Stochastic Dynamics in Biomolecular Systems

im Fachbereich Physik der Freien Universität Berlin
eingereichte Dissertation

zur Erlangung des akademischen Grades
eines Doktors der Naturwissenschaften (Dr. rer. nat.)

vorgelegt von

Yann von Hansen

Berlin, 2013

Erster Gutachter:	Prof. Dr. Roland R. Netz, Freie Universität Berlin
Zweiter Gutachter:	Prof. Dr. Igor M. Sokolov, Humboldt-Universität Berlin
Tag der Disputation:	20. Dezember 2013

CONTENTS

CHAPTER 1

INTRODUCTION AND OUTLINE

All science is either physics or stamp collecting.

Ernest Rutherford (1871-1937)

In biological and soft matter systems, the dynamics of atoms, molecules and supramolecular assemblies differ drastically from the motion of macroscopic objects we know from our everyday life. Unlike balls on a billiard table or satellites traveling through space—the motion of which is governed by simple physical laws and predetermined by a few initial conditions—the paths of microscopic objects embedded in a soft or fluid environment are characterized by rapid and seemingly random fluctuations. Indeed, the trajectories of objects at the nano- and microscale, similarly to stock prices displayed on financial charts, are characterized by a continuous, fractal-like up and down and knowledge of the past and present states provides, at best, limited information on the future evolution.

1.1 The Chaotic Brownian Dance

Although the random motion of charcoal powder on the surface of alcohol was already documented in 1784 by Jan Ingen-Housz [1], the discovery of the erratic and incessant motion of particles in a fluid is commonly attributed to the botanist Robert Brown, who studied pollen grains under a microscope in 1827 and observed the "vivid motion on immersion in water" of the micrometer-sized "particles contained in the grains of pollen" [2]. Brown excluded life as a driving factor [3], the underlying cause for the motion however remained elusive until the beginning of the twentieth century despite ongoing experimental studies revealing the influence of particle size, fluid viscosity, and temperature on the dynamics [4–6].

In 1905 and 1906, the explanation for the jittery motion observed by Ingen-Housz and Brown was proposed independently by William Sutherland [7], Albert Einstein [8–10], and Marian von Smoluchowski [11]: The continuous kicks of the surrounding solvent molecules—invisible even under the microscope—were identified as the cause for the thermal motion of suspended particles. It was Einstein's achievement to establish the link between two at that time disconnected phenomena: the erratic Brownian motion of individual particles and the thermodynamic laws of diffusion already known since the mid of the 19th century [12].

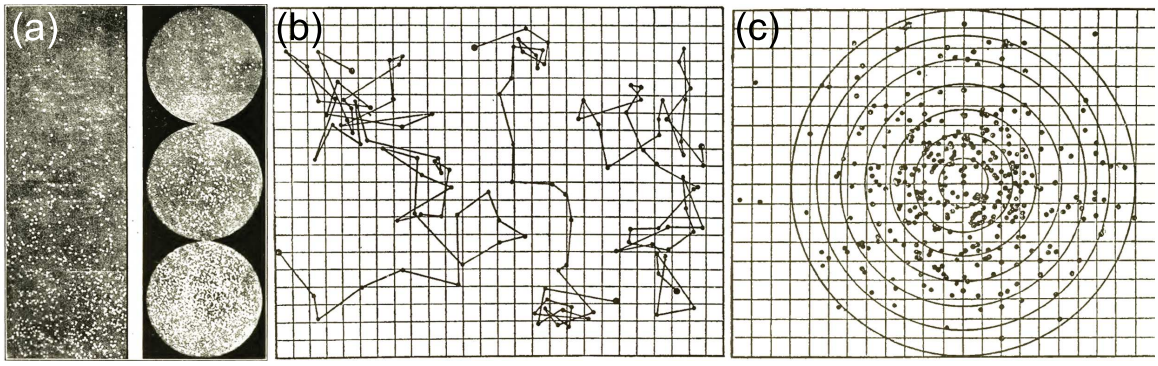

Figure 1.1:
Overview of Perrin's seminal work on Brownian motion: a) Equilibrium distribution of granules of gamboge and mastic at different heights above the object glass of the microscope, b) three sample trajectories of individual mastic granules in the lateral plane obtained from joining by straight lines the positions in consecutive configurations taken at 30 seconds intervals, and c) distribution of 365 lateral displacement vectors. All figures are adapted from Ref. [15].

Extensive subsequent experimental work by Jean-Baptiste Perrin and coworkers [13–15] allowed to verify the theoretical prediction $D = k_B T/\zeta_0$, nowadays called Einstein-relation, where D denotes the diffusion coefficient, k_B the Boltzmann constant, T the temperature (in Kelvin), and ζ_0 the particle's friction coefficient; the latter is $\zeta_0 = 6\pi\eta_0 a$ for a spherical particle of radius a in a solvent of shear viscosity η_0 according to Stokes [16] and thus independently accessible experimentally. Perrin chose several independent experimental pathways to measure the value of k_B and thereby to determine the Avogagro number $N_A = R_{id}/k_B$, the universal gas constant being denoted by R_{id}: (i) By evaluating the equilibrium distributions of granules at different heights above the object glass of the microscope as shown in Fig. 1.1a, (ii) from the mean square displacement (MSD) of the stochastic particle trajectories in the lateral plane, three samples being reproduced in Fig. 1.1b, (iii) by comparison of the time dependent distributions of hundreds of lateral displacement vectors (indicated in Fig. 1.1c) to the theoretical predictions, and (iv) by analyzing the Brownian rotation of granules. Perrin's precise estimate of the Avogadro number unambiguously confirmed the molecular nature of matter, an achievement for which he was awarded the Nobel prize in physics in 1926.

Interestingly, the mathematical concepts for the explanation of Brownian motion are already contained in Louis Bachelier's Ph.D. thesis *Théorie de la spéculation* from 1900 [17] dealing with the stochastic analysis of the French stock and option markets. Bachelier's work however remained unnoticed, until being rediscovered by Merton, Black and Scholes, who, based on similar arguments, established in 1973 the theoretical fundament for derivative pricing in mathematical finance [18, 19].

Einstein's and Smoluchowski's work, reviewed extensively in honor of the 100th anniversary of the discovery of Brownian motion [20–23], pointed out the need for a probabilistic description of the dynamics at the microscopic scale, where individual realizations are generally unreproducible and a statistical treatment therefore is inevitable. The early theoretical studies on Brownian motion can thus be considered as the fundament for the entire field of stochastic processes, which revolutionized (non-)equilibrium statistical physics and has since then contributed to the understanding of complex phenomena in biology, chemistry, nanotechnology,

ecology, economy, and other areas [22]. Over the years, two complementary ways of mathematically tackling stochastic dynamics have evolved:

- Individual trajectories, such as those in Fig. 1.1b, are described in terms of stochastic differential equations, first introduced by Langevin [24] and put on solid mathematical ground later by Itô [25, 26], Stratonovich [27], and others [28, 29]. The Langevin equation includes, in addition to the usual terms in Newton's equation of motion, a stochastic component reflecting the interactions with the noisy environment. Generalized Langevin equations for the dynamics of slow degrees of freedom in complex systems can be derived from the deterministic Liouville equations using the projector formalism [30–33]. Although exact analytical solutions are restricted to particular cases, the Langevin equation constitutes an intuitive form of accounting for the random aspects of the dynamics, and its numerical implementation is of wide practical relevance for computer simulations of stochastic systems [28].

- On the contrary, the time evolution of the trajectory ensemble as a whole, e.g., the displacement distribution in Fig. 1.1c, may be captured by partial differential equations, nowadays known as Fokker-Planck (FP) equations [34–36]. Early examples include Smoluchowski's generalized diffusion equation for the overdamped motion of a particle in an external potential [37]. Related approaches suitable to capture the stochastic dynamics within a finite number of states are known as master equations or Markov models [33, 38].

1.2 Stochastic Dynamics in Biological Systems

Why are stochastic processes essential to understand the dynamics of biological systems? Biological cells, the basic structural and functional units in all living organisms, are small entities with typical diameters on the order of $1 - 100$ μm, which contain many different components such as genetic material, organelles, the cytoskeleton and the cytosol [39]. The latter consists of a crowded, aqueous solution of various macromolecular assemblies and in particular proteins, which are involved in tasks as diverse as enzymatic activity, cell signaling, gene regulation, ligand binding, intracellular transport, or cell motility. On even smaller scales, the selective transport of molecules and ions through lipid membranes as well as folding and conformational changes of proteins are essential processes for proper cellular function. All the above mentioned processes take place on the micro- and nanometer scale and thus inevitably are subject to thermal fluctuations. Probabilistic rather than deterministic concepts are therefore required for a (quantitative) understanding of biological function at the cellular and molecular level [40, 41]. Physics at these scales is being probed experimentally and modeled theoretically as outlined in the following.

Due to recent advances in optics, fluorescence, micro-fluidics, and nanotechnology, a wide range of experimental techniques are nowadays available to sensitively probe the dynamics of biological cells and molecules. Fluorescent labels are used in combination with super-resolution microscopy to image and track specific components within living cells [42] and, on a smaller scale, to probe the dynamics of ligand-protein binding as well as in- and out-of-equilibrium dynamics of internal molecular coordinates by site-specific labeling of the molecules [43, 44]. In addition, single-molecule techniques based on atomic force microscopy or optical and magnetic tweezers reveal detailed spectroscopic information about individual molecules in equilibrium or under the influence of an external mechanical force or torque [45].

When it comes to specific biophysical systems, theoretical approaches nowadays often rely on computer simulations with various levels of resolution and complexity, which can provide microscopic details inaccessible experimentally. Moreover, thanks to increasing computational resources, simulation studies begin to reach time scales, which allow a direct comparison with experiments [46].

However, the fluctuating time series recorded in experiments and simulations are by themselves just as informative as the trajectories of Brownian particles depicted in Fig. 1.1b. Statistical analysis and in particular adapted theoretical models thus remain crucial to gain physical insight into cellular and molecular dynamics. In recent years, fundamental advances in non-equilibrium statistical physics [47, 48] and unified frameworks for single-molecule kinetics [49, 50] have helped to extract meaningful information from experimental data. To name a few explicit examples of successful theoretical approaches, the analysis of atomistic simulations based on a master equation approach [51] has helped to clarify the mechanisms and time scales of secondary structure formation in short peptides [52]. Markov models have revealed the complex folding and unfolding pathways of proteins [53, 54] and have established the relation between experimental observables and specific conformational changes of the molecules in simulations [55]. Furthermore, theoretical advances based on the Langevin equation have contributed to a broader understanding of the dynamics of semiflexible polymers in excellent agreement with experiments [56, 57], and the working principles of molecular motors, efficient molecular machines converting chemical energy into mechanical or electrical work, have been deciphered [41, 58].

Over a century after the discovery of Brownian motion, continuously refined theoretical instruments based on the groundbreaking work of Einstein and Smoluchowski play, more than ever, a fundamental role in contemporary biophysics research. In particular, dynamic processes with characteristics deviating strongly from the ordinary diffusion laws have attracted considerable interest during the last decades [59–62]. Although the present thesis mostly focuses on dynamics at the molecular scale, it is worth mentioning that similar concepts are also employed to model a variety of other complex phenomena: Examples range from gene regulation networks [63], biological evolution [64], and search strategies of living organisms [59, 65] to traffic jams on the cellular level as well as in the macroscopic world [20, 66].

1.3 Outline of This Work

As argued above, devising methods to reliably and efficiently extract the physically relevant information contained in stochastic signals constitutes a major challenge in theoretical biophysics research. The aims of the present thesis are twofold: (i) Based on data from atomistic simulations, we demonstrate how molecular mechanisms can be identified via a detailed trajectory analysis, and (ii) we establish refined stochastic models to quantitatively analyze and predict the statistical properties of fluctuating observables in biophysical simulations and experiments.

The Chapters 2 to 4 form the first part of the thesis and are based on the analysis of fluctuating time series from molecular dynamics (MD) simulations of aqueous systems. Among others, we employ a method relying on the calculation of mean first-passage times (MFPTs), which was first developed in Ref. [x] and which has since then successfully been applied in other contexts [viii][67]. The approach rests on mapping the dynamics on the FP equation, thereby disentangling free-energetic and friction contributions, which allows an interpretation of the kinetics in terms of an intuitive physical picture.

- Water is the most abundant liquid on earth and of enormous importance for life [68]. Yet, many of the fascinating aspects of water still remain unexplained [69]. In Chapter 2, the dynamics of individual water and solute molecules in bulk water are studied based on simulations run by Dr. Felix Sedlmeier. We resolve the anisotropic translational and rotational diffusive properties of water molecules and determine the diffusivity profile for the relative motion of a chosen pair of water molecules. The latter exhibits a pronounced drop within the first coordination shell, pointing towards major contributions of orthogonal degrees of freedom in hydrogen-bond formation and breakage kinetics.
- Next, we focus on the biologically more relevant problem of water near lipid membranes and investigate the dynamics of hydration water in the vicinity of lipid bilayers in Chapter 3 based on MD simulations run by Prof. Dr. Stephan Gekle. Our analysis reveals anomalous dynamics over extended time scales and a reversed diffusional anisotropy in the vicinity of the membrane compared to homogeneous surfaces, where the interfacial water mobilities are quantitatively described by boundary hydrodynamic theory.
- Numerous studies have shown that problems as complex as protein folding can equally be interpreted as a diffusive search through an effective, low-dimensional free energy landscape [70–75]. Chapter 4 is devoted to the conformational changes of a small alanine-based peptide in MD simulations run by Prof. Dr. Joachim Dzubiella and Dr. Immanuel Kalcher. We elucidate the influence of ionic co-solutes on the peptide kinetics by identifying ion-specific changes of both free energy and diffusivity, and relate the observed differences between sodium and potassium salts to particularly long-lived conformations involving the binding of single ions to the peptide.

In the second part of the thesis formed by the Chapters 5 to 8, we develop theoretical methods to quantitatively analyze and predict the spectral properties of equilibrium fluctuations in biophysical experiments and simulations.

- Single-molecule techniques [43–45] have revolutionized the experimental possibilities for studying microscopic kinetics in biological systems. In Chapter 5, we devise a method for the spectral analysis of dual trap optical tweezers, which are used to study individual molecules, e.g., nucleic acids or proteins [53, 76–78]. Our approach includes the theoretical modeling of the experimental signal processing and is based on the statistical properties of the recorded signals. In collaboration with our experimental colleagues Alexander Mehlich and Benjamin Pelz from the group of Prof. Dr. Matthias Rief, the accuracy of the Bayesian method is explicitly demonstrated. The comparison to experimental data also underlines the importance of hydrodynamic retardation effects in the fluid.
- We address a more fundamental problem in Chapter 6, namely the influence of nonlinearities in the equations of motion governing the stochastic, thermal motion of a system. For a one-dimensional system, an expansion of typical dynamic observables in powers of the thermal noise strength is derived and the findings are validated by comparison to numerical simulations. In addition, our approach sheds light on the limitations of the dynamic convolution theory (DCT) [ix] and of the widely employed signal analysis based on strictly linear models.
- Cytoskeletal semiflexible biopolymers such as actin and microtubules are involved in a variety of vital tasks ranging from maintaining the cell shape to cellular motion, intracellular transport, and cell division [39, 40]. In Chapter 7, the thermal motion of single

semiflexible polymers is investigated by means of dynamic mean-field theory and Brownian dynamics simulations. We resolve the influence of the mechanical properties of the filament as well as of hydrodynamic screening caused by nearby surfaces on various dynamic observables and compare our findings to experimental results on f-actin [79].

- Biological materials such as the cytoskeleton are characterized by remarkable mechanical properties, which are only partially understood [80]. Given the complexity and size of these structures, explicit simulations of the overall dynamics are currently not feasible. To study the viscoelasticity of extended polymeric networks, we therefore in Chapter 8 generalize the DCT from Ref. [ix]. Using our approach, the micro- and macrorheological properties of crosslinked networks, e.g., the shear or compression response, are readily computed given the linear response properties of the filaments and the network structure. We in particular focus on the influence of orientational degrees of freedom at the network nodes and the flexibility of crosslinkers, which are known to be crucial components in cytoskeletal network structures [81].

The overall results of this thesis are briefly summarized in Chapter 9, where we also discuss possible future lines of work. Longer calculations, complementary material and technical details are found in the Appendices A-G.

CHAPTER 2

DYNAMICS OF INDIVIDUAL MOLECULES IN BULK WATER

Bibliographic information: Parts of this chapter and of Appendix C have previously been published. Reprinted with permission from Ref. [v].

The unique properties of liquid water are relevant for a broad range of processes in biology, chemistry, and physics, as well as for technological applications [69]. A prominent goal of recent research has been to relate macroscopic properties of water, in particular its notable anomalies and singularities, to the microscopic structure and thus to the hydrogen (H) bonding pattern between individual water molecules [82]. This goal has only partly been achieved. Indeed, even for the most elementary kinetic process of breaking a single H-bond between two water molecules that are embedded in the bulk liquid matrix, various viewpoints exist: In an early application of transition path sampling, it was found that in roughly half of the cases of an H-bond breaking event a new bond forms right afterwards [83], supporting Stillinger's switching-of-allegiance description of the local water dynamics [82]. In later simulation works, the water reorientation during this H-bond switching was shown to occur quite abruptly [84], in line with the pronounced rotational-translational motion coupling of individual water molecules [85]. The non-exponential H-bond relaxation was shown to be due to a coupling of bond forming/breaking dynamics and the relative diffusion of water pairs [86]. It is however not related to the local environment of H-bond forming water molecules [87], which is surprising in light of the above mentioned H-bond switching scenario. Clearly, the H-bond dynamics is intimately related to the kinetics of other processes, e.g., protein folding [88] or solute dissociation [89], so clarifying the kinetics of the binding and unbinding of water molecules is without doubt of fundamental importance.

In this chapter, we analyze the stochastic trajectories of individual molecules in bulk water based on molecular dynamics (MD) simulations, which are shortly described in Sec. 2.1. Dynamics of individual molecules are considered in Sec. 2.2, and the relative dynamics of pairs of water molecules are studied in Sec. 2.3. Our main findings are summarized in Sec. 2.4, while technical aspects and longer calculations are covered in the Appendices B and C.

2.1 Molecular Dynamics Simulations

MD simulations of the SPC/E [90] water model are performed with the GROMACS simulation package [91, 92]. Systems consisting of 895 and 2180 water molecules are simulated in a cubic box with periodic boundary conditions. At $T = 300$ K the box sizes are roughly $3.0 \times 3.0 \times 3.0\,\mathrm{nm}^3$ and $4.0 \times 4.0 \times 4.0\,\mathrm{nm}^3$, respectively. We perform simulations at temperatures $T = 280$, 300, 320, 340, and 360 K for the small system and at $T = 300$ K for the large system, both at a pressure of $P = 1$ bar. We also perform simulations at $T = 300$ K of bulk water with one additional solute molecule: a sodium, caesium, chloride or iodide ion or a methane molecule. The systems are equilibrated first in an NVT ensemble (constant particle number, volume and temperature) for 50 ps and then in an NPT ensemble (constant particle number, pressure and temperature) for 100 ps. Production runs are performed subsequently for 10 ns and configurations are saved each 10 fs for the small system and each 100 fs for the large system. In addition, we also perform one 1 ns simulation of the small system, where configurations are saved every 2 fs, i.e., after each simulation time step. A Berendsen weak coupling thermostat and barostat [93] with a relaxation time of 1 ps is used for temperature and pressure control. All non-bonded interactions are cut off at a radius of 0.9 nm. Long-range electrostatic interactions are treated by the particle mesh Ewald method [94, 95] with tinfoil boundary conditions. An analytical long-range correction for the Lennard-Jones interaction is applied to energy and pressure.

The MD simulations analyzed in this chapter have been performed by Dr. Felix Sedlmeier from the Technical University of Munich.

2.2 Dynamics of Single Water and Solute Molecules

Due to translational and rotational invariance of bulk water, individual molecules do not have a preferential position or orientation in the simulation box or, in other words, the associated free energy landscape is unstructured and flat. Under these circumstances, the analysis of the molecular trajectories in terms of the mean square displacement (MSD) is meaningful in the sense that the long-time MSDs reveal the diffusion coefficients of individual molecules. Overall water and solute diffusion coefficients are resolved in Sec. 2.2.1, while we focus on the anisotropy of translational and orientational water dynamics in Sec. 2.2.2.

2.2.1 Overall translational diffusion

In this section, we disregard the internal molecular water structure and quantify the dynamics in terms of the fluctuating position trajectories $\boldsymbol{r}_\mathrm{O}(t)$ of the molecules' oxygen (O) atoms. The motion of the water molecules is characterized by the time-dependent MSD

$$\langle (\Delta \boldsymbol{r}_\mathrm{O}(t))^2 \rangle \equiv \langle (\boldsymbol{r}_\mathrm{O}(t' + t) - \boldsymbol{r}_\mathrm{O}(t'))^2 \rangle, \tag{2.1}$$

where $\langle \ldots \rangle$ denotes the thermal expectation value, which is calculated by averaging over both all SPC/E water molecules in the simulation as well as the reference time t'. For temperatures T ranging from 280 to 360 K, water MSDs are shown in Fig. 2.1: While the MSDs display a quadratic dependence on time characteristic for ballistic motion on the femtosecond time scale, a smooth crossover to a diffusive scaling is observed for $t \sim 10$ ps. As for the case of the

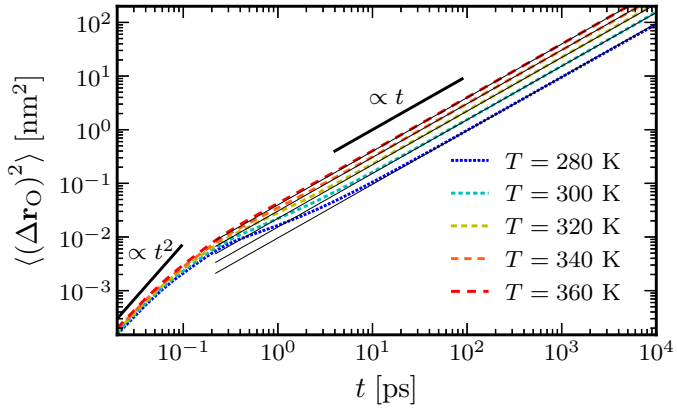

Figure 2.1:
Overall MSDs of SPC/E water molecules (Eq. 2.1) in bulk water at various temperatures T (*dashed colored lines*). Linear fits to the data are displayed as *thin black lines*, resulting diffusion coefficients (Eq. 2.2) are given in Tab. 2.1.

colloids in Perrin's experiment (cf. Sec. 1.1), the diffusion constant of a single water molecule is by definition obtained from the long-time behavior of the MSD

$$D_{H_2O} \equiv \lim_{t\to\infty} \frac{\langle(\Delta \boldsymbol{r}_O(t))^2\rangle}{6t}. \tag{2.2}$$

Since the MSDs computed from MD simulations are subject to statistical noise on time scales beyond ~ 1 ns, we decide to fit the MSD data in the time range 10 ps $< t < 10^3$ ps only. The linear fits are shown as thin black lines in Fig. 2.1 and the resulting SPC/E diffusion coefficients are given in Tab. 2.1, where they are compared to results from experiments and other simulation studies. Fig. 2.2 reveals an Arrhenius-like temperature dependence of the SPC/E diffusion coefficients within the investigated range of temperatures in agreement with experiment [97].

For reference, we also resolve the diffusion coefficients of various isotropic solutes in bulk SPC/E water at a temperature of $T = 300$ K. Similarly as before, the diffusion coefficients are obtained from linear fits to the long-time MSDs shown in Fig. 2.3, the corresponding values are given in Tab. 2.2. We note that the diffusion coefficients of the charged solutes are smaller than the water diffusion coefficient implying a higher hydrodynamic radius, although the bare ionic radii are smaller than the radius of a water molecule. The underlying reasons for this at first sight contradictory observation are theoretically well understood [101] and partially in accordance with the simple picture that ions do not diffuse as isolated entities but together with the tightly bound water molecules of the first hydration shell [101].

2.2.2 Anisotropy of translational and rotational water diffusion

Realizing that water molecules, in contrast to the isotropic solutes considered above, are characterized by an internal structure and thus by an unambiguous orientation, we in the following take a closer look at the SPC/E water dynamics and resolve all translational and rotational entries of the underlying grand-diffusivity matrix. For this purpose, we define an internal coordinate frame $(\hat{\boldsymbol{e}}_x, \hat{\boldsymbol{e}}_y, \hat{\boldsymbol{e}}_z)$ as indicated in Fig. 2.4: The z-axis is selected to point in direction of the

T [K]	D_{H_2O} [nm^2/ns]	
	Simulations (SPC/E)	Experiments
278	—	1.313 [96]
280	1.60 ± 0.02	1.44 [97]
298	2.75 [98], 2.70 [99]	2.22 – 2.61 [96, 97, 100]
300	2.55 ± 0.05	—
318	—	3.575 [96]
320	3.70 ± 0.05	—
340	5.08 ± 0.05	—
360	6.60 ± 0.05	—

Table 2.1:
Temperature dependence of the diffusion coefficient D_{H_2O} of individual water molecules in bulk water. Simulation results for the SPC/E water model obtained from Eq. 2.2 are compared to results from previous simulation studies and to experimental findings, both with references in square brackets.

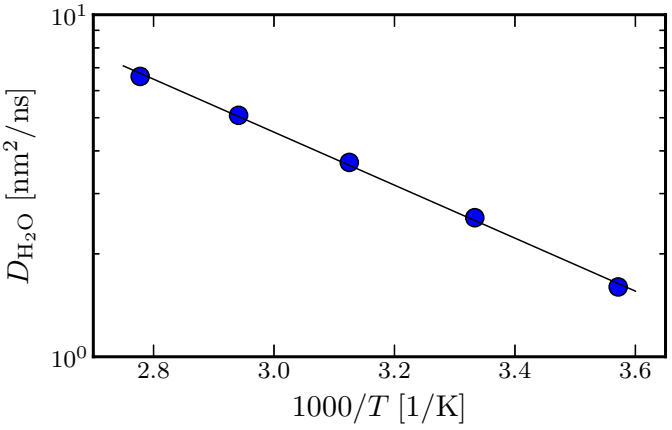

Figure 2.2:
Arrhenius plot of the SPC/E water diffusion coefficient: *Blue circles* denote results from Tab. 2.1, the *black line*, $D_{H_2O}(T) \approx 956 \exp(-1783.6\,\mathrm{K}/T)$ nm^2/ns, reveals the Arrhenius-like dependence of the diffusion coefficients in the studied temperature range.

Solute	D_{sol} [nm^2/ns]
CH_4	≈ 2.2
Na^+	≈ 1.1
Cs^+	≈ 1.9
Cl^-	≈ 1.6
I^-	≈ 1.6

Table 2.2:
Translational diffusion coefficients of isotropic solutes at $T = 300$ K in bulk SPC/E water obtained from linear fits to the long-time MSDs in Fig. 2.3.

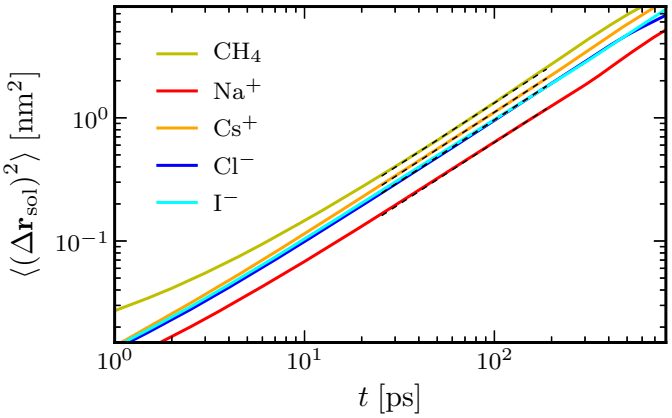

Figure 2.3:
MSDs of isotropic solutes in bulk SPC/E water at $T = 300$ K (*colored lines*). The *dashed black lines* denote linear fits used to determine the solute diffusion coefficients D_{sol} given in Tab. 2.2.

water dipole vector and the x-axis to be parallel to the vector connecting the two H-atoms. The origin of the internal coordinate frame is chosen so that the SPC/E molecule is mirror-symmetric to the $x = 0$ and $y = 0$ planes and is located at a distance δz above the position of the oxygen atom. In the following, the distance δz is varied to study the effect of the position of the internal coordinate frame on the resulting dynamics.

Clearly, since the molecules do not have a preferential orientation in the simulation box, the MSDs of the motion along the lab coordinate axis are not suited to reveal a possible molecular anisotropy. As an intuitive analogue, one may think of a diffusing ellipsoidal colloid, which is characterized by three in general distinct diffusion coefficients [102, 103]. Thermal averages of the colloid's motion in the lab coordinate frame, however, do not reflect this anisotropy since the colloid reorients over time and motion along all internal axes thus contributes equally to the lab frame observables.

In order to disentangle the contributions of the dynamics along the internal axes, we define internal coordinates and angles

$$r_\alpha(t) \equiv \int_{-\infty}^{t} \mathrm{d}t'\, v_\alpha(t'), \qquad \varphi_\alpha(t) \equiv \int_{-\infty}^{t} \mathrm{d}t'\, \omega_\alpha(t'), \qquad \alpha = x, y, z, \tag{2.3}$$

where v_α and ω_α denote the translational and angular velocities along/around the internal axis α. Temporal increments of these variables are given by

$$\Delta r_\alpha(t) \equiv r_\alpha(t) - r_\alpha(0) = \textstyle\int_0^t \mathrm{d}t'\, v_\alpha(t') \approx \sum_{i=1}^{m} \delta r_\alpha(i\,\delta t), \qquad \alpha = x, y, z, \tag{2.4}$$

$$\Delta \varphi_\alpha(t) \equiv \varphi_\alpha(t) - \varphi_\alpha(0) = \textstyle\int_0^t \mathrm{d}t'\, \omega_\alpha(t') \approx \sum_{i=1}^{m} \delta \varphi_\alpha(i\,\delta t), \qquad \alpha = x, y, z, \tag{2.5}$$

where $m \equiv t/\delta t$ and δt denotes the time resolution of the simulation output, and where the reference time is set to 0 for simplicity. In the last step, the integrals over the velocities are

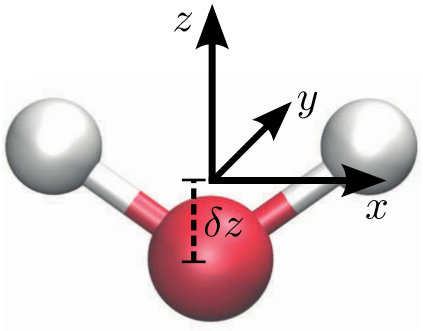

Figure 2.4:
Internal coordinate frame used to reveal the anisotropy in the translational and rotational dynamics of water molecules in MD simulations: The z-direction points in the direction of the water dipole and the x-axis is chosen parallel to the vector connecting the two H-atoms. The origin of the coordinate frame is located within the two symmetry planes of the molecule and at a distance δz above the water's oxygen atom.

approximated by sums over the (small) increments δr_α and $\delta\varphi_\alpha$ between subsequent configurations

$$\delta r_\alpha(i\,\delta t) \equiv \frac{1}{2}\Big(\boldsymbol{r}\big(i\,\delta t\big) - \boldsymbol{r}\big((i-1)\,\delta t\big)\Big)\cdot\Big(\hat{\boldsymbol{e}}_\alpha\big((i-1)\,\delta t\big) + \hat{\boldsymbol{e}}_\alpha\big(i\,\delta t\big)\Big), \tag{2.6}$$

$$\delta\varphi_\alpha(i\,\delta t) \equiv \frac{1}{2}\sum_{\beta,\gamma}\varepsilon_{\alpha\beta\gamma}\,\hat{\boldsymbol{e}}_\beta\big(i\,\delta t\big)\cdot\hat{\boldsymbol{e}}_\gamma\big((i-1)\,\delta t\big), \tag{2.7}$$

where $\boldsymbol{r} = \boldsymbol{r}_\mathrm{O} + \delta z\,\hat{\boldsymbol{e}}_\mathrm{z}$ is the position of the origin of the molecule's internal coordinate frame, the $\hat{\boldsymbol{e}}_\alpha$ are unit vectors in the directions of the internal coordinate axis and $\varepsilon_{\alpha\beta\gamma}$ denotes the Levi-Civita symbol

$$\varepsilon_{\alpha\beta\gamma} \equiv \begin{cases} 1 & \text{if } (\alpha,\beta,\gamma) \text{ is an even permutation of } (x,y,z),\\ -1 & \text{if } (\alpha,\beta,\gamma) \text{ is an odd permutation of } (x,y,z),\\ 0 & \text{else.}\end{cases} \tag{2.8}$$

Note that the definition of the internal coordinates in Eq. 2.3 based on the unambiguous translational and angular velocities in the comoving local coordinate frame is essential to obtain trajectories, from which the various diffusion coefficients can be disentangled. In particular, our definition of the internal angles in Eq. 2.3 directly reveals the rotation around a single axis in contrast to the definition in Ref. [104], where rotations around two axes mix. In practice, the MSDs are calculated from the Eqs. 2.6 and 2.7, where the time resolution δt needs to be selected small enough, i.e., so small that the resulting MSDs do not depend on the particular choice of δt. Here, we simply select a time resolution of $\delta t = 2$ fs, which corresponds to the integration time step in the MD simulation.

For a non-orthotropic rigid body, the overdamped translational and rotational motions are generally coupled [102, 103], see Appendix B for an explicit derivation. However, given the

internal coordinate frame of the SPC/E molecule in Fig. 2.4 and based on symmetry arguments detailed in Appendix B.1, we expect a grand-diffusivity matrix of the form

$$\boldsymbol{\mathcal{D}} = \begin{pmatrix} D_x & 0 & 0 & 0 & D_{xy}^{\text{trans, rot}} & 0 \\ 0 & D_y & 0 & D_{yx}^{\text{trans, rot}} & 0 & 0 \\ 0 & 0 & D_z & 0 & 0 & 0 \\ 0 & D_{xy}^{\text{rot, trans}} & 0 & D_x^{\text{rot}} & 0 & 0 \\ D_{yx}^{\text{rot, trans}} & 0 & 0 & 0 & D_y^{\text{rot}} & 0 \\ 0 & 0 & 0 & 0 & 0 & D_z^{\text{rot}} \end{pmatrix}, \tag{2.9}$$

where the six diagonal elements are the translational and rotational diffusion coefficients and where the four off-diagonal elements reflect the correlations in the translational and rotational motion.

Similarly as before, the translational and rotational diffusion coefficients are obtained from the long-time dependence of the corresponding MSDs

$$D_\alpha \equiv \lim_{t\to\infty} \frac{\langle (\Delta r_\alpha(t))^2 \rangle}{2t}, \qquad D_\alpha^{\text{rot}} \equiv \lim_{t\to\infty} \frac{\langle (\Delta \varphi_\alpha(t))^2 \rangle}{2t}, \qquad \alpha = x, y, z, \tag{2.10}$$

and the off-diagonal elements in Eq. 2.9 are deduced from the cross-correlations of the temporal increments in the local variables

$$D_{\alpha\beta}^{\text{trans, rot}} = D_{\beta\alpha}^{\text{rot, trans}} \equiv \lim_{t\to\infty} \frac{\langle \Delta r_\alpha(t) \Delta \varphi_\beta(t) \rangle}{2t}, \qquad \alpha, \beta = x, y, z. \tag{2.11}$$

For $\delta z = 0$, i.e., for a local coordinate frame centered in the oxygen atom, the resulting translational MSDs $\langle (\Delta r_\alpha)^2 \rangle$ along the internal coordinates are shown in Fig. 2.5a: The curves are slightly different already in the ballistic regime, since the center of mass is located at a distance $\delta z \approx 0.0064$ nm from the oxygen atom and inertial rotational motion around x and y therefore mixes in. The colored curves clearly separate on time scales around ~ 0.1 ps, with the motion along y being clearly faster than that along x or z. The translational MSDs enter the diffusive regime around ~ 10 ps and the sum of the three translational MSDs (dash-dotted yellow line) as expected approximately coincides with the overall MSD from Fig. 2.1, which for reference is shown as larger gray line in Fig. 2.5a. Thinner dashed black lines denote linear fits to the data used to determine the corresponding diffusion coefficients.

The angular MSDs $\langle (\Delta \varphi_\alpha)^2 \rangle$ displayed in Fig. 2.5b differ from each other in the ballistic regime due to the different moments of inertia; here, the rotational motion around x is enhanced compared to that around z and y. The orientational MSDs are characterized by a pronounced plateau at times around ~ 30 fs attributed to the fast librational motion in the H-bonded water network [104]; subsequently, the curves cross over to the linear regime on the picosecond time scale. Note that the curves for x and z intersect so that diffusive rotational motion around z is faster than the one around x.

The two non-vanishing cross-correlations $\langle \Delta r_x \Delta \varphi_y \rangle$ and $\langle \Delta r_y \Delta \varphi_x \rangle$ are shown in Fig. 2.5c: The cross-correlations of translations along y and rotations around x (blue curve) take positive values over the entire time range resolved and enter the diffusive regime for $t \gtrsim 10$ ps. The center of mass of the molecule being located at $\delta z \approx 0.0064$ nm, the cross-correlations of translations along x and rotations around y (red curve) are negative (indicated by a dashed line) in the inertial time regime but cross over to positive values for $t \gtrsim 1$ ps. Despite an

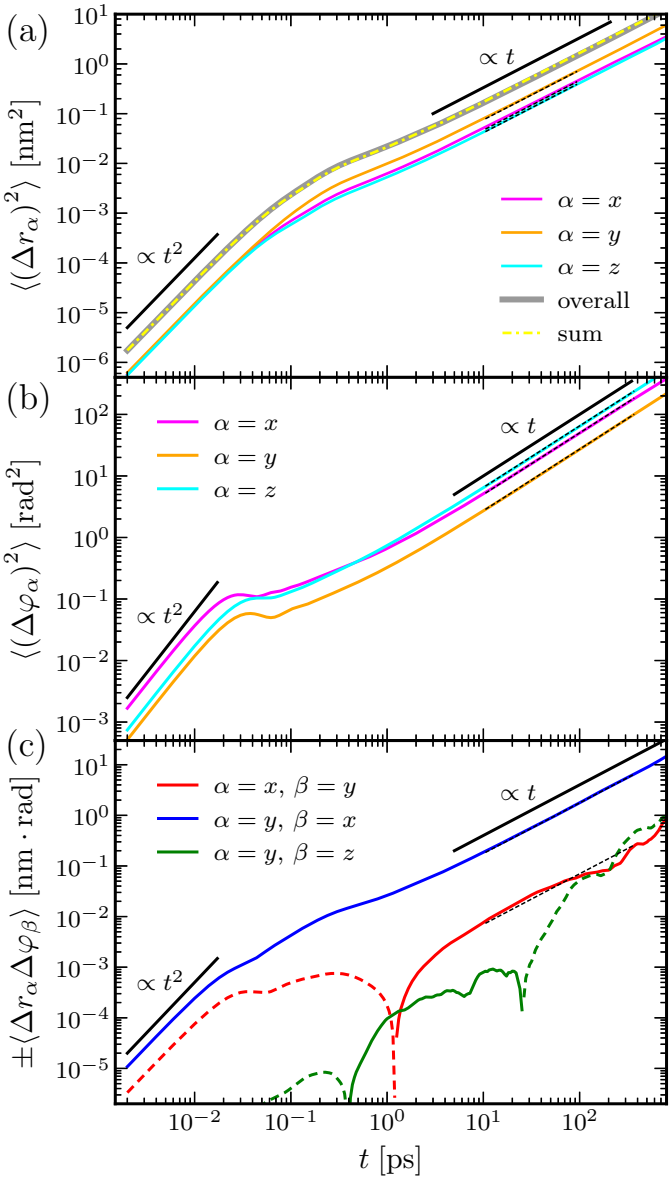

Figure 2.5:
Anisotropic dynamics of single SPC/E water molecules in bulk water at $T = 300$ K resolved via Eqs. 2.4 and 2.5 from MD simulation data for $\delta z = 0$: a) Translational MSDs, b) rotational MSDs, and c) cross-correlations in the temporal increments of positional and angular variables. Negative values of the cross-correlations are indicated by *dashed colored lines*. In all panels, *thinner dashed black lines* denote linear fits to the data in the time range shown.

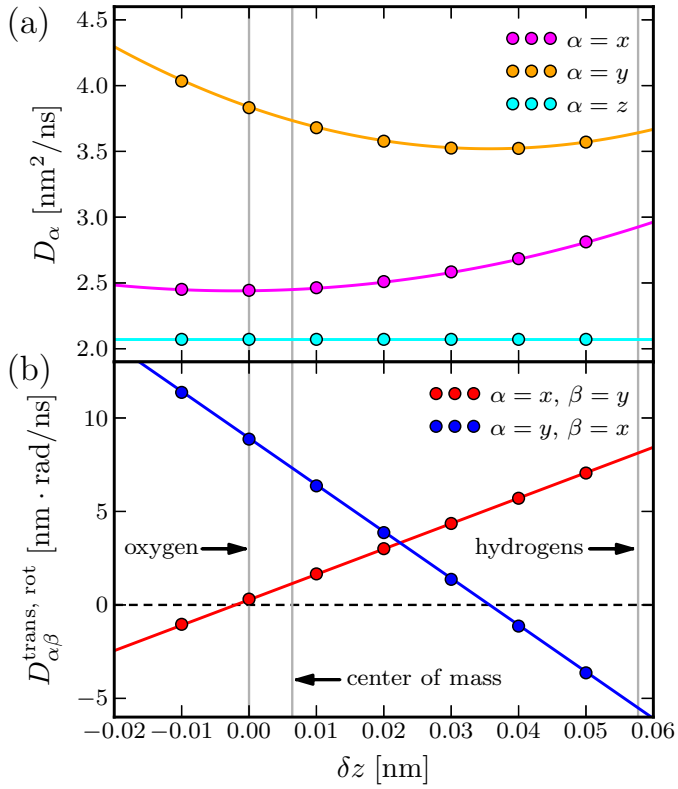

Figure 2.6:
Influence of the distance δz between the origin of the internal coordinate frame and the water's oxygen (Fig. 2.4) on the diffusion coefficients: a) Translational diffusion coefficients (Eq. 2.10), b) off-diagonal elements of the grand-diffusivity matrix (Eq. 2.11) reflecting correlations of the translations along axis α and rotations around axis β. *Symbols* denote data points calculated from MD data (Fig. 2.5) according to the Eqs. 2.10 and 2.11, *lines* denote quadratic and linear fits (Eqs. 2.12 and 2.13).

appreciable statistical uncertainty of the cross-correlations $\langle \Delta r_x \Delta \varphi_y \rangle$ in the diffusive regime, these are clearly suppressed by a factor ~ 25 compared to $\langle \Delta r_y \Delta \varphi_x \rangle$ as is seen from Fig. 2.5c. As a measure for the statistical uncertainty in the data, we show an estimate for one of the vanishing cross-correlations, $\langle \Delta r_y \Delta \varphi_z \rangle$, as a green line in Fig. 2.5c.

To investigate the influence of the distance δz between the origin of the internal coordinate frame and the oxygen atom (Fig. 2.4), we repeat the same kind of analysis for various values of δz and determine the entries of the grand-diffusivity matrix (Eq. 2.9) via Eqs. 2.10 and 2.11. The coefficients resulting from the MD trajectory analysis are shown as colored circles in Fig. 2.6: As expected from symmetry arguments (Appendix B.1), the translational diffusion coefficients in Fig. 2.6a scale as

$$D_x = D_x^0 + D_y^{\text{rot}}(\delta z - \delta z')^2, \qquad D_y = D_y^0 + D_x^{\text{rot}}(\delta z - \delta z'')^2, \qquad D_z = D_z^0, \tag{2.12}$$

where $\delta z'$ and $\delta z''$ are a priori unknown, while the off-diagonal elements of the grand-diffusivity matrix linearly depend on δz

$$D_{xy}^{\text{trans, rot}} = D_{yx}^{\text{rot, trans}} = D_y^{\text{rot}}(\delta z - \delta z'), \qquad D_{yx}^{\text{trans, rot}} = D_{xy}^{\text{rot, trans}} = -D_x^{\text{rot}}(\delta z - \delta z''). \tag{2.13}$$

Water axis α	D_α^0 [nm^2/ns]	D_α^{rot} [rad^2/ns]
x	≈ 2.4	≈ 250
y	≈ 3.5	≈ 135
z	≈ 2.1	≈ 325

Table 2.3:
Minimal translational and rotational SPC/E water diffusion coefficients along/around the internal axes at $T = 300$ K. Based on the above coefficients, the grand-diffusivity matrix (Eq. 2.9) is calculated for arbitrary δz using the Eqs. 2.12 and 2.13 and the roots of the colored lines in Fig. 2.6b: $\delta z' \approx -0.002$nm and $\delta z'' \approx 0.035$nm.

The rotational diffusion coefficients D_α^{rot}, which result from the angular MSDs in Fig. 2.5b, do not depend on δz (Eqs. 2.7 and B.19) and are therefore not shown. Fits of the Eqs. 2.12 and 2.13 to the MD diffusion coefficients are shown as colored lines in Fig. 2.6 and yield the minimal diffusion coefficients D_x^0, D_y^0, D_z^0 as well as the values for $\delta z'$ and $\delta z''$. The resulting values for the minimal translational and the rotational diffusion coefficients along/around the three internal axes are given in Tab. 2.3.

Note that the position $\delta z' \approx -0.002$ nm, for which translations along x and rotations around y are uncorrelated, does *not* coincide with the position $\delta z'' \approx 0.035$ nm, for which translations along y and rotations around x are uncorrelated. In other words, no position of the internal coordinate frame exists, for which the grand-diffusivity matrix is completely diagonal and diffusional translations along and rotations about all axes are completely independent.

Summarizing, we find that both the translational and orientational diffusive motions of individual water molecules in bulk water are characterized by a pronounced anisotropy: The translational diffusion coefficients differ by factors of up to ~ 1.8 if the origin of the internal coordinate frame in Fig. 2.4 lies between oxygen and hydrogen atoms ($0 \leq \delta z \lesssim 0.06$ nm), and the rotational diffusion coefficients differ by factors of up to ~ 2.4. The ordering of the rotational diffusion coefficients, $D_z^{\mathrm{rot}} > D_x^{\mathrm{rot}} > D_y^{\mathrm{rot}}$, is exactly opposite of the translational ones, $D_y^0 > D_x^0 > D_z^0$, but unlike (orthotropic) ellipsoidal bodies [102, 103] no internal coordinate frame can be found for which all cross-correlations in the translations and rotations of the SPC/E molecule vanish.

This complex anisotropic diffusion behavior of individual water molecules is yet another remarkable property of water and presumably a consequence of the intricate dynamics of H-bonds between neighboring water molecules in the liquid matrix. To gain further insight into the process of H-bond formation and breakage in water, we in the following focus on the relative dynamics of a selected pair of water molecules.

2.3 Relative Dynamics of Pairs of Water Molecules

For the stochastic analysis of the relative dynamics of pairs of water molecules, we adopt the concept of diffusion along a reaction coordinate (RC), which has been fruitful for exploring the underlying mechanisms of high-dimensional dynamics as in the case of protein folding, for which various approaches to identify suitable RCs [105–107] and to locate or characterize transition states [108, 109] have been developed. Here, we select the separation between two oxygen atoms of the water molecules as the naive RC and show that a consistent description of

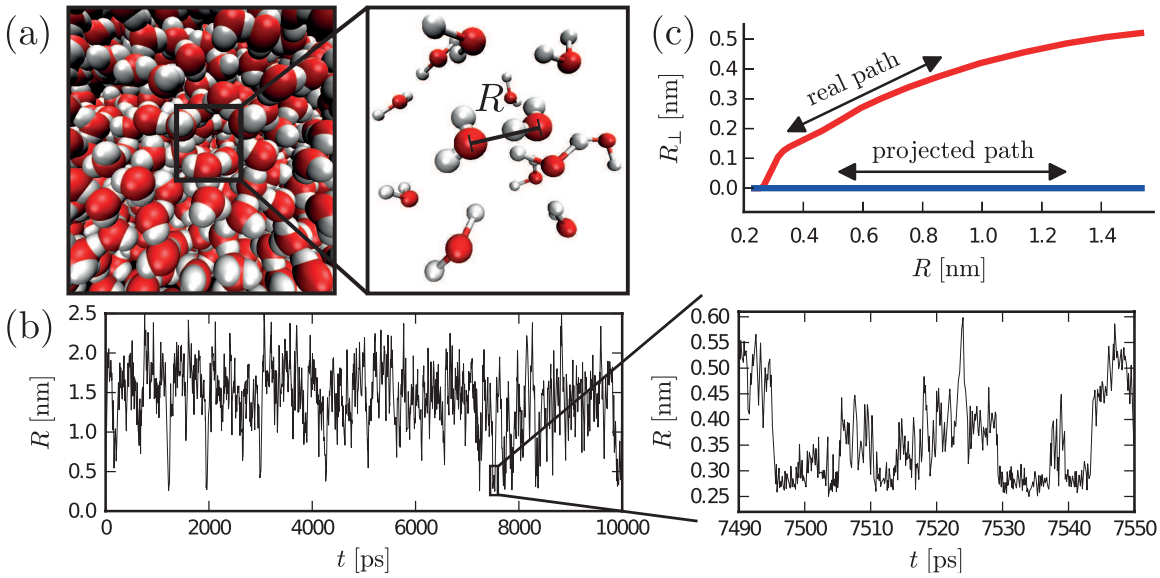

Figure 2.7:
a) Snapshot of a bulk-water MD simulation visualized via VMD [110], a simulation movie is included as supplementary material [111]. The radial separation between the oxygen atoms is denoted by R in the enlarged section. b) Typical time series $R(t)$ at $T = 300$ K, the magnification reveals fluctuations on the sub-picosecond time scale. c) Illustrative reaction path involving a component $R_\perp$ orthogonal to R, cf. Sec. 2.3.7.

the dynamics along the separation coordinate can be obtained. In fact, our stochastic analysis in terms of the Fokker-Planck (FP) equation with coordinate-dependent free energy and diffusivity allows us to quantify to which extent degrees of freedom that are orthogonal to our selected RC are involved in the reaction. As a main result, we find the relative translational friction in the first coordination shell to be more than six-fold increased compared to bulk water. Application of transition rate theory without taking this local friction change into account underestimates typical bond-breakage times by a factor of two.

Our analysis is based on the trajectories of the separation R between the oxygen atoms of all mutual water pairs in the simulation box, see Fig. 2.7a-b for a snapshot and an example trajectory. A corresponding movie, which visualizes the relative dynamics of a selected water pair in the MD simulation, has been created with VMD [110] and is included as supplementary material [111].

A brief review of the FP equation, on which our analysis is based, is given in Sec. 2.3.1. The trajectory analysis is described in Sec. 2.3.2 and results are presented in the Secs. 2.3.3 and 2.3.4. Various aspects of the results are discussed in the Secs. 2.3.5-2.3.7.

2.3.1 Fokker-Planck equation for radial dynamics

In the overdamped limit, the FP equation

$$\frac{\partial}{\partial t} P_{3D}(\boldsymbol{R}, t) = -\nabla_{\boldsymbol{R}} \cdot \boldsymbol{J}(\boldsymbol{R}), \tag{2.14}$$

describes the time evolution of the probability density function (PDF) P_{3D} of observing a (three dimensional) separation vector $\boldsymbol{R}$ between the two water molecules at time t, where the probability flux density

$$\boldsymbol{J}(\boldsymbol{R}) = -P_{3D}(\boldsymbol{R},t)\overleftrightarrow{\boldsymbol{\mu}}_{3D}(\boldsymbol{R})\cdot\nabla_{\boldsymbol{R}}U(\boldsymbol{R}) - \overleftrightarrow{\boldsymbol{D}}_{3D}(\boldsymbol{R})\cdot\nabla_{\boldsymbol{R}}P_{3D}(\boldsymbol{R},t),$$

has two contributions: (i) the overdamped motion due to an (effective) potential U and (ii) diffusion with a (possibly) position dependent diffusion tensor $\overleftrightarrow{\boldsymbol{D}}_{3D}$. Using the Einstein relation $\overleftrightarrow{\boldsymbol{D}}_{3D} = k_B T\overleftrightarrow{\boldsymbol{\mu}}_{3D}$ linking mobility and diffusivity via the thermal energy $k_B T$, Eq. 2.14 can be rewritten as

$$\frac{\partial}{\partial t}P_{3D}(\boldsymbol{R},t) = \nabla_{\boldsymbol{R}}\cdot\left(\mathrm{e}^{-U(\boldsymbol{R})/(k_B T)}\,\overleftrightarrow{\boldsymbol{D}}_{3D}(\boldsymbol{R})\cdot\nabla_{\boldsymbol{R}}\left(\mathrm{e}^{U(\boldsymbol{R})/(k_B T)}\,P_{3D}(\boldsymbol{R},t)\right)\right). \tag{2.15}$$

For the relative dynamics of two water molecules along their radial distance $R \equiv |\boldsymbol{R}|$, the diffusion tensor

$$\overleftrightarrow{\boldsymbol{D}}_{3D} = \begin{pmatrix} D_R & 0 & 0 \\ 0 & D_\Theta & 0 \\ 0 & 0 & D_\Phi \end{pmatrix}, \tag{2.16}$$

is diagonal when introducing spherical coordinates (R,Θ,Φ). Since internal orientational coordinates of the molecules are neglected and due to symmetry, the effective inter-molecular potential U depends on R only. The angular coordinates Θ and Φ can thus be integrated out [112], and the time evolution of the radial PDF

$$P(R,t) \equiv \int_0^{2\pi}\mathrm{d}\Phi\int_0^{\pi}\mathrm{d}\Theta\,\sin\Theta\,R^2\,P_{3D}(R,\Theta,\Phi,t), \tag{2.17}$$

specifying the probability of finding a radial distance R at time t, is then described by the simpler equation

$$\frac{\partial}{\partial t}P(R,t) = \frac{\partial}{\partial R}\left(R^2\mathrm{e}^{-U(R)/(k_B T)}\,D_R(R)\frac{\partial}{\partial R}\left(\mathrm{e}^{U(R)/(k_B T)}\,\frac{P(R)}{R^2}\right)\right), \tag{2.18}$$

where the pair radial diffusivity D_R may depend on R. It is useful to absorb the factors R^2 in Eq. 2.18 by defining a free energy $F \equiv U - 2k_B T\log(R) + \text{const.}$ [112] to recover the usual form of the one-dimensional FP equation [36, 38]

$$\frac{\partial}{\partial t}P(R,t) = \frac{\partial}{\partial R}\left(D_R(R)\mathrm{e}^{-F(R)//(k_B T)}\,\frac{\partial}{\partial R}\left(\mathrm{e}^{F(R)/(k_B T)}\,P(R,t)\right)\right). \tag{2.19}$$

The free energy $F(R) = -k_B T\log\langle P(R)\rangle + \text{const.}$ is obtained by Boltzmann inversion of the equilibrium probability $\langle P(R)\rangle$. Determining $D_R(R)$ is more subtle: Different procedures have been proposed in the context of protein folding [113–115][x] or interfacial water diffusion [116–119][viii]. Here, we obtain $D_R(R)$ directly from measured mean first-passage times (MFPTs): For diffusive dynamics described by Eq. 2.19, the MFPT τ_{fp} of first reaching a target separation R_t when starting off from R is given by [120]

$$\tau_{fp}(R,R_t) = \int_R^{R_t}\mathrm{d}R'\,\frac{\mathrm{e}^{F(R')/(k_B T)}}{D_R(R')}\int_{R_{min}}^{R'}\mathrm{d}R''\,\mathrm{e}^{-F(R'')/(k_B T)}, \tag{2.20}$$

assuming a reflective (zero-flux) boundary condition at R_{min} and $R_{\mathrm{min}} \leq R \leq R_{\mathrm{t}}$. By differentiation, one readily gets [x]

$$D_R(R) = -\frac{\mathrm{e}^{F(R)/(k_{\mathrm{B}}T)}}{\partial \tau_{\mathrm{fp}}(R, R_{\mathrm{t}})/\partial R} \int_{R_{\mathrm{min}}}^{R} \mathrm{d}R' \, \mathrm{e}^{-F(R')/(k_{\mathrm{B}}T)}. \tag{2.21}$$

Extracting MFPT curves τ_{fp} from simulation data thus allows to determine the separation dependent diffusivity $D_R(R)$ governing the dynamics in the free energy landscape $F(R)$.

2.3.2 Mean first-passage time data analysis

The relative dynamics of all pairs of water molecules within the 10 ns long MD trajectory are resolved using their minimal image distance with a spatial resolution of $\delta R = 0.002$ nm and a temporal resolution of $\delta t = 20$ fs. All paths starting within a distance $\delta R/2$ from R and crossing $R_{\mathrm{t}} - \delta R/2$ at a time t_{fp} later contribute to the MFPT $\tau_{\mathrm{fp}} = \langle t_{\mathrm{fp}} \rangle$ and to the first-passage time (FPT) distribution f_{fp}. Due to the periodicity of the system, the trajectories along the coordinate R is only meaningful for $R \leq L_{\mathrm{b}}/2$ with box size L_{b}; we therefore only consider target distances $R_{\mathrm{t}} < L_{\mathrm{b}}/2$. Note that the absolute values of the MFPT curves $\tau_{\mathrm{fp}}(R, R_{\mathrm{t}})$ sensibly depend on the time resolution δt of the underlying trajectory as discussed in detail in Appendix C.1.

The derivative $\partial \tau_{\mathrm{fp}}(R, R_{\mathrm{t}})/\partial R$ in Eq. 2.21 is determined by fitting a straight line to τ_{fp} within a region of width 0.032 nm around R (corresponding to 17 data points). This width is empirically found to smooth out the statistical noise in the MFPT curves without hiding the relevant variations of the diffusivity. The integral in Eq. 2.21 is evaluated numerically, the equilibrium PDF $\langle P(R) \rangle$ is linearly interpolated and the reflective boundary is set to $R_{\mathrm{min}} = 0.235$ nm. Applying the same kind of procedure based on simulations of 2180 water molecules in a cubic box of edge length $L_{\mathrm{b}} \approx 4$ nm allows to consider targets R_{t} up to 1.9 nm without introducing artifacts due to the periodicity of the simulation box and thus resolving the diffusivity D_R over a larger range of separations R; finite size effects in the diffusivity profiles are not observed.

We have thoroughly checked that for all numerical steps of the data analysis, varying the spatial and temporal resolutions as well as the position of the reflective boundary R_{min} had no significant impact on the resulting diffusivity profiles.

2.3.3 Mean first-passage times and resulting diffusivity profile

Pair-correlation functions $g_{\mathrm{OO}}(R)$ displaying the distribution of oxygen-oxygen separations R at various temperatures are shown in Fig. 2.8a, where the maxima indicate the positions of the respective coordination shells. The free energy

$$F(R) \equiv -2k_{\mathrm{B}}T \log R - k_{\mathrm{B}}T \log \left(g_{\mathrm{OO}}(R) \right), \tag{2.22}$$

exhibits a barrier of about 1 $k_{\mathrm{B}}T$ at $T = 300$ K for crossing from the first to the second coordination shell as seen in Fig. 2.11a. MFPT curves τ_{fp} extracted from the simulation data for targets R_{t} ranging from 0.4 to 1.4 nm for $T = 300$ K are shown in Fig. 2.8b. They are converted, using Eq. 2.21, into diffusivity profiles $D_R(R)$ shown in Fig. 2.8c. We observe rather good agreement between the curves for different target separations R_t, which is strictly expected only for a pure Markovian process described by a one-dimensional FP equation. As will be discussed later on, this suggests that water bond breakage, defined as the passage from the first to the second coordination shell, is to a good approximation Markovian. The deviations seen when $|R_t - R| \to 0$

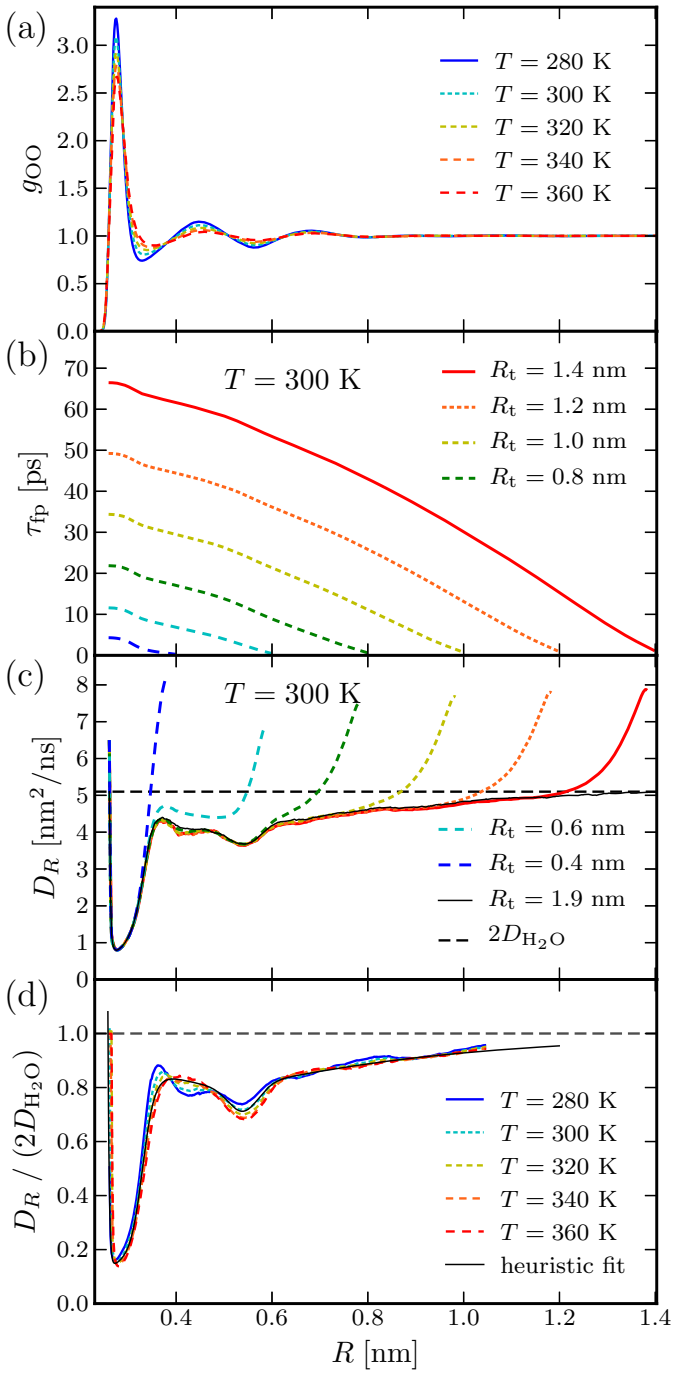

Figure 2.8:
a) Pair correlation function g_{OO} from MD simulations at various temperatures. b) MFPT curves τ_{fp} from MD data for $T = 300$ K and several target separations R_t. c) Diffusivity profiles D_R at $T = 300$ K from the distributions in (a) and the MFPTs in (b) using the Eqs. 2.21 and 2.22, *same color coding* as in (b). d) Diffusivity profiles rescaled by the relative bulk diffusivity 2 D_{H_2O} for various temperatures.

are expected, since on the short spatial scales associated with those first-passage events water motion is not diffusive; in fact, the crossover between ballistic and diffusive motion of single water molecules occurs at length scales of around 0.1 nm, cf. Fig. 2.1. For increasing separation, all curves saturate at the expected of value of twice the diffusion constant of a single water molecule, $\lim_{R\to\infty} D_R(R) = 2D_{H_2O} \approx 5.1\ \mathrm{nm}^2/\mathrm{ns}$, denoted by a dashed line in Fig. 2.8c.

As our main finding, the diffusivity profile exhibits a pronounced drop within the first coordination shell and reaches a minimum value of $D_R \approx 0.79\ \mathrm{nm}^2/\mathrm{ns}$ about six times smaller than in bulk, while only factors ~ 2 have previously been observed in simpler systems [121, 122]. The thin, black line in Fig. 2.8c is obtained by evaluating MFPTs to a target separation $R_t = 1.9$ nm based on simulation data of the larger box with edge length $L_b \approx 4.0$ nm.

Diffusivity profiles corresponding to distinct target separations R_t deviate from each other in two respects: (i) Non-Markovian dynamics on short time and length scales lead to modifications for $|R - R_t| \lesssim 0.25$ nm as discussed above, and (ii) an increasing statistical uncertainty with increasing $|R - R_t|$ due to a decreasing number of recorded transition events contributing to the corresponding MFPTs. Smooth and reliable diffusivity profiles are thus obtained by joining the regions $R_t - 0.45\ \mathrm{nm} \leq R < R_t - 0.35$ nm of the diffusivity profiles corresponding to targets $R_t = 0.5, 0.6, \ldots, 1.4$ nm.

The resulting diffusivity profiles rescaled by twice the bulk diffusion constant D_{H_2O} are shown for various temperatures in Fig. 2.8d. Interestingly, deviations over a temperature span of 80 K are very small; the main features of the profile, including the six-fold decrease within the first coordination shell, are accurately described by the heuristic formula

$$\begin{aligned} D_R(R) \approx 2D_{H_2O}\Bigg(&10.76 - 0.68\ \exp\left(-9\frac{\tilde{R}}{4}\right) - 0.1\ \exp\left(-\frac{1}{5}(27 - 50\tilde{R})^2\right) \\ &+ 10\tanh\left(50(1 - 4\tilde{R})\right) - 0.34\tanh\left(13.2 - 40\tilde{R}\right) + 0.1\tanh\left(4.1 - 10\tilde{R}\right)\Bigg), \end{aligned} \tag{2.23}$$

which is shown as thin black line in Fig. 2.8d and where $\tilde{R} \equiv R/\mathrm{nm}$. From the Arrhenius-like temperature dependence of the bulk diffusion coefficient, cf. Fig. 2.2, it directly follows that the entire diffusivity profile for relative motion obeys an Arrhenius law over the studied temperature range.

2.3.4 Maxima in the mean first-passage times at small separations

According to Eq. 2.20 the MFPT-curve $\tau_{fp}(R, R_t)$ is a strictly decreasing function of R; in contrast, as can be seen in Fig. 2.9a, which shows a close-up of the MFPTs of Fig. 2.8b at small separations, the MFPT curves obtained from MD simulation data show a maximum at separations $R \approx 0.26$ nm. Since according to Eq. 2.21 a vanishing/positive slope of an MFPT-curve implies a diverging/negative diffusivity, the concept of Markovian dynamics obviously breaks down at such small separations. The diffusivity profiles in Fig. 2.8c-d are therefore only resolved for separations $R \geq 0.265$ nm.

Though being counterintuitive at first sight, these maxima in the MFPTs can easily be understood by considering the average oxygen-oxygen separation $\langle R(t)\rangle_{R_0}$ of an ensemble of water pairs starting with defined initial separation R_0 at time $t = 0$. SPC/E-water molecules interact via Coulomb and via Lennard-Jones (LJ) interactions: For small separations the repulsive part of the LJ-potential significantly contributes to the total energy of a water pair, e.g., $U_{LJ} \approx 13.5\ k_B T$

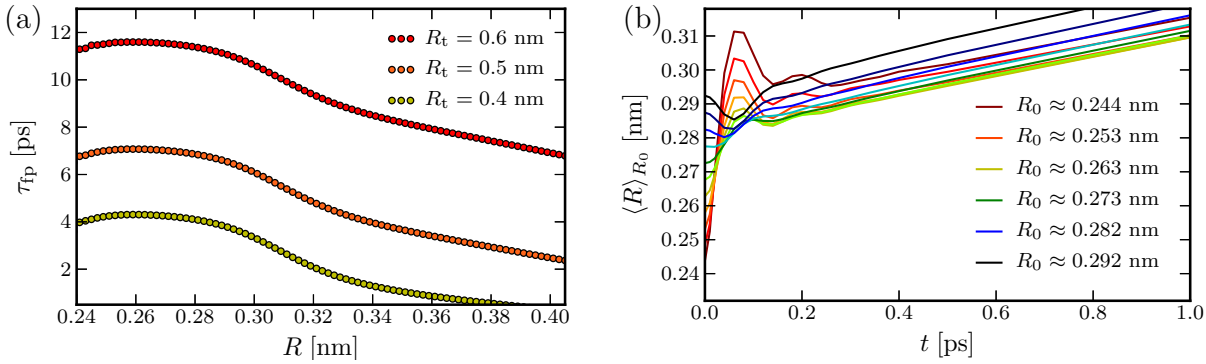

Figure 2.9:
a) Enlarged view of the MFPT curves τ_{fp} from Fig. 2.8b. b) Average oxygen-oxygen separations for water pairs with defined initial separation R_0, only every second curve is shown in the legend.

for $R = 0.25$ nm and $T = 300$ K. The corresponding water pair is thus expected to be quickly driven apart due to the repulsive LJ-force. Fig. 2.9b indeed reveals that the average distance between water molecules starting at separations $R_0 \lesssim 0.25$ nm increases strongly within fractions of picoseconds. The oscillations seen in the curve for $R_0 \approx 0.244$ nm nicely match the time scale of inter-oxygen vibrations, which is found to be on the order of $0.1 - 0.2$ ps [87]. Due to the repulsive LJ-interaction for $R \lesssim 0.25$ nm, the average separations of water pairs starting out at $R_0 \approx 0.244$ nm and at $R_0 \approx 0.282$ nm are very similar on time scales $t \gtrsim 1$ ps. In particular, they exceed the average separation of pairs starting in the range $0.255 \text{ nm} < R_0 < 0.275$ nm. The maxima observed in the MFPT curves of Fig. 2.9a thus are a direct consequence of mutual LJ-repulsion.

2.3.5 Fokker-Planck kinetics with and without diffusivity profile

To what extent is this local friction increase relevant for the water-bond breakage kinetics? To quantify the relevance of the change in local friction, we compare in Fig. 2.10a the MFPT curves from MD data already shown in Fig. 2.8b (colored lines) to analytical predictions resulting from Eq. 2.20 using the diffusivity profiles $D_R(R)$ (solid lines) shown in Fig. 2.8c as well as calculations employing a constant diffusivity $D_R = 2D_{H_2O}$ (dashed lines). The solid lines by construction match the MD data nicely, where the vertical shift is caused by the 20 fs time discretization of the underlying MD trajectory, cf. Appendix C.1 for a detailed analysis of the sensitivity of MFPT curves on the temporal discretization of the trajectory. It is seen that the assumption of a constant diffusivity leads to a considerable underestimation of the MFPTs. The time to reach the target separation $R_t = 0.4$ nm from the first coordination shell ($R \lesssim 0.28$ nm) is underestimated by a factor of roughly one half.

The accuracy of the FP approach involving the diffusivity profile is demonstrated by comparing first-passage time (FPT) distributions: Fig. 2.10b contrasts the FPT histogram from MD data for $R_t = 0.4$ nm with FPT distributions from the numerical solution of the FP equation (numerical details are given in Appendix C.2), again using the flat diffusivity $2D_{H_2O}$ and the actual diffusivity profile $D_R(R)$. Only the FP approach including the $D_R(R)$ profile correctly reproduces the entire FPT distribution from MD simulations and in particular also the exponential tail of the distribution, as shown by the plot using the logarithmic scale on the right. Systematic

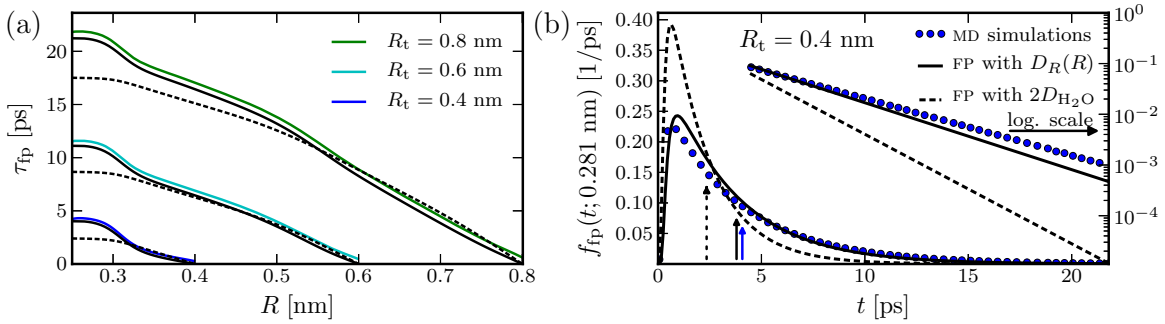

Figure 2.10:
a) MFPTs from MD simulations (*solid colored lines*, same data as in Fig. 2.8b), and from the FP description (Eq. 2.20) for several target separations R_t. b) FPT distribution to reach a separation $R_t = 0.4$ nm for water pairs starting within the first coordination shell ($R = 0.281 \pm 0.001$ nm). Histograms from MD simulations at $T = 300$ K (*blue circles*) are compared to the numerical solution of the FP Eq. 2.19. Data are shown on both linear and logarithmic scales, vertical arrows indicate the mean of the distributions. Other examples are found in Appendix C.2. FP results for a constant diffusivity $2D_{H_2O}$ are displayed as *dashed black lines*, those for the diffusivity profile $D_R(R)$ from Fig. 2.8c as *solid black lines*.

discrepancies are observed on short time scales $\lesssim 1$ ps where the MD data show more "fast" transitions than the FP description. These effects are caused by ballistic motion of water molecules and cannot be captured by a Markovian description.

2.3.6 Testing the quality of the reaction coordinate

Although our procedure does not strictly depend on the fact that the separation R is a "good" RC, the whole mapping on a one-dimensional FP equation will certainly be more meaningful if this is the case. To check the quality of our RC, we divide R into a bound region A for $R < R_A = 0.275$ nm, an unbound region B for $R \geq R_B = 0.47$ nm and the intermediate region for $0.275\text{ nm} < R < 0.47$ nm, which roughly encompasses the free energy barrier seen in Fig. 2.11a. For a diffusive process described by the FP equation (Eq. 2.19), the committor $\pi_X(R)$ specifying the probability of first reaching the region $X \in \{A, B\}$ when starting from R is a solution of the stationary backward FP equation [38]

$$e^{F(R)/(k_B T)} \frac{\partial}{\partial R} \left(e^{-F(R)/(k_B T)} D_R(R) \frac{\partial \pi_X(R)}{\partial R} \right) = 0. \tag{2.24}$$

The committor fulfills the boundary conditions $\pi_X(R_Y) = \delta_{XY}$, with δ_{XY} denoting the Kronecker symbol. The solutions are

$$\pi_A(R) = \frac{1}{\mathcal{N}} \int_R^{R_B} dR' \, \frac{e^{F(R')/(k_B T)}}{D_R(R')}, \qquad \pi_B(R) = 1 - \pi_A(R) = \frac{1}{\mathcal{N}} \int_{R_A}^{R} dR' \, \frac{e^{F(R')/(k_B T)}}{D_R(R')}, \tag{2.25}$$

with the common normalization factor

$$\mathcal{N} \equiv \int_{R_A}^{R_B} dR' \, \frac{e^{F(R')/(k_B T)}}{D_R(R')}. \tag{2.26}$$

In Fig. 2.11b, we show the committors $\pi_A(R)$ and $\pi_B(R)$, which specify the probability of first reaching region A and B, respectively: Estimates from MD data (circles) as well as from the exact solution of the FP equation (Eqs. 2.25 and 2.26) employing constant bulk (dashed line) or true diffusivity profile (solid line) are displayed. Agreement between solid lines and MD data is quite good, although deviations close to region A are discernible and might point to residual barrier-crossing events orthogonal to the coordinate R [83].

The probability $P(\mathrm{TP}|R)$ that a path passing through R is a transition path (TP), i.e., a path directly connecting the regions A and B, is given by [109]

$$P(\mathrm{TP}|R) = 2\pi_\mathrm{A}(R)\pi_\mathrm{B}(R) = 2\pi_\mathrm{A}(R)(1-\pi_\mathrm{A}(R)), \tag{2.27}$$

where the factor 2 takes into account that a TP can start in A and reach B or vice versa. The probability $P(\mathrm{TP}|R)$ reaches its maximum value 0.5 at the transition state denoted by $R^\ddagger$ [123], where $\pi_\mathrm{A}(R^\ddagger) = \pi_\mathrm{B}(R^\ddagger) = 0.5$. A "good" RC is characterized by a maximum value of the TP probability near this diffusive limit of 0.5 [109]. In contrast, for "poor" RCs, which do not single out the transition states, this maximum is considerably lower; the reason is that for "poor" RCs excursions starting and ending in A and excursions starting and ending in B dominate all along the coordinate so that TPs are rare everywhere between A and B [89, 108].

Committor and TP probabilities are estimated by analyzing all simulation paths within the region $R \in [R_\mathrm{A}, R_\mathrm{B}] = [0.275\ \mathrm{nm}, 0.47\ \mathrm{nm}]$ within a time window of 100 ps, where the time resolution is $\delta t = 0.01$ ps. $P(\mathrm{TP}|R)$ from MD data in Fig. 2.11c reaches a maximal value of $P(\mathrm{TP}|R^\ddagger) \approx 0.38$, where the position $R^\ddagger$ is slightly displaced from the FP prediction by about 0.02 nm. Though caution is recommended in interpreting the TP probability test [124], we conclude that the separation R is an acceptable RC unlike in the similar problem of ion unbinding [89].

2.3.7 Interpretation of the diffusivity profile

Based on these findings, it is possible to give a quite intuitive interpretation of the diffusivity profile. Assuming that the relative dynamics of two water molecules can be described as a diffusive process along a single path $\boldsymbol{R}$ in the full high-dimensional configuration space, the projection onto one single coordinate, in this case the oxygen-oxygen separation R, generally leads to considerable changes in free energy and diffusivity.

For convenience we assume the path $\boldsymbol{R}(s),\ s \in [0, L]$ of total contour length L being arc-length parametrized, i.e., $|\mathrm{d}\boldsymbol{R}(s)/\mathrm{d}s| = 1 \quad \forall s \in [0, L]$. In doing so, we implicitly assume that the reactive flux tube is quite narrow, i.e., that the idea of a single, dominating path makes sense [107]. The vector $\boldsymbol{R} \equiv (R, \boldsymbol{R}_\perp)$ is split up into the coordinate R and an ortogonal, vectorial component $\boldsymbol{R}_\perp$, implying

$$\left|\frac{\mathrm{d}\boldsymbol{R}(s)}{\mathrm{d}s}\right| = \sqrt{\left|\frac{\mathrm{d}\boldsymbol{R}_\perp(s)}{\mathrm{d}s}\right|^2 + \left(\frac{\mathrm{d}R}{\mathrm{d}s}\right)^2} = 1, \quad \forall\, s \in [0, L]. \tag{2.28}$$

We assume a one-to-one correspondence between the arc-length variable s and the relative separation R, i.e., a path which does not take any value of R more than once. In this case, the coordinate R is just a reparametrization of s. As is well-known [120][x], such a reparametriza-

tion can sensibly alter the free energy and the diffusivity; more precisely, the corresponding profiles along the coordinates R and s are connected via

$$F(R) = F_s(s) + k_\mathrm{B}T \log\left(\frac{\mathrm{d}R}{\mathrm{d}s}\right), \quad D_R(R) = D_s(s)\left(\frac{\mathrm{d}R}{\mathrm{d}s}\right)^2. \tag{2.29}$$

Combining the Eqs. 2.28 and 2.29, one deduces

$$\left|\frac{\mathrm{d}\boldsymbol{R}_\perp}{\mathrm{d}s}\right| = \sqrt{1-\left(\frac{\mathrm{d}R}{\mathrm{d}s}\right)^2} = \sqrt{1-\frac{D_R(R(s))}{D_s(s)}}, \tag{2.30}$$

meaning that the knowledge of the diffusivity profile $D_R(R)$ along the coordinate R allows to draw conclusions on the shape of the path $\boldsymbol{R}(s)$. In particular, a reduction of the diffusivity $D_R(R)$ along a chosen RC R is a signature of pronounced contributions to the reaction path that are orthogonal to the RC. Deviations of the diffusivity from the value $D_s(s)$ thus indicate a non-negligible component of the path tangent perpendicular to R. Since only the magnitude of this perpendicular tangent component can be accessed and thus the direction of the path remains uncertain, the path $\boldsymbol{R}$ cannot be completely reconstructed from the knowledge of $D_R(R)$. However, the definition of

$$R_\perp \equiv \int_{R_0}^{R} \mathrm{d}R' \left|\frac{\mathrm{d}\boldsymbol{R}_\perp}{\mathrm{d}R'}\right| = \int_{R_0}^{R} \mathrm{d}R' \sqrt{\frac{D_s(s(R'))}{D_R(R')}-1}, \tag{2.31}$$

allows to visualize the path in the $(R, R_\perp)$-plane starting from a reference coordinate R_0. Choosing a constant $D_s(s) = 2D_{\mathrm{H_2O}}$ for illustrative purposes, we show in Fig. 2.7c a fictitious path in the plane $(R, R_\perp)$ that would be consistent with the diffusivity profile $D_R(R)$ actually extracted from MD simulations. We observe that the pictorial reaction path has large contributions orthogonal to R within the first coordination shell, where the diffusivity profile shows its prominent drop, i.e., for relative separations 0.26 nm $\lesssim R \lesssim$ 0.34 nm. This is in agreement with previous simulation results suggesting that the orthogonal degrees of freedom involved in water-bond breakage are of angular nature [84, 85].

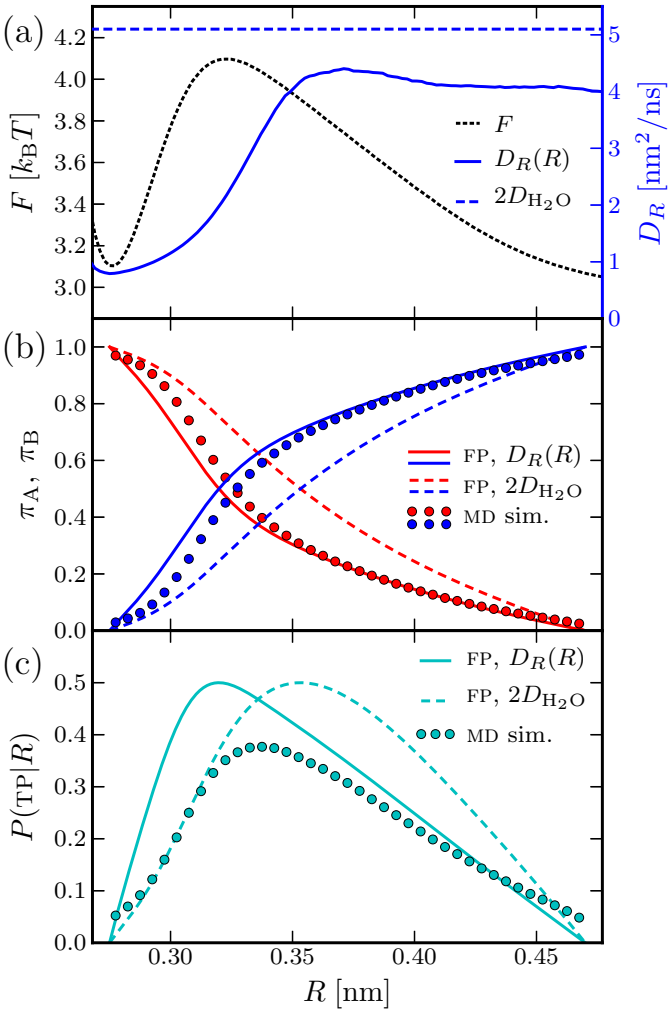

Figure 2.11:
a) Free energy and diffusivity profiles for separations between the first and second coordination shell and a temperature $T = 300$ K. b) Commitment probabilities π_A and π_B (Eqs. 2.25 and 2.26). c) Transition path probability $P(\mathrm{TP}|R)$ (Eq. 2.27). In (b) and (c), simulation results (*circles*) are compared to FP estimates based on the diffusivity profile $D_R(R)$ (*solid lines*) and based on a constant diffusivity $2D_{\mathrm{H_2O}}$ (*dashed lines*).

2.4 Conclusions

Based on the analysis of the stochastic trajectories obtained from MD simulations, we have resolved the diffusion coefficients of individual water and solute molecules in bulk SPC/E water. Distinguishing between translations along and rotations around the individual internal coordinate axes of the water molecules, we have found a pronounced anisotropy of the translational and rotational dynamics as well as non-vanishing correlations in the translational and orientational motion.

The diffusivity profile characterizing the relative dynamics of a selected pair of water molecules drops by a factor of more than six within the first coordination shell compared to large separations, where both molecules diffuse independently. Although the absolute diffusivities show an Arrhenius-like temperature dependence, the shape of the diffusivities for the relative motion is found to be temperature-insensitive between 280 and 360 K. The form of the diffusivity profile is necessary to reproduce dynamic properties, e.g., FPT distributions observed in the simulations, and can be interpreted in terms of a reaction path which is distorted with respect to the resolved separation coordinate R.

We cautiously remark that a distorted reaction path is only one of a few mechanisms that would modify the local diffusivity; orthogonal energetic barriers, which are, based on our results shown in Fig. 2.11, presumably small in the present case but dominate in related problems [89], and competing reaction paths [55] or flux-tube width variations [107, 125] are additional complications. The charm of our approach is that it allows for a consistent description of the kinetics even without a detailed knowledge of the transition path and the involved relevant degrees of freedom.

A better understanding of H-bond breakage and formation processes presumably requires an extension of the analysis to a larger configuration space, e.g., including orientational degrees of freedom of the molecules, and the application of concepts such as transition path theory [107] or Markov-state-modeling [126]. We in particular expect the observed anisotropy in the dynamics of individual water molecules to play a key role for a better understanding of the complex rearrangement processes in the H-bonded network.

CHAPTER 3

WATER DYNAMICS AT BIOLOGICAL INTERFACES

Bibliographic information: Parts of this chapter have previously been published. Reprinted with permission from Ref. [iii]. Copyright 2013 by the American Physical Society.

Lipid bilayers are fundamental building blocks of all living matter [127]. Most membrane physiological functions involve transport of molecules within the membrane plane or between the membrane and the bulk compartments [128]. In all these situations, the dynamics of the membrane hydration water are believed to be important [129] and has been experimentally studied by radioactive labeling [130], nuclear magnetic resonance (NMR) [131], inelastic neutron scattering [132], fluorescence spectroscopy [133], infrared adsorption [134] and THz spectroscopy techniques [135]. Experimentally, the long-time dynamics of molecules in bacterial cells [42] and crowded fluids [136] as well as transmembrane-protein motion [137] have been found to deviate strongly from the ordinary diffusion law, which has been suggested to be of physiological relevance in preventing prospective reaction partners to prematurely run away from each other [42].

In atomistic simulations, lateral lipid diffusion has been found to be anomalous over extended intermediate time scales for different compositions [138], to exhibit cooperative motion [139] and to reflect internal degrees of freedom [140]. Transmembrane proteins diffuse even slower and show enhanced anomalous diffusion behavior [141]. The dynamics of membrane hydration water have been considered in few theoretical works: Water diffusion perpendicular to the membrane plane has been simulated in order to predict transmembrane water transport [142, 143] and water dynamics as relevant to NMR experiments [144]. Water diffusion at a fixed distance away from the bilayer surface has been extracted from molecular dynamics (MD) simulations [145], but the spatially resolved tensorial diffusivity of the hydration water has not been considered yet.

Here, we examine the dynamics of individual water molecules in the vicinity of a dipalmitoylphosphatidylcholine (DPPC) bilayer based on the trajectory analysis of extensive MD simulations. Once the free energy profile perpendicular to the membrane plane is accounted for in the stochastic analysis, water diffusion is found to be strongly reduced next to the membrane. We reveal anisotropic diffusion behavior of the hydration water that markedly differs from the one at solid surfaces, where the water diffusion is also substantially slowed down but in quantitative agreement with continuum hydrodynamic theory. As we show by coarse-grained simulations, this anisotropy can be traced back to the transient but long-lived corrugated free

energy landscape imposed by the lipids. The lateral water dynamics consequently show the characteristics of obstructed diffusion, similar to the dynamics in crowded fluids [136]. We expect the diffusion of other solutes at membranes to exhibit similar features and thus our findings to be relevant for a broad range of physiological processes ranging from intercellular signaling to drug delivery.

The chapter is organized as follows: The simulation methods are presented in Sec. 3.1 and the dynamics of water molecules parallel and perpendicular to the membrane are analyzed in the Secs. 3.2 and 3.3 respectively. We compare the water diffusion anisotropy near lipid membranes to the one at solid, homogeneous surfaces in Sec. 3.4, reveal the influence of the bilayer structure on the lateral dynamics in Sec. 3.5, and summarize the main results of the chapter in Sec. 3.6.

3.1 Methods

3.1.1 Molecular dynamics simulations

Our simulation setup resembles that of previous studies [146–148] and consists of a lipid bilayer composed of 72 DPPC molecules and 2278 SPC/E water molecules, see the simulation snapshot in Fig. 3.1a. Simulations are based on the DPPC force field from Ref. [149] and are run using the GROMACS 4.0.7 package [91] in the NVT ensemble starting from a pre-equilibrated box as described in Ref. [148]. The box dimensions are $4.597 \times 5.090 \times 6.839$ nm^3 corresponding to a mean area of ≈ 0.65 nm^2 per DPPC molecule. The average temperature is fixed at 320 K using a Berendsen thermostat and the integration time step is set to 2 fs. For the covalent bonds to hydrogens in the DPPC molecules rigid constraints are used [150], while the water geometry is constrained using SETTLE [151]. A plain cut-off at 0.9 nm is used for short-range van der Waals interactions. Electrostatics are treated on the particle-mesh Ewald level [94, 95] with a real-space cutoff of 0.9 nm.

For the constrained simulations evaluated in Sec. 3.2.3, approximately 10% of the water molecules within initial separations $|z - z_0| \leq 0.15$ nm from various distances z_0 from the membrane mid-plane are randomly selected and harmonically constrained around their initial z-positions with a spring constant of 6640 kJ/(mol nm^2), while being free in x- and y-direction. Neighboring values of z_0 being separated by 0.5 nm, in total only roughly 6 % of the 2278 water molecules are z-constrained in these simulations.

Production runs have a total length of approximately 6.5 μs and frames for analysis are written every 0.05 ps (unconstrained simulations) and every 2 ps (constrained simulations). The total simulation length used for the evaluation of the lateral mean square displacements (MSDs) in the unconstrained simulations is roughly 600 ns, and approximately 400 ns for the constrained simulations. The perpendicular diffusivity is evaluated from mean first-passage times (MFPTs) based on the unconstrained simulations with a total length of roughly 6 μs.

Recent systematic studies on systems similar to ours [152–154] have investigated a possible influence of the finite system size used in MD simulations. Quantifying internal dynamics and collective structural properties of the lipids, they have found 36 lipids per leaflet as used in our simulations to be sufficient to obtain reliable results which are not modified when going to larger system sizes. Therefore, and since we find the lateral water dynamics next to the membrane to become Markovian on sub-nanometer length scales and on time scales of a few nanoseconds in Sec. 3.2.4, we expect at most a minor influence of the system size on our results.

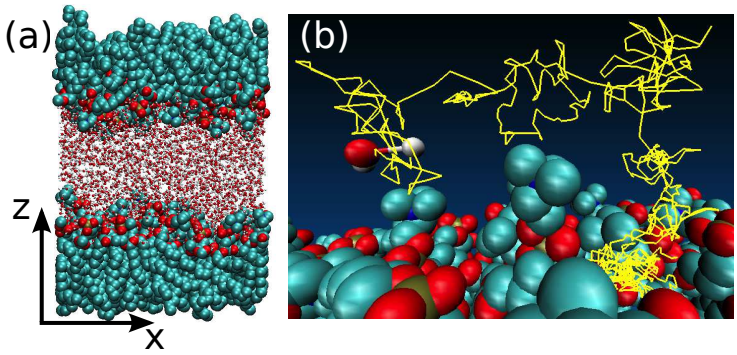

Figure 3.1:
a) Snapshot of the simulation box. b) Trajectory of a water molecule in the vicinity of the membrane in the MD simulation: The *yellow* path of 100 ps duration starts in the lower right. A corresponding movie is included as supplementary material [111].

The MD simulations analyzed in this chapter have been performed by Prof. Dr. Stephan Gekle from the University of Bayreuth.

3.1.2 Monte Carlo simulations

To estimate the effect of the bilayer structure on the lateral water dynamics, we perform Monte Carlo (MC) simulations in the transient free energy landscapes from MD simulations

$$F_{z_0,\tau}(x,y) \equiv -k_B T \log\left(\overline{\rho}_{z_0,\tau}(x,y)/\rho_0\right), \tag{3.1}$$

where $\overline{\rho}_{z_0,\tau}$ denotes the lateral water density at a distance z_0 from the membrane mid-plane averaged over a time τ and where $\rho_0 \approx 32\ \mathrm{nm}^{-3}$ denotes the bulk water number density. The lateral water densities $\overline{\rho}_{z_0,\tau}$ are resolved with a spatial resolution $\delta x \approx \delta y \approx 0.1$ nm by averaging the distribution of water molecules over a 0.5 nm thick slab centered around z_0, an example density profile for $z_0 = 2$ nm and $\tau = 50$ ps is shown in Fig. 3.2.

MC simulations are performed based on the following protocol: The motion along the two spatial directions is independent and within a time step δt the position of the random walker at the lattice position (x_i, y_j) changes according to the Metropolis algorithm

$$(x_i,y_j) \longrightarrow \begin{cases} (x_{i-1},y_i) & \text{with prob. } \min\left[\frac{1}{2}, \frac{\overline{\rho}_{z_0,\tau}(x_{i-1},y_j)}{2\overline{\rho}_{z_0,\tau}(x_i,y_j)}\right] \\ (x_{i+1},y_i) & \text{with prob. } \min\left[\frac{1}{2}, \frac{\overline{\rho}_{z_0,\tau}(x_{i+1},y_j)}{2\overline{\rho}_{z_0,\tau}(x_i,y_j)}\right] \\ (x_i,y_i) & \text{with prob. } 1 - \min\left[\frac{1}{2}, \frac{\overline{\rho}_{z_0,\tau}(x_{i-1},y_j)}{2\overline{\rho}_{z_0,\tau}(x_i,y_j)}\right] - \min\left[\frac{1}{2}, \frac{\overline{\rho}_{z_0,\tau}(x_{i+1},y_j)}{2\overline{\rho}_{z_0,\tau}(x_i,y_j)}\right] \end{cases}, \tag{3.2}$$

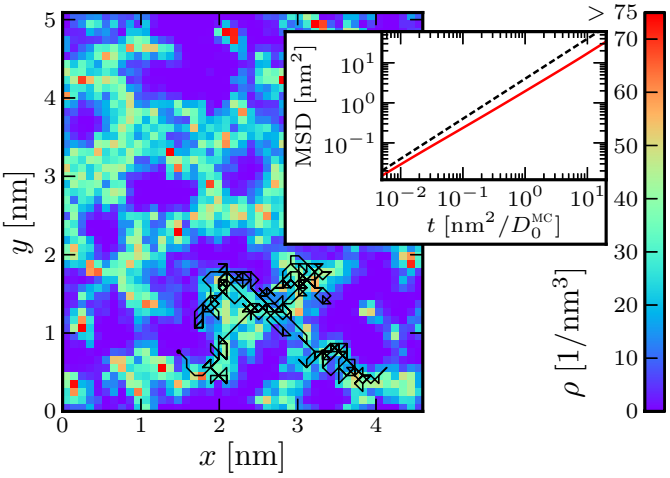

Figure 3.2:
Water density profile $\overline{\rho}_{z_0,\tau}(x,y)$ averaged in a slab $|z - z_0| \leq 0.25$ nm around a distance $z_0 = 2$ nm from the membrane mid-plane over a time window $\tau = 50$ ps with lateral discretization $\delta x \approx \delta y \approx 0.1$ nm. A sample MC trajectory of 500 steps is shown as *thin black line*. Inset: The lateral MSD from MC simulations (*red line*) and the reference MSD in an unstructured environment, $4D_0^{\mathrm{MC}}t$, (*dashed black line*) are shown.

and

$$(x_i, y_j) \longrightarrow \begin{cases} (x_i, y_{j-1}) & \text{with prob. } \min\left[\frac{1}{2}, \frac{\overline{\rho}_{z_0,\tau}(x_i,y_{j-1})}{2\overline{\rho}_{z_0,\tau}(x_i,y_j)}\right] \\ (x_i, y_{j+1}) & \text{with prob. } \min\left[\frac{1}{2}, \frac{\overline{\rho}_{z_0,\tau}(x_i,y_{j+1})}{2\overline{\rho}_{z_0,\tau}(x_i,y_j)}\right] \\ (x_i, y_j) & \text{with prob. } 1 - \min\left[\frac{1}{2}, \frac{\overline{\rho}_{z_0,\tau}(x_i,y_{j-1})}{2\overline{\rho}_{z_0,\tau}(x_i,y_j)}\right] - \min\left[\frac{1}{2}, \frac{\overline{\rho}_{z_0,\tau}(x_i,y_{j+1})}{2\overline{\rho}_{z_0,\tau}(x_i,y_j)}\right] \end{cases}, \quad (3.3)$$

where periodic boundary conditions are used. The time step δt in the MC simulations is related to the lateral diffusion coefficient in an unstructured environment D_0^{MC} via $\delta t \equiv (\delta x)^2 / (2D_0^{\mathrm{MC}}) \approx (\delta y)^2 / (2D_0^{\mathrm{MC}})$. For each set of parameters (z_0, τ), trajectories of $2 \cdot 10^7$ MC steps each are generated in 25 independent density profiles. A sample MC trajectory of 500 steps is shown as a thin black line in Fig. 3.2.

3.2 Water Dynamics Parallel to the Lipid Membrane

3.2.1 Unconstrained simulations

Water motion parallel to the membrane surface is characterized by the MSDs

$$\langle (\Delta x(t))^2 \rangle_{z_0} \equiv \langle \left(x(t' + t) - x(t')\right)^2 \rangle_{z_0}, \qquad \langle (\Delta y(t))^2 \rangle_{z_0} \equiv \langle \left(y(t' + t) - y(t')\right)^2 \rangle_{z_0}, \quad (3.4)$$

of the x- and y-coordinates of the water oxygen. In Eq. 3.4, $\langle \ldots \rangle_{z_0}$ denotes the double average over the reference time t' and all the water molecules, for which $|z(t' + \tau) - z_0| \leq 0.25$ nm is fulfilled for the entire time span $0 \leq \tau \leq t$, i.e., only trajectories which remain within an

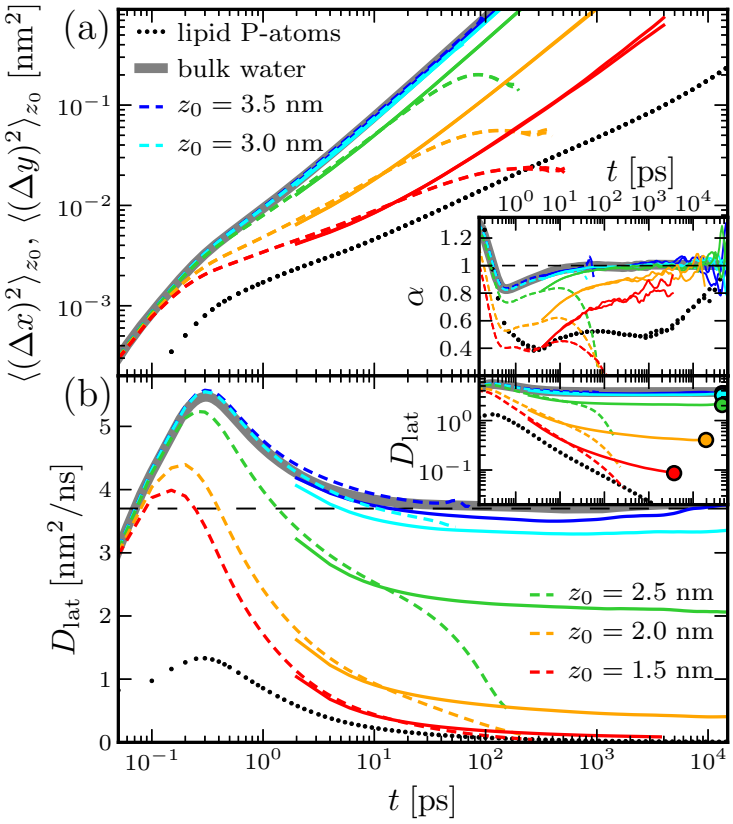

Figure 3.3:
a) Lateral MSDs (Eq. 3.4) for water at different distances z_0 from the membrane center (*colored lines*), for lipid heads (*black dots*), and for bulk water (adapted from Fig. 2.1, *gray lines*, mostly hidden under the $z_0 = 3.5$ nm water data). Inset: Corresponding local exponents α (Eq. 3.8). b) Resulting time-dependent diffusion coefficients D_{lat} (Eq. 3.9). Inset: Double-logarithmic representation of the same data, *filled colored circles* denote upper bounds for the long-time diffusion coefficients. In all panels and insets, the *same color coding* is used, and data for unconstrained and harmonically trapped water molecules are displayed as *dashed* and *solid lines*, respectively.

interval of 0.5 nm centered around a prescribed distance z_0 from the membrane mid-plane are considered. In order to avoid artifacts due to the diffusion of the membrane as a whole, we have subtracted the lateral center-of-mass position of the nearest membrane leaflet from the water coordinates [155, 156].

Lateral water MSDs for different distances z_0 from the membrane center (denoted by different colors) are shown as dashed lines in Fig. 3.3a. The perfect agreement of the MSDs for x and y testifies to the statistical data quality. While the sub-picosecond dynamics are independent of z_0, on larger time scales the MSDs differ considerably depending on the distance from the membrane mid-plane [145]: Whereas water molecules in the center of the water slab ($z_0 = 3.5$ nm) show MSD curves that are indistinguishable from those in bulk water studied in Sec. 2.2.1 (thick gray line), closer to the membrane the water MSD curves approach the lateral MSDs of the lipids' phosphorus atoms (black dots).

Note that the MSD curves for $z_0 \leq 2.5$ nm in Fig. 3.3a (green, orange and red dashed lines) saturate and then begin to decrease for times $t \gtrsim 50$ ps. As we show next, these artifacts are

due to the fact that the trajectory ensemble which serves to calculate the MSD (Eq. 3.4) changes over time [116].

3.2.2 Alternative definitions of the lateral mean square displacement

According to Eq. 3.4, only those trajectory segments contribute to the lateral MSD values, for which $|z(t'+\tau) - z_0| \leq 0.25$ nm for all times $0 \leq \tau \leq t$. When the time t increases, fewer and fewer trajectories fulfill this criterion, i.e., the trajectory ensemble contributing to the MSD values at time t_2 is a subset of the trajectory ensemble over which MSD-values at time $t_1 < t_2$ are calculated. To estimate the influence of the time-dependent trajectory-ensembles, we also consider MSDs

$$\begin{aligned} \langle (\Delta x(t))^2 \rangle_{z_0,\, t_{\mathrm{ref}}} &\equiv \langle \big(x(t'+t) - x(t')\big)^2 \rangle_{z_0,\, t_{\mathrm{ref}}}, \\ \langle (\Delta y(t))^2 \rangle_{z_0,\, t_{\mathrm{ref}}} &\equiv \langle \big(y(t'+t) - y(t')\big)^2 \rangle_{z_0,\, t_{\mathrm{ref}}}, \end{aligned} \tag{3.5}$$

for which the condition $|z(t'+\tau) - z_0| \leq 0.25$ nm holds for all times $0 \leq \tau \leq t_{\mathrm{ref}}$, where t_{ref} denotes a certain fixed reference time. Corresponding curves for reference times $t_{\mathrm{ref}} = 50$ ps and 100 ps are compared in Fig. 3.4a to the dashed curves from Fig. 3.3a. The curves corresponding to Eq. 3.5 reflect the time evolution of the second moment of a fixed trajectory ensemble and are monotonously increasing with time. The spurious effects in Fig. 3.3a (decrease or saturation of the MSD curves) thus are a consequence of the time-dependent trajectory ensemble: As is seen from Fig. 3.4a, water molecules which remain for a long time within a 0.5 nm interval in z-direction are also less mobile laterally [116].

Both the definitions of the lateral MSDs in the Eqs. 3.4 and 3.5 are very restrictive with respect to the motion of the molecules in z-direction since only those trajectory segments are considered, which do not leave the prescribed interval around z_0 (not even once!). Water MSD curves therefore become statistically unreliable for t or $t_{\mathrm{ref}} \gtrsim 100$ ps, because very few water trajectories stay within a given interval around z_0 for such long times. Long-time MSDs, from which the lateral diffusion coefficients can be inferred, thus cannot be resolved based on the definitions in the Eqs. 3.4 and 3.5. We therefore consider the alternative definitions of the lateral MSDs

$$\begin{aligned} \langle (\Delta x(t))^2 \rangle_{z_0,\, \mathrm{beg.}} &\equiv \langle \big(x(t'+t) - x(t')\big)^2 \rangle_{z_0,\, \mathrm{beg.}}, \\ \langle (\Delta y(t))^2 \rangle_{z_0,\, \mathrm{beg.}} &\equiv \langle \big(y(t'+t) - y(t')\big)^2 \rangle_{z_0,\, \mathrm{beg.}}, \end{aligned} \tag{3.6}$$

where the z-coordinate is required to lie within the slab around z_0 at the beginning of a trajectory segment ($\tau = 0$) only, i.e., $|z(t') - z_0| \leq 0.25$ nm, as well as

$$\begin{aligned} \langle (\Delta x(t))^2 \rangle_{z_0,\, \mathrm{beg.\&end}} &\equiv \langle \big(x(t'+t) - x(t')\big)^2 \rangle_{z_0,\, \mathrm{beg.\&end}}, \\ \langle (\Delta y(t))^2 \rangle_{z_0,\, \mathrm{beg.\&end}} &\equiv \langle \big(y(t'+t) - y(t')\big)^2 \rangle_{z_0,\, \mathrm{beg.\&end}}, \end{aligned} \tag{3.7}$$

where the average is taken over trajectories, for which $|z(t'+\tau) - z_0| \leq 0.25$ nm is fulfilled at the two reference times $\tau = 0$ and $\tau = t$, while no restriction is imposed for intermediate times $0 < \tau < t$. Note that in contrast to the Eqs. 3.4 and 3.5, where x and y denote the coordinates of the oxygen relative to the nearest lipid leaflet, x and y denote the coordinates of the water

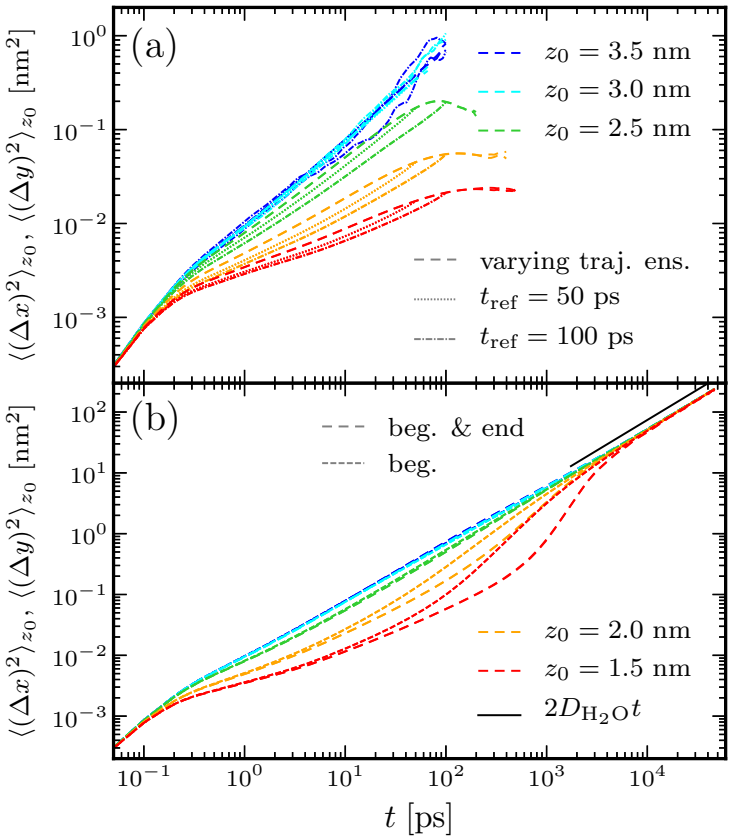

Figure 3.4:
Comparison of various MSD definitions: a) Lateral MSDs from Fig. 3.3a (varying trajectory ensemble, Eq. 3.4) are shown as *dashed lines*, while (*dashed-*)*dotted lines* denote lateral MSDs according to Eq. 3.5 (fixed trajectory ensemble) for reference times $t_{\mathrm{ref}} = 50$ ps and $t_{\mathrm{ref}} = 100$ ps. b) Lateral MSDs according to the Eqs. 3.6 and 3.7 are shown as differently *dashed lines*, and the *solid black line* denotes the bulk water MSD with $D_{\mathrm{H_2O}} \approx 3.7$ nm^2/ns from Tab. 2.1. In both panels, the *color coding* discriminates between different separations z_0 from the membrane mid-plane, analogous to Fig. 3.3.

oxygen in the laboratory frame in the Eqs. 3.6 and 3.7, since the trajectories are not restricted to the vicinity of a specific leaflet.

Corresponding MSD curves are shown in Fig. 3.4b: While the MSD curves for trajectories only starting as well as starting and ending next to the membrane ($z_0 \lesssim 2.0$ nm) are clearly suppressed on time scales of tens to hundreds of picoseconds, all MSD curves converge to a common linear MSD $2\overline{D}_{\mathrm{lat}}t$ on the nanosecond time scale. Although the statistical uncertainty in the curves in Fig. 3.4b is negligible, these are not suited to determine the z-dependence of the lateral diffusivity profile, since the long-time MSDs reflect the slab-averaged lateral diffusion coefficient $\overline{D}_{\mathrm{lat}} \approx 2$ nm^2/ns only. This is significantly smaller than the bulk diffusion constant $D_{\mathrm{H_2O}} \approx 3.7$ nm^2/ns at $T = 320$ K from Sec. 2.2.1, indicating an overall reduced lateral diffusivity of the membrane hydration water compared to bulk as is clearly seen from the comparison to the solid black line in Fig. 3.4b.

3.2.3 Constrained simulations

To reliably determine lateral MSDs on the nanosecond time scale and resolve the z-dependent diffusivity profile for lateral motion, we therefore resort to simulations where roughly 6% of the 2278 water molecules are harmonically constrained in z-direction as described in Sec. 3.1.1. The resulting MSDs are shown as solid lines in Fig. 3.3 and compare well to the unconstrained MSDs (dashed lines) on times up to ~ 20 ps.

The local slopes of the MSD data in the double-logarithmic representation reflect the time-dependent exponent, which for a general function $f(t)$ is defined as

$$\alpha(t) \equiv \frac{\mathrm{d}\log\left(f(t)\right)}{\mathrm{d}\log\left(t\right)} = \frac{t}{f(t)}\frac{\mathrm{d}f(t)}{\mathrm{d}t}. \tag{3.8}$$

Time-dependent exponents of the MSD data are shown in the inset of Fig. 3.3a: For bulk-like water (blue curves), we observe a smooth transition from superdiffusive behavior $\alpha > 1$ for times $t \lesssim 200$ fs to a subdiffusive regime with $\alpha \approx 0.9$ on the picosecond time scale, and a subsequent crossover to the exponent $\alpha = 1$, associated with normal diffusion, for $t \gtrsim 10$ ps. When approaching the membrane, the anomalous diffusion regime extends to time scales of up to nanoseconds and the exponents α decrease. For water molecules in direct proximity of the membrane ($z_0 = 1.5$ nm), typical MSD exponents are ≈ 0.4, similar to those of the lipid head-groups themselves [138, 140], demonstrating a tight coupling of water and lipid motions further analyzed in Sec. 3.5.

Time-dependent lateral diffusion coefficients

$$D_{\mathrm{lat}}(t; z_0) \equiv \frac{\langle (\Delta x(t))^2 + (\Delta y(t))^2 \rangle_{z_0}}{4t}, \tag{3.9}$$

from both constrained and unconstrained simulations, are shown as solid and dashed lines in Fig. 3.3b using the same color coding as in Fig. 3.3a. While the superdiffusive regime at short times gives rise to an increasing diffusion coefficient, a maximum in the sub-picosecond range and a slow subsequent saturation are observed. The diffusion coefficients in the membrane vicinity continue to decrease even beyond several nanoseconds, as is best seen in the double-logarithmic representation of the data in the inset of Fig. 3.3b, where upper bounds for the long-time diffusion coefficients are indicated by colored circles.

3.2.4 Mean first-passage time analysis for motion parallel to the membrane

Estimates for the lateral diffusion coefficients have been obtained from the long-time MSDs above. They can equally be determined by an MFPT analysis, cf. Sec. 2.3.1 and Refs. [viii][x]. For this, trajectories $r(t)$ of the radial lateral distance of the z-constrained molecules from a (randomly selected) reference point in the two-dimensional plane are analyzed. Due to translation invariance in the lateral plane, the equilibrium probability density function of radial distances is of entropic nature only, i.e., $\mathrm{e}^{-F(r)/(k_{\mathrm{B}}T)} \propto r$. According to Eq. 2.21, the radial diffusivity profile then can be reconstructed from

$$D_r(r) = -\frac{1/r}{\partial\tau_{\mathrm{fp}}(r, r_{\mathrm{t}})/\partial r} \int_0^r \mathrm{d}r'\, r' = -\frac{r}{2\partial\tau_{\mathrm{fp}}(r, r_{\mathrm{t}})/\partial r}\,. \tag{3.10}$$

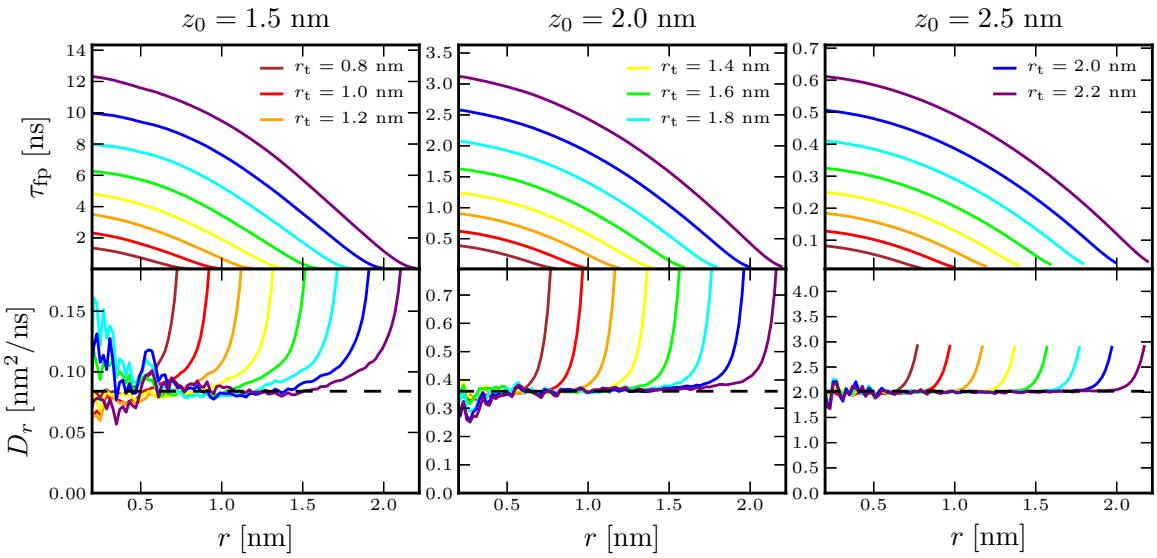

Figure 3.5:
Top panels: MFPTs to first reach a radial distance r_t from a given reference point in the lateral plane, when starting off from r; data for three distances z_0 from the membrane mid-plane are shown. Bottom panels: Corresponding lateral diffusivity profiles (*colored lines*) calculated from the MFPTs in the top panels using Eq. 3.10; diffusion coefficients obtained from the long-time MSDs in Fig. 3.3b are shown as *horizontal dashed black lines*.

Similarly to the analysis in Sec. 2.3.2, radial MFPTs are resolved with a spatial resolution of 0.01 nm and the MFPT derivatives in Eq. 3.10 are approximated by fitting straight lines to the MFPT data within intervals of 0.15 nm to minimize the influence of statistical uncertainties. The resulting diffusivity profiles for the lateral motion at different distances z_0 from the membrane center are shown in Fig. 3.5 As expected, the diffusivity profiles for different radial target distances r_t converge to a common and constant value for $r_t - r$ large enough. The estimates for the lateral diffusion coefficients from the radial MFPT analysis nicely agree with the estimates extracted from the long-time MSDs (filled colored circles in the inset of Fig. 3.3b), which are shown as horizontal dashed black line in the lower panels of Fig. 3.5.

3.3 Water Dynamics Perpendicular to the Lipid Membrane

We next turn to water diffusion perpendicular to the membrane surface, i.e., along the z-direction in Fig. 3.1a. Several methods have been used to extract diffusivity profiles in similar inhomogeneous systems before [116, 119, 142]. Here, we employ the same MFPT analysis as before to disentangle the contributions of free energy and diffusivity to the water kinetics.

The free energy $F(z)$ and MFPTs $\tau_{fp}(z, z_t)$ to first reach a target distance z_t from the membrane mid-plane given a start at z are resolved with a spatial resolution of 0.01 nm based on the trajectories of the 2278 water molecules in the unconstrained MD data. In analogy to Eq. 2.21, the diffusivity profile is then obtained via

$$D_z(z) = -\frac{e^{F(z)/(k_B T)}}{\partial \tau_{fp}(z, z_t)/\partial z} \int_{z_{refl}}^{z} dz'\, e^{-F(z')/(k_B T)}, \tag{3.11}$$

where the MFPT derivatives are again approximated by fitting straight lines to the MFPT data within intervals of 0.15 nm width to minimize the influence of statistical uncertainties, analogous to the analysis in Sec. 3.2.4. In Eq. 3.11, we impose a reflective boundary at $z_{\text{refl}} = 0.475$ nm corresponding to a value of the free energy of roughly 12 $k_{\text{B}}T$. Similarly as in Sec. 2.3.2, the precise position of the reflecting boundary has a negligible influence on the form of the resulting diffusivity profiles.

The water density $\rho(z)$, the corresponding Gibbs dividing surface (GDS) and the associated free energy profile

$$F(z) \equiv -k_{\text{B}}T \log\left(\rho(z)/\rho_0\right), \tag{3.12}$$

where $\rho_0 \approx 32/\text{nm}^3$ denotes the bulk water number density, are shown in Fig. 3.6a. MFPTs for different target distances z_{t} as extracted from MD trajectories are presented in Fig. 3.6b. Diffusivity profiles resulting from Eq. 3.11 are denoted by solid lines in Fig. 3.6c using the same color coding as in Fig. 3.6b: The diffusivity profiles reveal bulk-like dynamics in a small region in the center of the slab only as is seen from the comparison to the diffusion coefficient $D_{\text{H}_2\text{O}} \approx 3.7\,\text{nm}^2/\text{ns}$ at $T = 320$ K from Sec. 2.2.1, which is indicated by a horizontal dashed line in Fig. 3.6c. When approaching the membrane the diffusivity smoothly decreases and levels off at values $\sim 0.2\,\text{nm}^2/\text{ns}$ in the lipid head group region, about a factor 20 smaller than in bulk.

We observe that diffusivity profiles from MFPT curves for different target distances z_{t} superimpose well except for $z_{\text{t}} - z \lesssim 0.25\,\text{nm} = \delta z$. These deviations are caused by non-Markovian effects on time scales $(\delta z)^2/D_z$ ranging from ~ 10 ps in the bulk-like region of the water slab to ~ 300 ps near the lipids. The overlap of the diffusivity profiles demonstrates that perpendicular diffusion on larger length and longer time scales is Markovian and accurately described by a diffusion equation including the free energy profile.

For comparison, we also indicate the upper bounds for the lateral diffusivity $D_{\text{lat}}(z)$ from the inset of Fig. 3.3b as open circles in Fig. 3.6c. While both perpendicular and parallel diffusion are slowed down in a region with a thickness of roughly 2 nm, a significant anisotropy $D_{\text{lat}}(z)/D_z(z) < 1$ is observed in the inset of Fig. 3.6c (filled circles) close to the membrane-surface: for $z_0 = 1.5$ nm, the lateral diffusivity is $D_{\text{lat}} \approx D_z/3$ only. This observation is in marked contrast to the water dynamics at solid homogeneous interfaces discussed in the following.

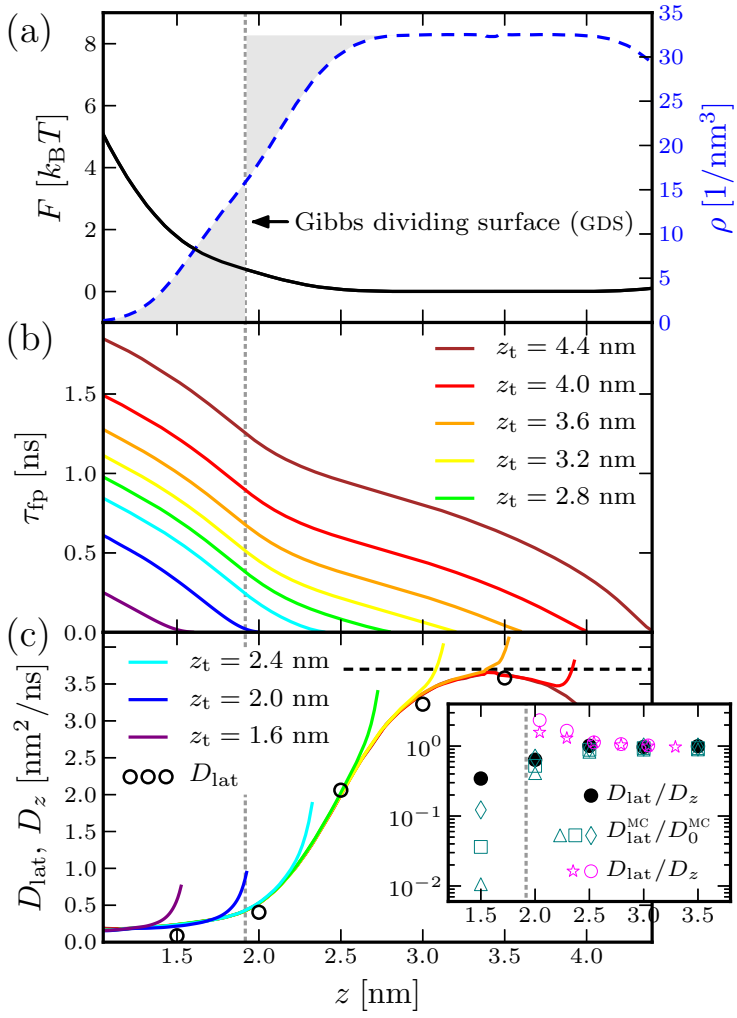

Figure 3.6:
a) Water density $\rho(z)$ and the corresponding free energy profile $F(z)$ (Eq. 3.12). b) Water MFPTs to first reach a target distance z_t when starting off from z. c) Perpendicular water diffusivity profiles $D_z(z)$ (*colored solid lines*) derived via Eq. 3.11. *Open circles* denote the long-time lateral diffusivities from the inset of Fig. 3.3b. Inset: Water diffusion anisotropy D_{lat}/D_z at the membrane (•), at solid homogeneous hydrophobic (⋆) and hydrophilic (○) surfaces (Fig. 3.7) discussed in Sec. 3.4, and lateral rescaled diffusion constant D_{lat}^{MC}/D_0^{MC} (△, □, ◇) from MC simulations (Fig. 3.11c) discussed in Sec. 3.5. The z-coordinates of the solid homogeneous surfaces have been adjusted so that the positions of the respective GDSs (vertical gray dashed line) agree.

3.4 Water Diffusion at Solid, Homogeneous Surfaces

In Fig. 3.7, we reproduce water free energy and diffusivity profiles at H- (hydrophobic) and OH-terminated (hydrophilic) diamond surfaces obtained using similar methods as described above, see Ref. [viii] for details. A corresponding simulation movie is included as supplementary material [111]. For a better comparison of the diffusivities at the lipid bilayer and at the solid homogeneous interfaces, the z-coordinates of the solid interfaces have been adjusted so that the positions of the GDSs agree for all interfaces. The position $z_{\mathrm{GDS}} \approx 1.92$ nm is indicated by gray dashed lines in the Figs. 3.6 and 3.7.

The bulk diffusion coefficient $D_{\mathrm{H_2O}} \approx 2.7\ \mathrm{nm^2/ns}$ at $T = 300$ K from Ref. [viii] is shown as horizontal dashed black line in Fig. 3.7d-f. Exactly opposite from the behavior at the lipid bilayer, the lateral diffusivity (blue squares) is larger than the perpendicular one (red circles) for all three surface polarities as expected based on continuum hydrodynamics as we show next.

3.4.1 Hydrodynamics at planar interfaces

For a comparison of water diffusivity profiles from MD simulations to estimates from continuum hydrodynamic theory for a solid no-slip sphere of radius a and bulk diffusion coefficient D_0, we set $D_0 = D_{\mathrm{H_2O}} \approx 2.7\ \mathrm{nm^2/ns}$ and $a = a_{\mathrm{hyd}}$, where the hydrodynamic radius of a water molecule is

$$a_{\mathrm{hyd}} \equiv \frac{k_{\mathrm{B}}T}{6\pi\eta_0 D_{\mathrm{H_2O}}} \approx 0.11\ \mathrm{nm}, \tag{3.13}$$

according to Stokes' law [16] and using the shear viscosity $\eta_0 \approx 0.71\ \mathrm{mPa \cdot s}$ of SPC/E water [99].

The H-terminated diamond surface used by us has been found to have a finite slip length $b \approx 2.5$ nm, the corresponding data from Ref. [99] is reproduced in Fig. 3.8a. The position of the interface in the hydrodynamic description is set to $z_{\mathrm{int}} = z_{\mathrm{GDS}} - a_{\mathrm{hyd}} \approx 1.81$ nm. Approximate expressions by Lauga and Squires [157] for the anisotropic mobilities of a no-slip sphere of radius a at a distance $h \equiv z - z_{\mathrm{int}}$ from a boundary with slip length b are reproduced in Appendix D.1: The analytical predictions for the sphere diffusivities $k_{\mathrm{B}}T\mu_{\parallel}^{\mathrm{LS}}$ (Eq. D.1) and $k_{\mathrm{B}}T\mu_{\perp}^{\mathrm{LS}}$ (Eq. D.2) are shown as solid lines in Fig. 3.7d.

As has been observed previously [99], the hydrophilic diamonds with 12.5 % and 25 % surface OH-groups used in the MD simulations are characterized by a region of increased viscosity in direct proximity of the interface, the corresponding data for 25 % OH is reproduced in Fig. 3.8b. For simplicity, we compare the diffusivity profiles to hydrodynamic theory in a medium of uniform viscosity in Fig. 3.7e-f. For this, the position of the no-slip interface is set to $z_{\mathrm{int}} = z_{v_0} - a_{\mathrm{hyd}}$. Here, z_{v_0} denotes the position, where the extrapolated shear velocity profile equals the velocity v_0 of the interface, as seen in Fig. 3.8b. The resulting positions of the interface are $z_{\mathrm{int}} \approx 2.05$ nm (12.5% OH) and $z_{\mathrm{int}} \approx 2.08$ nm (25% OH). The mobilities of a sphere of radius a at a distance $h \equiv z - z_{\mathrm{int}}$ from a no-slip wall are covered in Appendix D.2: The diffusivity profile for lateral motion is well approximated by $k_{\mathrm{B}}T\mu_{\parallel}^{\mathrm{PJ}}$ (Eq. D.6) and the one for motion perpendicular to the interface is given by $k_{\mathrm{B}}T\mu_{\perp}^{\mathrm{SJ}}$ (Eq. D.7), the corresponding expressions are drawn as solid colored lines in Fig. 3.7e-f.

Apart from oscillations in the mobilities due to molecular interfacial layering, the continuum theory is in excellent agreement with the MD data for all three surfaces in Fig. 3.7d-f. This is particularly meaningful since no adjustable fit parameter is introduced, i.e., the shear viscosity as well as the slip and stagnation lengths have independently been determined [99].

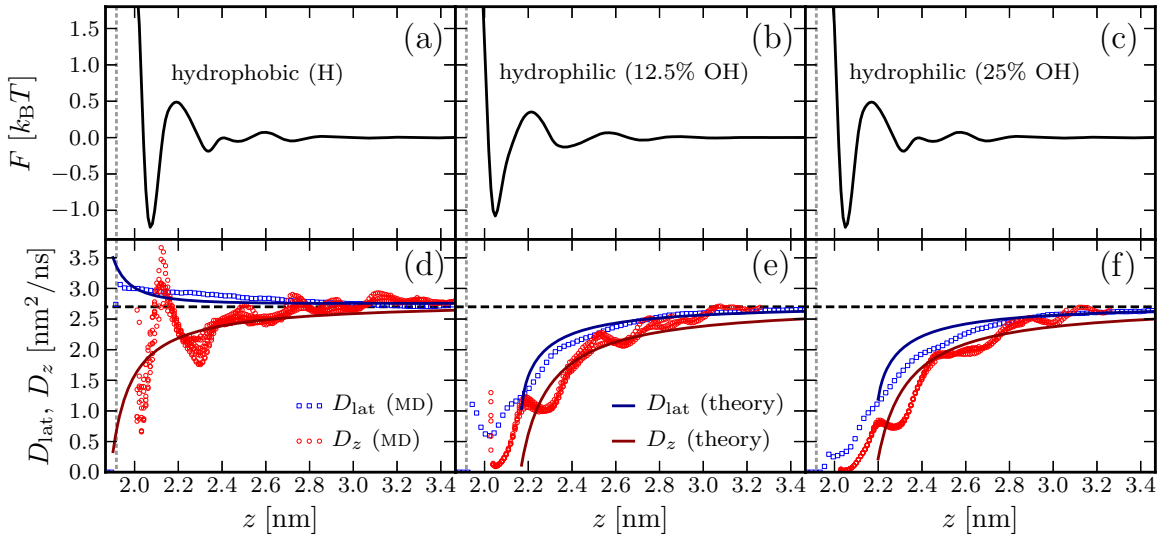

Figure 3.7:
a), b), and c) Water free energy profiles at hydrophobic/-philic solid surfaces from MD simulations [viii]. d), e), and f) Diffusivity profiles for motion parallel and perpendicular to the surfaces from MD simulations (*symbols*) [viii] and estimates from hydrodynamic theory (*lines*, cf. Sec. 3.4.1 for details); the *horizontal dashed black line* denotes the bulk diffusion coefficient $D_{H_2O} \approx 2.7$ nm^2/ns at $T = 300$ K [viii]. The *vertical dashed gray lines* denote the positions of the GDSs.

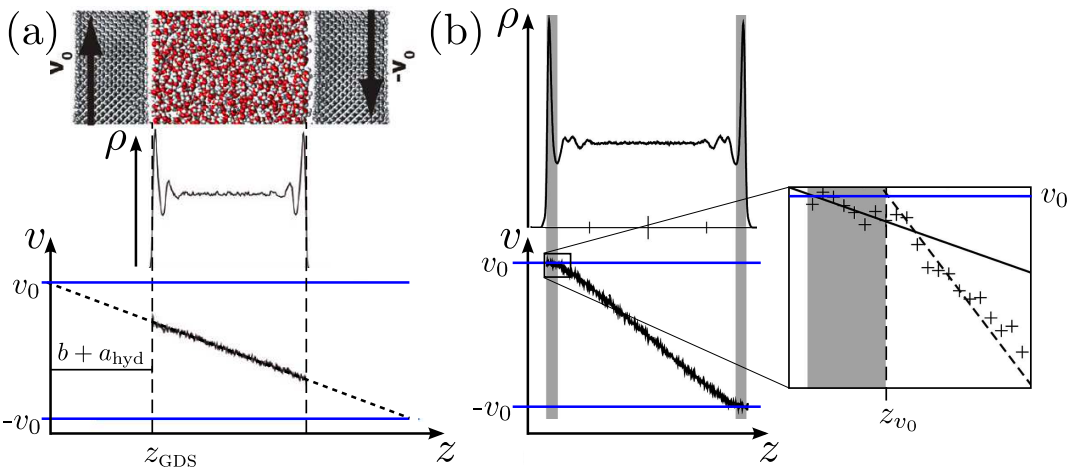

Figure 3.8:
Shear simulations of water slabs confined by hydrophobic/-philic diamond surfaces from Ref. [99]. a) Hydrophobic H-terminated diamond: Simulation setup, water density profile and water velocity profile (from top to bottom). b) Hydrophilic diamond (25% surface OH-groups): Water density profile (top), water velocity profile (bottom) and magnification of the *gray-shaded* interfacial stagnation layer. Adapted with permission from Ref. [99]. Copyright 2009 American Chemical Society.

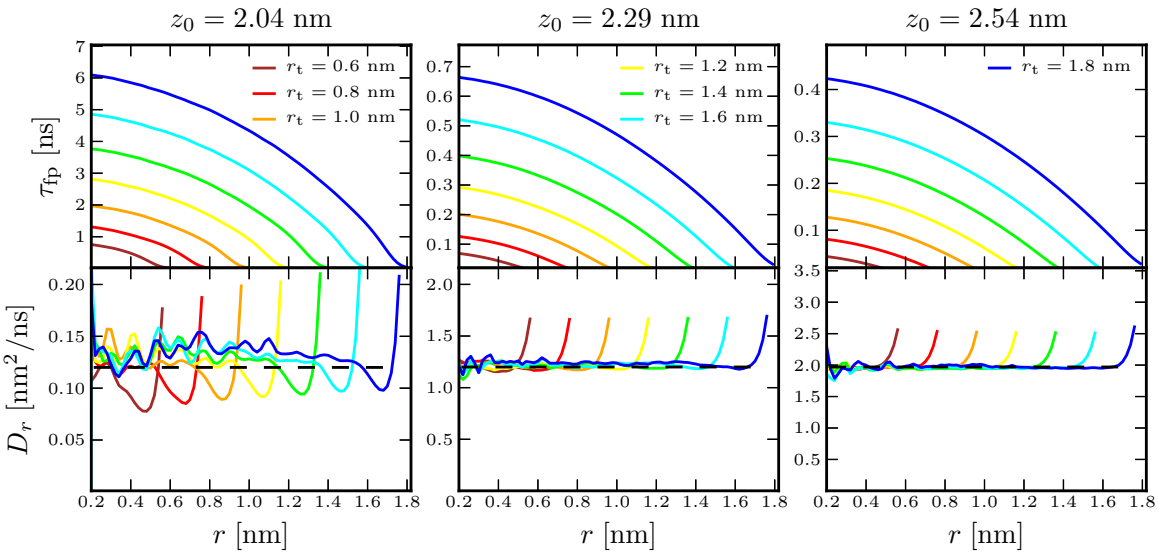

Figure 3.9: Same as Fig. 3.5 but for the lateral dynamics at the diamond with 25 % surface-OH density.

Both continuum hydrodynamics and MD simulations show that the lateral diffusivity at solid surfaces is larger than the perpendicular one, in contrast to the membrane scenario. This is highlighted in the inset of Fig. 3.6c, where we compare the ratio D_{lat}/D_z for hydrophobic and hydrophilic solid surfaces (magenta stars and magenta open circles, results have been averaged over 0.25 nm) with the membrane results (black filled circles).

3.4.2 Mean first-passage time analysis for motion parallel to a solid surface

Similarly as in Sec. 3.2.4, diffusion coefficients for the motion parallel to the solid, homogeneous surfaces can also be obtained from a radial MFPT-analysis. In the top panels of Fig. 3.9, radial MFPT-curves for the lateral motion of a subset of z-constrained water molecules in the vicinity of the diamond with 25 % surface-OH density are shown. Corresponding diffusivity profiles are displayed in the bottom panels of Fig. 3.9 and mostly fall on the dashed horizontal lines, which favorably agree with the estimates from Fig. 3.7. Note that for the molecules in the first interfacial solvent layer ($z_0 = 2.04$ nm), the overlap in the diffusivity profiles for distinct target separations r_t is worse than for larger separations z_0 from the interface; in particular, a pronounced dip in the diffusivity profiles at $r \approx r_t - 0.1$ nm is observed. The cause are the regularly distributed OH-groups on the diamond surface, which break the lateral translation symmetry, on which the analysis via Eq. 3.10 is based, on a molecular length scale.

As has been argued in Sec. 3.3, the length scale from which on the water diffusion becomes Markovian, and thus the description in terms of the usual diffusion equation adequate, is set by the distance δr, from which on the radial diffusivity profiles for various target distances r_t agree. At homogeneous, solid surfaces the length scale $\delta r \approx 0.2$ nm is independent of the distance to the interface as is seen from the bottom panels in Fig. 3.9, where for example the diffusivity profiles for $r_t = 1.4$ nm (green curves) are essentially flat for $r \lesssim 1.2$ nm for all values of z_0 shown.

In contrast, for motion parallel to the lipid bilayer the values for δr depend on the distance z_0 from the membrane mid-plane: As is seen from the bottom panels of Fig. 3.5, the diffusivity profile for $r_t = 1.6$ nm (green curve) is constant for $r \lesssim 1.4$ nm at a distance $z_0 = 2.5$ nm, whereas for $z_0 = 1.5$ nm convergence is observed for values $r \lesssim 1$ nm only. The Markovianity length scale thus increases from values around $\delta r \approx 0.2$ nm for $z_0 = 2.5$ nm to $\delta r \approx 0.6$ nm for $z_0 = 1.5$ nm indicating an influence of the interface on the character of the lateral motion. The associated time scales $(\delta r)^2/D_{\mathrm{lat}}$ range from ~ 20 ps for $z_0 = 2.5$ nm to ~ 4 ns for $z_0 = 1.5$ nm in agreement with the time scales for the transition to normal diffusion with exponent $\alpha = 1$ observed in the lateral MSD curves (Fig. 3.3a). The increase of δr when approaching the membrane reflects the increasing transient lateral heterogeneity imposed by the lipids, which is studied in further detail below.

3.5 Influence of the Lateral Bilayer Structure

To understand the discrepancy between water diffusion next to solid, homogeneous surfaces, where the anisotropy $D_{\mathrm{lat}}/D_z > 1$ is in agreement with boundary hydrodynamic theory, and in the lipid interfacial region, where an anisotropy $D_{\mathrm{lat}}/D_z < 1$ and a markedly increased length scale δr are observed, we examine the lateral bilayer structure. For this, we calculate lateral water density profiles $\overline{\rho}_{z_0,\tau}(x,y)$ that are averaged over a time τ for different distances z_0 from the membrane mid-plane as described in Sec. 3.1.2.

The lateral water density profiles $\overline{\rho}_{z_0,\tau}(x,y)$ in Fig. 3.10 reveal a transient heterogenous and strongly structured water distribution: In particular for $z_0 = 1.5$ nm and $z_0 = 2$ nm, the density profiles are characterized by a considerable roughness and fractal structure remaining nearly invariant on time scales of up to hundreds of picoseconds, while the densities in the bulk region of the water slab ($z_0 = 3.5$ nm) show small statistical fluctuations only, which quickly average out.

To estimate the effect of the bilayer structure and dynamics on the lateral water diffusion, we perform MC simulations in the two dimensional free energy landscapes $F_{z_0,\tau}(x,y)$ defined in Eq. 3.1 as described in Sec. 3.1.2. MC trajectories serve to calculate lateral MSDs by computing time and ensemble averages (Eq. 3.4). In the case, where the density profiles divide up into separate partitions, trajectories are initiated in each of them and MSDs are calculated from a weighted average of the MSDs in the individual partitions. The statistical weights are proportional to the relative number of water molecules in the partitions so that the lateral distributions of water molecules in the MC trajectory ensemble and in the density profiles from MD simulations agree.

Lateral MSDs (Eq. 3.4), corresponding exponents α (Eq. 3.8) and time-dependent diffusion coefficients (Eq. 3.9) from MC simulations are shown in Fig. 3.11a-c. For $z_0 \lesssim 2.0$ nm, the lateral MSDs in the MC simulations are characterized by a pronounced subdiffusive regime and a decreased long-time diffusion coefficient, which both are characteristic features for obstructed diffusion in rough environments [136, 137]. Both the distance from the membrane z_0 as well as the choice of the averaging time τ affect the MSD curves: The density profiles $\overline{\rho}_{z_0,\tau}$ being considerably rougher for short averaging times, MSD values, local exponents and diffusion coefficients are reduced compared to larger values of τ, for which the profiles are "washed out" and lateral motion in the MC simulations therefore faster. A similar dependency is observed when changing the lateral cell dimensions δx and δy (data not shown).

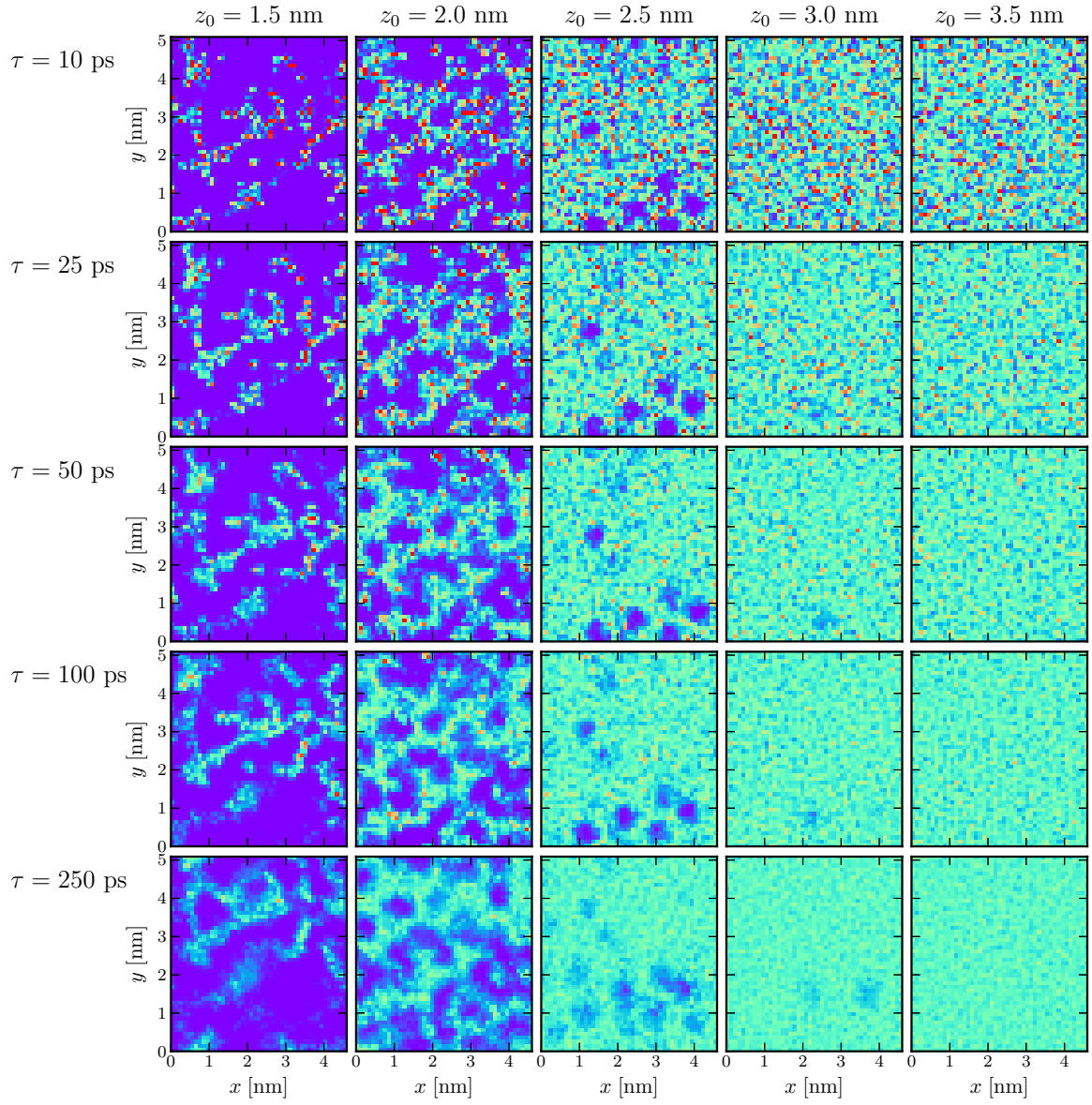

Figure 3.10:
Water number densities $\overline{\rho}_{z_0,\tau}$ averaged in z-direction over $|z - z_0| \leq 0.25$ nm and times τ ranging from 10 ps (top) to 250 ps (bottom) for distances from the membrane mid-plane ranging from $z_0 = 1.5$ nm (left) to $z_0 = 3.5$ nm (right). Lateral cell dimension are $\delta x \approx \delta y \approx 0.1$ nm and the *color coding* denotes water densities ranging from 0 (*purple*) to 75 nm^{-3} (*red*), cf. the legend in Fig. 3.2.

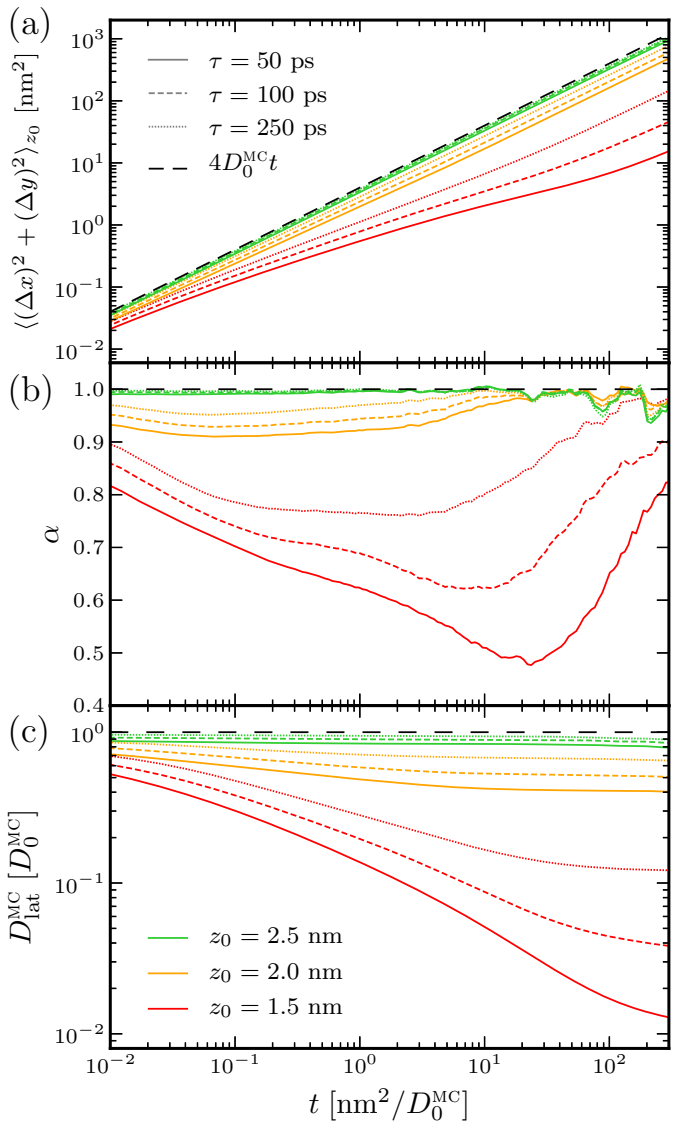

Figure 3.11:
a) Lateral MSDs (Eq. 3.4), b) corresponding local exponents (Eq. 3.8), and c) time-dependent diffusion coefficients (Eq. 3.9) from lattice MC simulations in density profiles $\overline{\rho}_{z_0,\tau}(x,y)$ for various averaging times τ and lateral bin dimensions $\delta x \approx \delta y \approx 0.1$ nm as shown in Fig. 3.10. In all panels, the *colors* indicate the distance z_0 from the membrane, analogous to the Figs. 3.3 and 3.4. Time is given in units of nm^2/D_0^{MC}, where D_0^{MC} denotes the bare diffusion coefficient in the MC simulations. The *dashed black lines* correspond to the MSD $4D_0^{\mathrm{MC}}t$ of normal diffusion in a homogeneous environment.

Because of the above sensitivity on the parameters drawing quantitative conclusions from the MC simulations is difficult. Moreover, the overall match of water dynamics in the MD and MC simulations would require time-dependent free energy landscapes. Nevertheless, the MC results clearly show that the roughness and fractal structure of the density profiles indeed gives rise to a ratio $D_{\mathrm{lat}}^{\mathrm{MC}}/D_0^{\mathrm{MC}}$ significantly smaller than one and to a pronounced subdiffusive regime in the MSDs with crossover times to diffusive dynamics increased by up to several orders of magnitude. The long-time ratios $D_{\mathrm{lat}}^{\mathrm{MC}}/D_0^{\mathrm{MC}}$ from Fig. 3.11c are shown as open triangles ($\tau =$ 50 ps), squares ($\tau = 100$ ps) and diamonds ($\tau = 250$ ps) in the inset of Fig. 3.6c. Note that the water diffusion anisotropy from the MC simulation, which comprises the obstructing free energy landscape due to the inhomogeneous lipid distribution but no hydrodynamic effects, is more pronounced than the anisotropy extracted from the membrane simulations (filled circles).

3.6 Conclusions

Summarizing, we have resolved both the lateral and the perpendicular diffusivity profile of water molecules next to a lipid bilayer. We find that the diffusivities of the membrane hydration water are reduced by more than one order of magnitude compared to bulk water. Furthermore, in contrast to solid, homogeneous surfaces, the lateral water diffusion next to the membrane is considerably slower than the perpendicular one.

The observed diffusion anisotropy of membrane hydration water results from the interplay of two competing effects: (i) Continuum hydrodynamics alone (Sec. 3.4.1) speed up the lateral diffusion compared to the perpendicular one, irregardless of the surface polarity, as confirmed by our MD simulations at solid homogeneous surfaces, implying $D_{\mathrm{lat}}/D_z > 1$, while (ii) the lateral diffusion dynamics are considerably slowed down by the transient but long-lived free energy landscape imposed by the lipids, implying $D_{\mathrm{lat}}/D_z < 1$, as shown by our coarse-grained MC simulations without hydrodynamics (Sec. 3.5). As seen in the inset of Fig. 3.6c, both effects roughly compensate for $z \gtrsim 2.5$ nm yielding almost isotropic diffusive properties, while the second effect dominates for $z \lesssim 2.5$ nm giving rise to a pronounced anisotropy with $D_{\mathrm{lat}}/D_z <$ 1 in the vicinity of the lipid leaflet.

Our findings imply that efficient transport parallel to the membrane surface necessarily also involves fluctuations perpendicular to the lipid leaflet as shown in Fig. 3.1b. In turn, attraction towards the lipid bilayer would constitute a simple mechanism for significantly suppressing lateral diffusive motion. We expect our results also to be relevant for the diffusion of solutes at the surfaces of proteins or other structured biological surfaces and to have implications for surface binding and reaction kinetics [158].

CHAPTER 4

ION-SPECIFICITY OF PEPTIDE CONFORMATIONAL DYNAMICS

Bibliographic information: Parts of this chapter have previously been published. Reprinted with permission from Ref. [vii]. Copyright 2010 American Chemical Society.

The application of stochastic concepts based on the Fokker-Planck (FP) equation are not restricted to the diffusional dynamics of solute and solvent molecules discussed in the preceding chapters. Indeed, the complex problem of protein folding is typically also interpreted in terms of a diffusive search through an effective, low-dimensional free energy landscape, where most of the countless degrees of freedom of the system have been integrated out [70–75]. In this scenario the effective diffusivity (or friction) arising from intrapeptide and peptide-solvent interactions as well as from orthogonal degrees of freedom typically varies considerably along the reaction coordinate (RC) [115][x]. In general, the internal friction constitutes a major contribution to the friction, so that solvent viscous drag and solvent-peptide interactions are not the only mechanisms that govern protein kinetics [159, 160]. Internal and solvent-induced friction processes may even be intimately connected as was demonstrated for the loop formation rate of unfolded peptides, where the strongly denaturing salt guanidine hydrochloride modifies internal friction by specific binding mechanisms [161, 162].

The investigation of the salt-specific action on proteins in general ("Hofmeister effects") has a long history [163] but the underlying mechanisms are still under exploration [164, 165]. In a recent series of experiments, for example, it has been shown that even the simple cations sodium (Na^+) and potassium (K^+) exhibit considerably different behavior in the interaction with protein surfaces, where Na^+ is favored over K^+ [166–168]. One apparent reason is the stronger attraction of sodium to acidic (anionic) surface groups, in particular to carbonyl and side chain carboxylate groups. While these static properties have received much attention lately [169], not much is known about their consequences to biomolecular kinetics. Experimental hints have been given in studies of Na^+- and K^+-specific polyglutamic acid aggregation kinetics [170], folding kinetics of halophilic ("salt-loving" and very acidic) proteins [171, 172], or DNA [173]. However, a detailed molecular understanding of the ion-specific action on biomolecular folding and assembly kinetics is still lacking. In particular for large concentrations ($c \gtrsim 1$ mol/l) salt effects are pronounced, highly sequence and salt-type specific; they typically lead to changes in protein solubility, stability, and/or denaturation that result in the so-called Hofmeister series for

the precipitation of proteins [163]. Although an order of magnitude higher than at typical physiological conditions ($c \sim 0.2$ mol/l), large salt concentrations play a central biochemical role in the broad field of protein crystallization [174], in food industry as fermentation additives [175], and for the function and stability of biotechnologically interesting halophilic (salt-loving) enzymes [176]. Additionally, the study of protein structures in high salinity solvents is instructive as salt-specific effects are amplified and, important from a computational perspective, can be sampled more efficiently in molecular dynamics (MD) simulations, a popular tool nowadays for the theoretical study of protein folding, function, and stability [177].

A ubiquitous and fundamental secondary structure element of proteins is the α-helix, which is stabilized by $(i, i+4)$ backbone hydrogen-bonds involving four amino acids (aa) per turn. The majority of short ($\lesssim 20$ aa) isolated helices derived from proteins are unstable in solution, unless specific side-chain interactions stabilize them. Among those it has been demonstrated that alanine-based peptides have the strongest intrinsic helix propensity [178–182]. A very instructive model peptide was experimentally introduced by Marqusee and Baldwin [178], who showed that alanine-based oligopeptides with an A(EAAAK)$_n$A pattern display a high α-helix propensity, which is probably stabilized by Glu^- (E) and Lys^+ (K) salt bridges along the folded peptide. Marqusee and Baldwin also found that the simple salt NaCl has a destabilizing effect on the α-helical configurations of these peptides. Indeed, in a recent explicit-water MD computer simulation [183] the structural behavior of the oligopeptide Ace-AEAAAKEAAAKA-Nme, in the following named the "EK" peptide, has been explored in detail, and the stabilizing and destabilizing mechanisms in various highly concentrated aqueous electrolyte solutions have been identified. Amongst others, it has been found that sodium (Na^+) destabilizes the helical structure more strongly than potassium (K^+); it was also previously recognized that the reason for the destabilization of the salt bridges and the hydrogen-bonds of the secondary structure lies in the higher affinity of Na^+ to carboxylate and carbonyl groups. In a recent follow-up study, the folding kinetics of the EK-peptide in pure aqueous solution have been investigated and interpreted in terms of diffusion in a reduced (one-dimensional) free energy landscape involving a local coordinate-dependent diffusivity [x].

The aim of this chapter is to extend these previous studies on the "EK"-peptide to the investigation of the specific effects of the salts KCl, NaCl, and NaI on peptide α-helical folding and unfolding kinetics. In particular, we explore how salts alter the mean folding and unfolding times and look for possible molecular reasons. Strong salt-specific effects are found in the mean folding times, which can be attributed to the binding of individual ions to multiple, anionic peptide groups inducing transient cross-links between peptide fragments. In consequence, not only equilibrium distributions of configurations are modified but also new, slow time scales in the peptide's configurational mobility arise due to enhanced internal friction. Salt effects are thus reflected in both modified free energy landscape and local changes of the effective diffusivity; our results demonstrate the highly specific action on protein folding kinetics by the individual binding of ions and, more generally, exemplify the intimate coupling between solvent and intrapeptide friction effects in protein folding. We believe that these mechanisms could be of general importance and transferable to a variety of biomolecular and polyelectrolyte systems.

The chapter is organized as follows: The simulation and analysis methods are introduced in Sec. 4.1 and the results are presented in Sec. 4.2, before being comprehensively discussed in Sec. 4.3. Our main findings are summarized in Sec. 4.4.

4.1 Methods

4.1.1 Molecular dynamics simulations

Our MD simulations are performed using the parallel module *sander.MPI* in the simulation package Amber9.0 with the ff03 force field for the peptides and the rigid and nonpolarizable TIP3P water for the solvent [184]. All simulated systems are maintained at a fixed pressure of $P = 1$ bar and a temperature $T = 300$ K by coupling to a Berendsen barostat and Langevin thermostat [184], respectively. The cubic and periodically repeated simulation box of edge length $L_b \simeq 3.6$ nm includes approximately 1500 water molecules. Electrostatic interactions are calculated by particle mesh Ewald summation, and all real-space interactions (electrostatics and van der Waals) have a cutoff of 0.9 nm. The peptide is generated using the *tleap* tool in the Amber package [184].

We investigate the helical folding and unfolding behavior of a 12 amino acid long peptide with the acetyl (Ace) and amine (Nme) capped sequence Ace-AEAAAKEAAAKA-Nme. This peptide can form three α-helical turns in the fully folded state, where Glu2 and Lys6, and Glu7 and Lys11, are potentially able to form a salt bridge, respectively [183]. The influence on α-helix folding kinetics of a large concentration of $\simeq 3.6 \pm 0.1$ mol/l of the simple monovalent salts NaCl, KCl, and NaI is investigated. We have simulated the system without salt for approximately 1.35 μs and including salt for roughly 2 μs for each salt type. We note here that the free energy along the RC q (see below) derived from replica-exchange MD trajectories at $T = 300$ K for the salt-free system gives very good agreement to the brute force approach [x], indicating a decent statistical sampling by our trajectories.

The considered salt concentrations result from 90 ion pairs in the simulation box. Cations and anions are modeled as nonpolarizable Lennard-Jones spheres with charge and interaction parameters as supplied by Dang [185], as the default Amber parameters are known to be faulty [186]. The Dang parameters show reasonable bulk thermodynamic properties in SPC/E water even for high concentrations [187]. Comparative calculations in TIP3P water show only small differences in hydration structure and no qualitative difference in the binding to peptide groups [188]. The parameters used are summarized in previous work on the equilibrium structure of the EK peptide in salt at a different temperature [183]. We are aware of the weaknesses of ionic MD force fields for quantitative predictions in biomolecular simulations, although a reasonable description of helicity and destabilization with NaCl has been observed when compared to experiments [183]. Since the destabilization seems to be overemphasized for NaCl, we do not claim to be quantitative in our work but focus on the discussion of the main effects and qualitative trends with the addition of salt; we believe these to be insensitive to the particular force field and relevant for a variety of experimental observations.

The MD simulations analyzed in this chapter have been performed by Prof. Dr. Joachim Dzubiella from the Helmholtz Zentrum Berlin and Humboldt University Berlin and Dr. Immanuel Kalcher from the Technical University of Munich.

4.1.2 Helicity and reaction coordinate

The trajectory analysis is performed using the *ptraj* tool in the Amber9.0 package [184]. The helicity, i.e., the α-helical fraction, is identified using the DSSP method by Kabsch and Sander [189]. We focus on the RC Q, which is defined as the root mean square distance from a fully helical reference structure, i.e., a structure with helicity equal to one, averaged over all atoms of the

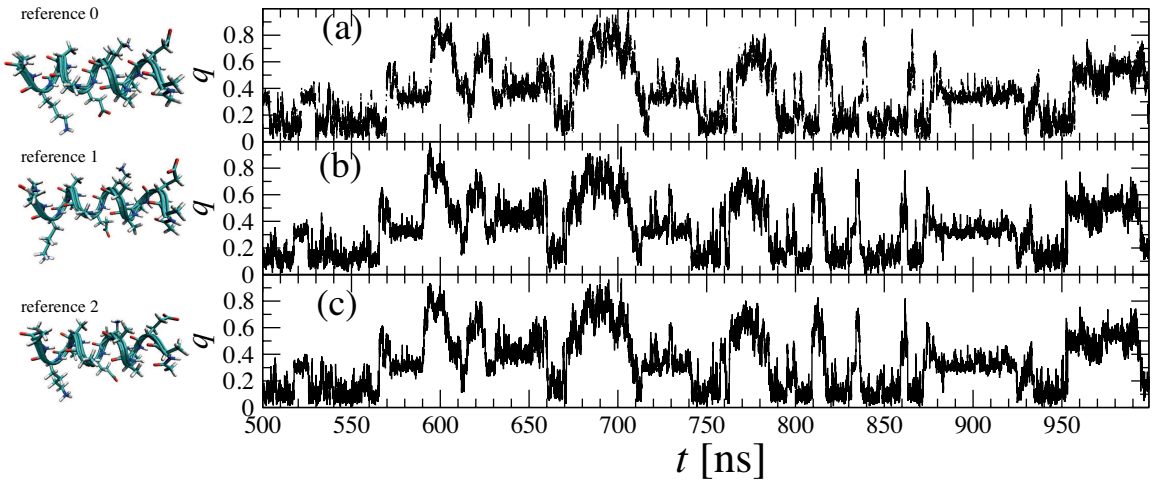

Figure 4.1:
Left: Three reference structures. *Right*: Time series of the RC q for these choices of the reference structures in the salt-free case. a) reference 0, b) reference 1, c) reference 2. The reference structures deviate from each other mainly in the arrangement of the E and K side chains. Reference 0 is the structure used for the kinetic analysis within this chapter.

peptide and which thus measures the deviation from the "native" state. This quantity was previously found to act as an adequate dynamic RC in the salt-free case [x].

Trajectories are recorded with a resolution of 20 ps, giving a total of $\sim$ 67500 data points for the simulations without salt and roughly 100000 data points for the runs including salt. For convenience, we define a rescaled RC by $q = (Q - Q^{\min})/(Q^{\max} - Q^{\min})$, so that the minimal and maximal values of the data points, denoted as $Q^{\min}$ and $Q^{\max}$, are projected on the RC values $q = 0$ and $q = 1$, respectively. The absolute minimum and maximum RC values are similar for all systems and are $Q^{\min} \simeq 0.1$ nm and $Q^{\max} \simeq 0.8$ nm.

To check the sensitivity of our results on the microscopic reference structure used for the definition of the RC, we calculated time series $q(t)$ for three different structures for the salt-free case. As is clearly seen from Fig. 4.1, the specific choice only has a minor influence on the form of the resulting time series, which therefore yield the same kinetic behavior. Similarly, we only observed a marginal influence of the reference structure on the resulting free energy landscapes, i.e., local variations on the order of fractions of the thermal energy $k_B T$, as shown in Fig. 4.2.

4.1.3 Bulk shear viscosities

In order to get a more complete picture of the solvent properties, we calculate bulk shear viscosities for NaCl, KCl, and NaI at the relevant concentrations in TIP3P water. We employ the same ionic force fields as above but perform the simulations with the GROMACS 4.0 [91, 92] package due to the implemented viscosity calculation methods. In these simulations, the periodically repeated box has an edge length of $L_b \simeq 4$ nm, with a total number of 1910 water molecules and 135 ion pairs. For the pure water simulation we use 2180 water molecules. After *NPT*-

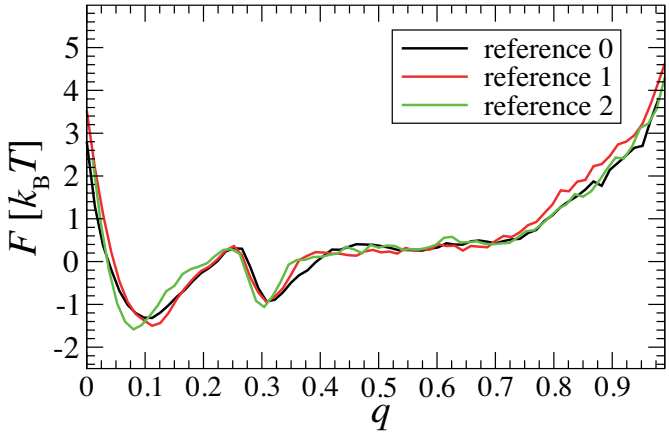

Figure 4.2: Free energy landscapes resulting from the same reference structures as in Fig. 4.1.

equilibration we proceed with an NVT-production run of 50 ns. We compare two approaches to calculate the viscosity: First, we employ the Green-Kubo (GK) formula [190, 191]

$$\eta_0 = \frac{V}{k_B T} \int_0^\infty \langle \sigma_{xz}(t_0)\sigma_{xz}(t_0+t)\rangle_{t_0} \, \mathrm{d}t, \tag{4.1}$$

involving an off-diagonal component, e.g., σ_{xz}, of the stress tensor only. We obtained averaged viscosities over a correlation time of 5 to 20 ps. The latter choice reflects the fact that the viscosity converges rapidly but exhibits large statistical errors for long correlation times [192]. Second, we perform a nonequilibrium perturbation method [190], in which an external force is applied in the NVT-simulation with the periodic acceleration profile

$$a_x(z) = A \cos\left(2\pi \frac{z}{L_b}\right), \tag{4.2}$$

L_b being the edge length of the box. The amplitude A needs to be chosen small enough in order not to drive the system out of the linear response regime and at the same time large enough to yield a decent signal-to-noise ratio. We set the amplitude to $A = 0.02\ \mathrm{nm \cdot ps^{-2}}$ and refer to previous work [190] for a more detailed discussion. We then obtain the viscosity by calculating the average velocity profile of all particles [190].

With the GK formula we find values of $\eta_0 = (0.31 \pm 0.01) \times 10^{-3}\ \mathrm{kg/(m \cdot s)}$ for pure TIP3P water, corroborating with previous studies [193], and $\eta_0^{\mathrm{salt}} = 0.58$, 0.74, and $(0.6 \pm 0.01) \times 10^{-3}\ \mathrm{kg/(m \cdot s)}$ for the KCl, NaCl, and NaI solutions at a concentration of 3.6 mol/l, respectively. The periodic perturbation method yields the same results within a 5% error range. Compared to experimental values [194] the MD simulation considerably overemphasizes the increase of the viscosity at this elevated salt concentration; indeed, the viscosity has experimentally been found to increase by only roughly 5% for KCl and $30 - 40$% for NaCl and NaI compared to pure water. This failure in describing the correct bulk viscosities of the electrolyte solutions must be attributed to inaccuracies in the force field. Note that the value for pure TIP3P water already considerably deviates from the experimental value $0.893 \times 10^{-3}\ \mathrm{kg/(m \cdot s)}$ at 298.15 K [195] by more than a factor of two.

4.1.4 Diffusional analysis

Similarly to Sec. 2.3.1, we assume that the stochastic time evolution of the probability $P(q,t)$ of finding a configuration with RC value q at time t is described by the one-dimensional FP equation [196]

$$\frac{\partial}{\partial t}P(q,t) = \frac{\partial}{\partial q}\left(D(q)\,\mathrm{e}^{-F(q)/(k_\mathrm{B}T)}\frac{\partial}{\partial q}\left(\mathrm{e}^{F(q)/(k_\mathrm{B}T)}\,P(q,t)\right)\right), \tag{4.3}$$

where $D(q)$ is the (in general q-dependent) diffusivity and $F(q) = -k_\mathrm{B}T\ln\langle P(q)\rangle$ is the free energy obtained by Boltzmann-inversion of the time-averaged normalized probability density function $\langle P(q)\rangle$. Similarly as in Ref. [x], we define round-trip times (RTTs)

$$\tau_\mathrm{RT}(q,q_\mathrm{t}) \equiv \mathrm{sign}(q-q_\mathrm{t})[\tau_\mathrm{fp}(q,q_\mathrm{t}) + \tau_\mathrm{fp}(q_\mathrm{t},q)], \tag{4.4}$$

which specify the average time needed for an excursion starting at q, reaching q_t at least once, and returning to q for the first time. Similarly as in Sec. 2.3.1, MFPTs for transitions starting at q and reaching q_t are denoted by $\tau_\mathrm{fp}(q,q_\mathrm{t})$ in Eq. 4.4. For a diffusive process described by the FP equation (Eq. 4.3) the RTT is given by the integral

$$\tau_\mathrm{RT}(q,q_\mathrm{t}) = \int_{q_\mathrm{t}}^{q}\mathrm{d}q'\,\frac{\mathrm{e}^{F(q')/(k_\mathrm{B}T)}}{D(q')}\int_0^1\mathrm{d}q''\,\mathrm{e}^{-F(q'')/(k_\mathrm{B}T)} = \int_{q_\mathrm{t}}^{q}\mathrm{d}q'\,\frac{1}{D(q')\langle P(q')\rangle}, \tag{4.5}$$

which is derived from Eq. 4.4 and the MFPT-formula in Eq. 2.20. Though Eq. 4.5 can in principle be inverted to obtain the diffusivity profile $D(q)$ from the slope of the RTT curves [x], we choose a complementary analysis method here to avoid artifacts due to insufficient statistical sampling. The FP approach assumes an underlying Markovian process and, as is easily seen from Eq. 4.5, RTT curves (as a function of q) for different target points q_t therefore only differ by a constant

$$\tau_\mathrm{RT}(q,q_\mathrm{t}) = \tau_\mathrm{RT}(q,q_\mathrm{t}') + \tau_\mathrm{RT}(q_\mathrm{t}',q_\mathrm{t}). \tag{4.6}$$

The assumption of Markovian behavior however generally breaks down at short times and for unsuitable RCs, i.e., RCs that do not single out the transition state as explicitly shown in Chapter 2 and Ref. [x].

In our analysis of the simulation time series $q(t)$ we discretize the RC in $N = 50$ intervals centered around $q^{(i)} = (2i-1)/100,\ i \in \{1,2,\ldots,50\}$; MFPTs between all possible pairs of bins are extracted from simulation data and converted into RTTs using Eq. 4.4. To simplify the analysis, we assume a flat diffusivity within each of the following regions: (i) values of the RC $q < q_{2/3}$ corresponding to an almost perfectly folded helix, (ii) one or two unfolded helical turns equivalent to $q_{2/3} \le q < q_{1/3}$, and (iii) mostly unfolded states characterized by RC values $q \ge q_{1/3}$, where the indices 1/3 and 2/3 denote the average helicity at these q-values. The values of the diffusivity in those three regions are used as fit parameters in Eq. 4.5 to best reproduce the RTT curves obtained from simulation data; the integral in Eq. 4.5 is computed numerically by linear interpolation of $\{\langle P(q^{(i)})\rangle\}_{i=1}^{50}$. Best fits to the round-trip data for different target points q_t allow the determination of the diffusivity (including an error estimate) for each

of the three regions. Alternatively, the diffusivity profile can also be obtained by fitting to the average RTT

$$\overline{\tau}_{\mathrm{RT}}(q^{(j)}) \equiv \frac{1}{N}\sum_{i=1}^{N}\tau_{\mathrm{RT}}(q^{(j)}, q^{(i)}), \tag{4.7}$$

which is less affected by statistical noise and which according to Eq. 4.6 is just shifted vertically with respect to the round-trip curve $\tau_{\mathrm{RT}}(q, q_{\mathrm{t}})$ for a specific target position q_{t}. The results of both fitting procedures are shown and discussed in Sec. 4.2.3.

4.2 Results

4.2.1 Equilibrium free energy landscapes

The RC time series of all investigated systems are shown in Fig. 4.3, where numerous folding and unfolding transitions on different time scales are discernible. Already at a first glance longer time scales (and fewer folding and unfolding transitions) are observed in the systems with the sodium salts, which will be quantified and discussed in more detail in the following. Free energy profiles $F(q)$ of all investigated systems are extracted from the trajectories $q(t)$ and plotted in Fig. 4.4 together with the (time-averaged) helicity resolved along the RC. In the salt-free case (black curve) in Fig. 4.4a, three minima are clearly visible: one at $q_1 \simeq 0.1$, a second at $q_2 \simeq 0.32$, and a third, shallow one at $q_3 = 0.58$. Judging from the helicity vs q, plotted in Fig. 4.4b, these minima seem to correspond mainly to (1) a full helix with three turns, (2) a partially unfolded helix with two neighboring turns, and (3) one helical turn as well as fully unfolded states. Representative simulation snapshots taken at corresponding q_i-values ($i = 1, 2, 3$) confirm this view and are shown in Fig. 4.4b. We note that the value of q_1, which in absolute units corresponds to $Q_1 \simeq 0.16$ nm, deviates from 0 (the reference state) due to thermal fluctuations.

For KCl, the free energy $F(q)$ is slightly shifted to favor unfolded states at larger q-values ($q_3 \simeq 0.67$), while the main features remain the same as without salt. The total helicity decreases slightly from 62% to 55%. For the sodium salts, NaCl and NaI, the fully folded state at q_1 becomes metastable, and the distribution is strongly shifted to the partially and fully unfolded states. In particular, the third minimum at q_3 deepens and broadens. Also in the systems with salt the minima mostly match with partially folded α-helical states as can be judged from the helicity vs q curve. All total helicities and positions of the minima in $F(q)$ are summarized in Tab. 4.1.

system	helicity	q_1	q_2	q_3	$q_{2/3}$	$q_{1/3}$
no salt	0.62	0.11	0.31	0.57	0.34	0.56
KCl	0.55	0.10	0.32	0.67	0.35	0.65
NaCl	0.39	0.08	0.28	0.59	0.30	0.52
NaI	0.34	0.09	0.31	0.65	0.32	0.53

Table 4.1:
Total helicity of the investigated systems and helicity at the positions in the free energy landscape shown in Fig. 4.4: locations of local minima are denoted by q_i, $i = 1, 2, 3$, and values of the RC, where the average helicity is $2/3$ or $1/3$, by $q_{2/3}$ and $q_{1/3}$ respectively.

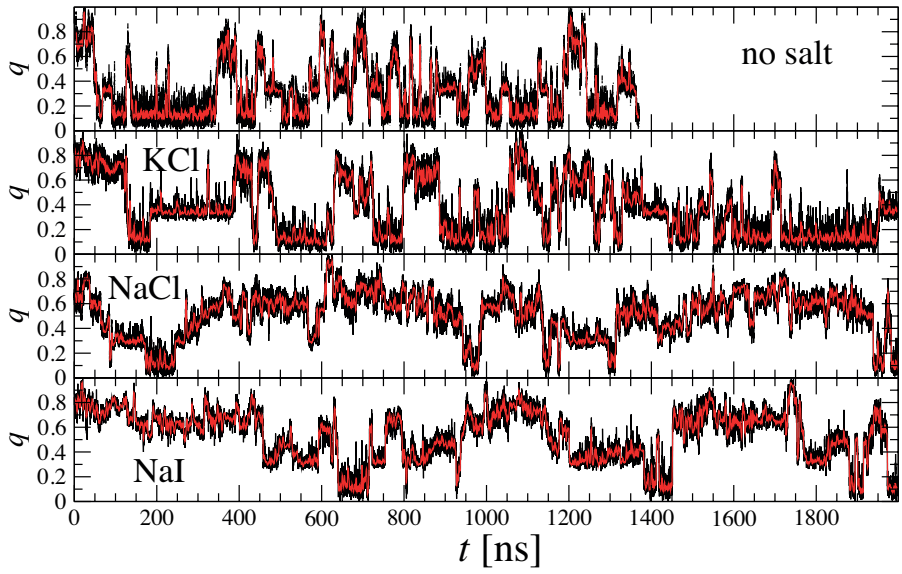

Figure 4.3:
Time series data for reaction coordinate q from the MD simulations in explicit water with varying salt type. Data in *black* shows the full 20 ps resolution, while data in *red* is smoothed over time windows of 2 ns.

For the NaCl and NaI salts the total helicity significantly decreases to about 39% and 34%, respectively. The main causes have been discovered previously [183] and are twofold: First, specific Na^+-binding to the glutamic acid side chain carboxylates interferes with EK salt bridging, and second, the binding of cations to backbone carbonyls perturbs secondary-structure forming hydrogen bonds [183]. In comparison to Na^+, the specific binding of K^+ is weak, and KCl thus behaves less destabilizing. We note that quantitatively these effects are force field dependent while the binding trends have been corroborated in many experiments and various simulation studies [166–168]. For completeness, we plot radial distribution functions $g(r)$ between the cations and the oxygen atoms from the backbone carbonyls and side chain carboxylates in Fig. 4.5: the dominance of sodium over potassium binding to the anionic peptide groups is obvious.

4.2.2 Long-lived structures and specific ion binding

Previous work on the EK-peptide stability in salt solution [183] revealed that due to Na^+-binding long-lived loop-forming configurations occupy the region of intermediate to large q-values, in addition to one-turn and random coil states also present without salt. In these looped configurations a single Na^+-ion is collectively trapped by a few peptide backbone carbonyls and side chain carboxylates. This leads to a partial wrapping of the oligomeric backbone around the ion. From a superficial inspection of our trajectories we find that these long-lived configurations involving tightly bound Na^+-ions can be stable on a $\simeq$ 1-10 ns time scale. Representative simulation snapshots which are dynamically selected, so that they exist for more than 2 ns are shown in Fig. 4.6: A sodium ion is bound and wrapped by the central part of the peptide, while the terminal parts exhibit partial helical turns in Fig. 4.6a. The bound sodium "locks"

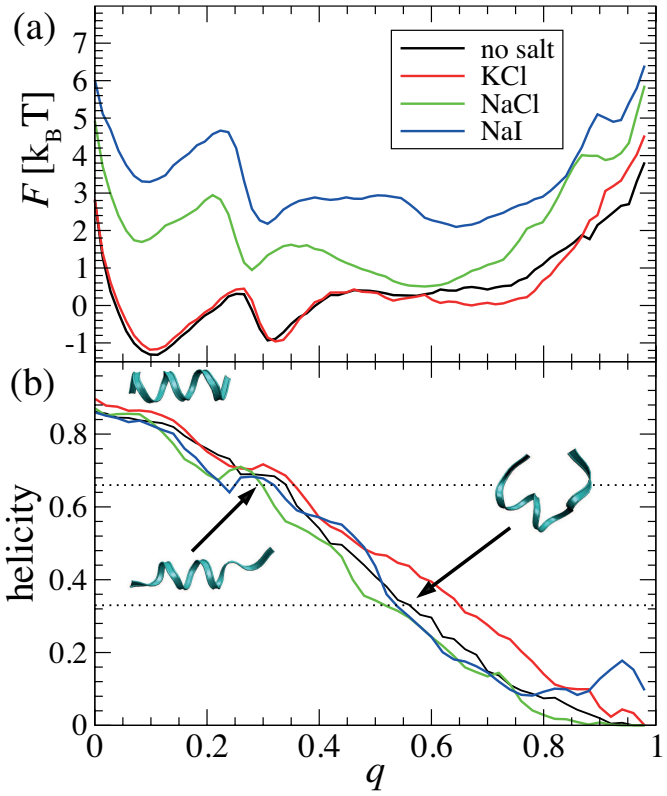

Figure 4.4:
a) Free energies $F(q)$ for the EK peptide in different salt solutions; the profiles are shifted vertically for better comparison. b) Average α-helicity of the peptide resolved by q. The snapshots illustrate the backbone structure of partially folded/unfolded states corresponding to values of the helicity indicated by arrows. Simulation snapshots are visualized using VMD [110].

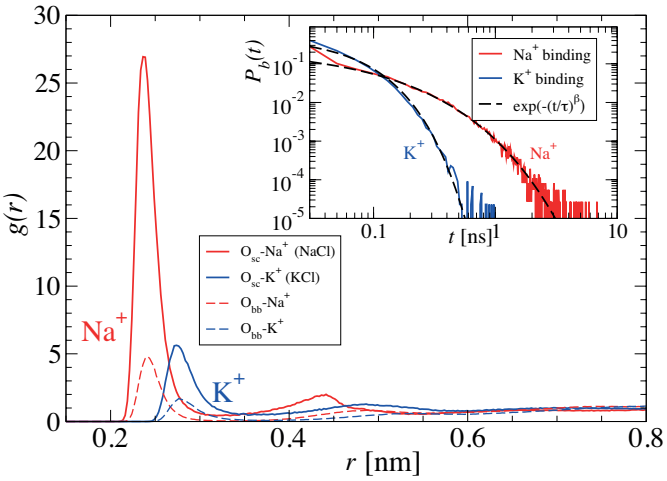

Figure 4.5:
Radial distribution function of cations around peptide oxygen atoms from the side chain (sc) carboxylates or backbone (bb) carbonyls. Inset: Residence time distribution for the cations in the first solvation shell of the peptide oxygen atoms. The distribution for K^+ can be fitted by a single exponential with a time constant of $\tau = 50$ ps, while the one for Na^+ obeys a stretched exponential with $\tau = 50$ ps and stretching exponent $\beta = 0.55$.

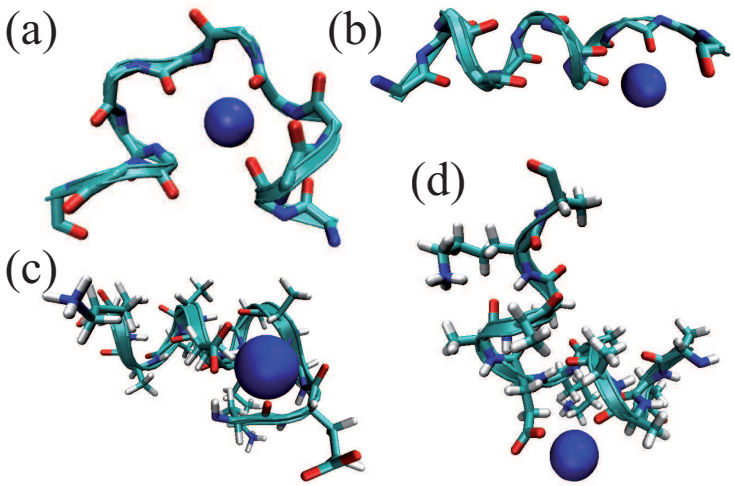

Figure 4.6:
Simulation snapshots of backbone configurations, in which a single Na^+-ion (*blue sphere*) is trapped by multiple oxygen binding sites (*red*). These snapshots are dynamically selected, so that the configurations shown existed for longer than 2 ns. In a) and b), no side chains are shown to better illustrate the binding to the backbone. In c) and d) all side chains are shown, since glutamic acid side chains are also involved in binding the cation.

this structure on times up to several nanoseconds. An example of a long-lived configuration, in which two neighboring turns are correctly folded, while the rest of the peptide forms a loop around the cation is shown in Fig. 4.6b. Often also the glutamic acid side chain is involved as displayed in Fig. 4.6c-d, where the cation not only binds to a backbone carbonyl but also to the headgroup of the E^- side chain. In all these situations the peptide is relatively compact with one or two turns correctly folded, corresponding to the q-region $0.25 \lesssim q \lesssim 0.65$, where the helicity is mostly between $2/3$ and $1/3$ (cf. Fig. 4.4b). Configurations of this type have not or only rarely have been found involving anions or a K^+-ion, so that their existence must be attributed to the relatively strong binding of the Na^+-ion.

A rigorous life-time analysis of the occurring configurations involving trapped ions is difficult to perform due to the variety and complexity of the somewhat amorphous structures. We therefore resort to the analysis of cation binding times. In the inset of Fig. 4.5, we plot the binding time distribution $P_b(t)$ of the cations K^+ and Na^+ in the first solvation shell of carboxylates and carbonyls, which defined by the location of the first minimum in the cation radial distribution function in Fig. 4.5. While the distribution decays exponentially for K^+ with a time constant of about 50 ps, we find a much slower, nonexponential behavior for Na^+ which can be best fitted by a stretched exponential of the form $\propto \exp(-(t/\tau)^\beta)$ with $\tau \simeq 50$ ps and $\beta = 0.55$. This indicates that long binding times on the order of nanoseconds are indeed possible and corroborate the existence of "trapped" unfolded configurations in which peptide parts tightly wrap around the cation.

We note that it is indeed well established that systems with multiple trapping or other manifestations of disorder can lead to anomalous kinetics [197]. In our investigated systems, the appearance and magnitude of trapping is controlled by the nature of the ions. The observed "stretched" exponentials resemble the slow relaxation in glass-forming liquids [198]. Anomalous kinetics in peptide and protein dynamics have been indeed observed in simulations and experiments for certain dynamic variables or RCs [199–201], and obviously question the general validity of Markovian approaches to predict long-time dynamics in protein folding. While this complex issue is still awaiting resolution, we proceed with the interpretation of helix folding in the framework of simple diffusion. Since the average folding-unfolding times ($\gtrsim 10$ ns) are typically much larger than the ion binding times (~ 50 ps), we expect the long-term dynamics to be adequately described in terms of memoryless diffusion in a free energy landscape.

4.2.3 Folding kinetics

We first analyze mean folding and unfolding times: In Fig. 4.7a, the MFPTs for folding from $q > q_1$ to q_1 given by $\tau_f(q, q_1) \equiv \tau_{fp}(q, q_1)$ are shown; the salt-specific values of q_1 are found in Tab. 4.1. Without salt the typical folding time is about $\tau_f \simeq 20 - 30$ ns in the region $q \gtrsim 0.3$ before it quickly drops down to 0 for q-values closely approaching q_1. In KCl $\tau_f(q, q_1)$ increases by a factor of about 2, while the sodium salts lead to a considerable slowing down of folding by one order of magnitude. The unfolding times $\tau_{uf}(q, q_3)$ ($q < q_3$), cf. Fig. 4.7b, show less variations between the salts. Without salt the typical unfolding time is about 30-40 ns while it may rise by a factor of 2-3 in NaCl or KCl. Note that for KCl both the folding and unfolding are slower than in the salt-free case although the free energy landscape is very similar.

To get a grasp on the folding kinetics involving fewer helical turns we have also resolved $\tau_f(q, q_2)$ for $q > q_2$ (folding by one or two turns to the two-turn state) and $\tau_{uf}(q, q_2)$ for $q < q_2$ (unfolding by one turn to the two-turn state), which are shown in Fig. 4.7c-d. The folding times decrease by a factor of about 2 when compared to the $q \to q_1$ folding, while the trends with

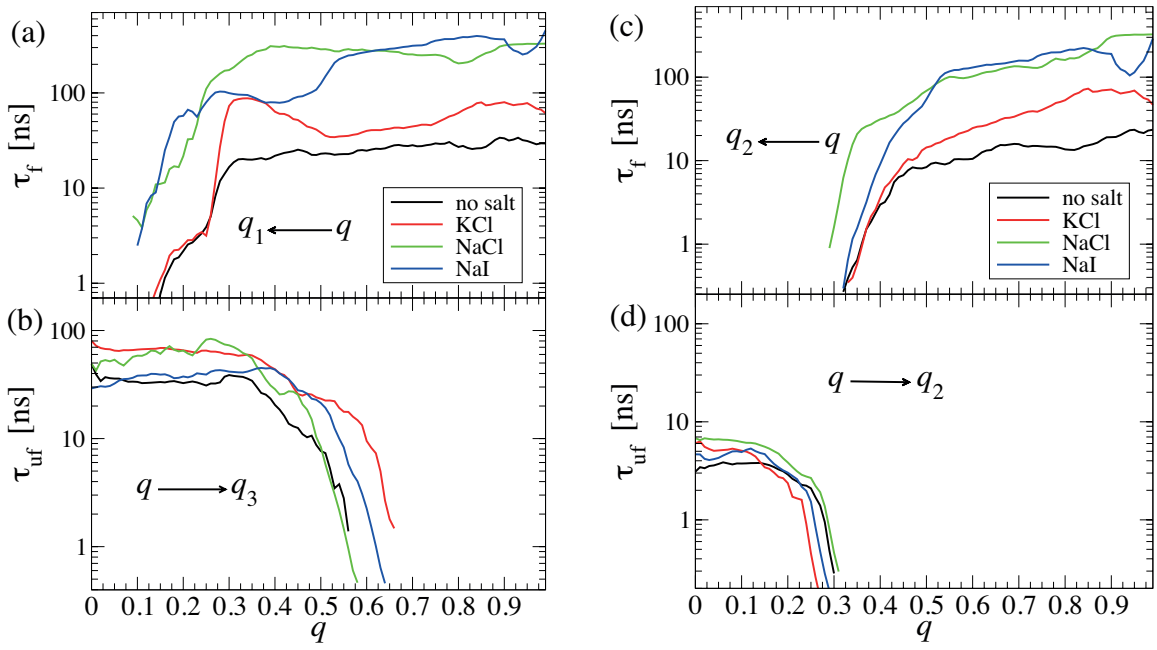

Figure 4.7:
a) MFPTs τ_f for folding from state q to q_1. b) MFPTs τ_{uf} for unfolding from state q to q_3. c) MFPTs τ_f for folding from state q to q_2. d) MFPTs τ_{uf} for unfolding from state q to q_2.

salt remain the same, in particular the one order of magnitude slower folding in the sodium salts. Unfolding times $\tau_{uf}(q, q_2)$ are relatively small, lying between $3 - 7$ ns. The variation between the salts is again more pronounced for the folding times compared to the unfolding times, which show a different ordering.

Note that the MFPTs shown in Fig. 4.7 are in part subject to substantial noise due to insufficient statistical sampling: for example, clear deviations from a monotonously increasing function (expected for diffusive dynamics) are observed in the KCl-folding times shown in Fig. 4.7a; this irregularity has its origin in an exceptionally long-lived (relative to the full trajectory duration) state of a specific peptide configuration in the KCl-time series in Fig. 4.3 within the time range 200 ns $\lesssim t \lesssim$ 400 ns. Briefly, this specific configuration is characterized by two helical turns and the Ace-cap being buried between the hydrophobic side chains of one Lys and one Ala group. This configuration, which does not involve bound ions, is found rather frequently in all trajectories but with typically much shorter life times.

4.2.4 Free energy and diffusivity profiles

We now turn to the interpretation of the mean folding times in terms of the free energy $F(q)$ and diffusivity profile $D(q)$. For statistical reasons leading to the above-mentioned anomalies, we have resolved the $D(q)$ profile only by three q-regions distinguishing: (i) mainly full-helix states corresponding to $q < q_{2/3}$, (ii) one- and two-turn states, i.e., $q_{2/3} \leq q < q_{1/3}$, and (iii) mainly unfolded states with $q \geq_{1/3}$. We assume that these states are separated by the q-values, where the average helicity is $2/3$ and $1/3$ in Fig. 4.4, the salt-specific values of $q_{2/3}$ and $q_{1/3}$ being summarized in Tab. 4.1. The RTT τ_{RT} in Eq. 4.5 then is a function of q involving up to four pa-

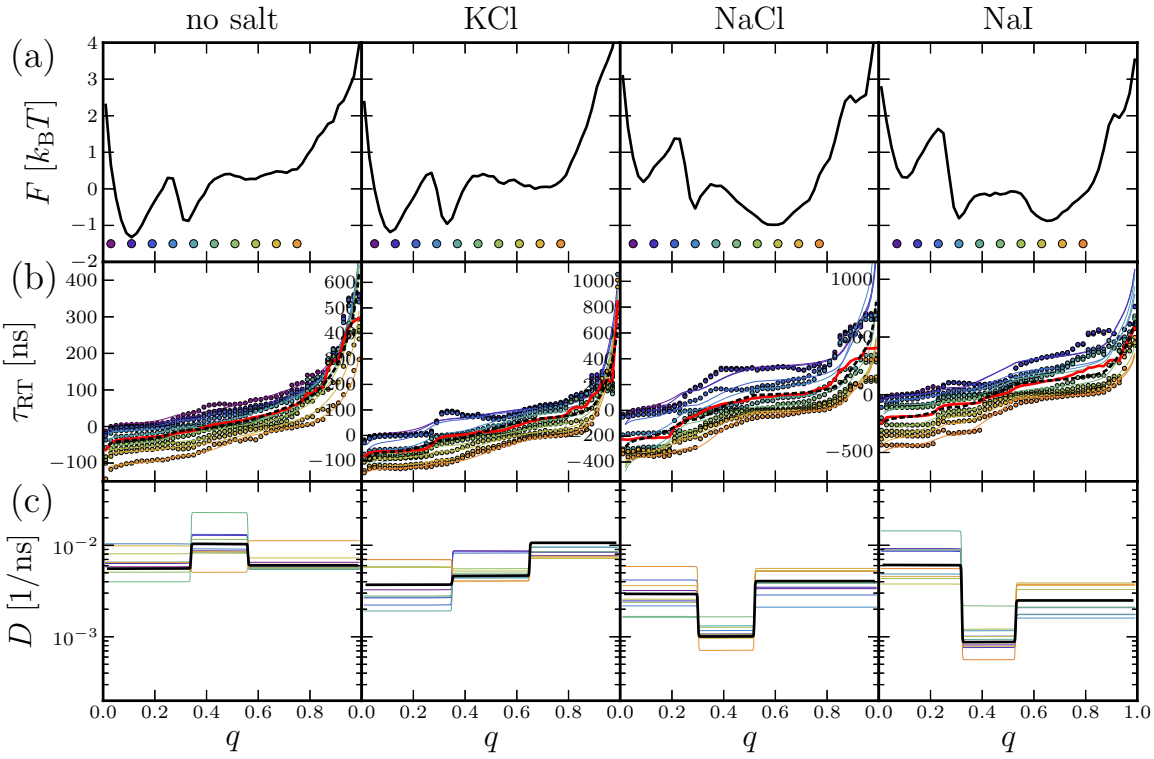

Figure 4.8:
a) Free energy landscapes with and without salt; *colored circles* show the positions of the target points q_t considered in the RTT analysis. b) RTTs from the $q(t)$ trajectories (*colored circles*, *same color coding* as in (a); *colored lines* show best fits of the RTT functions to the simulation data. Averaged RTTs (Eq. 4.7) are shown as *thick red lines*, the corresponding best fits are displayed as *dashed black lines*. c) Diffusivity profiles resulting from best fits to the data shown in (b) as explained in Sec. 4.2.4.

rameters: the target position q_t, and the diffusivities D_f, D_{pf}, and D_{uf} in the folded (f), partially folded (pf), and unfolded (uf) regions.

Free energy landscapes for the systems with and without salt are shown in Fig. 4.8a, where colored circles denote the positions of target points q_t considered in the RTT analysis. RTTs extracted from the simulation trajectory $q(t)$ by combining MFPTs according to Eq. 4.4 are shown as colored circles in Fig. 4.8b, where the color-coding denotes the target positions shown in Fig. 4.8a and where the average round-trip curves defined in Eq. 4.7 are displayed as thicker red lines. We now adjust the three diffusivity values D_f, D_{pf}, and D_{uf} in such a way to best reproduce the RTT data extracted from the simulation trajectories: Best fits are shown as lines in Fig. 4.8a, where colored thin lines correspond to fits to RTT data belonging to specific targets q_t and the thicker dashed black lines correspond to best fits to the average RTTs (Eq. 4.7). The diffusivity profiles corresponding to these fits are shown in Fig. 4.8c, again using the same color coding.

Clearly, insufficient statistical sampling and deviations from pure Markovian dynamics along q lead to irregularities in the round-trip data of Fig. 4.8b: Round-trip curves corresponding to distinct targets q_t are not just strictly shifted vertically with respect to each other (cf. Eq. 4.6) and—in particular for KCl—non-monotonous behavior is observed for some of the target po-

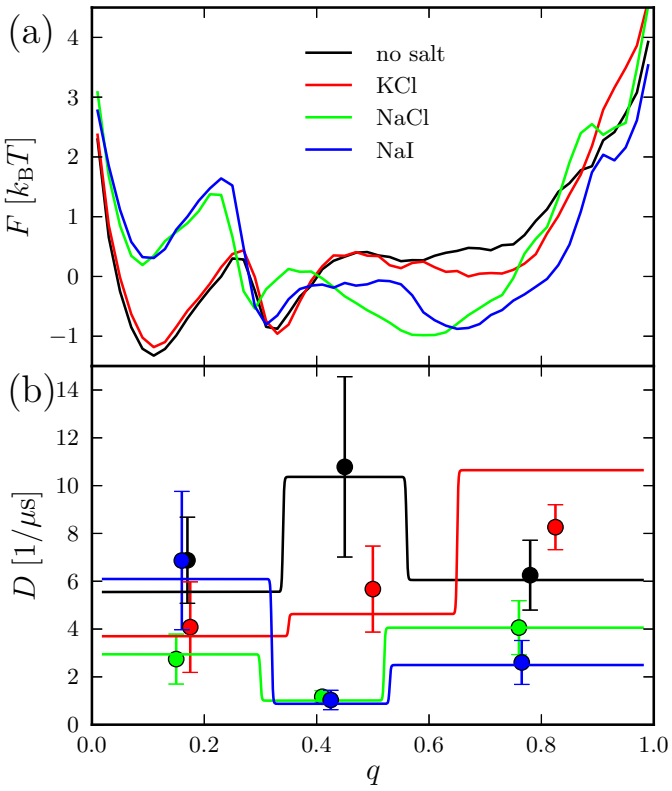

Figure 4.9:
a) Free energy landscapes (same data as in Fig. 4.4a). b) Diffusivity profiles for all investigated systems resolved by three regions $q < q_{2/3}$, $q_{2/3} \leq q \leq q_{1/3}$, and $q \geq_{1/3}$, which correspond to the fully helical, two-turn, and one-turn as well as unfolded states, respectively. *Symbols with error bars* result from fits to the ensemble of RTTs for different targets q_t (colored lines in Fig. 4.8c), while the diffusivity profiles resulting from fits to the average RTT curve (black lines in Fig. 4.8c) are displayed as *solid lines*.

sitions, similarly to the artifacts seen in the average folding times in Fig. 4.7a. It is therefore not astonishing that the resolved diffusivities (thin colored lines in Fig. 4.8) sensitively depend on the target position q_t. In Fig. 4.9b, the means and standard deviations of the thin, colored diffusivity profiles in Fig 4.8c are displayed as circles with error bars, while the solid lines display the fit results to the average RTT curve, which is less affected by statistical noise (thicker black lines in Fig 4.8c). As is seen from Fig. 4.9b, both analysis methods yield estimates, which coincide within error bars (the only exception being KCl for $q > q_{1/3}$), by this clearly validating our approach.

First of all, we observe that the diffusivity profiles in Fig. 4.9b are not flat, a feature discussed previously for this peptide in the salt-free case [x]. The inhomogeneities reflect variations of the multidimensional configurational mobility of the peptide projected onto the one-dimensional RC q, cf. Sec. 2.3.7. After including the salt, a few significant changes to $D(q)$ are visible within the large error bars: first, in the solution with sodium salts there is a moderate decrease of the effective diffusivity by $30-60\%$ in the large q-region, $q > q_{1/3}$, where the peptide is mostly unfolded. In contrast, with KCl the diffusivity seems to increase by $30-60\%$ in the unfolded regions. Second, a drastic drop in diffusivity is observed for all salts in the central region $q_{2/3} <$

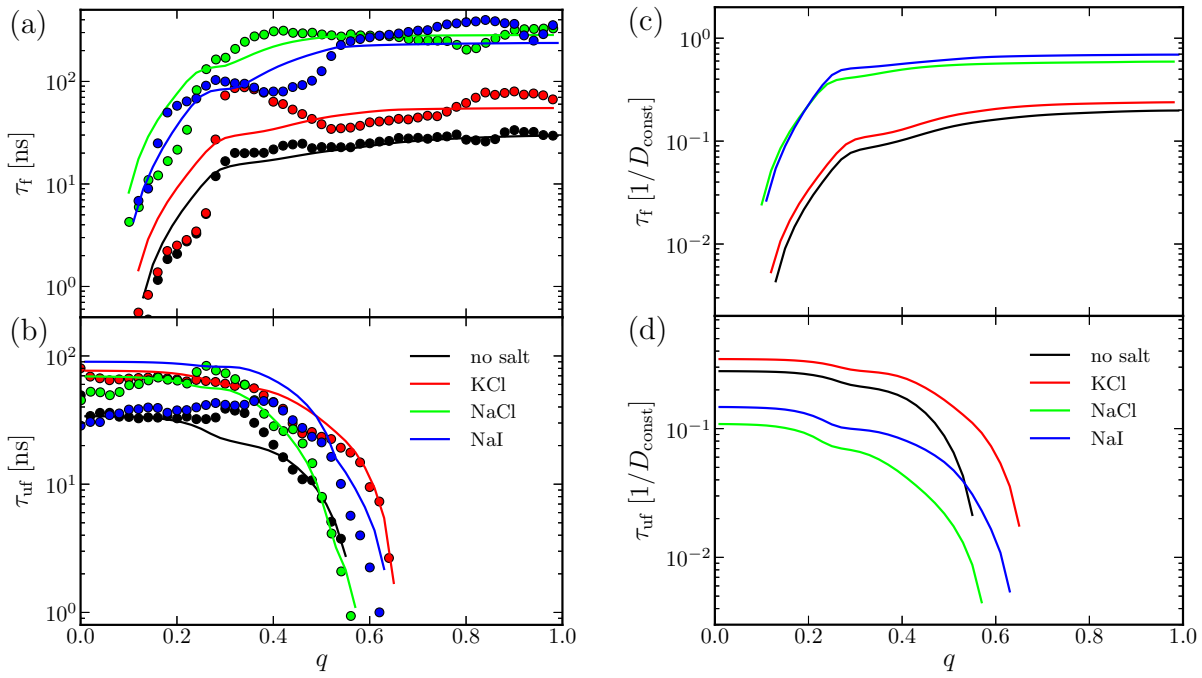

Figure 4.10:
a) Average folding and b) unfolding times from the reduced FP description using the diffusion profiles denoted by *solid lines* in Fig. 4.9b (*lines*) and from the original time series (*circles*, same data as in Fig. 4.7a-b). c) Average folding and d) unfolding times from the reduced FP description assuming a flat diffusivity profile; times are displayed in units of the inverse diffusion constant D_{const}.

$q < q_{1/3}$, where the peptide features one or two α-helical turns. The decrease is about one order of magnitude for the sodium salts NaCl and NaI. Finally, we find a smaller decrease of the diffusivity again in the completely folded states $q < q_{2/3}$, where the diffusion drops by about $30 - 60\%$ for the KCl and NaCl salts.

Although the resolution of $D(q)$ is small, we emphasize that it can almost quantitatively reproduce the folding and unfolding times plotted in Fig. 4.7. MFPTs for folding and unfolding from the reduced FP approach using the free energy landscape and the diffusivity profiles in Fig. 4.9 obtained by fitting to $\overline{\tau}_{\text{RT}}$ are compared in Fig. 4.10a-b to the raw simulation data (already shown in Fig. 4.7a-b). Note that the predictions of the reduced FP description are qualitatively in agreement with the simulation data, especially for longer times where non-Markovian effects become negligible, in contrast to what one would expect from a naive look at the different free energies. This observation is corroborated by the comparison to Fig. 4.10c-d displaying average folding and unfolding times resulting from an FP description involving a state-independent diffusivity, i.e., a diffusion constant $D(q) = D_{\text{const}}$. In particular, a flat and salt-independent diffusivity cannot account for the salt-dependent ordering of the folding and unfolding times seen in Fig. 4.10a-b. Conversely, this implies that the knowledge of the salt-specific changes in the equilibrium *free energy* (Fig. 4.9a) is not sufficient to draw conclusions about the salt-specific folding and unfolding *dynamics*. Similarly to Sec. 2.3.5, this comparison thus demonstrates that only the combination of free energy and diffusivity profiles (Fig. 4.9a-b) yields the complete picture of the kinetics.

4.3 Discussion

Thus, while no clear-cut trends in the change of the diffusivity profile with salt can be recognized, clearly the diffusivity mainly decreases with salt, along with a significant drop in the partially folded states in the intermediate q-region. Importantly, the changes of $D(q)$ with salt are obviously not just a rescaling of $D(q)$ of the salt-free system as if the action would just stem from a nonspecific change due to a different bulk viscosity. In particular, the very few cases for which a viscosity argument applies could be for NaCl and KCl in the low q-region, $q < q_{2/3}$, or for NaCl and NaI in the high q-region, $q > q_{1/3}$: Here, the diffusivity is reduced by a factor of 2, roughly the same as for the viscosity increase discussed in Sec. 4.1.3. Since there is no general trend, however, we must conclude that the change of the diffusivity profile originates from a combination of bulk viscosity effects and specific cosolute binding to the peptide. We believe that viscosity effects may be more important in the large q-region than in the low q-region, because large scale coil rearrangements in the solvent are frequent in the former, while changes along the RC are mainly governed by internal mechanisms in the latter case. Here, only minor configurational rearrangements like the expulsion of one water molecule or one ion, or the forming and breaking of internal hydrogen-bonds take place. From this perspective it is interesting to see the diffusivity increase in the high q-region for KCl, while from viscosity arguments only it should decrease by a factor of 2.

However, given the diffusivity profiles in Fig. 4.9b, the large increase of folding times in the Figs. 4.7a and 4.7c for the sodium salts must thus be attributed not only to the changes in the free energy landscape but more dominantly, to the strongly reduced diffusivity in the intermediate q -region, $q_{2/3} \lesssim q \lesssim q_{1/3}$. The faster unfolding and the weaker dependence of unfolding vs folding times on salt type (cf. Figs. 4.7b and 4.7d) seems to arise from a cancelation effect, where the small diffusivity in the intermediate q-regions is counterbalanced by the low unfolding barriers in the free energy landscape.

What are the molecular reasons for the major changes in the diffusivity profiles in the electrolytes solutions? On the basis of our structural and ion binding analysis in Sec. 4.2.2, it is now easy to argue that the prominent drop in the effective diffusivity in the sodium salts is a consequence of the long-lived configurations similar to those shown in Fig. 4.6. The long-lived character of these conformations is clearly observed in trajectory analysis and also manifested in the long binding times of cations on a nanosecond time scale shown in Fig. 4.5. While the form of the free energy landscape does not depend on the lifetime of these states (just what fraction of time they are sampled), the long life times are clearly reflected in the intermediate q-region of the diffusivity profiles. Due to the stronger binding of Na^+ vs K^+ to the peptide oxygen atoms, the effect is less drastic in the KCl solution than for the sodium salts.

4.4 Conclusions

In this chapter, we have investigated the specific effects of salt at molar concentrations on the α-helical folding kinetics of a short, alanine-based and salt-bridge-forming peptide by means of molecular simulations and a diffusional analysis. Mean folding times have been found to considerably depend on salt type with folding times varying over one order of magnitude. The molecular basis for this is the previously observed stronger binding affinity of Na^+- vs K^+-ions to anionic peptide groups thereby transiently cross-linking multiple groups in the peptide. These binding processes increase the internal friction and induce a new, slow time scale. Within

an analysis in terms of an effective diffusivity in a one-dimensional free energy landscape, these new time scales are expressed by a strong and salt-specific variation of the local diffusivity. A recent simulation study of a fully charged polyglutamic acid chain in salt solution has shown that segmental relaxation kinetics are significantly slowed because of the same molecular mechanisms [188].

Therefore, adsorption of ions not only alter the equilibrium but also the kinetic properties of protein folding by direct binding mechanisms. Whether a general relation between preferential adsorption [202] and changes in the kinetics can be drawn may be an interesting topic for further research. Given the current insights it seems likely, however, that the change in the kinetics not only depends on the amount of adsorbed ions but also on the nature of the individual ion peptide interactions.

As we have demonstrated, molecular simulations can provide valuable information to understand the complex mechanisms in solvent-protein interactions and thereby protein stability and folding. The molecular mechanism found may be of general importance to understand cosolute effects on protein folding kinetics and shed more light onto experimentally observed cation-specific slowing down of (bio-)polyelectrolyte kinetics [170, 173], in particular for halophilic proteins [171, 172]. Similar mechanisms may be at work in polymer melts [203], so that more experimental studies are highly desirable. In particular, the novel long-lived loop-forming configurations in the denatured/unfolded states, in which sodium or similarly strong binders are bound and immobilized by the peptide backbone, may be experimentally accessible by nuclear magnetic resonance [204] or time-resolved Förster resonance energy transfer measurements [162] probing salt-specific peptide relaxation and kinetics.

Furthermore, the action of complex denaturants such as guanidinium and urea deserve further attention, and systematic studies on specific salt effects should follow. The guanidinium cation, for instance, has been shown to decrease friction in neutral $(\mathrm{GlySer})_n$ peptides [161, 162]. We expect also a strong influence of other specifically binding cations on anionic peptides, such as lithium, or polyvalent cations, such as Mg^{2+} or Ca^{2+}. Large effects may also be anticipated by exchanging the anion, which has been found to considerably alter the unfolding kinetics of a halophilic protein [171, 172].

CHAPTER 5

SPECTRAL ANALYSIS OF DUAL TRAP OPTICAL TWEEZER EXPERIMENTS

Bibliographic information: Parts of this chapter and of Appendix E have previously been published. Reprinted with permission from Ref. [iv]. Copyright 2012, AIP Publishing LLC.

Recent years have seen an ever increasing use of optical tweezers as sensitive tools for the manipulation and observation of single molecules [205], including a number of studies focusing on the mechanical properties of nucleic acids and proteins [53, 76, 77, 206]. As a result of technological development, spatial resolution with sub-nanometer precision and sampling rates reaching the MHz range [207, 208] are by now possible and allow unprecedented insights into molecular structure and dynamics. Similarly to micro-rheological studies [209–211], dual trap optical tweezers exhibit a number of advantages, including a higher "signal-to-noise" ratio and a minimized influence of instrumental drift [212] and therefore are preferred to single trap setups, when high precision is a concern.

Typical extension traces recorded in equilibrium single-molecule experiments display fluctuating trajectories with discrete jumps of the extension trace baseline: The standard analysis consists in computing the moving average of the time series to identify distinct molecular conformations, their average extension, equilibrium probabilities and inter-state kinetics [53, 77]. The thermal fluctuations of the tethered beads—often referred to as "noise"—are thus generally disregarded, although their spectral properties are a signature of the viscoelastic properties of the experimental construct and therefore interesting by themselves. In fact, based on coarse grained simulations of such a single-molecule experiment, the contributions of the experimental handles, of hydrodynamic interactions, and—most importantly—of the molecule under study to the measured fluctuations of the beads in their respective traps, could be disentangled [ix].

Here, we provide a framework for the quantitative spectral analysis of data from actual dual trap optical tweezer experiments. As will be shown, this involves a detailed understanding of instrumental characteristics as well as a controlled way of inferring undetermined parameters from experimental data.

The chapter is organized as follows: We start with a description of our experimental setup in Sec. 5.1. The fluctuation-dissipation theorem (FDT) relating thermal equilibrium fluctuations and linear force response of mechanical objects is reviewed in the general context of optical

tweezer experiments in Sec. 5.2.1, while the more specific case of two unconnected beads is treated in Sec. 5.2.2. Low Reynolds number hydrodynamics and the resulting frequency dependence of self- and cross-mobilities are covered in the Secs. 5.3.1 and 5.3.2, respectively. We model the signal processing in a dual trap optical tweezer setup including polarization crosstalk, (parasitic) filtering, and instrumental noise and discuss the influence of the finite sampling rate on self- and cross power spectral densities (PSDs) in the Secs. 5.4.1 and 5.4.2. The statistical properties of auto- and cross-periodograms [213] of the experimental time series in Sec. 5.5.1 form the basis for the maximum-likelihood method presented in Sec. 5.5.2, which by Bayesian inference allows to determine optimal values for the model parameters. Judging whether the theoretical model used is indeed adequate may be done by quantifying the deviations between fit and experimental data as explained in Sec. 5.5.3. The overall procedure for the spectral analysis is summarized in Sec. 5.5.4. As an application of the maximum-likelihood method, we suggest a calibration scheme for dual trap optical tweezers based on three measurements in Sec. 5.6. It can be viewed as a generalization of a calibration technique, which for single trap setups is by now standard [214–218]. We consider a pair of unconnected but hydrodynamically interacting beads trapped in their respective laser foci in Sec. 5.7 and explicitly demonstrate the influence of instrumental effects and of finite statistics on the auto- and cross-periodograms of the measured signals. For a carefully calibrated setup, PSDs estimated from experimental data agree with the theoretical predictions taking into account the frequency dependence of hydrodynamic interactions (HI) arising from the finite time for vortex diffusion in the fluid [219–221]. Our main findings are summarized in Sec. 5.8, while more technical aspects are found in Appendix E: Various filter effects are discussed in Appendix E.1, a minimal model explaining the observed crosstalk asymmetry is presented in Appendix E.2, statistical properties of auto- and cross-periodograms are explicitly calculated in Appendix E.3, basic characteristics of the discrete Fourier transformation (DFT) are reviewed in Appendix E.4, and the properties of normally distributed random variables on logarithmic plots are discussed in Appendix E.5.

For more complex experimental situations, where a pair of trapped beads are e.g. tethered via double stranded DNA handles to a protein, we suggest a two-step procedure to reliably determine the viscoelastic properties of the molecular tether: (i) a calibration run as described in Sec. 5.6 without the tethering macromolecular construct to fix the instrumental parameters, and (ii) a production run with the tether construct to determine the tether parameters. In both steps, the same maximum-likelihood method (Sec. 5.5.2) can be used, the only difference lying in the thermal PSDs (Sec. 5.2.1) and in the set of parameters to be determined.

5.1 Dual Trap Optical Tweezers

The experimental setup used for trapping and tracking micron-sized beads is a custom-built high-resolution dual trap optical tweezer with back-focal plane detection (see Fig. 5.1b) similar to setups described elsewhere [212, 217, 222, 223]. The light of a 4 W linear polarized diode pumped Nd:YVO4 solid state cw laser system emitting at 1064 nm (Spectra-Physics, California, USA) passes a Faraday isolator (Electro-Optics Technology, Inc., Michigan, USA) before getting expanded and collimated by the first telescope. A first computer controlled and motorized $\lambda/2$-plate followed by a polarizing beam splitter (PBS) cube (order number PTW 2.10 or PTW 2.20, Bernhard Halle, Germany) controls the overall laser power passing into the successive optical parts. A second $\lambda/2$-plate sets the relative laser power in the two orthogonally

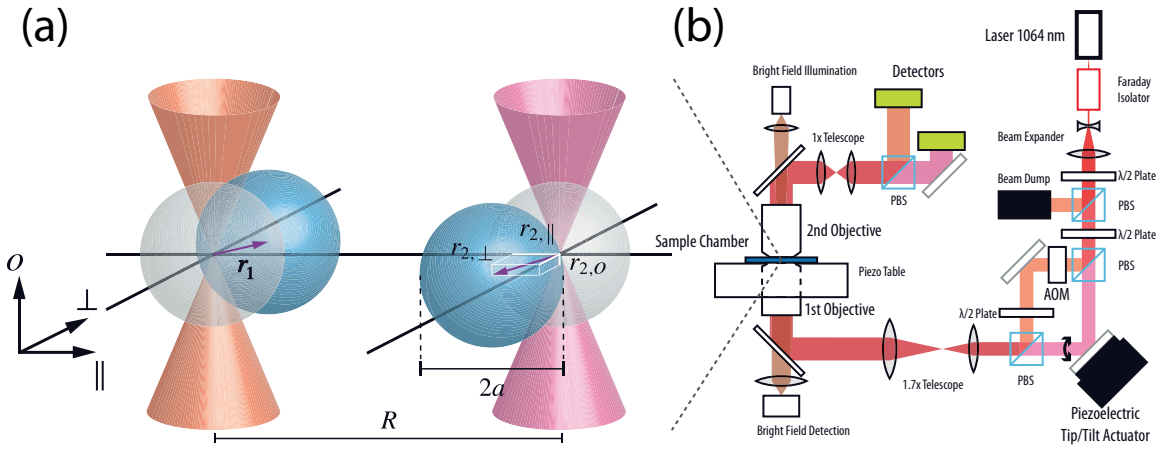

Figure 5.1:
a) Zoom-in into the dual trap optical tweezer sample chamber: The notation for the coordinates of the beads (*blue*) relative to the trap centers (*gray*) is used throughout the chapter. b) Schematic of the overall experimental setup described in Sec. 5.1.

polarized trapping beams separated by a second PBS. One of the beams is reflected by a mirror mounted on a two axis piezoelectric tip/tilt actuator (Mad City Labs, Wisconsin, USA) providing lateral displacement of the corresponding trap in the specimen plane. The other beam is frequency shifted using an acousto-optical modulator (Gooch & Housego, Great Britain) to reduce interference artifacts [224]. After recombination of the two trapping beams with a third PBS a second telescope expands the beams to overfill the back aperture of the focusing objective (63x/1.20 W Corr, C-Apochromat, Zeiss, Germany). The objective focuses the beams to two diffraction-limited spots in the sample chamber. The use of a water-immersion objective permits trapping deep inside the sample chamber. The distance from the cover slip is set to 20 μm and therewith is much larger than typical inter-bead distances. The hydrodynamic influence of the cover-slip surface is therefore neglected in Sec. 5.3. After passing the sample chamber placed on a piezoelectric table (Physik Instrumente, Germany), the forward scattered light of the trapped beads is collimated with a second identical objective. The beams are split by polarization and imaged onto two position sensing devices (DL100-7PCBA3, Pacific Silicon Sensor Inc., California, USA). Due to depolarization in the optical path and the intrinsic non-perfect separation and conservation of polarization upon transmission through and reflection by the PBSs, each of the detector signals to a certain degree also reflects the motion of the bead in the "wrong" trap; this effect, known as polarization crosstalk [225], is explicitly considered in the signal processing described in Sec. 5.4.1. All components are mounted on a vibration isolated optical table (M-ST-46-12, Newport Corporation, Irvine, USA). Optical paths are enclosed to minimize the effect of air fluctuations. Custom-built electronics are used for processing the analog position signals including an individual offset correction, normalization and amplification for each channel [214, 226]. Before recording, all signals are filtered with an 8th order Butterworth filter with 3dB-frequency set at 200 kHz and further amplified (Model 3384 Filter, Kron-Hite, Massachusetts, USA). For real-time steering and data acquisition a custom-written LabVIEW program runs on a field-programmable gate array (FPGA)-board (NI PCI-7833R 3M, National Instruments, Texas, USA). Data is recorded with a sampling rate of 100 kHz. Mea-

surements are performed at a temperature of $22.6 \pm 0.3^\circ$ C using silica beads with 1.0 μm in diameter (Bangs Laboratories, Indiana, USA) diluted in phosphate buffered saline (P4417, Sigma Aldrich, St. Louis, USA). The sample chamber consists of two cover slips separated by stripes of Nescofilm (Bando Chemical Industries Ltd., Japan) forming a channel, which is sealed with vacuum grease after filling. The dimensions of the sample chamber are about $9 \times 18 \times 0.1$ mm^3.

Optical tweezer experiments have been performed by Alexander Mehlich and Benjamin Pelz under the supervision of Prof. Dr. Matthias Rief at the Technical University of Munich.

5.2 Force Response and Thermal Motion

5.2.1 General formulation

In a dual trap optical tweezer experiment, the thermal motion of the two beads in their respective traps reflects the viscoelastic properties of the experimental construct. For simplicity, we restrict the following discussion to the case, in which all spatial components decouple; the necessary conditions for this to happen are detailed in Sec. 5.2.2. The thermal cross-correlation function of the bead coordinates r_i and r_j is defined as

$$S_{ij}^{\mathrm{th}}(t) \equiv \langle r_i(0) r_j(t) \rangle = \langle r_i(t') r_j(t'+t) \rangle_{t'} \equiv \lim_{T\to\infty} \frac{1}{T} \int_{-T/2}^{T/2} \mathrm{d}t'\, r_i(t') r_j(t'+t), \quad i,j \in \{1,2\}, \tag{5.1}$$

where the equivalence of equilibrium average $\langle \ldots \rangle$ and temporal average $\langle \ldots \rangle_{t'}$ holds in ergodic systems and where the measurement time is denoted by T. Correlation functions in thermal equilibrium are of interest because they reflect the linear force response properties of the system; in fact, the FDT [227] states

$$J_{ij}(t) = \begin{cases} -(k_{\mathrm{B}}T)^{-1}\, \mathrm{d}S_{ij}^{\mathrm{th}}(t)/\mathrm{d}t & \text{for } t \geq 0, \\ 0 & \text{for } t < 0, \end{cases} \tag{5.2}$$

where $k_{\mathrm{B}}T$ denotes the thermal energy and J_{ij} the corresponding response function. In the past, the interplay of (instantaneous) HI and the harmonic laser trap potential [228–230] as well as the relaxation dynamics of DNA [231] were measured resolving auto- and cross-correlation functions of the bead's positions.

Here, working in frequency space turns out to be more convenient for the following reasons: (i) Retardation/memory effects in the (integro-differential) equations of motions cause difficulties when calculating temporal correlation functions, while they are easily taken into account in frequency space as shown in Sec. 5.2.2, (ii) relevant instrumental effects such as crosstalk, signal filtering, and instrumental noise can be accounted for as detailed in Sec. 5.4, and (iii) the maximum-likelihood method presented in Sec. 5.5.2 makes it straightforward to quantitatively evaluate experimental estimates for auto- and cross-PSDs, defined as the Fourier transformations (cf. Appendix A.2) of the corresponding thermal correlation functions

$$S_{ij}^{\mathrm{th}}(\omega) \equiv \int_{-\infty}^{\infty} \mathrm{d}t\, S_{ij}^{\mathrm{th}}(t) \mathrm{e}^{\mathrm{i}\omega t}, \qquad i,j \in \{1,2\}. \tag{5.3}$$

Note that if time reversal symmetry holds, temporal correlation functions $S_{ij}^{\mathrm{th}}(t)$ as well as their Fourier transformations, the PSDs $S_{ij}^{\mathrm{th}}(\omega)$, are real and even functions. According to the cross-correlation theorem, PSDs and the Fourier components of the stochastic motion are related via

$$S_{ij}^{\mathrm{th}}(\omega)\, 2\pi\, \delta(\omega - \omega') = \langle r_i(\omega) r_j^{\star}(\omega') \rangle, \qquad i,j \in \{1,2\} \tag{5.4}$$

where $(\dots)^{\star}$ denotes the complex conjugate. PSDs can thus directly be estimated experimentally by calculating averaged auto- and cross-periodograms from the stochastic trajectories as detailed in Sec. 5.5.1.

For simple systems as the one in Sec. 5.2.2, thermal PSDs can be obtained easily from the stochastic equations of motion; for more complex constructs, it may be easier to calculate linear response functions J_{ij} relating average oscillation and external driving force amplitudes on the linear level

$$\langle r_i(\omega) \rangle = \sum_{j=1}^{2} J_{ij}(\omega)\, f_j^{\mathrm{ext}}(\omega) + \mathcal{O}\left(\left(f^{\mathrm{ext}} \right)^2 \right), \qquad i \in \{1,2\}. \tag{5.5}$$

Overall, the experimental object of study—two micron-sized beads in optical traps potentially connected via a molecular tether and embedded in a fluid—is completely characterized by two self-response functions J_{11} and J_{22} relating forces and displacements on the same bead and, in the absence of time reversal breaking, one cross-response function $J_{12} = J_{21}$ relating force and displacement amplitudes of different beads. Dynamic (de-)convolution theory [ix] provides a framework for iteratively calculating these three response functions from the mechanical response characteristics of the individual components, i.e., the beads in the optical traps, the elements of the molecular tether and HI between the various components. The corresponding thermal PSDs are then obtained using the FDT in frequency space

$$S_{ij}^{\mathrm{th}}(\omega) = \frac{2 k_{\mathrm{B}} T}{\omega} \operatorname{Im}\left[J_{ij}(\omega) \right], \qquad i,j \in \{1,2\}, \tag{5.6}$$

where $\operatorname{Im}[\dots]$ denotes the imaginary part. Because of causality ($J_{ij}(t) = 0$ for times $t < 0$), real and imaginary parts of the response functions in frequency space are related by Kramers-Kronig relations [227]. Recording the equilibrium fluctuations of the system and estimating the PSDs S_{ij}^{th} is therefore sufficient for completely characterizing the system's force response via Eq. 5.6.

5.2.2 Two hydrodynamically interacting beads

The stochastic, thermal motion of two unconnected beads in the trapping potentials of two laser foci is described by a set of differential equations, which in the frequency domain reads

$$-\mathrm{i}\,\omega \begin{pmatrix} \boldsymbol{r}_1(\omega) \\ \boldsymbol{r}_2(\omega) \end{pmatrix} = \begin{pmatrix} \overleftrightarrow{\boldsymbol{\mu}}_{11}(\omega) & \overleftrightarrow{\boldsymbol{\mu}}_{12}(\omega) \\ \overleftrightarrow{\boldsymbol{\mu}}_{21}(\omega) & \overleftrightarrow{\boldsymbol{\mu}}_{22}(\omega) \end{pmatrix} \cdot \begin{pmatrix} \boldsymbol{f}_1^{\mathrm{trap}}(\omega) + \boldsymbol{f}_1^{\mathrm{ext}}(\omega) + m_1\, \omega^2 \boldsymbol{r}_1(\omega) \\ \boldsymbol{f}_2^{\mathrm{trap}}(\omega) + \boldsymbol{f}_2^{\mathrm{ext}}(\omega) + m_2\, \omega^2 \boldsymbol{r}_2(\omega) \end{pmatrix} + \begin{pmatrix} \boldsymbol{v}_1^{\mathrm{st}}(\omega) \\ \boldsymbol{v}_2^{\mathrm{st}}(\omega) \end{pmatrix}. \tag{5.7}$$

Here, the 3×3 mobility tensors $\overleftrightarrow{\boldsymbol{\mu}}_{ij}$ relate the forces on bead j, i.e., forces due to the trapping potential $\boldsymbol{f}_j^{\mathrm{trap}}$, external forces $\boldsymbol{f}_j^{\mathrm{ext}}$ and inertial ones (m_1 and m_2 denoting the beads' masses), to the velocity $-\mathrm{i}\,\omega \boldsymbol{r}_i$ of bead i; the stochastic contribution to the motion of bead i is denoted by $\boldsymbol{v}_i^{\mathrm{st}}$.

The motion along the individual spatial coordinates in Eq. 5.7 decouples if the main axis of the elliptic laser foci coincide with the Cartesian coordinates [214] *and* if the mobility tensors

are diagonal. While the first condition can be achieved via careful alignment of the instrument [223], the second requirement is satisfied in an unbounded fluid if the axis connecting the trap centers is parallel to one of the coordinate axes (cf. Sec. 5.3.2). To simplify the notation, we restrict ourselves to two identical beads ($m \equiv m_1 = m_2$) in the following, and distinguish motion along the optical axis (o) as well as along ($\parallel$) and perpendicular ($\perp$) to the inter-trap axis as shown in Fig. 5.1a.

The thermal motion of the two beads held in harmonic traps along the spatial coordinate α is then described by the simpler set of equations of motion

$$-\mathrm{i}\,\omega \begin{pmatrix} r_{1,\alpha}(\omega) \\ r_{2,\alpha}(\omega) \end{pmatrix} = \begin{pmatrix} \mu_{\mathrm{self}}(\omega) & \mu^{\alpha}_{\mathrm{cross}}(\omega) \\ \mu^{\alpha}_{\mathrm{cross}}(\omega) & \mu_{\mathrm{self}}(\omega) \end{pmatrix} \cdot \begin{pmatrix} (-\kappa_{1,\alpha} + m\,\omega^2) r_{1,\alpha}(\omega) + f^{\mathrm{ext}}_{1,\alpha}(\omega) \\ (-\kappa_{2,\alpha} + m\,\omega^2) r_{2,\alpha}(\omega) + f^{\mathrm{ext}}_{2,\alpha}(\omega) \end{pmatrix} + \begin{pmatrix} v^{\mathrm{st}}_{1,\alpha}(\omega) \\ v^{\mathrm{st}}_{2,\alpha}(\omega) \end{pmatrix}, \quad (5.8)$$

where the trap strengths $\kappa_{i,\alpha}$ and, in particular, the cross-mobilities $\mu^{\alpha}_{\mathrm{cross}}$ in general depend on the spatial coordinate $\alpha \in \{\parallel, \perp, o\}$. The frequency dependence of self- and cross-mobilities is a consequence of the hydrodynamic flow field created around a moving sphere discussed in Sec. 5.3. The stochastic velocity contributions $v^{\mathrm{st}}_{i,\alpha}$ in Eq. 5.8 are due to thermal kicks of solvent molecules and are normally distributed random variables with vanishing mean

$$\left\langle v^{\mathrm{st}}_{i,\alpha} \right\rangle = 0, \qquad i \in \{1,2\}, \qquad \alpha \in \{\parallel, \perp, o\}, \quad (5.9)$$

and correlations

$$\left\langle v^{\mathrm{st}}_{i,\alpha}(\omega) v^{\mathrm{st}\,\star}_{j,\alpha}(\omega') \right\rangle = 4\pi\, k_{\mathrm{B}} T\, \mathrm{Re}\left[\delta_{ij} \mu_{\mathrm{self}}(\omega) + \left(1 - \delta_{ij}\right) \mu^{\alpha}_{\mathrm{cross}}(\omega)\right] \delta(\omega - \omega'), \quad (5.10)$$

where δ_{ij} is the Kronecker symbol and where $\mathrm{Re}[\dots]$ denotes the real part. Eq. 5.8 being linear, solving for $r_{i,\alpha}$ is straightforward; for each of the spatial directions α, thermal PSDs $S^{\alpha,\mathrm{th}}_{ij}$ can then be either calculated directly using Eq. 5.4 or by identifying response functions J^{α}_{ij} defined via Eq. 5.5 and using the FDT (Eq. 5.6).

Though being in general characterized by a weaker trapping strength, the coordinate o is equivalent to the coordinate $\perp$ from a hydrodynamic point of view due to symmetry, cf. Sec. 5.3. Since bead displacements along $\perp$ are easier to access experimentally than the ones along o [232], we restrict the following discussion to the coordinates $\parallel$ and $\perp$. Note that for tethered beads, motion along o and $\perp$ will in general couple to the equations of motion for $r_{i,\parallel}$ even in a perfectly aligned setup. These nonlinear contributions (discussed extensively in Chapter 6) can however be suppressed using longer tethers and smaller bead sizes [212][ix].

5.3 Low Reynolds Number Hydrodynamics

5.3.1 Flow-field around an oscillating sphere

The Reynolds number characterizing the relative importance of inertial compared to viscous forces in a hydrodynamic flow is typically small for the thermal motion of micron-sized objects in water: for a bead of radius a moving with velocity v through a fluid of kinematic viscosity $\nu \equiv \eta_0/\rho$, with the fluid's shear viscosity being denoted by η_0 and its mass density by ρ, one has $\mathrm{Re} \sim av/\nu$. The equipartition theorem $k_{\mathrm{B}} T \sim m \left\langle v^2 \right\rangle$, where the bead's mass is denoted by m, allows to estimate the Reynolds numbers for the thermal motion of a micron-sized bead in water, $\mathrm{Re} \sim \sqrt{k_{\mathrm{B}} T/m}\, a/\nu \sim 10^{-3} \ll 1$. Hydrodynamics are thus adequately described by

the linearized Navier-Stokes (or transient Stokes) equation, which for an incompressible fluid reads

$$\rho\,\partial \boldsymbol{u}/\partial t = \eta_0\,\nabla^2 \boldsymbol{u} - \nabla p, \qquad \nabla \cdot \boldsymbol{u} = 0, \tag{5.11}$$

where $\boldsymbol{u}$ denotes the velocity and p the pressure field in the fluid. Taking the curl of Eq. 5.11 yields a diffusion equation for the vorticity $\boldsymbol{\Omega} \equiv \nabla \times \boldsymbol{u}$: vortices due to forces or torques acting on objects in a viscous fluid thus diffusively propagate in space, the characteristic time scale for diffusion over a distance R being $\tau_R \equiv R^2/\nu$. A prominent consequence of the finite time scale for vortex diffusion is the frequency dependence of the self-mobility μ_{self} (the inverse of the sphere's drag coefficient): For a no-slip sphere of radius a in an unbounded and incompressible fluid, the exact result found by Stokes [16] reads

$$\mu_{\text{self}}^{\text{Stokes}}(\omega) = \mu_0 / \left(1 + \lambda_{\text{in}} a + \lambda_{\text{in}}^2 a^2/9\right). \tag{5.12}$$

where

$$\lambda_{\text{in}} \equiv \sqrt{-\mathrm{i}\,\frac{\omega}{\nu}} = \frac{\sqrt{-\mathrm{i}\,\omega\tau_a}}{a}, \qquad \mathrm{Re}\left[\lambda_{\text{in}}\right] > 0. \tag{5.13}$$

The penetration depth in the fluid is $1/\left|\lambda_{\text{in}}\right|$ and $\tau_a \equiv a^2/\nu$ is the characteristic time scale for vortex diffusion on length scales comparable to the bead's radius a. The self-mobility thus deviates from the quasi-stationary self-mobility $\mu_0 \equiv 1/(6\pi\eta_0 a)$ for frequencies $\omega \gtrsim \tau_a^{-1}$. Though theoretically known for over a century, the frequency dependence in Eq. 5.12—responsible for power law tails in the velocity autocorrelation function and resonances in PSDs—is of ongoing interest [207, 208, 233, 234].

The velocity field around an oscillating sphere with a no-slip boundary condition on its surface is calculated employing a standard singularity ansatz involving the Green's function for a force Stokeslet [16, 235]. For a sphere in an incompressible fluid, cross-sections of the velocity field for various values of $\omega\tau_a$ are shown in Fig. 5.2; animations visualizing the time evolution of these velocity fields are included as supplementary material [236]. The direction of the velocity field is denoted by streamlines (black lines with arrow heads), its amplitude by the color coding, which is the same in all snapshots and animations, emphasizing the attenuation of the velocity field at higher frequencies. At low frequencies the time dependence in Eq. 5.11 can be neglected: in the "creeping flow" limit, forces are *instantaneously* propagated through the fluid. The animations for values $\omega \lesssim 10^{-4}/\tau_a$ indeed show a flow-field that is almost immediately built up all over the displayed cross-section; the flow-field in Fig. 5.2a is long-ranged decaying as $1/R$ with corrections accounting for the finite bead size at small separations $R \sim a$. In contrast, retardation/memory effects become noticeable, when the time scale τ_R for vortex diffusion over a distance R becomes comparable to the oscillation period: the flow direction changes and the velocity magnitude is attenuated as seen in Fig. 5.2b. For further increasing frequencies, vorticity effects not only appear at the edges of the displayed cross-section but also in the sphere's vicinity. For $\omega = 1/\tau_a$ (Fig. 5.2c), the subsequent creation of vortices and their diffusion towards the sides is best seen. For even larger frequencies ($\omega\tau_a \gtrsim 10$) shown in the series of animations [236], the flow-field is completely changed: it is now dominated by the dipole contribution with magnitude decaying like $1/R^3$ and with frequency as $1/\omega$, while vorticity effects are restricted to the direct proximity of the sphere. The external force acting on and the velocity of the sphere are related by the frequency-dependent self-mobility given in Eq. 5.12. Their amplitudes are shown as red and blue arrows within the spheres in Fig. 5.2 and

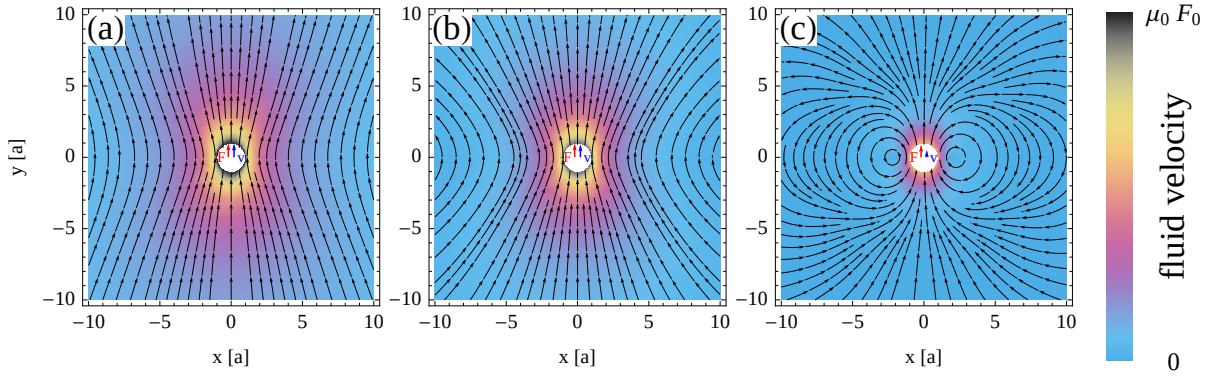

Figure 5.2:
Cross-sections of the flow field around an oscillating no-slip sphere in an incompressible fluid for various driving frequencies: a) $\omega = 10^{-4}/\tau_a$, b) $\omega = 10^{-2}/\tau_a$, c) $\omega = 1/\tau_a$. *Streamlines* indicate the direction of the velocity field and the *color coding* its magnitude, where F_0 is the driving force amplitude and $\mu_0 = 1/(6\pi\eta_0 a)$ the quasi-static sphere mobility. Spatial coordinates are given in units of the sphere radius a, frequencies in units of $\tau_a^{-1} = \nu/a^2$, the kinematic viscosity of the fluid being denoted by ν. Amplitudes of the driving force acting on and the velocity of the sphere are shown as *red* and *blue arrows* within the spheres. The figures above show the configuration of the flow-field, when the sphere velocity is maximal. Animations showing the time evolution of these flow fields are included as supplementary material [236].

in the animations [236]; the phase shift and the decrease of the sphere's self-mobility are clearly discernible in the regime $\omega\tau_a \gtrsim 1$.

Similarly to the sphere's self-mobility (Eq. 5.12), the strength of the HI, i.e., the entrainment of objects by the flow fields shown in Fig. 5.2, also depends on the driving frequency as discussed in Sec. 5.3.2. For the spheres of radius $a = 500$ nm used in our experiment, the vorticity time scale in water is $\tau_a \approx 0.26$ μs; in the snapshots (Fig. 5.2) and animations [236], the angular frequency $\omega = 10^{-2}/\tau_a$ thus corresponds to a driving frequency $f \approx 6$ kHz.

5.3.2 Frequency dependence of self- and cross-mobilities

Calculating the HI between two spheres of radius a at radial distance R constitutes a challenging problem from a mathematical point of view, because the no-slip boundary conditions on the sphere's surfaces have to be fulfilled *simultaneously*. Since no closed-form solution is known, one has to rely on approximations of varying complexity and accuracy, which are discussed in the following. A series expansion of self- and cross-mobilities in powers of a/R and $\lambda_{\text{in}}a$ by van Saarloos and Mazur [237] (vSM) yields self-mobilities

$$\mu_{\text{self}}^{\text{vSM}}(\omega) = \mu_0 \left(1 - \lambda_{\text{in}}a + \frac{8}{9}\lambda_{\text{in}}^2 a^2 - \frac{7}{9}\lambda_{\text{in}}^3 a^3\right), \tag{5.14}$$

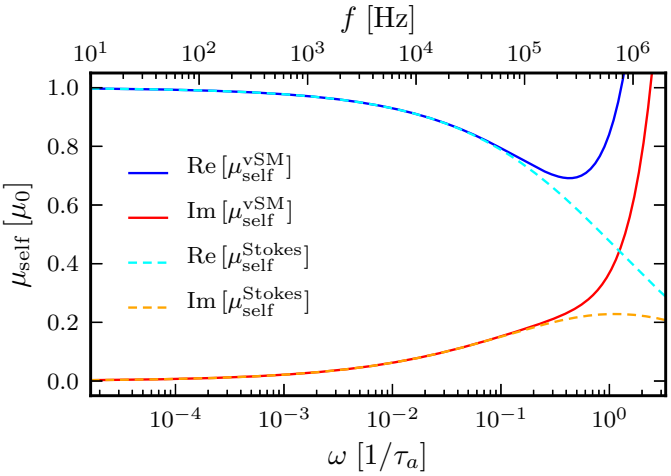

Figure 5.3:
Dependence of real and imaginary parts of the self-mobility of a sphere on the driving frequency ω. In the low-frequency limit, the quasi-stationary self-mobility $\mu_0 \equiv 1/(6\pi\eta_0 a)$ of a sphere of radius a in a fluid of shear viscosity η_0 is recovered. On the bottom, the angular frequency ω is rescaled by $\tau_a \equiv a^2/\nu$, the top frequency scale corresponds to the experimental case where $\tau_a \approx 0.26$ μs (beads of radius $a = 500$ nm in water). The exact result by Stokes (*dashed lines*, Eq. 5.12) and the approximate expressions (*solid lines*, Eq. 5.14) nicely match over the entire range of frequencies resolved in our experiment ($f \lesssim 100$ kHz).

and cross-mobilities

$$\begin{aligned}\frac{\mu_{\mathrm{cross}}^{\alpha,\mathrm{vSM}}(\omega)}{\mu_0} &= \frac{3a}{4R}\mathrm{e}^{-\lambda_{\mathrm{in}}R}\left(1+\frac{5}{9}\lambda_{\mathrm{in}}^2a^2+\frac{1}{6}\lambda_{\mathrm{in}}^3a^3\right)\left[1+\delta_{\alpha,\parallel}\right]\\ &-\left(\frac{a^3}{R^3}+\frac{9a}{2\lambda_{\mathrm{in}}^2R^3}-\frac{\left(5\lambda_{\mathrm{in}}^2a^2+9\right)\left(\lambda_{\mathrm{in}}^2R^2+2\lambda_{\mathrm{in}}R+2\right)a}{4\lambda_{\mathrm{in}}^2R^3}\mathrm{e}^{-\lambda_{\mathrm{in}}R}\right)\left[\frac{1}{3}-\delta_{\alpha,\parallel}\right],\end{aligned} \tag{5.15}$$

where $\delta_{\parallel,\parallel} = 1$ and $\delta_{\perp,\parallel} = \delta_{o,\parallel} = 0$. A comparison of the approximate expression for the spheres' self-mobility (Eq. 5.14) and the exact result by Stokes (Eq. 5.12) is shown in Fig. 5.3: both nicely match over the entire frequency range accessible in our experiment ($f \lesssim 100$ kHz).

The frequency dependence of the cross-mobilities parallel and perpendicular to the inter-bead axis are shown for two different ratios of inter-bead separation R to bead radius a as solid lines in Fig. 5.4. In the low-frequency limit $\omega\tau_R \to 0$, the cross-mobilities in Eq. 5.15 reduce to the principal components of the Rotne-Prager (RP) tensor [238] commonly employed in Brownian hydrodynamics simulations [239]

$$\frac{\mu_{\mathrm{cross}}^{\alpha,\mathrm{RP}}}{\mu_0} = \frac{3a}{4R}\left[1+\delta_{\alpha,\parallel}\right]+\frac{3a^3}{2R^3}\left[\frac{1}{3}-\delta_{\alpha,\parallel}\right], \qquad \alpha \in \{\parallel,\perp,o\}, \tag{5.16}$$

with dominant $1/R$-scaling and corrections accounting for the finite bead size a. These quasi-stationary cross-mobilities are indicated by horizontal arrows in Fig. 5.4.

The finite time scale τ_R for the vorticity to diffuse over length scales comparable to the bead separation R is reflected in the frequency dependence of real and imaginary parts of the cross-

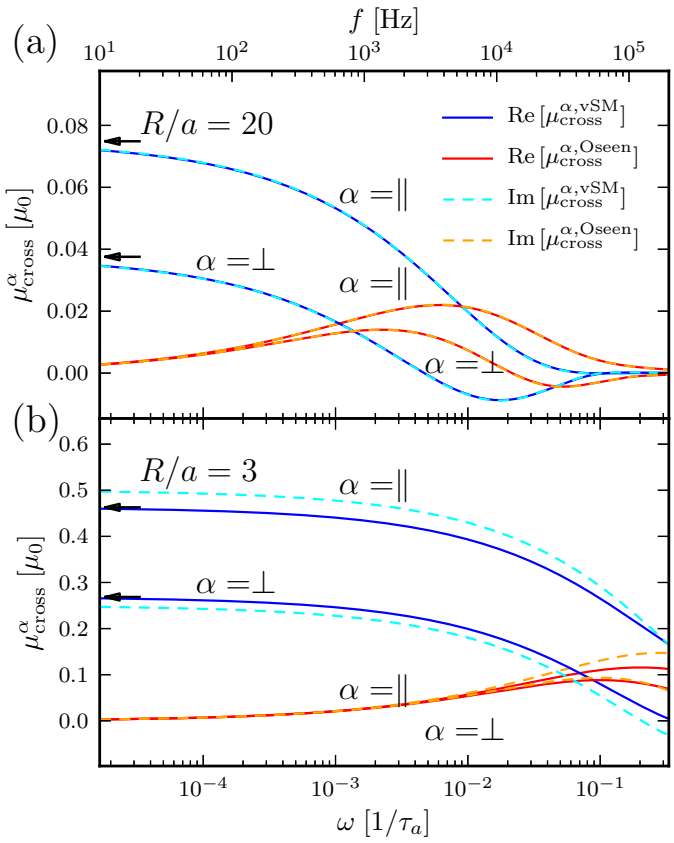

Figure 5.4:
Frequency dependence of cross-mobilities parallel ($\alpha = \parallel$) and perpendicular ($\alpha = \perp$) to the inter-bead axis for two different ratios of inter-bead separation R to bead radius a: a) $R/a = 20$, b) $R/a = 3$. Cross-mobilities for spheres of finite radius (*solid lines*, Eq. 5.15) are compared to the Oseen result for point-like particles (*dashed lines*, Eq. 5.17) and to quasi-static HI (*horizontal arrows*, Eq. 5.16). Cross-mobilities are given in units of the quasi-static Stokes self-mobility $\mu_0 \equiv 1/(6\pi\eta_0 a)$ for a sphere of radius a in a fluid of shear viscosity η_0; the angular frequency is rescaled by the characteristic time scale τ_a for vortex diffusion over the length scale of the bead's radius a, the top frequency scale corresponds to experimental conditions ($\tau_a \approx 0.26\ \mu$s).

mobilities as seen in Fig. 5.4; corrections to the quasi-static limit denoted by horizontal arrows, set in at frequencies $\omega \sim 1/\tau_R$ and thus become apparent at smaller frequencies for the case of large separations $R/a = 20$ as compared to $R/a = 3$. In contrast, corrections accounting for the finite size of the beads are important at small separations ($R/a = 3$) and become irrelevant at larger ones ($R/a = 20$): in the limit $a/R \to 0$ the expressions for the cross-mobilities (Eq. 5.15) reduce, as expected, to the Oseen result for point-forces [102, 240]

$$\frac{\mu_{\text{cross}}^{\alpha,\text{Oseen}}}{\mu_0} = \frac{3a\left(1-\mathrm{e}^{-\lambda_{\text{in}}R}(\lambda_{\text{in}}R+1)\right)}{\lambda_{\text{in}}^2R^3}\,\delta_{\alpha,\parallel} + \frac{3a}{2}\,\frac{\mathrm{e}^{-\lambda_{\text{in}}R}\left(\lambda_{\text{in}}^2R^2+\lambda_{\text{in}}R+1\right)-1}{\lambda_{\text{in}}^2R^3}\Big[1-\delta_{\alpha,\parallel}\Big], \quad (5.17)$$

shown as dashed lines in Fig. 5.4. In the frequency and distance range, in which $|\lambda_{\text{in}}|\,R \gg 1$ but still $|\lambda_{\text{in}}|\,a \ll 1$, Eq. 5.15 reduces to [237]

$$\frac{\mu_{\text{cross}}^{\alpha,\text{vSM}}(\omega)}{\mu_0} \approx -\left(\frac{9}{2}\frac{a}{\lambda_{\text{in}}^2R^3} + \frac{a^3}{R^3}\right)\left[\frac{1}{3}-\delta_{\alpha,\parallel}\right], \qquad \alpha \in \{\parallel,\perp,o\}, \quad (5.18)$$

revealing the existence of a second dynamic regime, in which HI are considerably weakened and decay as $1/R^3$. Note that since $|\lambda_{\text{in}}|\,a \ll 1$, in the above expression the first term $\propto \omega^{-1}$ dominates over the second one accounting for the finite size of the beads.

As discussed in the last paragraphs, the strength of the HI depends on the relative distance and orientation of the two beads, which introduces nonlinearities in the equations of motion (Eqs. 5.7 and 5.8). The fact that the bead's positional fluctuations (in our setup on the order of $\sqrt{k_{\text{B}}T/\kappa} \approx 5$ nm) are relatively small compared to the average inter-bead separation $R \sim 1.5-10\ \mu$m justifies the pre-averaging [241] of the equations of motion, i.e., replacing the actual cross-mobilities by the (constant) cross-mobilities for the average bead configuration.

Previous experimental studies have mostly focused on the quasi-stationary limit (Eq. 5.16): The interplay of instantaneous HI and the finite relaxation times in the harmonic trapping potentials of optical tweezers are responsible for time-delayed anti-correlations in the beads' positions [228–230]. Similarly, translation-rotation coupling, though decaying as $1/R^2$ and therefore weaker, is equally observable combining optical tweezers with polarization microscopy [242, 243]. The frequency dependence of the HI has been addressed in a series of experiments [219–221] based on the point-particle limit derived by Oseen (Eq. 5.17), thereby neglecting corrections for the finite size of the beads.

5.4 Signal Processing in a Dual Trap Optical Tweezer Experiment

The electrical signals recorded in a dual trap optical tweezer setup as described in Sec. 5.1 generally differ from the actual trajectories of the two beads due to various instrumental effects [214, 225, 244] including polarization crosstalk, filtering of the position sensing device and amplification electronics as well as instrumental noise. The consequences of these instrumental effects on the PSDs are discussed in Sec. 5.4.1. Experimentally, PSDs are estimated based on discretely sampled and finite trajectories, the resulting effects are addressed in Sec. 5.4.2.

Notation: The following discussion equally applies to the signals corresponding to both spatial coordinates $\alpha = \parallel$ and $\alpha = \perp$. To avoid an overloaded notation, indices and superscripts α are therefore omitted. An overview of frequently used symbols throughout this chapter is found in Tab. 5.1.

Quantity	Symbol	Definition
Spatial direction	α	$\in \{\parallel, \perp, o\}$
Bead / Signal indices	i, j	$\in \{1, 2\}$
Bead coordinate	r_i	
Linear response function	J_{ij}	Eq. 5.5
Thermal correlation function / PSD	S_{ij}^{th}	Eqs. 5.1, 5.3 & 5.4
(Virtual) filter function	f_i	Eq. E.13
Electrical signal	z_i	Eqs. 5.19 & 5.20
Electrical PSD	S_{ij}	Eq. 5.24
Electrical DFT component	Z_i	Eq. E.41
Sampling interval	Δt	
Sampling rate	f_{sampl}	$= 1/\Delta t$
Nyquist frequency	f_{Nyq}	$= f_{\mathrm{sampl}}/2$
# of data points per time window	N	
Duration of a time window	T	$= N\Delta t$
Periodogram	P_{ij}	Eq. 5.27
# of independent time windows	N_{w}	
# of discrete frequencies per block	N_{b}	
# of blocked frequencies resolved	N_{f}	
Averaged periodogram	$\overline{P}_{ij}$	Eq. 5.32

Table 5.1:
Overview of the notation used in this chapter; sub- and superscripts α are omitted in the text, if the discussion equally applies to all spatial directions.

5.4.1 Crosstalk, signal filtering and instrumental noise

The use of a single laser for both optical traps induces polarization crosstalk between the channels [225], meaning that changes in the positions r_1 and r_2 of *both* beads contribute to each of the detected signals

$$\tilde{z}_i(t) \equiv \int_{-\infty}^{\infty} \mathrm{d}t' \; f_i(t-t') \sum_{j=1}^{2} \epsilon_{ij} r_j(t') \qquad i \in \{1,2\}, \tag{5.19}$$

with amplitudes $\epsilon_{11} \gg \epsilon_{12}$ and $\epsilon_{22} \gg \epsilon_{21}$ and where f_i denotes the filter kernel in channel i. Clearly, $f_i(t) = 0$ for $t < 0$ due to causality. Filtering can be due to the position sensing device detecting the centroid of the laser spot intensity [216, 244], the amplification electronics or other factors, which are discussed in detail in Appendix E.1. In addition, the recorded signals are affected by stationary additive and independent instrumental noise

$$z_i(t) = \tilde{z}_i(t) + \eta_i(t), \qquad i \in \{1,2\}, \tag{5.20}$$

with vanishing mean

$$\langle \eta_i(t) \rangle = 0, \tag{5.21}$$

and correlations

$$\langle \eta_i(t)\eta_j(t') \rangle = S_{ij}^{\mathrm{noise}}(t-t'), \qquad \langle \eta_i(t) z_j(t') \rangle = 0. \tag{5.22}$$

In the actual experimental setup, contributions to the noise η_i include vibrations of the optical components in the optical path, electronic noise in the detectors as well as shot noise. Using the Eqs. 5.19 and 5.20 and the above statistical properties of the instrumental noise, the PSD of the electrical signals, defined by

$$\langle z_i(\omega) z_j^\star(\omega') \rangle = 2\pi\, \delta(\omega - \omega')\, S_{ij}(\omega), \tag{5.23}$$

can be related to the thermal PSDs S_{ij}^{th} defined in Sec. 5.2.1 and the noise PSDs S_{ij}^{noise},

$$S_{ij}(\omega) \equiv f_i(\omega) f_j^\star(\omega) \sum_{k,l=1}^{2} \epsilon_{ik}\epsilon_{jl} S_{kl}^{\mathrm{th}}(\omega) + S_{ij}^{\mathrm{noise}}(\omega). \tag{5.24}$$

Due to crosstalk, filter and noise characteristics, these PSDs S_{ij} may dramatically differ from the thermal PSDs S_{ij}^{th}, in particular: (i) The cross-PSD S_{12} can be dominated by S_{11}^{th} or S_{22}^{th} due to crosstalk, if $\epsilon_{21} S_{11}^{\mathrm{th}} \gtrsim \epsilon_{22} S_{12}^{\mathrm{th}}$ or $\epsilon_{12} S_{22}^{\mathrm{th}} \gtrsim \epsilon_{11} S_{12}^{\mathrm{th}}$, which is always true for zero crossings of S_{12}^{th}, (ii) although all thermal PSDs S_{ij}^{th} ($i, j \in \{1, 2\}$) are real (cf. Sec. 5.2.1), the cross-PSD S_{12} may have a non-vanishing imaginary part, if the filter characteristics of the two position sensing devices and electronics differ so that $\mathrm{Im}\,[f_1 f_2^\star] \neq 0$, see Appendix E.1 for details, and (iii) auto-PSDs S_{ii} are generally more affected by instrumental noise than cross-PSDs, since the instrumental noise in the two channels is found to be (almost) independent, $S_{ii}^{\mathrm{noise}} \gg S_{ij}^{\mathrm{noise}}$, $i \neq j$.

5.4.2 Influence of time resolution and overall measurement time

Discretely sampled experimental signals form the basis of the spectral analysis and are used to estimate auto- and cross-PSDs applying a DFT on the recorded time series. The use of a DFT instead of a continuous Fourier transformation introduces systematic artifacts as detailed in Appendix E.4. Most prominently, due to the finite sampling interval Δt one obtains estimates for the aliased PSDs

$$S_{ij}^{\mathrm{al.}}(\omega_n) \equiv \sum_{m=-\infty}^{\infty} S_{ij}\left(\omega_n + m\frac{2\pi}{\Delta t}\right), \tag{5.25}$$

at discrete frequencies

$$\omega_n \equiv \frac{2\pi n}{T}, \tag{5.26}$$

where $T = N\Delta t$ is the length of the time series and n is an integer. The double-infinite sum over all integers m in Eq. 5.25 is in practice approximated numerically using suitable lower and upper cutoffs, see Appendix E.4 for details.

5.5 Relating Experiment and Theory

In equilibrium optical tweezer experiments, the recorded signals reflect the stochastic, thermal fluctuations of the beads in the setup: Periodograms calculated from experimental time series therefore are random variables, the statistical properties of which are discussed in Sec. 5.5.1, while the explicit calculations are found in Appendix E.3. Based on these statistics, a maximum-likelihood method is proposed in Sec. 5.5.2, which allows to determine unknown parameters by a global fit of auto- and cross-PSDs to the periodogram values. Quantifying the deviations

between fit and experimental data may serve to validate the underlying model as shown in Sec. 5.5.3. The overall spectral analysis is summarized in Sec. 5.5.4.

5.5.1 Statistical properties of auto- and cross-periodograms

The thermal motion of the beads being stochastic, the signals $z_i(t)$ recorded over a time window T, their Fourier components $z_i(\omega)$ as well as real and imaginary parts of the periodograms

$$P_{ij}(n) \equiv \frac{1}{T} z_i(\omega_n) z_j^\star(\omega_n), \tag{5.27}$$

are stochastic quantities. Leakage effects (cf. Appendix E.4) being negligible as long as the window time T is much larger than all relevant time scales in the system [214], the expectation values of real and imaginary parts of the periodograms by definition (cf. Eqs. 5.23 and 5.27) coincide with the corresponding real and imaginary parts of the PSDs

$$\left\langle \mathrm{Re}\left[P_{ij}(n)\right]\right\rangle = \mathrm{Re}\left[S_{ij}(\omega_n)\right], \tag{5.28}$$

$$\left\langle \mathrm{Im}\left[P_{ij}(n)\right]\right\rangle = \mathrm{Im}\left[S_{ij}(\omega_n)\right]. \tag{5.29}$$

However, the values of individual periodograms are broadly distributed around these expectation values as is seen from the variances of these quantities. From the explicit calculations in Appendix E.3 resulting in the Eqs. E.38-E.40, one obtains [213]

$$\Sigma^2\left[\mathrm{Re}\left[P_{ij}\right]\right] = \frac{1}{2}\left(S_{ii}S_{jj} + \mathrm{Re}\left[S_{ij}\right]^2 - \mathrm{Im}\left[S_{ij}\right]^2\right), \tag{5.30}$$

$$\Sigma^2\left[\mathrm{Im}\left[P_{ij}\right]\right] = \frac{1}{2}\left(S_{ii}S_{jj} - \mathrm{Re}\left[S_{ij}\right]^2 + \mathrm{Im}\left[S_{ij}\right]^2\right), \tag{5.31}$$

where $\Sigma^2[\dots] \equiv \left\langle (\dots)^2\right\rangle - \langle \dots\rangle^2$ denotes the second central moment and the frequency arguments have for simplicity been omitted. For auto-periodograms ($i = j$), which by definition are real and positive, $\Sigma^2[\mathrm{Re}\,[P_{ii}]] = S_{ii}^2$ since $\mathrm{Im}\,[S_{ii}] \equiv 0$ in Eq. 5.30; the statistical uncertainty thus coincides with the expectation value S_{ii}. More specifically, one can show that the values of the auto-periodogram P_{ii} are exponentially distributed [214, 245, 246]. Note that periodogram values are non-self-averaging, meaning that increasing the signal length T yields periodogram estimates for a larger set of discrete frequencies and reduces leakage effects (cf. Appendix E.4) but has no influence on the periodogram statistics.

For the real and imaginary parts of the cross-periodograms ($i \neq j$), the situation is even worse, since the statistical uncertainties will in general exceed the expectation values due to the dominance of the term $S_{ii}S_{jj}$ in the Eqs. 5.30 and 5.31; in the general case where $S_{ij} \neq 0$, the form of the probability density functions (PDFs) for real and imaginary parts of the cross-periodograms are not simple [213].

The previous statements, which are based on the use of the continuous Fourier transformation, also apply to the periodograms based on the DFT of discretely sampled time series, if the PSDs S_{ij} in the Eqs. 5.28-5.31 are replaced by their aliased equivalents $S_{ij}^{\mathrm{al.}}$ defined in Eq. 5.25, see Appendix E.3 for details.

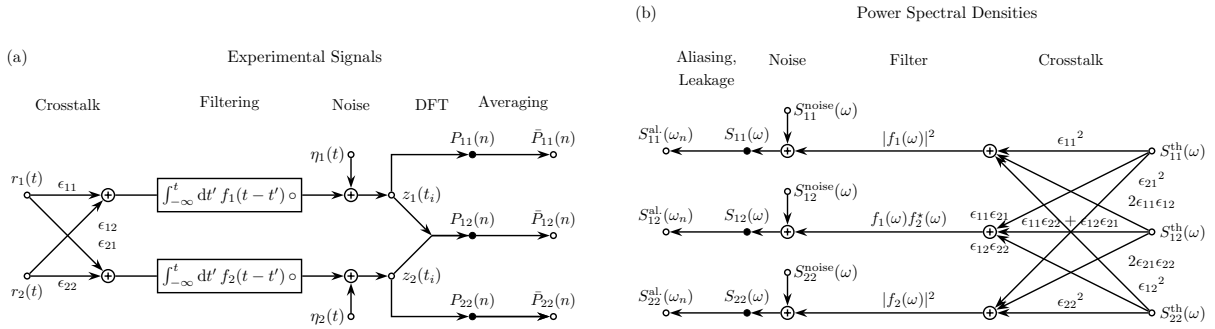

Figure 5.5:
Visualization of the signals in a typical dual trap optical tweezer experiment as described in the Secs. 5.4 and 5.5.1. a) Signal processing as described by the Eqs. 5.19 and 5.20; averaged periodograms $\overline{P}_{ij}$ obtained via DFT from the discretely sampled stochastic trajectories yield experimental estimates for the aliased PSDs $S_{ij}^{\mathrm{al.}}$. b) Relation between auto- and cross-PSDs S_{ij}^{th} of the beads' thermal motion and aliased electrical PSDs $S_{ij}^{\mathrm{al.}}$ according to the Eqs. 5.24 and 5.25. Unknown parameters in the PSDs can be determined via a global maximum-likelihood fit to $\overline{P}_{ij}$ as explained in Sec. 5.5.2.

The way to deal with the above mentioned statistical uncertainties is of course to average periodograms over N_{w} statistically independent time windows and (possibly) over blocks of N_{b} discrete, neighboring frequencies, yielding averaged periodograms

$$\overline{P}_{ij}(n) \equiv \frac{1}{N_{\mathrm{w}} N_{\mathrm{b}}} \sum_{k=1}^{N_{\mathrm{w}}} \sum_{l} P_{ij}^{(k)}(l), \tag{5.32}$$

where the superscript (k) discriminates the periodogram values of different time windows and the index l runs over the block of N_b frequencies around ω_n. Note that "blocking" may cause artifacts: for a single trap blocking effects are negligible as long as $N_{\mathrm{b}} \ll \kappa\mu_0 T/(2\pi)$, see Ref. [214] for further details. According to the central limit theorem, the statistical uncertainty Σ of the averaged periodograms is reduced by a factor $1/\sqrt{N_{\mathrm{w}} N_{\mathrm{b}}}$ with respect to the periodograms of individual time windows; the values of $\overline{P}_{ij}$ thus represent statistically more reliable experimental estimates of the PSD S_{ij}.

Clearly, not the individual values of the auto- and cross-PSDs S_{ij} are of interest but the values of the parameters in the theoretical model, which yield the best agreement between theory and experimental data, i.e., the averaged auto- and cross-periodograms $\overline{P}_{ij}$ at the discrete frequencies ω_n resolved experimentally. A controlled way of inferring these parameters from the data taking into account the statistical aspects discussed in this section is given by the maximum-likelihood method described in Sec. 5.5.2. A schematic summarizing the signal processing described in Sec. 5.4 and the relationship between periodograms and PSDs discussed above is found in Fig. 5.5.

5.5.2 Maximum-likelihood fits of power spectral densities

The theoretical auto- and cross-PSDs S_{ij} of the electrical signals involve parameters both on the level of the thermal motion of the experimental object (trap strengths, particle radii, etc., cf. Secs. 5.2 and 5.3) as well as on the level of the signal processing in the instrument (amplification,

polarization crosstalk, parasitic filtering, etc., cf. Sec. 5.4 and Appendix E.1). For averaged periodograms $\overline{P}_{ij}$ (Eq. 5.32) calculated from experimental time series, optimal parameter values can be obtained by Bayesian inference, which thus constitutes the missing link between theory and experiment in Fig. 5.5. The strength of the method consists in the fact that the statistical aspects discussed in Sec. 5.5.1 are inherently taken into account.

In general, given some measured data, the most likely parameters (params) are those maximizing the conditional probability $\mathcal{P}\left(\text{params}|\text{data}\right)$. Using Bayes' theorem

$$\mathcal{P}\left(\text{params}|\text{data}\right) = \frac{\mathcal{P}\left(\text{data}|\text{params}\right)\mathcal{P}\left(\text{params}\right)}{\mathcal{P}\left(\text{data}\right)}, \tag{5.33}$$

and assuming a uniform prior distribution of the parameters, i.e., $\mathcal{P}\left(\text{params}\right) = \text{const.}$, maximizing $\mathcal{P}\left(\text{params}|\text{data}\right)$ turns out to be equivalent to maximizing the conditional probability $\mathcal{P}\left(\text{data}|\text{params}\right)$ of observing some data given a set of parameters. In the present case, the data consists of the ensemble of averaged periodogram vectors

$$\overline{\boldsymbol{P}} \equiv \left(\overline{P}_{11}, \overline{P}_{22}, \text{Re}\left[\overline{P}_{12}\right], \text{Im}\left[\overline{P}_{12}\right]\right)^{\text{T}}, \tag{5.34}$$

at each of the N_f discrete frequencies resolved in the spectral analysis. Periodograms of distinct time windows are independent random variables drawn from a PDF with finite first and second moments given in Sec. 5.5.1 and Appendix E.3. According to the central limit theorem, when averaging over a large number $N_\text{w}N_\text{b}$ of realizations, the PDF for an averaged periodogram vector $\overline{\boldsymbol{P}}$ converges to a multivariate normal PDF characterized by the expectation vector

$$\left\langle\overline{\boldsymbol{P}}\right\rangle = \boldsymbol{S}^{\text{al.}} \equiv \left(S_{11}^{\text{al.}}, S_{22}^{\text{al.}}, \text{Re}\left[S_{12}^{\text{al.}}\right], \text{Im}\left[S_{12}^{\text{al.}}\right]\right)^{\text{T}}, \tag{5.35}$$

and a covariance matrix resulting from the periodogram covariances calculated in Appendix E.3,

$$\boldsymbol{V}^{\text{al.}} \equiv \frac{1}{N_\text{w}N_\text{b}} \times \begin{pmatrix} {S_{11}^{\text{al.}}}^2 & \text{Re}\left[S_{12}^{\text{al.}}\right]^2 + \text{Im}\left[S_{12}^{\text{al.}}\right]^2 & S_{11}^{\text{al.}}\text{Re}\left[S_{12}^{\text{al.}}\right] & S_{11}^{\text{al.}}\text{Im}\left[S_{12}^{\text{al.}}\right] \\ \text{Re}\left[S_{12}^{\text{al.}}\right]^2 + \text{Im}\left[S_{12}^{\text{al.}}\right]^2 & {S_{22}^{\text{al.}}}^2 & S_{22}^{\text{al.}}\text{Re}\left[S_{12}^{\text{al.}}\right] & S_{22}^{\text{al.}}\text{Im}\left[S_{12}^{\text{al.}}\right] \\ S_{11}^{\text{al.}}\text{Re}\left[S_{12}^{\text{al.}}\right] & S_{22}^{\text{al.}}\text{Re}\left[S_{12}^{\text{al.}}\right] & \frac{1}{2}\left(S_{11}^{\text{al.}}S_{22}^{\text{al.}} + \text{Re}\left[S_{12}^{\text{al.}}\right]^2 - \text{Im}\left[S_{12}^{\text{al.}}\right]^2\right) & \text{Re}\left[S_{12}^{\text{al.}}\right]\text{Im}\left[S_{12}^{\text{al.}}\right] \\ S_{11}^{\text{al.}}\text{Im}\left[S_{12}^{\text{al.}}\right] & S_{22}^{\text{al.}}\text{Im}\left[S_{12}^{\text{al.}}\right] & \text{Re}\left[S_{12}^{\text{al.}}\right]\text{Im}\left[S_{12}^{\text{al.}}\right] & \frac{1}{2}\left(S_{11}^{\text{al.}}S_{22}^{\text{al.}} - \text{Re}\left[S_{12}^{\text{al.}}\right]^2 + \text{Im}\left[S_{12}^{\text{al.}}\right]^2\right) \end{pmatrix}, \tag{5.36}$$

where the (discrete) frequency arguments n and ω_n are again omitted for simplicity. Periodogram values at different frequencies being (approximately) independent [213], the overall conditional probability of observing a certain ensemble of averaged periodograms given a particular set of parameters is just the product of the N_f multivariate normal PDFs

$$\mathcal{P}(\text{data}|\text{params}) = \prod_n \left(\frac{1}{4\pi^2\sqrt{\det(\boldsymbol{V}^{\text{al.}}(\omega_n))}}\, \text{e}^{-\frac{1}{2}\left(\overline{\boldsymbol{P}}(n) - \boldsymbol{S}^{\text{al.}}(\omega_n)\right)^{\text{T}} \cdot \boldsymbol{V}^{\text{al.}\,-1}(\omega_n) \cdot \left(\overline{\boldsymbol{P}}(n) - \boldsymbol{S}^{\text{al.}}(\omega_n)\right)} \right). \tag{5.37}$$

For a given ensemble of averaged periodograms, the optimal set of parameters is obtained by maximizing the above conditional probability with respect to these parameters; by rea-

son of numerical stability, it is however preferred to minimize the negative log-likelihood $-\log\left(\mathcal{P}(\text{data}|\text{params})\right)$, which up to a constant equals

$$\sum_n \left(\frac{1}{2} \left(\overline{\boldsymbol{P}}(n) - \boldsymbol{S}^{\text{al.}}(\omega_n) \right)^{\text{T}} \cdot \boldsymbol{V}^{\text{al.}\,-1}(\omega_n) \cdot \left(\overline{\boldsymbol{P}}(n) - \boldsymbol{S}^{\text{al.}}(\omega_n) \right) + \frac{1}{2} \log \left[\det \left(\boldsymbol{V}^{\text{al.}}(\omega_n) \right) \right] \right). \tag{5.38}$$

The maximum-likelihood method for determining the optimal set of parameters in the theoretical model consists of performing a minimization of Eq. 5.38 in the (multidimensional) parameter space; since the second term in Eq. 5.38 can be neglected if $\sqrt{N_\text{w} N_\text{b}(n)} \gg 1$, one is left with minimizing the sum of normalized squared deviations

$$\text{SNSD} \equiv \sum_n \left(\overline{\boldsymbol{P}}(n) - \boldsymbol{S}^{\text{al.}}(\omega_n) \right)^{\text{T}} \cdot \boldsymbol{V}^{\text{al.}\,-1}(\omega_n) \cdot \left(\overline{\boldsymbol{P}}(n) - \boldsymbol{S}^{\text{al.}}(\omega_n) \right), \tag{5.39}$$

which corresponds to a standard multidimensional least-square fit, for which a handy implementation in C/C++ has been provided by M. Lourakis [247].

Note that in the case of one trap and thus a single signal, $V^{\text{al.}} = {S_{11}^{\text{al.}}}^2/(N_\text{w} N_\text{b})$ and Eq. 5.38 (again up to a constant) reduces to

$$\sum_n \left(\frac{N_\text{w} N_\text{b}(n)}{2} \left(\frac{\overline{P}_{11}(n)}{S_{11}^{\text{al.}}(\omega_n)} - 1 \right)^2 + \log \left(S_{11}^{\text{al.}}(\omega_n) \right) \right). \tag{5.40}$$

This is the quantity which is commonly minimized for the calibration of single trap setups [214].

5.5.3 Deviations between fits and data

Once Eq. 5.39 has been minimized numerically, the encountered minimal value

$$\text{SNSD}_\text{min} \equiv \min_\text{params} \text{SNSD}, \tag{5.41}$$

quantifies the remaining squared deviations between averaged experimental periodograms and theoretical PSDs. The fit quality can be judged based on the sample average of the normalized deviations per experimental observable

$$\chi^2_\text{fit} = \frac{1}{N_{\overline{\boldsymbol{P}}} N_\text{f}} \text{SNSD}_\text{min}, \tag{5.42}$$

where N_f denotes the number of discrete frequencies resolved in the spectral analysis and $N_{\overline{\boldsymbol{P}}}$ is the dimension of the periodogram vector $\overline{\boldsymbol{P}}$ defined in Eq. 5.34. The expectation value of χ^2_fit being 1, the encountered value of χ^2_fit is an indicator for the quality of the theoretical modeling of the experimental signals: both values $\chi^2_\text{fit} \gg 1$ and $\chi^2_\text{fit} \ll 1$ indicate deficits in the model and comparing χ^2_fit-values may help to discriminate between various potentially appropriate models.

In some cases, it is helpful to restrict the computation of SNSD and χ^2_fit to a subset of the observables in $\overline{\boldsymbol{P}}$ to localize the source of the deviations observed. If for example only P_{11} and $\text{Re}\left[P_{12}\right]$ are considered, only the first and third columns and rows in $\boldsymbol{V}^{\text{al.}}$ are taken into account and one sets $N_{\overline{\boldsymbol{P}}} = 2$ in Eq. 5.42.

5.5.4 Power spectral analysis in a nutshell

Overall, the auto- and cross-power spectral analysis of optical tweezer experiments proposed in this chapter involves the following procedure:

1. Determine the analytical form of the auto- and cross-PSDs S_{ij}^{th} describing the thermal fluctuations of the beads, which are the experimentally accessible parts of the overall construct under study (Sec. 5.2).

2. Identify the relations between bead positions and detected signals (Sec. 5.4) and deduce the analytical form of the auto- and cross-PSDs S_{ij}.

3. Perform the actual experiment and calculate averaged auto- and cross periodograms $\overline{P}_{ij}$ from the experimental time series via Eqs. 5.27 and 5.32.

4. Perform a numerical minimization of Eq. 5.39 to determine the optimal parameter values compatible with the data.

5. Judge on the validity of the theoretical model based on the deviations between best fits and the experimental data (Sec. 5.5.3).

In a first step, this procedure allows a precise calibration of the instrument by three consecutive calibration measurements as shown in Sec. 5.6. In a second step, additional unknown parameters of more complex experimental constructs, characterizing for example the viscoelastic properties of the molecular tether under study, can be determined.

5.6 Calibration of Dual Trap Optical Tweezers

A series of three measurements is proposed for the calibration of a dual trap optical tweezer setup: (i) both traps empty, in the following named Cal. I, (ii) first trap occupied, second one empty (Cal. II), and (iii) second trap occupied, first one empty (Cal. III). In Cal. I, all thermal PSDs vanish, $S_{ij}^{\text{th}} = 0,\ \forall i,j$, and therefore according to Fig. 5.5a the recorded periodograms $\overline{P}_{ij}$ result from the instrumental noise only. In Cal. II, only the thermal PSD S_{11}^{th} is non-zero reflecting the stochastic motion of a single bead in the first optical trap [214] and similarly S_{22}^{th} is the only non-vanishing thermal PSD in Cal. III. Explicit expressions for the thermal PSD of a single bead in a harmonic trap are for example found in Ref. [214].

Detector output voltages are recorded with 100 kHz sampling rate over a time window of 60 s for each of the calibration experiments. The time series are analyzed using 6000 windows of $T = 10$ ms duration each, and blocking neighboring periodogram values resulting in blocked periodogram values at 84 distinct discrete frequencies in the range of 100 Hz to 50 kHz. The averaged periodograms resulting from the spectral analysis are denoted as symbols in Fig. 5.6, where top and bottom figures show data corresponding to the spatial direction parallel and perpendicular to the inter-trap axis, respectively.

The averaged periodograms from Cal. I shown in Fig. 5.6a reveal that the instrumental noise recorded by the two detectors is to a major extent independent, demonstrated by the fact that typical amplitudes of the cross-periodograms $\overline{P}_{12}$ are suppressed by one order of magnitude or more with respect to the auto-periodogram values $\overline{P}_{11}$ and $\overline{P}_{22}$. The functional form of the instrumental noise-PSDs S_{ij}^{noise}, the Fourier transformations of the noise correlation functions

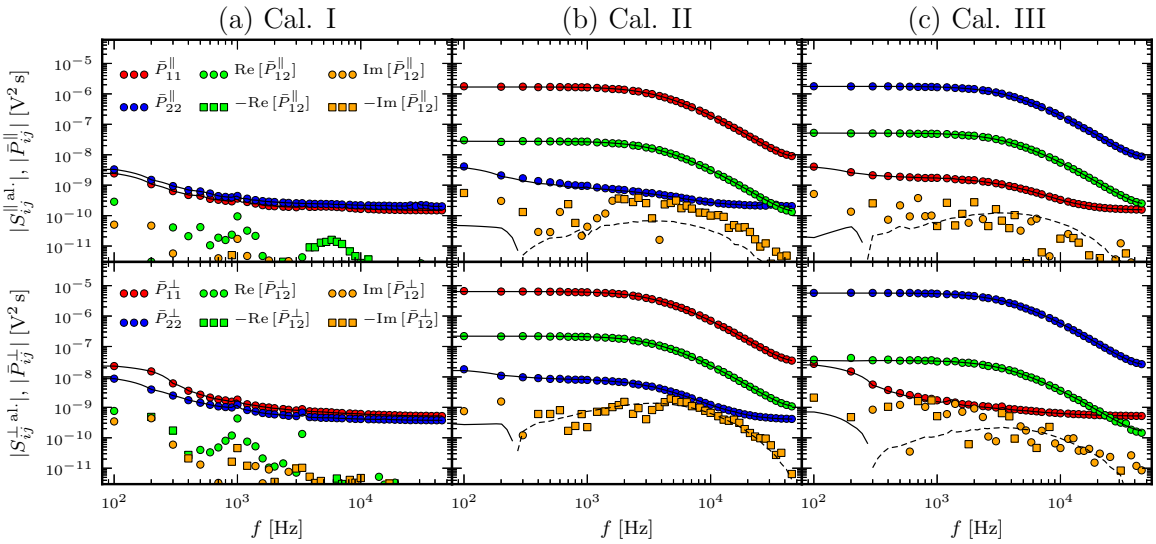

Figure 5.6:
Results of the three calibration measurements described in Sec. 5.6: a) no trapped beads, b) first trap occupied and second one empty, c) vice versa. Averaged experimental periodograms $\overline{P}^{\alpha}_{ij}$ are denoted by *symbols*, theoretical PSDs $S^{\alpha\,\mathrm{al.}}_{ij}$, based on a global maximum-likelihood fit to the data (Sec. 5.5.2) are shown as *lines*, where *dashed lines* correspond to negative values of the PSDs; fit values are given in Tab. 5.2. Results for the spatial coordinates parallel to the inter-trap axis ($\alpha = \parallel$) are shown in the upper row, those for the perpendicular direction ($\alpha = \perp$) in the lower one.

in Eq. 5.22, can be modeled as a uniform white-noise background spectrum superimposed by a $1/f$-PSD as well as a number of spikes at well-defined frequencies (data not shown). Given that, according to Eq. 5.24, noise PSDs simply yield an additive contribution to the detected PSDs S_{ij}, we restrict ourselves to directly use the values of the averaged periodograms in Fig. 5.6a as reliable estimates of the aliased noise PSDs for the analysis of the subsequent experiments. Assuming stationarity and statistical independence of the time windows, the expected statistical error for the averaged auto-periodograms is in fact on the order of one percent or below, depending on the block size.

According to Fig. 5.5b, one expects contributions of the thermal motion of the bead in the first trap, S^{th}_{11}, and of the instrumental noise, S^{noise}_{ij}, to the measured periodograms of Cal. II. The averaged periodograms $\overline{P}_{11}$ (red circles) in Fig. 5.6b in fact reflect the typical Lorentzian shape of S^{th}_{11}. Due to polarization crosstalk ($\epsilon_{21} \neq 0$) the thermal motion of the bead is also observed in the real part of the cross-periodograms, Re $\left[\overline{P}_{12}\right]$, shown as green symbols, though reduced in amplitude by a factor $\epsilon_{21}/\epsilon_{11}$ with respect to $\overline{P}_{11}$. The auto-periodogram of the second signal $\overline{P}_{22}$ (blue circles) is clearly dominated by the instrumental noise, the thermal motion of the bead introducing only slight changes with respect to Cal. I in Fig. 5.6a. The imaginary parts of the cross-periodogram values, Im $\left[\overline{P}_{12}\right]$ (orange symbols), result from an asymmetry in the signal filtering properties of the two channels as well as from the statistical uncertainty and will be discussed later. Up to this point, the undetermined parameters are the trap strength κ_1 in S^{th}_{11}, the V/nm conversion factors ϵ_{11} and ϵ_{21} as well as parameters ϕ_i and τ_i ($i \in \{1, 2\}$) reflecting the parasitic filtering properties of the two position sensing devices and entering the filter functions f_1 and f_2, see Appendix E.1 for further details. The situation for

Quantity	Symbol	Values $\parallel$	Values $\perp$	Units
Trap strength	κ_1	0.21 ± 0.021	0.21 ± 0.007	pN/nm
	κ_2	0.21 ± 0.018	0.20 ± 0.012	pN/nm
Amplitudes	ϵ_{11}	32 ± 1.1	61 ± 1.0	mV/nm
	ϵ_{12}	0.93 ± 0.034	0.34 ± 0.021	mV/nm
	ϵ_{21}	0.52 ± 0.025	2.10 ± 0.037	mV/nm
	ϵ_{22}	32 ± 1.2	56 ± 1.0	mV/nm
Pol. crosstalk	$\epsilon_{12}/\epsilon_{11}$	2.9	0.56	%
	$\epsilon_{21}/\epsilon_{22}$	1.6	3.7	%
Fraction of	ϕ_1	0.6 ± 0.054	0.63 ± 0.038	—
fast electrons	ϕ_2	0.6 ± 0.040	0.61 ± 0.023	—
Electr. relax.	τ_1	5.7 ± 1.5	5.5 ± 1.0	μs
time scale	τ_2	6.1 ± 1.5	6.6 ± 0.8	μs
Normalized sq.	χ^2_{fit}	18	8.7	—
deviations	$\chi^2_{\text{fit, red}}$	1.8	2.1	—

Table 5.2:
Calibration results: Best fit parameters obtained from global maximum-likelihood fits to the averaged periodograms in Fig. 5.6 as described in Sec. 5.6.

Cal. III is analogous to the previous discussion of Cal. II except for indices 1 and 2 interchanged, which adds the three additional parameters κ_2, ϵ_{12} and ϵ_{22}.

Since voltage amplitudes and polarization crosstalk differ for both spatial directions, we treat the corresponding data sets for $\alpha = \parallel$ and $\alpha = \perp$ separately. We use $\eta_0 = 0.949 \cdot 10^{-3}$ N s/m^2 and $\nu = 0.951 \cdot 10^{-6}$ m^2/s for the dynamic and kinematic viscosity of water at the experimental temperature $T = 22.6^\circ$ C and the radius $a = 500$ nm given by the manufacturer for both beads. The values of the 10 parameters are determined by a global maximum-likelihood fit to averaged auto- and cross-periodograms from Cal. II and III as described in Sec. 5.5.2. Best fits to the data are shown as black lines in Fig. 5.6, values of the fit parameters including confidence intervals are found in Tab. 5.2. As expected, the fit values for the trap stiffnesses κ_1 and κ_2 as well as for the detector properties (ϕ_1, ϕ_2, τ_1, τ_2) for the two orthogonal spatial directions $\parallel$ and $\perp$ in Tab. 5.2 agree within error.

In Fig. 5.6, the agreement of experimental data and fits for the auto-PSDs S_{11} and S_{22} and the real part of the cross-PSD, Re $[S_{12}]$, is excellent over the entire range of frequencies for both Cal. II and III. As is seen from Tab. 5.2, the sample average of the squared normalized deviations of the data from the PSD values χ^2_{fit} defined in Eq. 5.42 is relatively large compared to the expectation value of 1, the reasons for which most likely are: (i) differences in the instrumental noise S^{noise}_{ij} in Cal. I compared to Cal. II or III, (ii) other non-stationary effects in the experimental setup, which are intrinsically difficult to model and to quantify, and (iii) an inconsistency between Cal. II and III concerning the imaginary parts of the cross-periodograms Im $[P_{12}]$, which is discussed at the end of this section. In fact, when restricting the computation of χ^2_{fit} to the quantities which are less sensitive to the above mentioned effects, i.e., P_{11} and Re $[P_{12}]$ in Cal. II as well as P_{22} and Re $[P_{12}]$ in Cal. III, one obtains reasonable values for the squared deviations denoted by $\chi^2_{\text{fit, red}}$ in Tab. 5.2.

Once the setup is calibrated as described, all instrumental parameters are set and the link between electrical PSDs S_{ij} and the thermal PSDs S_{ij}^{th} is thus established, as is seen from the signal processing summarized in Fig. 5.5b. For more complicated experimental constructs, e.g., single molecules tethered to the beads, additional unknown parameters characterizing the viscoelastic properties of the molecule under study and entering the thermal PSDs S_{ij}^{th} of the overall experimental construct [ix], can in a second step be determined from the measured auto- and cross-periodograms $\overline{P}_{ij}$ employing the same maximum-likelihood fitting method. Here, we demonstrate in Sec. 5.7 that—without additional adjustable parameters—the periodograms recorded for two hydrodynamically interacting beads are in excellent agreement with the theoretical predictions over the entire range of frequencies resolved and for different trap separations. We thereby demonstrate the accuracy of the calibration method and the influence of the frequency dependence of the HI discussed in Sec. 5.3 on the PSDs.

However, some additional comments on the calibration spectra and the fit results are worth to be mentioned before proceeding:

- The radii of micron-sized beads used in optical tweezer experiments may vary from one bead to another due to finite sample variance. Determining the bead radii using a standard approach [217] involves a low-frequency oscillation of the piezo stage and adds the two parameters a_1 and a_2 to be determined when calibrating the instrument. Based on the peak amplitudes of $\overline{P}_{11}$ in Cal. II and $\overline{P}_{22}$ in Cal. III at the driving frequency of 30 Hz (data not shown), we found bead radii 500 ± 5 nm in perfect agreement with the manufacturer's specifications (cf. Sec. 5.1). We therefore use a fixed bead radius $a_1 = a_2 = a = 500$ nm in all our modeling. Note that the oscillation of the piezo stage also induces a periodic signal in the "empty" channel (2 in Cal. II and 1 in Cal. III), the amplitude and relative phase of which is less straightforward to interpret; values of the cross-periodogram and the auto-periodogram of the empty channel at the driving frequency have therefore not been considered when determining a_1 and a_2. In asymmetric setups, the bead masses m_1 and m_2 in Eq. 5.7 would have to be adjusted and our common radius a in the expressions for the self-mobilities (Eqs. 5.12 and 5.14) would have to be replaced by a_1 and a_2, respectively; expressions for the corresponding cross-mobilities replacing Eq. 5.15 are found in Ref. [237].

- As is clearly seen from Tab. 5.2, the polarization crosstalk amplitudes in the two channels and for the two spatial directions differ considerably ranging from 0.56 to 3.7 percent. Moreover, the importance of crosstalk is larger in channel 1 for the $\parallel$-direction, while it is dominant in channel 2 for the $\perp$-direction. This observed asymmetry is presumably a consequence of the orthogonally polarized light in the two traps and the fact that the two spatial directions are detected in different layers of the position sensing devices, see Appendix E.2 for a minimal model explaining this crosstalk asymmetry.

- According to our model for the signal processing in Sec. 5.4, the ratio of real and imaginary parts of the cross-PSDs results from the filtering properties in the two channels and is given by $\text{Re}\,[f_1 f_2^\star] \,/\text{Im}\,[f_1 f_2^\star]$ and thus independent of the thermal PSDs S_{ij}^{th}, which are purely real (cf. Sec. 5.2.1). In contrast, the ratio of real and imaginary parts of the cross-periodogram values in Fig. 5.6, given by the distance of the periodogram values in the logarithmic plots, differ for Cal. II and Cal. III. The filtering properties of the detectors thus seem to slightly differ depending on which of the traps is occupied and which one is empty. Separate maximum-likelihood fits to the data of Cal. II and Cal. III yielded

marginally better fits (not shown), the fit values however remained essentially unchanged compared to the results of the global fit to both experimental data sets in Tab. 5.2.

5.7 Discussion

The experimental setup being calibrated as described in Sec. 5.6, we now compare theoretical PSDs resulting from the Eqs. 5.8, 5.24, and 5.25 and using the fit parameters in Tab. 5.2 to averaged, experimental periodograms for two hydrodynamically interacting beads fluctuating in their respective laser traps. For trap separations R ranging from 10 down to 1.5 μm, averaged periodograms are calculated from the four voltage time series $(z_{1,\parallel}, z_{2,\parallel}, z_{1,\perp}, z_{2,\perp})$ with an overall duration of 30 seconds by analyzing time windows of $T = 10$ ms length each. The importance of hydrodynamic retardation effects are highlighted in Sec. 5.7.1, while the influence of instrumental effects, i.e., polarization crosstalk, (parasitic) filtering and instrumental noise, as well as of finite statistics is discussed in Sec. 5.7.2.

5.7.1 Retarded vs instantaneous hydrodynamics

Theoretical PSDs based on frequency-dependent HI between finite-sized beads described by Eq. 5.15 (black lines) as well as averaged periodograms from experimental data (colored symbols) are shown for various distances R between the trap centers and for motion parallel and perpendicular to the inter-trap axis in Fig. 5.7. Both auto-PSDs S_{11} and S_{22} and, in particular, the cross-PSD S_{12} are affected by the varying strength of the HI with changing trap separation or spatial direction. Over the entire resolved frequency range of 100 Hz $-$ 50 kHz, excellent agreement between theoretical predictions and experimental data is observed. Note that no additional fit parameters are used in Fig. 5.7, demonstrating the accuracy of both the modeling of the signal processing in Sec. 5.4 as well as of the instrumental calibration in Sec. 5.6.

To stress the importance of the frequency dependence of the HI discussed in Sec. 5.3.2, we also plot theoretical predictions based on instantaneous HI described by the components of the RP tensor (Eq. 5.16) as light blue lines in Fig. 5.7. The comparison reveals that the frequency dependence of the cross-mobilities shown in Fig. 5.4 arising from the finite time of vortex propagation in the fluid is essential for a quantitative match of theory and experiment. As expected, the influence of the frequency dependence is more prominent at large separations than at smaller ones, where the idealized picture of instantaneous HI constitutes a better, though still approximate description (cf. Sec. 5.3.2).

Remaining deviations between theoretically predicted and recorded spectra are mainly attributed to uncertainties in the calibration fit parameters (see Tab. 5.2), non-stationary instrumental effects and slight dependencies of the system parameters on the trap configuration. In particular, the signal amplitude ϵ_{11} of our mobile trap was found to vary within some percent when the trap is displaced over length scales of several μm (data not shown). If a quantitative evaluation of the spectra is intended, it is therefore recommended to perform the calibration measurements in a similar configuration as the actual experiment is done. In addition, at high frequencies systematic deviations may result from limitations in the model, e.g., for the parasitic filtering covered in Appendix E.1, and for separations $R \lesssim 3a$, the uncertainty in the absolute distance R and the neglect of higher order corrections for self- and cross-mobilities [102] may play a role. Finally, alignment inaccuracies of the instrument (cf. Sec. 5.2.2) or crosstalk between the spatial directions within each of the position sensing devices [214] may be respon-

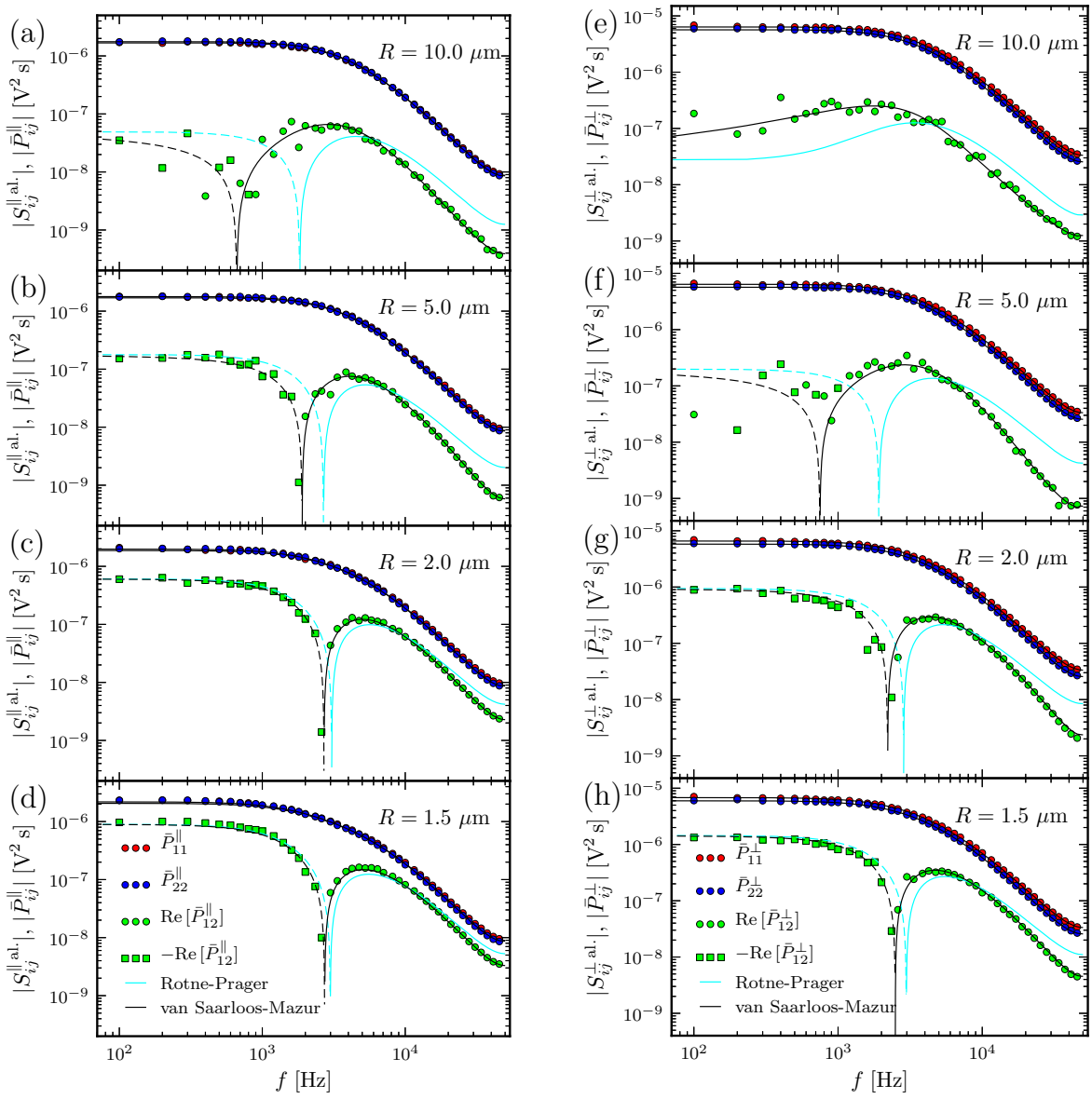

Figure 5.7:
Auto- and cross-PSDs of the fluctuations parallel (a-d) and perpendicular (e-h) to the inter-trap axis for various trap separations R: *Symbols* denote averaged experimental periodograms $\overline{P}_{ij}^{\parallel}$ and $\overline{P}_{ij}^{\perp}$, *lines* the theoretical predictions for the aliased PSDs $S_{ij}^{\parallel\mathrm{al.}}$ and $S_{ij}^{\perp\mathrm{al.}}$ according to the Eqs. 5.24 and 5.25: *black lines* include the full frequency dependence of the HI (Eq. 5.15), while *cyan lines* correspond to instantaneous HI (Eq. 5.16). Positive values of the averaged experimental periodograms are denoted by *circles*, negative ones by *squares*; similarly, *solid* and *dashed lines* respectively denote positive and negative PSD values.

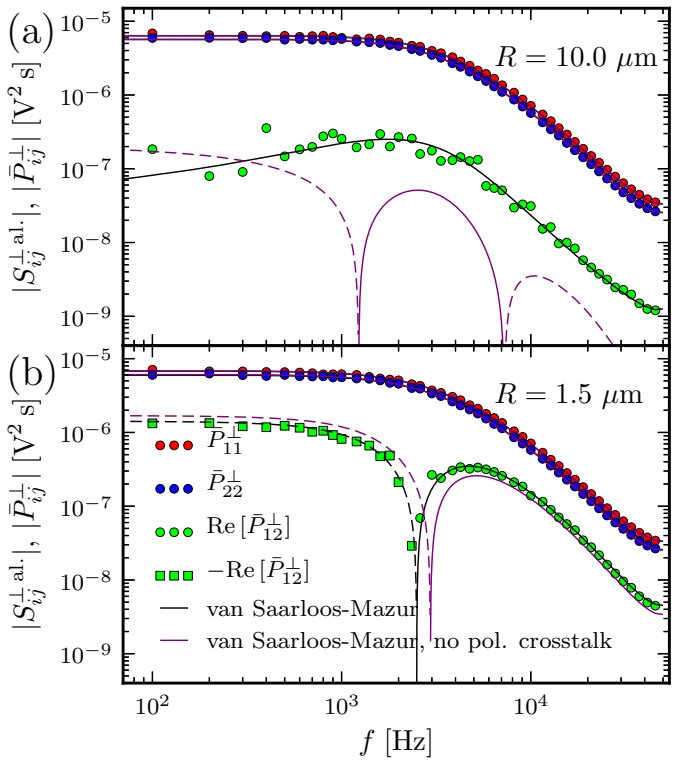

Figure 5.8:
Influence of polarization crosstalk: Theoretical PSDs accounting for polarization crosstalk are shown as *black lines* (same as in Fig. 5.7), theoretical PSDs neglecting polarization crosstalk are denoted as *purple lines*; since auto-PSDs are only marginally affected by polarization crosstalk, *black* and *purple lines* for S_{11} and S_{22} overlap. *Symbols* denote experimental data (same as in Fig. 5.7).

sible for residual deviations; both effects have been neglected in the present analysis but can in principle be accounted for using the full three-dimensional theory (Sec. 5.2.2) and a refined model for the signal processing involving all four recorded signals, thereby generalizing the approach taken in Sec. 5.4.

5.7.2 Instrumental effects and finite statistics

As schematically indicated in Fig. 5.5b, the electrical PSDs S_{ij} deviate from the thermal PSDs of the beads S_{ij}^{th} due to three instrumental effects: polarization crosstalk, (parasitic) filtering and instrumental noise. Their influence on the calibration and hydrodynamic spectra in the Figs. 5.6 and 5.7 is discussed in the following.

The importance of polarization crosstalk for the calibration process has been covered in Sec. 5.6; its influence on the PSDs of two hydrodynamically interacting beads is illustrated by comparing experimental data and theoretical curves from the Figs. 5.7e and 5.7h to theoretical predictions for the PSDs, which do not account for crosstalk setting $\epsilon_{12} = \epsilon_{21} = 0$. The corresponding PSDs are shown as purple lines in Fig. 5.8 together with the original data and curves from Fig. 5.7. For a trap separation $R = 10\ \mu$m (Fig. 5.8a), where due to weak HI the thermal cross-PSD S_{12}^{th} is small in amplitude compared to the thermal auto-PSDs S_{11}^{th} and S_{22}^{th}, the observed

cross-PSD of the electrical signals S_{12} is dominated by the thermal auto-PSDs, which couple in due to polarization-crosstalk. Experimental data is consequently ill-represented when polarization crosstalk is neglected, as shown in Fig. 5.8a. For smaller trap separations ($R = 1.5\ \mu$m in Fig. 5.8b), where HI are stronger, the frequency dependence of the thermal cross-PSD S_{12}^{th} is better reflected in S_{12}, though including polarization crosstalk remains necessary for a quantitative agreement between theory and experimental data. As expected, the black and purple lines for the auto-PSDs overlap mostly in Fig. 5.8, since the polarization crosstalk affects the auto-PSDs to a minor extent only. We conclude that a quantitative analysis of experimental (cross-)periodograms requires accounting for crosstalk to disentangle the contributions of thermal auto- and cross-PSDs.

The effects of the parasitic filtering of the position sensing devices (cf. Appendix E.1) on the auto-periodograms measured in single trap optical tweezer experiments have been discussed in detail before [216, 244, 248]. For dual trap setups, deviations in the filter properties of the two devices have as additional consequence a non-vanishing imaginary part of the cross-PSD, $\mathrm{Im}\left[S_{12}\right]$, as discussed in Sec. 5.4.1 and exemplified in Appendix E.1.

The influence of the instrumental noise is seen in the calibration measurements of Cal. II and III in Fig. 5.6b-c; the discussion in this paragraph focuses on Cal. II but equally applies to Cal. III with indices 1 and 2 interchanged. In the absence of noise, according to the schematic in Fig. 5.5b, one expects roughly equivalent shapes for $\overline{P}_{11}$, $\mathrm{Re}\left[\overline{P}_{12}\right]$, and $\overline{P}_{22}$, slight differences being attributed to the individual filter functions f_1 and f_2 and the relative magnitudes being set by the ratio $\epsilon_{11}/\epsilon_{21} \gg 1$. However, the averaged periodogram values $\overline{P}_{22}$ are mostly dominated by the instrumental noise, since $S_{22}^{\mathrm{noise}} \gtrsim \epsilon_{21}^2 S_{11}^{\mathrm{th}}$.

Finally, some comments on the statistical uncertainty in the data: In Fig. 5.6b-c, one observes a noticeable larger scatter of the cross-periodogram values $\mathrm{Re}\left[\overline{P}_{12}\right]$ around the theoretical estimate $\mathrm{Re}\left[S_{12}\right]$ compared to the auto-periodogram values. This effect is best seen for large frequencies in the bottom panel of Fig. 5.6c corresponding to the $\perp$ direction, where the polarization crosstalk is the weakest. According to the periodogram statistics discussed in Sec. 5.5.1, the relative statistical uncertainty of $\mathrm{Re}\left[P_{12}\right]$ (Eq. 5.30) is

$$\frac{\sqrt{\Sigma^2[\mathrm{Re}\left[P_{12}\right]]}}{\mathrm{Re}\left[S_{12}\right]} \approx \sqrt{\frac{\frac{1}{2}\left((S_{11}^{\mathrm{noise}} + \epsilon_{12}^2 S_{22}^{\mathrm{th}})\epsilon_{22}^2 S_{22}^{\mathrm{th}} + (\epsilon_{12}\epsilon_{22} S_{22}^{\mathrm{th}})^2\right)}{\left(\epsilon_{12}\epsilon_{22} S_{22}^{\mathrm{th}}\right)^2}} = \sqrt{1 + \frac{S_{11}^{\mathrm{noise}}}{2\epsilon_{12}^2 S_{22}^{\mathrm{th}}}}, \tag{5.43}$$

which exceeds the expected relative statistical uncertainty of auto-periodogram values ($= 1$, cf. Sec. 5.5.1), whenever the instrumental noise in the "empty" signal dominates over the contribution of the thermal bead motion. The instrumental noise in the two signals z_1 and z_2 being (mostly) independent, the expectation value $\left\langle \mathrm{Re}\left[\overline{P}_{12}\right]\right\rangle = \mathrm{Re}\left[S_{12}\right]$ are relatively insensitive to instrumental noise, the statistical uncertainty in the cross-periodogram values is however increased. For the case of two hydrodynamically interacting beads, the contribution of noise to the observed PSDs is rather small; taking into account instrumental noise is thus in the first place important to account for the increased statistical uncertainty of cross-periodogram values when calibrating the experimental setup as described in Sec. 5.6.

The averaged periodograms $\overline{P}_{ij}$ shown in the Figs. 5.6-5.8 result from the spectral analysis of at least 3000 signal windows and from blocking periodogram values corresponding to neighboring frequencies; for independent samples, the statistical uncertainty of the averaged periodograms is thus reduced by a factor $\leq 1/\sqrt{3000} \sim 0.02$ compared to the bare periodograms. Nevertheless, for the cross-periodograms the statistical uncertainty still may be comparable

or even exceed the magnitude of the expectation value, cf. Sec. 5.5.1. As an example, the periodogram values Re $\left[\overline{P}_{12}\right]$ considerably scatter around the theoretical predictions Re $[S_{12}]$ in the top panels of Fig. 5.7. If the statistical uncertainty exceeds the magnitude of the expectation value, plotting the absolute periodogram values on a logarithmic scale leads to a spurious, smooth frequency dependence, which is a signature of the statistical uncertainty only and which can easily be misinterpreted, see Appendix E.5 for further details. Such a spurious behavior is for example observed for the periodogram values Im $\left[\overline{P}_{12}\right]$ in Cal. III shown in Fig. 5.6c.

The statistical aspects discussed in the previous two paragraphs are rather subtle; it is therefore recommended to fit auto- and cross-periodograms simultaneously rather than independently by applying the Bayesian inference fitting method presented in Sec. 5.5.2, which inherently accounts for the statistical properties of auto- and cross-periodograms and which was used within this chapter for the calibration of a dual trap optical tweezer instrument.

5.8 Conclusions

In summary, we have presented a theoretical description of the signal processing in a typical dual trap optical tweezer experiment, and have proposed a maximum-likelihood method based on the statistical properties of auto- and cross-periodograms for the power spectral analysis of the experimentally recorded fluctuations. We have shown how—in a first calibration step—the method can be used to determine the instrumental parameters involved in the signal processing as well as the optical trapping strengths by combining data from three consecutive measurements. Using two unconnected but hydrodynamically interacting beads trapped in the respective laser potentials as simple model system, we could demonstrate a number of different aspects including: (i) the frequency-dependence of the hydrodynamic coupling arising from the finite time of vortex diffusion in the viscous fluid, (ii) the influence of crosstalk, (parasitic) filtering and instrumental noise on the recorded periodograms, and (iii) potential caveats in the interpretation of experimental data due to finite statistics. We expect the present Bayesian inference method paired with dynamic (de-)convolution theory [ix] to enable experimentalists in a second step to recover the viscoelastic force response characteristics of the molecule of study from the measured equilibrium fluctuations of the overall experimental construct, e.g., the molecule tethered via handles to the two beads trapped in their respective laser foci.

CHAPTER 6

DYNAMICS OF THERMALLY FLUCTUATING NONLINEAR SYSTEMS

Bibliographic information: Parts of this chapter and of Appendix F have previously been published. Reprinted from Ref. [ii]. With kind permission of The European Physical Journal (EPJ).

A common way of studying the dynamics of a system consists in probing its response to externally applied non-stationary fields. Linear response is of particular interest not only because it yields the dominant contribution for small driving amplitudes, but also because it is easily obtained from the system's thermal equilibrium fluctuations, cf. Chapter 5.

As a matter of fact, the exact analytical forms of equilibrium correlation functions and dynamic susceptibilities are often tedious or impossible to obtain for nonlinear systems. Expressions employed in the evaluation of experimental or simulation data are therefore often phenomenological or based on linearized equations [249]. Examples are ubiquitous and include various types of spectroscopic techniques ranging from the dielectric characterization of liquid systems [250] to single-molecule force spectroscopy [206].

Previous attempts to theoretically tackle the problem of nonlinearities in the equations of motion of thermally fluctuating systems are mainly based on the Fokker-Planck (FP) equation. While exact solutions have been derived for a few particular cases [251, 252], most methods rely on approximations: examples comprise the expansion of the observables in eigenfunctions of the FP operator [253] and perturbative approaches for the system's response to external driving [254, 255].

Here, we systematically analyze the influence of nonlinearities in the equations of motion of thermally fluctuating systems by expanding typical dynamic observables in powers of the thermal noise strength and corroborate our analytical findings by comparison to the results of numerical simulations. As we show based on explicit examples, linear models are very successful for parametrizing two-point correlation functions. Caution is however advised, when it comes to the interpretation of the (fitted) parameter values, since the underlying physics may be completely missed. In addition, many practical applications effectively probe the dynamics of a multi-component system, which is more complex than the bare object of interest. Theoretical methods relating the dynamics of a composite system to the dynamic properties of its building blocks thus are essential to disentangle the individual contributions and to recover the relevant information about the object of primary interest from measured data. In this context, the advan-

tages and limitations of a recently introduced method [ix] serving this goal are discussed based on our expansion of dynamic observables in powers of the thermal noise strength.

Although the problem in the remainder of the chapter is phrased in terms of a mechanical system characterized by its position and driven by a mechanical force, our approach is very general as outlined in Sec. 6.1 and therefore in principle applicable to any pairs of observables and conjugated fields, e.g., polarization and electric field, magnetization and magnetic field, etc.

The chapter is organized as follows: In Sec. 6.1, we derive the general functional form of equilibrium correlation and force response functions of a thermally fluctuating system from the underlying equations of motion. As an example, we consider in Sec. 6.2 the overdamped diffusion of a particle in three different potential landscapes, for which we explicitly evaluate our analytical expressions and compare them to results from numerical simulations. We critically discuss the role of strictly linear models for the analysis of fluctuating dynamics based on two-point correlation functions in Sec. 6.3 and explicitly show how the evaluation of higher order correlation functions may easily unmask nonlinearities in the dynamics. In Sec. 6.4, we focus on the dynamics of composite systems and reveal the limitations of the linear dynamic convolution theory (DCT) of Ref. [ix], for which we derive a first-oder correction term, which is even relevant for the spectral properties of the equilibrium fluctuations in the limit of vanishing external force strength. The main results of the chapter are summarized in Sec. 6.5, while details on the spectral analysis as well as parts of the calculations are found in Appendix F.

6.1 Expansion in Powers of the Thermal Noise Strength

For simplicity, we consider the ergodic dynamics of a one-dimensional system characterized by the position x. Our approach is general in the sense that—beyond the analyticity of the equations of motion—no prerequisites are needed. In particular, the formalism is restricted neither to overdamped nor to Markovian dynamics. An extension of the formalism to multiple variables and/or higher dimensions is amenable, but not pursued here.

The expansions of the force profile and the trajectory of the system are introduced in Sec. 6.1.1, the expansions for the resulting thermally averaged observables are derived in Sec. 6.1.2 and a short discussion of our analytical findings is found in Sec. 6.1.3.

6.1.1 Equations of motion and athermal force response

The equation of motion of the system is formulated in terms of the functional

$$\mathcal{F}_t[x] = f(t), \tag{6.1}$$

which yields the force f acting on the system at time t in dependence of the system's entire trajectory $x(t)$. The above formulation of the equation of motion explicitly includes non-local dependencies between x and f such as frictional memory-kernels. The inverse relation between force and position trajectories, i.e., the (numerical) solution of the equation of motion, is expressed in terms of the functional

$$\mathcal{X}_t[f] = x(t), \tag{6.2}$$

which yields the position x of the system at time t given the entire force profile $f(t)$. For convenience, we restrict the discussion to systems, where $\mathcal{F}_t[0] = 0$ and $\mathcal{X}_t[0] = 0$; for bound systems,

this can always be achieved by an appropriate shift of the reference point along the x-axis. We expand the functional in Eq. 6.2 and obtain

$$\begin{aligned} x(t) = \mathcal{X}_t[f] = \int \mathrm{d}t' \underbrace{\left.\frac{\delta \mathcal{X}_t[f]}{\delta f(t')}\right|_{f=0}}_{j_1(t-t')} f(t') + \frac{1}{2}\int \mathrm{d}t' \int \mathrm{d}t'' \underbrace{\left.\frac{\delta^2 \mathcal{X}_t[f]}{\delta f(t')\delta f(t'')}\right|_{f=0}}_{j_2(t-t',t-t'')} f(t')f(t'') \\ + \frac{1}{6}\int \mathrm{d}t' \int \mathrm{d}t'' \int \mathrm{d}t''' \underbrace{\left.\frac{\delta^3 \mathcal{X}_t[f]}{\delta f(t')\delta f(t'')\delta f(t''')}\right|_{f=0}}_{j_3(t-t',t-t'',t-t''')} f(t')f(t'')f(t''') + \ldots, \end{aligned} \tag{6.3}$$

thereby defining athermal force response functions j_1, j_2, etc., which only depend on the time differences $t - t'$, $t - t''$, etc. because of time translation invariance. Note that the athermal response functions vanish as soon as one of the temporal arguments is negative due to causality. Switching to Fourier domain, one obtains

$$\begin{aligned} x(\omega) = \int \mathrm{d}\omega' \, j_1(\omega') f(\omega') \delta(\omega - \omega') + \frac{1}{2}\frac{1}{2\pi}\int \mathrm{d}\omega' \int \mathrm{d}\omega'' \, j_2(\omega', \omega'') f(\omega') f(\omega'') \delta(\omega - (\omega' + \omega'')) \\ + \frac{1}{6}\frac{1}{(2\pi)^2}\int \mathrm{d}\omega' \int \mathrm{d}\omega'' \int \mathrm{d}\omega''' \, j_3(\omega', \omega'', \omega''') f(\omega') f(\omega'') f(\omega''') \delta(\omega - (\omega' + \omega'' + \omega''')) + \ldots, \end{aligned} \tag{6.4}$$

where the employed convention for the Fourier transformation and details on the notation are found in Appendix A.2. Similarly, expanding the functional in Eq. 6.1 and taking the Fourier transformation, one obtains

$$\begin{aligned} f(\omega) = \int \mathrm{d}\omega' \, g_1(\omega') x(\omega') \delta(\omega - \omega') + \frac{1}{2}\frac{1}{2\pi}\int \mathrm{d}\omega' \int \mathrm{d}\omega'' \, g_2(\omega', \omega'') x(\omega') x(\omega'') \delta(\omega - (\omega' + \omega'')) \\ + \frac{1}{6}\frac{1}{(2\pi)^2}\int \mathrm{d}\omega' \int \mathrm{d}\omega'' \int \mathrm{d}\omega''' \, g_3(\omega', \omega'', \omega''') x(\omega') x(\omega'') x(\omega''') \delta(\omega - (\omega' + \omega'' + \omega''')) + \ldots, \end{aligned} \tag{6.5}$$

where corresponding functions g_i have been defined. Real and imaginary parts of the functions g_1, g_2, g_3, etc. denote the linear, quadratic, and cubic conservative and dissipative contributions to the equations of motion respectively. The functions j_i and g_i have the following important properties: (i) they are symmetric with respect to a permutation of the arguments, i.e., $j_2(\omega, \omega') = j_2(\omega', \omega)$, $g_2(\omega, \omega') = g_2(\omega', \omega)$, $j_3(\omega, \omega', \omega'') = j_3(\omega', \omega, \omega'') = j_3(\omega'', \omega, \omega') = \ldots$, etc, and (ii) being the Fourier transformations of real valued functions, they fulfill $j_1^\star(\omega) = j_1(-\omega)$, $j_2^\star(\omega, \omega') = j_2(-\omega, -\omega')$, etc.

The overall dynamic properties of the system are equivalently encoded in the sets of functions $\{j_i\}$ or $\{g_i\}$, where knowledge of the j_i's permits the calculation of the system trajectory from the force acting on it via Eq. 6.4, and conversely knowledge of the g_i's allows to determine the force associated with a given trajectory using Eq. 6.5.

Each of these sets can (in principle) be calculated from the other one by inserting Eq. 6.5 into Eq. 6.4, grouping together all terms with equal powers of x, and satisfying the equality term by term for arbitrary $x(\omega)$. The resulting equations (specified in Appendix F.1) give rise to a hierarchy of relations, the first ones of which read

$$j_1(\omega) = \frac{1}{g_1(\omega)}, \tag{6.6}$$

$$j_2(\omega, \omega') = -\frac{g_2(\omega, \omega') j_1(\omega + \omega')}{g_1(\omega) g_1(\omega')} = -\frac{g_2(\omega, \omega')}{g_1(\omega) g_1(\omega') g_1(\omega + \omega')}, \tag{6.7}$$

$$j_3(\omega,\omega',\omega'') = -\frac{j_1(\omega+\omega'+\omega'')g_3(\omega,\omega',\omega'') + j_2(\omega,\omega'+\omega'')g_1(\omega)g_2(\omega',\omega'')}{g_1(\omega)g_1(\omega')g_1(\omega'')} \\ - \frac{j_2(\omega',\omega+\omega'')g_1(\omega')g_2(\omega,\omega'') + j_2(\omega'',\omega+\omega')g_1(\omega'')g_2(\omega,\omega')}{g_1(\omega)g_1(\omega')g_1(\omega'')}, \tag{6.8}$$

etc., allowing to recursively calculate the athermal response functions j_1, j_2, etc. from the g_i-functions, which are easily read off from the equations of motion. The equivalent inverse relations for the functions g_i are obtained by interchanging j and g in the above expressions. For linear systems, the only non-vanishing functions are g_1 and j_1. In turn, any nonlinearity in the equations of motion leads to at least one additional non-vanishing g_i-function and in consequence to a whole series of non-zero athermal response functions j_i.

6.1.2 Thermally averaged dynamic observables

In the general framework of a Langevin equation, the overall force acting on the system $f \equiv f_{\text{ext}} + f_{\text{st}}$ consists of a superposition of an external driving f_{ext} and a stochastic thermal force f_{st}. In equilibrium, the statistical properties of the stochastic force, which is assumed to be independent of the external driving, are

$$\langle f_{\text{st}}(\omega)\rangle = 0, \qquad \left\langle f_{\text{st}}(\omega) f_{\text{st}}(\omega')\right\rangle = 4\pi k_{\text{B}} T \zeta'(\omega)\delta(\omega+\omega') \equiv \sigma_{\text{st}}^2(\omega,\omega'). \tag{6.9}$$

According to the fluctuation-dissipation theorem (FDT), the linear dissipative part in the equation of motion and the fluctuating thermal force are linked

$$\zeta'(\omega) = -\frac{\text{Im}\left[g_1(\omega)\right]}{\omega}. \tag{6.10}$$

Here, ζ' denotes the real part of the (in general) frequency dependent friction coefficient

$$\zeta(\omega) = \zeta'(\omega) + \zeta''(\omega). \tag{6.11}$$

According to the definition of the Fourier transformation in Appendix A.2, Eq. 6.9 translates into

$$\langle f_{\text{st}}(t)\rangle = 0, \qquad \left\langle f_{\text{st}}(t) f_{\text{st}}(t')\right\rangle = 2k_{\text{B}} T \zeta'(t-t') = k_{\text{B}} T \zeta\left(|t-t'|\right), \tag{6.12}$$

where $\zeta'(t)$ denotes the inverse Fourier transform of the real part of the friction coefficient $\zeta'(\omega)$, and $\zeta(t)$ corresponds to the memory kernel of the associated generalized Langevin equation in time domain [256].

The thermal noise strength $k_{\text{B}} T \zeta'(\omega)$ is by definition (Eqs. 6.9 and 6.12) a real and even function of frequency. We only consider the case, in which the friction coefficient is independent of the system's state x, which, for a one-dimensional systems, can always be achieved by an appropriately chosen coordinate transformation [36], cf. Sec. 2.3.7.

We restrict the following discussion to linear dissipative contributions to the equation of motion only: The real and imaginary parts of the Fourier components $f_{\text{st}}(\omega)$ are then normally distributed variables with variance $\sigma_{\text{st}}^2/2$, and higher moments are straightforward to calculate: Odd moments vanish due to symmetry, i.e.,

$$\left\langle f_{\text{st}}(\omega) f_{\text{st}}(\omega') f_{\text{st}}(\omega'')\right\rangle = 0, \tag{6.13}$$

$$\left\langle f_{\text{st}}(\omega) f_{\text{st}}(\omega') f_{\text{st}}(\omega'') f_{\text{st}}(\omega''') f_{\text{st}}(\omega^{\text{IV}})\right\rangle = 0, \tag{6.14}$$

etc., and even moments can be broken down to factors of second moments, e.g.,

$$\begin{aligned}\left\langle f_{\mathrm{st}}(\omega) f_{\mathrm{st}}(\omega') f_{\mathrm{st}}(\omega'') f_{\mathrm{st}}(\omega''')\right\rangle &= \frac{1}{2!\,2^2} \sum_{\mathcal{P}\{\omega,\omega',\omega'',\omega'''\}} \sigma^2_{\mathrm{st}}(\omega,\omega')\sigma^2_{\mathrm{st}}(\omega'',\omega''') \\ &= \sigma^2_{\mathrm{st}}(\omega,\omega')\sigma^2_{\mathrm{st}}(\omega'',\omega''') + \sigma^2_{\mathrm{st}}(\omega,\omega'')\sigma^2_{\mathrm{st}}(\omega',\omega''') + \sigma^2_{\mathrm{st}}(\omega,\omega''')\sigma^2_{\mathrm{st}}(\omega',\omega''),\end{aligned} \tag{6.15}$$

and

$$\begin{aligned}&\left\langle f_{\mathrm{st}}(\omega) f_{\mathrm{st}}(\omega') f_{\mathrm{st}}(\omega'') f_{\mathrm{st}}(\omega''') f_{\mathrm{st}}(\omega^{\mathrm{IV}}) f_{\mathrm{st}}(\omega^{\mathrm{V}})\right\rangle \\ &= \frac{1}{3!\,2^3} \sum_{\mathcal{P}\{\omega,\ldots,\omega^{\mathrm{V}})\}} \sigma^2_{\mathrm{st}}(\omega,\omega')\sigma^2_{\mathrm{st}}(\omega'',\omega''')\sigma^2_{\mathrm{st}}(\omega^{\mathrm{IV}},\omega^{\mathrm{V}}),\end{aligned} \tag{6.16}$$

etc., where $\mathcal{P}\{\ldots\}$ denotes the ensemble of permutations of the elements in $\{\ldots\}$ and the symmetry $\sigma^2_{\mathrm{st}}(\omega',\omega) = \sigma^2_{\mathrm{st}}(\omega,\omega')$ has been used in Eq. 6.15.

Note that systems with nonlinearities in the dissipative contributions to the equations of motion, i.e., $\mathrm{Im}\,[g_i(\omega)] \neq 0$ for $i > 1$, would also require corrections in the higher-order correlations of the thermal forces (Eqs. 6.15 and 6.16).

Fluctuating dynamics in thermal equilibrium

We first focus on the unperturbed system ($f_{\mathrm{ext}} = 0$) subject to thermal forces only. Taking the thermal average of Eq. 6.4 yields

$$\begin{aligned}\langle x(\omega)\rangle = \Bigg(&k_{\mathrm{B}}T \int \mathrm{d}\omega'\; j_2(\omega',-\omega')\zeta'(\omega') + \frac{(k_{\mathrm{B}}T)^2}{4\pi} \int \mathrm{d}\omega' \int \mathrm{d}\omega''\; j_4(\omega',-\omega',\omega'',-\omega'')\zeta'(\omega')\zeta'(\omega'') \\ &+ \mathcal{O}\left((k_{\mathrm{B}}T)^3\right)\Bigg)\delta(\omega) = x_{\mathrm{avg}}\, 2\pi\,\delta(\omega),\end{aligned} \tag{6.17}$$

where x_{avg} denotes the average state of the system. As is evident from the above equation, for finite thermal noise strength the average position x_{avg} does in general differ from the reference point of the expansion $x = 0$. A dynamic quantity of common interest is the power spectral density (PSD) of the equilibrium fluctuations $S(\omega)$ defined by

$$S(\omega)\, 2\pi\,\delta(\omega+\omega') \equiv \left\langle \Delta x(\omega)\Delta x(\omega')\right\rangle, \tag{6.18}$$

and thus nothing else than the Fourier transformation of the temporal auto-correlation function $S(t) \equiv \langle \Delta x(t'+t)\Delta x(t')\rangle$, where deviations around the mean are denoted as

$$\Delta x(t) \equiv x(t) - x_{\mathrm{avg}} \quad \text{or} \quad \Delta x(\omega) \equiv x(\omega) - x_{\mathrm{avg}}\, 2\pi\,\delta(\omega). \tag{6.19}$$

Performing the thermal average in Eq. 6.18 using Eq. 6.4 and the relations from the Eqs. 6.9 and 6.13-6.16, one obtains

$$\begin{aligned}
S(\omega) = {} & 2k_{\mathrm{B}}T\zeta'(\omega)\,|j_1(\omega)|^2 \\
& + \frac{(k_{\mathrm{B}}T)^2}{\pi}\left(2\zeta'(\omega)\int \mathrm{d}\omega'\ \mathrm{Re}\left[j_1(\omega)j_3(-\omega,\omega',-\omega')\right]\zeta'(\omega')\right. \\
& \qquad \left. + \int \mathrm{d}\omega'\ \left|j_2(\omega',\omega-\omega')\right|^2\zeta'(\omega')\zeta'(\omega-\omega')\right) \\
& + \frac{(k_{\mathrm{B}}T)^3}{\pi^2}\left(\frac{1}{2}\zeta'(\omega)\int \mathrm{d}\omega'\int \mathrm{d}\omega''\ \mathrm{Re}\left[j_1(\omega)j_5(-\omega,\omega',-\omega',\omega'',-\omega'')\right]\zeta'(\omega')\zeta'(\omega'')\right. \\
& \qquad + \int \mathrm{d}\omega'\int \mathrm{d}\omega''\ \mathrm{Re}\left[j_2(\omega',\omega-\omega')j_4(-\omega',\omega'-\omega,\omega'',-\omega'')\right]\zeta'(\omega')\zeta'(\omega-\omega')\zeta'(\omega'') \\
& \qquad + \frac{1}{3}\int \mathrm{d}\omega'\int \mathrm{d}\omega''\ \left|j_3(\omega',\omega'',\omega-\omega'-\omega'')\right|^2\zeta'(\omega')\zeta'(\omega'')\zeta'(\omega-\omega'-\omega'') \\
& \qquad \left. + \frac{1}{2}\zeta'(\omega)\left|\int \mathrm{d}\omega'\ j_3(\omega,\omega',-\omega')\zeta'(\omega')\right|^2\right) + \mathcal{O}\left((k_{\mathrm{B}}T)^4\right).
\end{aligned} \tag{6.20}$$

The first term, which depends on the athermal linear response j_1 of the system as well as on the frequency-dependence of the friction coefficient, is linear in the thermal noise strength and known from linearized fluctuation theory [253]. It is the only term contributing to the response of a linear system, for which all athermal response functions except j_1 are zero, cf. Sec. 5.2.2. In turn, nonlinearities in the equations of motion contribute terms to the equilibrium PSD, which scale as $(k_{\mathrm{B}}T\zeta')^n$ with $n > 1$ and thus become more and more important with increasing strength of the thermal noise.

Similarly, higher order correlation and cumulant functions can be calculated from the Eqs. 6.4, 6.9 and 6.13-6.16. In particular, we focus on the fourth order cumulant Y defined via

$$\begin{aligned}
Y(\omega_1,\omega_2,\omega_3)\,2\pi\,\delta(\omega_1+\omega_2+\omega_3+\omega_4) \equiv {} & \langle\Delta x(\omega_1)\Delta x(\omega_2)\Delta x(\omega_3)\Delta x(\omega_4)\rangle - \langle\Delta x(\omega_1)\Delta x(\omega_2)\rangle\langle\Delta x(\omega_3)\Delta x(\omega_4)\rangle \\
& - \langle\Delta x(\omega_1)\Delta x(\omega_3)\rangle\langle\Delta x(\omega_2)\Delta x(\omega_4)\rangle - \langle\Delta x(\omega_1)\Delta x(\omega_4)\rangle\langle\Delta x(\omega_2)\Delta x(\omega_3)\rangle.
\end{aligned} \tag{6.21}$$

Explicit evaluation of the above expression yields

$$\begin{aligned}
Y(\omega_1,\omega_2,\omega_3) = {} & 8(k_{\mathrm{B}}T)^3 j_1(\omega_1)\zeta'(\omega_1)j_1(\omega_2)\zeta'(\omega_2)j_1(\omega_3)\zeta'(\omega_3)j_1(-\omega_1-\omega_2-\omega_3)\zeta'(-\omega_1-\omega_2-\omega_3) \\
& \times\left(\frac{j_3(\omega_1,\omega_2,\omega_3)}{j_1(-\omega_1-\omega_2-\omega_3)\zeta'(-\omega_1-\omega_2-\omega_3)} + \frac{j_3(-\omega_1-\omega_2-\omega_3,\omega_2,\omega_3)}{j_1(\omega_1)\zeta'(\omega_1)}\right. \\
& \qquad \left. + \frac{j_3(\omega_1,-\omega_1-\omega_2-\omega_3,\omega_3)}{j_1(\omega_2)\zeta'(\omega_2)} + \frac{j_3(\omega_1,\omega_2,-\omega_1-\omega_2-\omega_3)}{j_1(\omega_3)\zeta'(\omega_3)}\right) + \mathcal{O}\left((k_{\mathrm{B}}T)^4\right).
\end{aligned} \tag{6.22}$$

The first term in the expansion of the function Y in powers of the thermal noise strength being already proportional to the athermal cubic force response function j_3, the function Y vanishes for strictly linear systems, where $j_3 = 0$. In turn, non-vanishing values of Y indicate nonlinear contributions to the equilibrium dynamics.

Thermal force response

In the case of a non-vanishing external driving force f_{ext}, the average response of the system

$$\begin{aligned}\langle \Delta x(\omega)\rangle = {} & j_1(\omega) f_{\mathrm{ext}}(\omega) + \frac{k_{\mathrm{B}}T}{2\pi}\int \mathrm{d}\omega'\, j_3(\omega,\omega',-\omega')\zeta'(\omega') f_{\mathrm{ext}}(\omega) \\ & + \frac{(k_{\mathrm{B}}T)^2}{8\pi^2}\int \mathrm{d}\omega' \int \mathrm{d}\omega''\, j_5(\omega,\omega',-\omega',\omega'',-\omega'')\zeta'(\omega')\zeta'(\omega'') f_{\mathrm{ext}}(\omega) \\ & + \frac{(k_{\mathrm{B}}T)^3}{48\pi^3}\int \mathrm{d}\omega' \int \mathrm{d}\omega'' \int \mathrm{d}\omega'''\, j_7(\omega,\omega',-\omega',\omega'',-\omega'',\omega''',-\omega''')\zeta'(\omega')\zeta'(\omega'')\zeta'(\omega''') f_{\mathrm{ext}}(\omega) \\ & + \mathcal{O}\left((k_{\mathrm{B}}T)^4\right) f_{\mathrm{ext}}(\omega) + \mathcal{O}(f_{\mathrm{ext}}^2),\end{aligned} \tag{6.23}$$

is obtained by taking the thermal average of Eq. 6.4, again employing the relations from the Eqs. 6.9, 6.15 and 6.16. Defining linear and higher order response functions J_1, J_2, etc. for the thermal force response similarly as before

$$\begin{aligned}\langle \Delta x(\omega)\rangle = {} & \int \mathrm{d}\omega'\, J_1(\omega') f_{\mathrm{ext}}(\omega')\delta(\omega-\omega') + \frac{1}{2}\frac{1}{2\pi}\int \mathrm{d}\omega' \int \mathrm{d}\omega''\, J_2(\omega',\omega'') f_{\mathrm{ext}}(\omega') f_{\mathrm{ext}}(\omega'')\delta(\omega-(\omega'+\omega'')) \\ & + \frac{1}{6}\frac{1}{(2\pi)^2}\int \mathrm{d}\omega' \int \mathrm{d}\omega'' \int \mathrm{d}\omega'''\, J_3(\omega',\omega'',\omega''') f_{\mathrm{ext}}(\omega') f_{\mathrm{ext}}(\omega'') f_{\mathrm{ext}}(\omega''')\delta(\omega-(\omega'+\omega''+\omega''')) + \ldots,\end{aligned} \tag{6.24}$$

we obtain expressions for the thermal linear force response function

$$\begin{aligned}J_1(\omega) = {} & j_1(\omega) + \frac{k_{\mathrm{B}}T}{2\pi}\int \mathrm{d}\omega'\, j_3(\omega,\omega',-\omega')\zeta'(\omega') \\ & + \frac{(k_{\mathrm{B}}T)^2}{8\pi^2}\int \mathrm{d}\omega' \int \mathrm{d}\omega''\, j_5(\omega,\omega',-\omega',\omega'',-\omega'')\zeta'(\omega')\zeta'(\omega'') \\ & + \frac{(k_{\mathrm{B}}T)^3}{48\pi^3}\int \mathrm{d}\omega' \int \mathrm{d}\omega'' \int \mathrm{d}\omega'''\, j_7(\omega,\omega',-\omega',\omega'',-\omega'',\omega''',-\omega''')\zeta'(\omega')\zeta'(\omega'')\zeta'(\omega''') \\ & + \mathcal{O}\left((k_{\mathrm{B}}T)^4\right),\end{aligned} \tag{6.25}$$

as well as for the higher order response functions

$$J_2(\omega,\omega') = j_2(\omega,\omega') + \frac{k_{\mathrm{B}}T}{2\pi}\int \mathrm{d}\omega''\, j_4(\omega,\omega',\omega'',-\omega'')\zeta'(\omega'') + \mathcal{O}\left((k_{\mathrm{B}}T)^2\right), \tag{6.26}$$

$$J_3(\omega,\omega',\omega'') = j_3(\omega,\omega',\omega'') + \frac{k_{\mathrm{B}}T}{2\pi}\int \mathrm{d}\omega'''\, j_5(\omega,\omega',\omega'',\omega''',-\omega''')\zeta'(\omega''') + \mathcal{O}\left((k_{\mathrm{B}}T)^2\right), \tag{6.27}$$

etc., contributing to the nonlinear thermal force response of the system. For a recent study on the thermal nonlinear force response of bistable systems, see Ref. [257]. As expected, the athermal response of the system (the first term in the Eqs. 6.25-6.27) is complemented by noise strength dependent terms involving higher order athermal response functions j_i with $i > 1$ and the real part of the frequency-dependent friction coefficient ζ'.

Note that the PSD of the equilibrium fluctuations (Eq. 6.20) can equally be calculated from the linear force response (Eq. 6.25) using the FDT

$$S(\omega) = \frac{2k_{\mathrm{B}}T}{\omega}\,\mathrm{Im}\left[J_1(\omega)\right] = \frac{2k_{\mathrm{B}}T}{\omega}\,\mathrm{Im}\left[j_1(\omega)\right] + \frac{(k_{\mathrm{B}}T)^2}{\pi\omega}\int \mathrm{d}\omega'\,\mathrm{Im}\left[j_3(\omega,\omega',-\omega')\right]\zeta'(\omega') + \frac{(k_{\mathrm{B}}T)^3}{4\pi^2\omega}\int \mathrm{d}\omega'\int \mathrm{d}\omega''\,\mathrm{Im}\left[j_5(\omega,\omega',-\omega',\omega'',-\omega'')\right]\zeta'(\omega')\zeta'(\omega'') + \mathcal{O}\left((k_{\mathrm{B}}T)^4\right). \tag{6.28}$$

In practice, calculating $S(\omega)$ via this second route may be easier than evaluating the integrals in Eq. 6.20.

6.1.3 Discussion of the analytical results

As follows from the derivations above, thermally fluctuating systems are in general characterized by force response and equilibrium correlation functions showing a complex functional dependence on the thermal noise strength. The results obtained in this section (Eqs. 6.20, 6.22 and 6.25-6.27) represent the first terms in a systematic expansion. The practical use of the first few terms in the Taylor expansion as valuable estimates for the overall series clearly depends on the convergence properties of the series as is discussed in Sec. 6.2 based on explicit examples of overdamped diffusion in three different potential landscapes. Previous studies focusing on similar systems provided approximate [258–260] and in a few cases also exact [251, 252] analytical expressions based on the corresponding FP equation. In contrast, our approach, which is based on the Langevin equation, is not restricted to Markovian dynamics; incorporating the effects of colored instead of white thermal noise thus does not constitute a problem. In addition, the single trajectory perspective taken in our approach is essential to understand the consequences for the dynamics of composite systems discussed in Sec. 6.4.

6.2 Examples: Overdamped Diffusion in a Potential Landscape

In the Secs. 6.2.2-6.2.4, we consider the overdamped motion of a particle with friction coefficient ζ_0 in three different external potentials $U(x)$. The corresponding equation of motion is

$$\zeta_0\frac{\mathrm{d}x(t)}{\mathrm{d}t} + \frac{\mathrm{d}U(x)}{\mathrm{d}x} = \mathcal{F}_t[x] = f_{\mathrm{st}}(t) + f_{\mathrm{ext}}(t). \tag{6.29}$$

The stochastic forces are assumed to be δ-correlated in time,

$$\left\langle f_{\mathrm{st}}(t)f_{\mathrm{st}}(t')\right\rangle = 2\zeta_0 k_{\mathrm{B}}T\delta(t-t'), \tag{6.30}$$

which according to the definitions in the Eqs. 6.9 and 6.12 implies

$$\zeta'(t) = \zeta_0\,\delta(t), \qquad \zeta'(\omega) = \zeta_0. \tag{6.31}$$

The normalized equilibrium probability density function (PDF) is

$$P_{\mathrm{eq}}(x) \equiv \frac{1}{Z}\,\mathrm{e}^{-U(x)/(k_{\mathrm{B}}T)}, \qquad Z \equiv \int \mathrm{d}x\,\mathrm{e}^{-U(x)/(k_{\mathrm{B}}T)}, \tag{6.32}$$

characterized by the mean and the variance

$$x_{\mathrm{avg}} \equiv \int \mathrm{d}x\; x\, P_{\mathrm{eq}}(x), \qquad \sigma_x^2 \equiv \int \mathrm{d}x\; (x - x_{\mathrm{avg}})^2\, P_{\mathrm{eq}}(x). \tag{6.33}$$

In the following, the potentials are chosen so that the potential minimum, around which the expansion is performed, is located at $x = 0$. The second derivative of the potential at the position of the minimum is denoted by α_0. Energy is measured in units of $k_{\mathrm{B}}T$, length in units of $\sqrt{k_{\mathrm{B}}T/\alpha_0}$ and time in units of ζ_0/α_0. In consequence, the units of the linear force response and of the PSD are $1/\alpha_0$ and $\zeta_0 k_{\mathrm{B}}T/\alpha_0^2$, respectively. Rescaled units are denoted by a tilde.

6.2.1 Numerical simulations

Numerical simulations of the Eqs. 6.29 and 6.30 in the potentials given in the Eqs. 6.34, 6.44 and 6.52 are performed using a simple Euler integration scheme with a time step $\delta\tilde{t} = 10^{-3}$. For each set of parameters, 10 independent simulations with $2 \cdot 10^{10}$ integration steps each are performed corresponding to a total simulation time $\tilde{T}_{\mathrm{sim}} = 2 \cdot 10^8$. The position x is written out with a time resolution of $\Delta\tilde{t} = 10^{-1}$ for the subsequent spectral analysis.

6.2.2 Harmonic potential with a quartic contribution

We consider potential landscapes of the form

$$U(x) = \frac{1}{2}\alpha_0 x^2 + \frac{1}{4}\beta x^4, \qquad \alpha_0 > 0, \quad \beta \geq 0, \tag{6.34}$$

where deviations from a harmonic potential are introduced through the parameter β determining the strength of the quartic contribution as shown in Fig. 6.1a. Fourier transformation of the equation of motion (Eq. 6.29) and comparison to Eq. 6.5 yield

$$\begin{aligned} &g_1(\omega) = -\mathrm{i}\omega\zeta_0 + \alpha_0, \qquad g_2(\omega,\omega') = 0, \qquad g_3(\omega,\omega',\omega'') = 6\beta, \\ &g_i(\omega,\ldots,\omega^{(i-1)}) = 0, \quad \forall\, i \geq 4, \end{aligned} \tag{6.35}$$

translating into

$$j_1(\omega) = \frac{1}{\alpha_0 - \mathrm{i}\zeta_0\omega}, \tag{6.36}$$

$$j_2(\omega,\omega') = 0, \tag{6.37}$$

$$j_3(\omega,\omega',\omega'') = \frac{-6\beta}{(\alpha_0 - \mathrm{i}\zeta_0\omega)(\alpha_0 - \mathrm{i}\zeta_0\omega')(\alpha_0 - \mathrm{i}\zeta_0\omega''))(\alpha_0 - \mathrm{i}\zeta_0(\omega+\omega'+\omega'')))}, \tag{6.38}$$

according to the Eqs. 6.6-6.8. The functions j_i with even i vanish due to symmetry, while those with odd i do not. The function j_5 is calculated via Eq. F.5, the resulting bulky expression is

however not shown explicitly. With this, the first terms in the expansions for the linear force response function (Eq. 6.25) and the equilibrium PSD (Eq. 6.20) read

$$\begin{aligned} J_1(\omega) = &\frac{1}{\alpha_0 - \mathrm{i}\zeta_0\omega} - \frac{3\tilde{\beta}}{\alpha_0(1-\mathrm{i}\zeta_0\omega/\alpha_0)^2} \\ &+ \frac{9\tilde{\beta}^2}{(1-\mathrm{i}\zeta_0\omega/\alpha_0)^2}\left(\frac{1}{\alpha_0-\mathrm{i}\zeta_0\omega} + \frac{2}{3\alpha_0-\mathrm{i}\zeta_0\omega} + \frac{1}{\alpha_0}\right) + \mathcal{O}\left(\tilde{\beta}^3\right), \end{aligned} \tag{6.39}$$

and

$$S(\omega) = \frac{2\zeta_0 k_\mathrm{B}T}{\alpha_0^2+\zeta_0^2\omega^2} - \frac{12\tilde{\beta}\zeta_0 k_\mathrm{B}T}{\left(\alpha_0+\zeta_0^2\omega^2/\alpha_0\right)^2} + \frac{18\tilde{\beta}^2\zeta_0 k_\mathrm{B}T\left(59\alpha_0^4+26\alpha_0^2\zeta_0^2\omega^2-\zeta_0^4\omega^4\right)}{\left(9+\zeta_0^2\omega^2/\alpha_0^2\right)\left(\alpha_0^2+\zeta_0^2\omega^2\right)^3} + \mathcal{O}\left(\tilde{\beta}^3\right), \tag{6.40}$$

where we have introduced the expansion parameter $\tilde{\beta} \equiv \beta k_\mathrm{B}T/\alpha_0^2$ controlling the importance of the subsequent terms in the above equations. The examination of the PSD in Eq. 6.40 reveals that the effect of the quartic part in the potential landscape is most pronounced in the low-frequency regime ($\omega \ll \alpha_0/\zeta_0$), while it is negligible in the opposite case, since the correction terms to the Lorentzian asymptotically scale as $\propto \omega^{-n}$ with $n \geq 4$ and thus only marginally affect the high-frequency behavior $S(\omega) \sim 2k_\mathrm{B}T/(\zeta_0\omega^2)$.

To assess the influence of the nonlinearity, we consider a series of potentials, in which the quartic contribution tuned by the value of $\tilde{\beta}$ in Eq. 6.34 is gradually increased. The potential landscapes and corresponding equilibrium PDFs are shown in Fig. 6.1a-b. Real and imaginary parts of the linear response function J_1 (Eq. 6.39) are shown in Fig. 6.1c-d: When the quartic contribution is increased, the real part of the quasi-static response decreases; at the same time, the position of the characteristic peak in the imaginary part is shifted towards higher frequencies and its peak height diminishes. Note that the apparent reversal of this trend for $\tilde{\beta} = 0.1$ is an artifact due to the slow convergence properties of the series in Eq. 6.39. Similarly, the terms in the Taylor expansion of the PSD (Eq. 6.40) are of alternating sign and the convergence based on the first three terms is rather poor for $\tilde{\beta} \gtrsim 0.1$ as is explicitly shown in the following. A better estimate is the corresponding Padé approximant [261] of order $[1,1]$, which for a Taylor series

$$S = S_0 + S_1\tilde{\beta} + \frac{1}{2}S_2\tilde{\beta}^2 + \mathcal{O}(\tilde{\beta}^3), \tag{6.41}$$

is given by

$$S^{[1,1]} \equiv \frac{2S_0S_1 + (2S_1^2 - S_0S_2)\beta}{2S_1 - S_2\beta}. \tag{6.42}$$

Based on Eq. 6.40, we obtain

$$S^{[1,1]}(\omega) = \frac{\zeta_0 k_\mathrm{B}T}{\alpha_0^2}\frac{2\zeta_0^2\omega^2\alpha_0^2\left(2-3\tilde{\beta}\right) + 6\alpha_0^4\left(6+23\tilde{\beta}\right)}{\zeta_0^4\omega^4\left(2-3\tilde{\beta}\right) + 2\alpha_0^2\zeta_0^2\omega^2\left(10+39\tilde{\beta}\right) + 3\alpha_0^4\left(6+59\tilde{\beta}\right)}, \tag{6.43}$$

which is free of singularities for $\tilde{\beta} < 2/3$.

In Fig. 6.2, the PSDs S (Eq. 6.40) and $S^{[1,1]}$ (Eq. 6.43) are compared to estimates from numerical simulations of the Eqs. 6.29, 6.30 and 6.34. Details about the spectral analysis of the simulation data are found in Appendix F.2. The purple line corresponds to the purely harmonic potential ($\tilde{\beta} = 0$), for which the PSD takes the form of a simple Lorentzian. As the quartic contribution to the potential is increased, the PSD values decrease significantly in the low frequency regime. As

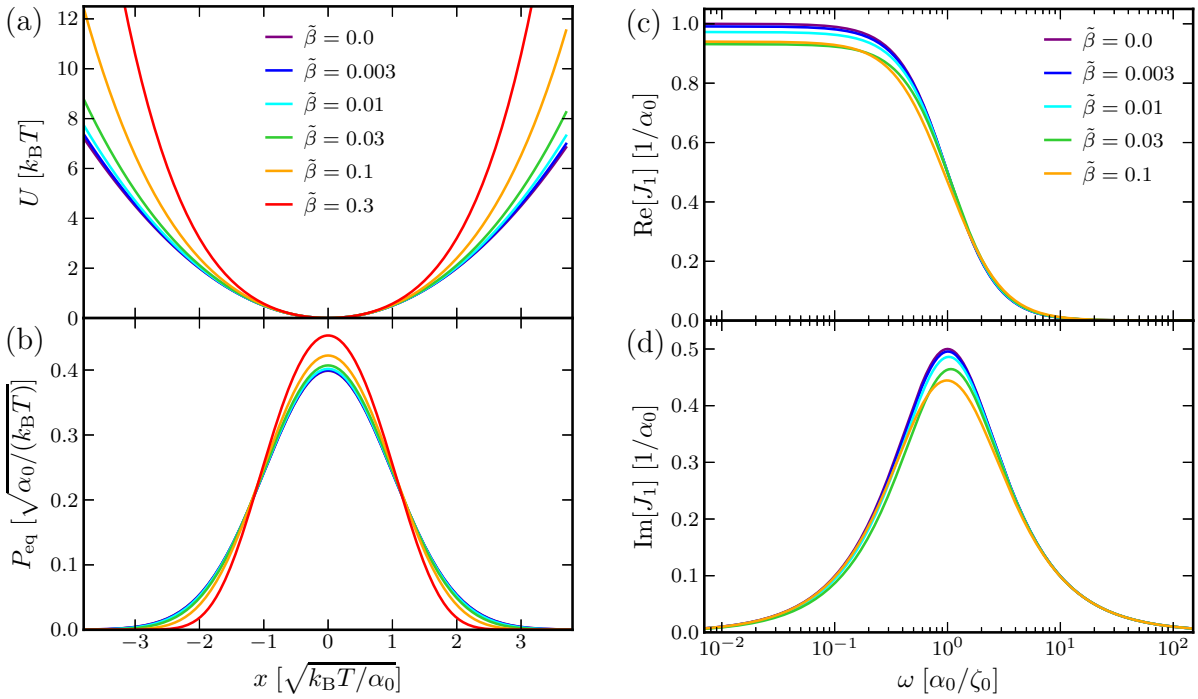

Figure 6.1:
a) Potential landscape (Eq. 6.34) and b) equilibrium PDF (Eq. 6.32) for different values of the rescaled quartic contribution $\tilde{\beta} \equiv \beta k_B T/\alpha_0^2$. c) Corresponding real and d) imaginary parts of the Taylor expansion of the linear response function J_1 (Eq. 6.39).

is seen from Fig. 6.2, the Padé approximants (solid lines) clearly represent the better estimate compared to the first three terms of the Taylor expansion (dashed lines). In fact, $S^{[1,1]}$ yields an excellent description of the data for $\tilde{\beta} \lesssim 0.1$ and even for $\tilde{\beta} = 0.3$ the maximal relative error remains on the order of 20% only.

6.2.3 Smoothed V-shape potential

Next, we consider potential landscapes

$$U(x) = F_0 x \tanh\left(\frac{\alpha_0 x}{2F_0}\right), \qquad \alpha_0 > 0, \quad F_0 > 0, \tag{6.44}$$

corresponding to a smoothed V-shape as shown in Fig. 6.3a. For $|x| \ll 2F_0/\alpha_0$, the potential is characterized by a quadratic dependence $U(x) \approx \alpha_0 x^2/2$, while it is linearly increasing, $U(x) \approx F_0\,|x|$, for $|x| \gg 2F_0/\alpha_0$. Fourier transformation of the equation of motion (Eq. 6.29) and comparison to Eq. 6.5 yield

$$\begin{aligned} &g_1(\omega) = -\mathrm{i}\omega\zeta_0 + \alpha_0, \quad g_3(\omega,\omega',\omega'') = -\alpha_0^3/F_0^2, \quad g_5(\omega,\omega',\omega'',\omega''',\omega^{\mathrm{IV}}) = 3\alpha_0^5/F_0^4, \quad \text{etc.} \\ &g_i(\omega,\ldots,\omega^{(i-1)}) = 0, \quad \forall\, i \text{ even}, \end{aligned} \tag{6.45}$$

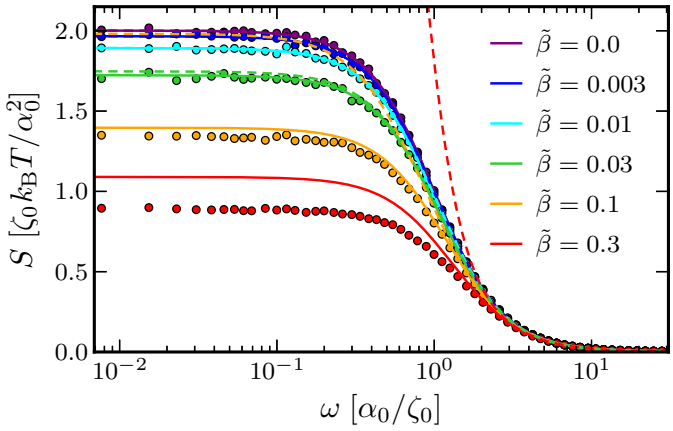

Figure 6.2:
PSDs for overdamped diffusion in a harmonic potential with rescaled quartic contribution $\tilde{\beta} \equiv \beta k_B T/\alpha_0^2$, *same color coding* as in Fig. 6.1. *Dashed lines* denote the first three terms in the Taylor expansion of S (Eq. 6.40), *solid lines* correspond to the Padé approximant $S^{[1,1]}$ (Eq. 6.43), and *colored circles* denote spectral estimates from numerical simulations. Note that *purple* and *blue dashed lines* perfectly overlap with the *solid ones* and that the *orange dashed line* is hardly discernible between the *purple* and *blue data points*.

translating into

$$j_1(\omega) = \frac{1}{\alpha_0 - i\zeta_0\omega}, \tag{6.46}$$

$$j_2(\omega, \omega') = 0, \tag{6.47}$$

$$j_3(\omega, \omega', \omega'') = \frac{\alpha_0^3}{F_0^2(\alpha_0 - i\zeta_0\omega)(\alpha_0 - i\zeta_0\omega')(\alpha_0 - i\zeta_0\omega'')(\alpha_0 - i\zeta_0(\omega + \omega' + \omega''))}, \tag{6.48}$$

according to the Eqs. 6.6-6.8. The functions j_i and g_i with even i vanish due to symmetry, while both the functions g_i and j_i with odd i do not. The function j_5 is calculated via Eq. F.5, the resulting bulky expression is however not shown explicitly. The first terms in the expansions of the linear force response function (Eq. 6.25) and the equilibrium PSD (Eq. 6.20) are

$$J_1(\omega) = \frac{1}{\alpha_0 - i\zeta_0\omega} + \frac{\alpha_0}{2\tilde{F}_0^2(\alpha_0 - i\zeta_0\omega)^2} + \frac{\alpha_0\left(7\alpha_0^2 - 2i\alpha_0\zeta_0\omega + \zeta_0^2\omega^2\right)}{8\tilde{F}_0^4(\alpha_0 - i\zeta_0\omega)^3(3\alpha_0 - i\zeta_0\omega)} + \mathcal{O}\left(\tilde{F}_0^{-6}\right), \tag{6.49}$$

and

$$S(\omega) = \frac{2\zeta_0 k_B T}{\alpha_0^2 + \omega^2\zeta_0^2} + \frac{2\alpha_0^2\zeta_0 k_B T}{\tilde{F}_0^2\left(\alpha_0^2 + \zeta_0^2\omega^2\right)^2} + \frac{2\alpha_0^2\zeta_0 k_B T\left(8\alpha_0^4 - \alpha_0^2\zeta_0^2\omega^2 - \zeta_0^4\omega^4\right)}{\tilde{F}_0^4\left(\alpha_0^2 + \zeta_0^2\omega^2\right)^3\left(9\alpha_0^2 + \zeta_0^2\omega^2\right)} + \mathcal{O}\left(\tilde{F}_0^{-6}\right), \tag{6.50}$$

where the expansion parameter $\tilde{F}_0^{-2} \equiv \alpha_0 k_B T/F_0^2$ is used and the harmonic potential is thus recovered in the limit $\tilde{F}_0 \to \infty$. Again, the effect of the nonlinearity in the potential landscape (Eq. 6.44) is most pronounced in the low-frequency regime ($\omega \ll \alpha_0/\zeta_0$), while it is negligible for $\omega \gg \alpha_0/\zeta_0$, since the correction terms to the Lorentzian asymptotically scale as $\propto \omega^{-n}$ with $n \geq 4$ and thus only marginally affect the high-frequency behavior $S(\omega) \sim 2k_B T/(\zeta_0\omega^2)$.

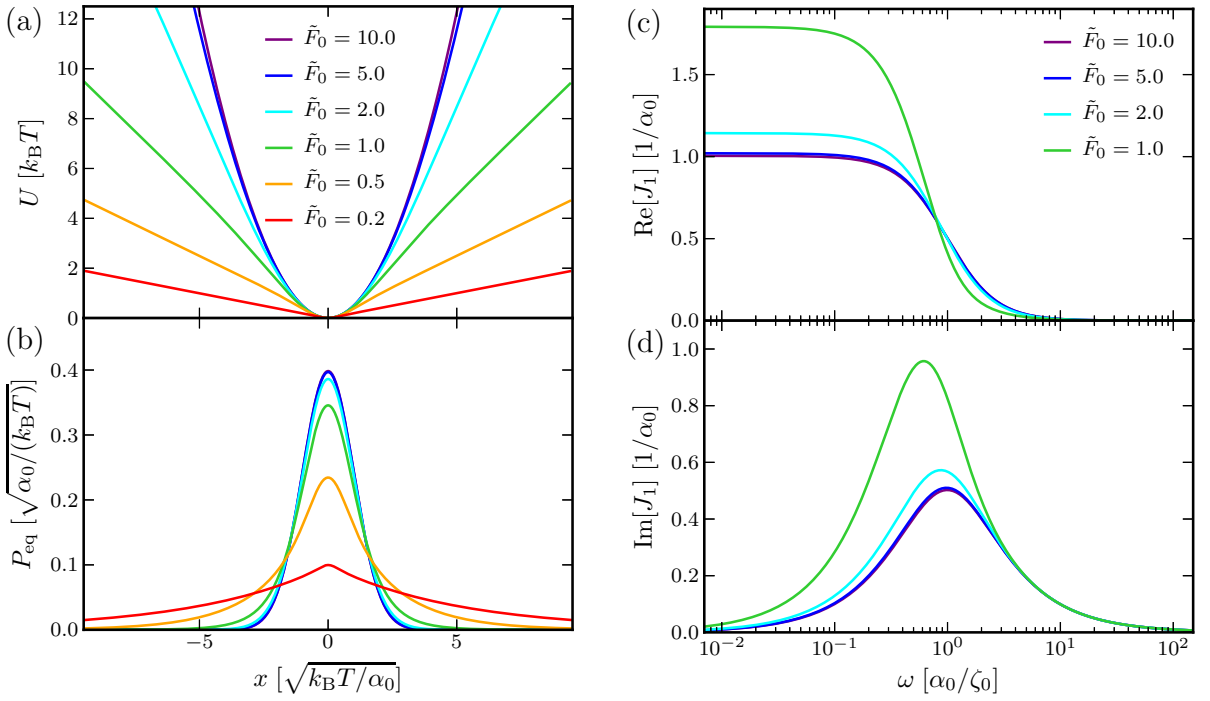

Figure 6.3:
a) Potential landscape (Eq. 6.44) and b) equilibrium PDF (Eq. 6.32) for different values of $\tilde{F}_0 \equiv F_0/\sqrt{\alpha_0 k_\mathrm{B}T}$. c) Corresponding real and d) imaginary parts of the first three terms in the Taylor expansion of the linear response function J_1 (Eq. 6.49).

To study the effect of the nonlinearity on the equilibrium fluctuations of the system, we consider overdamped motion in a series of potentials characterized by different values of $\tilde{F}_0 \equiv F_0/\sqrt{\alpha_0 k_\mathrm{B}T}$. Potential landscapes and corresponding equilibrium PDFs are shown in Fig. 6.3a-b, real and imaginary parts of the linear force response functions are displayed in Fig. 6.3c-d: When gradually decreasing the value of $\tilde{F}_0$ in Eq. 6.44, the quasi-stationary force response and the peak amplitude of the imaginary part increase, while the characteristic frequency decreases. Increasing the degree of nonlinearity (by decreasing the value $\tilde{F}_0$) thus has the opposite effect on the linear force response than in Sec. 6.2.2, which shows that nonlinearities act differently depending on the specificities of the potential.

To assess the accuracy of the analytical results, we compare results from numerical simulations of the Eqs. 6.29, 6.30 and 6.44 to the first three terms of the Taylor expansion of the equilibrium PSD (Eq. 6.50) in Fig. 6.4. We observe excellent quantitative agreement between simulation results (circles) and the analytical estimates (solid lines) for $\tilde{F}_0 \gtrsim 2$. For $\tilde{F}_0 = 1$, the first three Taylor terms for S are still in qualitative agreement with the data, but relative deviations of $\sim 30\%$ are discernible for small frequencies. For $\tilde{F}_0 = 0.2$ (red curve), the first three terms in Eq. 6.50 yield (unphysical) negative values in the intermediate frequency range, thereby indicating the slow convergence of the series for such large nonlinearities.

In the limit $\tilde{F}_0 \to 0$, the exact form of the potential at the origin becomes irrelevant for the resulting two-point correlation functions and a potential of the form $U(x) = F_0\,|x|$ should

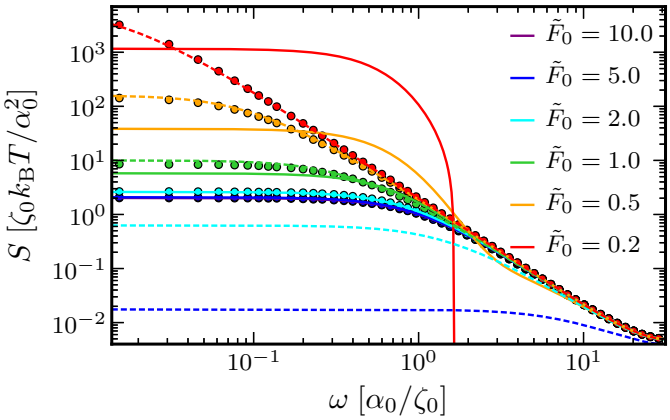

Figure 6.4:
PSDs for overdamped motion in a smoothed V-shape potential (Eq. 6.44) for different values of $\tilde{F}_0 \equiv F_0/\sqrt{\alpha_0 k_B T}$, *same color coding* as in Fig. 6.3. *Solid lines* denote the first three terms in the Taylor expansion of S (Eq. 6.50) and *colored circles* denote spectral estimates from numerical simulations. *Dashed lines* correspond to the PSD $S_\vee$ in a cuspidal V-shape potential (Eq. 6.51). *Purple symbols* and *lines* are mostly superimposed by the *blue symbols* and *lines*.

therefore accurately capture the dynamics. For the problem of overdamped diffusion in such a cuspidal V-shape potential the exact functional form of the PSD has been derived [251]

$$S_\vee(\omega) = \frac{2k_B T}{\zeta_0 \omega^2}\left(1 + \frac{1}{2}\left(\frac{\tilde{F}_0^2 \alpha_0}{\zeta_0 \omega}\right)^2 \left(1 - \sqrt{\frac{1+\sqrt{1+\left(\frac{4\zeta_0\omega}{\tilde{F}_0^2\alpha_0}\right)^2}}{2}}\right)\right), \tag{6.51}$$

and is displayed as dashed colored lines in Fig. 6.4. Indeed, numerical data and the above expression agree well for $\tilde{F}_0 \ll 1$, while for $\tilde{F}_0 \gg 1$ the values of the PSD are underestimated by several orders of magnitude for small frequencies. Thus, depending on the value of $\tilde{F}_0$, either Eq. 6.50 or Eq. 6.51 represent the better analytical estimate.

6.2.4 Symmetric double-well potential

Finally, as an example for a highly nonlinear system, we examine the overdamped dynamics in a double-well potential, which has extensively been studied in the literature and is of particular interest in the context of stochastic resonance [253, 254, 262, 263]. We consider a symmetric double-well potential of the form

$$U(x) = \frac{1}{2}\alpha_0 x^2 - \frac{\alpha_0}{4}\sqrt{\frac{\alpha_0}{2\Delta U}}x^3 + \frac{\alpha_0^2}{64\Delta U}x^4, \qquad \alpha_0 > 0, \quad \Delta U > 0, \tag{6.52}$$

as shown in Fig. 6.5a. The potential is characterized by an energy barrier of magnitude ΔU located at $x = 2\sqrt{2\Delta U/\alpha_0}$ separating two minima at $x = 0$ and $x = 4\sqrt{2\Delta U/\alpha_0}$. Again, the

second derivative of the potential in the minima is given by α_0. Fourier transformation of Eq. 6.29 and comparison with Eq. 6.5 yield

$$\begin{aligned} g_1(\omega) &= -\mathrm{i}\omega\zeta_0 + \alpha_0, \qquad g_2(\omega,\omega') = -\frac{3\alpha_0}{2}\sqrt{\frac{\alpha_0}{2\Delta U}}, \\ g_3(\omega,\omega',\omega'') &= \frac{3\alpha_0^2}{8\Delta U}, \qquad g_i(\omega,\ldots,\omega^{(i-1)}) = 0, \quad \forall\, i \geq 4, \end{aligned} \tag{6.53}$$

translating into

$$j_1(\omega) = \frac{1}{\alpha_0 - \mathrm{i}\zeta_0\omega}, \tag{6.54}$$

$$j_2(\omega,\omega') = \frac{3\alpha_0\sqrt{\alpha_0}}{2\sqrt{2\Delta U}\,(\alpha_0 - \mathrm{i}\zeta_0\omega)\,(\alpha_0 - \mathrm{i}\zeta_0\omega')\,(\alpha_0 - \mathrm{i}\zeta_0(\omega+\omega'))}, \tag{6.55}$$

according to the Eqs. 6.6 and 6.7. The functions j_3, j_4 and j_5 are calculated based on the Eqs. F.3-F.5, the resulting bulky expressions are however not shown. With this, we obtain the linear force response function (Eq. 6.25)

$$\begin{aligned} J_1(\omega) = &\frac{1}{\alpha_0 - \mathrm{i}\zeta_0\omega} + \frac{3\alpha_0(5\alpha_0 - \mathrm{i}\zeta_0\omega)}{8\Delta\tilde{U}(\alpha_0 - \mathrm{i}\zeta_0\omega)^2(2\alpha_0 - \mathrm{i}\zeta_0\omega)} \\ &+ \frac{9\alpha_0\left(182\alpha_0^4 - 211\mathrm{i}\alpha_0^3\zeta_0\omega - 78\alpha_0^2\zeta_0^2\omega^2 + 19\mathrm{i}\alpha_0\zeta_0^3\omega^3 + 2\zeta_0^4\omega^4\right)}{64(\Delta\tilde{U})^2(\alpha_0 - \mathrm{i}\zeta_0\omega)^3(2\alpha_0 - \mathrm{i}\zeta_0\omega)^2(3\alpha_0 - \mathrm{i}\zeta_0\omega)} + \mathcal{O}\left((\Delta\tilde{U})^{-3}\right), \end{aligned} \tag{6.56}$$

and the equilibrium PSD (Eq. 6.20)

$$\begin{aligned} S(\omega) = &\frac{2\zeta_0 k_\mathrm{B}T}{\alpha_0^2 + \zeta_0^2\omega^2} - \frac{3\zeta_0 k_\mathrm{B}T\left(\alpha_0^2\zeta_0^2\omega^2 - 23\alpha_0^4\right)}{4\Delta\tilde{U}\left(\alpha_0^2 + \zeta_0^2\omega^2\right)^2\left(4\alpha_0^2 + \zeta_0^2\omega^2\right)} \\ &+ \frac{9\alpha_0^2\zeta_0 k_\mathrm{B}T\left(6932\alpha_0^8 + 449\alpha_0^6\zeta_0^2\omega^2 - 1849\alpha_0^4\zeta_0^4\omega^4 + 27\alpha_0^2\zeta_0^6\omega^6 + \zeta_0^8\omega^8\right)}{32(\Delta\tilde{U})^2\left(\alpha_0^2 + \zeta_0^2\omega^2\right)^3\left(4\alpha_0^2 + \zeta_0^2\omega^2\right)^2\left(9\alpha_0^2 + \zeta_0^2\omega^2\right)} + \mathcal{O}\left((\Delta\tilde{U})^{-3}\right), \end{aligned} \tag{6.57}$$

where the expansion parameter is $(\Delta\tilde{U})^{-1} \equiv k_\mathrm{B}T/\Delta U$ and the harmonic potential is thus recovered in the limit of large barrier heights $\Delta\tilde{U} \to \infty$. In the following, we consider overdamped dynamics in a series of double-well potentials, in which the rescaled height of the energy barrier $\Delta\tilde{U}$ is progressively decreased. Potential landscapes and corresponding equilibrium PDFs are shown in Fig. 6.5. The first three terms of the Taylor expansion of the PSD (Eq. 6.57) are compared to estimates from numerical simulations of the Eqs. 6.29, 6.30 and 6.52 in Fig. 6.6a. Good agreement between theoretical and numerical estimates is found for large frequencies only, while large deviations are observed in particular for small frequencies, where the contribution of inter-well hopping to the PSD is dominant. For reference, the standard Lorentzian representing the first term in the Taylor expansion of the PSD (Eq. 6.57) is drawn as a dashed black line. The differences between the actual PSD values and the Lorentzian comprise several orders of magnitudes for small frequencies and thus it is not astonishing that the first three terms of alternating sign in the Taylor series are not sufficient to yield quantitative agreement over the whole range of frequencies. In the inset of Fig. 6.6, a close view of the region indicated by a gray rectangle is shown, where the vertical axis is rescaled to better distinguish the

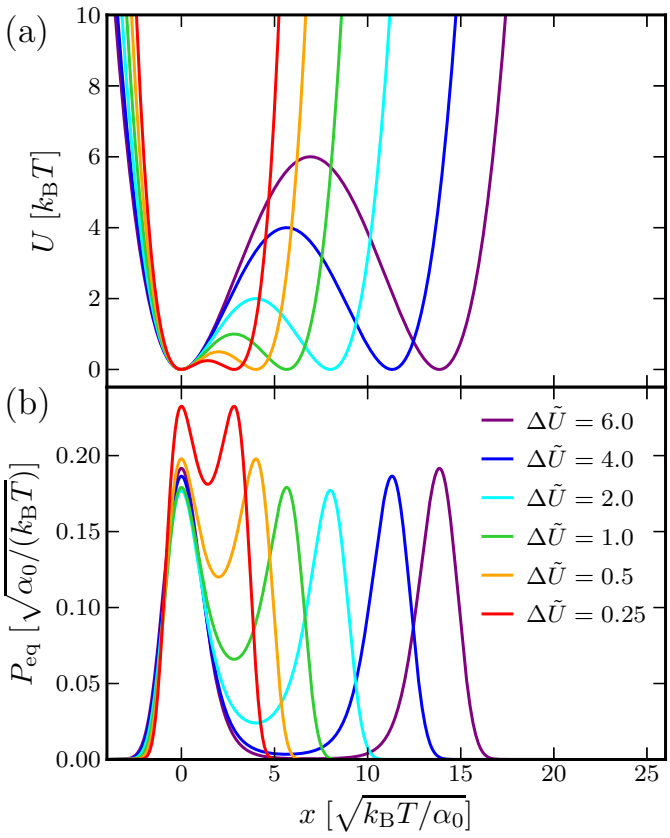

Figure 6.5:
a) Symmetric double-well potential (Eq. 6.52) and b) corresponding equilibrium PDF (Eq. 6.32) for different values of the rescaled height of the energy barrier $\Delta\tilde{U} \equiv \Delta U/k_\mathrm{B}T$.

individual curves and data points. As expected, the deviations between numerical data and theoretical curves set in at larger frequencies the smaller the value of the energy barrier $\Delta\tilde{U}$. The slow convergence of the Taylor series for small values of $\Delta\tilde{U}$ is emphasized by the fact that the red curve corresponding to $\Delta\tilde{U} = 0.25$ takes (unphysical) negative values for intermediate frequencies.

6.2.5 Range of validity of the expansions for the model systems

We conclude that already slight nonlinearities have a significant effect on the linear force response function J_1 and the equilibrium PSD S of a thermally fluctuating system. Increasing nonlinear contributions affect the low-frequency regime first, the high-frequency dynamics being trivially linear. For the case of overdamped diffusion in a harmonic potential with a quartic contribution (Sec. 6.2.2), these changes can quantitatively be captured over the full frequency range by the first three terms of the Taylor expansions in the Eqs. 6.39 and 6.40 as long as $\beta k_\mathrm{B}T/\alpha_0^2 \lesssim 0.03$. Moreover, the Padé approximant of the equilibrium PSD (Eq. 6.43) still yields reasonable agreement with the data for quartic contributions $\beta k_\mathrm{B}T/\alpha_0^2 \lesssim 0.3$. For the case of a smoothed V-shape potential (Sec. 6.2.3), the first three terms in the Taylor expansions in the Eqs. 6.49 and 6.50 yield accurate predictions for $F_0/\sqrt{\alpha_0 k_\mathrm{B}T} \gtrsim 1$. In turn, the analytical expres-

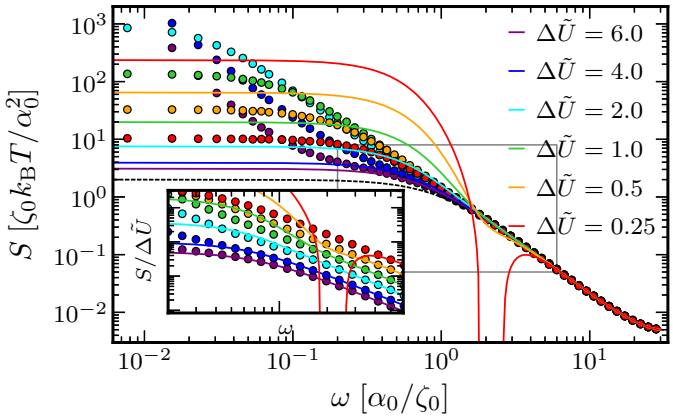

Figure 6.6:
PSDs for overdamped motion in a symmetric double-well potential (Eq. 6.52) with different barrier heights $\Delta\tilde{U} \equiv \Delta U/k_B T$. *Solid colored lines* denote the first three terms in the Taylor expansion of S (Eq. 6.57) and *colored circles* denote spectral estimates from numerical simulations, *same color coding* as in Fig. 6.5. The *dashed black line* indicates the first term in Eq. 6.57. The inset shows a close view of the rectangular region indicated by the *gray box*; the vertical axis of the inset is rescaled by $\Delta\tilde{U}$ for clarity.

sion for the PSD associated with overdamped diffusion in a cuspidal V-potential [251] becomes adequate for $F_0/\sqrt{\alpha_0 k_B T} \lesssim 1$. For a highly nonlinear system such as diffusion in a double-well potential (Sec. 6.2.4), the first few terms in the Taylor expansion are not sufficient to quantitatively capture the entire frequency dependence of the PSD irrespective of the barrier height $\Delta\tilde{U}$.

Although the limits of the series expansions in Sec. 6.1 are independent of the expansion point, for asymmetric bi- or multistable systems, a better convergence of the first few terms may be obtained via a Boltzmann-weighted average over the expansions around the minima in the individual wells.

6.3 Use and Misuse of Strictly Linear Models

A standard approach when characterizing the fluctuating dynamics of observables consists in estimating the associated two-point correlation function (in time or frequency domain) and interpreting it based on a strictly linear model. For overdamped dynamics, this is equivalent to fitting the temporal two-point correlation function by a single exponential, or the PSD data by the first term in the expansions of the PSDs in the Eqs. 6.40, 6.50 and 6.57, i.e., a Lorentzian

$$S_{\text{fit}}(\omega) = \frac{2\zeta^{\text{fit}} k_B T}{\left(\alpha^{\text{fit}}\right)^2 + \left(\zeta^{\text{fit}}\right)^2 \omega^2}, \tag{6.58}$$

where the friction coefficient ζ^{fit} and the potential strength α^{fit} are used as fit parameters. To explicitly show the limitations of such an approach, we fit the PSD data from numerical simulations of overdamped diffusion in the monostable but anharmonic potentials of the Secs. 6.2.2 and 6.2.3 to the functional form of Eq. 6.58, details on the fitting procedure are found in Appendix F.3.

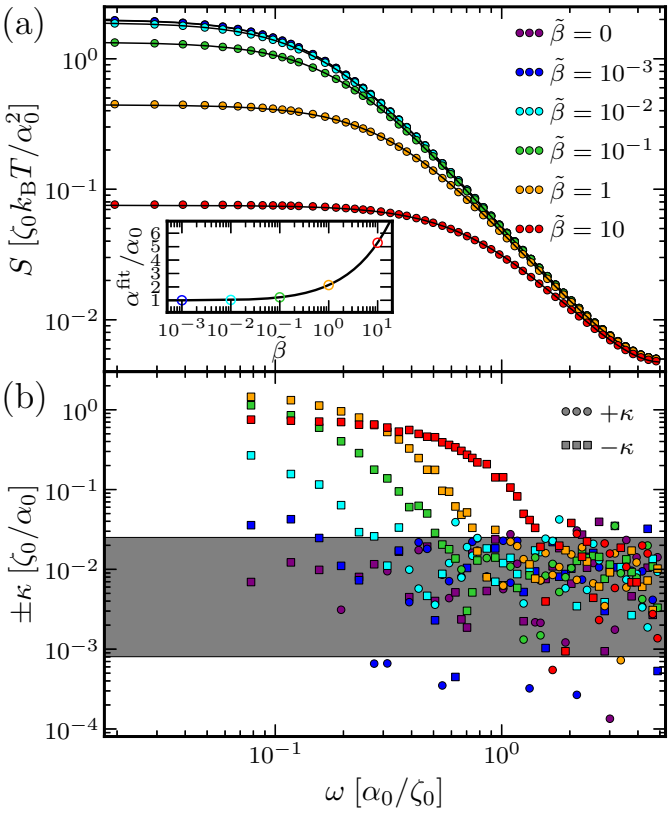

Figure 6.7:
a) PSDs for overdamped motion in the potential U (Eq. 6.34) for different values of the rescaled quartic contribution $\tilde{\beta} \equiv \beta k_B T/\alpha_0^2$: *Colored circles* denote estimates from numerical simulations, *black lines* denote fits to a strictly linear model (Eq. 6.58), see Appendix F.3 for details. Inset: Fit values α^{fit} are shown as *open colored circles*, fit values $\zeta^{\mathrm{fit}} \approx \zeta_0$ are independent of $\tilde{\beta}$ and are not shown. *Purple data points* are mostly hidden under the *blue* ones. b) Estimates for the spectral kurtosis κ (Eq. 6.59) resolved from numerical data, where *circles* and *squares* denote positive and negative values respectively. *Gray-shaded areas* indicate the 90%-confidence interval for strictly linear dynamics, see Appendix F.4 for details.

For the quadratic potential with a quartic contribution (Eq. 6.34), this kind of analysis provides almost perfect fits to the data independent of the degree of nonlinearity as is seen from Fig. 6.7a, where fits to the simulation data are displayed as black lines. A similar conclusion is drawn from Fig. 6.8a, where we show corresponding data and fits for diffusion in the V-shape potential (Eq. 6.44). The frequency dependence of the equilibrium PSDs thus does not or only very weakly deviate from a Lorentzian (Eq. 6.58) even for strongly nonlinear dynamics. While this observation explains the wide use and success of linear models, it in turn also implies that an apparent agreement of the spectral data with a Lorentzian fit cannot serve to validate or reject the hypothesis of strictly linear dynamics. Moreover, the information content of the fit values is rather limited: Indeed, the fit values α^{fit} shown in the insets of the Figs. 6.7a and 6.8a are well captured by the function $k_B T/\sigma_x^2$ (shown as black line in the insets) meaning that the fit values merely reflect the width σ_x of the equilibrium PDF (Eq. 6.33). Similarly, we obtain

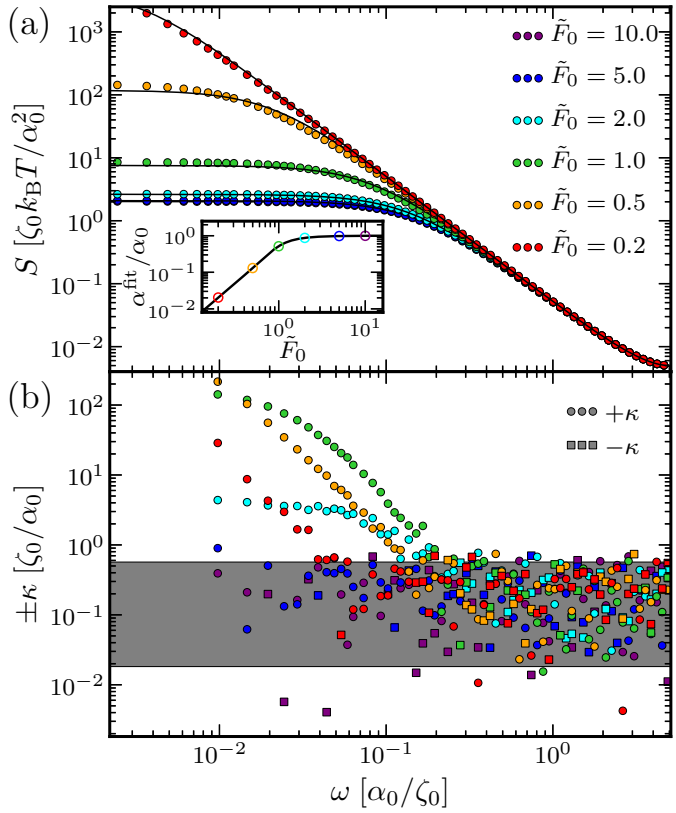

Figure 6.8:
Same as Fig. 6.7 but for overdamped diffusion in a V-shape potential (Eq. 6.44). Fit values $\zeta^{\rm fit} \approx \zeta_0$ are independent of $\tilde{F}_0$ and not shown.

$\zeta^{\rm fit} \approx \zeta_0$ for all fits shown in the Figs. 6.7a and 6.8a, as expected due to the trivially linear high-frequency behavior of the dynamics.

In order to identify possible nonlinear contributions to the dynamics, the analysis of higher-order correlation or response functions is therefore required. Here, we resolve the spectral kurtosis

$$\kappa(\omega) \equiv \frac{Y(\omega,-\omega,\omega)}{S(\omega)^2} = 8k_B T\zeta'(\omega)\,\mathrm{Re}\left[\frac{j_3(\omega,-\omega,\omega)}{j_1(-\omega)}\right] + \mathcal{O}\left((k_B T)^2\right), \tag{6.59}$$

where the leading term in the expansion on the right hand side results from the Eqs. 6.20 and 6.22. Since $\kappa(\omega) = 0$ for strictly linear dynamics, non-zero values of the spectral kurtosis indicate nonlinearities in the dynamics. Estimates for the spectral kurtosis from numerical simulations (see Appendix F.2 for the details on the spectral analysis) are shown in the Figs. 6.7b and 6.8b. While all systems considered are (within error) linear in the high-frequency regime, nonlinearities clearly come to light at smaller frequencies. While the overdamped diffusion in the harmonic potential with a quartic contribution is characterized by a negative spectral kurtosis, the kurtosis is positive for the motion in the V-shape potential. Given enough data (see Appendix F.4 for details on the statistical aspects), even weak nonlinearities such as for $\tilde{\beta} = 10^{-3}$

and $\tilde{\beta} = 10^{-2}$ are reliably revealed in the spectral kurtosis (blue data points in Fig. 6.7b), while the PSD-values are (by eye) indistinguishable from those for $\tilde{\beta} = 0$ in Fig. 6.7a.

The spectral kurtosis of the overdamped dynamics in the double-well potential (Eq. 6.52) is shown in Fig. 6.9b, the corresponding discussion is however deferred to the following section, where the data is discussed in the context of the superposition of two independent subsystems.

Overall, we find that linear models generally are well-suited to parametrize two-point correlation functions independently of the nature of the underlying dynamics. Caution is therefore advised before taking the fit values and thus implicitly the assumption of a linear model at face value. Resolving higher-order correlation/response functions and analyzing the dependence of PSD (Eq. 6.20) or response functions (Eqs. 6.25-6.27) on the thermal noise strength represent complementary approaches to unmask nonlinearities in the fluctuating dynamics and thus to confirm or to reject the linearity hypothesis.

6.4 Dynamics of Composite Systems

In the following, we consider the dynamics in a system resulting from the combination of two independent subsystems named $\mathfrak{A}$ and B. Each of these systems is described by separate sets of correlation and response functions, in particular the linear force response is given by

$$J_1^{\mathfrak{A}}(\omega) = \lim_{f_{\text{ext}}^{\mathfrak{A}} \to 0} \frac{\langle x_{\mathfrak{A}}(\omega) \rangle_{\mathfrak{A}}}{f_{\text{ext}}^{\mathfrak{A}}(\omega)}, \qquad J_1^{\mathfrak{B}}(\omega) = \lim_{f_{\text{ext}}^{\mathfrak{B}} \to 0} \frac{\langle x_{\mathfrak{B}}(\omega) \rangle_{\mathfrak{B}}}{f_{\text{ext}}^{\mathfrak{B}}(\omega)}, \tag{6.60}$$

where $\langle \ldots \rangle_{\mathfrak{A}}$ and $\langle \ldots \rangle_{\mathfrak{B}}$ denote averages over the thermal fluctuations of the respective subsystems.

The case of superposition is treated in Sec. 6.4.1, and the more complex case of mechanical coupling, for which the linear DCT was introduced in Ref. [ix], is discussed in Sec. 6.4.2.

6.4.1 Superposition

A simple composite system results from the superposition of the two independent subsystems as indicated in Fig. 6.10a: The composite system is characterized by the variable

$$x = x_{\mathfrak{A}} + x_{\mathfrak{B}}, \tag{6.61}$$

while both subsystems feel the same external force

$$f_{\text{ext}} = f_{\text{ext}}^{\mathfrak{A}} = f_{\text{ext}}^{\mathfrak{B}}. \tag{6.62}$$

Assuming that the two subsystems remain independent when being superposed, the force responses simply add up

$$J_i = J_i^{\mathfrak{A}} + J_i^{\mathfrak{B}}, \quad \forall\, i, \tag{6.63}$$

and in particular the PSD of the composite system is just the sum of the individual PSDs

$$S(\omega) = S^{\mathfrak{A}}(\omega) + S^{\mathfrak{B}}(\omega). \tag{6.64}$$

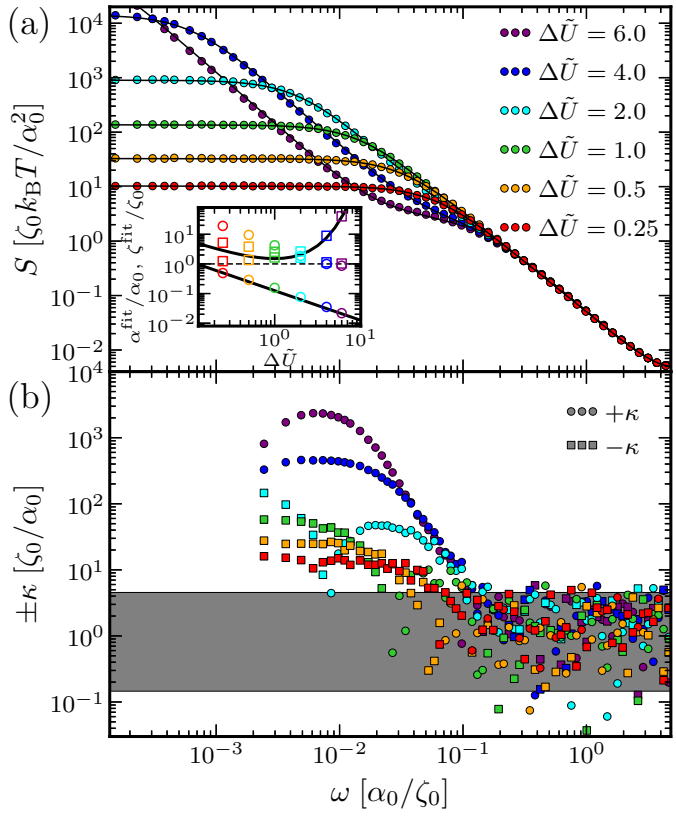

Figure 6.9:
a) PSDs for overdamped diffusion in a double-well potential (Eq. 6.52) for different values of the rescaled barrier height $\Delta\tilde{U} \equiv \Delta U/k_B T$: *Colored circles* denote estimates from numerical simulations, *black lines* denote fits to the superposition of two Lorentzians (Eq. F.12), see Appendix F.3 for details. Inset: Fit values $\alpha_{1,2}^{\mathrm{fit}}$ are shown as *colored open circles*, the fit values $\zeta_{1,2}^{\mathrm{fit}}$ as *open colored squares*, the *solid black lines* are given in Eq. 6.66. b) Estimates for the spectral kurtosis κ (Eq. 6.59) resolved from numerical data, where *circles* and *squares* denote positive and negative values respectively. *Gray-shaded areas* indicate the 90%-confidence interval for strictly linear dynamics, see Appendix F.4 for details.

Overdamped diffusion in a double-well potential

The superposition principle is often used to approximate the dynamics in bistable systems [257]. For the overdamped dynamics in the double-well (dw) potential of Sec. 6.2.4, the overall coordinate

$$x_{\mathrm{dw}} = x_{\mathrm{inter}} + x_{\mathrm{intra}}, \tag{6.65}$$

can be thought of a discrete stochastic variable x_{inter} discretely switching between the positions of the potential minima and of a continuous variable x_{intra} describing the dynamics within the corresponding wells.

Approximating the PSDs S_{inter} and S_{intra} both by a Lorentzian (Eq. 6.58) and adjusting the four parameters in the fit procedure (see Appendix F.3 for details), we obtain the solid lines in Fig. 6.9a. The fits nicely match the data from numerical simulations over the entire frequency range resolved and for all values of $\Delta\tilde{U}$. The fit values are displayed in the inset, where values for α^{fit} and ζ^{fit} are denoted by open circles and squares, respectively. For barrier heights $\Delta\tilde{U} \gtrsim 1$,

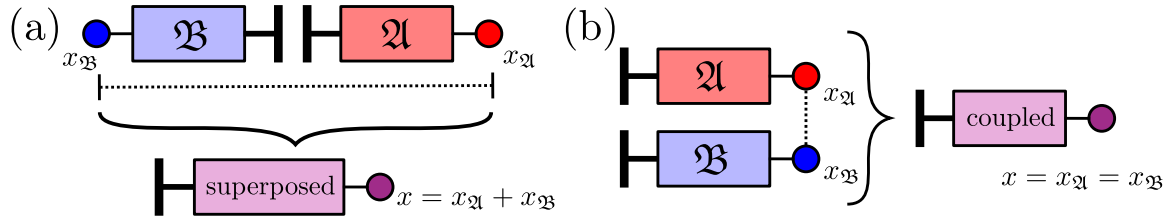

Figure 6.10:
a) The superposition of two independent mechanical subsystems of type $\mathfrak{A}$ and $\mathfrak{B}$ yields a composite system with coordinate $x = x_{\mathfrak{A}} + x_{\mathfrak{B}}$. b) The mechanical coupling of $\mathfrak{A}$ and $\mathfrak{B}$ enforces the same positions of both subsystems; the equivalent composite system is characterized by the coordinate $x = x_{\mathfrak{A}} = x_{\mathfrak{B}}$.

the fit values for the inter-well process are well approximated by estimates from Kramers' rate theory (Appendix F.5),

$$\alpha_{\text{inter}}^{\text{fit}} = \frac{\alpha_0}{8\Delta\tilde{U}}, \qquad \zeta_{\text{inter}}^{\text{fit}} = \frac{\pi\,\zeta_0\,\mathrm{e}^{\Delta\tilde{U}}}{4\sqrt{2}\Delta\tilde{U}}, \tag{6.66}$$

which are displayed as solid black lines in the inset of Fig. 6.9a, while the intra-well process is characterized by $\zeta_{\text{intra}} \approx \zeta_0$ and $\alpha_{\text{intra}} \approx \alpha_0$ (indicated by a broken horizontal line) as expected.

The nice agreement between the PSD data and the fits in Fig. 6.9a does however not represent a validation of the underlying assumption that the dynamics indeed result from the superposition of two independent stochastic processes. It also does not allow a judgement about the linearity of the dynamics. In fact, the spectral kurtosis (Eq. 6.59) of the stochastic fluctuations of the diffusive motion in the double-well potential, which is shown in Fig. 6.9b, emphasizes the highly nonlinear character of the dynamics: For intermediate frequencies, the spectral kurtosis is positive, while it takes negative values in the limit $\omega \to 0$.

6.4.2 Mechanical coupling

In contrast to the superposition described above, the mechanical coupling of the subsystems $\mathfrak{A}$ and $\mathfrak{B}$, which is relevant for practical applications [ix], is equivalent to the requirement

$$x \equiv x_{\mathfrak{A}} = x_{\mathfrak{B}}, \tag{6.67}$$

where x denotes the position of the overall system as depicted in Fig. 6.10b. For this to be fulfilled, the forces on the subsystems will generally differ, and the overall force on the coupled system then is

$$f = f^{\mathfrak{A}} + f^{\mathfrak{B}}. \tag{6.68}$$

If the force-free positions of both subsystems agree, one directly infers from the expansion in Eq. 6.5 and the coupling constraints (Eq. 6.67)

$$g_i = g_i^{\mathfrak{A}} + g_i^{\mathfrak{B}}, \quad \forall\, i, \tag{6.69}$$

Inserting the g_i-functions of the coupled system into the Eqs. 6.6-6.8 then allows to calculate the PSD (Eq. 6.20) or the force response functions (Eqs. 6.25-6.27). Note that the knowledge of all athermal g_i-functions of the subsystems are thus required to calculate dynamic quantities

of the composite system. Unlike in the case of the superposition (Sec. 6.4.1), the thermal linear response functions $J_1^{\mathfrak{A}}$ and $J_1^{\mathfrak{B}}$ of the subsystems do in general not contain enough information to calculate the thermal linear response function J_1 of the coupled system.

Dynamic convolution theory

The DCT from Ref. [ix] provides a method of estimating the linear force response of mechanically coupled objects based on the linear response functions of the individual components. For systems with only one degree of freedom and linear response functions given by Eq. 6.60, the DCT predictions reduce to the result from Ref. [264], namely

$$\begin{aligned} J_1^{\mathrm{DCT}}(\omega) \equiv& \frac{J_1^{\mathfrak{A}}(\omega) J_1^{\mathfrak{B}}(\omega)}{J_1^{\mathfrak{A}}(\omega) + J_1^{\mathfrak{B}}(\omega)} = \left(\frac{1}{J_1^{\mathfrak{A}}(\omega)} + \frac{1}{J_1^{\mathfrak{B}}(\omega)} \right)^{-1} \\ &\overset{(6.60)}{=} \lim_{f_{\mathrm{ext}}^{\mathfrak{A}} \to 0} \lim_{f_{\mathrm{ext}}^{\mathfrak{B}} \to 0} \left(\frac{f_{\mathrm{ext}}^{\mathfrak{A}}(\omega)}{\langle x_{\mathfrak{A}}(\omega) \rangle_{\mathfrak{A}}} + \frac{f_{\mathrm{ext}}^{\mathfrak{B}}(\omega)}{\langle x_{\mathfrak{B}}(\omega) \rangle_{\mathfrak{B}}} \right)^{-1} \\ &\overset{(6.67)}{=} \lim_{f_{\mathrm{ext}}^{\mathfrak{A}} \to 0} \lim_{f_{\mathrm{ext}}^{\mathfrak{B}} \to 0} \left(\frac{f_{\mathrm{ext}}^{\mathfrak{A}}(\omega)}{\langle x(\omega) \rangle_{\mathfrak{A}}} + \frac{f_{\mathrm{ext}}^{\mathfrak{B}}(\omega)}{\langle x(\omega) \rangle_{\mathfrak{B}}} \right)^{-1} \\ &\approx \lim_{f_{\mathrm{ext}}^{\mathfrak{A}} \to 0} \lim_{f_{\mathrm{ext}}^{\mathfrak{B}} \to 0} \left(\frac{f_{\mathrm{ext}}^{\mathfrak{A}}(\omega) + f_{\mathrm{ext}}^{\mathfrak{B}}(\omega)}{\langle x(\omega) \rangle} \right)^{-1} \overset{(6.68)}{=} \lim_{f_{\mathrm{ext}} \to 0} \frac{\langle x(\omega) \rangle}{f_{\mathrm{ext}}(\omega)} \equiv J_1(\omega), \end{aligned} \tag{6.70}$$

where the definitions of the linear force response functions (Eq. 6.60), the coupling constraints (Eq. 6.67), and the additivity of the forces (Eq. 6.68) have been used as indicated by the equation numbers above the equalities. The approximation step in Eq. 6.70 consists in identifying the averages with respect to the thermal forces of the subsystems, i.e., $\langle x(\omega) \rangle_{\mathfrak{A}}$ and $\langle x(\omega) \rangle_{\mathfrak{B}}$, with the thermal average in the coupled system $\langle x(\omega) \rangle$. To better understand the consequences of this approximation, we expand both sides of Eq. 6.70 in powers of the thermal noise strength employing Eq. 6.25 for the thermal linear response functions $J_1^{\mathfrak{A}}$ and $J_1^{\mathfrak{B}}$ of the subsystems as well as for the thermal linear response J_1 of the composite system. For the DCT estimate on the left side of Eq. 6.70, we obtain

$$\begin{aligned} J_1^{\mathrm{DCT}}(\omega) =& \frac{j_1^{\mathfrak{A}}(\omega) j_1^{\mathfrak{B}}(\omega)}{j_1^{\mathfrak{A}}(\omega) + j_1^{\mathfrak{B}}(\omega)} + \frac{k_{\mathrm{B}} T}{2\pi} \frac{1}{\left(j_1^{\mathfrak{A}}(\omega) + j_1^{\mathfrak{B}}(\omega) \right)^2} \times \\ & \int \mathrm{d}\omega' \left(j_1^{\mathfrak{A}}(\omega)^2 j_3^{\mathfrak{B}}(\omega, \omega', -\omega') \zeta'_{\mathfrak{B}}(\omega') + j_1^{\mathfrak{B}}(\omega)^2 j_3^{\mathfrak{A}}(\omega, \omega', -\omega') \zeta'_{\mathfrak{A}}(\omega') \right) + \mathcal{O}\left((k_{\mathrm{B}} T)^2 \right), \end{aligned} \tag{6.71}$$

while the expansion of the right side of Eq. 6.70 yields

$$J_1(\omega) = j_1(\omega) + \frac{k_{\mathrm{B}} T}{2\pi} \int \mathrm{d}\omega' \, j_3(\omega, \omega', -\omega') \left(\zeta'_{\mathfrak{A}}(\omega') + \zeta'_{\mathfrak{B}}(\omega') \right) + \mathcal{O}\left((k_{\mathrm{B}} T)^2 \right), \tag{6.72}$$

where

$$j_1(\omega) = \frac{1}{g_1(\omega)} = \frac{1}{g_1^{\mathfrak{A}}(\omega) + g_1^{\mathfrak{B}}(\omega)} = \frac{1}{1/j_1^{\mathfrak{A}}(\omega) + 1/j_1^{\mathfrak{B}}(\omega)} = \frac{j_1^{\mathfrak{A}}(\omega) j_1^{\mathfrak{B}}(\omega)}{j_1^{\mathfrak{A}}(\omega) + j_1^{\mathfrak{B}}(\omega)}, \tag{6.73}$$

according to the Eqs. 6.6 and 6.69. Similarly, the function j_3 in Eq. 6.72 results from the Eqs. 6.6-6.8 and the coupling constraints (Eq. 6.69), more specifically

$$\begin{aligned} j_3(\omega,\omega',-\omega') =& \frac{1}{(g_1^{\mathfrak{A}}(\omega)+g_1^{\mathfrak{B}}(\omega))^2\left|g_1^{\mathfrak{A}}(\omega')+g_1^{\mathfrak{B}}(\omega')\right|^2}\Bigg(- g_3^{\mathfrak{A}}(\omega,\omega',-\omega') - g_3^{\mathfrak{B}}(\omega,\omega',-\omega') \\ &+ \frac{(g_2^{\mathfrak{A}}(\omega,-\omega')+g_2^{\mathfrak{B}}(\omega,-\omega'))(g_2^{\mathfrak{A}}(\omega',\omega-\omega')+g_2^{\mathfrak{B}}(\omega',\omega-\omega'))}{g_1^{\mathfrak{A}}(\omega-\omega')+g_1^{\mathfrak{B}}(\omega-\omega')} \\ &+ \frac{(g_2^{\mathfrak{A}}(\omega,\omega')+g_2^{\mathfrak{B}}(\omega,\omega'))(g_2^{\mathfrak{A}}(\omega+\omega',-\omega')+g_2^{\mathfrak{B}}(\omega+\omega',-\omega'))}{g_1^{\mathfrak{A}}(\omega+\omega')+g_1^{\mathfrak{B}}(\omega+\omega')} \\ &+ \frac{(g_2^{\mathfrak{A}}(\omega,0)+g_2^{\mathfrak{B}}(\omega,0))(g_2^{\mathfrak{A}}(\omega',-\omega')+g_2^{\mathfrak{B}}(\omega',-\omega'))}{g_1^{\mathfrak{A}}(0)+g_1^{\mathfrak{B}}(0)}\Bigg). \end{aligned} \tag{6.74}$$

Obviously, the first terms in the Eqs. 6.71 and 6.72 do agree, while already the terms $\propto k_\mathrm{B}T$ in general deviate from each other. The DCT prediction thus represents a zero-order approximant to the actual linear force response of the coupled system.

The deviations become most apparent in the simple case, in which two subsystems of the same type are coupled, i.e., for $\mathfrak{B}=\mathfrak{A}$: The DCT prediction (Eq. 6.71) then reduces to

$$J_1^{\mathrm{DCT}}(\omega) = \frac{1}{2}J_1^{\mathfrak{A}}(\omega) = \frac{1}{2}j_1^{\mathfrak{A}}(\omega) + \frac{k_\mathrm{B}T}{4\pi}\int \mathrm{d}\omega'\; j_3^{\mathfrak{A}}(\omega,\omega',-\omega')\zeta'_{\mathfrak{A}}(\omega') + \mathcal{O}\left((k_\mathrm{B}T)^2\right). \tag{6.75}$$

while the exact linear response of the system (Eq. 6.72) is

$$J_1(\omega) = \frac{1}{2}j_1^{\mathfrak{A}}(\omega) + \frac{k_\mathrm{B}T}{8\pi}\int \mathrm{d}\omega'\; j_3^{\mathfrak{A}}(\omega,\omega',-\omega')\zeta'_{\mathfrak{A}}(\omega') + \mathcal{O}\left((k_\mathrm{B}T)^2\right), \tag{6.76}$$

since $g_i = 2g_i^{\mathfrak{A}}$ (Eq. 6.69) and thus $j_i = j_i^{\mathfrak{A}}/2^i$ according to the Eqs. 6.6-6.8. In this simple example, the DCT thus overestimates the J_1-contribution, which scales linearly with $k_\mathrm{B}T$, by a factor of two; inspection of the next order terms in the expansion reveals that contributions to J_1 which scale $\propto (k_\mathrm{B}T)^n$ are overestimated by a factor of 2^n in the DCT prediction.

The above results explain why the DCT, which enforces the equivalence of the expectation values $\langle x_{\mathfrak{A}}\rangle_{\mathfrak{A}} = \langle x_{\mathfrak{B}}\rangle_{\mathfrak{B}}$ only and not of the instantaneous positions, fails to capture even the linear dynamics of composite systems involving a highly nonlinear subsystem [265]. Nevertheless, the DCT provides a good approximation [ix], when the temperature-independent term is "dominant" in the expansion (Eq. 6.25). As can directly be deduced from the Eqs. 6.71 and 6.72, the DCT in particular is exact in the following two cases: (i) for arbitrary systems in the limit $k_\mathrm{B}T \to 0$, where the dynamics becomes deterministic and the linear force response is governed by $j_1^{\mathfrak{A}}$ and $j_1^{\mathfrak{B}}$ only, and (ii) for strictly linear systems at arbitrary temperature T, i.e., for systems where $g_1^{\mathfrak{A}}$ and $g_1^{\mathfrak{B}}$ are the only non-vanishing g_i-functions.

First-order correction to the dynamic convolution theory

Based on the relations derived in Sec. 6.1, systematic corrections to the DCT estimate J_1^{DCT} can be calculated. For example, if in addition to the linear force response functions the quadratic and cubic response functions of the subsystems, i.e., $J_2^{\mathfrak{A}}$, $J_2^{\mathfrak{B}}$, $J_3^{\mathfrak{A}}$, and $J_3^{\mathfrak{B}}$, are known, a first-order

correction $\Delta J_1^{\mathrm{DCT}}$ can be calculated so that the corrected DCT prediction and the exact linear response function of the coupled system agree up to $\mathcal{O}\left((k_{\mathrm{B}}T)^2\right)$, i.e.,

$$J_1^{\mathrm{DCT}}(\omega) + \Delta J_1^{\mathrm{DCT}}(\omega) = J_1(\omega) + \mathcal{O}\left((k_{\mathrm{B}}T)^2\right). \tag{6.77}$$

The correction term results from the difference of the terms of $\mathcal{O}(k_{\mathrm{B}}T)$ in the Eqs. 6.72 and 6.71, using the thermal response functions of the subsystems as zero-order approximants for the athermal ones. More specifically,

$$\begin{aligned}\Delta J_1^{\mathrm{DCT}}(\omega) = \frac{k_{\mathrm{B}}T}{2\pi} P \int \mathrm{d}\omega' \, \frac{1}{\mathrm{i}\,\omega'} \Bigg(& \tilde{j}_3(\omega,\omega',-\omega') \left(\frac{J_1^{\mathfrak{A}}(\omega')}{\left|J_1^{\mathfrak{A}}(\omega')\right|^2} + \frac{J_1^{\mathfrak{B}}(\omega')}{\left|J_1^{\mathfrak{B}}(\omega')\right|^2} \right) \\ & - \frac{J_1^{\mathfrak{A}}(\omega)^2 J_3^{\mathfrak{B}}(\omega,\omega',-\omega')}{\left(J_1^{\mathfrak{A}}(\omega) + J_1^{\mathfrak{B}}(\omega)\right)^2} \frac{J_1^{\mathfrak{B}}(\omega')}{\left|J_1^{\mathfrak{B}}(\omega')\right|^2} - \frac{J_1^{\mathfrak{B}}(\omega)^2 J_3^{\mathfrak{A}}(\omega,\omega',-\omega')}{\left(J_1^{\mathfrak{A}}(\omega) + J_1^{\mathfrak{B}}(\omega)\right)^2} \frac{J_1^{\mathfrak{A}}(\omega')}{\left|J_1^{\mathfrak{A}}(\omega')\right|^2} \Bigg),\end{aligned} \tag{6.78}$$

where P denotes the Cauchy principal value of the integral and the zero-order approximants for the linear friction coefficients arise from the Eqs. 6.6, 6.10 and 6.25

$$\tilde{\zeta}'_{\mathfrak{a}}(\omega) \equiv \frac{\mathrm{Im}\left[J_1^{\mathfrak{a}}(\omega)\right]}{\omega\left|J_1^{\mathfrak{a}}(\omega)\right|^2} = \frac{\mathrm{Im}\left[j_1^{\mathfrak{a}}(\omega)\right]}{\omega\left|j_1^{\mathfrak{a}}(\omega)\right|^2} + \mathcal{O}(k_{\mathrm{B}}T) = -\frac{1}{\omega}\mathrm{Im}\left[g_1^{\mathfrak{a}}(\omega)\right] + \mathcal{O}(k_{\mathrm{B}}T) = \zeta'_{\mathfrak{a}}(\omega) + \mathcal{O}(k_{\mathrm{B}}T), \tag{6.79}$$

as well as symmetry arguments have been used to simplify the integral in Eq. 6.78. Analogous to the recursive relations in the Eqs. 6.6-6.8, the zero-order approximant for the cubic athermal response function of the coupled system $\tilde{j}_3$ is calculated from

$$\begin{aligned}\tilde{j}_3(\omega,\omega',\omega'') = & -\frac{\tilde{j}_1(\omega+\omega'+\omega'')\tilde{g}_3(\omega,\omega',\omega'') + \tilde{j}_2(\omega,\omega'+\omega'')\tilde{g}_1(\omega)\tilde{g}_2(\omega',\omega'')}{\tilde{g}_1(\omega)\tilde{g}_1(\omega')\tilde{g}_1(\omega'')} \\ & - \frac{\tilde{j}_2(\omega',\omega+\omega'')\tilde{g}_1(\omega')\tilde{g}_2(\omega,\omega'') + \tilde{j}_2(\omega'',\omega+\omega')\tilde{g}_1(\omega'')\tilde{g}_2(\omega,\omega')}{\tilde{g}_1(\omega)\tilde{g}_1(\omega')\tilde{g}_1(\omega'')},\end{aligned} \tag{6.80}$$

$$\tilde{j}_2(\omega,\omega') = -\frac{\tilde{g}_2(\omega,\omega')\tilde{j}_1(\omega+\omega')}{\tilde{g}_1(\omega)\tilde{g}_1(\omega')}, \tag{6.81}$$

$$\tilde{j}_1(\omega) = \frac{1}{\tilde{g}_1(\omega)}, \tag{6.82}$$

where the zero-order approximants for the g_i-functions of the coupled system are given by

$$\begin{aligned}&\tilde{g}_1(\omega) = \tilde{g}_1^{\mathfrak{A}}(\omega) + \tilde{g}_1^{\mathfrak{B}}(\omega), \qquad \tilde{g}_2(\omega,\omega') = \tilde{g}_2^{\mathfrak{A}}(\omega,\omega') + \tilde{g}_2^{\mathfrak{B}}(\omega,\omega'), \\ &\tilde{g}_3(\omega,\omega',\omega'') = \tilde{g}_3^{\mathfrak{A}}(\omega,\omega',\omega'') + \tilde{g}_3^{\mathfrak{B}}(\omega,\omega',\omega'').\end{aligned} \tag{6.83}$$

The zero-order approximants of the subsystems are finally expressed in terms of the individual linear, quadratic, and cubic thermal response functions based on the Eqs. 6.25-6.27 and the relations from the Eqs. F.1-F.3 in Appendix F

$$\tilde{g}_1^{\mathfrak{a}}(\omega) = \frac{1}{J_1^{\mathfrak{a}}(\omega)}, \qquad \mathfrak{a} \in \{\mathfrak{A},\mathfrak{B}\}, \tag{6.84}$$

$$\tilde{g}_2^{\mathfrak{a}}(\omega,\omega') = -\frac{J_2^{\mathfrak{a}}(\omega,\omega')\tilde{g}_1^{\mathfrak{a}}(\omega+\omega')}{J_1^{\mathfrak{a}}(\omega)J_1^{\mathfrak{a}}(\omega')}, \tag{6.85}$$

$$\begin{aligned}\tilde{g}_3^{\mathfrak{a}}(\omega,\omega',\omega'') = &- \frac{\tilde{g}_1^{\mathfrak{a}}(\omega+\omega'+\omega'')J_3^{\mathfrak{a}}(\omega,\omega',\omega'') + \tilde{g}_2^{\mathfrak{a}}(\omega,\omega'+\omega'')J_1^{\mathfrak{a}}(\omega)J_2^{\mathfrak{a}}(\omega',\omega'')}{J_1^{\mathfrak{a}}(\omega)J_1^{\mathfrak{a}}(\omega')J_1^{\mathfrak{a}}(\omega'')} \\ &- \frac{\tilde{g}_2^{\mathfrak{a}}(\omega',\omega+\omega'')J_1^{\mathfrak{a}}(\omega')J_2^{\mathfrak{a}}(\omega,\omega'') + \tilde{g}_2^{\mathfrak{a}}(\omega'',\omega+\omega')J_1^{\mathfrak{a}}(\omega'')J_2^{\mathfrak{a}}(\omega,\omega')}{J_1^{\mathfrak{a}}(\omega)J_1^{\mathfrak{a}}(\omega')J_1^{\mathfrak{a}}(\omega'')}.\end{aligned} \tag{6.86}$$

Summarizing, the knowledge of the linear, quadratic, and cubic thermal response functions of the two subsystems $\mathfrak{A}$ and $\mathfrak{B}$ allows via Eqs. 6.84-6.86 to approximate the g_i-functions of the subsystems and of the coupled system (Eq. 6.83). The inverse procedure (Eqs. 6.80-6.82) then yields $\tilde{j}_3$ which approximates the athermal cubic response function j_3 of the coupled system and which is used together with Eq. 6.79 in the integral of Eq. 6.78 to calculate the first-order correction to the DCT prediction.

Higher order correction terms for the DCT can systematically be derived based on the relations from Sec. 6.1 in a similar manner as exemplified above.

6.5 Conclusions

In conclusion, we have derived perturbation expansions for equilibrium correlation functions (Eqs. 6.20 and 6.22) and force response functions (Eqs. 6.25-6.27) to account for nonlinearities in the equations of motion of thermally fluctuating systems. The non-trivial dependence of these quantities on the thermal noise strength has been illustrated using overdamped diffusion in three different potential landscapes as simple model systems and the accuracy of the analytical predictions has been tested by comparison to results from numerical simulations.

We have explicitly shown that discriminating between linear and nonlinear dynamic models is an intrinsically difficult task based on two-point correlation functions only. However, evaluating higher order correlation and cumulant functions, e.g., the spectral kurtosis, or probing the nonlinear response of the system are valuable methods to detect nonlinearities. In addition, nonlinearities leave specific fingerprints in the dynamic quantities, which become apparent when the temperature of the system is varied. The spectral analysis approach taken in this chapter is particularly relevant, when the equilibrium PDF of the signal, from which the nonlinearities are trivially read off, is not directly accessible. This is for example the case, when the measured signal is (intentionally) filtered by the experimental or data acquisition equipment as seen in Chapter 5, thereby irrevocably distorting the signal's equilibrium PDF [78]. Accounting for linear filters in the spectral analysis, as done in Sec. 5.4.1, is in contrast straightforward.

Finally, we have studied the dynamics of composite systems, in particular mechanically coupled ones. We have revealed the range of validity of the linear DCT [ix] and have derived a first-order correction to account for nonlinearities in the dynamics of the subsystems.

Our approach is based on the Langevin equation and very general: It allows to readily compute the first terms in the expansion of any dynamic quantity of interest once the stochastic equation of motion has been specified. We therefore expect a variety of possible applications for the analysis of simulations and experiments of thermally fluctuating systems. The specific monostable systems (Secs. 6.2.2 and 6.2.3) may serve to detect nonlinearities of atomic force microscopy and optical tweezer experiments. This is particularly important, because the *small* equilibrium fluctuations of the cantilevers/beads in these instruments (cf. Chapter 5) are used for calibration purposes [214, 266], while actual experimental force measurements often involve *large* deflections and therefore are sensibly affected by nonlinear contributions in the potential. The analytical formulas for the PSDs (Eqs. 6.43 and 6.50) thus constitute a valuable starting point to identify and quantify these nonlinearities and to improve the accuracy of microscopic force measurements.

CHAPTER 7

DYNAMICS OF SEMIFLEXIBLE POLYMERS AT INTERFACES

Bibliographic information: Parts of this chapter and of Appendix D have previously been published. Reprinted with permission from Ref. [vi]. Copyright 2011, American Institute of Physics.

Semiflexible polymers are of interest in various fields of science and technology due to their abundance in biological and synthetic systems. Examples of biological relevance include double-stranded DNA and cytoskeletal filaments such as actin and microtubules. The theoretical interest in semiflexible polymer dynamics [56, 57, 267–271] has been spurred since the manipulation and observation of single polymer filaments has become feasible experimentally. A variety of refined experimental techniques allow to precisely follow and analyze conformations and dynamics of single polymers in all kinds of different environments, e.g., under confinement in nanotubes and nanoslits [272, 273]. To give explicit examples, the internal relaxation dynamics of f-actin have been resolved by fluorescence videomicroscopy [79], and the end-monomer dynamics of dsDNA have been investigated by fluorescence correlation spectroscopy [274, 275]. Although polymers are often confined due to practical reasons in such experiments, hydrodynamic interactions (HI) are—if considered at all—generally included in existing theories [276] assuming a boundless fluid. Though the importance of HI has been demonstrated in a range of simulation studies on force- or shear-driven filaments [267–269, 271, 277, 278], the question how the internal equilibrium dynamics of a polymer change, when nearby surfaces alter the HI between different parts of the polymer, has received little attention and the influence of surface-induced hydrodynamic screening on semiflexible polymer dynamics has thus remained elusive.

Within this chapter, we focus on a single semiflexible polymer, which is confined to a layer at fixed separation from a planar hydrodynamic boundary at which a no-slip boundary condition is enforced; the strength of the HI thus varies depending on the distance to the wall. Polymer dynamics are studied by means of Brownian hydrodynamics simulations and compared with a hydrodynamic mean-field theory (MFT). Our study demonstrates the complexity of semiflexible polymer dynamics resulting from a subtle interplay of chain connectivity, internal bending and stretching stiffness as well as (screened) HI. We find the importance of the HI to vary among the different dynamic observables considered: while the mean square displacements (MSDs) of vectorial quantities such as the end-monomer position or the end-to-end vector sensitively de-

pend on the HI strength, this dependence is much less pronounced for the MSDs of a scalar quantity such as the end-to-end distance. In the scalar case, on the other hand, a pronounced dependence of dynamic scaling exponents on the ratio of the bending and stretching stiffnesses and on the ratio of contour and persistence lengths appears in the data, in qualitative agreement with our reanalysis of experimental data for the internal relaxation dynamics of f-actin [79]. Interestingly, the crossover from Zimm-type behavior in bulk to Rouse-type behavior in the MSDs of vectorial quantities at the hydrodynamic boundary is rather weak and the free-draining limit is not completely reached even when the polymer distance from the wall is on the order of the monomer size. An interesting question in the future thus concerns the relevance of hydrodynamics for the dynamics of biopolymers *in vivo* with omnipresent confining surfaces and the crowded environment of cellular systems [279].

The chapter is organized as follows: The essentials of low Reynolds-number hydrodynamics near a planar surface, which are used in both simulations and theory, are shortly revisited in Sec. 7.1. The Brownian hydrodynamics scheme is described in Sec. 7.2.1; for the theoretical description of semiflexible polymer dynamics, a hydrodynamic mean-field approach [56] is adapted to the present context, details of which are found in Sec. 7.2.2. The results of hydrodynamic simulations and of the theory are presented and discussed in Sec. 7.3, while the main implications of our findings are exposed in Sec. 7.4. The entries of the hydrodynamic interaction tensor used for simulation purposes and within the analytical theory are found in Appendix D.3.

7.1 Hydrodynamics near a Planar No-Slip Boundary

We assume the planar hydrodynamic boundary being placed in the xy-plane at $z = 0$ of the coordinate system. The no-slip boundary condition at the wall implies that all components of the solvent flow field vanish at the boundary. The quasi-stationary incompressible Stokes equation (cf. Eq. 5.11)

$$\nabla p(\boldsymbol{r}) - \eta_0 \nabla^2 \boldsymbol{u}(\boldsymbol{r}) = \boldsymbol{f}(\boldsymbol{r}), \qquad \nabla \cdot \boldsymbol{u}(\boldsymbol{r}) = 0, \tag{7.1}$$

relating pressure p, shear viscosity η_0, fluid velocity $\boldsymbol{u}$ and an external force density $\boldsymbol{f}$, can be solved using a standard Green's function technique [280]. The solution satisfying the no-slip condition at $z = 0$, named the Blake tensor $\overleftrightarrow{\boldsymbol{\mu}}^{\mathrm{B}}$, is derived using the method of images [281]

$$\overleftrightarrow{\boldsymbol{\mu}}^{\mathrm{B}}(\boldsymbol{r}, \boldsymbol{r}') = \overleftrightarrow{\boldsymbol{\mu}}^{\mathrm{O}}(\boldsymbol{R}) - \overleftrightarrow{\boldsymbol{\mu}}^{\mathrm{O}}(\overline{\boldsymbol{R}}) + \overleftrightarrow{\boldsymbol{\mu}}^{\mathrm{D}}(\overline{\boldsymbol{R}}) - \overleftrightarrow{\boldsymbol{\mu}}^{\mathrm{SD}}(\overline{\boldsymbol{R}}), \tag{7.2}$$

where $\boldsymbol{r}' = (x', y', z')^{\mathrm{T}}$ is the position of the Stokeslet, the image Stokeslet has coordinates $\overline{\boldsymbol{r}'} = (x', y', -z')^{\mathrm{T}}$, and where we have defined the relative vectors $\boldsymbol{R} \equiv \boldsymbol{r} - \boldsymbol{r}'$ and $\overline{\boldsymbol{R}} \equiv \boldsymbol{r} - \overline{\boldsymbol{r}'}$. The Oseen tensor $\overleftrightarrow{\boldsymbol{\mu}}^{\mathrm{O}}$, the Stokes doublet $\overleftrightarrow{\boldsymbol{\mu}}^{\mathrm{D}}$, and the source doublet $\overleftrightarrow{\boldsymbol{\mu}}^{\mathrm{SD}}$ are 3×3-tensors with entries

$$\mu^{\mathrm{O}}_{\alpha\beta}(\boldsymbol{R}) = \frac{1}{8\pi\eta_0 R}\left(\delta_{\alpha\beta} + \frac{R_\alpha R_\beta}{R^2}\right), \qquad \alpha, \beta \in \{x, y, z\}, \tag{7.3}$$

$$\mu^{\mathrm{D}}_{\alpha\beta}(\overline{\boldsymbol{R}}) = \frac{2z'^2(1 - 2\delta_{\beta z})}{8\pi\eta_0}\left(\frac{\delta_{\alpha\beta}}{\overline{R}^3} - \frac{3\overline{R}_\alpha \overline{R}_\beta}{\overline{R}^5}\right), \qquad \alpha, \beta \in \{x, y, z\}, \tag{7.4}$$

$$\mu^{\mathrm{SD}}_{\alpha\beta}(\overline{\boldsymbol{R}}) = \frac{2z'(1-2\delta_{\beta z})}{8\pi\eta_0}\left(\frac{\delta_{\alpha\beta}\overline{R}_z}{\overline{R}^3} - \frac{\delta_{\alpha z}\overline{R}_\beta}{\overline{R}^3} + \frac{\delta_{\beta z}\overline{R}_\alpha}{\overline{R}^3} - \frac{3\overline{R}_\alpha\overline{R}_\beta\overline{R}_z}{\overline{R}^5}\right), \qquad \alpha,\beta\in\{x,y,z\}, \tag{7.5}$$

where $R \equiv |\boldsymbol{R}|$ and $\overline{R} \equiv |\overline{\boldsymbol{R}}|$. The hydrodynamic entrainment effect of the motion of a finite sized sphere of radius a located at $\boldsymbol{r}$ on another equal-sized sphere at $\boldsymbol{r}'$ is approximated by a multipole expansion [282, 283] to second order in the bead radius a

$$\overleftrightarrow{\boldsymbol{\mu}}^{\mathrm{RPB}}(\boldsymbol{r},\boldsymbol{r}') \equiv \left(1 + \frac{a^2}{6}\nabla^2_{\boldsymbol{r}} + \frac{a^2}{6}\nabla^2_{\boldsymbol{r}'}\right)\overleftrightarrow{\boldsymbol{\mu}}^{\mathrm{B}}(\boldsymbol{r},\boldsymbol{r}'), \tag{7.6}$$

which in analogy to the procedure in an unbounded fluid is called the Rotne-Prager [238] (RP) level of the Blake tensor. The approximate expression for the HI between finite sized spheres in Eq. 7.6 is used in both simulations and theory as detailed in Sec. 7.2, the explicit entries of the tensor are found in Appendix D.3.

7.1.1 Self-mobilities near a planar no-slip interface

The no-slip boundary at the wall not only alters HI between different particles, but also affects the particles' self-mobilities. Approximate expressions [282, 283] for the dependence of the self-mobility of a sphere on the separation z to the wall are obtained by considering the limit

$$\overleftrightarrow{\boldsymbol{\mu}}^{\mathrm{RPB}}_{\mathrm{self}}(z) \equiv \lim_{\boldsymbol{r}\to\boldsymbol{r}'}\overleftrightarrow{\tilde{\boldsymbol{\mu}}}^{\mathrm{RPB}}(\boldsymbol{r},\boldsymbol{r}') = \begin{pmatrix} \mu^{\mathrm{RPB}}_{\parallel}(z) & 0 & 0 \\ 0 & \mu^{\mathrm{RPB}}_{\parallel}(z) & 0 \\ 0 & 0 & \mu^{\mathrm{RPB}}_{\perp}(z) \end{pmatrix}, \tag{7.7}$$

where $\overleftrightarrow{\tilde{\boldsymbol{\mu}}}^{\mathrm{RPB}}$ is the RP level of the tensor $\overleftrightarrow{\tilde{\boldsymbol{\mu}}}^{\mathrm{B}}$, in which—compared to the Blake tensor $\overleftrightarrow{\boldsymbol{\mu}}^{\mathrm{B}}$ in Eq. 7.2—the first Oseen contribution $\overleftrightarrow{\boldsymbol{\mu}}^{\mathrm{O}}(\boldsymbol{r},\boldsymbol{r}')$, which has a singularity at $\boldsymbol{r}=\boldsymbol{r}'$, is replaced by the diagonal 3×3 matrix $\mu_0\overleftrightarrow{\mathbf{1}}$, $\mu_0 \equiv 1/(6\pi\eta_0 a)$ being the bare Stokes self-mobility of a sphere of radius a in a solvent of viscosity η_0 [16]. One obtains renormalized self-mobilities parallel ($\parallel$) and perpendicular ($\perp$) to the boundary, which depend on the distance z from the wall

$$\mu^{\mathrm{RPB}}_{\parallel}(z) = \mu_0\left(1 - \frac{9a}{16z} + \frac{1}{8}\left(\frac{a}{z}\right)^3 + \mathcal{O}\left(\left(\frac{a}{z}\right)^4\right)\right), \tag{7.8}$$

$$\mu^{\mathrm{RPB}}_{\perp}(z) = \mu_0\left(1 - \frac{9a}{8z} + \frac{1}{2}\left(\frac{a}{z}\right)^3 + \mathcal{O}\left(\left(\frac{a}{z}\right)^4\right)\right). \tag{7.9}$$

In Fig. 7.1, the expressions in the Eqs. 7.8 and 7.9 (dashed lines), which only approximately fulfill the no-slip boundary condition on the bead's surface, are compared to more elaborate and experimentally tested results [284], shown as solid lines, which correctly reproduce the short-range lubrication effects: The expression for the self-mobility parallel to the wall obtained by Perkins and Jones [285] (PJ) and Stimson's and Jeffery's (SJ) exact result for the self-mobility perpendicular to the surface [103, 286], which have already been used in Sec. 3.4.1, are reproduced in Appendix D.2.

In Fig. 7.1 differences between the exact and the approximate self-mobilities are only noticeable for distances $z/a \lesssim 2$. For the sake of consistency of self-mobilities and inter-bead HI described by the RP level of the Blake tensor (Eq. 7.6), we resort to the approximate expressions

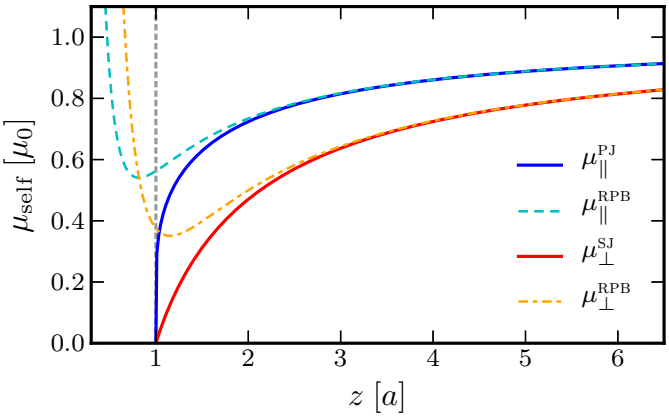

Figure 7.1:
Parallel ($\parallel$) and perpendicular ($\perp$) self-mobilities of a sphere of radius a located at a distance z from a planar no-slip wall ($z = 0$). The approximations of the Eqs. 7.8 and 7.9 (*dashed lines*) are compared to the PJ result (Eq. D.6, *solid blue line*), and to the exact SJ expression for the perpendicular mobility (Eq. D.7, *solid red line*). Self-mobilities are given in units of the bare self-mobility $\mu_0 = 1/(6\pi\eta_0 a)$ in a fluid of shear viscosity η_0. The region $z < a$ is inaccessible due to excluded-volume effects.

in the Eqs. 7.8 and 7.9 even for $z/a < 2$. Since the continuum description of hydrodynamics is expected to break down in any case in the limit $z/a \to 1$, since single molecules have a non-vanishing mobility even when they are in direct contact with a surface, we do not attribute any experimental significance to the deviations between our approximate and the exact expressions in Fig. 7.1.

7.1.2 Screening of hydrodynamic interactions near a planar no-slip interface

HI are long-ranged, decaying as $1/R$ in an unbounded fluid. The term hydrodynamic screening is employed to describe the weakening of these HI, for example in the presence of nearby surfaces. Within the following discussion we restrict ourselves to the scenario schematically depicted in Fig. 7.2, where two equal-sized spheres of radius a are found at a distance z from the no-slip interface and at a separation R from each other along the x-axis of the coordinate frame. As illustrated in Fig. 7.2, the hydrodynamic flow-field created by a force $\boldsymbol{f}$ acting on one of the spheres also causes a motion with velocity $\boldsymbol{v} = \overleftrightarrow{\boldsymbol{\mu}}^{\mathrm{RPB}} \cdot \boldsymbol{f}$ of the other one.

In Fig. 7.3a-c, the strengths of the HI at different distances from the wall are compared: The diagonal entries of the RP level of the Blake tensor $\overleftrightarrow{\boldsymbol{\mu}}^{\mathrm{RPB}}$ (Eq. 7.6 with specific entries in Appendix D.3) are shown as a function of the inter-particle distance R. For HI along the connection vector (Fig. 7.3a), HI remain long-ranged decaying as $1/R$ for $R \ll z$, but cross over to a $1/R^3$-scaling for $R \gg z$. The strength of the HI perpendicular to this axis decays faster ($\propto 1/R^5$) as seen in Fig. 7.3b-c. Note also the sign change in μ_{zz}^{RPB} in Fig. 7.3c which turns from positive to negative for $R/z \approx 0.9$. To characterize the strength of the HI for a certain relative configuration of two spheres, we define the scalar quantity

$$H(R,z) \equiv \sqrt{\frac{1}{3}\sum_{\alpha,\beta}\mu_{\alpha\beta}^{\mathrm{RPB}\,2}}, \qquad \langle \boldsymbol{v}^2 \rangle_f = \langle \boldsymbol{f}^{\mathrm{T}} \cdot \overleftrightarrow{\boldsymbol{\mu}}^{\mathrm{RPB}\,\mathrm{T}} \cdot \overleftrightarrow{\boldsymbol{\mu}}^{\mathrm{RPB}} \cdot \boldsymbol{f} \rangle_f \equiv H^2(R,z)\ |\boldsymbol{f}|^2\,, \tag{7.10}$$

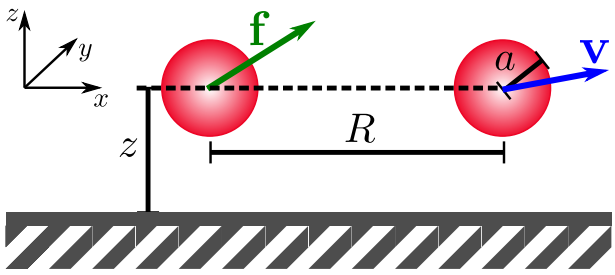

Figure 7.2:
Schematic illustration of the bead configuration for which the diagonal elements of the hydrodynamic interaction tensor (Eq. 7.6) relating the force $\boldsymbol{f}$ acting on one of the beads and the velocity $\boldsymbol{v}$ of the other one are plotted in Fig. 7.3: both spheres are located at the same height z above the no-slip interface, the vector of length R connecting the sphere centers points along the x-direction.

which relates the average root mean square velocity of one sphere, $\sqrt{\langle v^2 \rangle_f}$, to the magnitude $|\boldsymbol{f}|$ of the force acting on the other one, and where $\langle \ldots \rangle_f$ denotes an average over the possible directions of the force. Dynamic scaling regimes in the motion of semiflexible polymers result from a subtle interplay of HI and monomer mobility, which both decrease when approaching the no-slip boundary: As is visible from the Langevin Eq. 7.13 underlying the Brownian dynamics (BD) simulation method in Sec. 7.2.1 as well as from the theoretical dynamic description in Sec. 7.2.2, a simultaneous drop of the HI *and* self-mobilities by the same factor is equivalent to a rescaling of time and thus does not affect dynamic scaling exponents. In turn, in order to see non-trivial dynamic effects embodied in changes of dynamic scaling exponents, the ratio between self- and cross-mobility must change. The unitless ratio

$$\tilde{H}(R,z) \equiv \frac{H(R,z)}{\sqrt{\frac{1}{3}\left(2\left(\mu_{\parallel}^{\mathrm{RPB}}(z)\right)^2 + \left(\mu_{\perp}^{\mathrm{RPB}}(z)\right)^2\right)}} \frac{\mu_0}{H_\infty(R)}, \tag{7.11}$$

quantifies the relative importance of hydrodynamics at a finite distance z from a no-slip boundary compared to an unbounded fluid, where

$$H_\infty(R) \equiv \lim_{z\to\infty} H(R,z) = \frac{\mu_0 a}{R}\sqrt{1+\frac{1}{8}\left(1-\frac{2a^2}{R^2}\right)^2}, \tag{7.12}$$

corresponds to the strength of the HI based on the RP-tensor [238] (Eq. D.9 in Appendix D.3). For the configuration shown in Fig. 7.2, the function $\tilde{H}$ in Eq. 7.11 is plotted for different values of the separation z in Fig. 7.3d. In the limit of large separations from the wall, $z/a \to \infty$, full HI described by the RP tensor are recovered ($\tilde{H} = 1$), while the free-draining limit corresponds to $\tilde{H} = 0$. As is clearly seen in Fig. 7.3d, the influence of the HI is continuously reduced with increasing inter-bead separation R and decreasing distance to the wall compared to the case of an unbounded fluid, though for small inter-bead separations it remains sizeable even for $z/a = 2$. The consequences arising from this complex behavior of the HI and self-mobilities for the dynamics of semiflexible polymers are discussed in Sec. 7.3.

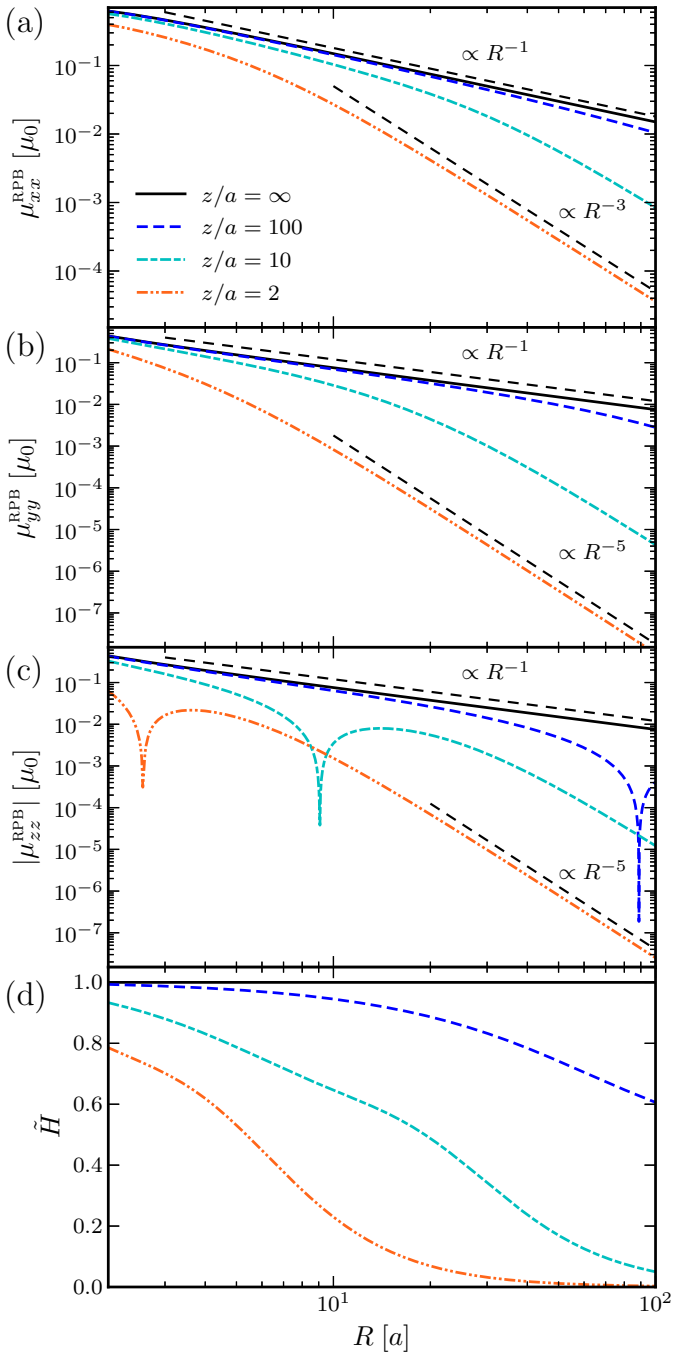

Figure 7.3:
Screened HI between spherical particles of radius a at a relative distance R and at equal height z above a no-slip interface as shown in Fig. 7.2. a), b), c) Diagonal entries of the RPB tensor (Eqs. D.8 and D.10-D.12 in Appendix D.3) for different distances z from the wall (*colored lines*); in the limit $z/a \to \infty$ the usual RP tensor (Eq. D.9 in Appendix D.3) is recovered (*solid black line*). In (c), the tensor element is positive for $R/z \lesssim 0.9$ and negative for $R/z \gtrsim 0.9$. d) Relative importance of HI compared to an unbounded fluid in terms of the unitless function $\tilde{H}$ (Eq. 7.11).

7.2 Methods

7.2.1 Brownian hydrodynamics simulations

We simulate the dynamics of a semiflexible polymer in solution adopting a standard hydrodynamic BD scheme [239], in which the polymer is modeled as a chain of M beads of radius a. According to Itô [29], the overdamped Langevin equation governing the time evolution of the position $\boldsymbol{r}_i = (x_i, y_i, z_i)^{\mathrm{T}}$ of bead i is given by

$$\frac{d\boldsymbol{r}_i(t)}{dt} = \sum_{j=1}^{M} \overleftrightarrow{\boldsymbol{\mu}}_{ij} \cdot \left(-\nabla_{\boldsymbol{r}_j} U(\boldsymbol{r}_1, \ldots, \boldsymbol{r}_M)\right) + k_{\mathrm{B}}T \left[\frac{\mathrm{d}\mu_{\perp}^{\mathrm{RPB}}(z)}{\mathrm{d}z}\right]_{z=z_i} \hat{\boldsymbol{e}}_z + \boldsymbol{v}_i^{\mathrm{st}}(t), \tag{7.13}$$

where $\hat{\boldsymbol{e}}_z$ denotes the unit vector in the z-direction. The mobility matrix $\overleftrightarrow{\boldsymbol{\mu}}$ composed of the 3×3-submatrices

$$\overleftrightarrow{\boldsymbol{\mu}}_{ij} = \delta_{ij} \overleftrightarrow{\boldsymbol{\mu}}_{\mathrm{self}}^{\mathrm{RPB}}(z_i) + (1 - \delta_{ij}) \overleftrightarrow{\boldsymbol{\mu}}^{\mathrm{RPB}}(\boldsymbol{r}_i, \boldsymbol{r}_j), \tag{7.14}$$

accounts for two effects: (i) the dependence of the self-mobility on the distance z_i of bead i from the wall (Eqs. 7.7-7.9), and (ii) the fact that a force $\boldsymbol{f}_j \equiv -\nabla_{\boldsymbol{r}_j} U$ acting on bead j creates a hydrodynamic flow-field in the fluid thereby entraining bead i (Eq. 7.6). The second term in Eq. 7.13 is due to the spatial variation of the beads' self-mobilities; it is introduced to compensate the flux caused by the position dependent random velocity contributions $\boldsymbol{v}_i^{\mathrm{st}}$ [239, 280], which are assumed to be Gaussian random vectors with hydrodynamic correlations according to the FDT

$$\langle \boldsymbol{v}_i^{\mathrm{st}}(t) \otimes \boldsymbol{v}_j^{\mathrm{st}}(t') \rangle = 2k_{\mathrm{B}}T \, \overleftrightarrow{\boldsymbol{\mu}}_{ij} \, \delta(t - t'). \tag{7.15}$$

The potential $U \equiv U_{\mathrm{WLC}} + U_{\mathrm{LJ}} + U_{\mathrm{conf}}$ determining the configuration-dependent forces felt by the beads consists of three terms

$$U_{\mathrm{WLC}} = \frac{\gamma}{4a} \sum_{i=1}^{M-1} (r_{i+1,i} - 2a)^2 + \frac{\kappa}{2a} \sum_{i=2}^{M-1} (1 - \cos\theta_i), \tag{7.16}$$

$$U_{\mathrm{LJ}} = w_{\mathrm{rep}} \sum_{i<j} \Theta(2a - r_{ij}) \left[\left(\frac{2a}{r_{ij}}\right)^{12} - 2\left(\frac{2a}{r_{ij}}\right)^{6} + 1\right], \tag{7.17}$$

$$U_{\mathrm{conf}} = \frac{g}{2} \sum_{i=1}^{M} (z_i - z_0)^2, \tag{7.18}$$

where $r_{ij} = |\boldsymbol{r}_i - \boldsymbol{r}_j|$ denotes the separation between the centers of the beads i and j, and θ_i is the angle between the bond vectors connecting beads $i-1$ and i, and beads i and $i+1$, respectively. The shifted harmonic potential between adjacent beads of usual strength $\gamma = 200\, k_{\mathrm{B}}T/a$ (cf. Sec. 7.3.2) keeps the contour length $L = (M-1)2a$ approximately fixed, a bending potential of strength κ between adjacent bonds takes care of the bending stiffness of the chain, and the pairwise truncated repulsive Lennard-Jones potential U_{LJ} of strength $w_{\mathrm{rep}} = 3\, k_{\mathrm{B}}T$ mimics excluded volume effects and prevents significant bead overlap, which otherwise would be a source of numerical instabilities. The harmonic potential U_{conf} of strength $g = 1\, k_{\mathrm{B}}T/a^2$ ensures an average distance z_0 of the polymer from the wall as illustrated in Fig. 7.4. By gradually varying the value of z_0, the influence of the hydrodynamic boundary condition at the wall on the motion of the polymer is sensitively resolved. In the limit of infinite separation from the wall

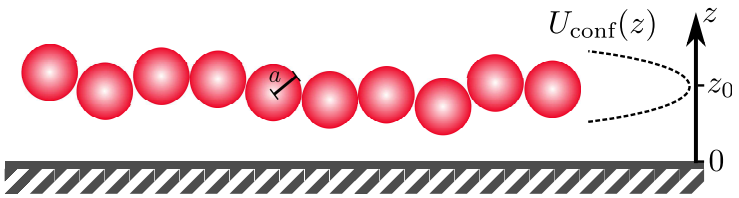

Figure 7.4:
Schematic of the simulation setup: A polymer chain consisting of M monomers of radius a is confined by the harmonic potential U_{conf} (Eq. 7.18) centered around z_0 and acting in the z-direction only.

the usual RP tensor [238] (Eq. D.9 in Appendix D.3) is recovered as hydrodynamic interaction tensor.

Eq. 7.13 is discretized and integrated numerically using a simple Euler algorithm. The time discretized form of the Langevin equation for bead i reads

$$\boldsymbol{r}_i(t+\delta t) = \boldsymbol{r}_i(t) + \left(\sum_{j=1}^{M} \overleftrightarrow{\boldsymbol{\mu}}_{ij} \cdot \boldsymbol{f}_j + k_{\mathrm{B}}T \left[\frac{\mathrm{d}\mu_{\perp}^{\mathrm{RPB}}(z)}{\mathrm{d}z} \right]_{z=z_i} \hat{\boldsymbol{e}}_z \right) \delta t + \delta \boldsymbol{r}_i^{\mathrm{st}}(t), \tag{7.19}$$

where the time step is denoted by δt, and the stochastic contributions $\delta \boldsymbol{r}_i^{\mathrm{st}}$ are Gaussian distributed random vectors with vanishing mean and correlations

$$\langle \delta \boldsymbol{r}_i^{\mathrm{st}}(t) \otimes \delta \boldsymbol{r}_j^{\mathrm{st}}(t) \rangle = 2k_{\mathrm{B}}T \, \overleftrightarrow{\boldsymbol{\mu}}_{ij} \delta t. \tag{7.20}$$

In the case of collisions with the wall, the z-component is reflected about $z = a$, while the updating scheme for the other components remains unchanged. The correlated stochastic contributions of Eq. 7.15 are obtained from uncorrelated Gaussian noise by means of a Cholesky decomposition of the hydrodynamic matrix $\overleftrightarrow{\boldsymbol{\mu}}$ (Eq. 7.14). In all the results below, lengths are measured in units of the bead radius a, energies in units of thermal energy $k_{\mathrm{B}}T$ and time in units of the monomeric time scale $\tau_{\mathrm{mon}} \equiv a^2/(k_{\mathrm{B}}T\mu_0)$.

7.2.2 Hydrodynamic mean-field theory

For the theoretical description of the polymer motion, we apply a dynamic mean-field approach which has proven useful for the description of semiflexible polymer dynamics in three dimensions in various contexts ranging from DNA end-monomer diffusion [56, 57] to DNA-protein binding dynamics [xi] and the dynamic force-response of pre-stressed filaments [287].

The simplest description of a semiflexible polymer is the worm-like chain (WLC) model: The polymer is represented by a continuous, differentiable space curve $\boldsymbol{r}(s)$ of contour length L. The associated elastic energy U_{WLC}, the continuum analogue of Eq. 7.16, is given by [288]

$$U_{\mathrm{WLC}}[\boldsymbol{r}(s)] = \frac{\kappa}{2} \int_{-L/2}^{L/2} \mathrm{d}s \, \left(\frac{\partial \boldsymbol{u}(s)}{\partial s} \right)^2. \tag{7.21}$$

Here, the arc-length variable ranging from $-L/2$ to $L/2$ is denoted by s, and the tangent vector $\boldsymbol{u} \equiv \partial \boldsymbol{r}/\partial s$ is constrained by local inextensibility to unit length, $\boldsymbol{u}^2(s) = 1, \ \forall s \in [-L/2, L/2]$.

The bending rigidity κ is related to the persistence length $l_\mathrm{p}^{d\mathrm{D}}$, the typical length scale on which tangent-tangent correlations decay

$$\left\langle \boldsymbol{u}(s)\cdot\boldsymbol{u}(s')\right\rangle = \mathrm{e}^{-|s-s'|/l_\mathrm{p}^{d\mathrm{D}}}, \qquad l_\mathrm{p}^{d\mathrm{D}} \equiv \frac{2\kappa}{(d-1)k_\mathrm{B}T}, \tag{7.22}$$

where d is the dimension. Here, we consider the case of two-dimensional confinement ($d = 2$); the configurational space being reduced compared to three dimensions, a polymer with given bending rigidity κ therefore appears stiffer in confinement: $l_\mathrm{p} \equiv l_\mathrm{p}^{3\mathrm{D}} = l_\mathrm{p}^{2\mathrm{D}}/2$.

The constraint in the tangent vector length leading to nonlinear equations of motion, an alternative, approximate model is required. Within a mean-field approach [289, 290] the local constraint is relaxed and replaced by the global and end-point conditions $\left\langle \int \mathrm{d}s\, \boldsymbol{u}^2(s)\right\rangle = L$ and $\left\langle \boldsymbol{u}^2(\pm L/2)\right\rangle = 1$. The resulting Gaussian mean-field Hamiltonian incorporates a finite extensibility in addition to the bending term

$$U_\mathrm{MF}[\boldsymbol{r}(s)] = \frac{\epsilon}{2}\int_{-L/2}^{L/2}\mathrm{d}s\, \left(\frac{\partial \boldsymbol{u}(s)}{\partial s}\right)^2 + \nu\int_{-L/2}^{L/2}\mathrm{d}s\, \boldsymbol{u}^2(s) + \nu_0\left(\boldsymbol{u}^2\left(-L/2\right) + \boldsymbol{u}^2\left(L/2\right)\right), \tag{7.23}$$

where the MFT parameters

$$\epsilon = l_\mathrm{p}^{2\mathrm{D}}k_\mathrm{B}T, \quad \nu = \frac{k_\mathrm{B}T}{2l_\mathrm{p}^{2\mathrm{D}}}, \quad \text{and} \quad \nu_0 = \frac{k_\mathrm{B}T}{2}, \tag{7.24}$$

are chosen so that the most prominent static equilibrium properties of the WLC, the tangent-tangent correlation function in Eq. 7.22 and other derived quantities such as the mean square end-to-end distance, are correctly reproduced [291].

The dynamic theory for the Gaussian semiflexible polymer is based on the hydrodynamic pre-averaging approach [292], analogous to that used for the Zimm model [241] in the case of flexible chains. Within that approximation, the time evolution of the position-vector of point s on the polymer contour within the x-y-plane is governed by the Langevin equation

$$\begin{aligned}
&\frac{\partial}{\partial s}\boldsymbol{r}(s,t) = -\int_{-L/2}^{L/2}\mathrm{d}s'\, \overleftrightarrow{\boldsymbol{\mu}}_\mathrm{avg}(s,s';z)\,\frac{\delta U_\mathrm{MF}}{\delta \boldsymbol{r}(s',t)} + \boldsymbol{v}^\mathrm{st}(s,t),\\
&\left\langle \boldsymbol{v}^\mathrm{st}(s,t)\otimes\boldsymbol{v}^\mathrm{st}(s',t')\right\rangle = 2k_\mathrm{B}T\,\overleftrightarrow{\boldsymbol{\mu}}_\mathrm{avg}(s,s';z)\,\delta(t-t').
\end{aligned} \tag{7.25}$$

Here the pre-averaged mobility tensor $\overleftrightarrow{\boldsymbol{\mu}}_\mathrm{avg}$ is used, which is a function of the contour points s and s' only and which does not depend on the actual spatial positions $\boldsymbol{r}(s,t)$ and $\boldsymbol{r}(s',t)$. The pre-averaged tensor takes the diagonal form

$$\overleftrightarrow{\boldsymbol{\mu}}_\mathrm{avg}(s,s';z) = \left[2a\mu_\parallel^\mathrm{RPB}(z)\delta(s-s') + \Theta\left(\left|s-s'\right|-2a\right)\mu_\mathrm{avg}^\mathrm{RPB}(s,s';z)\right]\overleftrightarrow{\mathbf{1}}, \tag{7.26}$$

thus incorporating the self-mobility $\mu_\parallel^\mathrm{RPB}$ parallel to the boundary (Eq. 7.8), and the pre-averaged HI between different parts of the polymer contour $\mu_\mathrm{avg}^\mathrm{RPB}$, which are cut off for distances $|s-s'| < 2a$ by the unit step function Θ. In Eq. 7.26, the 2×2 unit matrix is denoted by $\overleftrightarrow{\mathbf{1}}$. The pre-averaged HI are obtained by averaging the 2×2 sub-block of the RP level of the Blake tensor

(Eq. 7.6) corresponding to the x- and y-components over all equilibrium configurations of the polymer

$$\overleftrightarrow{\boldsymbol{\mu}}^{\mathrm{RPB}}_{\mathrm{avg}}(s,s';z) = \int \mathrm{d}\boldsymbol{R}\ \overleftrightarrow{\boldsymbol{\mu}}^{\mathrm{RPB}}(\boldsymbol{R};z)\, P_{\mathrm{eq}}(\boldsymbol{R};s,s') = \mu^{\mathrm{RPB}}_{\mathrm{avg}}(s,s';z)\overleftrightarrow{\mathbf{1}}, \tag{7.27}$$

with the Gaussian equilibrium probability density function of (two dimensional) distances $\boldsymbol{R}$ between s and s'

$$\begin{aligned} P_{\mathrm{eq}}(\boldsymbol{R};s,s') &= \frac{1}{\pi\sigma^2(s-s')}\,\mathrm{e}^{-\boldsymbol{R}^2/\sigma^2(s-s')}, \\ \sigma^2(\Delta s) &\equiv 2l_{\mathrm{P}}^{2\mathrm{D}}\left(\Delta s - l_{\mathrm{P}}^{2\mathrm{D}}(1-\mathrm{e}^{-\Delta s/l_{\mathrm{P}}^{2\mathrm{D}}})\right). \end{aligned} \tag{7.28}$$

Note that the steric effect of the wall does not need to be accounted for, since polymer configurations are anyways restricted to a two-dimensional layer. The explicit functional form of $\mu^{\mathrm{RPB}}_{\mathrm{avg}}$ entering the Eqs. 7.26 and 7.27 is found in Eq. D.16 in Appendix D.3.

The pre-averaged Langevin Eq. 7.25 can be solved through a normal mode decomposition, with the eigenmodes fulfilling free-end boundary conditions at $s = \pm L/2$. Since the MFT-parameters (Eq. 7.24) are all just multiplied by the constant factor $2/3$ compared to three dimensions, the free-end boundary conditions and the form of the normal modes described in detail elsewhere [56] remain unchanged. The eigenmode expansion yields a set of ordinary differential equations coupled by a hydrodynamic interaction matrix; once this matrix is diagonalized [56, 241], the problem is reduced to simple Langevin equations for the decoupled normal mode amplitudes $\boldsymbol{P}_n(t)$ with stochastic contributions $\boldsymbol{Q}_n(t)$

$$\begin{aligned} &\frac{\partial}{\partial t}\boldsymbol{P}_0(t) = \boldsymbol{Q}_0(t), \qquad \frac{\partial}{\partial t}\boldsymbol{P}_n(t) = -\Lambda_n\boldsymbol{P}_n(t) + \boldsymbol{Q}_n(t), \quad n = 1,\ldots,N, \\ &\langle Q_n(t)\otimes Q_m(t')\rangle = 2k_{\mathrm{B}}T\delta_{nm}M_n\overleftrightarrow{\mathbf{1}}\delta(t-t'). \end{aligned} \tag{7.29}$$

The two-dimensional vectors $\boldsymbol{P}_n(t)$ and $\boldsymbol{Q}_n(t)$ are related to the polymer conformation $\boldsymbol{r}(s,t)$ and to the stochastic velocities $\boldsymbol{v}^{\mathrm{st}}(s,t)$ through the expansions

$$\boldsymbol{r}(s,t) = \sum_{n=0}^{N}\boldsymbol{P}_n(t)\Psi_n(s), \qquad \boldsymbol{v}^{\mathrm{st}}(s,t) = \sum_{n=0}^{N}\boldsymbol{Q}_n(t)\Psi_n(s), \tag{7.30}$$

where the scalar functions $\Psi_n(s)$ are the decoupled normal modes. The modes are ordered in such a way that the eigenvalues Λ_n (inverse relaxation times) increase with n. We set the high-frequency cutoff N for the mode number to $N = \lceil L/8a \rceil$, which has previously been shown to give good agreement at small scales with BD simulations in three dimensions [56], [xi]. The precise choice of the mode number cutoff does not influence the polymer motion on length scales much larger than the monomer radius a and is therefore only relevant on time scales $t \lesssim \tau_{\mathrm{mon}}$. The inverse relaxation times Λ_n and the fluctuation-dissipation parameters M_n can directly be derived from the tensor $\overleftrightarrow{\boldsymbol{\mu}}^{\mathrm{RPB}}_{\mathrm{avg}}$ evaluated numerically in the normal mode basis. Full details of this procedure together with the explicit form of the normal modes $\Psi_n(s)$ have been given before [56].

Using the Langevin equations in Eq. 7.29 and the normal mode decomposition (Eq. 7.30), we obtain the MSD of the polymer's ends

$$\begin{aligned}\left\langle (\Delta \boldsymbol{r}_{\mathrm{e}}(t))^2 \right\rangle &\equiv \left\langle \left(r_{\mathrm{e}}(t'+t) - r_{\mathrm{e}}(t')\right)^2 \right\rangle = \left\langle \left(\boldsymbol{r}\left(\pm L/2, t'+t\right) - \boldsymbol{r}\left(\pm L/2, t'\right)\right)^2 \right\rangle \\ &= 4D_{\mathrm{pol}}^{\mathrm{2D}} t + 4k_{\mathrm{B}}T \sum_{n=1}^{N} \frac{M_n}{\Lambda_n} \Psi_n^2\left(\pm L/2\right) \left(1 - \mathrm{e}^{-\Lambda_n t}\right),\end{aligned} \tag{7.31}$$

where the (z-dependent) center-of-mass diffusion constant of the polymer is

$$D_{\mathrm{pol}}^{\mathrm{2D}} \equiv k_{\mathrm{B}}T M_0 \Psi_0^2\left(\pm L/2\right). \tag{7.32}$$

Similarly, the MSD of the end-to-end vector is expressed in terms of the MFT normal modes

$$\begin{aligned}\left\langle (\Delta \boldsymbol{R}_{\mathrm{ee}}(t))^2 \right\rangle &\equiv \left\langle (\boldsymbol{R}_{\mathrm{ee}}(t) - \boldsymbol{R}_{\mathrm{ee}}(0))^2 \right\rangle \\ &= \left\langle \left(\left(\boldsymbol{r}\left(L/2, t\right) - \boldsymbol{r}\left(-L/2, t\right)\right) - \left(\boldsymbol{r}\left(L/2, 0\right) - \boldsymbol{r}\left(-L/2, 0\right)\right)\right)^2 \right\rangle \\ &= 4k_{\mathrm{B}}T \sum_{n=1,\,\mathrm{odd}}^{N} \frac{M_n}{\Lambda_n} \left(\Psi_n\left(L/2\right) - \Psi_n\left(-L/2\right)\right)^2 \left(1 - \mathrm{e}^{-\Lambda_n t}\right),\end{aligned} \tag{7.33}$$

where the reference time t' has for simplicity been set to 0.

Note that the polymer's bending stiffness and the z-dependent HI enter the above equations via the parameters M_n and Λ_n as well as via the normal modes Ψ_n. The temporal dependence of the dynamic quantities in the Eqs. 7.31 and 7.33 for different distances z from the no-slip wall are compared to BD results in Sec. 7.3.1.

7.3 Results and Discussion

In the following, we discuss the results from extensive hydrodynamic BD simulations of polymers of contour length $L/a = 100$ (corresponding to $M = 51$ beads) and three dimensional persistence lengths l_{p}/a ranging from 40 to 320 at various average distances z_0 from the wall; a simulation snapshot of two polymer conformations is shown in Fig. 7.5. The simulation time step is $\delta t = 0.06\, a/(\mu_0 \gamma)$, which corresponds to $\delta t = 3 \cdot 10^{-4}\, \tau_{\mathrm{mon}}$ for the stretching elasticity $\gamma = 200\, k_{\mathrm{B}}T/a$ used in all hydrodynamic and most of the free-draining simulations. Observables are averaged over up to 16 trajectories of length $3 \cdot 10^5\, \tau_{\mathrm{mon}}$ each, after an initial thermalization period of $3 \cdot 10^3\, \tau_{\mathrm{mon}}$. For comparison, we also perform free-draining BD simulations, using a diagonal hydrodynamic matrix $\overleftrightarrow{\boldsymbol{\mu}}_{ij} = \mu_0 \delta_{ij} \overleftrightarrow{\mathbf{1}}$ in the Eqs. 7.14 and 7.15, and also set up a free-draining version of the MFT by replacing $\overleftrightarrow{\boldsymbol{\mu}}_{\mathrm{avg}}(s, s')$ by $2a\mu_0 \delta(s - s') \overleftrightarrow{\mathbf{1}}$ in Eq. 7.26.

7.3.1 End-monomer and end-to-end vector dynamics

We first discuss the time dependence of the end-monomer and the end-to-end vector MSDs and their sensitivity to bending stiffness and hydrodynamic screening. As is illustrated in the inset of Fig. 7.5, the end-monomer MSD $\left\langle (\Delta \boldsymbol{r}_{\mathrm{e}})^2 \right\rangle$ reduces to the center-of-mass MSD, $4D_{\mathrm{pol}}^{\mathrm{2D}} t$, once the

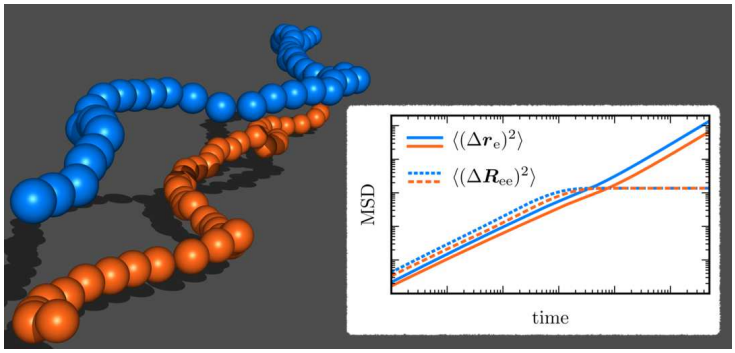

Figure 7.5:
BD simulation snapshot showing conformations of a polymer consisting of 51 beads (contour length $L/a = 100$) and persistence length $l_p/a = 40$ subject to a harmonic confining potential centered around $z_0/a = 10$ (*blue*) and $z_0/a = 2$ (*orange*). The graph displays MFT results for the end-monomer MSD $\langle(\Delta \boldsymbol{r}_e)^2\rangle$ (Eq. 7.31, *solid lines*) and the end-to-end vector MSD (Eq. 7.33, *dashed lines*).

largest relaxation time Λ_1^{-1} is reached, while the end-to-end vector MSD $\langle(\Delta \boldsymbol{R}_{ee})^2\rangle$ levels off at twice the equilibrium mean square end-to-end distance $\sigma^2(L)$ for times $t \gtrsim \Lambda_1^{-1}$ (cf. Eq. 7.28).

The end-monomer MSD $\langle(\Delta \boldsymbol{r}_e)^2\rangle$ in the x-y-plane for polymers of contour length $L/a = 100$ and four different persistence lengths l_p are shown in Fig. 7.6, in which symbols denote hydrodynamic and free-draining simulation results and the lines correspond to the MFT expression in Eq. 7.31. The overall match of simulations and MFT is good, in agreement with our previous results for the bulk case [56, 57, 270]. Note that no fitting parameter is used in the MFT. Two distinct effects are clearly identified in both simulation and theory: (i) when decreasing the distance to the wall, the curves are shifted to larger times, i.e., the overall dynamics are slowed down, and (ii) the slope of the curves on the double-logarithmic scale corresponding to the exponent of the underlying power law decreases. These are non-trivial effects, since they depend on the subtle interplay between wall-induced self-mobility and HI, which both decrease when approaching the wall as shown in the Figs. 7.1 and 7.3. The curves in the double-logarithmic representation show deviations from perfect straight lines, we adopt the concept of a local exponent [56], which in analogy to Sec. 3.2.3 is defined as

$$\alpha(t) \equiv \frac{d \log f(t)}{d \log t}, \tag{7.34}$$

for a general function $f(t)$. The time dependent local exponent $\alpha(t)$ is estimated at each time t by fitting straight lines to the double logarithmic plot of MSD data points at times t_i within a small range around t, defined by the condition $\left|\log_{10}(t_i/t)\right| < 0.15$. The local exponents of the end-point MSDs are shown in the panels below the MSD data in Fig. 7.6. For short times, they exhibit plateaus extending over several decades in time; a crossover to the center-of-mass exponent 1 sets in around the largest polymer relaxation time Λ_1^{-1}, which is designated by a vertical arrow in the Figs. 7.6 and 7.7 and increases by approximately a factor 5 when HI are gradually turned off. Note that even for shorter times than Λ_1^{-1} the exponents start to oscillate; these extended crossover-regions reflect rotations of the entire polymer which for stiff filaments are captured by the first eigenmode [57, 291]. Insufficient sampling leads to statistical

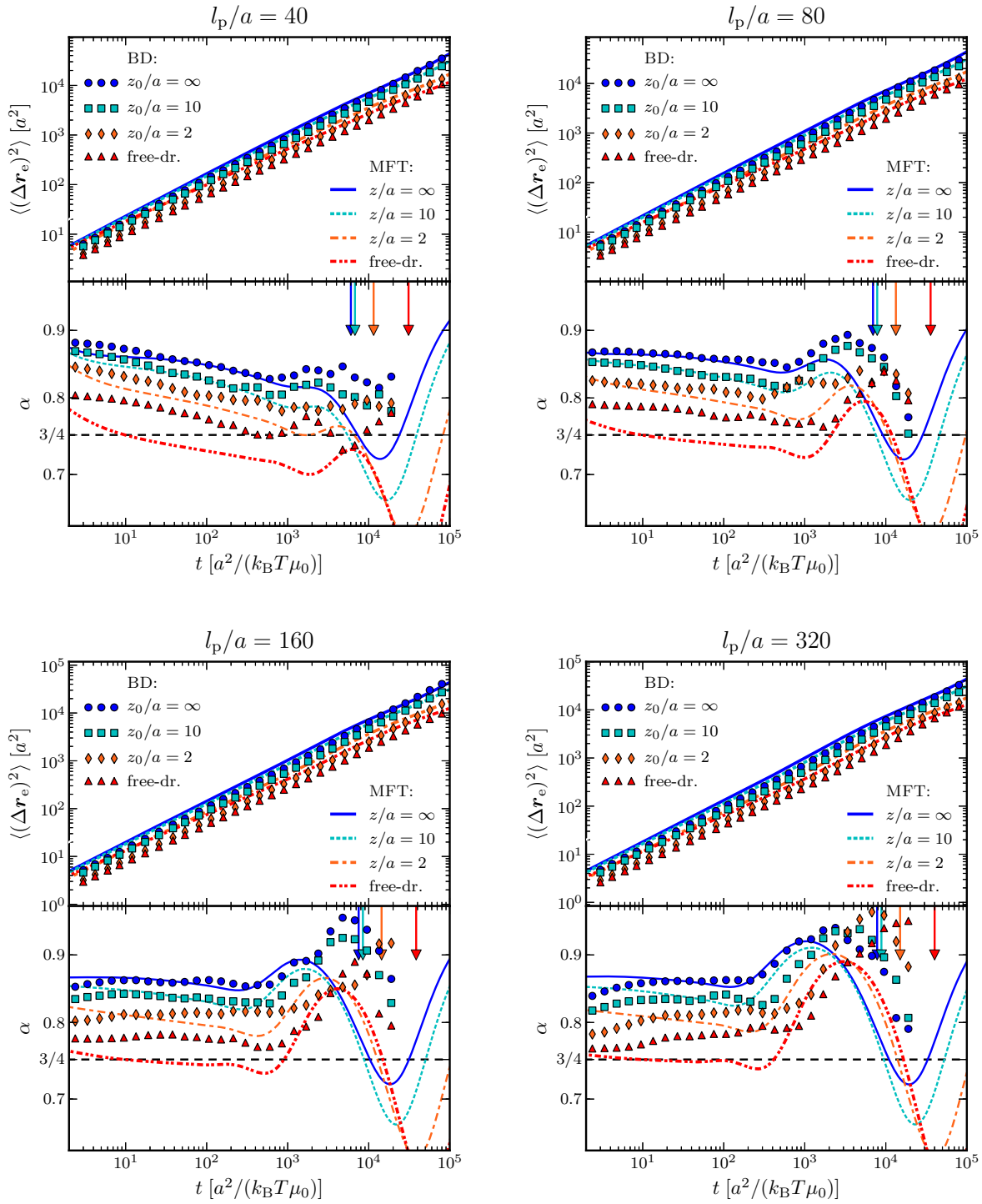

Figure 7.6:
In-plane dynamics of polymers of length $L/a = 100$ and various persistence lengths l_p/a held at an average distance z_0 from a no-slip wall. The dynamics are characterized in terms of the end-monomer MSDs (Eq. 7.31, top panels) and the corresponding local exponents (Eq. 7.34, bottom panels). *Symbols* denote results of hydrodynamic and free-draining BD simulations and *lines* predictions of the two dimensional MFT. *Vertical arrows* designate the largest MFT-relaxation times Λ_1^{-1}.

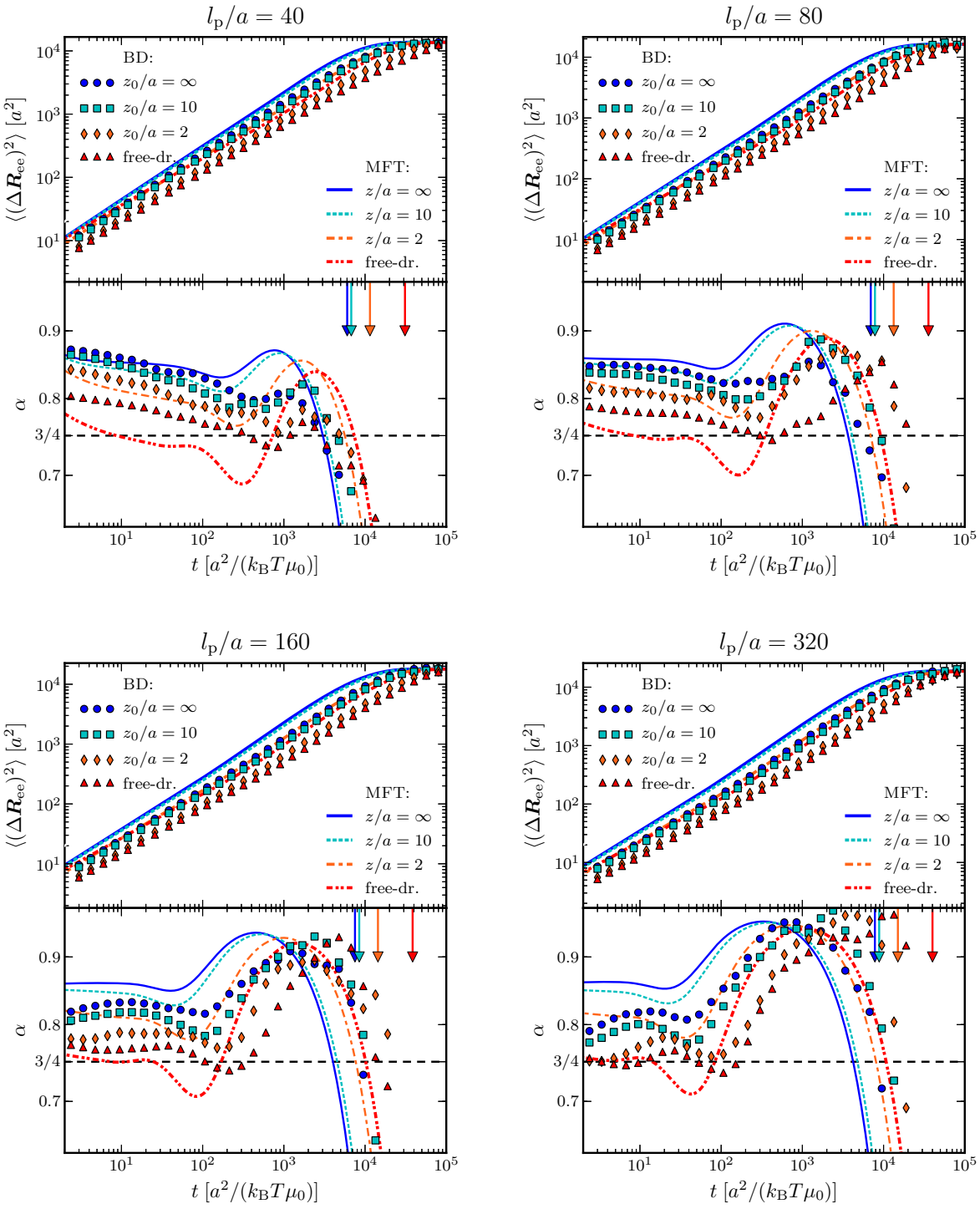

Figure 7.7:
Same as Fig. 7.6 but for the end-to-end vector MSDs (Eq. 7.33, top panels) and the corresponding local exponents α (Eq. 7.34, bottom panels).

noise in the simulated local exponents for times $t \gtrsim 10^3\ \tau_{\mathrm{mon}}$ so that the crossovers are only partially seen in the simulation data. When decreasing the distance to the wall, the values of the exponent are continuously reduced and approach the scaling behavior of the free-draining limit, where for very stiff and inextensible polymers without HI a typical scaling exponent of $3/4$ is expected [56, 292]. We briefly recall previous results for the the scale-dependent dynamics of semiflexible polymers in bulk [56, 57, 270]: In the weak stiffness range $a < l_{\mathrm{p}} < L$, the exponent α for the end-point MSD has been shown to continuously change as a function of time and to show a pronounced minimum roughly at the largest internal polymer time scale. Only in the limit $a \ll L \ll l_{\mathrm{p}}$ asymptotic scaling is observed and in the absence of HI, the classical WLC exponent $\alpha \approx 3/4$ is realized for times $t < \Lambda_1^{-1}$. In the presence of HI, all exponents are increased by a constant shift of roughly 0.1 and thus the asymptotic WLC exponent is more on the order $\alpha \approx 0.85$. Those results from hydrodynamic simulations and hydrodynamic MFT could be rationalized by scaling theory and eigenmode analysis [56] and have quantitatively been compared to experimental time-resolved data for DNA [57, 270].

Remarkably, the dynamic crossover from hydrodynamic to free-draining behavior in Fig. 7.6 sets in at relatively small distances z_0 from the wall. Indeed, the dynamics for $z_0/a = 2$, i.e., at a monomeric separation of the polymer from the wall, are characterized by a considerably higher exponent than the free-draining one, meaning that HI—though screened—still contribute substantially to the relaxation dynamics. Note that this is not an artifact due to the use of approximate self-mobilities and HI of finite sized beads in hydrodynamic simulations and the MFT, since even at separations of two monomer radii from the wall these approximations compare well to the exact expressions in Fig. 7.1. Similar trends are seen in the MSD of the end-to-end vector $\langle(\Delta \boldsymbol{R}_{\mathrm{ee}})^2\rangle$ in Fig. 7.7, which saturates at twice the mean square end-to-end distance of the polymer for $t \gg \Lambda_1^{-1}$. Again a slow-down of the dynamics and a decrease of the local exponent are observed when HI are reduced due to the nearby wall; local exponents are reversely ordered due to this slow-down for $t \gtrsim \Lambda_1^{-1}$.

The quantitative agreement of the MSDs in BD simulations and in the MFT is less impressive in the confined geometry than in the three-dimensional case [57], the MSDs generally being overestimated by the theory. The reasons for the reduced accuracy of the theory in the present case are manifold: (i) Within the MFT the polymer is treated as completely confined to two dimensions, while small out of plane fluctuations are possible in the simulation, (ii) as has been argued in Ref. [57], long ranged HI are one factor for the success of the MFT in three dimensions; conversely, a worsening of the theory is thus expected, when the wall is approached and in consequence HI are gradually weakened, (iii) in analogy with the critical behavior of lattice spin systems [293], mean-field theory and similarly also the pre-averaging approximation of the hydrodynamic tensor are expected to perform better in higher dimension; the reduced accuracy of the two-dimensional theory can therefore be, at least in part, attributed to the lower dimension. However, the general trends induced by the interaction with the no-slip boundary, which are best seen in the local exponents (bottom panels in the Figs. 7.6 and 7.7), are reliably reproduced by the MFT.

Considerably stiffer and longer chains, where the different dynamic regimes are clearly separated in time, are not accessible yet by means of simulations because of the overwhelming computational costs. In contrast, the mean-field approach is equally applicable here. MFT results for a chain with $L/a = l_{\mathrm{p}}/a = 500$ shown in Fig. 7.8 confirm the previous observations: When approaching the wall, hydrodynamic screening shifts the crossovers to larger times and simultaneously decreases the (local) exponent, though not quite reaching the free-draining limit with

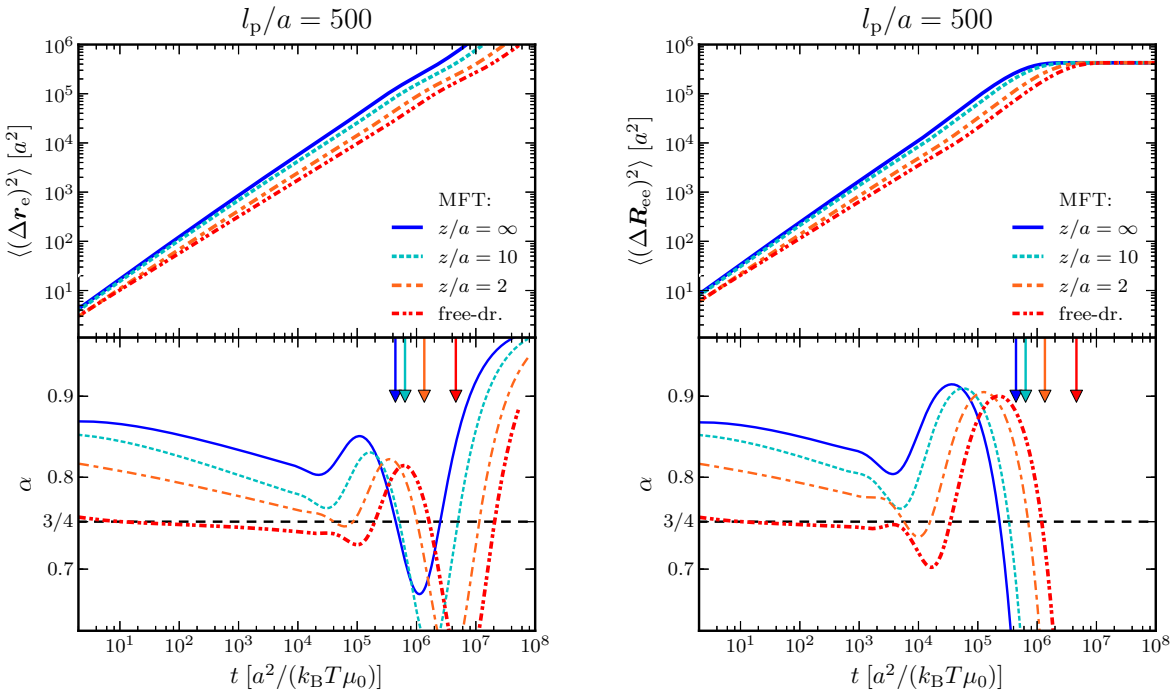

Figure 7.8:
MFT results for in-plane dynamics of a polymer of contour and persistence lengths $L/a = l_p/a = 500$: The top panels show the end-monomer MSD (left, Eq. 7.31) and the end-to-end vector MSD (right, Eq. 7.33) and the bottom panels the corresponding local exponents (Eq. 7.34) for various distances z from the wall as well as in the free-draining limit. Vertical arrows designate the largest MFT-relaxation times Λ_1^{-1}.

exponent 3/4 even at wall-separations on the order of the monomer size. Clearly, the strength of the HI is the most relevant parameter for determining the dynamic scaling exponents in the Figs. 7.6-7.8, while the ratio l_p/L, ranging from 0.4 to 3.2, is of comparatively minor importance for the MSDs of the vectorial quantities considered so far.

7.3.2 Dynamics of the scalar end-to-end distance

Experimentally, end-to-end relaxation dynamics have been studied using end-labeled f-actin filaments [79], which are enclosed in a 1 μm thick chamber to keep the fluorescent markers in the focal plane of the microscope. The dynamics of filaments of contour lengths L ranging from 5.9 to 25.6 μm and persistence length $l_p \approx 15.7$ μm [79] have been quantified in terms of the MSD of the (scalar) end-to-end distance

$$\begin{aligned}\left\langle\left(\Delta\left|\boldsymbol{R}_{ee}\right|(t)\right)^2\right\rangle &\equiv \left\langle\left(\left|\boldsymbol{R}_{ee}(t'+t)\right| - \left|\boldsymbol{R}_{ee}(t')\right|\right)^2\right\rangle \\ &= \left\langle\left(\left|\boldsymbol{r}\left(L/2, t'+t\right) - \boldsymbol{r}\left(-L/2, t'+t\right)\right| - \left|\boldsymbol{r}\left(L/2, t'\right) - \boldsymbol{r}\left(-L/2, t'\right)\right|\right)^2\right\rangle,\end{aligned} \tag{7.35}$$

which obviously differs from the end-to-end vector MSD in Eq. 7.33. In their work, Le Goff et al. suggest a linear rescaling of the time and MSD variables in order to collapse the MSD data set

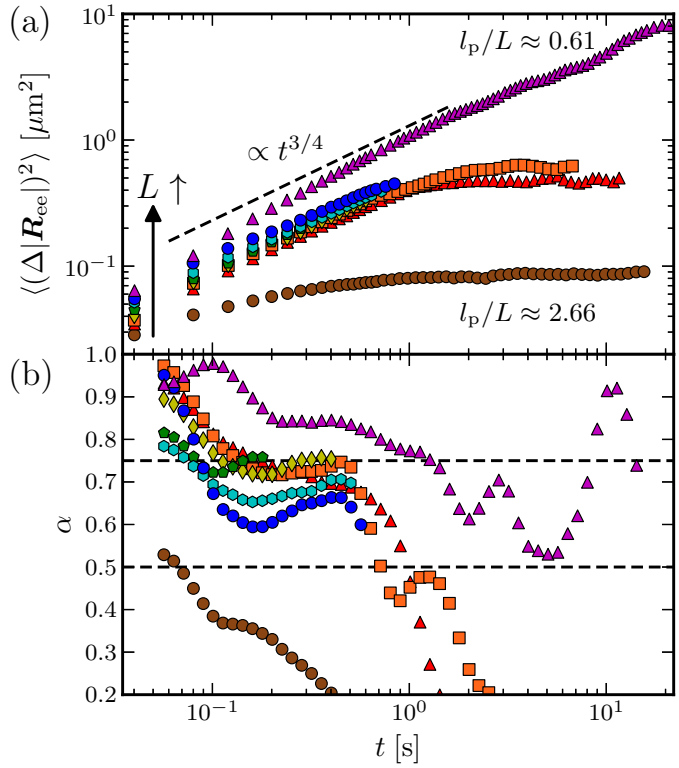

Figure 7.9:
a) Experimental MSDs of the scalar end-to-end distance of f-actin filaments of contour length $L = 5.9, 10.4, 10.7, 11.8, 11.8, 11.9, 12.9$, and 25.6 μm (from bottom to top, data digitized from the inset of Fig. 3 in Ref. [79]; only those parts of the data set are used, which could unambiguously be assigned to a certain contour length L). Assuming a persistence length $l_p \approx 15.7\mu$m [79], the ratio l_p/L varies between 0.61 and 2.66 (from top to bottom). b) Corresponding local exponents (Eq. 7.34).

onto a single master curve, which at short times reduces to a power law scaling with exponent $\alpha = 3/4$. Interestingly, our re-analysis of the experimental data in terms of local exponents reveals smooth crossovers from values between 0.8 and 1.0 at short times to values around 0.7 before the exponents quickly drop towards 0. The original data as well as the corresponding local exponents, both affected by significant statistical noise, are shown in Fig. 7.9. Plateau regions with an approximately constant exponent (cf. Figs. 7.6-7.8) are not observed. Note that a linear rescaling of time $\tilde{t} \equiv c_t t$ and of the dynamic observable $\tilde{f}(\tilde{t}) \equiv c_f f(c_t t)$ with c_t and c_f constants, leaves the local exponent (Eq. 7.34) unchanged: $\tilde{\alpha}(\tilde{t}) = \alpha(c_t t)$. The rescaling therefore cannot be the reason for the apparent plateaus of the exponents in the original data analysis. Rather, the graphical averaging over various filament lengths seems to wash out the variations of the exponent as a function of time and when comparing different filament lengths with each other.

Unfortunately, the isotropic MFT in the formulation of Sec. 7.2.2 does not allow the evaluation of the scalar end-to-end distance MSD measured in the experiments. Also, a direct comparison of experiments and hydrodynamic simulations is unfeasible because of the immense computational costs associated with contour lengths $L/a \sim \mathcal{O}(10^3)$. The MSD of the scalar end-to-end distance from BD simulations of chain length $L/a = 100$ are shown in Fig. 7.10. As in the case

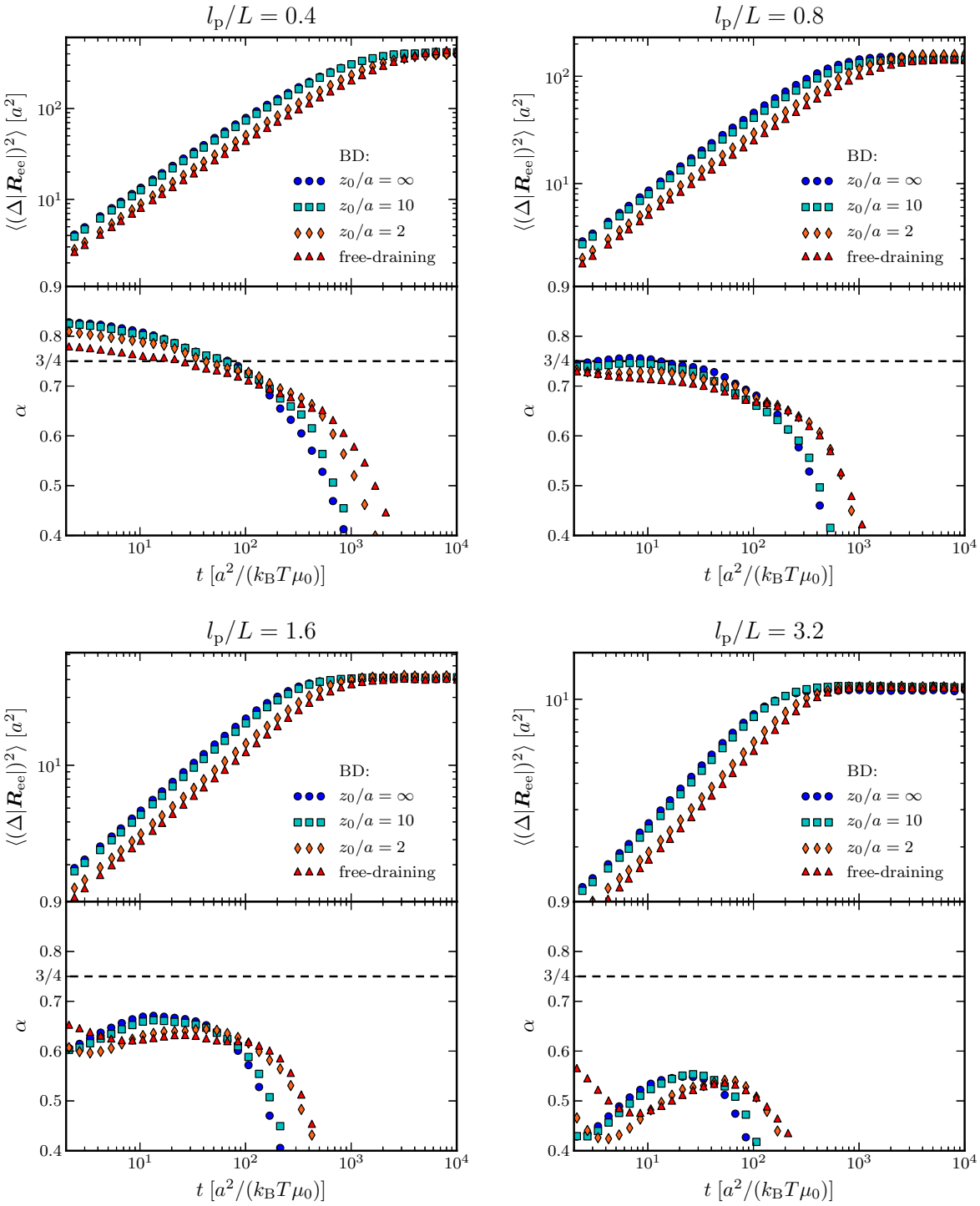

Figure 7.10:
Scalar end-to-end distance MSD from hydrodynamic BD simulations of a polymer of length $L/a = 100$ and varying stiffness l_p/L for several average distances z_0 from the confining wall (top panels) as well as corresponding the local exponents α (bottom panels). For comparison results from free-draining BD simulations are shown using *red triangles*.

of the end-to-end vector MSD in Fig. 7.7, the weakening of the HI leads to a slowdown of the overall relaxation dynamics, the saturation crossover being shifted to larger times. However, the scalar end-to-end distance saturates at considerably smaller times since the slow rotational mode of the entire filament is factored out in this observable. In accordance with the experimental data in Fig. 7.9, the local exponents are rather characterized by smooth crossovers than by constant values. Most strikingly, the comparison of the simulation results in Fig. 7.10 reveals a strong dependence of the local exponents on the ratio l_p/L: Typical values of $\alpha \gtrsim 0.8$ for $l_p/L = 0.4$, $\alpha \approx 0.7 - 0.75$ for $l_p/L = 0.8$, $\alpha \approx 0.65$ for $l_p/L = 1.6$, and $\alpha \approx 0.5$ for $l_p/L = 3.2$ are identified, in agreement with results previously obtained for the fluctuations of unconstrained filaments [57]. For a fixed ratio l_p/L, the strength of the HI varying with the distance z_0 from the boundary only slightly affects the local exponents. Hydrodynamics thus seem to be of minor importance for the dynamic scaling of the scalar end-to-end distance MSD, in contrast to the vectorial MSDs in the Figs. 7.6 and 7.7. This is not surprising, as hydrodynamics most strongly affect the center-of-mass translation and the rotation of the filament, both of which are factored out in the scalar end-to-end distance. This finding suggests to use free-draining simulations for a more detailed analysis of the dynamic scaling behavior of the scalar end-to-end distance.

The fact that the local exponents in Fig. 7.10 tend towards $1/2$ instead of $3/4$ with increasing ratio l_p/L is easily understood by realizing that we keep the harmonic bond-stretching parameter in Eq. 7.16 constant at a value $\gamma = 200\, k_B T/a$ in our simulations, while varying the bending stiffness κ. As a consequence, the free-draining scalar end-to-end relaxation becomes dominated by stretching relaxation [294] with characteristic exponent $1/2$ in the limit $\kappa \to \infty$, whereas the weakly-bending WLC exponent $3/4$ is expected only in the idealized limit of a perfectly inextensible semiflexible chain. To substantiate this suggestion, we compare the scalar end-to-end MSDs of free-draining simulations with $\gamma = 200\, k_B T/a$ and $\gamma = 1000\, k_B T/a$ in Fig. 7.11a-b. Indeed, for $lp/L \gtrsim$ one finds higher exponents in the less extensible cases denoted by open symbols in Fig. 7.11a-b. In turn, variations of the chain extensibility only marginally affect end-to-end relaxation dynamics in the flexible regime $l_p/L \lesssim 1$, since here the relaxation is dominated by bending fluctuations. For biopolymers probed experimentally, the stretching and bending stiffness constants are not independent quantities. Rather, the ratio of the stretching and bending energy parameters,

$$\frac{\gamma a^2}{4\kappa}, \tag{7.36}$$

presumably is rather constant and on the order of unity as in the case of an isotropic elastic cylinder [295]. Since higher values of the stretching parameter γ require a reduced simulation time step δt (cf. beginning of Sec. 7.3), an increase of γ is currently unfeasible for simulations including HI (the simulation time for a single hydrodynamic trajectory with 10^9 time steps lasting approximately 40 days on a standard single-core computer). We therefore continue our discussion with free-draining simulations, which does not seem to be a serious restriction since the results in Fig. 7.10 indicate that HI are rather unimportant for the MSD of the scalar end-to-end distance anyways. In Fig. 7.11c-d, we show results from free-draining simulations, in which γ and κ have simultaneously been modified to keep the ratio in Eq. 7.36 equal to 1.25. As is clearly seen, the trends observed in Fig. 7.10 remain unchanged: when increasing the ratio l_p/L, the local exponents gradually decrease (below $3/4$), in qualitative agreement with the experimental data shown in Fig. 7.9.

We cautiously remark that experimentally the ratio l_p/L is varied by choosing filaments of different contour lengths L while keeping the persistence length l_p fixed. In our simulations,

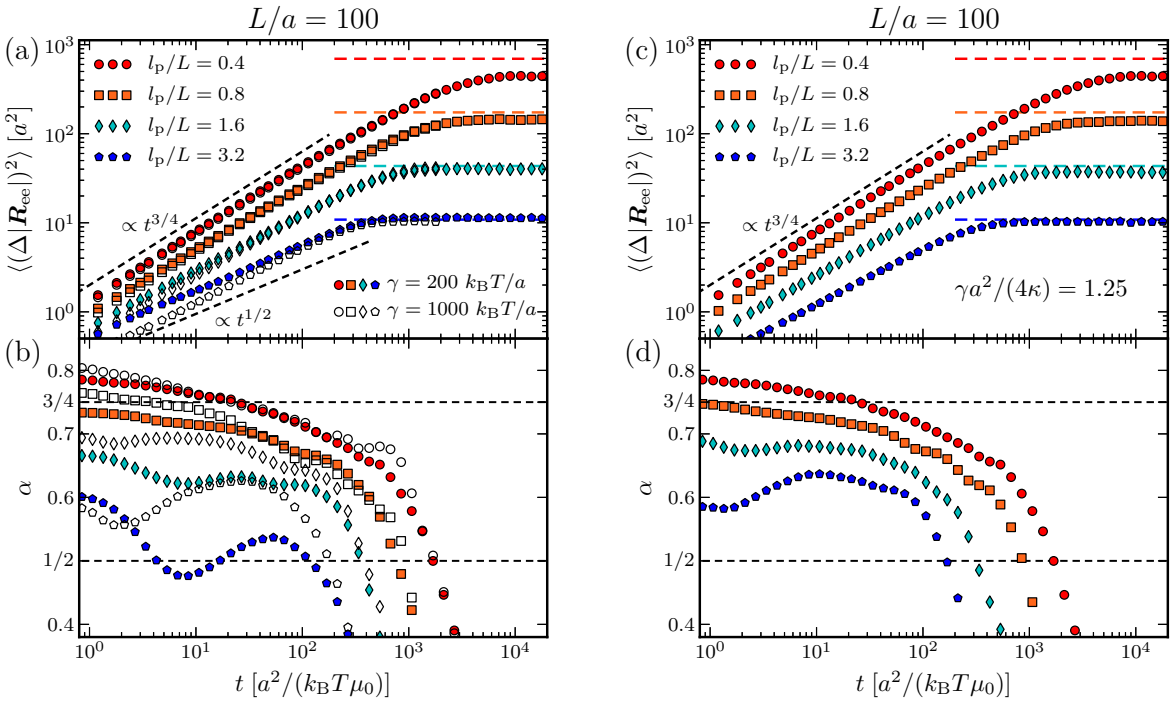

Figure 7.11:
a) Influence of the stiffness l_p/L and the stretching force constant γ on the end-to-end distance MSD (Eq. 7.35) and b) corresponding local exponents (Eq. 7.34) in free-draining BD simulations of a polymer of length $L/a = 100$. Results obtained with the standard stretching force constant $\gamma = 200\ k_BT/a$ (*filled symbols*) and $\gamma = 1000\ k_BT/a$ (*open symbols*) are compared. c) and d) Same as (a) and (b) but from simulations with a constant ratio of bending and stretching energy parameters in Eq. 7.36.

the persistence length l_p is varied while keeping L fixed. These two scenarios are not strictly equivalent since an additional length scale, the monomer radius a, is present in the problem, giving a second dimensionless length-scale ratio L/a. In order to look into this, we show in Fig. 7.12 MFT results of the end-monomer and end-to-end vector MSDs for filaments of varying length to monomer radius ratio L/a but constant ratio $l_p/L = 1$. The dependence on the monomer radius a can be scaled out in the free-draining limit or, in other words, free-draining relaxation dynamics are characterized by the ratio l_p/L only as is clearly seen from the dashed lines in the bottom panels of Fig. 7.12, where the data is rescaled by the polymer length L. On the other hand, HI give rise to a genuine logarithmic dependence of the dynamics on the ratio L/a as is seen from the solid lines in the bottom panels of Fig. 7.12.

The dilemma is that our simulations do not span a large enough range of ratios l_p/L and L/a in order to extract the full scaling behavior, while the MFT cannot be used to calculate the experimentally measured scalar end-to-end distance MSD. Nevertheless, it is conceivable that the scaling in terms of one parameter only, namely the ratio l_p/L, observed in the MFT for the MSDs of the vectorial observables without HI (Fig. 7.12), also holds for the scalar end-to-end distance MSD, for which the hydrodynamic effects have been shown to be rather unimportant in simulations (Fig. 7.10). This suggestion is enforced by the observation that experimental and simulation results for the scalar end-to-end distance MSD in the Figs. 7.9 and 7.11c-d show similar behavior for matching values of l_p/L, although the values of L/a are very different. Based

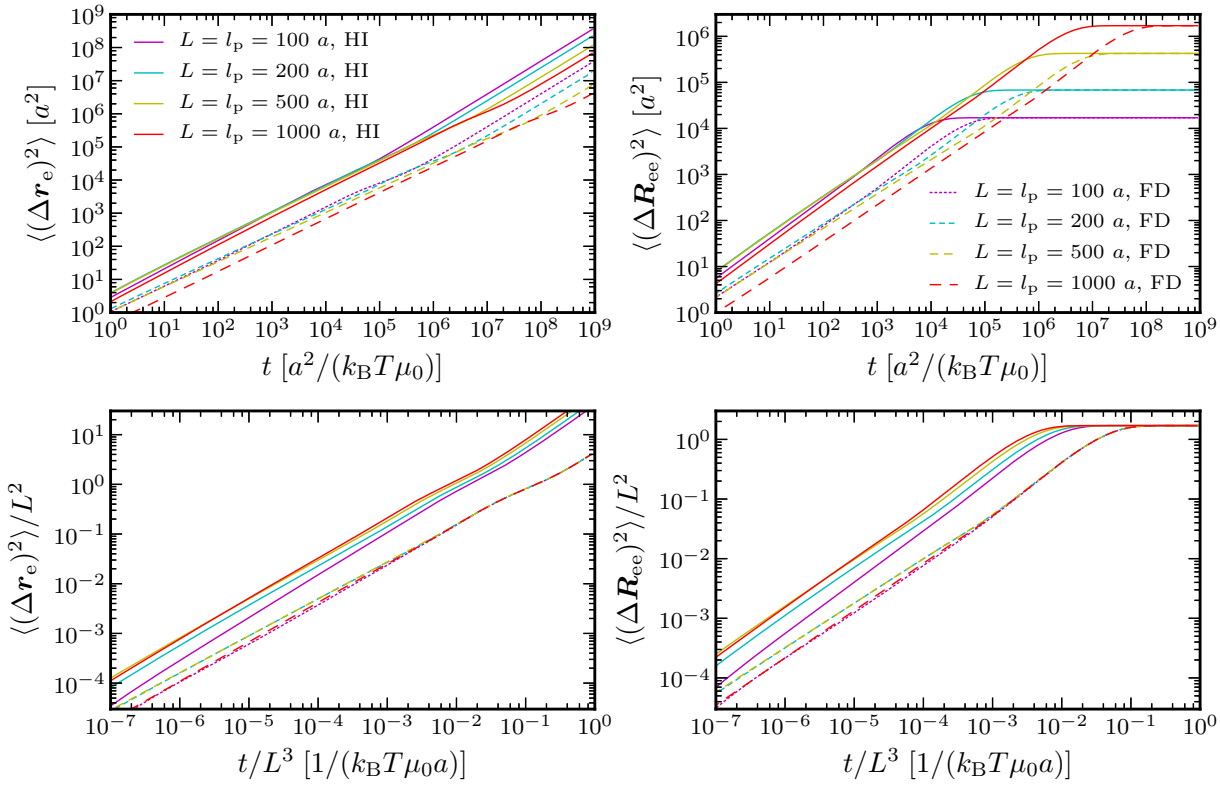

Figure 7.12:
Top left: MFT results for the end-monomer position vector MSD (Eq. 7.31) with HI (*solid lines*) and in the free-draining (FD) limit (*dashed lines*) for filaments of varying contour length L and persistence length l_p but constant ratio $l_p/L = 1$. Bottom left: A rescaling of time and MSD by the polymer length L yields a collapse of the free-draining MSDs on a master curve, deviations at small times arise from differences in the mode-number cutoff N, cf. Sec. 7.2.2. In the presence of HI, no collapse is obtained. Right: Corresponding plots for the end-to-end vector MSD (Eq. 7.33).

on the similar qualitative trends seen in the restricted experimental and simulation data sets displayed in Fig. 7.9 and Fig. 7.11c-d, we are led to the following tentative conclusions: (i) Local exponents for the scalar end-to-end distance MSD do not show characteristic plateau values but rather continously decrease with increasing time, and (ii) the dynamic scaling varies with polymer stiffness l_p/L, where values of $\alpha \gtrsim 3/4$ are observed for more flexible chains ($l_p/L < 1$), while exponents $\alpha \lesssim 3/4$ are characteristic for stiffer filaments ($l_p/L > 1$). These observations crucially depend on the presence of stretching fluctuations, as indeed experimentally present for elastic biopolymers. The strength of the HI, which have sizeable effects on the MSDs of vectorial observables, mainly reduces to a temporal rescaling for the case of the scalar end-to-end distance MSD. Given these results, the collapse of experimental scalar end-to-end MSDs for different l_p/L on a single master-curve [79], calls for further experimental investigations in light of the presence of stretching fluctuations as described by an extensible WLC model with a finite ratio of the bending and stretching stiffnesses (Eq. 7.36).

7.4 Conclusions

In summary, we have presented results from hydrodynamic and free-draining BD simulations of a single semiflexible filament in the vicinity of a hydrodynamic no-slip wall. By varying the distance to the boundary, the influence of hydrodynamic screening on typical dynamic quantities such as the end-monomer and end-to-end vector MSD of the polymer filament have been resolved. The weakening of the HI when approaching the wall is clearly reflected in these observables. Though being less accurate than in the three dimensional case, the adaptation of the hydrodynamic MFT captures the trends seen in the simulations, i.e., the slowing down of the overall dynamics and the crossover towards free-draining dynamic scaling when approaching the wall. In addition, the theoretical approach allows to consider polymer lengths inaccessible in simulations.

Our analysis reveals that (screened) HI contribute differently to different dynamic variables: MSDs of vectorial quantities such as the end-monomer position and the end-to-end vector show distinct plateaus in their local exponents, which are similar over a broad range of bending stiffnesses and gradually decrease when approaching the surface. Nevertheless, hydrodynamics continue to be important at polymer-wall separations on the order of the monomer-size and the free-draining limit therefore remains an inaccurate approximation to the actual dynamics, even very close to planar surfaces. To what extent similar reservations hold in other geometries or in non-dilute polymer solutions remains for future investigations.

On the other hand, rotations of the entire filament are factored out in the scalar end-to-end distance MSDs, and the corresponding dynamic scaling exponents rather result from an interplay of stretching and bending stiffness, while the role of hydrodynamic screening is mainly reduced to a temporal rescaling. The non-universal dependence of the scaling exponent on the persistence length to contour length ratio l_p/L seen in the free-draining simulations qualitatively agrees with a similar dependence seen in our reanalysis of experimental data for f-actin filaments [79] and crucially depends on the fact that chain stretching fluctuations are included in the theoretical modeling, as appropriate for elastic biopolymers.

On the basis of our findings, the characterization of previous experimental data in terms of a single dynamic scaling exponent appears oversimplified. Experiments resolving more dynamic observables than the usual scalar end-to-end MSD, extending the analysis to a larger range of stiffnesses l_p/L, and rigorously identifying the hydrodynamic influence of nearby boundaries would certainly be helpful in shed more light on the rich and complex relaxation dynamics of semiflexible polymers.

CHAPTER 8

BOTTOM-UP APPROACH TO THE VISCOELASTICITY OF POLYMER NETWORKS

Bibliographic information: Parts of this chapter and of Appendix G have previously been published. Reprinted from Ref. [i]. With kind permission of The European Physical Journal (EPJ).

The salient mechanical properties of biological materials such as proteins [296], the cytoskeleton [80, 297] and bone-like materials [298] have spurred interest in the question how the viscoelasticity of materials result from the underlying constituents and the materials' structures. Experimentally, the viscoelastic properties of a variety of hard and soft, complex materials are nowadays probed by micro- and macroscopic techniques [299–301], which have continuously been refined over the last decades. Given the complexity of the—often hierarchical—naturally occurring structures, the influence of individual building blocks on the materials' large-scale properties has been addressed experimentally by studying reconstituted model systems [302, 303].

On the theoretical side, typical features of the viscoelasticity of polymeric networks could be linked to the properties of the constituting semiflexible polymers [304, 305]. Various models for randomly placed semiflexible filaments [306, 307] and site-diluted random networks of filaments supporting both stretching forces and bending torques have been studied numerically and analytically in the quasi-static (zero-frequency) limit with a focus on the rigidity percolation threshold, the crossover between affine and non-affine elastic response and nonlinear elastic effects [308–312]. Despite ever increasing computational resources, explicit numerical calculations for large-scale structures remain time-consuming and have therefore mostly been restricted to probing quasi-static response properties. In recent work, the phonon spectrum and the frequency-dependent shear modulus of disordered central-force-lattices close to the rigidity limit have been studied [313, 314]. However, many details of how the micro- and macrorheological properties of a material result from characteristics of the structural building blocks still remain elusive.

Here, we present a theoretical framework that allows to explicitly calculate the entire frequency spectrum of the linear micro- and macro-viscoelastic response functions in complex networks of arbitrary topology. The input to our dynamic convolution theory (DCT) are the rheological properties of the structural components and the connectivity of the network. We focus on polymeric networks, where the dynamical properties of the individual semiflexible

filaments forming the network are either known theoretically or can be accessed via single-molecule experiments [79] or explicit simulations [287]. The viscoelastic properties of the constituting filaments are characterized by frequency-dependent self- and cross-response functions between all pairs of orientational and translational degrees of freedom at the filaments' ends. The connectivity of the network is encoded in the topology matrix; though applicable to arbitrary structures, we only consider square lattices in our explicit calculations. The mechanical properties of the network nodes modeling the crosslinker molecules play a central role [311, 315]: Depending on the network's topology, the angular constraints imposed by the crosslinkers quantitatively or even qualitatively affect the resulting viscoelastic properties of the network as is explicitly shown. We consider both microrheological and macrorheological properties: In the former a point force is applied on the lattice and the local response is measured, in the latter the network is sheared or compressed by uniform force distributions acting on the network boundaries. By a mapping on continuum viscoelastic theory we also determine the corresponding viscoelastic bulk moduli. The actual dynamic convolution step is performed numerically, the computational costs however are moderate even for networks consisting of hundreds of nodes.

For simplicity, we restrict the discussion to two dimensions, but it is straightforward to extend the formalism to three dimensions. The chapter is organized as follows: The DCT is formulated in Sec. 8.1, the linear force-response properties of individual semiflexible filaments are studied in Sec. 8.2 and used in Sec. 8.3 to calculate the micro- and macrorheological properties of crosslinked semiflexible polymer networks. Our main results are summarized in Sec. 8.4, while complementary considerations about viscoelastic continua are found in Appendix G.

8.1 Dynamic Convolution Theory

In the following, we present a DCT for two dimensional mechanical networks, thereby generalizing the one dimensional theory used in the context of single-molecule experiments [ix]. Linear force response properties of the constituents of the network are covered in Sec. 8.1.1, the convolution step resulting from connecting the end-points of isolated elements is explained in Sec. 8.1.2, and the overall procedure is summarized in Sec. 8.1.3. Possible applications as well as limitations of the theory are discussed in Sec. 8.1.4; an explicit example for the reorientation effects of mechanical elements is given in Sec. 8.1.5.

8.1.1 Dynamic linear force response of individual elements

We consider two dimensional networks built of mechanical elements consisting of a discrete number of end-points denoted by capital black letters, e.g., $\mathfrak{A}$, $\mathfrak{B}$, $\mathfrak{C}$, $\mathfrak{D}$, etc. Networks result from coupling the end-points of various mechanical elements as described in Sec. 8.1.2. In the following, we focus on two-point elements of type $\mathfrak{AB}$, $\mathfrak{CD}$, etc., which we call basic elements and which serve as building blocks for more complex structures.

The state of a basic element of type $\mathfrak{AB}$ is characterized by the Cartesian end-point coordinates $x^{\mathfrak{A}}$, $y^{\mathfrak{A}}$, $x^{\mathfrak{B}}$, and $y^{\mathfrak{B}}$ as well as the two terminal tangent angles $\varphi^{\mathfrak{A}}$ and $\varphi^{\mathfrak{B}}$. Motion in this six-dimensional coordinate space is due to thermal fluctuations as well as internal and external

forces. In frequency space, the linear response of the system to external forces $f_x^{\mathfrak{A}}$, $f_y^{\mathfrak{A}}$, $f_x^{\mathfrak{B}}$, and $f_y^{\mathfrak{B}}$ and torques $\tau^{\mathfrak{A}}$ and $\tau^{\mathfrak{B}}$ acting on the end-points and -orientations is given by

$$\left\langle \begin{pmatrix} x^{\mathfrak{A}}(\omega) \\ y^{\mathfrak{A}}(\omega) \\ \varphi^{\mathfrak{A}}(\omega) \\ x^{\mathfrak{B}}(\omega) \\ y^{\mathfrak{B}}(\omega) \\ \varphi^{\mathfrak{B}}(\omega) \end{pmatrix} \right\rangle = \begin{pmatrix} \boldsymbol{J}_{\mathfrak{A}\mathfrak{A}}(\omega) & \boldsymbol{J}_{\mathfrak{A}\mathfrak{B}}(\omega) \\ \boldsymbol{J}_{\mathfrak{B}\mathfrak{A}}(\omega) & \boldsymbol{J}_{\mathfrak{B}\mathfrak{B}}(\omega) \end{pmatrix} \cdot \begin{pmatrix} f_x^{\mathfrak{A}}(\omega) \\ f_y^{\mathfrak{A}}(\omega) \\ \tau^{\mathfrak{A}}(\omega) \\ f_x^{\mathfrak{B}}(\omega) \\ f_y^{\mathfrak{B}}(\omega) \\ \tau^{\mathfrak{B}}(\omega) \end{pmatrix}, \qquad \omega \neq 0, \tag{8.1}$$

with the 3×3 response matrices

$$\boldsymbol{J}_{\mathfrak{a}\mathfrak{b}}(\omega) \equiv \begin{pmatrix} J_{\mathfrak{a}\mathfrak{b}}^{xx}(\omega) & J_{\mathfrak{a}\mathfrak{b}}^{xy}(\omega) & J_{\mathfrak{a}\mathfrak{b}}^{x\varphi}(\omega) \\ J_{\mathfrak{a}\mathfrak{b}}^{yx}(\omega) & J_{\mathfrak{a}\mathfrak{b}}^{yy}(\omega) & J_{\mathfrak{a}\mathfrak{b}}^{y\varphi}(\omega) \\ J_{\mathfrak{a}\mathfrak{b}}^{\varphi x}(\omega) & J_{\mathfrak{a}\mathfrak{b}}^{\varphi y}(\omega) & J_{\mathfrak{a}\mathfrak{b}}^{\varphi\varphi}(\omega) \end{pmatrix}, \qquad \mathfrak{a}, \mathfrak{b} \in \{\mathfrak{A}, \mathfrak{B}\}, \tag{8.2}$$

where $\langle \ldots \rangle$ in Eq. 8.1 denotes an average with respect to the thermal fluctuations and $\omega \neq 0$ is the oscillation frequency, which is typically omitted in the following to simplify the notation. $\boldsymbol{J}_{\mathfrak{A}\mathfrak{A}}$ and $\boldsymbol{J}_{\mathfrak{B}\mathfrak{B}}$ being symmetric and $\boldsymbol{J}_{\mathfrak{A}\mathfrak{B}} = \boldsymbol{J}_{\mathfrak{B}\mathfrak{A}}^{\mathrm{T}}$ due to time-reversal symmetry, the linear response properties of such a two-point element are encoded in 21 in principle independent complex functions of frequency ω.

Local and global coordinate frames

In general, the linear response matrices $\boldsymbol{J}_{\mathfrak{a}\mathfrak{b}}$ depend on the (average) orientation of the element in the global coordinate frame (x, y). To unmask this orientational dependence, it is convenient to define a local orthogonal coordinate frame $(\parallel, \perp)$, where the $\parallel$-direction points from $\mathfrak{A}$ to $\mathfrak{B}$. The relationship between the local frame and the global one is established via a rotation matrix

$$\boldsymbol{T}(\Phi) = \begin{pmatrix} \cos\Phi & -\sin\Phi & 0 \\ \sin\Phi & \cos\Phi & 0 \\ 0 & 0 & 1 \end{pmatrix}, \tag{8.3}$$

where Φ is the angle between the x- and the $\parallel$-direction, see Fig. 8.1a for a schematic. Clearly, the forces and coordinates in the respective coordinate frames are related via

$$\begin{pmatrix} x^{\mathfrak{a}} \\ y^{\mathfrak{a}} \\ \varphi^{\mathfrak{a}} \end{pmatrix} = \boldsymbol{T}(\Phi) \cdot \begin{pmatrix} r_{\parallel}^{\mathfrak{a}} \\ r_{\perp}^{\mathfrak{a}} \\ \varphi^{\mathfrak{a}} \end{pmatrix}, \quad \begin{pmatrix} f_x^{\mathfrak{a}} \\ f_y^{\mathfrak{a}} \\ \tau^{\mathfrak{a}} \end{pmatrix} = \boldsymbol{T}(\Phi) \cdot \begin{pmatrix} f_{\parallel}^{\mathfrak{a}} \\ f_{\perp}^{\mathfrak{a}} \\ \tau^{\mathfrak{a}} \end{pmatrix}, \qquad \mathfrak{a} \in \{\mathfrak{A}, \mathfrak{B}\}. \tag{8.4}$$

Note that the terminal angle $\varphi_{\mathfrak{a}}$ is not transformed, since we focus on average oscillation amplitudes at non-zero frequency only. Indeed, time-averaged values of the angular variables, which obviously depend on the orientation Φ of the element, are reflected in the $\omega = 0$ component, which is not considered here. Accordingly, the relationship between the response matrices in the local and the global frames is given by

$$\boldsymbol{J}_{\mathfrak{a}\mathfrak{b}} = \boldsymbol{T}(\Phi) \cdot \tilde{\boldsymbol{J}}_{\mathfrak{a}\mathfrak{b}} \cdot \boldsymbol{T}(-\Phi), \qquad \mathfrak{a}, \mathfrak{b} \in \{\mathfrak{A}, \mathfrak{B}\}, \tag{8.5}$$

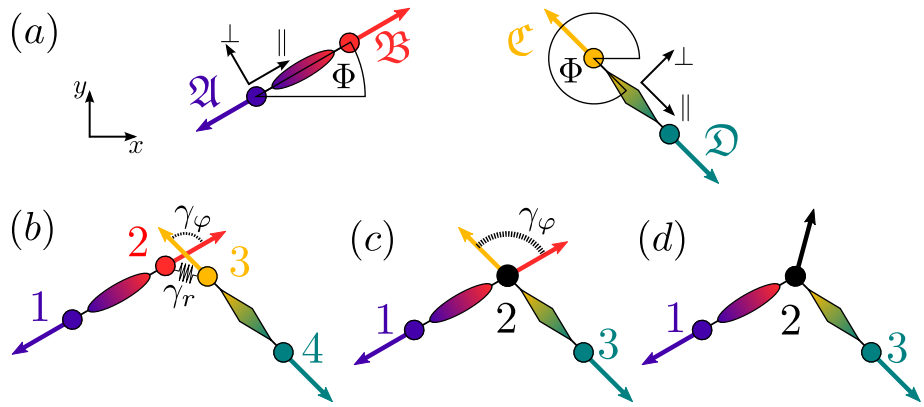

Figure 8.1:
a) Two-point elements of type $\mathfrak{AB}$ and $\mathfrak{CD}$ including the local coordinate frames $(\parallel, \perp)$ with orientation Φ with respect to the global coordinate frame (x, y). b), c), and d) Networks resulting from a serial alignment of $\mathfrak{AB}$ and $\mathfrak{CD}$ as discussed in Sec. 8.1.2; network nodes are denoted by 1, 2, 3, and 4.

where response matrices in the local coordinate frame $(\parallel, \perp)$ are denoted by a tilde.

Symmetry

Symmetry reduces the number of non-vanishing and independent response functions. For objects, which (on average) are mirror-symmetric with respect to the $\perp$-axis, the response matrices in the local coordinate frame take the form

$$\tilde{\boldsymbol{J}}_{\mathfrak{ab}} \equiv \begin{pmatrix} J_{\mathfrak{ab}}^{\parallel\parallel} & 0 & 0 \\ 0 & J_{\mathfrak{ab}}^{\perp\perp} & J_{\mathfrak{ab}}^{\perp\varphi} \\ 0 & J_{\mathfrak{ab}}^{\varphi\perp} & J_{\mathfrak{ab}}^{\varphi\varphi} \end{pmatrix}, \qquad \mathfrak{a}, \mathfrak{b} \in \{\mathfrak{A}, \mathfrak{B}\}, \tag{8.6}$$

and according to Eq. 8.5, the response matrices in the global coordinate frame are then given by

$$\boldsymbol{J}_{\mathfrak{ab}} = \begin{pmatrix} J_{\mathfrak{ab}}^{\parallel\parallel}\cos^2\Phi + J_{\mathfrak{ab}}^{\perp\perp}\sin^2\Phi & (J_{\mathfrak{ab}}^{\parallel\parallel} - J_{\mathfrak{ab}}^{\perp\perp})\cos\Phi\sin\Phi & -J_{\mathfrak{ab}}^{\perp\varphi}\sin\Phi \\ (J_{\mathfrak{ab}}^{\parallel\parallel} - J_{\mathfrak{ab}}^{\perp\perp})\cos\Phi\sin\Phi & J_{\mathfrak{ab}}^{\parallel\parallel}\sin^2\Phi + J_{\mathfrak{ab}}^{\perp\perp}\cos^2\Phi & J_{\mathfrak{ab}}^{\perp\varphi}\cos\Phi \\ -J_{\mathfrak{ab}}^{\varphi\perp}\sin\Phi & J_{\mathfrak{ab}}^{\varphi\perp}\cos\Phi & J_{\mathfrak{ab}}^{\varphi\varphi} \end{pmatrix}, \qquad \mathfrak{a}, \mathfrak{b} \in \{\mathfrak{A}, \mathfrak{B}\}. \tag{8.7}$$

The overall number of independent and non-vanishing response functions is thus reduced to 13: eight self-response functions relating forces/torques on and translational/angular motion of one of the ends: $J_{\mathfrak{AA}}^{\parallel\parallel}$, $J_{\mathfrak{AA}}^{\perp\perp}$, $J_{\mathfrak{BB}}^{\parallel\parallel}$, $J_{\mathfrak{BB}}^{\perp\perp}$ (translation), $J_{\mathfrak{AA}}^{\varphi\varphi}$, $J_{\mathfrak{BB}}^{\varphi\varphi}$ (orientation), $J_{\mathfrak{AA}}^{\perp\varphi}$, $J_{\mathfrak{BB}}^{\perp\varphi}$ (orientation-translation coupling) and five cross-response functions relating forces/torques on and translational/angular motion of different ends: $J_{\mathfrak{AB}}^{\parallel\parallel}$, $J_{\mathfrak{AB}}^{\perp\perp}$ (translation), $J_{\mathfrak{AB}}^{\varphi\varphi}$ (orientation), $J_{\mathfrak{AB}}^{\perp\varphi}$, $J_{\mathfrak{AB}}^{\varphi\perp}$ (orientation-translation coupling), where the latter two are in general independent.

For elements with equivalent end-points $\mathfrak{A}$ and $\mathfrak{B}$, the number of independent response functions is further reduced to eight, since $J_{\mathfrak{BB}}^{\parallel\parallel} = J_{\mathfrak{AA}}^{\parallel\parallel}$, $J_{\mathfrak{BB}}^{\perp\perp} = J_{\mathfrak{AA}}^{\perp\perp}$, $J_{\mathfrak{BB}}^{\varphi\varphi} = J_{\mathfrak{AA}}^{\varphi\varphi}$, $J_{\mathfrak{BB}}^{\perp\varphi} = -J_{\mathfrak{AA}}^{\perp\varphi}$, and $J_{\mathfrak{AB}}^{\varphi\perp} = -J_{\mathfrak{AB}}^{\perp\varphi}$. For the case of a single, homogeneous semiflexible filament the eight independent linear response functions are resolved and discussed in Sec. 8.2.

As has been stressed above, the linear response properties of a particular element in the global Cartesian coordinate frame depend on its (average) orientation Φ in the network (cf. Eqs. 8.5 and 8.7). We therefore use different labels, e.g., $\mathfrak{AB}$ and $\mathfrak{CD}$, for differently oriented elements of the same type, thereby unambiguously relating a label, e.g., $\mathfrak{AB}$, to a particular set of dynamic linear response matrices $\boldsymbol{J}_{\mathfrak{AA}}(\omega)$, $\boldsymbol{J}_{\mathfrak{AB}}(\omega)$ and $\boldsymbol{J}_{\mathfrak{BB}}(\omega)$ in the global coordinate frame.

8.1.2 Connection of individual elements

To simplify the notation, we define generalized force and position vectors

$$\boldsymbol{F}_{\mathfrak{a}}(\omega) \equiv \begin{pmatrix} f_x^{\mathfrak{a}}(\omega) \\ f_y^{\mathfrak{a}}(\omega) \\ \tau^{\mathfrak{a}}(\omega) \end{pmatrix}, \qquad \boldsymbol{R}_{\mathfrak{a}}(\omega) \equiv \begin{pmatrix} x^{\mathfrak{a}}(\omega) \\ y^{\mathfrak{a}}(\omega) \\ \varphi^{\mathfrak{a}}(\omega) \end{pmatrix}, \qquad \mathfrak{a} \in \{\mathfrak{A}, \mathfrak{B}\}, \tag{8.8}$$

and inverting Eq. 8.1, we obtain

$$\begin{pmatrix} \boldsymbol{F}_{\mathfrak{A}}(\omega) \\ \boldsymbol{F}_{\mathfrak{B}}(\omega) \end{pmatrix} = \begin{pmatrix} \boldsymbol{G}_{\mathfrak{AA}}(\omega) & \boldsymbol{G}_{\mathfrak{AB}}(\omega) \\ \boldsymbol{G}_{\mathfrak{BA}}(\omega) & \boldsymbol{G}_{\mathfrak{BB}}(\omega) \end{pmatrix} \cdot \langle \begin{pmatrix} \boldsymbol{R}_{\mathfrak{A}}(\omega) \\ \boldsymbol{R}_{\mathfrak{B}}(\omega) \end{pmatrix} \rangle \equiv \begin{pmatrix} \boldsymbol{J}_{\mathfrak{AA}}(\omega) & \boldsymbol{J}_{\mathfrak{AB}}(\omega) \\ \boldsymbol{J}_{\mathfrak{BA}}(\omega) & \boldsymbol{J}_{\mathfrak{BB}}(\omega) \end{pmatrix}^{-1} \cdot \langle \begin{pmatrix} \boldsymbol{R}_{\mathfrak{A}}(\omega) \\ \boldsymbol{R}_{\mathfrak{B}}(\omega) \end{pmatrix} \rangle, \tag{8.9}$$

with dynamic stiffness matrices $\boldsymbol{G}_{\mathfrak{AA}}$, $\boldsymbol{G}_{\mathfrak{BB}}$, and $\boldsymbol{G}_{\mathfrak{AB}}$ of dimension 3×3 each. Building networks out of isolated elements implies coupling their translational and angular degrees of freedom. Various coupling mechanisms, which give rise to pairwise coupling forces between the end-points $\mathfrak{a}$ and $\mathfrak{b}$ of different or the same element, are conceivable:

1. Harmonic coupling around an equilibrium position/orientation $\boldsymbol{R}_0 \equiv \left(x^0, y^0, \varphi^0\right)^{\mathrm{T}}$ implies a potential energy

$$U(t) = \frac{1}{2} \left(\boldsymbol{R}_{\mathfrak{b}}(t) - \boldsymbol{R}_{\mathfrak{a}}(t) - \boldsymbol{R}_0\right)^{\mathrm{T}} \cdot \boldsymbol{\Gamma} \cdot \left(\boldsymbol{R}_{\mathfrak{b}}(t) - \boldsymbol{R}_{\mathfrak{a}}(t) - \boldsymbol{R}_0\right), \tag{8.10}$$

   where the matrix

$$\boldsymbol{\Gamma} \equiv \begin{pmatrix} \gamma_r & 0 & 0 \\ 0 & \gamma_r & 0 \\ 0 & 0 & \gamma_\varphi \end{pmatrix}, \tag{8.11}$$

   contains the harmonic spring constants for translational and angular degrees of freedom γ_r and γ_φ. In frequency domain, such a harmonic coupling implies additional nodal forces

$$\boldsymbol{F}_{\mathfrak{a}}^{\mathrm{harm}}(\omega) = \boldsymbol{\Gamma} \cdot \left(\boldsymbol{R}_{\mathfrak{b}}(\omega) - \boldsymbol{R}_{\mathfrak{a}}(\omega)\right), \qquad \boldsymbol{F}_{\mathfrak{b}}^{\mathrm{harm}}(\omega) = -\boldsymbol{F}_{\mathfrak{a}}^{\mathrm{harm}}(\omega), \qquad \omega \neq 0, \tag{8.12}$$

   which are independent of the equilibrium state $\boldsymbol{R}_0$ for $\omega \neq 0$.

2. Coupling due to internal friction [67] generates additional nodal forces

$$\boldsymbol{F}_{\mathfrak{a}}^{\mathrm{frict}}(\omega) = -\mathrm{i}\,\omega\,\boldsymbol{Z} \cdot \left(\boldsymbol{R}_{\mathfrak{b}}(\omega) - \boldsymbol{R}_{\mathfrak{a}}(\omega)\right), \qquad \boldsymbol{F}_{\mathfrak{b}}^{\mathrm{frict}}(\omega) = -\boldsymbol{F}_{\mathfrak{a}}^{\mathrm{frict}}(\omega), \tag{8.13}$$

where the matrix

$$\boldsymbol{Z} \equiv \begin{pmatrix} \zeta_r & 0 & 0 \\ 0 & \zeta_r & 0 \\ 0 & 0 & \zeta_\varphi \end{pmatrix}, \tag{8.14}$$

contains the friction coefficients for translational and angular degrees of freedom denoted by ζ_r and ζ_φ, respectively.

3. Combinations of harmonic and internal frictional coupling [316] as defined in the Eqs. 8.12 and 8.13.

The underlying assumption behind the DCT is that the range of validity of the linear force response equations (Eqs. 8.1 or 8.9) extends to the sum of (arbitrarily small) external forces $\boldsymbol{F}_\mathfrak{a}$ *and* coupling forces. This is indeed true for linear systems and is a very good approximation if the effect of the nonlinearities is small, cf. discussion in Sec. 6.4.2.

In the following, we consider two elements of type $\mathfrak{AB}$ and $\mathfrak{CD}$, which are arranged in series and in parallel, before describing the procedure for arbitrary network types. To distinguish the degrees of freedom of the end-points of isolated elements and those of the nodes in the network, the latter ones are denoted by arabic numbers $1, 2, 3$, etc.

Serial alignment

A serial alignment of the elements $\mathfrak{AB}$ and $\mathfrak{CD}$ is achieved by harmonically coupling the ends $\mathfrak{B}$ and $\mathfrak{C}$ as schematically shown in Fig. 8.1b, where the network's degrees of freedom are $\boldsymbol{R}_1 \equiv \boldsymbol{R}_\mathfrak{A}$, $\boldsymbol{R}_2 \equiv \boldsymbol{R}_\mathfrak{B}$, $\boldsymbol{R}_3 \equiv \boldsymbol{R}_\mathfrak{C}$, and $\boldsymbol{R}_4 \equiv \boldsymbol{R}_\mathfrak{D}$. Under the above assumptions, the dynamic force balance in the network is

$$\begin{pmatrix} \boldsymbol{F}_1 \\ \boldsymbol{F}_2 \\ \boldsymbol{F}_3 \\ \boldsymbol{F}_4 \end{pmatrix} = \begin{pmatrix} \boldsymbol{F}_\mathfrak{A} \\ \boldsymbol{F}_\mathfrak{B} \\ \boldsymbol{F}_\mathfrak{C} \\ \boldsymbol{F}_\mathfrak{D} \end{pmatrix} = \begin{pmatrix} \boldsymbol{G}_{\mathfrak{AA}} & \boldsymbol{G}_{\mathfrak{AB}} & 0 & 0 \\ \boldsymbol{G}_{\mathfrak{BA}} & \boldsymbol{G}_{\mathfrak{BB}} + \boldsymbol{\Gamma} & -\boldsymbol{\Gamma} & 0 \\ 0 & -\boldsymbol{\Gamma} & \boldsymbol{G}_{\mathfrak{CC}} + \boldsymbol{\Gamma} & \boldsymbol{G}_{\mathfrak{CD}} \\ 0 & 0 & \boldsymbol{G}_{\mathfrak{DC}} & \boldsymbol{G}_{\mathfrak{DD}} \end{pmatrix} \cdot \langle \begin{pmatrix} \boldsymbol{R}_1 \\ \boldsymbol{R}_2 \\ \boldsymbol{R}_3 \\ \boldsymbol{R}_4 \end{pmatrix} \rangle, \tag{8.15}$$

where the degree of coupling between the nodes 2 and 3 is tuned by the spring constants γ_r and γ_φ in the matrix $\boldsymbol{\Gamma}$ (Eq. 8.11).

In the limit of large coupling constants, i.e., for $\gamma_r, \gamma_\varphi \to \infty$, the number of independent degrees of freedom is reduced by three, since the degrees of freedom at the nodes 2 and 3 then are identical. After this decimation of degrees of freedom (DDF), the remaining degrees of freedom of the network visualized in Fig. 8.1d are $\boldsymbol{R}_1 \equiv \boldsymbol{R}_\mathfrak{A}$, $\boldsymbol{R}_2 \equiv \boldsymbol{R}_\mathfrak{B} = \boldsymbol{R}_\mathfrak{C}$, $\boldsymbol{R}_3 \equiv \boldsymbol{R}_\mathfrak{D}$, and the dynamic force balance is

$$\begin{pmatrix} \boldsymbol{F}_1 \\ \boldsymbol{F}_2 \\ \boldsymbol{F}_3 \end{pmatrix} = \begin{pmatrix} \boldsymbol{F}_\mathfrak{A} \\ \boldsymbol{F}_\mathfrak{B} \\ 0 \end{pmatrix} + \begin{pmatrix} 0 \\ \boldsymbol{F}_\mathfrak{C} \\ \boldsymbol{F}_\mathfrak{D} \end{pmatrix} = \left(\begin{pmatrix} \boldsymbol{G}_{\mathfrak{AA}} & \boldsymbol{G}_{\mathfrak{AB}} & 0 \\ \boldsymbol{G}_{\mathfrak{BA}} & \boldsymbol{G}_{\mathfrak{BB}} & 0 \\ 0 & 0 & 0 \end{pmatrix} + \begin{pmatrix} 0 & 0 & 0 \\ 0 & \boldsymbol{G}_{\mathfrak{CC}} & \boldsymbol{G}_{\mathfrak{CD}} \\ 0 & \boldsymbol{G}_{\mathfrak{DC}} & \boldsymbol{G}_{\mathfrak{DD}} \end{pmatrix} \right) \cdot \langle \begin{pmatrix} \boldsymbol{R}_1 \\ \boldsymbol{R}_2 \\ \boldsymbol{R}_3 \end{pmatrix} \rangle, \tag{8.16}$$

where external forces $\boldsymbol{F}_\mathfrak{B}$ and $\boldsymbol{F}_\mathfrak{C}$ on the central node add up. The total linear force response of the network is contained in the grand-response matrix of dimension 9×9

$$\boldsymbol{\mathcal{J}}^{\text{serial}} = \begin{pmatrix} \boldsymbol{G}_{\mathfrak{AA}} & \boldsymbol{G}_{\mathfrak{AB}} & 0 \\ \boldsymbol{G}_{\mathfrak{BA}} & \boldsymbol{G}_{\mathfrak{BB}} + \boldsymbol{G}_{\mathfrak{CC}} & \boldsymbol{G}_{\mathfrak{CD}} \\ 0 & \boldsymbol{G}_{\mathfrak{DC}} & \boldsymbol{G}_{\mathfrak{DD}} \end{pmatrix}^{-1}. \tag{8.17}$$

An intermediate scenario ($\gamma_r \to \infty$, γ_φ finite) with two translational and two angular degrees of freedom at the central node after the DDF, is schematically shown in Fig. 8.1c.

Parallel alignment

Similarly, $\mathfrak{AB}$ and $\mathfrak{CD}$ can be aligned in parallel by harmonically coupling $\mathfrak{A}$ to $\mathfrak{C}$ and $\mathfrak{B}$ to $\mathfrak{D}$; employing the same notation for the network nodes as above, the dynamic force balance is

$$\begin{pmatrix} \boldsymbol{F}_1 \\ \boldsymbol{F}_2 \\ \boldsymbol{F}_3 \\ \boldsymbol{F}_4 \end{pmatrix} = \begin{pmatrix} \boldsymbol{F}_\mathfrak{A} \\ \boldsymbol{F}_\mathfrak{B} \\ \boldsymbol{F}_\mathfrak{C} \\ \boldsymbol{F}_\mathfrak{D} \end{pmatrix} = \begin{pmatrix} \boldsymbol{G}_{\mathfrak{AA}} + \boldsymbol{\Gamma} & \boldsymbol{G}_{\mathfrak{AB}} & -\boldsymbol{\Gamma} & 0 \\ \boldsymbol{G}_{\mathfrak{BA}} & \boldsymbol{G}_{\mathfrak{BB}} + \boldsymbol{\Gamma} & 0 & -\boldsymbol{\Gamma} \\ -\boldsymbol{\Gamma} & 0 & \boldsymbol{G}_{\mathfrak{CC}} + \boldsymbol{\Gamma} & \boldsymbol{G}_{\mathfrak{CD}} \\ 0 & -\boldsymbol{\Gamma} & \boldsymbol{G}_{\mathfrak{DC}} & \boldsymbol{G}_{\mathfrak{DD}} + \boldsymbol{\Gamma} \end{pmatrix} \cdot \langle \begin{pmatrix} \boldsymbol{R}_1 \\ \boldsymbol{R}_2 \\ \boldsymbol{R}_3 \\ \boldsymbol{R}_4 \end{pmatrix} \rangle, \tag{8.18}$$

assuming the same coupling matrix $\boldsymbol{\Gamma}$ (Eq. 8.11) for both ends. Similarly as above, in the limit of large coupling constants, i.e., for $\gamma_r, \gamma_\varphi \to \infty$, the number of independent degrees of freedom is reduced by six. After this DDF, the remaining network nodes are $\boldsymbol{R}_1 \equiv \boldsymbol{R}_\mathfrak{A} = \boldsymbol{R}_\mathfrak{C}$ and $\boldsymbol{R}_2 \equiv \boldsymbol{R}_\mathfrak{B} = \boldsymbol{R}_\mathfrak{D}$ and we obtain the dynamic force balance

$$\begin{pmatrix} \boldsymbol{F}_1 \\ \boldsymbol{F}_2 \end{pmatrix} = \begin{pmatrix} \boldsymbol{F}_\mathfrak{A} \\ \boldsymbol{F}_\mathfrak{B} \end{pmatrix} + \begin{pmatrix} \boldsymbol{F}_\mathfrak{C} \\ \boldsymbol{F}_\mathfrak{D} \end{pmatrix} = \left(\begin{pmatrix} \boldsymbol{G}_{\mathfrak{AA}} & \boldsymbol{G}_{\mathfrak{AB}} \\ \boldsymbol{G}_{\mathfrak{BA}} & \boldsymbol{G}_{\mathfrak{BB}} \end{pmatrix} + \begin{pmatrix} \boldsymbol{G}_{\mathfrak{CC}} & \boldsymbol{G}_{\mathfrak{CD}} \\ \boldsymbol{G}_{\mathfrak{DC}} & \boldsymbol{G}_{\mathfrak{DD}} \end{pmatrix} \right) \cdot \langle \begin{pmatrix} \boldsymbol{R}_1 \\ \boldsymbol{R}_2 \end{pmatrix} \rangle, \tag{8.19}$$

where individual external forces on both network nodes sum up. The linear force response of the network is consequently encoded in the grand-response matrix of dimension 6×6

$$\boldsymbol{\mathcal{J}}^{\text{parallel}} = \begin{pmatrix} \boldsymbol{G}_{\mathfrak{AA}} + \boldsymbol{G}_{\mathfrak{CC}} & \boldsymbol{G}_{\mathfrak{AB}} + \boldsymbol{G}_{\mathfrak{CD}} \\ \boldsymbol{G}_{\mathfrak{BA}} + \boldsymbol{G}_{\mathfrak{DC}} & \boldsymbol{G}_{\mathfrak{BB}} + \boldsymbol{G}_{\mathfrak{DD}} \end{pmatrix}^{-1}. \tag{8.20}$$

Arbitrary networks

Mechanical networks of arbitrary complexity can be constructed by softly coupling or decimating the degrees of freedom of the isolated building blocks. The underlying rules for calculating the network's grand-stiffness matrix $\boldsymbol{\mathcal{G}} \equiv \boldsymbol{\mathcal{J}}^{-1}$ remain unchanged: The DDF implies identical oscillation amplitudes of the corresponding degrees of freedom, and the forces in the network arise from the superposition of the individual external forces and soft coupling forces. Formally, the entries of the grand-stiffness matrix for a network consisting of N nodes are

$$\boldsymbol{\mathcal{G}}_{ij}(\omega) = \sum_{\mathfrak{a},\mathfrak{b}} \left(\boldsymbol{\mathcal{T}}_{i\mathfrak{a}} \cdot \boldsymbol{G}_{\mathfrak{ab}}(\omega) \cdot \boldsymbol{\mathcal{T}}_{j\mathfrak{b}}{}^{\mathrm{T}} \right) + \frac{1}{2} \left(\boldsymbol{\mathcal{C}}_{ij} + \boldsymbol{\mathcal{C}}_{ji}{}^{\mathrm{T}} \right), \qquad i,j \in \{1,\ldots,N\}, \tag{8.21}$$

where the indices $\mathfrak{a}$ and $\mathfrak{b}$ run over all different kinds of end-points in the network, i.e., $\mathfrak{A}$, $\mathfrak{B}$, $\mathfrak{C}$, etc., and the topology matrices $\boldsymbol{\mathcal{T}}_{i\mathfrak{a}}$ relate the degrees of freedom of the element's end-point $\mathfrak{a}$ to those of the network node i and thus in particularly specify which of the degrees of freedom are decimated. Soft coupling due to harmonic potentials and/or internal friction effects between the degrees of freedom of network nodes i and j are encoded in the matrices $\boldsymbol{\mathcal{C}}_{ij}$ entering Eq. 8.21. The pairwise character of the coupling forces (Eqs. 8.12 and 8.13) implies

$$\sum_j \sum_l \left(\boldsymbol{\mathcal{C}}_{ij}\right)_{kl} = 0 \quad \Leftrightarrow \quad \left(\boldsymbol{\mathcal{C}}_{ii}\right)_{kk} = -\sum_j \sum_l (1 - \delta_{ij}\delta_{kl}) \left(\boldsymbol{\mathcal{C}}_{ij}\right)_{kl}, \qquad \forall\, i,k, \tag{8.22}$$

where the indices i and j refer to nodes and the indices k and l to the corresponding degrees of freedom. The definition of a *network node* is rather flexible: In the following, we define a network node as the set of two translational degrees of freedom (along x and y) and one or more angular degrees of freedom. The grand-response and stiffness matrices $\boldsymbol{\mathcal{J}}$ and $\boldsymbol{\mathcal{G}}$ thus are of dimension $3N \times 3N$ or larger.

Coming back to the serial and parallel examples for illustration purposes, the networks of the harmonically coupled elements $\mathfrak{AB}$ and $\mathfrak{CD}$ (Eqs. 8.15 and 8.18) correspond to the simple topology matrices

$$\begin{array}{c} \\ 1 \\ 2 \\ 3 \\ 4 \end{array}\!\!\begin{array}{c} \begin{array}{cccc} \mathfrak{A} & \mathfrak{B} & \mathfrak{C} & \mathfrak{D} \end{array} \\ \begin{pmatrix} \mathbf{1}_{3\times3} & 0 & 0 & 0 \\ 0 & \mathbf{1}_{3\times3} & 0 & 0 \\ 0 & 0 & \mathbf{1}_{3\times3} & 0 \\ 0 & 0 & 0 & \mathbf{1}_{3\times3} \end{pmatrix} \end{array} = \boldsymbol{\mathcal{T}}^{\text{serial}} = \boldsymbol{\mathcal{T}}^{\text{parallel}}, \qquad \mathbf{1}_{3\times3} \equiv \begin{pmatrix} 1 & 0 & 0 \\ 0 & 1 & 0 \\ 0 & 0 & 1 \end{pmatrix}, \tag{8.23}$$

translating between alphabetical and numerical indices in this trivial network, in which each end-point by itself forms a network node. For the serial case, the non-vanishing coupling matrices are

$$\boldsymbol{\mathcal{C}}_{22}^{\text{serial}} = \boldsymbol{\mathcal{C}}_{33}^{\text{serial}} = -\boldsymbol{\mathcal{C}}_{23}^{\text{serial}} = -\boldsymbol{\mathcal{C}}_{32}^{\text{serial}} = \boldsymbol{\Gamma}, \tag{8.24}$$

specifying that the degrees of freedom of nodes 2 and 3 are coupled via $\boldsymbol{\Gamma}$ (Eq. 8.11), and

$$\begin{aligned} &\boldsymbol{\mathcal{C}}_{11}^{\text{parallel}} = \boldsymbol{\mathcal{C}}_{22}^{\text{parallel}} = \boldsymbol{\mathcal{C}}_{33}^{\text{parallel}} = \boldsymbol{\mathcal{C}}_{44}^{\text{parallel}} = \\ &-\boldsymbol{\mathcal{C}}_{13}^{\text{parallel}} = -\boldsymbol{\mathcal{C}}_{24}^{\text{parallel}} = -\boldsymbol{\mathcal{C}}_{31}^{\text{parallel}} = -\boldsymbol{\mathcal{C}}_{42}^{\text{parallel}} = \boldsymbol{\Gamma}, \end{aligned} \tag{8.25}$$

in the parallel scenario, where the nodes 1 and 3 as well as 2 and 4 are coupled respectively. In turn, the grand-stiffness matrices for the serial and parallel alignment of the elements $\mathfrak{AB}$ and $\mathfrak{CD}$ after the DDF (Eqs. 8.16 and 8.19) follow via Eq. 8.21 from the topology matrices

$$\begin{array}{c} \\ 1 \\ 2 \\ 3 \end{array}\!\!\begin{array}{c} \begin{array}{cccc} \mathfrak{A} & \mathfrak{B} & \mathfrak{C} & \mathfrak{D} \end{array} \\ \begin{pmatrix} \mathbf{1}_{3\times3} & 0 & 0 & 0 \\ 0 & \mathbf{1}_{3\times3} & \mathbf{1}_{3\times3} & 0 \\ 0 & 0 & 0 & \mathbf{1}_{3\times3} \end{pmatrix} \end{array} = \boldsymbol{\mathcal{T}}^{\text{serial}}, \qquad \begin{array}{c} \\ 1 \\ 2 \end{array}\!\!\begin{array}{c} \begin{array}{cccc} \mathfrak{A} & \mathfrak{B} & \mathfrak{C} & \mathfrak{D} \end{array} \\ \begin{pmatrix} \mathbf{1}_{3\times3} & 0 & \mathbf{1}_{3\times3} & 0 \\ 0 & \mathbf{1}_{3\times3} & 0 & \mathbf{1}_{3\times3} \end{pmatrix} \end{array} = \boldsymbol{\mathcal{T}}^{\text{parallel}}, \tag{8.26}$$

indicating that for the serial alignment the degrees of freedom of the end-points $\mathfrak{B}$ and $\mathfrak{C}$ are decimated and form the network node 2. For the parallel alignment, the degrees of freedom of the end-points $\mathfrak{A}$ and $\mathfrak{C}$ as well as $\mathfrak{B}$ and $\mathfrak{D}$ are forced to coincide and after the DDF form the network nodes 1 and 2, respectively. In both cases, the coupling matrices vanish, i.e.,

$$\boldsymbol{\mathcal{C}}_{ij}^{\text{serial}} = \boldsymbol{\mathcal{C}}_{ij}^{\text{parallel}} = 0, \quad \forall\, i, j. \tag{8.27}$$

The formulation in Eq. 8.21 is however not restricted to networks built out of two-point elements. As an example for a more complex network structure, which can be studied within the DCT framework, we consider the network structure schematically drawn in Fig. 8.2b. The building blocks shown in Fig. 8.2a are: (i) the two-node elements of type $\mathfrak{AB}$ and $\mathfrak{CD}$, which could represent linear objects such as unbranched polymers, (ii) a single-node element $\mathfrak{E}$, which could represent a small globular molecule or a colloid, and (iii) a three-node element $\mathfrak{FGH}$, which could represent a branched polymer.

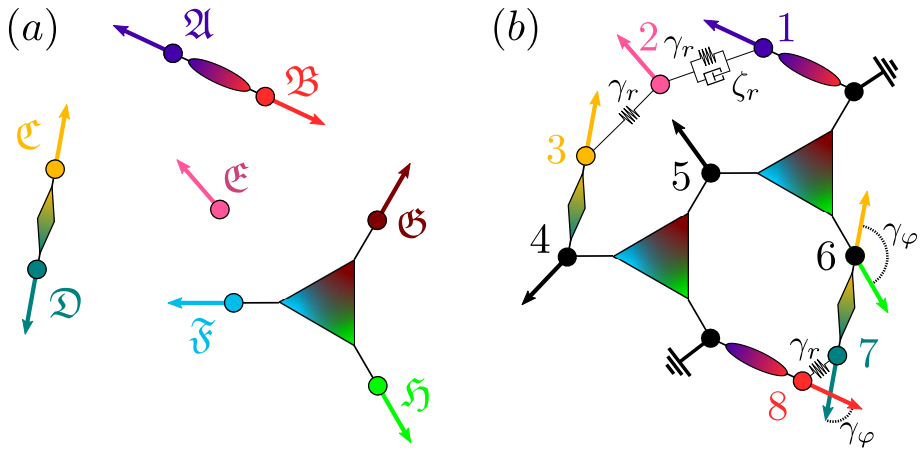

Figure 8.2:
a) Individual elements of type $\mathfrak{AB}$, $\mathfrak{CD}$, $\mathfrak{E}$, and $\mathfrak{FGH}$. b) Complex network of 8 mobile and 2 anchored nodes constructed from the elements shown in (a) as well as various coupling elements, see Sec. 8.1.2 for details.

The topology matrices corresponding to the network structure in Fig. 8.2b are

$$\begin{array}{c} \\ 1 \\ 2 \\ 3 \\ 4 \\ 5 \\ 6 \\ 7 \\ 8 \end{array} \begin{array}{c} \begin{array}{cccccccc} \mathfrak{A} & \mathfrak{B} & \mathfrak{C} & \mathfrak{D} & \mathfrak{E} & \mathfrak{F} & \mathfrak{G} & \mathfrak{H} \end{array} \\ \begin{pmatrix} \mathbf{1}_{3\times3} & 0 & 0 & 0 & 0 & 0 & 0 & 0 \\ 0 & 0 & 0 & 0 & \mathbf{1}_{3\times3} & 0 & 0 & 0 \\ 0 & 0 & \mathbf{1}_{3\times3} & 0 & 0 & 0 & 0 & 0 \\ 0 & 0 & 0 & \mathbf{1}_{3\times3} & 0 & \mathbf{1}_{3\times3} & 0 & 0 \\ 0 & 0 & 0 & 0 & 0 & \mathbf{1}_{3\times3} & \mathbf{1}_{3\times3} & 0 \\ 0 & 0 & \mathbf{1}'_{4\times3} & 0 & 0 & 0 & 0 & \mathbf{1}_{4\times3} \\ 0 & 0 & 0 & \mathbf{1}_{3\times3} & 0 & 0 & 0 & 0 \\ 0 & \mathbf{1}_{3\times3} & 0 & 0 & 0 & 0 & 0 & 0 \end{pmatrix} \end{array} = \boldsymbol{\mathcal{T}}, \tag{8.28}$$

with

$$\mathbf{1}_{4\times3} \equiv \begin{pmatrix} 1 & 0 & 0 \\ 0 & 1 & 0 \\ 0 & 0 & 1 \\ 0 & 0 & 0 \end{pmatrix}, \quad \mathbf{1}'_{4\times3} \equiv \begin{pmatrix} 1 & 0 & 0 \\ 0 & 1 & 0 \\ 0 & 0 & 0 \\ 0 & 0 & 1 \end{pmatrix}. \tag{8.29}$$

Eq. 8.28 specifies that the network node 1 is of type $\mathfrak{A}$, node 2 of type $\mathfrak{E}$, node 3 of type $\mathfrak{C}$, node 7 of type $\mathfrak{D}$, and node 8 of type $\mathfrak{B}$. Moreover, end-points of type $\mathfrak{D}$ and $\mathfrak{F}$ form node 4 after the DDF, and similarly $\mathfrak{F}$ and $\mathfrak{G}$ form node 5. Network node 6 is special in the sense that it comprises four degrees of freedom, since the translational degrees of freedom of the end-points of type $\mathfrak{C}$ and $\mathfrak{H}$ are decimated, while the angular ones remain independent; this property is encoded in the matrices $\mathbf{1}_{4\times3}$ and $\mathbf{1}'_{4\times3}$ in Eq. 8.28. Two of the network nodes in Fig. 8.2b are anchored, i.e., they are externally held fixed: In the upper right, the node formed by end-points of type $\mathfrak{B}$ and $\mathfrak{G}$ is immobile and therefore does not enter the grand-stiffness matrix. The same applies to the network node in the lower left formed by end-points of type $\mathfrak{A}$ and $\mathfrak{H}$.

The only non-vanishing coupling matrices in the network shown in Fig. 8.2b are

$$\boldsymbol{\mathcal{C}}_{11} = -\boldsymbol{\mathcal{C}}_{12} = -\boldsymbol{\mathcal{C}}_{21} = \begin{pmatrix} \gamma_r - \mathrm{i}\,\omega\,\zeta_r & 0 & 0 \\ 0 & \gamma_r - \mathrm{i}\,\omega\,\zeta_r & 0 \\ 0 & 0 & 0 \end{pmatrix},$$

$$\boldsymbol{\mathcal{C}}_{22} = \begin{pmatrix} 2\gamma_r - \mathrm{i}\,\omega\,\zeta_r & 0 & 0 \\ 0 & 2\gamma_r - \mathrm{i}\,\omega\,\zeta_r & 0 \\ 0 & 0 & 0 \end{pmatrix}, \qquad \boldsymbol{\mathcal{C}}_{33} = -\boldsymbol{\mathcal{C}}_{23} = -\boldsymbol{\mathcal{C}}_{32} = \begin{pmatrix} \gamma_r & 0 & 0 \\ 0 & \gamma_r & 0 \\ 0 & 0 & 0 \end{pmatrix}, \tag{8.30}$$

$$\boldsymbol{\mathcal{C}}_{66} = \begin{pmatrix} 0 & 0 & 0 & 0 \\ 0 & 0 & 0 & 0 \\ 0 & 0 & \gamma_\varphi & -\gamma_\varphi \\ 0 & 0 & -\gamma_\varphi & \gamma_\varphi \end{pmatrix}, \qquad \boldsymbol{\mathcal{C}}_{77} = \boldsymbol{\mathcal{C}}_{88} = -\boldsymbol{\mathcal{C}}_{78} = -\boldsymbol{\mathcal{C}}_{87} = \begin{pmatrix} \gamma_r & 0 & 0 \\ 0 & \gamma_r & 0 \\ 0 & 0 & \gamma_\varphi \end{pmatrix},$$

and reflect the viscoelastic coupling indicated by springs and dashpots in Fig. 8.2b: The translational degrees of freedom of the network nodes 2 and 3 are harmonically coupled via the force constant γ_r, those of the network nodes 1 and 2 are in addition subject to internal friction with a friction coefficient ζ_r. In addition, the translational degrees of freedom of the network nodes 7 and 8 are harmonically coupled via the force constant γ_r and the angular ones via the torque constant γ_φ. The latter is also the case for the two angular degrees of freedom of network node 6, which resembles node 2 in Fig. 8.1c, where translational degrees of freedom of $\mathfrak{B}$ and $\mathfrak{C}$ are decimated, while the angles are harmonically coupled.

Network response and boundary conditions

Once all elements of $\boldsymbol{\mathcal{G}}(\omega)$ for a specific frequency ω are calculated according to Eq. 8.21, the dynamic force balance in the network reads

$$\begin{pmatrix} \boldsymbol{F}_1(\omega) \\ \boldsymbol{F}_2(\omega) \\ \vdots \\ \boldsymbol{F}_N(\omega) \end{pmatrix} = \boldsymbol{\mathcal{G}}(\omega) \cdot \langle \begin{pmatrix} \boldsymbol{R}_1(\omega) \\ \boldsymbol{R}_2(\omega) \\ \vdots \\ \boldsymbol{R}_N(\omega) \end{pmatrix} \rangle. \tag{8.31}$$

The linear force response in the network

$$\langle \begin{pmatrix} \boldsymbol{R}_1(\omega) \\ \boldsymbol{R}_2(\omega) \\ \vdots \\ \boldsymbol{R}_N(\omega) \end{pmatrix} \rangle = \boldsymbol{\mathcal{J}}(\omega) \cdot \begin{pmatrix} \boldsymbol{F}_1(\omega) \\ \boldsymbol{F}_2(\omega) \\ \vdots \\ \boldsymbol{F}_N(\omega) \end{pmatrix}, \tag{8.32}$$

is encoded in the grand linear response matrix $\boldsymbol{\mathcal{J}}(\omega)$, which is obtained by inversion of $\boldsymbol{\mathcal{G}}(\omega)$.

Individual entries of the grand-response matrix $\boldsymbol{\mathcal{J}}(\omega)$ or linear combinations thereof describe the dynamic linear force response of the nodes to a given external force distribution on the network. For example, $\boldsymbol{\mathcal{J}}_{ii}(\omega)$ specifies the frequency dependent translational and orientational response of the network node i to a force and torque acting on it, and $\boldsymbol{\mathcal{J}}_{ji}(\omega)$ quantifies the response of the network node j to a force and torque on node i. Similarly, linear shear, compression and twist response between network nodes i and j are encoded in the entries of $(\boldsymbol{\mathcal{J}}_{ii}(\omega) + \boldsymbol{\mathcal{J}}_{jj}(\omega) - \boldsymbol{\mathcal{J}}_{ij}(\omega) - \boldsymbol{\mathcal{J}}_{ji}(\omega))/2$. This also means that if external forces are applied

to a subset of the nodes only and only the motion of these nodes is of interest, the dimension of the grand-response matrix $\mathcal{J}$ can be reduced by retaining only the corresponding rows and columns as is easily seen from Eq. 8.32.

As has been mentioned above, anchored nodes do not enter the grand-stiffness matrix $\mathcal{G}$. Inversely, the process of anchoring nodes in the network is equivalent to discarding the corresponding rows and columns from the grand-stiffness matrix $\mathcal{G}$ in Eq. 8.31. Note that the operations of reducing the dimension of a matrix and inverting it do in general not commute, which reflects the fact that the two kinds of boundary conditions, no external force vs no motion, are in general different.

8.1.3 Dynamic convolution theory in a nutshell

We summarize the steps to be taken to calculate the linear force response in networks of arbitrary topology and complexity:

1. Identify the network's building blocks, i.e., the isolated elements of type $\mathfrak{AB}$, $\mathfrak{CD}$, etc., and determine their linear response matrices $\boldsymbol{J}_{\mathfrak{ab}}(\omega)$, which depend on the average orientation of the element in the network according to Eq. 8.5. Linear response properties can be obtained either from theory or based on equilibrium simulations using the fluctuation-dissipation theorem (FDT). For elements with internal symmetries, the linear response matrices $\boldsymbol{J}_{\mathfrak{ab}}(\omega)$ can be calculated from the smaller set of independent response functions using Eq. 8.7.

2. Identify the network's structure, i.e., the number of non-anchored network nodes N, the network's topology matrices $\boldsymbol{\mathcal{T}}_{i\mathfrak{a}}$ and the coupling matrices $\boldsymbol{\mathcal{C}}_{ij}$.

3. For each frequency ω of interest:
   a) Calculate the entries of the grand dynamic stiffness matrix $\mathcal{G}$ according to Eq. 8.21.
   b) Obtain the grand-response matrix $\mathcal{J} = \mathcal{G}^{-1}$ by numerical inversion and calculate the network's response to an external force/torque distribution via Eq. 8.32.

Multi-step approach

The computational costs for the inversion of the grand-stiffness matrix quickly increase with its dimension. Under certain conditions, the following multi-step approach based on the discussion in Sec. 8.1.2 may be more efficient but still exact:

1. Divide the overall network into smaller subnetworks. For each of these subnetworks:
   a) Calculate the response matrix $\mathcal{J}_{\text{sub}}$ as described above.
   b) Obtain a matrix $\mathcal{J}'_{\text{sub}}$ of reduced dimension by discarding rows and columns in $\mathcal{J}_{\text{sub}}$, which correspond to network nodes, which fulfill all of the following properties:
      - These nodes are not connected to elements of other subnetworks in any of the following steps.
      - No external forces are applied to these nodes.
      - Resolving the response of these nodes is not desired.

See Sec. 8.1.2 for why the reduction in dimensionality is possible under these circumstances.

2. Use the subnetwork matrices of reduced dimension $\{\mathcal{J}'_{\text{sub}}\}$ as input to calculate the grand-response matrix of the overall network.

The above procedure can be applied recursively, i.e., the grand-response matrix obtained in (2.) can be used as input $\mathcal{J}_{\text{sub}}$ in (1.a) to study even larger structures. This multi-step approach is of particular interest for hierarchical structures, in which the number of relevant network nodes does not considerably increase in each iteration step.

8.1.4 Applicability and limitations of the dynamic convolution theory

The DCT framework being very general, it can serve to study the micro- and macrorheological properties of a whole spectrum of systems including colloidal suspensions as well as cytoskeletal networks. While pairwise (hydrodynamic) interactions between the colloids are the constitutive elements in the first case, the linear force response properties of polymeric meshworks result from the characteristics of the isolated filaments and the crosslinkers as is shown in Sec. 8.3.

As mentioned above, the constraints at the network nodes are enforced *on average* only and the force balance is based on *average* oscillation amplitudes within the DCT (Eq. 8.21 and 8.31). The DCT can therefore be viewed as a dynamic mean-field theory, which is exact for linear elements, for which the linear force response (Eq. 8.1) is valid for arbitrary force amplitudes, as well as for deterministic dynamics, where $\boldsymbol{R}_i = \langle \boldsymbol{R}_i \rangle$. If nonlinear contributions are small, the DCT generally provides a good first-order approximation, for which correction terms can systematically be derived, cf. Sec. 6.4.2.

Being a linear theory, the range of validity of the DCT is determined by the linear response regime of the network's constituents. For networks of nonlinear elements such as semiflexible filaments, the DCT can only provide insight into the linear response around the equilibrium structure of the network, which however can easily be determined using well-established techniques [309]. For the case of a polymer network under external prestress, the dynamic linear force response functions of the filaments parametrically depend on the applied force. Similarly, the DCT does not account for changes of the overall orientation of individual elements, specified by the angle Φ in the Eqs. 8.5 and 8.7 and in Fig. 8.1a, due to thermal forces. Consequently, the DCT provides an accurate estimate over the full frequency range only as long as the fluctuations $\boldsymbol{R}_i$ are small enough so that changes in the orientation angles Φ remain negligible.

The effects of orientational changes can be taken into account by averaging the network's grand-response matrix $\mathcal{J}$ over the equilibrium distribution of the components' orientations. Note however that the predictions of the DCT are accurate only for frequencies, which are larger than the typical (macroscopic) reorientation frequencies of the network, see Sec. 8.1.5 for an explicit example. Similarly, the force response of networks with multiple topologies can be studied using the DCT by averaging the elements of the grand-response matrix over the equilibrium ensemble of different network topologies. Again, this approach is restricted to the range of frequencies, which are larger than the frequencies at which topological changes of the network occur.

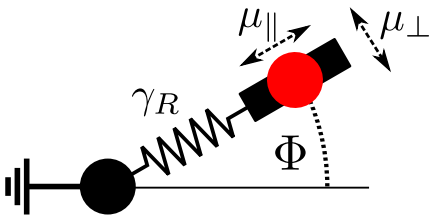

Figure 8.3:
Schematic of the simple model system treated in Sec. 8.1.5: The node is characterized by the anisotropic mobilities $\mu_\parallel$ and $\mu_\perp$ for motion along the two axis of the local coordinate frame (defined by the angle Φ). The node is attached via a harmonic spring of strength γ_R and equilibrium length R_0 to an anchored reference point, around which it is free to rotate.

8.1.5 Reorientation of a mechanical element

As discussed in Sec. 8.1.4, one important assumption for the derivation of the DCT is that the size of the thermal and force-induced fluctuations of the mechanical components are so small that changes of the overall element orientations can be neglected. If this is not the case, one can average the resulting grand-response matrix $\mathcal{J}$, which explicitly depends on the spatial orientations of the individual components (Eq. 8.5), over the equilibrium distribution of the orientations. Note however that this approach is adequate only in the frequency range $\omega \gg \omega_{\text{orient}}$, where $1/\omega_{\text{orient}}$ is the smallest time scale for the reorientation of individual components in the network.

As a simple example, we consider the system schematically drawn in Fig. 8.3: The mobile end-point is connected via a harmonic spring of equilibrium length R_0 and spring constant γ_R to the origin of the coordinate frame and is free to rotate around it. The motion of the object along the two local axes $(\parallel, \perp)$ is characterized by the mobilities $\mu_\parallel$ and $\mu_\perp$ respectively. The linear force response functions in the local coordinate frame are obtained from the linear, overdamped equations of motion and read

$$J^{\parallel\parallel}(\omega) = \mu_\parallel \frac{\mu_\parallel \gamma_R + \mathrm{i}\,\omega}{(\mu_\parallel \gamma_R)^2 + \omega^2}, \qquad J^{\perp\perp}(\omega) = \frac{\mathrm{i}\,\mu_\perp}{\omega}. \tag{8.33}$$

In the following, we focus on situations where $R_0^2 \gamma_R / (k_\mathrm{B} T) \gg 1$, i.e., we assume that the magnitude of the thermal equilibrium fluctuations along the $\parallel$-direction are much smaller than the equilibrium length of the spring R_0. Under these conditions, the problem can be solved analytically, since the orientational dynamics captured by the angle $\Phi \approx r_\perp / R_0$ and the radial dynamics of $R \equiv R_0 + r_\parallel$ decouple. The Green's functions for (i) free angular diffusion on the periodic interval $[0, 2\pi)$ with diffusion coefficient $D_\Phi \approx k_\mathrm{B} T \mu_\perp / R_0^2$ and (ii) overdamped elongational diffusion with mobility $\mu_\parallel$ in a harmonic potential of strength γ_R centered around R_0 can be obtained analytically [36, 38]. It is then straightforward to calculate the equilibrium correlation function for the spatial coordinates

$$x = R\cos\Phi, \qquad y = R\sin\Phi, \tag{8.34}$$

yielding

$$\begin{aligned}\langle x(t)x(0)\rangle_{R,\Phi} = \langle y(t)y(0)\rangle_{R,\Phi} &= \langle R(t)R(0)\rangle_R \langle \cos(\Phi(t))\cos(\Phi(0))\rangle_\Phi \\ &= \frac{1}{2}\left(\frac{k_\mathrm{B}T}{\gamma_R}\mathrm{e}^{-\mu_\parallel\gamma_R t} + R_0^2\right)\mathrm{e}^{-D_\Phi t}.\end{aligned} \tag{8.35}$$

Using the FDT, we deduce the frequency dependence of the linear force response functions

$$J^{xx}(\omega) = J^{yy}(\omega) = \frac{1}{2}\left(\mu_\parallel\frac{\mu_\parallel\gamma_R + \mathrm{i}\,\omega}{(\mu_\parallel\gamma_R)^2+\omega^2} + \mu_\perp\frac{\mu_\perp k_\mathrm{B}T/R_0^2 + \mathrm{i}\,\omega}{(\mu_\perp k_\mathrm{B}T/R_0^2)^2+\omega^2}\right). \tag{8.36}$$

As is easily seen, the above result indeed reduces to one of the Boltzmann averaged diagonal entries of Eq. 8.7

$$J^{xx}(\omega) \approx \frac{1}{2}\left(J^{\parallel\parallel}(\omega) + J^{\perp\perp}(\omega)\right) = \frac{1}{2\pi}\int_0^{2\pi}\mathrm{d}\Phi\ \left(J^{\parallel\parallel}(\omega)\cos^2\Phi + J^{\perp\perp}(\omega)\sin^2\Phi\right) \tag{8.37}$$

in the range of frequencies $\omega \gg \omega_\mathrm{orient} \equiv \mu_\perp k_\mathrm{B}T/R_0^2$, where the right hand side of Eq. 8.37 corresponds to the Boltzmann average over the uniformly distributed angle Φ. For low frequencies, on the other hand, temperature dependent contributions are found in Eq. 8.36, which are not captured by the approximate expression in Eq. 8.37 and which point to the nonlinear intrinsic nature of the system, cf. Sec. 6.1.2.

Similarly, the high-frequency response of the system in Fig. 8.3, if preferentially oriented due to an external potential depending on Φ, would result from the corresponding Boltzmann-weighted average of Eq. 8.7 with internal response functions given in Eq. 8.33.

8.2 Dynamics of Isolated Semiflexible Filaments

We resolve the various linear force response functions of isolated semiflexible polymers, which are then used in Sec. 8.3 to study the rheological properties of extended network structures.

8.2.1 Brownian dynamics simulations

Similarly as in Sec. 7.2.1, semiflexible filaments are modeled as standard bead-spring polymers, in which the M beads representing individual monomers interact via the wormlike chain (WLC) potential

$$U_\mathrm{WLC} = \frac{\gamma}{4a}\sum_{i=1}^{M-1}(|\boldsymbol{r}_{i+1}-\boldsymbol{r}_i| - 2a)^2 + \frac{\kappa}{2a}\sum_{i=2}^{M-1}(1-\cos\theta_i), \tag{8.38}$$

where the stretching elasticity is denoted by γ and the bending stiffness by κ, yielding a persistence length $l_\mathrm{p} \equiv \kappa/k_\mathrm{B}T$ in three dimensions. In Eq. 8.38, the monomer positions are denoted by $\boldsymbol{r}_i$ and the angles between consecutive bonds by θ_i, similarly as in Sec. 7.2.1. In the BD simulations, the beads move according to the overdamped and free-draining stochastic equations of motion

$$\frac{d\boldsymbol{r}_i(t)}{dt} = -\mu_i\frac{\partial U_\mathrm{WLC}(\boldsymbol{r}_1,\ldots,\boldsymbol{r}_M)}{\partial\boldsymbol{r}_i} + \boldsymbol{v}_i^\mathrm{st}(t), \qquad i\in\{1,\ldots,M\}, \tag{8.39}$$

$$\langle \boldsymbol{v}_i^{\mathrm{st}}(t) \otimes \boldsymbol{v}_j^{\mathrm{st}}(t') \rangle = 2k_{\mathrm{B}}T\mu_i\delta_{ij} \overleftrightarrow{\mathbf{1}}\, \delta(t-t'), \qquad i,j \in \{1,\ldots,N\}, \tag{8.40}$$

where $k_{\mathrm{B}}T$ denotes the thermal energy and $\boldsymbol{v}_i^{\mathrm{st}}$ the stochastic contribution to the velocity of bead i. The beads' self-mobilities are

$$\mu_i = \mu_0 \left(1 + \delta_{i1} + \delta_{iM}\right), \tag{8.41}$$

where the Stokes self-mobility of a sphere of radius a in a solvent of shear viscosity η_0 is $\mu_0 \equiv 1/(6\pi\eta_0 a)$ [16] and δ_{ij} denotes the Kronecker symbol. The end-momoners in the simulation are modeled as beads of radius $a/2$ and all others as beads of radius a; in this way, the serial alignment of several polymers gives rise to a longer polymer with uniform mobility μ_0 for all monomers except the ones at the two ends.

The equations of motion (Eq. 8.39) together with the WLC potential (Eq. 8.38) are intrinsically nonlinear equations in the monomer coordinates. However, in the case of stiff filaments with $\kappa/(Lk_{\mathrm{B}}T) = l_{\mathrm{p}}/L \gg 1$, the linearization of the equations of motion around the state of minimal configurational energy yields the dominant contribution to the linear response function of the filament as is shown in Sec. 8.2.3.

In contrast, Gaussian polymers described by the potential

$$U_{\mathrm{gauss}} = \frac{3k_{\mathrm{B}}T}{2r_0^2} \sum_{i=1}^{M-1} \left|\boldsymbol{r}_{i+1} - \boldsymbol{r}_i\right|^2, \tag{8.42}$$

with average squared bond lengths r_0^2, yield linear equations of motion. The dynamic force response of a Rouse polymer is consequently purely linear and independent of the thermal noise strength, cf. Sec. 6.1.2.

8.2.2 Correlation analysis

We identify the first and the Mth monomer with the points $\mathfrak{A}$ and $\mathfrak{B}$ of the equivalent mechanical element $\mathfrak{AB}$: The $\|$-direction of the local coordinate frame is then defined by the filament's end-to-end vector $\boldsymbol{r}_M - \boldsymbol{r}_1$ and the end-orientations are specified by the end-tangents, i.e., the orientations of the bonds between the two terminal beads $\boldsymbol{r}_1 - \boldsymbol{r}_2$ and $\boldsymbol{r}_M - \boldsymbol{r}_{M-1}$.

As explained in Sec. 8.1.1, due to symmetry there are only eight independent and non-vanishing linear response functions in the local coordinate frame: the four self-response functions $J_{\mathfrak{BB}}^{\|\|}$, $J_{\mathfrak{BB}}^{\perp\perp}$, $J_{\mathfrak{BB}}^{\varphi\varphi}$, $J_{\mathfrak{BB}}^{\perp\varphi}$ as well as the cross-response functions $J_{\mathfrak{AB}}^{\|\|}$, $J_{\mathfrak{AB}}^{\perp\perp}$, $J_{\mathfrak{AB}}^{\perp\varphi}$, and $J_{\mathfrak{AB}}^{\varphi\varphi}$. In the absence of thermal forces ($k_{\mathrm{B}}T = 0$), these are simply obtained by linearizing the equations of motion (Eq. 8.39) around the state of minimal configurational energy $U_{\mathrm{WLC}} = 0$ corresponding to a straight polymer configuration with relaxed bond lengths, cf. Sec. 6.1.2. This set of response functions is denoted as athermal in the following. At finite thermal noise strength, linear response functions are obtained from the (cross-)correlations in the local coordinate frame resolved from numerical simulations of Eq. 8.39

$$\tilde{\boldsymbol{C}}_{\mathfrak{ab}}(t) \equiv \left\langle \Delta\tilde{\boldsymbol{R}}_{\mathfrak{a}}(t) \otimes \Delta\tilde{\boldsymbol{R}}_{\mathfrak{b}}(t) \right\rangle = \left\langle \left(\tilde{\boldsymbol{R}}_{\mathfrak{a}}(t) - \tilde{\boldsymbol{R}}_{\mathfrak{a}}(0)\right) \otimes \left(\tilde{\boldsymbol{R}}_{\mathfrak{b}}(t) - \tilde{\boldsymbol{R}}_{\mathfrak{b}}(0)\right) \right\rangle, \tag{8.43}$$

where the reference time has been set to 0 for simplicity. Similarly as in Sec. 2.2.2, the temporal increments of the local coordinates (denoted by a tilde) are defined via the integral over the velocities

$$\Delta\tilde{\boldsymbol{R}}_{\mathfrak{a}}(t) \equiv \begin{pmatrix} \Delta r_{\parallel}^{\mathfrak{a}}(t) \\ \Delta r_{\perp}^{\mathfrak{a}}(t) \\ \Delta\varphi^{\mathfrak{a}}(t) \end{pmatrix} = \int_0^t \mathrm{d}t' \begin{pmatrix} \dot{r}_{\parallel}^{\mathfrak{a}}(t') \\ \dot{r}_{\perp}^{\mathfrak{a}}(t') \\ \dot{\varphi}^{\mathfrak{a}}(t') \end{pmatrix}, \qquad \mathfrak{a} \in \{\mathfrak{A}, \mathfrak{B}\}, \tag{8.44}$$

in the coordinate frame $(\parallel, \perp)$, which is defined by the filament's end-to-end orientation and fluctuates over time. See Fig. 8.4 for a simulation snapshot showing the six fluctuating time series forming the basis for computing the correlations in Eq. 8.43. We make use of the FDT

$$\tilde{\boldsymbol{J}}_{\mathfrak{a}\mathfrak{b}}(t) = \begin{cases} \frac{1}{2k_{\mathrm{B}}T}\frac{\mathrm{d}}{\mathrm{d}t}\tilde{\boldsymbol{C}}_{\mathfrak{a}\mathfrak{b}}(t), & t > 0, \\ 0, & t < 0, \end{cases} \qquad \mathfrak{a}, \mathfrak{b} \in \{\mathfrak{A}, \mathfrak{B}\}, \tag{8.45}$$

to convert the information content of the correlation functions into linear response functions. Note the factor $-1/2$ in the above formulation of the FDT compared to Eq. 5.2, which involves the correlations of the positional variables rather than the correlations of the temporal increments in the coordinates considered here.

In practice, each of the correlation functions in Eq. 8.43 is approximated by an expression of the type

$$C(t) \approx c_0\,|t| + \sum_{j=1}^{n} c_j(1 - \mathrm{e}^{-\lambda_j|t|}), \tag{8.46}$$

where c_0, c_1, λ_1, c_2, λ_2, etc. are constants used as fit parameters. According to the FDT (Eq. 8.45), the corresponding response functions in frequency space take the form

$$J(\omega) \approx \frac{\mathrm{i}\,c_0}{2k_{\mathrm{B}}T\omega} + \frac{1}{2k_{\mathrm{B}}T}\sum_{j=1}^{n}\frac{c_j\lambda_j}{\lambda_j - \mathrm{i}\,\omega}. \tag{8.47}$$

Given the $\mathfrak{A}$-$\mathfrak{B}$-symmetry of the filaments, odd relaxation modes along the polymer contour yield contributions of opposite signs to the self- and cross-correlation functions in Eq. 8.43. The correlations of symmetric/antisymmetric combinations of the end-point coordinates therefore reflect contributions of the even/odd normal modes only. Fitting these combinations rather than the self- and cross-correlation functions is advisable, since the number of independent fit parameters in each fit is reduced and the results consequently more reliable [317].

8.2.3 Linear force response of single filaments

We consider filaments of M beads, corresponding to an (average) contour length $L = (M-1)2a$; the stretching elasticity is set to $\gamma = 400\ k_{\mathrm{B}}T/a$ and the bending stiffness to the value $\kappa = 100\ k_{\mathrm{B}}T\,a$ expected for an isotropic elastic cylinder, cf. Eq. 7.36. A BD simulation snapshot and sample trajectories of the six fluctuating degrees of freedom of the polymer ends are shown in Fig. 8.4, the corresponding movie is included as supplementary material [318].

For short filaments of $M = 4$ beads with a corresponding ratio of persistence to contour length $l_{\mathrm{p}}/L \approx 16.7$, self- and cross-correlation functions from 50 independent BD simulations of up to 10^{11} integration steps of duration $10^{-4}\ a^2/(\mu_0 k_{\mathrm{B}}T)$ are shown in Fig. 8.5 together with best fits to the data (Eq. 8.46) displayed as black lines. Real and imaginary parts of the resulting linear force response functions in frequency space (Eq. 8.47) are shown as red and blue

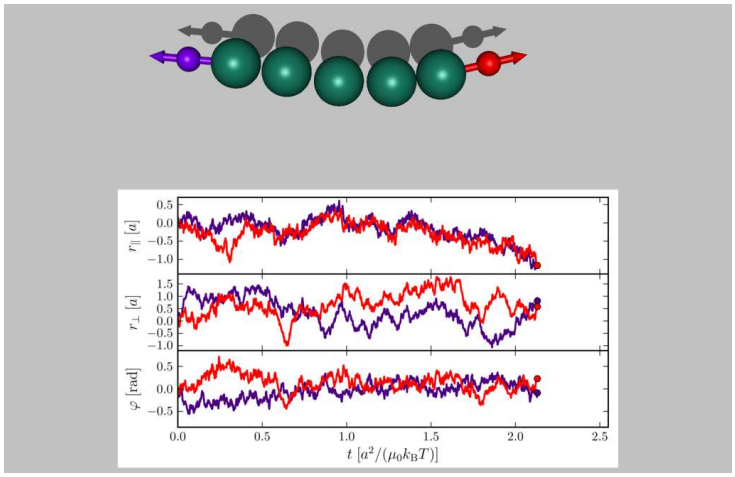

Figure 8.4:
Snapshot of a BD simulation of $M = 7$ beads and $l_p/L \approx 8.3$ including the six fluctuating end-point coordinates. The corresponding movie is included as supplementary material [318].

lines in Fig. 8.6, where positive values are displayed by solid and negative by dashed lines. In the high-frequency range ($\omega \to \infty$), cross-response functions relating force and displacements on different ends of the filament are clearly suppressed compared to the corresponding self-response functions revealing that the effect of forces/torques is mostly restricted to the direct proximity of the respective monomer. In the quasi static limit ($\omega \to 0$) in turn, forces and torques induce translations and/or rotations of the entire filament and self- and cross-response functions therefore are of comparable magnitude.

Athermal force response functions from linearizing the equations of motion around the perfectly straight polymer configuration with relaxed bond lengths are included as orange and light blue lines in Fig. 8.6; in fact, they are almost perfectly superimposed by the red and blue lines from BD simulations discussed above. Minor differences are discernible in the low-frequency regime of the parallel response, as is best seen in the insets of Fig. 8.6a displaying an 8-fold magnification of the data. These deviations are due to contributions of bending fluctuations to the parallel response, a finite temperature effect, which by definition is not contained in the athermal response functions. For the force response involving the perpendicular and orientational degrees of freedom in Fig. 8.6b-d, both sets of response functions agree even better; the residual differences in the cross-response functions at higher frequencies are attributed to inaccuracies in the fit parameters. In summary, the comparison of both sets of response functions certifies that temperature dependent contributions are small and restricted to the parallel direction as expected for such a high ratio l_p/L. We therefore expect the DCT to produce accurate results as discussed in Sec. 6.4.2. The set of linear force response functions for a longer filament ($L/a = 12$) are shown in Fig. 8.8 and discussed in Sec. 8.3.1.

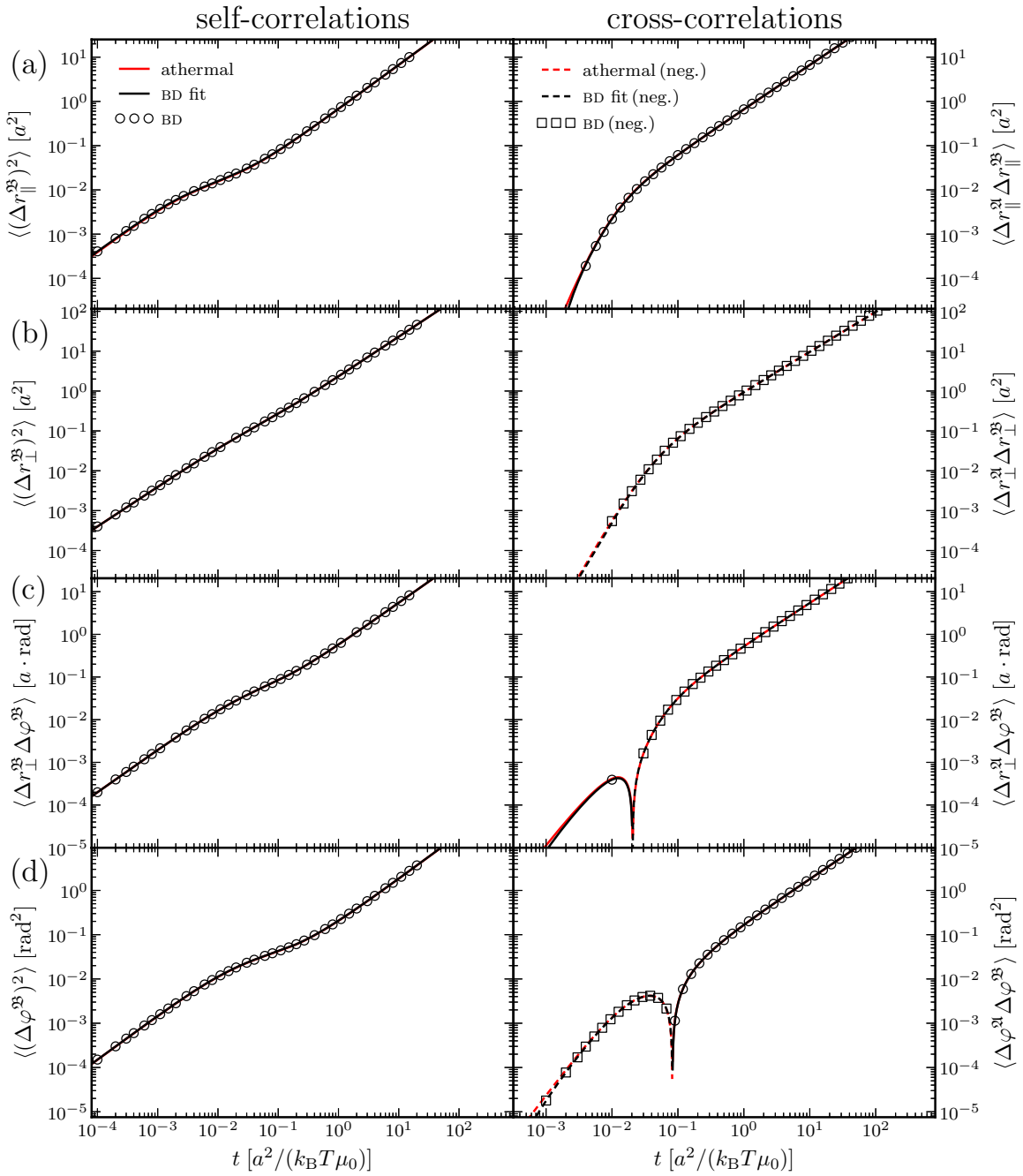

Figure 8.5:
Temporal correlations (Eq. 8.43) of an isolated semiflexible filament of contour length $L/a = 6$ (4 beads) and persistence length $l_\mathrm{p}/a = 100$. *Symbols* denote estimates from numerical simulations and *black lines* best fits to the data as described in Sec. 8.2.2, *red lines* denote athermal response functions (mostly superimposed by the BD fits). Positive/negative values are displayed as *circles/squares* and *solid/dashed lines*, respectively. The estimated relative errors of self-/cross-correlations from simulations are less than 0.5 %/10 %.

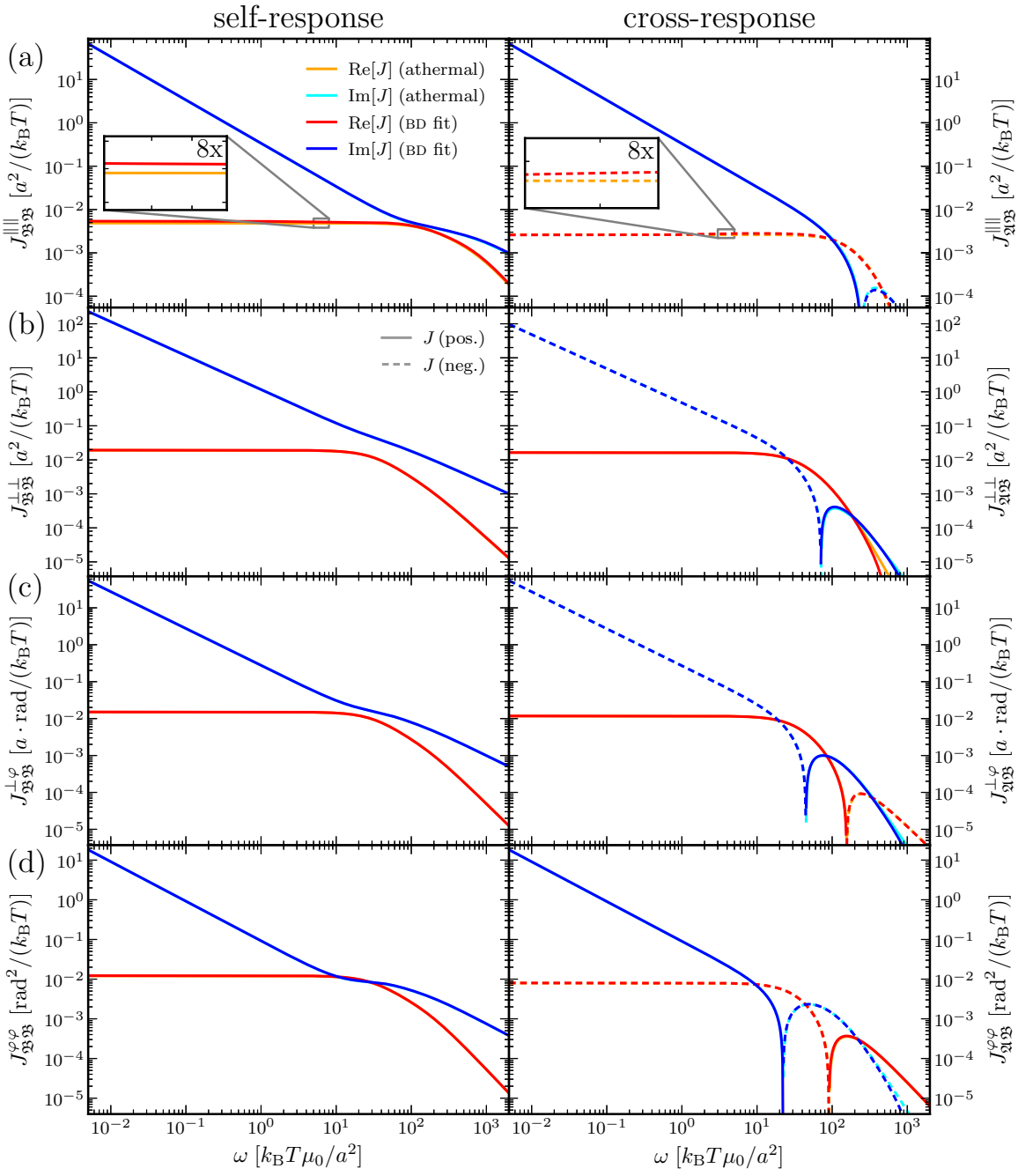

Figure 8.6:
Self- and cross-response of an isolated semiflexible filament of contour length $L/a = 6$ and $l_p/L \approx 16.7$: Linear response functions obtained from the correlation functions in Fig. 8.5 via the FDT (Eq. 8.45) are compared to the athermal ones, which are almost perfectly superimposed by the BD data. Positive/negative values are displayed as *solid/dashed lines*. Magnified parts of the graphs are shown in the insets.

8.3 Semiflexible Polymer Networks

Starting from semiflexible filaments described in Sec. 8.2, we use the DCT of Sec. 8.1 to resolve the viscoelastic properties of polymeric networks. We discuss the serial alignment of two filaments as a test case in Sec. 8.3.1 and calculate micro- and macrorheological properties of extended crosslinked polymeric networks in the Secs. 8.3.2 and 8.3.3.

As is known from studies on reconstituted systems of filamentous actin and various actin binding proteins (ABPs), the types of crosslinks and network structures formed depend drastically on the kind and concentration of the ABPs [80, 81]. As an example, the degrees of freedom of actin filaments crosslinked by heavy meromyosin (HMM) are only loosely coupled [81], corresponding to the situation schematically shown in Fig. 8.1b with finite γ_r but small or vanishing γ_φ. In small concentrations, ABPs such as α-actinin or filamin tend to form crosslinks as depicted in Fig. 8.1c, where translational degrees of freedom are tightly coupled but fibers are not preferentially oriented [81], corresponding to a small or vanishing value of γ_φ. In turn, ABPs such as fascin and Arp2/3 bind actin fibers under a preferential angle of 0° and 70°, respectively [319, 320] and can therefore be modeled via large values of γ_φ.

In the following, we consider network nodes as schematically shown in Fig. 8.1c, where the translational degrees of freedom of all filament ends at a given node are decimated ($\gamma_r \to \infty$) and the degree of coupling between the end-tangent orientations depends on the coupling strength γ_φ. We consider three different cases: (i) $\gamma_\varphi = 0$ called *free*, (ii) non-vanishing but finite values of γ_φ called *flex*, and (iii) the limiting case $\gamma_\varphi \to \infty$ called *fix* (corresponding to Fig. 8.1d).

8.3.1 Test case: Concatenating two short filaments

As a test of the DCT, we concatenate two semiflexible filaments of contour length $L/a = 6$ (4 beads) covered in Sec. 8.2 and compare the force response predictions to results from explicit simulations of a semiflexible filament of contour length $L/a = 12$ (7 beads). The DCT network results from the serial alignment of two identical elements as schematically indicated in Fig. 8.7 and, depending on the type of crosslinker, formally corresponds to the topology matrices

$$\begin{array}{c} \\ 1 \\ 2 \\ 3 \end{array}\!\!\begin{array}{c} \begin{array}{cc} \mathfrak{A} & \mathfrak{B} \end{array} \\ \begin{pmatrix} \mathbf{1}_{3\times3} & 0 \\ \mathbf{1}_{3\times3} & \mathbf{1}_{3\times3} \\ 0 & \mathbf{1}_{3\times3} \end{pmatrix} \end{array} = \boldsymbol{\mathcal{T}}^{\,fix}, \qquad \begin{array}{c} \\ 1 \\ 2 \\ 3 \end{array}\!\!\begin{array}{c} \begin{array}{cc} \mathfrak{A} & \mathfrak{B} \end{array} \\ \begin{pmatrix} \mathbf{1}_{3\times3} & 0 \\ \mathbf{1}'_{4\times3} & \mathbf{1}_{4\times3} \\ 0 & \mathbf{1}_{3\times3} \end{pmatrix} \end{array} = \boldsymbol{\mathcal{T}}^{\,flex} = \boldsymbol{\mathcal{T}}^{\,free}, \tag{8.48}$$

where the matrices $\mathbf{1}_{4\times3}$ and $\mathbf{1}'_{4\times3}$ are defined in Eq. 8.29. For crosslinkers of type *flex* and *free*, the node 2 thus consists of two translational and two angular degrees of freedom. For a crosslinker of type *flex*, the latter ones are coupled by the only non-vanishing coupling matrix

$$\boldsymbol{\mathcal{C}}_{22}^{\,flex} \equiv \begin{pmatrix} 0 & 0 & 0 \\ 0 & 0 & 0 \\ 0 & \gamma_\varphi & -\gamma_\varphi \\ 0 & -\gamma_\varphi & \gamma_\varphi \end{pmatrix}. \tag{8.49}$$

In the following, we compare the frequency dependence of the eight linear response functions of the composed filament resulting from the DCT calculation to those from explicit BD simulations and to the set of athermal response functions arising from linearizing the equations of motion along the polymer conformation of minimal configurational energy.

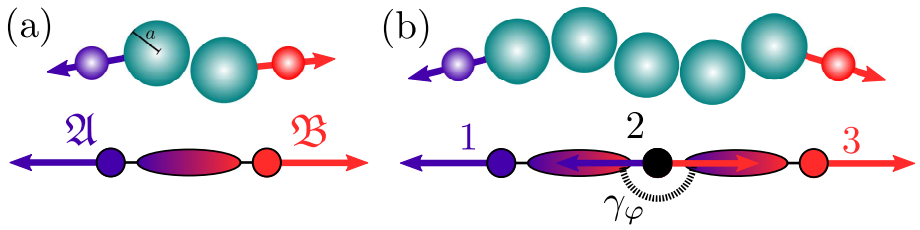

Figure 8.7:
a) BD and DCT representations of a short semiflexible polymer consisting of 4 beads and contour length $L/a = 6$. b) BD representation of a semiflexible filament of contour length $L/a = 12$ and the corresponding DCT representation resulting from concatenating two of the short filaments from (a). The end-tangent orientations at the central node are coupled by a harmonic potential of strength γ_φ.

BD and athermal response functions are shown as lines in Fig. 8.8: Similarly as in Sec. 8.2.3, the athermal response functions are mostly superimposed by lines from BD simulations; noticeable differences are again restricted to the parallel response shown in Fig. 8.8a. The ratio of persistence to contour length $l_p/L \approx 8.3$ being reduced by a factor of 2 compared to Sec. 8.2.3, the deviations due to finite temperature contributions are more pronounced compared to those in Fig. 8.6a. In turn, the athermal response functions are again excellent estimates for the remaining response functions involving translations along the perpendicular direction and end-tangent orientations as is seen from Fig. 8.8b-d.

The DCT calculation is based on the response functions of the short filament ($L/a = 6$) as resolved from BD simulations (red and blue lines in Fig. 8.6). DCT results for the polymer of length $L/a = 12$ are shown as symbols in Fig. 8.8, where different colors correspond to different types of crosslinkers at the central network node in Fig. 8.7b: The crosslinker of type *flex* corresponds to an angular coupling strength $\gamma_\varphi = \kappa/2a = 50\ k_B T$ (red and blue symbols), a crosslinker of type *free* to the case of totally independent end-tagents, i.e., $\gamma_\varphi = 0$, (golden and light blue symbols), and a crosslinker of type *fix* to the limiting case $\gamma_\varphi \to \infty$ (brown and green symbols), which formally corresponds to the serial connection discussed in Sec. 8.1.2 with $\mathfrak{CD} = \mathfrak{AB}$.

The overall agreement between self- and cross-response functions from explicit simulations and from the DCT with the appropriately chosen value $\gamma_\varphi = \kappa/2a$ (*flex*, cf. Eq. 8.38) is excellent. Small deviations are only found in the low frequency range of the parallel response as is best seen in the insets of Fig. 8.8a, where the red circles are displaced from the red line. Note that the DCT results based upon the finite temperature BD response functions from Fig. 8.6 still are better than the athermal estimates, which are displayed as orange and light blue lines, cf. inset of Fig. 8.8a. The agreement between the blue/red symbols and lines in Fig. 8.8b-d corresponding to response functions involving translations along the perpendicular direction and end-tangent orientations is excellent.

The DCT estimates corresponding to crosslinkers of type *fix* and *free* do only agree with the parallel BD response functions in Fig. 8.8a, where brown/golden and green/light blue symbols are hidden behind red/blue symbols corresponding to a crosslinker of type *flex*. Indeed, the parallel response of the filament is independent of the crosslinker type due to symmetry. In contrast, the other response properties of the filament in Fig. 8.8b-d deviate from the DCT estimates for crosslinkers of type *fix* and *free*. Deviations for the crosslinker of type *fix* are mostly quantitative and highlighted in the insets of Fig. 8.8b-d showing magnified parts of the response functions at intermediate frequencies. For the crosslinker of type *free* on the other hand,

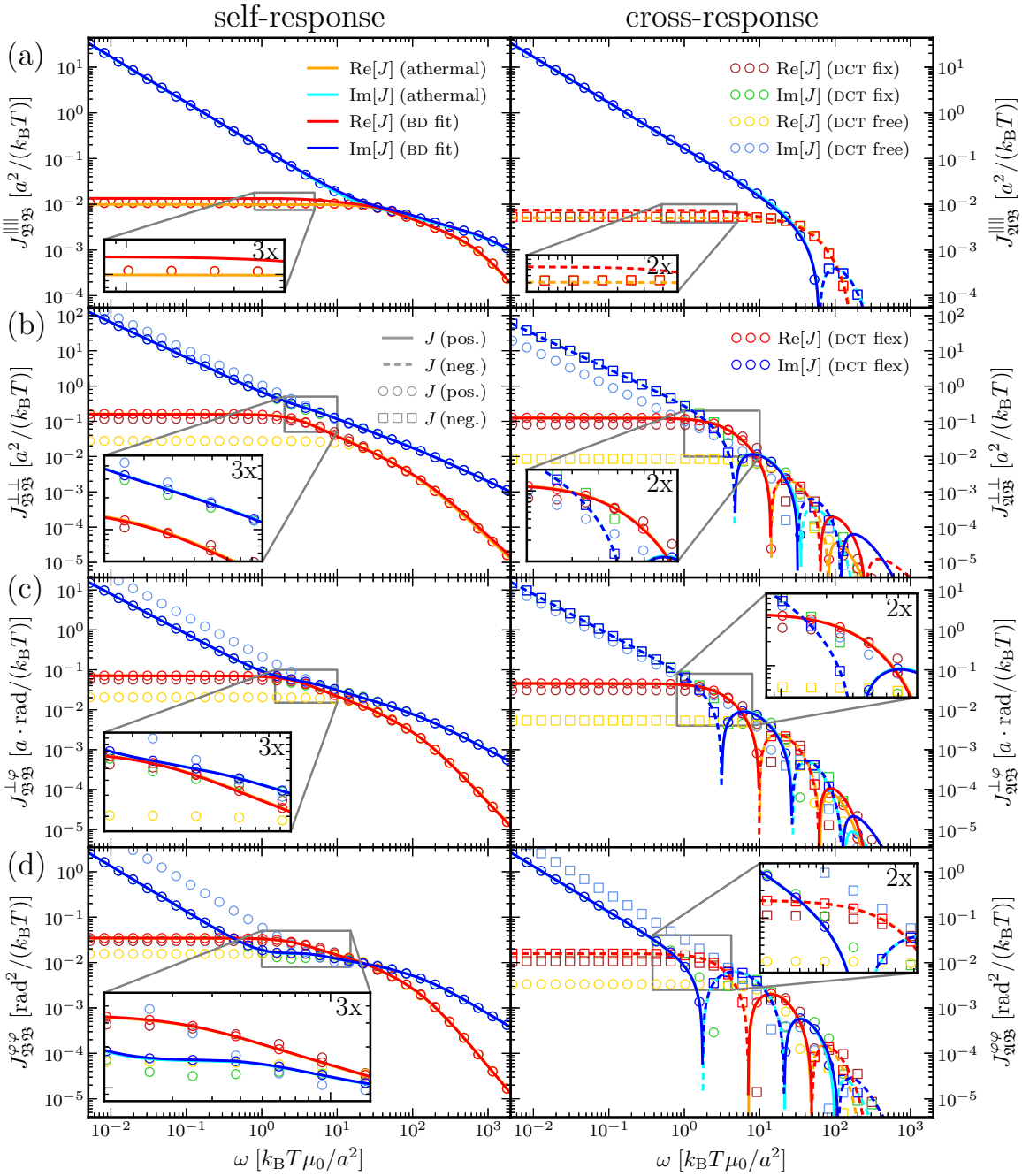

Figure 8.8:
Self- and cross-response of an isolated semiflexible filament of contour length $L/a = 12$ (7 beads) and $l_p/L \approx 8.3$: *Lines* show the response functions from BD correlation functions (*red and blue lines*, correlation data not shown) and athermal ones (*orange and light blue lines*, mostly superimposed by the BD data). *Symbols* denote DCT estimates based on the BD results of Fig. 8.6 for the serial alignment of two filaments of contour length $L/a = 6$ as indicated in Fig. 8.7b with crosslinkers of type *fix*, *free* and *flex* at the central network node, see Sec. 8.3.1 for details. Positive/negative values are displayed as *solid/dashed lines* or *circles/squares*. Magnified parts of the graphs are shown in the insets.

the perpendicular and orientational cross-response is not even qualitatively captured (wrong sign in the low-frequency range in the right panels of Fig. 8.8b-d). The comparison underlines the importance of angular degrees of freedom and the form of the coupling for the resulting dynamic properties of concatenated objects.

The test of the DCT being successful, we now proceed to more extended networks, for which we use the semiflexible filaments of contour length $L/a = 12$ (7 beads) discussed in this section as building blocks. We use the athermal response functions from the linearization of the equations of motion as input to the DCT, since they compare well to the thermal force response functions of the polymer as shown in Fig. 8.8 and are not subject to fit inaccuracies. The filaments are rather stiff, the ratio of persistence to contour length being $l_\mathrm{p}/L \approx 8.3$, thus implying a network mesh size $\xi \approx L$.

We distinguish four different scenarios regarding the crosslinker flexibility: (i) $\gamma_\varphi = 0$, i.e., end-tangents are free to move independently (*free*), (ii) a harmonic coupling of strength $\gamma_\varphi = 50\, k_\mathrm{B}T$ between the end-tangent orientations of filaments facing each other at one node (*flex_fil*), (iii) a harmonic coupling of strength $\gamma_\varphi = 50\, k_\mathrm{B}T$ acting on the end-tangent orientations of all pairs of neighboring filaments at one node (*flex_all*), (iv) no flexibility corresponding to the limit $\gamma_\varphi \to \infty$, where after the DDF each node is characterized by a single angular variable only (*fix*).

8.3.2 Microrheology

In experimental microrheology, the motion of thermally fluctuating or externally driven colloidal particles are tracked to probe the viscoelastic properties of the surrounding medium [80, 210]. Instead of explicitly modeling a probe particle, we directly resolve both translational and orientational linear response functions of individual network nodes using the DCT as explained in Sec. 8.1.2.

In the following, we consider square arrays of semiflexible filaments as depicted in Fig. 8.9: While the network in Fig. 8.9a is free to move as a whole in response to external forces, the nodes on the edges of the array in Fig. 8.9b are externally held fixed, by this anchoring the overall network. Using the DCT, we calculate the translational and orientational linear self-response of the central node displayed in red in both networks in Fig. 8.9; we vary the size l of the array and distinguish between crosslinkers of type *fix* and *free*.

Results for the network with free boundaries (Fig. 8.9a) are shown in Fig. 8.10, where real and imaginary parts of the response are shown as solid and dashed lines, respectively. Because of the square symmetry, the translational response is isotropic and labeled as J_trans in Fig. 8.10, while the orientational response to an external torque is labeled as J_orient. The response of the network is viscous, i.e., $\mathrm{Im}\,[J] > \mathrm{Re}\,[J]$, both in the limit of large and small frequencies. The high-frequency response is determined by the local network structure around the central node only and therefore independent of the network size; in contrast, the low-frequency response results from macroscopic deformations of the network and thus shows a pronounced dependence on the ratio of edge length to mesh size l/ξ. The influence of the crosslinker type is seen by comparing results in the left and right panels of Fig. 8.10: while the qualitative behavior remains similar, quantitative changes are observed over the entire frequency spectrum. For large frequencies, the microrheological response is more pronounced in the networks, where the filaments' end-tangents at the network nodes are *free* to adjust independently to the imposed stress, compared to the networks with crosslinkers of type *fix*. For the latter ones, at low frequencies the entire network is constrained to move/rotate uniformly in response to the force/torque on the central node (left panels of Fig. 8.10). For crosslinkers of type *free* on the

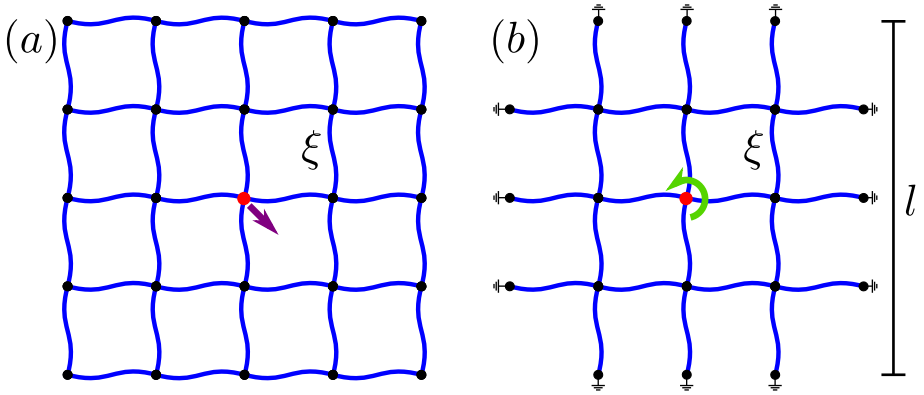

Figure 8.9:
Square arrays of edge length l built of crosslinked semiflexible filaments, the mesh size is denoted by ξ. The meshwork is a) free to diffuse and b) anchored by the edge-nodes, which are held fixed. The linear response of the *red* central nodes to forces and torques indicated by the *purple* and *green arrows* is resolved by means of the DCT. The corresponding response functions are shown in the Figs. 8.10 and 8.11.

other hand, a quasi-static force on the central node in Fig. 8.9a induces a uniform motion of all filaments in a row only and therefore yields a larger imaginary part of the response in the right panels of Fig. 8.10. For intermediate frequencies and increasing array size, we observe the appearance of a viscoelastic regime, i.e., $\mathrm{Re}\,[J] \approx \mathrm{Im}\,[J]$, in the translational response. For both types of crosslinkers, the frequency dependence in this regime is roughly $1/\sqrt{\omega}$ as expected for a predominantly elastic medium embedded in a viscous environment, see Appendix G.3, where a $1/\sqrt{\omega}$ behavior is obtained for the response of a Maxwell and Kelvin-Voigt material in the respective frequency ranges. This intermediate $1/\sqrt{\omega}$-regime is however shifted to lower frequencies for crosslinkers of type *fix*.

The orientational response at intermediate frequencies is characterized by real and imaginary parts with different frequency dependences: The imaginary part tends to fall off with a slightly smaller exponent than the real part of the response, as indicated by the dashed lines $\propto \omega^{-3/4}$ and $\propto \omega^{-1/2}$ in the bottom panels of Fig. 8.10. Moreover, the characteristic minimum of the imaginary part is more pronounced for crosslinkers of type *fix*. Increasing the array size l leads to a reduction of the imaginary part of the orientational response at low frequencies, while the real part is almost independent of the array size over the whole range of frequencies.

Corresponding results for the anchored network of Fig. 8.9b are shown in Fig. 8.11: The high-frequency response of the central node in the network is not influenced by the boundary condition on the edges of the square arrays. It however induces an elastic low-frequency response, $\mathrm{Re}\,[J] \gg \mathrm{Im}\,[J]$, reflecting the fact that overall translations/rotations of the array are inhibited. The influence of the different types of crosslinkers is of qualitative nature only in both the translational and the orientational response. Note that the orientational response quickly converges with increasing array size l over the overall range of frequencies in contrast to the translational response of the network.

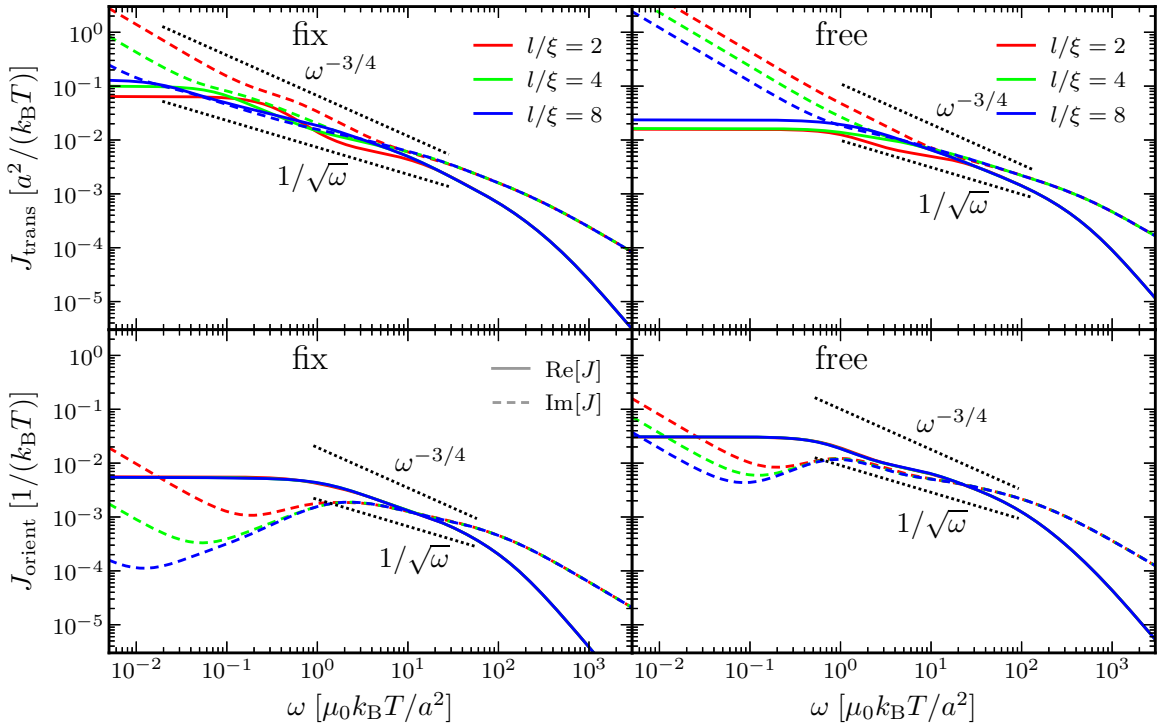

Figure 8.10:
Translational (top) and orientational (bottom) linear self-response of the central node in the unanchored square network of semiflexible filaments shown in Fig. 8.9a for various ratios of edge length to mesh size l/ξ and crosslinkers of type *fix* (left) and *free* (right); real/imaginary parts are displayed as *solid/dashed lines*.

8.3.3 Macrorheology

Next, the macrorheological properties of crosslinked polymeric networks are studied using the DCT: In this scenario, slabs of varying thickness d and infinite lateral extension subject to interfacial shear or compression stress are considered. As known from continuum viscoelastic theory, cf. Appendix G.1, the response generally depends on the orientation of the network with respect to the slab axes. We consider rectangular networks as shown in Fig. 8.12, where the angle between the slab axes and the filaments in the polymeric network is denoted by ϑ. By applying forces of opposite sign parallel/perpendicular to the slab orientation on the interfacial networks nodes (red nodes in Fig. 8.12), the linear shear/compression response of the polymeric slabs is probed. Due to the translational invariance of the problem, only one unit cell of width w with periodic boundary conditions (marked by dashed vertical lines in Fig. 8.12) needs to be considered within the DCT calculation.

The linear shear response of slabs of various thicknesses d is shown in Fig. 8.13 for all four types of crosslinkers. The high-frequency response, which is a probe of the slab's interfacial structure only, varies little with respect to network orientation and crosslinker type and is independent of the ratio of slab thickness to mesh size d/ξ. In turn, we observe a prominent dependence on the slab dimension in the low-frequency regime. As to the influence of the network geometry and the crosslinkers, the comparison of the left and right panels of Fig. 8.13

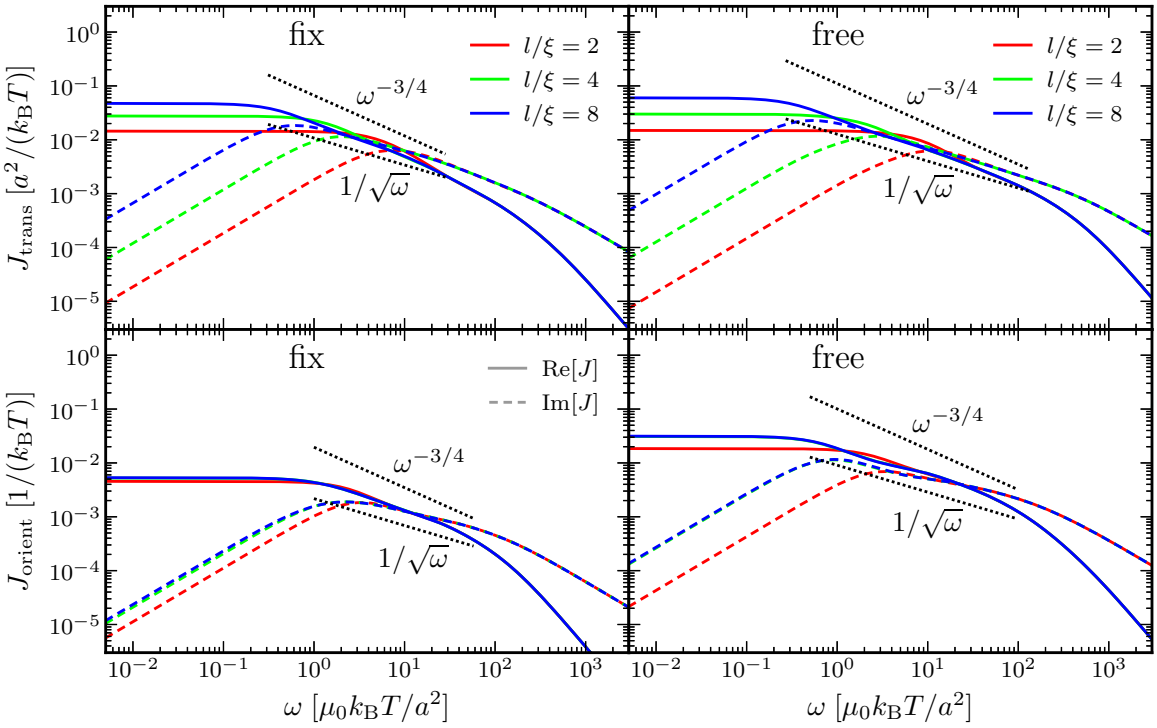

Figure 8.11: Same as Fig. 8.10 but for the anchored network shown in Fig. 8.9b.

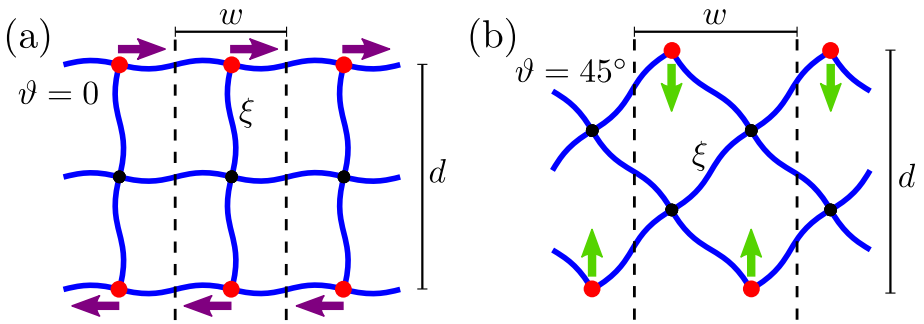

Figure 8.12:
Slabs of thickness d and infinite lateral extension constructed from square networks of semiflexible polymers. The orientation of the network structure with respect to the slab is: a) $\vartheta = 0°$, b) $\vartheta = 45°$. Macroscopic rheological properties are resolved by means of the DCT by applying forces of opposite direction on the interfacial network nodes (*red*): Shear stress is indicated by the *purple arrows* in (a), compression by the *green arrows* in (b). Unit cells of width w and with periodic boundary conditions used in the calculation are indicated by *dashed vertical lines*. Corresponding shear and compression response functions are shown in the Figs. 8.13 and 8.15.

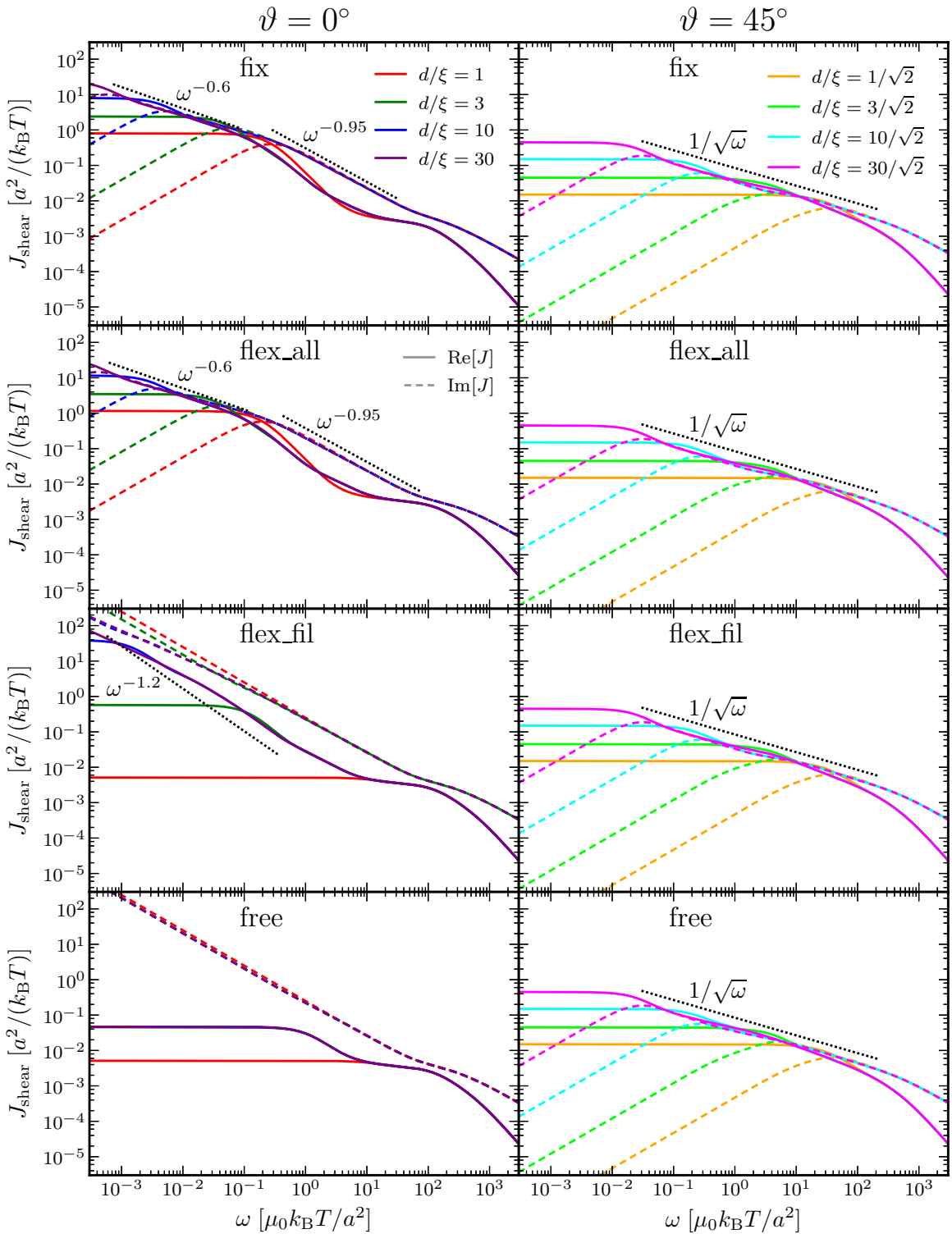

Figure 8.13:
Linear shear response of slabs of rectangular crosslinked semiflexible polymer networks with orientation $\vartheta = 0°$ (left) and $\vartheta = 45°$ (right) with respect to the slab axes as shown in Fig. 8.12 for various ratios of slab thickness to mesh size d/ξ and crosslinkers of type *fix*, *flex_all*, *flex_fil* and *free* (from top to bottom); real/imaginary parts are displayed as *solid/dashed lines*.

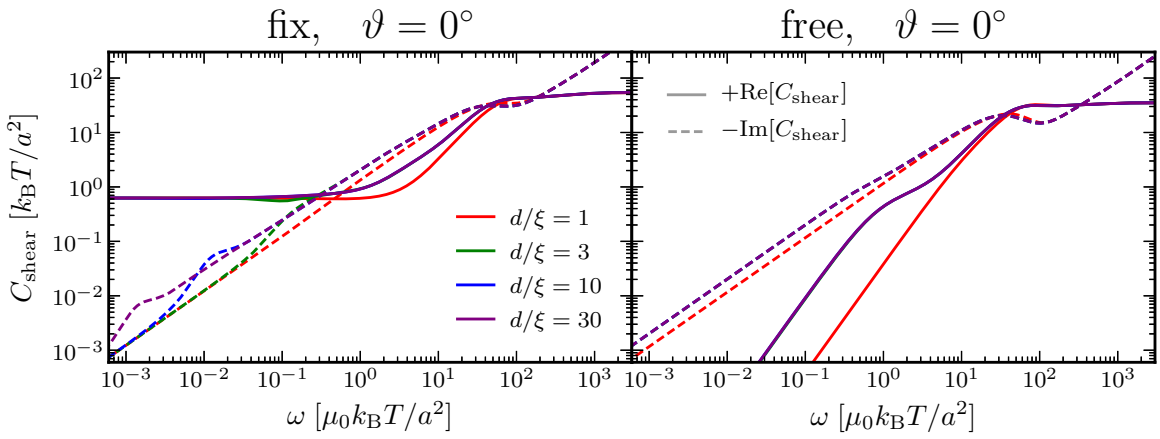

Figure 8.14:
Frequency-dependent viscoelastic moduli of an equivalent continuum model (Appendix G) associated with the shear response of Fig. 8.13. Shear moduli for the networks with crosslinkers of type *fix* (left) and of type *free* (right), both with orientation $\vartheta = 0°$ are shown. *Colors* denote the slab thickness d, where *green* and *blue* curves are mostly hidden behind the *purple* ones. *Solid* and *dashed lines* denote the real and the negative imaginary parts of the moduli respectively.

reveals that the slab response depends drastically on the crosslinker type for $\vartheta = 0°$, while it is crosslinker type independent for $\vartheta = 45°$ as will be discussed below. The frequency dependence of the slabs' shear response allows to classify the networks by comparison to results from continuum viscoelasticity, as detailed in Appendix G.3.

For $\vartheta = 0°$ (left panels of Fig. 8.13), the low-frequency behavior of the slab's shear response for *fix* and *flex_all*, $J(\omega) \approx a_1 + \mathrm{i}\,\omega a_2$ with constants a_1 and a_2, points towards a predominantly elastic material, where the quasi-static shear modulus slightly depends on the crosslinker type, cf. Eq. G.29 in Appendix G.3. In contrast, the shear response for *flex_fil* and *free*, $J(\omega) \approx a_1 + \mathrm{i}\,a_2/\omega$ with constants a_1 and a_2, is completely different, indicating a predominantly viscous material at small frequencies, cf. Eq. G.25 in Appendix G.3. In the latter case, the shear stress is balanced by the rotation of the filaments oriented perpendicular to the slab interface ("soft mode"): For crosslinkers of type *flex_fil*, the bending rigidity along the filaments induces a non-zero elastic coupling between the two interfaces and the low-frequency response thus depends on the slab thickness d. In turn, for crosslinkers of type *free* the low-frequency shear response is independent of the slab thickness for $d/\xi \geq 2$, since the effect of the shear stress remains limited to the two interfacial regions only. The latter observation is in agreement with predictions from continuum theory for a viscous material embedded in a viscous solvent, cf. Eq. G.25 in Appendix G.3.

For all type of crosslinkers, the response in the intermediate frequency range is characterized by power laws with different exponents as indicated by the black dotted lines in Fig. 8.13 and pronounced plateaus in the real part of the response function. The shear response functions of the discrete networks can further be rationalized by a mapping on the viscoelastic modulus C_{shear} of an equivalent continuum via Eq. G.23, as explained in Appendix G.4. For the two extreme cases in Fig. 8.13, i.e., the crosslinker types *fix* and *free* in the top left and bottom left panels, the corresponding viscoelastic moduli are shown in Fig. 8.14: Apart from the smallest slab with $d/\xi = 1$, the viscoelastic moduli for different slab thicknesses agree relatively well

over the entire frequency range. The comparison of the left and right panels of Fig. 8.14 reveals the influence of the crosslinker type: While for crosslinkers of type *fix* both low- and high-frequency moduli are of the Kelvin-Voigt type, i.e., $C_{\mathrm{KV}} \simeq \mu - \mathrm{i}\,\omega\eta$ with constants μ and η, the low-frequency moduli of the network with crosslinkers of type *free* correspond to those of a Maxwell material with $C_{\mathrm{M}} \simeq -\mathrm{i}\,\omega\eta + \omega^2\eta^2/\mu$ (again with constants μ and η), which is predominantly viscous at small frequencies.

Note that the results in Fig. 8.13 correspond to the linear response of networks with (approximately) orthogonally oriented filaments at all network nodes as indicated in Fig. 8.12. To quantitatively predict the response measured in actual shear experiments, an average over all equilibrium configurations of the network orientations would be necessary, see discussion in the Secs. 8.1.4 and 8.1.5. Based on Fig. 8.13, we expect only minor changes for the networks with crosslinkers of type *fix* and *flex_all*, but more pronounced changes for the networks with crosslinkers of type *flex_fil* and *free*. For the latter ones, the appearance of the characteristic "soft mode" discussed above is however expected to survive also in these disordered networks.

For $\vartheta = 45^\circ$, the symmetry of the network (cf. Fig. 8.12b) implies the same deformations for all filaments' end-tangents at a network node in response to applied shear stress. In consequence, the crosslinker type penalizing differences in the end-tangents' orientations has no influence at all on the linear shear response of the slab; indeed, the response functions in the right panels of Fig. 8.13 are independent of the crosslinker type. The low-frequency response of the slabs is elastic, while intermediate frequency regimes are characterized by a roughly Rouse-like frequency dependence $1/\sqrt{\omega}$ resembling the high-frequency response of a Maxwell material (Eq. G.27) or the intermediate frequency response of a Kelvin-Voigt material embedded in a viscous solvent, cf. Appendix G.3.

In Fig. 8.15, we display the compression response of the same polymeric slabs shown in Fig. 8.12. Unlike the case of applied shear, no qualitative differences of the slab response are observed: The slabs show an elastic low-frequency response independently of the orientation of the polymers and of the crosslinker type. We therefore only display results for crosslinkers of type *fix* and *free* in Fig. 8.15. For $\vartheta = 0^\circ$ (left panels of Fig. 8.15), the crosslinker type has no influence on the low-frequency compression response of the slab and induces only minor changes for larger frequencies, e.g., marginally different power law exponents in the intermediate viscoelastic frequency regime. For $\vartheta = 45^\circ$ (right panels of Fig. 8.15), the constraints on the filaments' end-tangents lead to a stiffening of the slab, which is reflected in a slightly reduced response over the entire frequency range for crosslinkers of type *fix* compared to those of type *free*.

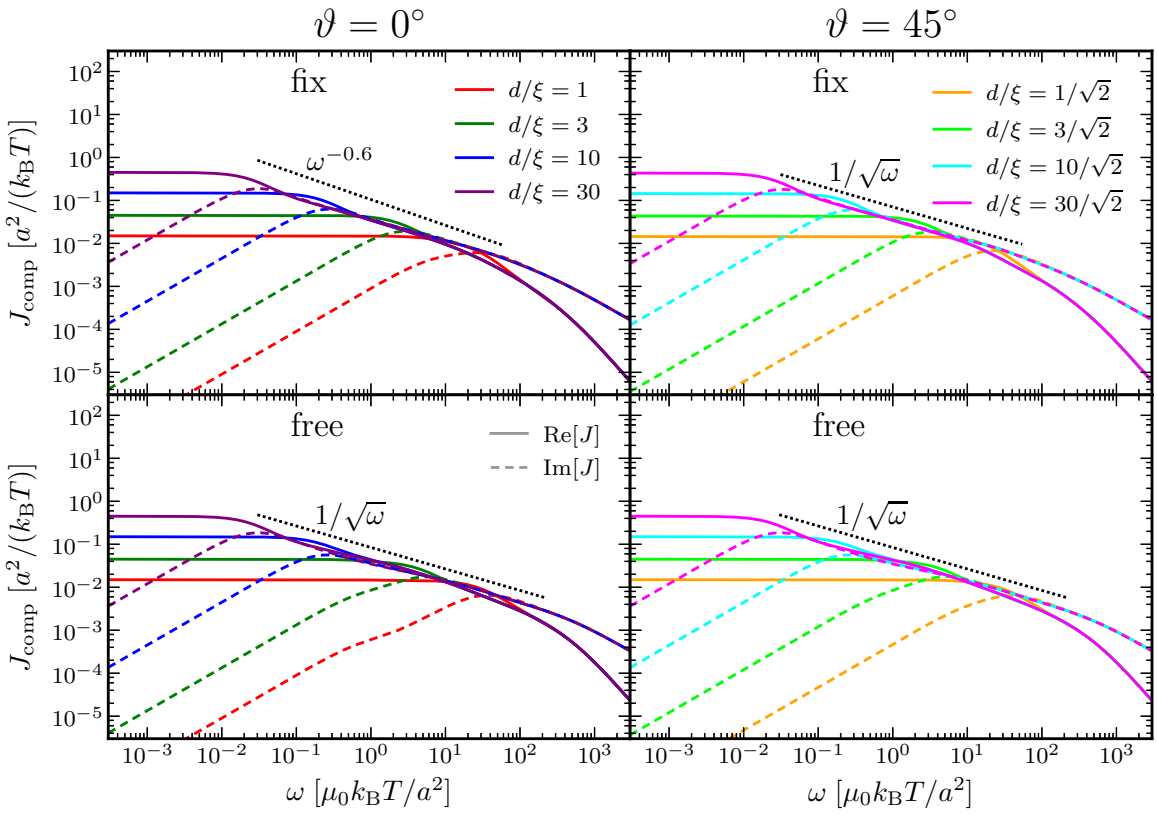

Figure 8.15:
Same as Fig. 8.13 but displaying the linear compression response of the polymeric slabs shown in Fig. 8.12.

8.4 Conclusions

In summary, we have presented a DCT, which provides a general framework for calculating micro- and macrorheological properties of extended networks of various types using as unique input the dynamic linear response properties of the network's building blocks as well as the network structure. The strength of the DCT consists in the accurate and numerically efficient prediction of the frequency dependent viscoelastic properties of extended networks, for which the computational costs of explicit simulations are overwhelming. The DCT thus bridges the gap between the dynamics of isolated network components, which are theoretically well understood, and large-scale structures probed experimentally.

Here, we have focused on crosslinked networks of semiflexible polymers as model systems for the cytoskeleton. In a first step, we have resolved the linear force response properties of isolated semiflexible filaments from explicit BD simulations. Using the DCT, we then have calculated the rheological properties of regular networks of crosslinked filaments. We have resolved the linear force/torque response of individual nodes in extended networks to study the microrheological properties, and have characterized the linear shear and compression response of polymeric slabs, which are so-called macrorheological quantities. Depending on the network size and geometry as well as on the crosslinker flexibility, we find new emerging viscoelastic behavior in the networks that markedly differs from the force response of isolated polymers. The crosslinkers, which couple the angular degrees of freedom at the network nodes—ranging from *fix* (rigid constraint) to *free* (no coupling)—have been found to quantitatively and in some cases also qualitatively alter the resulting micro- and macrorheological properties of the meshwork. Our results demonstrate that angular degrees of freedom and the specific properties of the crosslinking proteins are essential for the understanding of the viscoelasticity of crosslinked semiflexible polymer networks. These effects therefore should be taken into consideration in future theoretical approaches to cytoskeletal mechanics.

Within this chapter, we have restricted the analysis to rectangular networks of a single filament type, but—with the DCT as a versatile tool at hand—revealing the influence of the filaments' bending stiffness and stretching modulus as well as of the network's topology and mesh size on the rheological properties of the network is straightforward. Future lines of investigations will include studying the effect of static prestress on the dynamic response of crosslinked semiflexible meshworks and extending the present analysis to multi-component and disordered networks, thereby focusing on the biologically relevant influence of structural heterogeneity and topological defects.

CHAPTER 9

SUMMARY AND OUTLOOK

The aim of the work described in the preceding chapters has been to quantitatively evaluate, interpret and model the stochastic dynamics of biophysical systems. Based on several examples, we have shown how the improved statistical analysis of fluctuating time series from simulation or experiment can serve to reveal new information and to provide microscopic insights. Furthermore, theoretical concepts have been developed to analytically capture the dynamics of nonlinear and polymeric systems.

In the first part of the thesis, we have evaluated the trajectories of atomistic molecular dynamics (MD) simulations. The mapping of the stochastic dynamics onto the Fokker-Planck (FP) equation with coordinate dependent diffusivity based on a mean first-passage time (MFPT) analysis turned out to be a versatile tool for disentangling free-energetic and friction contributions.

We have studied the dynamics of bulk water in Chapter 2 and have found a pronounced translational and rotational anisotropy in the diffusional dynamics by analyzing the MD trajectories of individual water molecules. Furthermore, applying the MFPT method to the relative separation dynamics of pairs of water molecules we have revealed a six-fold higher friction for tightly coordinated water compared to molecules at large relative separations. This friction increase can be interpreted in terms of a dominant reaction path that involves additional orthogonal coordinates. Our findings reflect the complex character of the dynamics in liquid water and are expected to be relevant for the hydration of ions and other solutes [250, 321] as well as for cellular and molecular processes involving the binding or the transfer of individual water molecules.

The diffusional dynamics of water molecules in the hydration layer of a lipid membrane have been explored in Chapter 3: In the vicinity of the bilayer, the diffusivity perpendicular to the membrane is reduced by a factor ~ 20 compared to bulk, while the lateral water motion exhibits anomalous dynamics up to several nanoseconds and is characterized by diffusion coefficients which are even smaller than the perpendicular ones. This is in sharp contrast to the water diffusion at solid, homogeneous surfaces, which are quantitatively predicted by boundary hydrodynamic theory. By comparison with coarse-grained simulations, we have explained this reversed anisotropy compared to homogenous surfaces by the transient, corrugated free energy landscape imposed by the slowly rearranging lipids. The characteristics of the dynamics at biological interfaces found for water are expected to also apply to small solutes and thus to be important for a variety of physiological transport processes ranging from intercellular signaling to drug delivery.

In Chapter 4, the influence of the salts KCl, NaCl, and NaI on the α-helical folding kinetics of an alanine-based oligopeptide has been investigated. Average folding and unfolding times in MD simulations turned out to be highly salt-specific: In particular, the folding times increase about one order of magnitude for the sodium salts. The drastic slowing down could be traced back to long-lived, compact configurations of the partially folded peptide, in which sodium ions are tightly bound by several carbonyl and carboxylate groups. The analysis of α-helical folding in the framework of diffusion in a one-dimensional free energy landscape further showed that the salts not only specifically modify equilibrium properties, but also induce kinetic barriers due to individual ion binding. In the sodium salts, for instance, the peptide's configurational diffusivity decreases about one order of magnitude, demonstrating the highly specific action of ions and highlighting the intimate coupling of intramolecular friction and solvent effects in protein folding.

In the second part of the thesis, theoretical concepts have been developed for a refined spectral analysis of experimental time series and for quantifying the influence of nonlinearities on the dynamics of fluctuating systems. Moreover, we have studied the dynamics of semiflexible polymers based on coarse grained simulations and have devised an analytical bottom-up approach to the viscoelasticity of polymeric networks.

Chapter 5 focuses on the thermal fluctuations of micron-sized beads in dual trap optical tweezer experiments. To quantitatively interpret the spectral properties of the measured signals, which contain complete dynamic information about the viscoelastic properties of the embedding medium and, if present, macromolecular constructs connecting the two beads, a detailed understanding of the instrumental characteristics is required. To this end, we have presented a theoretical description of the signal processing including polarization crosstalk and instrumental noise. To infer unknown parameters from experimental time series, a maximum-likelihood method based on the statistical properties of the stochastic signals has been derived. We have tested our approach for a simple model system, a pair of unconnected but hydrodynamically interacting spheres. The comparison to theoretical predictions based on instantaneous as well as retarded hydrodynamic interactions (HI) emphasizes the importance of hydrodynamic retardation effects due to vorticity diffusion in the fluid. Overall, the accurate modeling of the stochastic signals in dual trap optical tweezers in conjunction with our Bayesian inference method provides a new framework for the quantitative spectral analysis of single-molecule experiments.

The effects of nonlinearities in the equations of motion of thermally fluctuating systems have been investigated in Chapter 6: We identified the first terms in the expansions of equilibrium correlation and force response functions in powers of the thermal noise strength. For simple model systems, our analytical results have been validated by comparison to numerical simulations. Our approach also exposes the limitations of the dynamic convolution theory (DCT) from Ref. [ix], for which we have derived a first-order correction. Clarifying the role of nonlinearities in the dynamics of thermally fluctuating systems is of fundamental importance and a prerequisite to assess the restrictions of the dynamical analysis based on strictly linear models, which is common in numerous contexts.

In Chapter 7, we have studied the dynamics of single semiflexible polymers by means of Brownian dynamics (BD) simulations and hydrodynamic mean-field theory (MFT). Special attention has been drawn to the influence of hydrodynamic screening near planar surfaces: When gradually decreasing the polymer-wall separation, a crossover from Zimm-type towards Rouse-type polymer dynamics is induced. This crossover is however rather weak and the free-

draining limit is not completely reached even at monomeric distances from the wall. Remarkably, the effect of surface-induced screening of HI sensitively depends on the type of the dynamic observable: For mean square displacements (MSDs) of vectorial quantities like the end-to-end-vector, HI are important and surface screening effects therefore are sizeable, while for MSDs of a scalar quantity like the end-to-end-distance HI are less important, but a pronounced dependence of dynamic scaling exponents on the persistence length to contour length ratio becomes noticeable in agreement with results from single-molecule experiments on f-actin [79].

Finally, we have developed an efficient method to link the equilibrium fluctuations of isolated semiflexible filaments to the viscoelasticity of extended polymeric networks in Chapter 8. The generalized DCT takes the anisotropic translational and orientational response functions of the filaments and the network structure as unique input. We have revealed new emerging viscoelastic behavior in the networks that markedly differs from the force response of isolated polymers and have found a particular influence of the crosslinker stiffness as well as the network geometry on the micro- and macrorheological properties of the crosslinked polymeric networks. The DCT thus bridges the gap between the dynamics of isolated network components, which are theoretically well understood, and large-scale structures probed experimentally.

Summarizing, this thesis demonstrates how new insights into the dynamics of complex biophysical systems, ranging from individual molecules to macromolecular assemblies, can be obtained via advanced stochastic models and methods. Throughout, our results have been validated by comparison to results from simulations and, whenever possible, to experimental data—a crucial measure to identify possible artifacts and to assess the limits of applicability of our analysis methods and analytical results. Based on these tests, we conclude that the theoretical concepts developed within the preceding chapters are complex enough to provide a quantitative understanding of the dynamics under consideration.

Yet, the systems and conditions studied in this thesis without doubt only reflect small parts of the complexity of actual biological structures and kinetics. Although bottom-up approaches combined with multiscale modeling provide a promising strategy for an overall understanding of the intricate phenomena in living cells, the present results obviously only constitute a first step on the path towards reaching this goal. Needless to say that our results are partially based on approximations, whose validity may deserve further attention in the future.

Prospective research efforts therefore could be targeted at extending our analysis to a broader class of systems, at including more (biologically relevant) details which are missing in the current description, and at combining and enhancing the various methods developed in this thesis. Possible directions for future investigations based on the present work are exposed in the remainder of this chapter.

Dynamics of water and solutes: SPC/E water molecules have been found to be characterized by anisotropic translational and rotational diffusion coefficients in MD simulations (Sec. 2.2). Clarifying the influence of the water model and extending the analysis to simulations reflecting the quantum nature of water represent possible lines for future investigations. The analysis method employed in Sec. 2.2 is however not restricted to water; revealing the anisotropy in the translational and rotational motion of other molecules employing the same method is straightforward and will hopefully contribute to a better understanding of the experimentally probed dynamics of solvent and solute molecules.

Furthermore, elucidating the relation between the internal anisotropy of the diffusional dynamics and the anisotropy of the motion observed at interfaces (Chapter 3) or, more generally,

the interplay of external fields and internal diffusional anisotropy for the resulting dynamics of individual molecules may be interesting subjects for future research.

Hydrogen-bond formation and breakage in liquids: The mapping of the relative dynamics of pairs of water molecules in MD simulations on the FP equation points towards the fact that orthogonal—presumably orientational [84, 322]—degrees of freedom, are involved in the process of hydrogen-bond formation and breakage in liquid water (Sec. 2.3). Preliminary results for the relative dynamics of water-solute pairs based on a similar kind of trajectory analysis indicate a pronounced influence of solute size and charge (data not shown).

To uncover the precise molecular mechanisms of bond formation and breakage in liquids an extension of the present one-dimensional analysis is required. Appropriate tools to investigate dynamics in a larger configuration space comprise Markov models [126], transition path sampling [108, 323], transition path theory [107], and techniques targeted at determining dominant reaction paths [324, 325]. For the latter, we expect the anisotropic diffusion coefficients of water molecules resolved in Sec. 2.2 to be of particular relevance.

Probing molecular friction: The DCT developed in Ref. [ix] provides an iterative approach to disentangle the contributions of various components to the thermal fluctuations in a complex mechanical network. Complemented by the Bayesian inference method and the modeling of the optical tweezer instrument (Chapter 5), a theoretical framework is available to quantitatively evaluate the information contained in the spectral properties of the fluctuating signals recorded with single-molecule force spectroscopic techniques applied to proteins and other complex macromolecules, and thereby to ultimately probe (internal) friction on the molecular scale.

Nonlinear effects: For one-dimensional systems, the influence of nonlinearities on the spectral properties of the thermal fluctuations has extensively been discussed (Chapter 6). The underlying analytical approach being very general, an extension of the formalism to more complex systems is conceivable. This would allow to assess the impact of approximations and linearizations, which are common in the analysis of stochastic dynamics, and to determine limits of applicability and corrections for linear theories such as the DCT from Ref. [ix] as well as its generalization to two dimensions in Chapter 8.

Semiflexible polymers: Studying polymer dynamics relative to an internal, comoving reference frame (Chapter 8) offers the possibility to reveal the anisotropic response properties of semiflexible filaments without the need of external forces orienting the filament in the simulation. Extending the present analysis to more flexible filaments with persistence to contour length ratio $l_\mathrm{p}/L \lesssim 1$ and to simulations including HI is straightforward. Moreover, an anisotropic dynamic MFT along the lines of Ref. [287], which captures the thermal fluctuations of the filament in the internal coordinate frame is conceivable. This would allow to consider filament lengths, which are probed experimentally [79] but inaccessible in BD simulations.

Rheology of polymeric meshworks: The generalized DCT has been used to calculate the rheological properties of regular semiflexible polymer networks in Chapter 8. The method being efficient and very general, the viscoelasticity of other network structures can equally be studied: Quantifying the effect of irregularities on the structural, geometrical, or crosslinker level in the meshwork would constitute the next logical step towards understanding the complexity of biological structures [326]. On the other hand, an extension of the method to include additional effects such as crosslinker (un-)binding would be conceptually interesting and particularly important for a quantitative explanation of experimental findings [81].

APPENDIX A

NOTATION

Given the diversity of topics covered within this thesis, the notation is not completely uniform across the chapters. The meaning of the symbols used to denote certain physical quantities is therefore specified separately within each chapter.

A.1 Acronyms and Symbols

Lists of frequently used acronyms and symbols are found in Tab. A.1 and A.2 respectively.

A.2 Fourier Transformation

Throughout the thesis, the following definition of the Fourier transformation $\mathcal{F}$ and its inverse $\mathcal{F}^{-1}$ for a function $f(t)$ are used

$$\begin{aligned} f(\omega) &= \mathcal{F}[f(t)] \equiv \int_{-\infty}^{\infty} \mathrm{d}t\, f(t) e^{\mathrm{i}\omega t}, \\ f(t) &= \mathcal{F}^{-1}[f(\omega)] \equiv \frac{1}{2\pi} \int_{-\infty}^{\infty} \mathrm{d}\omega\, f(\omega) e^{-\mathrm{i}\omega t}. \end{aligned} \tag{A.1}$$

Functions in time and frequency domain are denoted by the same variables. Using the above convention the convolution theorem takes the form

$$\mathcal{F}[f * g\,(t)] = f(\omega) g(\omega), \tag{A.2}$$

$$\mathcal{F}[f(t) g(t)] = \frac{1}{2\pi} f * g\,(\omega), \tag{A.3}$$

where the convolution between the functions f and g is defined as

$$f * g\,(t) \equiv \int_{-\infty}^{\infty} \mathrm{d}t'\, f(t') g(t - t'). \tag{A.4}$$

Acronym	Meaning
BD	Brownian dynamics
DFT	Discrete Fourier transform
DCT	Dynamic convolution theory
FDT	Fluctuation-dissipation theorem
FP	Fokker-Planck
FPT	First-passage time
GROMACS	Groningen machine for chemical simulations
HI	Hydrodynamic interactions
LJ	Lennard-Jones
MD	Molecular dynamics
MFPT	Mean first-passage time
MSD	Mean square displacement
PDF	Probability density function
PSD	Power spectral density
RC	Reaction coordinate
RP	Rotne-Prager
RPB	Rotne-Prager-Blake
SPC/E	Extended simple point charge model [90]
VMD	Visual molecular dynamics [110]
WLC	Wormlike chain

Table A.1: List of frequently used acronyms.

Symbol	Meaning
D	Diffusion coefficient, diffusivity
F	Free energy
$k_B T$	Thermal energy
a	Bead radius
μ_0, ζ_0	Quasi-static mobility, quasi-static friction coefficient
η	Shear viscosity
ζ, $\overleftrightarrow{\zeta}$	Friction coefficient, (tensorial) friction density
γ, κ	Stretching and bending elasticity
$\Delta x(t)$	Temporal increment of the observable x
J, J_1	Thermal linear force response function
S	Power spectral density

Table A.2:
List of frequently used symbols, which are decorated with indices and/or superscripts depending on the specific context in the various chapters.

APPENDIX B

OVERDAMPED MOTION OF A RIGID BODY

Steady flows around single particles of particular shapes and the resulting resistance and mobility functions have extensively been discussed in the literature [102, 103]. Here we take a complementary approach and derive relations for the diffusion coefficients of a rigid body, which is characterized by a certain tensorial friction density $\overleftrightarrow{\zeta}$ rather than by a particular shape of its surface, to derive the functional form of the grand-diffusivity matrix in Sec. 2.2.2.

We consider a rigid-body undergoing quasi-static, overdamped translational motion with velocity $\boldsymbol{V}$ and rotational motion with angular velocity $\boldsymbol{\Omega}$ with respect to a reference point $\boldsymbol{R}$. The velocity field within the body

$$v(\boldsymbol{r}) = \boldsymbol{V} + \boldsymbol{\Omega} \times (\boldsymbol{r} - \boldsymbol{R}), \tag{B.1}$$

implies a local force density

$$\boldsymbol{f}(\boldsymbol{r}) = \overleftrightarrow{\zeta}(\boldsymbol{r}) \cdot \boldsymbol{v}(r) = \overleftrightarrow{\zeta}(\boldsymbol{r}) \cdot \left(\boldsymbol{V} + \boldsymbol{\Omega} \times (\boldsymbol{r} - \boldsymbol{R})\right), \tag{B.2}$$

where $\overleftrightarrow{\zeta}$ denotes the local tensorial friction density. The resulting overall force

$$\boldsymbol{F} = \int \mathrm{d}\boldsymbol{r}\, \boldsymbol{f}(\boldsymbol{r}) = \int \mathrm{d}\boldsymbol{r}\, \overleftrightarrow{\zeta}(\boldsymbol{r}) \cdot \left(\boldsymbol{V} + \boldsymbol{\Omega} \times (\boldsymbol{r} - \boldsymbol{R})\right), \tag{B.3}$$

and torque

$$\boldsymbol{M} = \int \mathrm{d}\boldsymbol{r}\ (\boldsymbol{r} - \boldsymbol{R}) \times \boldsymbol{f}(\boldsymbol{r}) = \int \mathrm{d}\boldsymbol{r}\ (\boldsymbol{r} - \boldsymbol{R}) \times \left(\overleftrightarrow{\zeta}(\boldsymbol{r}) \cdot \left(\boldsymbol{V} + \boldsymbol{\Omega} \times (\boldsymbol{r} - \boldsymbol{R})\right)\right), \tag{B.4}$$

acting on the body are obtained by integration. These are linearly related to the rigid body translational and angular velocities via

$$\begin{pmatrix} \boldsymbol{F} \\ \boldsymbol{M} \end{pmatrix} = \begin{pmatrix} \boldsymbol{Z}^{FV} & \boldsymbol{Z}^{F\Omega} \\ \boldsymbol{Z}^{MV} & \boldsymbol{Z}^{M\Omega} \end{pmatrix} \cdot \begin{pmatrix} \boldsymbol{V} \\ \boldsymbol{\Omega} \end{pmatrix}, \tag{B.5}$$

where the entries of the 6×6-dimensional grand-friction matrix are

$$Z_{ij}^{FV} \;=\; \int \mathrm{d}\boldsymbol{r}\, \zeta_{ij}(\boldsymbol{r}) = Z_{ji}^{FV}, \qquad i,j \in \{1,2,3\}, \tag{B.6}$$

$$Z_{ij}^{F\Omega} = \sum_{k,l} \epsilon_{kjl} \int \mathrm{d}\boldsymbol{r}\, \zeta_{ik}(\boldsymbol{r})\,(r_l - R_l)\,, \qquad i,j \in \{1,2,3\}, \tag{B.7}$$

$$Z_{ij}^{MV} = \sum_{k,l} \epsilon_{ilk} \int \mathrm{d}\boldsymbol{r}\, \zeta_{kj}(\boldsymbol{r})\,(r_l - R_l) = Z_{ji}^{F\Omega}, \qquad i,j \in \{1,2,3\}, \tag{B.8}$$

$$Z_{ij}^{M\Omega} = \sum_{k,l,m,n} \epsilon_{ikm}\epsilon_{jln} \int \mathrm{d}\boldsymbol{r}\, \zeta_{kl}(\boldsymbol{r})\,(r_m - R_m)\,(r_n - R_n) = Z_{ji}^{M\Omega}, \qquad i,j \in \{1,2,3\}, \tag{B.9}$$

where the entries of the Levi-Civita tensor (Eq. 2.8) are denoted by ϵ_{ijk} and where the symmetry of the tensorial friction density $\zeta_{ij} = \zeta_{ji}$ has been used. The grand-friction matrix being symmetric, the motion of the rigid-body thus in general depends on the 21 independent matrix entries specified above.

The matrix entries coupling torque and translational motion or force and angular motion linearly depend on the coordinates of the reference point $\boldsymbol{R}$ (Eqs. B.7 and B.8), while the matrix entries coupling torque and angular motion quadratically depend on the R_i (Eq. B.9). Note however that—unlike in the related but simpler problem of inertial motion of a rigid body—a diagonalization of the grand-friction matrix via an appropriate choice of the reference point $\boldsymbol{R}$ and the orientation of the coordinate frame is in general *not* possible due to the tensorial character of friction.

B.1 Grand-Friction and -Diffusivity Matrices for SPC/E Water

The rigid SPC/E water molecule considered in Sec. 2.2.2 is mirror-symmetric with respect to the $x = 0$ and $y = 0$ planes of the internal coordinate frame shown in Fig. 2.4. The friction density therefore fulfills

$$\zeta_{ij}(\boldsymbol{R}+\boldsymbol{r}) = (1-2\delta_{ki})\left(1-2\delta_{kj}\right)\zeta_{ij}(\boldsymbol{R}+\boldsymbol{r}^{(k)}), \qquad r_i^{(k)} \equiv (1-2\delta_{ik})r_i, \qquad i,j \in \{1,2,3\}, \tag{B.10}$$

for $k = 1$ and $k = 2$, where $\boldsymbol{R}$ denotes the origin of the internal coordinate frame in Fig. 2.4. With this, one obtains the diagonal elements of the grand-friction matrix

$$Z_{ii}^{FV} = \int \mathrm{d}\boldsymbol{r}\, \zeta_{ii}(\boldsymbol{r}), \qquad i \in \{1,2,3\}, \tag{B.11}$$

and

$$Z_{11}^{M\Omega} = \int \mathrm{d}\boldsymbol{r}\, \left[\zeta_{22}(\boldsymbol{r})(r_3-R_3)^2 + \zeta_{33}(\boldsymbol{r})(r_2-R_2)^2 - 2\zeta_{23}(\boldsymbol{r})(r_2-R_2)(r_3-R_3)\right], \tag{B.12}$$

$$Z_{22}^{M\Omega} = \int \mathrm{d}\boldsymbol{r}\, \left[\zeta_{11}(\boldsymbol{r})(r_3-R_3)^2 + \zeta_{33}(\boldsymbol{r})(r_1-R_1)^2 - 2\zeta_{13}(\boldsymbol{r})(r_1-R_1)(r_3-R_3)\right], \tag{B.13}$$

$$Z_{33}^{M\Omega} = \int \mathrm{d}\boldsymbol{r}\, \left[\zeta_{11}(\boldsymbol{r})(r_2-R_2)^2 + \zeta_{22}(\boldsymbol{r})(r_1-R_1)^2 - 2\zeta_{12}(\boldsymbol{r})(r_1-R_1)(r_2-R_2)\right], \tag{B.14}$$

where the symmetry of the friction tensor, $\zeta_{ij} = \zeta_{ji}$, has been used to simplify the integrands. The only non-zero off-diagonal elements of the grand-friction matrix are

$$Z_{12}^{F\Omega} = Z_{21}^{MV} = \int \mathrm{d}\boldsymbol{r}\, \left[\zeta_{11}(\boldsymbol{r})(r_3-R_3) - \zeta_{13}(\boldsymbol{r})(r_1-R_1)\right], \tag{B.15}$$

$$Z_{21}^{F\Omega} \;= Z_{12}^{MV} \;= \int \mathrm{d}\boldsymbol{r}\; \left[\zeta_{23}(\boldsymbol{r})(r_2 - R_2) - \zeta_{22}(\boldsymbol{r})(r_3 - R_3)\right]. \tag{B.16}$$

For the remaining freedom in the R_3-coordinate of the reference point, various possibilities exist: It can be chosen to make $Z_{12}^{F\Omega} = Z_{21}^{MV}$ vanish and $Z_{22}^{M\Omega}$ minimal by setting it to

$$R_3' \equiv \frac{\int \mathrm{d}\boldsymbol{r}\; \left[\zeta_{11}(\boldsymbol{r})r_3 - \zeta_{13}(\boldsymbol{r})(r_1 - R_1)\right]}{\int \mathrm{d}\boldsymbol{r}\; \zeta_{11}(\boldsymbol{r})}, \tag{B.17}$$

or to make $Z_{21}^{F\Omega} = Z_{12}^{MV}$ vanish and $Z_{11}^{M\Omega}$ minimal by setting it to

$$R_3'' \equiv \frac{\int \mathrm{d}\boldsymbol{r}\; \left[\zeta_{22}(\boldsymbol{r})r_3 - \zeta_{23}(\boldsymbol{r})(r_2 - R_2)\right]}{\int \mathrm{d}\boldsymbol{r}\; \zeta_{22}(\boldsymbol{r})}. \tag{B.18}$$

In general, it will however not be possible to meet both conditions and thus to completely decouple translational and angular motions by an appropriate choice of the reference point. Alternatively, one could select the value of R_3 which minimizes the norm of the grand-friction matrix, i.e., the sum of squared matrix elements.

The inversion of the grand-friction matrix yields the grand-mobility matrix, which up to a factor $k_\mathrm{B}T$ corresponds to the diffusivity matrix. In dependence of R_3, the grand-diffusivity matrix takes the form

$$\boldsymbol{\mathcal{D}} = \begin{pmatrix} D_x^0 + D_y^{\mathrm{rot}}(R_3 - R_3')^2 & 0 & 0 & 0 & D_y^{\mathrm{rot}}(R_3 - R_3') & 0 \\ 0 & D_y^0 + D_x^{\mathrm{rot}}(R_3 - R_3'')^2 & 0 & -D_x^{\mathrm{rot}}(R_3 - R_3'') & 0 & 0 \\ 0 & 0 & D_z^0 & 0 & 0 & 0 \\ 0 & -D_x^{\mathrm{rot}}(R_3 - R_3'') & 0 & D_x^{\mathrm{rot}} & 0 & 0 \\ D_y^{\mathrm{rot}}(R_3 - R_3') & 0 & 0 & 0 & D_y^{\mathrm{rot}} & 0 \\ 0 & 0 & 0 & 0 & 0 & D_z^{\mathrm{rot}} \end{pmatrix}, \tag{B.19}$$

where the minimal translational diffusion coefficients are

$$D_x^0 = \frac{k_\mathrm{B}T}{\int \mathrm{d}\boldsymbol{r}\; \zeta_{11}(\boldsymbol{r})}, \qquad D_y^0 = \frac{k_\mathrm{B}T}{\int \mathrm{d}\boldsymbol{r}\; \zeta_{22}(\boldsymbol{r})}, \qquad D_z^0 = \frac{k_\mathrm{B}T}{\int \mathrm{d}\boldsymbol{r}\; \zeta_{33}(\boldsymbol{r})}. \tag{B.20}$$

The angular diffusion coefficients in Eq. B.19 are

$$\begin{aligned} \frac{D_x^{\mathrm{rot}}}{k_\mathrm{B}T} &= \left(\int \mathrm{d}\boldsymbol{r}\; \left[\zeta_{22}(\boldsymbol{r})(r_3 - R_3'')^2 + \zeta_{33}(\boldsymbol{r})(r_2 - R_2)^2 - 2\zeta_{23}(\boldsymbol{r})(r_2 - R_2)(r_3 - R_3'')\right] \right)^{-1} \\ &= \left(\int \mathrm{d}\boldsymbol{r}\; \left[\zeta_{22}(\boldsymbol{r}) \left(r_3^2 - \left(R_3''\right)^2\right) + \zeta_{33}(\boldsymbol{r})(r_2 - R_2)^2 - 2\zeta_{23}(\boldsymbol{r})(r_2 - R_2)r_3\right] \right)^{-1}, \end{aligned} \tag{B.21}$$

$$\begin{aligned} \frac{D_y^{\mathrm{rot}}}{k_\mathrm{B}T} &= \left(\int \mathrm{d}\boldsymbol{r}\; \left[\zeta_{11}(\boldsymbol{r})(r_3 - R_3')^2 + \zeta_{33}(\boldsymbol{r})(r_1 - R_1)^2 - 2\zeta_{13}(\boldsymbol{r})(r_1 - R_1)(r_3 - R_3')\right] \right)^{-1} \\ &= \left(\int \mathrm{d}\boldsymbol{r}\; \left[\zeta_{11}(\boldsymbol{r})(r_3^2 - \left(R_3'\right)^2) + \zeta_{33}(\boldsymbol{r})(r_1 - R_1)^2 - 2\zeta_{13}(\boldsymbol{r})(r_1 - R_1)r_3\right] \right)^{-1}, \end{aligned} \tag{B.22}$$

which reflect the minimal values of the Eqs. B.12 and B.13 with respect to R_3 and where the coordinates R_3' and R_3'' are given in the Eqs. B.17 and B.18, as well as

$$\frac{D_z^{\mathrm{rot}}}{k_{\mathrm{B}}T} = \left(\int \mathrm{d}\boldsymbol{r} \left[\zeta_{11}(\boldsymbol{r})(r_2 - R_2)^2 + \zeta_{22}(\boldsymbol{r})(r_1 - R_1)^2 - 2\zeta_{12}(\boldsymbol{r})(r_1 - R_1)(r_2 - R_2) \right] \right)^{-1} . \quad \text{(B.23)}$$

The functional form of the grand-diffusivity matrix in Eq. B.19 serves as starting point for the analysis of the diffusional properties of SPC/E molecules in bulk water in Sec. 2.2.2. The correspondence between Eq. B.19 on the one hand and the Eqs. 2.9, 2.12 and 2.13 on the other one is: $R_3 - R_3' = \delta z - \delta z'$ and $R_3 - R_3'' = \delta z - \delta z''$. The resulting values for the diagonal and off-diagonal elements of the grand-diffusivity matrix are found in Tab. 2.3.

APPENDIX C

FIRST-PASSAGE TIMES

Based on data from Chapter 2, we discuss the influence of the time resolution of a trajectory on the estimated mean first-passage times (MFPTs) in Sec. C.1. The numerical solution of the Fokker-Planck (FP) equation, which serves to calculate MFPTs and first-passage time (FPT) distributions associated with a given free energy and diffusivity profile, is reviewed in Sec. C.2.

C.1 Finite Time Resolution of a Trajectory

Several MFPT curves obtained from the same simulation run by only varying the time resolution δt employed for the MFPT analysis in Sec. 2.3.2 are shown in Fig. C.1: We observe that MFPTs obtained for $\delta t = 1$ ps are, depending on the target R_t, roughly $2-6$ ps larger than the estimates from the analysis with $\delta t = 0.02$ ps. As we show in the following, the reason for the differences between the MFPT curves, are excursions beyond R_t and back, which are not registered due to the finite time resolution δt. Since the first *observed* passage time possibly by far exceeds the *actual* FPT, the finite time resolution thus also affects the estimate of the MFPT. Note that the curves in Fig. C.1 are mainly shifted vertically with respect to each other and that within the statistical uncertainty the choice of a specific time resolution had no visible effect on the shape of the resulting diffusivity profile, which according to Eq. 2.21 depends on the slope of the MFPT curves only (comparison not shown).

Note that the vertical shifts in Fig. C.1 are larger than the resolution δt of the trajectories. To demonstrate the influence of δt on the observed MFPT curves, we use a simple model system: free diffusion of a particle along the coordinate x with diffusion constant D_p, where a reflecting boundary at $x = 0$ restricts the particle position to the positive part of the coordinate axis. The corresponding Green's function is

$$G(x|x_0;t) = \frac{1}{\sqrt{4\pi D_\mathrm{p} t}} \left(\mathrm{e}^{-\frac{(x-x_0)^2}{4D_\mathrm{p}t}} + \mathrm{e}^{-\frac{(x+x_0)^2}{4D_\mathrm{p}t}} \right) \Theta(x), \tag{C.1}$$

where $\Theta(x)$ denotes the Heaviside step function. Since the process is Markovian, the probability density function (PDF) of finding the particle at position x at time $t + \delta t$ depends on the PDF at time t only

$$P(x;t+\delta t) = \int_0^\infty \mathrm{d}x'\, G(x|x';\delta t) P(x';t). \tag{C.2}$$

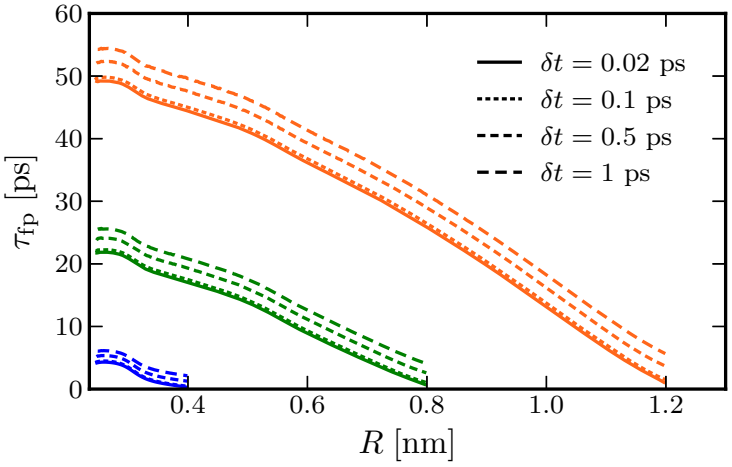

Figure C.1:
Dependence of the MFPT curves τ_{fp} on the time resolution δt of the underlying trajectories. Results for several target separations $R_{\mathrm{t}} = 1.2$ nm (*orange*), $R_{\mathrm{t}} = 0.8$ nm (*green*) and $R_{\mathrm{t}} = 0.4$ nm (*blue*) determined from molecular dynamics (MD) simulation data at $T = 300$ K.

According to Eq. 2.20 the MFPT of reaching x_{t} when starting out from x for a flat diffusivity $D(x) = D_{\mathrm{p}}$ and free energy profiles $F(x) = \text{const.}$ is given by

$$\tau_{\mathrm{fp}}(x, x_{\mathrm{t}}) = \tau_{\mathrm{d}} \left(1 - \left(\frac{x}{x_{\mathrm{t}}} \right)^2 \right), \tag{C.3}$$

where $\tau_{\mathrm{d}} \equiv x_{\mathrm{t}}^2 / (2D_{\mathrm{p}})$ denotes the characteristic time for diffusion over the length x_{t}.

We show in Fig. C.2 that MFPTs obtained from a trajectory with finite time resolution differ from the MFPT calculated in the continuum, because paths will possibly cross the target and come back many times before a position $x \geq x_{\mathrm{t}}$ is first recorded in the trajectory with finite time resolution. A lower bound for MFPT estimates based on trajectories with finite time resolution is obtained by the following numerical procedure:

1. At time $t = 0$ the particle is located at x_0, i.e., the PDF and the probability of finding the particle left of the target read

$$P(x; t = 0) = \delta(x - x_0), \qquad P_{\mathrm{left}}(t = 0) = 1. \tag{C.4}$$

Since no transitions beyond the target have been observed yet, the current MFPT estimate is $\tilde{\tau}_{\mathrm{fp}} = 0$. The PDF at time $t = \delta t$ according to Eq. C.2 thus simply is

$$P(x; t = \delta t) = G(x | x_0; \delta t), \tag{C.5}$$

which is evaluated numerically along x with a resolution $\delta x / x_{\mathrm{t}} = 0.03$.

The following steps are repeated until the exit condition is met:

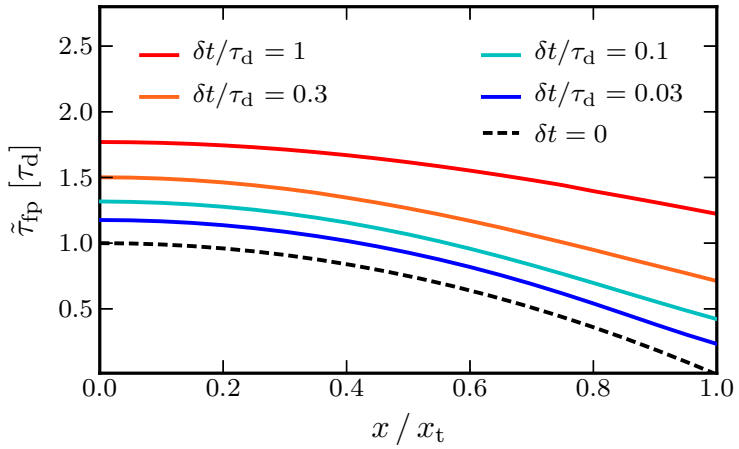

Figure C.2:
MFPT curves for reaching x_t in the case of free diffusion next to a reflecting wall at $x = 0$ for different time resolutions δt of the underlying trajectory: *Solid colored lines* are obtained by the numerical procedure described in Sec. C.1, the *dashed black line* denotes the continuum MFPTs (Eq. C.3). The characteristic diffusion time is $\tau_d \equiv x_t^2/(2D_p)$, where D_p denotes the particle's diffusion constant.

2. Linearly interpolate the discrete values of $P(x;t)$ to obtain a continuous function and calculate the probability of still finding the particle left of the target by numerical integration

$$P_{left}(t) = \int_0^{x_t} \mathrm{d}x\, P(x,t). \tag{C.6}$$

The fraction $\Delta P_{left} = P_{left}(t-\delta t) - P_{left}(t)$ of particles is thus found on the right of the target ($x > x_t$) for the first time.

3. The fraction ΔP_{left} has crossed the target between time $t - \delta t$ and time t and contributes to the observed MFPT, which is updated accordingly: $\tilde{\tau}_{fp} = \tilde{\tau}_{fp} + (t - \delta t)\,\Delta P_{left}$.

4. *If* $P_{left}(t) < 0.001$, i.e., if less than 0.1 % of the particles have not been observed right of the target at least once, *then* exit the loop and return the MFPT estimate $\tilde{\tau}_{fp}$. *Otherwise*:

   a) Starting from the linearly interpolated version of the current PDF $P(x;t)$, calculate the PDF $P(x;t+\delta t)$ on a discrete grid with $\delta x/x_t = 0.03$ by numerically integrating Eq. C.2. Use x_t as upper integration limit thereby neglecting the fraction of particles ΔP_{left} which have been found right of the target.

   b) Set $t = t + \delta t$ and go back to (2).

The MFPT curves resulting from the procedure described above are shown in Fig. C.2 and reveal the same characteristics as the MFPT curves from MD simulation data in Fig. C.1: Increasing δt shifts up vertically the curves and distortions of the curves are only observed for $\delta t \gtrsim \tau_{fp}$. As is clearly seen, one has $\tilde{\tau}_{fp} > \tau_{fp} + \delta t$ for the smaller values of δt: The deviations are thus *not* caused because the FPT is recorded with an uncertainty on the order of the time resolution, but because the first observed passage time in the discretely sampled trajectory can exceed by far the FPT in the continuous trajectory.

C.2 Numerical Solution of the Fokker-Planck Equation

We briefly review the numerical solution of the FP equation used to calculate MFPTs and FPT-distributions associated with a given pair of free energy and diffusivity profiles.

When discretizing the spatial coordinate R into N bins of width δR, the FP equation (Eq. 2.19) takes the form of a master equation [327]

$$\frac{\partial P_i(t)}{\partial t} = \sum_{j=1}^{N} W_{ij} P_j(t), \tag{C.7}$$

where $P_i(t)$ denotes the probability of observing a relative separation R within bin i, i.e., $R \in [R_i - \delta R/2, R_i + \delta R/2)$, at time t. The entries of the tridiagonal matrix of transition rates W_{ij} for a transition from bin j to bin i depend on both the free energy F and the diffusivity D

$$W_{i,i+1} = \frac{D_i + D_{i+1}}{2\,(\delta R)^2} \exp\left(-\frac{F_i - F_{i+1}}{2k_\mathrm{B}T}\right), \qquad i = 1, \ldots, N-1 \tag{C.8}$$

where $F_i \equiv F(R_i)$ and $D_i \equiv D_R(R_i)$. Due to detailed balance and probability conservation the remaining non-zero transition rates of the tridiagonal matrix are

$$W_{i+1,i} = \exp\left(-\frac{F_{i+1} - F_i}{k_\mathrm{B}T}\right) W_{i,i+1}, \qquad W_{ii} \equiv -\sum_{j \neq i} W_{ji} = -W_{i-1,i} - W_{i+1,i}. \tag{C.9}$$

The linear transformation $\tilde{P}_i(t) = \exp(\beta F_i/2) P_i(t)$ with $\beta \equiv (k_\mathrm{B}T)^{-1}$ converts Eq. C.7 into a simple differential equation involving a tridiagonal, symmetric matrix with entries $\tilde{W}_{ij}$

$$\frac{\partial \tilde{P}_i(t)}{\partial t} = \sum_{j=1}^{N} \tilde{W}_{ij} \tilde{P}_j(t) \quad \text{with} \quad \tilde{W}_{ij} \equiv \mathrm{e}^{\beta F_i/2}\, W_{ij}\, \mathrm{e}^{-\beta F_j/2}, \tag{C.10}$$

which is readily solved in terms of a matrix exponential

$$\tilde{P}_i(t) = \sum_{j=1}^{N} \left(\mathrm{e}^{\tilde{\mathbf{W}}t}\right)_{ij} \tilde{P}_j(0) \;\Leftrightarrow\; P_i(t) = \sum_{j=1}^{N} \mathrm{e}^{-\beta F_i/2} \left(\mathrm{e}^{\tilde{\mathbf{W}}t}\right)_{ij} \mathrm{e}^{\beta F_j/2} P_j(0) \equiv \sum_{j=1}^{N} G_{ij}(t) P_j(0), \tag{C.11}$$

where the Green's function G_{ij} specifies the probability of ending up in bin i within a time interval t given a start in bin j. The matrix exponential in Eq. C.11 is computed numerically by diagonalization of the symmetric matrix $\tilde{\mathbf{W}} = \mathbf{Q} \cdot \mathbf{\Lambda} \cdot \mathbf{Q}^{-1}$, with $\mathbf{Q}$ being the matrix of eigenvectors and $\mathbf{\Lambda}$ being the diagonal matrix of eigenvalues of $\tilde{\mathbf{W}}$. The matrix exponential is then simply given by

$$\mathrm{e}^{\tilde{\mathbf{W}}t} = \mathbf{Q} \cdot \mathrm{e}^{\mathbf{\Lambda}t} \cdot \mathbf{Q}^{-1}, \qquad \left(\mathrm{e}^{\mathbf{\Lambda}t}\right)_{ij} = \delta_{ij} \mathrm{e}^{\lambda_i t}. \tag{C.12}$$

For the case of relative SPC/E water dynamics, a bin width $\delta R = 0.002$ nm is used. A reflective boundary condition ($W_{0,1} = W_{1,0} = 0$) is imposed at $R_\mathrm{min} = 0.235$ nm corresponding to a value of the free energy $F \approx 18\, k_\mathrm{B}T$.

FPT distributions are obtained by imposing an absorbing boundary condition at the target position R_t, thus disregarding paths in the time evolution of G_{ij} which have already reached

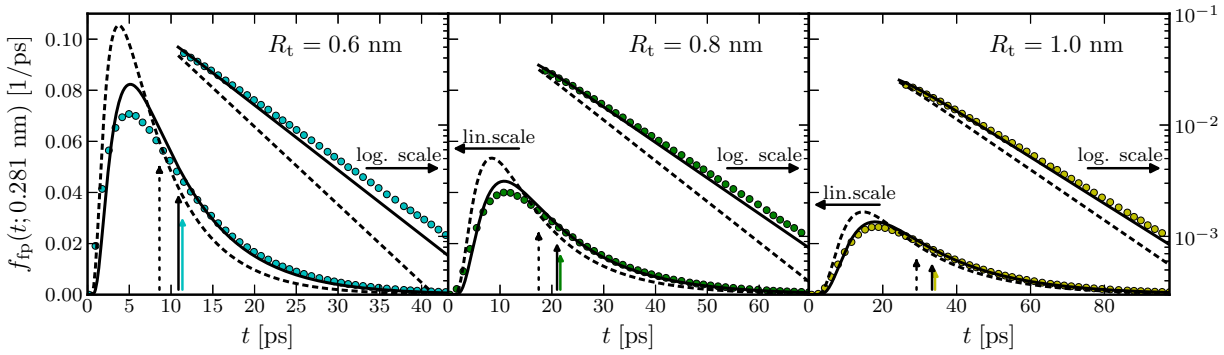

Figure C.3:
Same as Fig. 2.10b but for other target separations R_t: FPT distributions for water pairs starting within the first coordination shell ($R_0 = 0.281$ nm) from MD simulations at $T = 300$ K (*colored circles*) are compared to the results from the numerical solution of the FP equation (Eq. C.15) with flat diffusivity $2D_{H_2O}$ (*dashed black lines*) and with diffusivity profiles $D_R(R)$ from Fig. 2.8c (*solid black lines*), vertical arrows indicate the mean of the corresponding distributions (Eq. C.16).

the target beforehand: the total number N of bins is selected so that the target R_t is part of bin $N+1$ and the absorbing boundary condition is implemented by setting

$$W_{N,N} = -W_{N-1,N} - W_{N+1,N}, \tag{C.13}$$

but neglecting the backward flux $W_{N,N+1}P_{N+1}(t)$ since $P_{N+1}(t) = 0\ \forall t$. The survival probability P^j_{surv} for a start in bin j is

$$P^j_{\text{surv}}(t) = \sum_{i=1}^{N} G_{ij}(t) = \sum_{i=1}^{N} \mathrm{e}^{-\beta F_i/2} \left(\mathrm{e}^{\tilde{\mathbf{W}}t}\right)_{ij} \mathrm{e}^{\beta F_j/2}, \tag{C.14}$$

which is evaluated numerically at times $t \in [0, 200\text{ ps}]$ with time resolution $\delta t = 0.1$ ps. The FPT distribution is approximated by the finite difference

$$f_{\text{fp}}(t + \delta t/2; j) \approx \frac{P^j_{\text{surv}}(t) - P^j_{\text{surv}}(t + \delta t)}{\delta t}. \tag{C.15}$$

The MFPT is obtained by taking the first moment of the FPT distribution

$$\tau_{\text{fp}} = \int_0^\infty \mathrm{d}t\ t f_{\text{fp}}(t) = \int_0^\infty \mathrm{d}t\ P_{\text{surv}}(t) \approx \delta t \left(\frac{1 + P^j_{\text{surv}}(N\,\delta t)}{2} + \sum_{n=1}^{N-1} P^j_{\text{surv}}(n\,\delta t) \right), \tag{C.16}$$

where we have set the upper cutoff to $N = 2000$.

FPT histograms from MD data and from the numerical solution of the FP equation described in this section for other target separations than the one shown in Fig. 2.10b are found in Fig. C.3. No significant impact on the FPT distributions has been observed when refining the discretization in space and/or time.

APPENDIX D

LOW REYNOLDS NUMBER HYDRODYNAMICS AT PLANAR INTERFACES

Interfaces alter the hydrodynamic flow field in a fluid and thus have implications on the motion of nearby objects. In the following, various analytical results used in the Chapters 3 and 7 for the quasi-stationary mobilities of spherical objects in a viscous and incompressible fluid next to a planar interface are reproduced. The dependence of the self-mobilities on the distance to the interface at surfaces with finite and vanishing slip-length are discussed in the Secs. D.1 and D.2 respectively. Hydrodynamic interactions (HI) between spherical objects next to a no-slip boundary described by the Rotne-Prager-Blake (RPB) tensor are covered in Sec. D.3.

D.1 Self-Mobilities at a Planar Interface with Finite Slip Length

Approximate expressions for the mobilities of a no-slip sphere of radius a at a distance h from an interface with finite slip length b have been derived in Ref. [157] by Lauga and Squires (LS). The mobility parallel to the interface is approximated by

$$\mu_{\parallel}^{\mathrm{LS}}(h) = \mu_0 \left(1 + \frac{3a}{8h}\left(1 - 2\mathcal{J}(\mathrm{Kn})\right)\right) + \mathcal{O}\left(\frac{a^3}{h^3}\right), \tag{D.1}$$

and the one perpendicular to the wall by

$$\mu_{\perp}^{\mathrm{LS}}(h) = \mu_0 \left(1 - \frac{3a}{4h}\left(1 + 2\mathcal{I}(\mathrm{Kn})\right)\right) + \mathcal{O}\left(\frac{a^3}{h^3}\right). \tag{D.2}$$

Here, the Knudsen number is $\mathrm{Kn} \equiv b/h$ and the functions

$$\mathcal{I}(\mathrm{Kn}) = \frac{\mathrm{Kn}(\mathrm{Kn}-1) + \mathrm{e}^{1/\mathrm{Kn}}\Gamma(0, 1/\mathrm{Kn})}{8\mathrm{Kn}^3}, \tag{D.3}$$

and

$$\mathcal{J}(\mathrm{Kn}) = \frac{-\mathrm{Kn}(3\mathrm{Kn}+1) + \mathrm{e}^{1/\mathrm{Kn}}(1+2\mathrm{Kn})^2\,\Gamma(0, 1/\mathrm{Kn})}{8\mathrm{Kn}^3} + 2\,\frac{\mathrm{e}^{2/\mathrm{Kn}}\,\Gamma(0, 2/\mathrm{Kn})}{\mathrm{Kn}}, \tag{D.4}$$

have been defined, which involve the incomplete Gamma function

$$\Gamma(\gamma, x) \equiv \int_x^\infty \mathrm{d}t\; t^{\gamma-1}\,\mathrm{e}^{-t}. \tag{D.5}$$

Note that the factor 2 in front of the second summand in Eq. D.4 is missing in Eq. 34b of Ref. [157] due to a typo.

The Eqs. D.1 and D.2 are used to approximate the diffusivity profiles of water molecules next to a solid, homogeneous surface with finite slip length in Sec. 3.4: The continuum estimates for the lateral and perpendicular diffusivities $D_{\mathrm{lat}} = k_{\mathrm{B}}T\mu_{\parallel}^{\mathrm{LS}}$ and $D_z = k_{\mathrm{B}}T\mu_{\perp}^{\mathrm{LS}}$ are shown as solid colored lines in Fig. 3.7d.

In the limit of vanishing slip length, $b \to 0$, the Eqs. D.1 and D.2 reduce to the approximate expressions for the mobilities of a sphere in the vicinity of a no-slip wall (Eqs. 7.8 and 7.9).

D.2 Self-Mobilities at a Planar No-Slip Interface

The expressions for the self-mobilities of a sphere of radius a at a distance h from a planar no-slip interface, are reproduced: The approximate expression for the self-mobility parallel to the interface obtained by Perkins and Jones [285] (PJ) reads

$$\mu_{\parallel}^{\mathrm{PJ}}(h) = \mu_0 \left(1 - \frac{8}{15}\log\left(1-\frac{a}{h}\right) + 0.029\,\frac{a}{h} + 0.04973\left(\frac{a}{h}\right)^2 - 0.1249\left(\frac{a}{h}\right)^3 + \dots\right)^{-1}. \tag{D.6}$$

In turn, Stimson's and Jeffery's (SJ) exact result for the self-mobility perpendicular to the surface [103, 286] is given by

$$\begin{aligned}\mu_{\perp}^{\mathrm{SJ}}(h) =& \frac{3\mu_0}{4\sinh\rho}\times \\ &\left(\sum_{n=1}^{\infty}\frac{n(n+1)}{(2n-1)(2n+3)}\left[\frac{2\sinh\left((2n+1)\rho\right)+(2n+1)\sinh(2\rho)}{4\sinh^2\left((n+\frac{1}{2})\rho\right)-(2n+1)^2\sinh^2(\rho)}-1\right]\right)^{-1},\end{aligned} \tag{D.7}$$

with $\rho \equiv \cosh^{-1}(h/a)$.

The above expressions are used to approximate the diffusivity profiles of water molecules next to solid, homogeneous surfaces characterized by a stagnation layer in Sec. 3.4: The continuum estimates for the lateral and perpendicular diffusivities $D_{\mathrm{lat}} = k_{\mathrm{B}}T\mu_{\parallel}^{\mathrm{PJ}}$ and $D_z = k_{\mathrm{B}}T\mu_{\perp}^{\mathrm{SJ}}$ are shown as solid colored lines in Fig. 3.7e-f. Furthermore, the Eqs. D.6 and D.7 are compared to approximate expressions (Eqs. 7.8 and 7.9) in Fig. 7.1 setting $h = z$.

D.3 Hydrodynamic Interactions at a Planar No-Slip Interface

Entries of the Rotne-Prager level of the Blake tensor

As outlined in Sec. 7.1 the Rotne-Prager level of the Blake tensor describing the approximate HI of finite sized particles near a planar no-slip wall at $z = 0$ is obtained from the Blake tensor $\overleftrightarrow{\boldsymbol{\mu}}^B$ by the operation

$$\begin{aligned}\overleftrightarrow{\boldsymbol{\mu}}^{\mathrm{RPB}}(\boldsymbol{r}_i,\boldsymbol{r}_j) &= \left[\left(1+\frac{a^2}{6}\nabla_{\boldsymbol{r}}^2+\frac{a^2}{6}\nabla_{\boldsymbol{r}'}^2\right)\overleftrightarrow{\boldsymbol{\mu}}^B(\boldsymbol{r},\boldsymbol{r}')\right]_{\boldsymbol{r}=\boldsymbol{r}_i,\boldsymbol{r}'=\boldsymbol{r}_j} \\ &= \overleftrightarrow{\boldsymbol{\mu}}^{RP}(\boldsymbol{r}_i-\boldsymbol{r}_j)-\overleftrightarrow{\boldsymbol{\mu}}^{RP}(\boldsymbol{r}_i-\bar{\boldsymbol{r}}_j)+\overleftrightarrow{\boldsymbol{\Delta\mu}}(\boldsymbol{r}_i,\boldsymbol{r}_j),\end{aligned} \tag{D.8}$$

where $\bar{\boldsymbol{r}}_j = (x_j, y_j, -z_j)^{\mathrm{T}}$ is the image position of particle j and where the definition of the Blake tensor (Eq. 7.2) as well as of the Rotne-Prager (RP) tensor [238]

$$\overleftrightarrow{\boldsymbol{\mu}}^{\mathrm{RP}}(\boldsymbol{R}) = \frac{1}{8\pi\eta_0 R}\left[\overleftrightarrow{\mathbf{1}}+\frac{\boldsymbol{R}\otimes\boldsymbol{R}}{r^2}\right]+\frac{a^2}{4\pi\eta_0 R^3}\left[\frac{\overleftrightarrow{\mathbf{1}}}{3}-\frac{\boldsymbol{R}\otimes\boldsymbol{R}}{R^2}\right], \tag{D.9}$$

are used. Compared to the case of an unbounded fluid, the hydrodynamic drag on bead i resulting from an external force acting on bead j is thus modified by two terms: (i) the RP-interaction with the image of bead j (second term in Eq. D.8) and (ii) the RP-level of the Stokes and source doublets (cf. Eqs. 7.4 and 7.5) at the position of the image

$$\overleftrightarrow{\boldsymbol{\Delta\mu}}(\boldsymbol{r}_i,\boldsymbol{r}_j) \equiv \left[\left(1+\frac{a^2}{6}\nabla_{\boldsymbol{r}}^2+\frac{a^2}{6}\nabla_{\boldsymbol{r}'}^2\right)\left(\overleftrightarrow{\boldsymbol{\mu}}^{D}(\boldsymbol{r}-\bar{\boldsymbol{r}}')-\overleftrightarrow{\boldsymbol{\mu}}^{SD}(\boldsymbol{r}-\bar{\boldsymbol{r}}')\right)\right]_{\boldsymbol{r}=\boldsymbol{r}_i,\boldsymbol{r}'=\boldsymbol{r}_j}, \tag{D.10}$$

for which we report the explicit entries in the following. Note that our expressions differ from a previously reported version of the tensor [328].

The indices α, β and z specify the entries of the matrix $\overleftrightarrow{\boldsymbol{\Delta\mu}}$ and the elements of the vector $\overline{\boldsymbol{R}} = \left(\overline{R}_x, \overline{R}_y, \overline{R}_z\right)^{\mathrm{T}} = \left(x_i - x_j, y_i - y_j, z_i + z_j\right)^{\mathrm{T}}$. The diagonal matrix entries are given by

$$\Delta\mu_{\alpha\alpha} = \frac{1}{4\pi\eta_0}\left(\frac{-z_i z_j}{\overline{R}^3}\left(1-3\frac{\overline{R}_\alpha^2}{\overline{R}^2}\right)+\frac{a^2\overline{R}_z^2}{\overline{R}^5}\left(1-5\frac{\overline{R}_\alpha^2}{\overline{R}^2}\right)\right), \quad \alpha\in\{x,y,z\}, \tag{D.11}$$

$$\Delta\mu_{zz} = \frac{1}{4\pi\eta_0}\left(\frac{z_i z_j}{\overline{R}^3}\left(1-3\frac{\overline{R}_z^2}{\overline{R}^2}\right)-\frac{a^2\overline{R}_z^2}{\overline{R}^5}\left(3-5\frac{\overline{R}_z^2}{\overline{R}^2}\right)\right), \tag{D.12}$$

the off-diagonal ones read

$$\Delta\mu_{\alpha\beta} = \frac{1}{4\pi\eta_0}\left(\frac{3z_i z_j\overline{R}_\alpha\overline{R}_\beta}{\overline{R}^5}-5a^2\frac{\overline{R}_\alpha\overline{R}_\beta\overline{R}_z^2}{\overline{R}^7}\right), \qquad \alpha\neq\beta\in\{x,y,z\}, \tag{D.13}$$

$$\Delta\mu_{\alpha z} = \frac{1}{4\pi\eta_0}\left(\frac{z_j\overline{R}_\alpha}{\overline{R}^3}\left(1-3\frac{z_i\overline{R}_z}{\overline{R}^2}\right)-\frac{a^2\overline{R}_\alpha\overline{R}_z}{\overline{R}^5}\left(2-5\frac{\overline{R}_z^2}{\overline{R}^2}\right)\right), \qquad \alpha\in\{x,y,z\}, \tag{D.14}$$

$$\Delta\mu_{z\alpha} = \frac{1}{4\pi\eta_0}\left(\frac{z_j\overline{R}_\alpha}{\overline{R}^3}\left(1+3\frac{z_i\overline{R}_z}{\overline{R}^2}\right) - 5\frac{a^2\overline{R}_\alpha\overline{R}_z^3}{\overline{R}^7}\right), \qquad \alpha \in \{x,y,z\}. \tag{D.15}$$

Altogether, the HI described by the Eqs. D.8- D.15 are equivalent to the expressions in Ref. [283]. Note the following typo in a previous publication by Kim and Netz [282]: In Eq. 2.14, the plus sign in front of the last line should be replaced by a minus sign in order to obtain the above expressions.

Pre-Averaged form of the Rotne-Prager level of the Blake tensor

For the two dimensional version of the mean-field theory in Sec. 7.2.2, the 2×2-submatrix of $\overleftrightarrow{\mu}^{\mathrm{RPB}}$ corresponding to the x- and y-coordinates is pre-averaged by using the two dimensional Gaussian probability density function given in Eq. 7.28. The right hand side of Eq. 7.27 yields

$$\begin{aligned}\frac{\mu_{\mathrm{avg}}^{\mathrm{RPB}}}{\mu_0} = {} & \frac{\sqrt{\pi}(4+9\tilde{\sigma}^2)\mathrm{erfc}\,(2/\tilde{\sigma})}{8\tilde{\sigma}^3} - \frac{\mathrm{e}^{-4/\tilde{\sigma}^2}}{4\tilde{\sigma}^2} + \frac{\mathrm{e}^{-4/\tilde{\sigma}^2}}{4\tilde{\sigma}^6\left(1+\tilde{z}^2\right)^{5/2}}\left(64\tilde{z}^4\left(1+\tilde{z}^2\right)^2\right. \\ & \left.+8\tilde{\sigma}^2\tilde{z}^2\left(1+\tilde{z}^2\right)\left(4+6\tilde{z}^2+3\tilde{z}^4\right)+\tilde{\sigma}^4\left(1+7\tilde{z}^2+15\tilde{z}^4+6\tilde{z}^6\right)\right) - \frac{\sqrt{\pi}}{8\tilde{\sigma}^7} \\ & \times \mathrm{e}^{4\tilde{z}^2/\tilde{\sigma}^2}\left(32\tilde{z}^4(8+3\tilde{\sigma}^2)+4\tilde{\sigma}^2\tilde{z}^2(32+9\tilde{\sigma}^2)+\tilde{\sigma}^4(4+9\tilde{\sigma}^2)\right)\mathrm{erfc}\left(2\frac{\sqrt{1+\tilde{z}^2}}{\tilde{\sigma}}\right),\end{aligned} \tag{D.16}$$

where $\tilde{\sigma}^2 \equiv \sigma^2(|s-s'|)/a^2$ denotes the normalized mean square distance between s and s' (Eq. 7.28), and $\tilde{z} \equiv z/a$. Note that the positive exponential in the last row of Eq. D.16 is a source of numerical error for values $z/a \gtrsim 25$ when using double precision numbers. In this case, an asymptotic expansion of the above expression for the limit $z/a \to \infty$ can be used.

APPENDIX E

OPTICAL TWEEZERS – SIGNAL PROCESSING, DATA ANALYSIS & STATISTICS

In the following, technical aspects of the spectral analysis of the optical tweezer experiments in Chapter 5 are provided: Various filtering sources entering the signal processing are covered in Sec. E.1, a minimal model explaining the observed crosstalk asymmetry is presented in Sec. E.2, periodogram covariances are derived in Sec. E.3, the use of the discrete Fourier transform (DFT) for the signal analysis is reviewed in Sec. E.4, and the appearance of normally distributed random variables on logarithmic scales is discussed in Sec. E.5.

E.1 Possible Forms of Filtering

Signal filtering can occur due to a number of different reasons, some examples are discussed in the following subsections. Subsequent application of various filters corresponds to the iterative convolution of the original signal with the various filter kernels in time domain or, more conveniently, to the multiplication with the product of transfer functions in frequency space, cf. Eq. A.2.

Filtering of the position sensing device

Due to the transparency of silicon to the employed laser light of 1064 nm wavelength, the electrical signal produced by the position sensing device differs from the actual dynamics of the centroid of the laser spot intensity [244, 248]. This parasitic or "virtual" filtering can be modeled [216, 248] via a transfer function

$$f_i^{\mathrm{pf}}(\omega) = \phi_i + \mathrm{i}\,\frac{1-\phi_i}{\mathrm{i}+\omega\tau_i}, \quad i \in \{1,2\}, \tag{E.1}$$

where ϕ_i is the fraction of fast (instantaneously detected) electrons and τ_i is the typical relaxation timescale of the slow electron fraction in channel i. Power spectral densities (PSDs) thus are modified by factors

$$f_i^{\mathrm{pf}}(\omega) f_j^{\mathrm{pf}^\star}(\omega) = \phi_i\phi_j + \frac{1-\phi_i\phi_j}{1+\mathrm{i}\,\omega(\tau_j-\tau_i)+\tau_i\tau_j\omega^2} + \mathrm{i}\,\omega\,\frac{\phi_j\tau_j(1-\phi_i)-\phi_i\tau_i(1-\phi_j)}{1+\mathrm{i}\,\omega(\tau_j-\tau_i)+\tau_i\tau_j\omega^2}, \tag{E.2}$$

which for $i = j$ reduce to

$$|f_i^{\mathrm{pf}}(\omega)|^2 = {\phi_i}^2 + \frac{1-\phi_i^2}{1+(\omega\tau_i)^2}, \tag{E.3}$$

which is purely real. In contrast, even slight asymmetries in the filtering properties of the two detectors result in a non-vanishing imaginary part of $f_1^{\mathrm{pf}} f_2^{\mathrm{pf}\star}$ as discussed in Sec. 5.6, see Fig. E.1a for typical frequency dependences.

Electric filter

The amplification device used in our setup acts as an 8th order Butterworth filter with $f_{3\mathrm{dB}} = 200$ kHz corresponding to transfer functions

$$f_i^{\mathrm{B8}}(\omega) = \frac{1}{B_8(\mathrm{i}\,\omega/(2\pi f_{3\mathrm{dB}}))}, \tag{E.4}$$

with B_8 being the 8th order Butterworth polynomial, so that

$$f_i^{\mathrm{B8}}(\omega) f_j^{\mathrm{B8}\star}(\omega) = \frac{1}{1+(\omega/(2\pi f_{3\mathrm{dB}}))^{16}}. \tag{E.5}$$

In Fig. E.1b, Butterworth filters are compared to first-order low-pass filters, for which

$$f_i^{\mathrm{lp}}(\omega) f_j^{\mathrm{lp}\star}(\omega) = \frac{1}{1+(\omega/(2\pi f_{3\mathrm{dB}}))^{2}}. \tag{E.6}$$

Temporal averaging

Temporal averaging also represents a form of low-pass filtering: For a uniform averaging of a signal over a time window τ_{av}, i.e., a filter kernel

$$f_i^{\mathrm{av}}(t) = \frac{1}{\tau_{\mathrm{av}}}\Theta(t)\Theta(\tau_{\mathrm{av}} - t), \tag{E.7}$$

where Θ denotes the Heaviside step function, one obtains

$$f_i^{\mathrm{av}}(\omega) f_i^{\mathrm{av}\star}(\omega) = \left(\frac{2}{\omega\tau_{\mathrm{av}}}\,\sin\left(\frac{\omega\tau_{\mathrm{av}}}{2}\right)\right)^2, \tag{E.8}$$

in frequency domain. In consequence, PSDs of the time-averaged signals are reduced in amplitude compared to unfiltered PSDs for frequencies $\omega \gtrsim 1/\tau_{\mathrm{av}}$ as is shown in Fig. E.1c.

Time delay between channels

The temporal shift of a signal by $\tau_{\mathrm{delay},\,i}$ corresponds to

$$f_i^{\mathrm{del}}(t) = \delta(t - \tau_{\mathrm{delay},\,i}), \qquad \tau_{\mathrm{delay},\,i} \geq 0, \tag{E.9}$$

and thus translates into

$$f_i^{\mathrm{del}}(\omega) = \exp\left(\mathrm{i}\omega\tau_{\mathrm{del},\,i}\right). \tag{E.10}$$

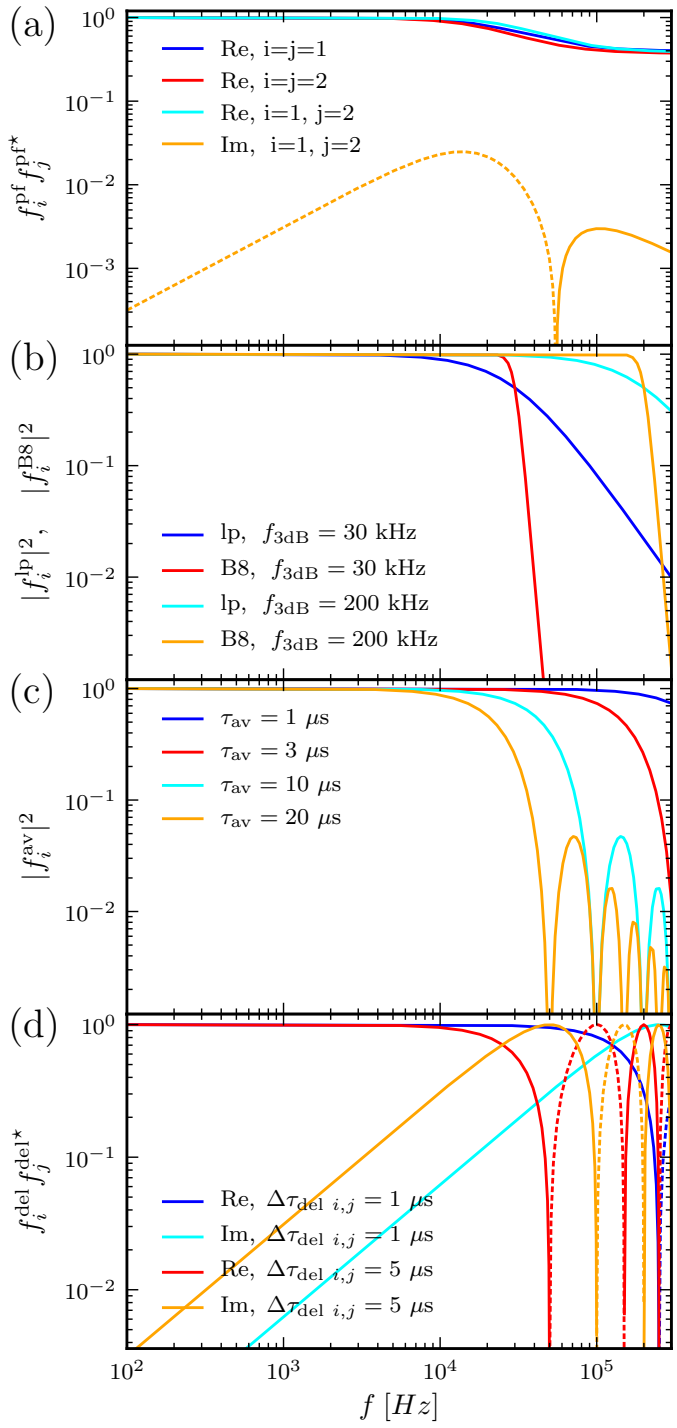

Figure E.1:
Attenuation $f_i f_j^\star$ resulting from various filtering sources as discussed in Sec. E.1: (a) parasitic filtering of the position sensing devices (Eq. E.2) using the parameters from Tab. 5.2 for the $\perp$ direction, (b) different electric low-pass filters (Eqs. E.5 and E.6), (c) uniform averaging of signals over a time window of duration τ_{av} (Eq. E.8), (d) time delay between the two recorded signals (Eq. E.11). Positive values of $f_i f_j^\star$ are drawn as solid lines, negative ones are dashed.

Auto-PSDs thus remain unaffected by time shifts, $|f_i(\omega)|^2 = 1$, while the cross-PSDs are multiplied by a complex factor

$$f_i^{\mathrm{del}}(\omega) f_j^{\mathrm{del}\star}(\omega) = \cos\left(\omega \Delta\tau_{\mathrm{del}\ i,j}\right) + \mathrm{i}\sin\left(\omega \Delta\tau_{\mathrm{del}\ i,j}\right), \tag{E.11}$$

with relative time delay between the channels

$$\Delta\tau_{\mathrm{del}\ i,j} \equiv \tau_{\mathrm{del},\ i} - \tau_{\mathrm{del},\ j}. \tag{E.12}$$

For $\Delta\tau_{\mathrm{del}\ i,j} \neq 0$, cross-PSDs are thus modified; two examples are shown in Fig. E.1d.

Overall transfer functions

Given the specifications of our signal recording hardware (Sec. 5.1), time averaging effects as well as temporal delays in the signal detection are negligible. The overall filter function for channel i is therefore given by

$$f_i(\omega) = f_i^{\mathrm{pf}}(\omega) f_i^{\mathrm{B8}}(\omega), \tag{E.13}$$

accounting for the parasitic filtering of the position sensing device (Eq. E.1) and for the Butterworth filter of the amplification device (Eq. E.4). The above expression involves two parameters ϕ_i and τ_i for each channel; these have been determined in the course of the instrumental calibration in Sec. 5.6.

E.2 Crosstalk Asymmetry

The calibration in Sec. 5.6 yields values for ϵ_{11}, ϵ_{12}, ϵ_{21}, and ϵ_{22}, which reflect the sensitivity of the recorded voltage signals to the motion of the beads in their respective traps. As is seen from Tab. 5.2, the relative crosstalk amplitudes $\epsilon_{12}/\epsilon_{11}$ and $\epsilon_{21}/\epsilon_{22}$ vary considerably (ranging from 0.56 to 3.7 percent) and depend on the spatial direction α. Moreover, in channel 1 the importance of crosstalk is larger for the $\parallel$-direction, while it is dominant for the $\perp$-direction in channel 2. In the following, we present a minimal model to explain this, at first sight counterintuitive, asymmetry.

Minimal model

Due to depolarization in the optical path and the intrinsic non-perfect separation and conservation of polarization upon transmission through and reflection by the polarization beam splitters (PBSs), the light in each of the two traps is not perfectly polarized. Distinguishing the polarizations along two orthogonal spatial directions x and y, the light intensities in the traps are

$$\boldsymbol{I}_{\mathrm{trap}\ 1} = \begin{pmatrix} 1-\phi_x \\ \phi_y \end{pmatrix} I_0, \qquad \boldsymbol{I}_{\mathrm{trap}\ 2} = \begin{pmatrix} \phi_x \\ 1-\phi_y \end{pmatrix} I_0, \tag{E.14}$$

where we have for simplicity assumed that the overall intensities in x- and y-polarization are equal ($= I_0$) and where $\phi_x \ll 1$ and $\phi_y \ll 1$ quantify the amount of light of "wrong" polarization in each of the traps. The light in trap 1 is thus mainly x-polarized, the one in trap 2 mainly y-polarized.

The PBS between sample chamber and detectors (cf. Fig. 5.1) is responsible for sending x-polarized light to detector 1 and y-polarized light to detector 2. However, due to the imperfect properties of the PBS, the incident light intensities on the detector surfaces are

$$\boldsymbol{I}_{\text{det 1, surface}} = \underbrace{\begin{pmatrix}(1-\psi_x)(1-\phi_x)\\ \psi_y\phi_y\end{pmatrix} I_0}_{\text{from trap 1}} + \underbrace{\begin{pmatrix}(1-\psi_x)\phi_x\\ \psi_y(1-\phi_y)\end{pmatrix} I_0}_{\text{from trap 2}}, \tag{E.15}$$

$$\boldsymbol{I}_{\text{det 2, surface}} = \underbrace{\begin{pmatrix}\psi_x(1-\phi_x)\\ (1-\psi_y)\phi_y\end{pmatrix} I_0}_{\text{from trap 1}} + \underbrace{\begin{pmatrix}\psi_x\phi_x\\ (1-\psi_y)(1-\phi_y)\end{pmatrix} I_0}_{\text{from trap 2}}, \tag{E.16}$$

where ψ_x reflects the fraction of x-polarized light, which is erroneously sent to detector 2, and ψ_y the fraction of y-polarized light arriving at detector 1. The experimentally recorded voltages are

$$z_{i,\alpha} = a_{i,\alpha} V_{i,\alpha}^{\text{out}} = a_{i,\alpha} \frac{V_{i,\alpha}^{\Delta}}{V_{i,\alpha}^{\Sigma}}, \qquad i \in \{1,2\}, \quad \alpha \in \{\parallel, \perp\}, \tag{E.17}$$

where $a_{i,\alpha}$ is the manually adjusted amplification factor of the corresponding channel, where the sum signal $V_{i,\alpha}^{\Sigma}$ is proportional to the overall light intensity, and where the difference signal $V_{i,\alpha}^{\Delta}$ is proportional to both the light intensity and the α-coordinate of the laser centroid on the position sensing device [214, 329].

It is important to note that position sensing for the spatial directions $\parallel$ and $\perp$ occurs in two different layers of the device (cf. Sec. 5.1). We assume without loss of generality that the detection of the $\parallel$-direction occurs in the top layer and obtain signals

$$z_{1,\parallel} = a_{1,\parallel} \frac{\big((1-\psi_x)(1-\phi_x) + \psi_y\phi_y\big)\, r_{1,\parallel} + \big((1-\psi_x)\phi_x + \psi_y(1-\phi_y)\big)\, r_{2,\parallel}}{(1-\psi_x) + \psi_y}, \tag{E.18}$$

$$z_{2,\parallel} = a_{2,\parallel} \frac{\big(\psi_x(1-\phi_x) + (1-\psi_y)\phi_y\big)\, r_{1,\parallel} + \big(\psi_x\phi_x + (1-\psi_y)(1-\phi_y)\big)\, r_{2,\parallel}}{\psi_x + (1-\psi_y)}. \tag{E.19}$$

The relative crosstralk amplitudes are then given by

$$\frac{\epsilon_{12}^{\parallel}}{\epsilon_{11}^{\parallel}} = \frac{(1-\psi_x)\phi_x + \psi_y(1-\phi_y)}{(1-\psi_x)(1-\phi_x) + \psi_y\phi_y} \approx \phi_x + \psi_y, \tag{E.20}$$

$$\frac{\epsilon_{21}^{\parallel}}{\epsilon_{22}^{\parallel}} = \frac{(\psi_x(1-\phi_x) + (1-\psi_y)\phi_y}{\psi_x\phi_x + (1-\psi_y)(1-\phi_y)} \approx \phi_y + \psi_x, \tag{E.21}$$

where the approximations result from retaining only terms linear in ϕ_x, ϕ_y, ψ_x and ψ_y. Overall, the crosstalk in channel 1 thus results from two effects: (i) the amount ϕ_x of x-polarized light in trap 2 and (ii) the fact that the PBS between sample chamber and detectors erroneously reflects or transmits a fraction ψ_y of the y-polarized light from trap 2 to detector 1. A certain part of the

light intensity being absorbed in the top layer of the position sensing device the light intensities relevant for the detection of the $\perp$-direction are

$$\boldsymbol{I}_{\text{det 1, 2}^{\text{nd}}\text{ layer}} = \underbrace{\begin{pmatrix} \vartheta_x(1-\psi_x)(1-\phi_x) \\ \vartheta_y\psi_y\phi_y \end{pmatrix} I_0}_{\text{from trap 1}} + \underbrace{\begin{pmatrix} \vartheta_x(1-\psi_x)\phi_x \\ \vartheta_y\psi_y(1-\phi_y) \end{pmatrix} I_0}_{\text{from trap 2}}, \tag{E.22}$$

$$\boldsymbol{I}_{\text{det 2, 2}^{\text{nd}}\text{ layer}} = \underbrace{\begin{pmatrix} \vartheta_x\psi_x(1-\phi_x) \\ \vartheta_y(1-\psi_y)\phi_y \end{pmatrix} I_0}_{\text{from trap 1}} + \underbrace{\begin{pmatrix} \vartheta_x\psi_x\phi_x \\ \vartheta_y(1-\psi_y)(1-\phi_y) \end{pmatrix} I_0}_{\text{from trap 2}}. \tag{E.23}$$

where the transmission coefficients for the two polarizations are denoted by ϑ_x and ϑ_y, respectively. The resulting signal amplitudes are

$$z_{1,\perp} = a_{1,\perp} \frac{\left(\vartheta_x(1-\psi_x)(1-\phi_x) + \vartheta_y\psi_y\phi_y\right) r_{1,\perp} + \left(\vartheta_x(1-\psi_x)\phi_x + \vartheta_y\psi_y(1-\phi_y)\right) r_{2,\perp}}{\vartheta_x\,(1-\psi_x) + \vartheta_y\psi_y}, \tag{E.24}$$

$$z_{2,\perp} = a_{2,\perp} \frac{\left(\vartheta_x\psi_x(1-\phi_x) + \vartheta_y(1-\psi_y)\phi_y\right) r_{1,\perp} + \left(\vartheta_x\psi_x\phi_x + \vartheta_y(1-\psi_y)(1-\phi_y)\right) r_{2,\perp}}{\vartheta_x\psi_x + \vartheta_y\,(1-\psi_y)}, \tag{E.25}$$

giving rise to relative crosstalk amplitudes

$$\frac{\epsilon_{12}^{\perp}}{\epsilon_{11}^{\perp}} = \frac{\vartheta_x(1-\psi_x)\phi_x + \vartheta_y\psi_y(1-\phi_y)}{\vartheta_x(1-\psi_x)(1-\phi_x) + \vartheta_y\psi_y\phi_y} \approx \phi_x + \frac{\vartheta_y}{\vartheta_x}\psi_y, \tag{E.26}$$

$$\frac{\epsilon_{21}^{\perp}}{\epsilon_{22}^{\perp}} = \frac{(\vartheta_x\psi_x(1-\phi_x) + \vartheta_y(1-\psi_y)\phi_y}{\vartheta_x\psi_x\phi_x + \vartheta_y(1-\psi_y)(1-\phi_y)} \approx \phi_y + \frac{\vartheta_x}{\vartheta_y}\psi_x. \tag{E.27}$$

Compared to Eqs. E.20 and E.26, the crosstalk contribution stemming from the PBS between sample chamber and detectors is thus modified due to the polarization-dependent transmission in the top layer of the position sensing device.

Conclusions

As is seen from the Eqs. E.20, E.21, E.26, and E.27, the relative crosstalk amplitudes for the two spatial directions depend on five parameters: the fractions ϕ_x and ϕ_y of "wrong" polarization in the traps, the properties ψ_x and ψ_y of the PBS between sample chamber and detectors, as well as the ratio of transmission coefficients ϑ_x/ϑ_y of the top layer of the position sensing device. PBSs are by construction asymmetric, i.e., in general $\phi_x \neq \phi_y$ and $\psi_x \neq \psi_y$; the four relative crosstalk amplitudes consequently are independent quantities. Note that in particular:

1. If the absorption in the first layer is polarization-independent ($\vartheta_x = \vartheta_y$), one obtains $\epsilon_{12}^{\perp}/\epsilon_{11}^{\perp} = \epsilon_{12}^{\parallel}/\epsilon_{11}^{\parallel}$ and $\epsilon_{21}^{\perp}/\epsilon_{22}^{\perp} = \epsilon_{21}^{\parallel}/\epsilon_{22}^{\parallel}$, i.e., relative crosstalk amplitudes for both spatial directions are equal in contradiction with our observations in Sec. 5.6.

2. If $\epsilon_{12}^{\perp}/\epsilon_{11}^{\perp} < \epsilon_{12}^{\parallel}/\epsilon_{11}^{\parallel}$, then $\vartheta_y < \vartheta_x$ as seen from the Eqs. E.20 and E.26. One thus expects $\epsilon_{21}^{\perp}/\epsilon_{22}^{\perp} > \epsilon_{21}^{\parallel}/\epsilon_{22}^{\parallel}$ from Eqs. E.21 and E.27 in accordance with the values in Tab. 5.2.

We conclude that the relative crosstalk amplitudes measured in the experiment can be explained based on the minimal model presented above: The observed asymmetry results from an interplay of three effects: (i) due to depolarization in the optical path and intrinsic non-perfect separation and conservation of polarization upon transmission through and reflection by the PBSs the light in the two traps is not perfectly polarized, (ii) non-perfect separation of polarization by the PBS between sample chamber and detectors, *as well as* (iii) different transmission properties of x- and y-polarized light in the top layer of the position sensing devices. We expect this asymmetry to disappear, if the polarization directions x and y are rotated with respect to the detectors in such a way that $\vartheta_x = \vartheta_y$.

E.3 Periodogram Covariances

We explicitly derive the periodogram covariances for an arbitrary number of signals $z_i(t)$ recorded over a time window T, again neglecting leakage effects (cf. Sec. E.4). According to the Secs. 5.2.2 and 5.4, the Fourier components of the signals

$$z_i(\omega_n) = \sum_j A_{ij}(\omega_n) v_j(\omega_n), \tag{E.28}$$

linearly depend on the stochastic Fourier components v_j representing thermal forces and instrumental noise, where the A_{ij} denote complex coefficients resulting from the underlying equations of motion and the signal processing in the instrument. For a stationary stochastic process, the real and imaginary parts of the stochastic Fourier components are assumed to be normally distributed random variables with vanishing mean and with (cross-)correlations

$$\left\langle \mathrm{Re}\left[v_i(\omega_n)\right] \mathrm{Re}\left[v_j(\omega_{n'})\right] \right\rangle = \left\langle \mathrm{Im}\left[v_i(\omega_n)\right] \mathrm{Im}\left[v_j(\omega_{n'})\right] \right\rangle = T\sigma_{ij}^2(\omega_n)\delta_{nn'}, \tag{E.29}$$

where σ_{ij}^2 denotes the corresponding variance and $\delta_{nn'}$ the Kronecker symbol, meaning that Fourier components corresponding to distinct frequencies are uncorrelated. Real and imaginary parts of the v_i components are independent due to time reversal symmetry and thus

$$\left\langle \mathrm{Re}\left[v_i(\omega_n)\right] \mathrm{Im}\left[v_j(\omega_{n'})\right] \right\rangle = 0. \tag{E.30}$$

Note that Eq. E.28 is quite general in the sense that it describes the electrical signals in any experimental setup, where the thermal motion of the compounds is described by linear integro-differential equations of motion (e.g., Eq. 5.8), the signal processing is linear (Eq. 5.19), and instrumental noise contributing to the signal is additive (Eq. 5.20), and the number of stochastic components v_i is not restricted. As a result, the periodograms

$$P_{ij}(\omega_n) \equiv \frac{1}{T} z_i(\omega_n) z_j^\star(\omega_n) = \frac{1}{T} \sum_{k,l} A_{ik} A_{jl}^\star v_k(\omega_n) v_l^\star(\omega_n), \tag{E.31}$$

are again (complex) random variables, the statistics of which can be inferred from the properties of the v_i-components given above.

In the following, the frequency dependence is implicitly assumed, although the argument ω_n is omitted to keep the notation simple. Basic algebra and Gaussian statistics yield

$$\left\langle v_i v_j^\star \right\rangle = 2T\sigma_{ij}^2, \tag{E.32}$$

$$\langle v_i v_j^\star v_k v_l^\star \rangle = 4T^2(\sigma_{ij}^2\sigma_{kl}^2 + \sigma_{il}^2\sigma_{jk}^2). \tag{E.33}$$

Real and imaginary parts of a periodogram are given by

$$\mathrm{Re}\left[P_{ij}\right] = \frac{1}{2}\frac{1}{T}\sum_{k,l}\left(A_{ik}A_{jl}^\star v_k v_l^\star + A_{ik}^\star A_{jl} v_k^\star v_l\right), \tag{E.34}$$

$$\mathrm{Im}\left[P_{ij}\right] = \frac{1}{2\mathrm{i}}\frac{1}{T}\sum_{k,l}\left(A_{ik}A_{jl}^\star v_k v_l^\star - A_{ik}^\star A_{jl} v_k^\star v_l\right). \tag{E.35}$$

In the limit $T \to \infty$, their expectation values by definition (cf. Eqs. 5.23 and 5.27) correspond to the real and imaginary parts of the corresponding PSDs

$$\left\langle \mathrm{Re}\left[P_{ij}\right]\right\rangle = 2\sum_{k,l}\mathrm{Re}\left[A_{ik}A_{jl}^\star\right]\,\sigma_{kl}^2 = \mathrm{Re}\left[S_{ij}\right], \tag{E.36}$$

$$\left\langle \mathrm{Im}\left[P_{ij}\right]\right\rangle = 2\sum_{k,l}\mathrm{Im}\left[A_{ik}A_{jl}^\star\right]\,\sigma_{kl}^2 = \mathrm{Im}\left[S_{ij}\right]. \tag{E.37}$$

Similarly, making use of Eq. E.33, higher moments of real and imaginary parts of the periodograms can be calculated. Gaussian statistics allow to reformulate the resulting expressions in terms of real and imaginary parts of the PSDs yielding covariances

$$\left\langle \mathrm{Re}\left[P_{ij}\right]\mathrm{Re}\left[P_{kl}\right]\right\rangle - \left\langle \mathrm{Re}\left[P_{ij}\right]\right\rangle\left\langle \mathrm{Re}\left[P_{kl}\right]\right\rangle = \frac{1}{2}\Big(\mathrm{Re}\left[S_{ik}\right]\mathrm{Re}\left[S_{jl}\right] + \mathrm{Im}\left[S_{ik}\right]\mathrm{Im}\left[S_{jl}\right] + \mathrm{Re}\left[S_{il}\right]\mathrm{Re}\left[S_{jk}\right] + \mathrm{Im}\left[S_{il}\right]\mathrm{Im}\left[S_{jk}\right]\Big), \tag{E.38}$$

$$\left\langle \mathrm{Re}\left[P_{ij}\right]\mathrm{Im}\left[P_{kl}\right]\right\rangle - \left\langle \mathrm{Re}\left[P_{ij}\right]\right\rangle\left\langle \mathrm{Im}\left[P_{kl}\right]\right\rangle = \frac{1}{2}\Big(\mathrm{Re}\left[S_{ik}\right]\mathrm{Im}\left[S_{jl}\right] - \mathrm{Im}\left[S_{ik}\right]\mathrm{Re}\left[S_{jl}\right] + \mathrm{Im}\left[S_{il}\right]\mathrm{Re}\left[S_{jk}\right] - \mathrm{Re}\left[S_{il}\right]\mathrm{Im}\left[S_{jk}\right]\Big), \tag{E.39}$$

$$\left\langle \mathrm{Im}\left[P_{ij}\right]\mathrm{Im}\left[P_{kl}\right]\right\rangle - \left\langle \mathrm{Im}\left[P_{ij}\right]\right\rangle\left\langle \mathrm{Im}\left[P_{kl}\right]\right\rangle = \frac{1}{2}\Big(\mathrm{Re}\left[S_{ik}\right]\mathrm{Re}\left[S_{jl}\right] + \mathrm{Im}\left[S_{ik}\right]\mathrm{Im}\left[S_{jl}\right] - \mathrm{Re}\left[S_{il}\right]\mathrm{Re}\left[S_{jk}\right] - \mathrm{Im}\left[S_{il}\right]\mathrm{Im}\left[S_{jk}\right]\Big). \tag{E.40}$$

Again, these approximations are strictly exact only in the limit $T \to \infty$. For the case of two detected signals ($k = i$, $l = j$), the variances resulting from the above expressions are given and discussed in Sec. 5.5.1; the overall covariance matrix for the averaged periodograms of two signals is found in Eq. 5.36.

E.4 Discrete Fourier Transformation

Consider a continuous signal $z(t)$ of infinite duration, which is sampled with a finite sampling rate $f_{\mathrm{sampl}} \equiv 1/\Delta t$ over a time window of duration $T \equiv N\Delta t$. Applying a DFT to $z(t)$ yields N discrete Fourier components

$$Z(n) \equiv \sum_{m=0}^{N-1} z(m\Delta t)\,\mathrm{e}^{\mathrm{i}\,2\pi mn/N} \approx \frac{z(\omega_n)}{\Delta t}, \tag{E.41}$$

where $z(\omega_n)$ denotes the value of the Fourier transformation of the original, continuous signal of infinite duration at the angular frequency $\omega_n \equiv 2\pi n/(N\Delta t)$ with n being integer. Due to the finite time resolution and the overall duration of the signal, the correspondence between discrete and continuous Fourier components in Eq. E.41 is only approximate. In the following, we review the relationship between discrete and continuous Fourier transformations and

point out which precautions have to be taken when working with DFTs [330]. Eq. E.41 can be reformulated as

$$Z(n) = \int_{-\infty}^{\infty} \mathrm{d}t \; \mathrm{Pulse}_T(t) \, \mathrm{Comb}_{\Delta t}(t) \, z(t) \, \mathrm{e}^{\mathrm{i}\omega_n t}, \tag{E.42}$$

where we defined the functions

$$\mathrm{Pulse}_T(t) \equiv \Theta(t + \Delta t/2)\Theta(-t + T - \Delta t/2), \tag{E.43}$$

$$\mathrm{Comb}_{\Delta t}(t) \equiv \sum_{m=-\infty}^{\infty} \delta(t - m\Delta t). \tag{E.44}$$

The discrete Fourier components Z thus correspond to the continuous Fourier transformation of the product of the rectangular pulse function Pulse_T, the Dirac comb function $\mathrm{Comb}_{\Delta t}$ and the continuous and infinite signal z. According to the convolution theorem (Eq. A.3)

$$Z(n) = (2\pi)^{-2} \, \mathrm{Pulse}_T * \mathrm{Comb}_{\Delta t} * z \, (\omega_n), \tag{E.45}$$

involving two convolutions: the first one arises from the finite window length T and is responsible for spectral leakage of the DFT, the second one is due to the finite sampling time interval Δt and causes aliasing.

Spectral leakage

The finite window time T causes a convolution with

$$\mathrm{Pulse}_T(\omega) = 2\frac{\sin(\omega T/2)}{\omega} \mathrm{e}^{\mathrm{i}\omega(T-\Delta t)/2}, \tag{E.46}$$

a highly oscillating function with side-lobes decaying as $1/\omega$. Fourier components around ω_n (mainly in a region of width $2\pi/T$) thus contribute to $Z(n)$ defined in Eq. E.41. The effect of spectral leakage can be reduced by using window functions [331], which smoothly fade in and out the signal and thereby reduce the side lobe amplitudes in frequency space at the cost of a wider central peak, see Appendix F.2 for an example. Spectral leakage causes prominent artifacts in the DFTs of periodic signals in case of a mismatch of window time and period of the signal. Since thermal PSDs however smoothly depend on frequency, leakage effects are of minor importance for the spectral analysis in Chapter 5 and can be further minimized by increasing the window length T.

Aliasing

The finite sampling interval Δt causes the convolution of the continuous Fourier transformation with

$$\mathrm{Comb}_{\Delta t}(\omega) = \frac{2\pi}{\Delta t} \sum_{m=-\infty}^{\infty} \delta\left(\omega + m\frac{2\pi}{\Delta t}\right). \tag{E.47}$$

According to the sampling theorem, Fourier components with frequencies $|\omega| > 2\pi f_{\mathrm{Nyq}} \equiv \pi/\Delta t$ are mapped onto Fourier components within the Nyquist interval. In the limit of large sample sizes ($N \to \infty$), Eq. E.45 reduces to

$$Z(n) = \frac{1}{\Delta t} \sum_{m=-\infty}^{\infty} z\left(\omega_n + m\frac{2\pi}{\Delta t}\right) \equiv \frac{1}{\Delta t} z^{\mathrm{al.}}(\omega_n), \tag{E.48}$$

the aliased version of the continuous Fourier transformation. For functions which quickly decay beyond the Nyquist interval, the effect of aliasing is most prominent at its edges ($|\omega| \lesssim 2\pi f_{\mathrm{Nyq}}$). Aliasing effects and the (mis-)use of anti-aliasing filters are discussed in detail in Ref. [214].

Calculating periodograms via discrete Fourier transform

The (cross-)PSD of two signals z_i and z_j is estimated by averaging periodograms

$$P_{ij}(n) \equiv \frac{\Delta t}{N} Z_i(n) Z_j^{\star}(n), \tag{E.49}$$

where Z_i and Z_j denote the DFTs of the time series z_i and z_j, which in practice are efficiently computed using a fast Fourier transformation algorithm. According to Eq. E.45 the expectation value is

$$\left\langle P_{ij}(n) \right\rangle = \frac{\Delta t}{2\pi} \int_{-\infty}^{\infty} \mathrm{d}\omega \; S_{ij}(\omega_n - \omega) \frac{1}{N} \left(\frac{\sin\left(N\omega\Delta t/2\right)}{\sin\left(\omega\Delta t/2\right)} \right)^2, \tag{E.50}$$

which, using Fejér's theorem, in the limit of large sample sizes N, reduces to the aliased PSD defined in Eq. 5.25

$$\lim_{N\to\infty} \left\langle P_{ij}(n) \right\rangle = \sum_{m=-\infty}^{\infty} S_{ij}\left(\omega_n + m\frac{2\pi}{\Delta t}\right). \tag{E.51}$$

The double-infinite sum is in our case approximated numerically using upper and lower cutoffs $m_{\max} = -m_{\min} = 5$, where cutoff errors are negligible due to the attenuation characteristics of the employed 8th order Butterworth filter, cf. Secs. 5.1 and E.1.

E.5 Normally Distributed Variables on Logarithmic Scales

As discussed in Sec. 5.5, the values of averaged periodograms $\bar{P}_{ij}$ are normally distributed random variables. The frequency dependence of periodograms and PSDs is generally displayed on logarithmic graphs. A short calculation demonstrates what has to be kept in mind, when interpreting such graphs.

The PDF for a normally distributed variable x with mean μ and variance σ^2 is given by

$$\mathcal{P}(x) = \frac{1}{\sqrt{2\pi\sigma^2}} \exp\left(-\frac{(x-\mu)^2}{2\sigma^2}\right), \tag{E.52}$$

and thus random variables x scatter around μ, if a linear axis is used. However, in a logarithmic plot, the variables shown are (taking into account the variable's sign)

$$y_{\pm} \equiv \log(\pm x) \;\Leftrightarrow\; x = \pm\exp(y_{\pm}). \tag{E.53}$$

This coordinate change affects the form of the PDF, which fulfills

$$\tilde{\mathcal{P}}_{\pm}(y_{\pm})\,|\mathrm{d}y_{\pm}| = \mathcal{P}(x)\mathrm{d}x. \tag{E.54}$$

The PDFs for the variables $y_{\pm}$ therefore read

$$\tilde{\mathcal{P}}_{\pm}(y_{\pm}) = \mathcal{P}(x)\left|\frac{\mathrm{d}x}{\mathrm{d}y_{\pm}}\right| = \frac{1}{\sqrt{2\pi\sigma^2}}\exp\left(y_{\pm} - \frac{(\pm\exp(y_{\pm}) - \mu)^2}{2\sigma^2}\right). \tag{E.55}$$

Note that $\mathcal{P}$ is peaked around $x^* = \mu$, while the PDFs $\tilde{\mathcal{P}}_{\pm}$ are peaked around

$$y_{\pm}^* = \log\left(\frac{\pm\mu + \sqrt{\mu^2 + 4\sigma^2}}{2}\right), \tag{E.56}$$

with limiting cases (assuming μ positive)

$$\lim_{\sigma\to 0}\exp\left(y_{+}^*\right) = \mu, \qquad \lim_{\mu\to 0}\exp\left(y_{\pm}^*\right) = \sigma. \tag{E.57}$$

As long as the statistical uncertainty is much smaller than the magnitude of the expectation value, random variables accumulate as expected around μ on a logarithmic plot. In the opposite case, random variables tend to scatter (with varying sign) around σ. Depending on the ratio of expectation value and statistical uncertainty, the absolute values of averaged cross-periodograms may therefore reflect the frequency dependence of the cross-PSD or its statistical uncertainty only as discussed in Sec. 5.7.2.

APPENDIX F

DYNAMICS OF THERMALLY FLUCTUATING NONLINEAR SYSTEMS – DETAILS

Additional information regarding the calculations and the analysis in Chapter 6 are provided: The bulky relations between the j_i- and g_i-functions are found in Sec. F.1, details concerning the spectral data analysis and the fitting procedures are given in Sec. F.2 and Sec. F.3 respectively, the statistical threshold for verifying the hypothesis of strictly linear dynamics is derived in Sec. F.4, and the Kramers' approximation for inter-well dynamics is discussed in Sec. F.5.

F.1 Relation between the j_i and g_i-Functions

The relations between the g_i- and j_i-functions are obtained by inserting Eq. 6.5 into Eq. 6.4, grouping together all terms with equal powers of x, and satisfying the equality term by term for arbitrary $x(\omega)$. The five first resulting equations are

$$j_1(\omega)g_1(\omega) = 1, \tag{F.1}$$

$$\sum_{\mathcal{P}(\{\omega,\omega'\})} \Big[j_1(\omega+\omega')g_2(\omega,\omega') + j_2(\omega,\omega')g_1(\omega)g_1(\omega') \Big] = 0, \tag{F.2}$$

$$\begin{aligned} \sum_{\mathcal{P}(\{\omega,\omega',\omega''\})} \Big[& j_1(\omega+\omega'+\omega'')g_3(\omega,\omega',\omega'') + 3j_2(\omega,\omega'+\omega'')g_1(\omega)g_2(\omega',\omega'') \\ & + j_3(\omega,\omega',\omega'')g_1(\omega)g_1(\omega')g_1(\omega'') \Big] = 0, \end{aligned} \tag{F.3}$$

$$\begin{aligned} \sum_{\mathcal{P}(\{\omega,\omega',\omega'',\omega'''\})} \Big[& j_1(\omega+\omega'+\omega''+\omega''')g_4(\omega,\omega',\omega'',\omega''') \\ & + 4j_2(\omega,\omega'+\omega''+\omega''')g_1(\omega)g_3(\omega',\omega'',\omega''') \\ & + 3j_2(\omega+\omega',\omega''+\omega''')g_2(\omega,\omega')g_2(\omega'',\omega''') \\ & + 6j_3(\omega,\omega',\omega''+\omega''')g_1(\omega)g_1(\omega')g_2(\omega'',\omega''') \\ & + j_4(\omega,\omega',\omega'',\omega''')g_1(\omega)g_1(\omega')g_1(\omega'')g_1(\omega''') \Big] = 0, \end{aligned} \tag{F.4}$$

and

$$\begin{aligned}\sum_{\mathcal{P}(\{\omega,\ldots,\omega^{\mathrm{IV}}\})}\Big[&j_1(\omega+\omega'+\omega''+\omega'''+\omega^{\mathrm{IV}})g_5(\omega,\omega',\omega'',\omega''',\omega^{\mathrm{IV}})\\&+5j_2(\omega,\omega'+\omega''+\omega'''+\omega^{\mathrm{IV}})g_1(\omega)g_4(\omega',\omega'',\omega''',\omega^{\mathrm{IV}})\\&+10j_2(\omega+\omega',\omega''+\omega'''+\omega^{\mathrm{IV}})g_2(\omega,\omega')g_3(\omega'',\omega''',\omega^{\mathrm{IV}})\\&+10j_3(\omega,\omega',\omega''+\omega'''+\omega^{\mathrm{IV}})g_1(\omega)g_1(\omega')g_3(\omega'',\omega''',\omega^{\mathrm{IV}})\\&+15j_3(\omega,\omega'+\omega'',\omega'''+\omega^{\mathrm{IV}})g_1(\omega)g_2(\omega',\omega'')g_2(\omega''',\omega^{\mathrm{IV}})\\&+10j_4(\omega,\omega',\omega'',\omega'''+\omega^{\mathrm{IV}})g_1(\omega)g_1(\omega')g_1(\omega'')g_2(\omega''',\omega^{\mathrm{IV}})\\&+j_5(\omega,\omega',\omega'',\omega''',\omega^{\mathrm{IV}})g_1(\omega)g_1(\omega')g_1(\omega'')g_2(\omega''')g_1(\omega^{\mathrm{IV}})\Big]=0,\end{aligned}\tag{F.5}$$

where $\mathcal{P}(\{\ldots\})$ denotes the ensemble of permutations of the elements in $\{\ldots\}$. Solving the above equations for j_1, j_2, etc. and taking the symmetry properties of the functions j_i and g_i into account, one obtains the Eqs. 6.6-6.8 as well as similar expressions for j_4 and j_5, which however are bulky and are therefore not shown.

F.2 Spectral Data Analysis

The spectral estimates from numerical simulations result from the statistical analysis of $M = T_{\mathrm{sim}}/T$ non-overlapping time windows of duration T. We take the discrete Fourier transformation (DFT) of each of the evenly sampled time series as defined by

$$X_n \equiv \sum_{j=0}^{N-1} w_j\, x(j\Delta t)\, \mathrm{e}^{\mathrm{i}\,2\pi jn/N}, \tag{F.6}$$

where the number of data points per time window is $N \equiv T/(\Delta t)$, where Δt is the time resolution of the trajectory and where $w_j \equiv 1-(1-2j/N)^2$ is the Welch window function employed to reduce leakage effects [331]. Estimates for the aliased power spectral densities

$$S^{\mathrm{al.}}(\omega_n) \equiv \sum_{j=-\infty}^{\infty} S\left(\omega_n + j\frac{2\pi}{\Delta t}\right), \tag{F.7}$$

at the frequency $\omega_n \equiv 2\pi n/(N\Delta t)$ are obtained by computing the sample averaged periodogram

$$\overline{P_n} \equiv \frac{\Delta t}{W_2}\overline{X_n X_{-n}} = \frac{\Delta t}{W_2}\frac{1}{M}\sum_{m=0}^{M-1} X_n^{(m)} X_{-n}^{(m)}, \qquad W_2 \equiv \sum_{j=0}^{N-1} w_j^2, \tag{F.8}$$

where $X_n^{(m)}$ denotes DFT-values for time window m and sample averages are denoted by overlines. For the aliased function

$$Y^{\mathrm{al.}}(\omega_n,-\omega_n,\omega_n) \equiv \sum_{j,k,l} Y\left(\omega_n + j\frac{2\pi}{\Delta t}, -\omega_n + k\frac{2\pi}{\Delta t}, \omega_n + l\frac{2\pi}{\Delta t}\right), \tag{F.9}$$

the unbiased estimator [332] is given by

$$\hat{Y}_n \equiv \frac{(\Delta t)^3}{W_4}\left(\frac{M+1}{M-1}\overline{|X_n|^4} - 2\frac{M}{M-1}\left(\overline{|X_n|^2}\right)^2\right), \qquad W_4 \equiv \sum_{j=0}^{N-1} w_j^4. \tag{F.10}$$

F.3 Fits to a Linear Model

Strictly linear overdamped dynamics are characterized by the power spectral density (PSD) given in Eq. 6.58. For the monostable potentials in the Secs. 6.2.2 and 6.2.3, the aliased PSD

$$S_{\text{fit}}^{\text{al.}}(\omega) = \sum_{j=-\infty}^{\infty} S_{\text{fit}}\left(\omega + j\frac{2\pi}{\Delta t}\right) = \frac{\Delta t\, k_{\text{B}} T \sinh\left(\alpha^{\text{fit}}\Delta t/\zeta^{\text{fit}}\right)}{\alpha^{\text{fit}}\left(\cosh\left(\alpha^{\text{fit}}\Delta t/\zeta^{\text{fit}}\right) - \cos(\omega\Delta t)\right)}, \tag{F.11}$$

serves as fit function. For the dynamics in the double-well potential (dw) of Sec. 6.2.4, which is approximated as the superposition of two independent stochastic processes in Sec. 6.4.1, the aliased PSD is approximated by

$$S_{\text{fit, dw}}^{\text{al.}}(\omega) = \frac{\Delta t\, k_{\text{B}} T \sinh\left(\alpha_1^{\text{fit}}\Delta t/\zeta_1^{\text{fit}}\right)}{\alpha_1^{\text{fit}}\left(\cosh\left(\alpha_1^{\text{fit}}\Delta t/\zeta_1^{\text{fit}}\right) - \cos(\omega\Delta t)\right)} + \frac{\Delta t\, k_{\text{B}} T \sinh\left(\alpha_2^{\text{fit}}\Delta t/\zeta_2^{\text{fit}}\right)}{\alpha_2^{\text{fit}}\left(\cosh\left(\alpha_2^{\text{fit}}\Delta t/\zeta_2^{\text{fit}}\right) - \cos(\omega\Delta t)\right)}, \tag{F.12}$$

where α_1^{fit}, α_2^{fit}, ζ_1^{fit}, and ζ_2^{fit} are the fit parameters.

Similarly as in Chapter 5, individual periodograms are exponentially distributed [213] for strictly linear dynamics and the statistical uncertainty of the averaged periodogram values therefore is

$$\sigma_{\overline{P_n}} = \frac{1}{\sqrt{M}}\, S^{\text{al.}}(\omega_n). \tag{F.13}$$

Neglecting leakage effects [331], best fits to the data are therefore obtained by minimizing the weighted sum of residuals

$$\Sigma^2 = \sum_{n=0}^{N-1}\left(\frac{\overline{P_n} - S^{\text{al.}}(\omega_n)}{\sigma_{\overline{P_n}}}\right)^2 = M\sum_{n=0}^{N-1}\left(\frac{\overline{P_n}}{S^{\text{al.}}(\omega_n)} - 1\right)^2, \tag{F.14}$$

thereby effectively penalizing relative deviations between numerical data and fit function as seen on the logarithmic plots in the Figs. 6.7a, 6.8a, and 6.9a.

F.4 Verifying the Hypothesis of Strictly Linear Dynamics

For a strictly linear system, the expectation value $\langle\hat{Y}_n\rangle = Y^{\text{al.}}(\omega_n, -\omega_n, \omega_n) = 0$ (Eq. 6.22). Individual values of $\hat{Y}_n$ however are (for large enough M) normally distributed around 0 with a standard deviation

$$\sigma_{\hat{Y}_n} \equiv 2\frac{W_2^2}{W_4}\Delta t\sqrt{\frac{M+1}{M(M-1)}}\left(S^{\text{al.}}(\omega_n)\right)^2 \approx \frac{W_2^2}{NW_4}\frac{2T}{\sqrt{T_{\text{sim}}/T}}\left(S^{\text{al.}}(\omega_n)\right)^2, \tag{F.15}$$

as again follows from the exponential distribution of periodograms and where $W_2^2/(NW_4)$ is a numerical prefactor depending on the window function only: It equals $\simeq 0.7$ for the Welch-window function employed in the present analysis and is 1 for a rectangular window function. Consequently, the estimates for the spectral kurtosis

$$\hat{\kappa}_n \equiv \frac{\hat{Y}_n}{\left(\overline{P}_n\right)^2}, \tag{F.16}$$

are expected to scatter around 0 with standard deviation

$$\sigma_{\hat{\kappa}_n} \approx \frac{W_2^2}{NW_4} \frac{2T}{\sqrt{T_{\mathrm{sim}}/T}}. \tag{F.17}$$

The hypothesis of strictly linear dynamics thus can only be rejected if the estimates $\hat{\kappa}_n$ are incompatible with what is expected for a linear system from a statistical point of view. As a reference, the 90%-confidence interval for $\pm\hat{\kappa}_n$-values for a strictly linear system ($0.063\ \sigma_{\hat{\kappa}_n} \lesssim \pm\kappa \lesssim 1.96\ \sigma_{\hat{\kappa}_n}$) are shaded in gray in the Figs. 6.7b, 6.8b and 6.9b.

Note that, for a fixed simulation time T_{sim}, the statistical uncertainty for the $\hat{\kappa}_n$-values (Eq. F.17) scales $\propto T^{3/2}$ with the duration of the time window employed for the spectral analysis. The choice for the window length T therefore represents a compromise between increasing the frequency range resolved in the analysis and minimizing leakage effects by increasing T on the one hand (cf. App. E.4), and reducing the statistical uncertainty in the numerical estimate for $\hat{\kappa}_n$ thus allowing to uncover weaker nonlinear contributions to the dynamics by decreasing T on the other hand. As is seen from Eq. F.17, a non-rectangular window function in Eq. F.6 thus has—in addition to reducing leakage effects—the advantage of reducing the statistical uncertainty of $\hat{\kappa}_n$.

F.5 Kramers' Approximation for Inter-Well Dynamics

The Kramers' escape rate [333] for the problem of overdamped diffusion in a double-well potential discussed in Sec. 6.2.4 is

$$k_{\mathrm{inter}} = \frac{\sqrt{-U''_{\mathrm{min}}U''_{\mathrm{max}}}}{2\pi\zeta_0}\, \mathrm{e}^{-\Delta U/k_{\mathrm{B}}T} = \frac{\alpha_0}{2\sqrt{2}\pi\zeta_0}\, \mathrm{e}^{-\Delta\tilde{U}}, \tag{F.18}$$

where $U''_{\mathrm{min}} = \alpha_0$ and $U''_{\mathrm{max}} = -\alpha_0/2$ are the curvatures of the potential U (Eq. 6.52) at the positions of the potential minima and maxima. The PSD

$$S_{\mathrm{inter}}(\omega) = \frac{(\Delta x)^2 k_{\mathrm{inter}}}{4k_{\mathrm{inter}}^2 + \omega^2} = \frac{16\sqrt{2}\pi\Delta U\zeta_0 \mathrm{e}^{\frac{\Delta U}{k_{\mathrm{B}}T}}}{\alpha_0^2 + 2\pi^2\zeta_0^2\omega^2\mathrm{e}^{\frac{2\Delta U}{k_{\mathrm{B}}T}}}, \tag{F.19}$$

is associated with a stochastic process switching at rate k_{inter} between the two potential minima with a mutual distance

$$\Delta x \equiv 4\sqrt{2\Delta U/\alpha_0}. \tag{F.20}$$

Equating Eq. F.19 and the Lorentzian fit function (Eq. 6.58) yields the expression for the fit values given in Eq. 6.66.

APPENDIX G

LINEAR CONTINUUM VISCOELASTIC THEORY

The linear viscoelasticity of continua, which is of relevance in Chapter 8, is shortly reviewed: Basic concepts and relations are introduced in Sec. G.1, the general response of a slab of finite thickness is derived in Sec. G.2, and the results for representative viscoelastic model materials are discussed in Sec. G.3.

G.1 Stress, Strain and Viscoelastic Moduli

We consider the continuum description of a viscoelastic medium: the reference configuration being specified by coordinates $\boldsymbol{r}_0$, the displacement at time t is given by

$$\boldsymbol{u}(\boldsymbol{r}_0, t) = \boldsymbol{r}(\boldsymbol{r}_0, t) - \boldsymbol{r}_0. \tag{G.1}$$

The following considerations apply to small deformations, i.e., $\left|\partial_j u_i\right| \ll 1$, for which the relation between stress and strain tensors is linear

$$\sigma_{ij} = \sum_{k,l} C_{ijkl}\, \varepsilon_{kl}, \tag{G.2}$$

where the entries of the strain tensor are

$$\varepsilon_{ij} \equiv \frac{1}{2}\left(\partial_i u_j(t) + \partial_j u_i(t)\right). \tag{G.3}$$

The symmetry of the strain and stress tensors imply that the entries C_{ijkl} of the fourth order viscoelastic tensor fulfill [334]

$$C_{ijkl} = C_{jikl} = C_{klij} = C_{ijlk}, \qquad \forall\, i,j,k,l. \tag{G.4}$$

In two dimensions, one is thus left with six independent moduli: C_{1111}, C_{1112}, C_{1122}, C_{1212}, C_{1222}, and C_{2222}.

Orthotropic materials

In the following, we consider materials with mutually orthogonal symmetry planes called orthotropic, for which

$$(1-\delta_{ij})C_{ijkk}=0, \qquad \forall\, i,j,k, \tag{G.5}$$

holds. In two dimensions, the number of in general independent and non-vanishing viscoelastic moduli is therefore reduced from six to four: C_{1111}, C_{2222}, C_{1122}, and C_{1212}. Examples are hexagonal or square networks, which both possess mutually orthogonal symmetry planes. Employing the Voigt notation, the stress-strain relation is given by

$$\begin{pmatrix}\sigma_{11}\\ \sigma_{22}\\ \sigma_{12}\end{pmatrix}=\begin{pmatrix}C_{1111} & C_{1122} & 0\\ C_{1122} & C_{2222} & 0\\ 0 & 0 & C_{1212}\end{pmatrix}\cdot\begin{pmatrix}\varepsilon_{11}\\ \varepsilon_{22}\\ 2\varepsilon_{12}\end{pmatrix}. \tag{G.6}$$

Rotations of the coordinate frame

For rotations of the coordinate frame described by a rotation matrix $\boldsymbol{T}$, the viscoelastic moduli transform according to

$$C'_{ijkl}=\sum_{m,n,o,p} T_{im}T_{jn}T_{ko}T_{lp}C_{mnop}\,. \tag{G.7}$$

For orthotropic continua with a symmetry under rotations about $\pi/2$, e.g., square materials, $C_{2222}=C_{1111}$ and the stress-strain relation is thus characterized by only three independent moduli. In turn, orthotropic continua with a symmetry under rotations about $\pi/3$, e.g., hexagonal materials, are examples for isotropic materials, for which $C_{2222}=C_{1111}$ and $C_{1122}=C_{1111}-2C_{1212}$, thus reducing the number of independent moduli to two: C_{1111} and C_{1212}.

In order to determine all viscoelastic moduli of an orthotropic material via the shear and compression response of a slab discussed in the following, one in general needs to probe the material in two different orientations with respect to the slab axes. When for example rotated about $\pm\pi/4$, one probes the viscoelastic moduli

$$C'_{2222} = \frac{1}{4}\left(C_{1111}+C_{2222}+2C_{1122}\right)+C_{1212}, \tag{G.8}$$

$$C'_{1212} = \frac{1}{4}\left(C_{1111}+C_{2222}-2C_{1122}\right), \tag{G.9}$$

from which C_{1111} and C_{1122} can then be inferred.

G.2 Viscoelastic Slab Response

In Fourier domain, the overdamped equations of motion of a viscoelastic medium embedded in a fluid are given by

$$-\mathrm{i}\,\omega\zeta u_i=\sum_j \partial_j\sigma_{ij}+f_i^{\mathrm{ext}}, \qquad i=1,2, \tag{G.10}$$

where $\boldsymbol{f}^{\mathrm{ext}}$ denotes the external force density and the frictional density ζ accounts for the interaction of the network with the surrounding solvent. In the following, we consider two-

dimensional slabs of thickness d in r_2 direction subject to a laterally homogeneous compression or shear force density acting with opposite sign on the bottom and top interfaces of the slab.

Compression

In the first case, the displacement profile is $\boldsymbol{u} = (0, u_2(r_2))^{\mathrm{T}}$ by symmetry and thus $\varepsilon_{22} = \partial_2 u_2$ is the only non-vanishing element of the deformation tensor. The elements of the stress tensor being

$$\sigma_{11}(r_2) = C_{1122}\partial_2 u_2(r_2), \qquad \sigma_{22}(r_2) = C_{2222}\partial_2 u_2(r_2), \qquad \sigma_{12} = \sigma_{21} = 0, \tag{G.11}$$

the equations of motion take the form

$$-\mathrm{i}\,\omega\zeta u_1 = 0, \tag{G.12}$$

$$-\mathrm{i}\,\omega\zeta u_2 = C_{2222}\,\partial_2^2 u_2 + f_2^{\mathrm{ext}}. \tag{G.13}$$

Shear

In the case of an applied shear stress, the displacement profile is $\boldsymbol{u} = (u_1(r_2), 0)^{\mathrm{T}}$ and thus $\varepsilon_{12} = \varepsilon_{21} = \partial_2 u_1/2$ are the only non-vanishing elements of the deformation tensor. The stress tensor elements therefore are $\sigma_{11} = 0$, $\sigma_{22} = 0$ and $\sigma_{12}(r_2) = \sigma_{21}(r_2) = C_{1212}\partial_2 u_1(r_2)$ yielding equations of motion

$$-\mathrm{i}\,\omega\zeta u_1 = C_{1212}\,\partial_2^2 u_1 + f_1^{\mathrm{ext}}, \tag{G.14}$$

$$-\mathrm{i}\,\omega\zeta u_2 = 0. \tag{G.15}$$

General notation and solution

Realizing that the equations for the deformations in response to compression and shear are of the same type, we use the general notation

$$-\mathrm{i}\,\omega\zeta u = C\partial_2^2 u + f^{\mathrm{ext}}, \tag{G.16}$$

in the following, where $u = u_2$ and $C = C_{2222}$ in the case of compression and $u = u_1$ and $C = C_{1212}$ when shear is applied. The one-dimensional linear differential equation of the above type is solved by Green's function techniques as sketched in the following

$$-\mathrm{i}\,\omega\zeta u_0(r_2, \omega; r_0) - C\partial_2^2 u_0(r_2, \omega; r_0) = \sigma_0\,\delta(r_2 - r_0). \tag{G.17}$$

The Fourier transformation mediating between r_2 and k_2 yields

$$-\mathrm{i}\,\omega\zeta u_0(k_2, \omega; r_0) + Ck_2^2 u_0(k_2, \omega; r_0) = \sigma_0\,\mathrm{e}^{\mathrm{i}k_2 r_0}, \tag{G.18}$$

implying

$$u_0(k_2, \omega; r_0) = \frac{\sigma_0\,\mathrm{e}^{\mathrm{i}k_2 r_0}}{-\mathrm{i}\,\omega\zeta + Ck_2^2} = \frac{\sigma_0}{-\mathrm{i}\,\omega\zeta}\,\frac{\mathrm{e}^{\mathrm{i}k_2 r_0}}{1 + k_2^2/\lambda_{\mathrm{ve}}^2}, \qquad \lambda_{\mathrm{ve}}^2 \equiv \frac{-\mathrm{i}\,\omega\zeta}{C}. \tag{G.19}$$

Back transformation yields

$$u_0(r_2, \omega; r_0) = \frac{\lambda_{\mathrm{ve}}}{-\mathrm{i}\,\omega\zeta}\frac{\sigma_0}{2}\mathrm{e}^{-\lambda_{\mathrm{ve}}|r_2 - r_0|}, \qquad \mathrm{Re}\,[\lambda_{\mathrm{ve}}] > 0, \tag{G.20}$$

where $\mathrm{Re}\,[\lambda_{\mathrm{ve}}]$ denotes the inverse viscoelastic penetration depth. For a slab geometry with opposite stresses acting on the top and bottom interface, a displacement profile, which is antisymmetric with respect to the slab's mid-plane ($r_2 = d/2$), is obtained by the linear superposition of two of the above solutions

$$u_{\pm}(r_2, \omega) \equiv u_0(r_2, \omega; d) - u_0(r_2, \omega; 0) = \frac{\lambda_{\mathrm{ve}}}{-\mathrm{i}\,\omega\zeta}\frac{\sigma_0}{2}\left(\mathrm{e}^{-\lambda_{\mathrm{ve}}|r_2 - d|} - \mathrm{e}^{-\lambda_{\mathrm{ve}}|r_2|}\right). \tag{G.21}$$

For a slab of finite thickness d, the surface force density at the top interface is

$$\sigma_{\mathrm{top}} \equiv C\,\partial_2 u_{\pm}(r_2, \omega)|_{r_2 = d} = \frac{\sigma_0}{2}\left(1 + \mathrm{e}^{-\lambda_{\mathrm{ve}} d}\right), \tag{G.22}$$

which for $\omega \neq 0$ deviates from σ_0. The interfacial response function of the continuum slab

$$J_{\mathrm{cont.}}(\omega) \equiv \frac{u_{\pm}(d, \omega)}{\sigma_{\mathrm{top}}} = \frac{\lambda_{\mathrm{ve}}}{-\mathrm{i}\,\omega\zeta}\frac{1 - \mathrm{e}^{-\lambda_{\mathrm{ve}} d}}{1 + \mathrm{e}^{-\lambda_{\mathrm{ve}} d}} = \frac{\lambda_{\mathrm{ve}}}{-\mathrm{i}\,\omega\zeta}\tanh\left(\frac{\lambda_{\mathrm{ve}} d}{2}\right), \tag{G.23}$$

reveals the influence of the slab thickness d, the frictional density ζ and of the viscoelastic moduli C_{2222} and C_{1212}, respectively.

Probing the viscoelastic moduli of an isotropic material thus requires the compression and shear response of a single slab only. For anisotropic but orthotropic media, the material has to be probed in two different orientations with respect to the slab axis: If the material is for example rotated by $\pi/4$, shear and compression moduli C'_{2222} and C'_{1212} allow to recover C_{1111} and C_{1122} using the relations from Sec. G.1.

G.3 Representative Viscoelastic Model Materials

Popular models for viscoelastic media include the Maxwell (M) and Kelvin-Voigt (KV) materials.

Maxwell material

Schematically, the Maxwell material results from the serial alignment of an elastic medium (modulus μ) and a viscous medium (viscosity η). Its viscoelastic modulus is given by

$$C_{\mathrm{M}} \equiv \left(\frac{1}{\mu} + \frac{1}{-\mathrm{i}\,\omega\eta}\right)^{-1}, \tag{G.24}$$

i.e., at small frequencies ($\omega \ll \mu/\eta$) the material behaves like a fluid, $C_{\mathrm{M}} \sim -\mathrm{i}\,\omega\eta$, while it shows elastic behavior, $C_{\mathrm{M}} \sim \mu$, at large frequencies ($\omega \gg \mu/\eta$). Performing a low frequency

expansion, one obtains a nonlinear deformation profile $u_{\pm}(r_2)$, in which the typical penetration depth is $1/\lambda_v \equiv \sqrt{\eta/\zeta}$. The interfacial response is given by

$$J_M(\omega) = \frac{i}{\omega}\frac{\lambda_v}{\zeta}\tanh\left(\frac{\lambda_v d}{2}\right) + \frac{\lambda_v d + \sinh(\lambda_v d)}{2\lambda_v \mu(1+\cosh(\lambda_v d))} + \mathcal{O}(\omega), \tag{G.25}$$

which in the limit of large slab thickness ($d\lambda_v \gg 1$) simplifies to

$$\lim_{d\to\infty} J_M(\omega) = \frac{i}{\omega}\frac{1}{\sqrt{\zeta\eta}} + \frac{\sqrt{\eta}}{2\sqrt{\zeta}\mu} + \mathcal{O}(\omega), \tag{G.26}$$

which is dominated by the viscous properties of the material. In the limit of large frequencies, one obtains

$$J_M(\omega) = \frac{1+i}{\sqrt{\omega}}\frac{1}{\sqrt{2\zeta\mu}} - \frac{1-i}{\omega^{3/2}}\frac{1}{2}\sqrt{\frac{\mu}{2\zeta\eta}} + \mathcal{O}(\omega^{-5/2}), \tag{G.27}$$

where the dominant terms of the real and imaginary part are equal. This high frequency-response is independent of the slab thickness d and dominated by the elastic material properties.

Kelvin-Voigt material

Similarly, the parallel alignment of an elastic medium (modulus μ) and a viscous medium (viscosity η) gives rise to the Kelvin-Voigt material with viscoelastic modulus

$$C_{KV} \equiv \mu - i\omega\eta, \tag{G.28}$$

which acts as an elastic solid, $C_{KV} \sim \mu$, for small frequencies ($\omega \ll \mu/\eta$) and behaves fluid-like, $C_{KV} \sim -i\omega\eta$, at large frequencies ($\omega \gg \mu/\eta$). Again, performing a low frequency expansion, one obtains the low frequency response

$$J_{KV}(\omega) = \frac{d}{2\mu} + i\omega d\,\frac{\zeta d^2 + 12\eta}{24\mu^2} + \mathcal{O}(\omega^2), \tag{G.29}$$

which is dominated by the elastic properties of the slab. In contrast, for large frequencies the interfacial response

$$J_{KV}(\omega) = \frac{i}{\omega}\frac{\lambda_v}{\zeta}\tanh\left(\frac{\lambda_v d}{2}\right) + \frac{1}{\omega^2}\frac{\lambda_v\mu\,(\lambda_v d + \sinh(\lambda_v d))}{2\zeta\eta\,(1+\cosh(\lambda_v d))} + \mathcal{O}(\omega^{-3}), \qquad \lambda_v \equiv \sqrt{\frac{\zeta}{\eta}}, \tag{G.30}$$

is dominated by the viscous material properties and reduces to

$$J_{KV}(\omega) = \frac{i}{\omega}\frac{1}{\sqrt{\zeta\eta}} + \frac{1}{\omega^2}\frac{\mu}{2\eta\sqrt{\zeta\eta}} + \mathcal{O}(\omega^{-3}), \tag{G.31}$$

for large slap thicknesses $\lambda_v d \gg 1$. Note that in an intermediate frequency range $\mu/(\zeta d^2) \ll \omega \ll \mu/\eta$, which becomes apparent for large enough slab thickness d, the response is characterized by real and imaginary parts of equal magnitude and frequency dependence $1/\sqrt{\omega}$, similarly to Eq. G.27.

G.4 Relating the Response of Continuum Models and Discrete Networks

The comparison of the shear and compression responses of polymeric slabs resolved using the dynamic convolution theory (DCT) in Chapter 8 and the predictions from continuum theory discussed in the previous subsections is rather insightful: We have seen in Sec. 8.3.3 that the Kelvin-Voigt and Maxwell materials indeed are good model systems for explaining the frequency dependences of the response functions in the Figs. 8.13 and 8.15.

For a quantitative analysis, note the difference in units between the above continuum response functions and the nodal response functions J in Sec. 8.3: The equivalence between both is established via $J_{\mathrm{cont.}}/w = J$, where w denotes the width of the periodic unit cells in Fig. 8.12. The friction density ζ results from the monomer density and equals $\zeta = L/(\xi^2 a \mu_0) \approx 1/(12\mu_0 a^2)$ for the square networks of filaments with contour length $L/a = 12$ considered in Sec. 8.3.3. The low-frequency elastic moduli μ and η of a Kelvin-Voigt material can be obtained from the slab response via Eq. G.29, and similarly those of a Maxwell-material result (for large enough slab thickness d) from the the slab response via Eq. G.26.

An example for a one-to-one mapping of the DCT response functions onto the above continuum theory reproducing also the fine structure of the response over the whole frequency range is shown in Fig. 8.14. Note that such a mapping can be challenging from a numerical point of view, since Eq. G.23 cannot explicitly be solved for the complex modulus C. Also, it is unclear whether a unique mapping $J \to C$ exists in all cases. Finally, the resulting moduli should be interpreted with care, since any continuum theory is expected to break down once the penetration depth $|\lambda_{\mathrm{ve}}|^{-1}$ becomes comparable to the network mesh size ξ.

List of Figures

List of Tables

List of Supplementary Material

The following simulation movies and animations are included as supplementary material:

1. Movies visualizing the motion of water molecules in MD simulations:
   a) MD_h2o_pair.mpg: Dynamics of pairs of water molecules in bulk water,
   b) MD_h2o_diamond.mpg: Dynamics of an individual water molecule in the vicinity of a diamond surface,
   c) MD_h2o_dppc.mpg: Dynamics of an individual water molecule in the vicinity of a DPPC membrane.
2. flow_field_*.swf: A series of animations showing the hydrodynamic flow field around an oscillating sphere in a viscous, incompressible fluid in the low Reynolds number regime at various driving frequencies.
3. BD_semiflexible_polymer.mp4: Movie visualizing the thermal motion of a short semiflexible polymer in a BD simulation and showing the six fluctuating end-point coordinates.

List of Publications

The present thesis is based on the following manuscripts, which have been published in peer-reviewed journals:

[i] Yann von Hansen, Sebastian Rode, and Roland R. Netz. Convolution theory for dynamic systems: A bottom-up approach to the viscoelasticity of polymeric networks. *The European Physical Journal E* **36 (12)**, 137 (2013),
doi:10.1140/*epje*/*i*2013-13137-5

[ii] Yann von Hansen and Roland R. Netz. Influence of nonlinearities on the dynamics of thermally fluctuating systems revealed by the expansion of dynamic observables in powers of the thermal noise strength. *The European Physical Journal B* **86 (10)**, 415 (2013),
doi:10.1140/*epjb*/*e*2013-40692-*y*

[iii] Yann von Hansen, Stephan Gekle, and Roland R. Netz. Anomalous anisotropic diffusion dynamics of hydration water at lipid membranes. *Physical Review Letters* **111 (11)**, 118103 (2013),
doi:10.1103/*PhysRevLett*.111.118103

[iv] Yann von Hansen, Alexander Mehlich, Benjamin Pelz, Matthias Rief, and Roland R. Netz. Auto- and cross-power spectral analysis of dual trap optical tweezer experiments using Bayesian inference. *Review of Scientific Instruments* **83 (9)**, 095116 (2012),
doi:10.1063/1.4753917

[v] Yann von Hansen, Felix Sedlmeier, Michael Hinczewski, and Roland R. Netz. Friction contribution to water-bond breakage kinetics. *Physical Review E* **84 (5)**, 051501(2011),
doi:10.1103/*PhysRevE*.84.051501

[vi] Yann von Hansen, Michael Hinczewski, and Roland R. Netz. Hydrodynamic screening near planar boundaries: Effects on semiflexible polymer dynamics. *The Journal of Chemical Physics* **134 (23)**, 235102 (2011),
doi:10.1063/1.3593458

[vii] Yann von Hansen, Immanuel Kalcher, and Joachim Dzubiella. Ion specificity in alpha-helical folding kinetics. *The Journal of Physical Chemistry B* **114 (43)**, 13815 (2010),
doi:10.1021/*jp*107495*f*

The following publications are related to the present thesis but not part of it:

[viii] Felix Sedlmeier, Yann von Hansen, Liang Mengyu, Dominik Horinek, and Roland R. Netz. Water dynamics at interfaces and solutes: Disentangling free energy and diffusivity contributions, *Journal of Statistical Physics* **145 (2)**, 240 (2011), *doi*:10.1007/s10955-011-0338-0

[ix] Michael Hinczewski, Yann von Hansen, and Roland R. Netz. Deconvolution of dynamic mechanical networks, *Proceedings of the National Academy of Sciences of the United States of America* **107 (50)**, 21493 (2010), *doi*:10.1073/*pnas*.1010476107

[x] Michael Hinczewski, Yann von Hansen, Joachim Dzubiella, and Roland R. Netz. How the diffusivity profile reduces the arbitrariness of protein folding free energies. *The Journal of Chemical Physics* **132 (24)**, 245103 (2010), *doi*:10.1063/1.3442716

The following publication is unrelated to the present work:

[xi] Yann von Hansen, Roland R. Netz, and Michael Hinczewski. DNA-protein binding rates: Bending fluctuation and hydrodynamic coupling effects. *The Journal of Chemical Physics* **132 (13)**, 135103 (2010), *doi*:10.1063/1.3352571

BIBLIOGRAPHY

[1] J. Ingen-Housz. Bemerkungen über den Gebrauch des Vergrößerungsglases. *Vermischte Schriften physisch medicinischen Inhalts* **2**, 122 (1784) : cited on p. 1

[2] R. Brown. A brief account of microscopical observations made in the months of June, July and August, 1827, on the particles contained in the pollen of plants; and on the general existence of active molecules in organic and inorganic bodies. *Phil. Mag.* **4 (21)**, 161 (1828) : cited on p. 1

[3] R. Brown. Additional remarks on active molecules. *Edinburgh Journal of Science* **1**, 314 (1829) : cited on p. 1

[4] S. Exner. Untersuchungen über Brown's Molecularbewegung. *Sitzungsber. d. k. Akad. d. Wissensch. zu Wien* **56**, 116 (1867) : cited on p. 1

[5] L. G. Gouy. Note sur le mouvement brownien. *J. de Phys.* **7 (2)**, 561 (1888) : cited on p. 1

[6] F. M. Exner. Notiz zu Brown's Molecularbewegung. *Ann. Phys.* **307**, 843 (1900) : cited on p. 1

[7] W. Sutherland. Dynamical theory of diffusion for non-electrolytes and the molecular mass of albumin. *Phil. Mag.* **9**, 781 (1905) : cited on p. 1

[8] A. Einstein. Über die von der molekularkinetischen Theorie der Wärme geforderte Bewegung von in ruhenden Flüssigkeiten suspendierten Teilchen. *Ann. Phys.* **322**, 549 (1905) : cited on p. 1

[9] A. Einstein. Eine neue Bestimmung der Moleküldimensionen. *Ann. Phys.* **324**, 289 (1906) : cited on p. 1

[10] A. Einstein. Zur Theorie der Brownschen Bewegung. *Ann. Phys.* **324**, 371 (1906) : cited on p. 1

[11] M. von Smoluchowski. Zur kinetischen Theorie der Brownschen Molekularbewegung und der Suspensionen. *Ann. Phys.* **326**, 757 (1906) : cited on p. 1

[12] A. Fick. Über Diffusion. *Ann. Phys.* **170**, 59 (1855) : cited on p. 1

[13] J. B. Perrin. L'agitation moléculaire et le mouvement brownien. *C. R. Acad. Sci.* **146**, 967 (1908) : cited on p. 2

[14] J. B. Perrin. Mouvement brownien et réalité moléculaire. *Ann. Chim. Phys.* **18**, 5 (1909) : cited on p. 2

[15] Jean-Baptiste Perrin. *Brownian Motion and Molecular Reality*. Taylor and Francis, London (1910) : cited on p. 2

[16] G.G. Stokes. On the effect of the internal friction of fluids on the motion of pendulums. *Trans. Camb. Philos. Soc.* **9**, [8] (1851) : cited on pp. 2, 40, 71, 119, and 153

[17] M. L. Bachelier. Théorie de la spéculation. *Ann. Sci. École Norm. S.* **17**, 21 (1900) : cited on p. 2

[18] R. C. Merton. Theory of rational option pricing. *Bell J. Econ.* **4 (1)**, 141 (1973) : cited on p. 2

[19] F. Black and M. Scholes. Pricing of options and corporate liabilities. *J. Polit. Econ.* **81 (3)**, 637 (1973) : cited on p. 2

[20] E. Frey and K. Kroy. Brownian motion: A paradigm of soft matter and biological physics. *Ann. Phys.* **14 (1-3)**, 20 (2005) : cited on pp. 2 and 4

[21] P. Hänggi and F. Marchesoni. Introduction: 100 years of Brownian motion. *Chaos* **15 (2)**, 026101 (2005) : cited on p. 2

[22] M. Haw. Einstein's random walk. *Phys. World* **18 (1)**, 19 (2005) : cited on pp. 2 and 3

[23] B. Duplantier. Brownian motion, "Diverse and undulating". *Prog. Math. P.* **47**, 201 (2006) : cited on p. 2

[24] P. Langevin. Sur la théorie du mouvement brownien. *C. R. Acad. Sci.* **146**, 530 (1908) : cited on p. 3

[25] K. Itô. Stochastic integral. *Proc. Imp. Acad. Tokyo* **20 (8)**, 519 (1944) : cited on p. 3

[26] K. Itô. On a stochastic integral equation. *Proc. Japan Acad.* **22 (2)**, 32 (1946) : cited on p. 3

[27] R. L. Stratonovich. A new representation for stochastic integrals and equations. *SIAM J. Control* **4**, 362 (1966) : cited on p. 3

[28] William T. Coffey and Yuri P. Kalmykov. *The Langevin Equation – With Applications to Stochastic Problems in Physics, Chemistry and Electrical Engineering*. World Scientific Publishing Co. Pte. Ltd., 3rd edition (2012) : cited on p. 3

[29] Nico G. van Kampen. *Stochastic Processes in Physics and Chemistry*. North Holland, 3rd edition (2007) : cited on pp. 3 and 123

[30] R. Zwanzig. Ensemble method in the theory of irreversibility. *J. Chem. Phys.* **33 (5)**, 1338 (1960) : cited on p. 3

[31] R. Zwanzig. Memory effects in irreversible thermodynamics. *Phys. Rev.* **124 (4)**, 983 (1961) : cited on p. 3

[32] H. Mori. Transport, collective motion, and Brownian motion. *Prog. Theor. Phys.* **33 (3)**, 423 (1965) : cited on p. 3

[33] Robert Zwanzig. *Nonequilibrium Statistical Mechanics*. Oxford University Press (2001) : cited on p. 3

[34] A. D. Fokker. Die mittlere Energie rotierender elektrischer Dipole im Strahlungsfeld. *Ann d. Phys.* **348**, 810 (1914) : cited on p. 3

[35] M. Planck. Über einen Satz der statistischen Dynamik und seine Erweiterung in der Quantentheorie. *Sitzber. K. Preuss. Aka.* pages 323–341 (1917) : cited on p. 3

[36] Hannes Risken. *The Fokker-Planck Equation – Methods of Solution and Applications*. Springer, Berlin, 3rd edition (1996) : cited on pp. 3, 18, 94, and 151

[37] M. von Smoluchowski. Über Brownsche Molekularbewegung unter Einwirkung äußerer Kräfte und deren Zusammenhang mit der verallgemeinerten Diffusionsgleichung. *Ann. Phys.* **48**, 1103 (1916) : cited on p. 3

[38] Crispin W. Gardiner. *Handbook of Stochastic Methods for Physics, Chemistry and the Natural Sciences*. Springer series in synergetics, 13. Springer, Berlin, 2nd edition (2002) : cited on pp. 3, 18, 23, and 151

[39] Erich Sackmann and Rudolf Merkel. *Lehrbuch der Biophysik*. Wiley-VCH Verlag (2010) : cited on pp. 3 and 5

[40] Rob Phillips, Jane Kondev, Julie Theriot, and Nigel Orme. *Physical Biology of the Cell*. Garland Science, Taylor & Francis Group (2009) : cited on pp. 3 and 5

[41] Philip Nelson. *Biological Physics – Energy, Information, Life*. W. H. Freeman and Company, New York, USA (2008) : cited on pp. 3 and 4

[42] I. Golding and E. C. Cox. Physical nature of bacterial cytoplasm. *Phys. Rev. Lett.* **96 (9)**, 098102 (2006) : cited on pp. 3 and 29

[43] R. Roy, S. Hohng, and T. Ha. A practical guide to single-molecule FRET. *Nat. Methods* **5 (6)**, 507 (2008) : cited on pp. 3 and 5

[44] N. G. Walter, C. Y. Huang, A. J. Manzo, and M. A. Sobhy. Do-it-yourself guide: How to use the modern single-molecule toolkit. *Nat. Methods* **5 (6)**, 475 (2008) : cited on pp. 3 and 5

[45] K. C. Neuman and A. Nagy. Single-molecule force spectroscopy: Optical tweezers, magnetic tweezers and atomic force microscopy. *Nat. Methods* **5 (6)**, 491 (2008) : cited on pp. 3 and 5

[46] D. E. Shaw, P. Maragakis, K. Lindorff-Larsen, S. Piana, R. O. Dror, M. P. Eastwood, J. A. Bank, J. M. Jumper, J. K. Salmon, Y. B. Shan, and W. Wriggers. Atomic-level characterization of the structural dynamics of proteins. *Science* **330 (6002)**, 341 (2010) : cited on p. 4

[47] C. Jarzynski. Nonequilibrium equality for free energy differences. *Phys. Rev. Lett.* **78 (14)**, 2690 (1997) : cited on p. 4

[48] G. E. Crooks. Nonequilibrium measurements of free energy differences for microscopically reversible Markovian systems. *J. Stat. Phys.* **90 (5-6)**, 1481 (1998) : cited on p. 4

[49] O. K. Dudko, G. Hummer, and A. Szabo. Intrinsic rates and activation free energies from single-molecule pulling experiments. *Phys. Rev. Lett.* **96 (10)**, 108101 (2006) : cited on p. 4

[50] O. K. Dudko, G. Hummer, and A. Szabo. Theory, analysis, and interpretation of single-molecule force spectroscopy experiments. *Proc. Natl. Acad. Sci. U.S.A.* **105 (41)**, 15755 (2008) : cited on p. 4

[51] N. V. Buchete and G. Hummer. Coarse master equations for peptide folding dynamics. *J. Phys. Chem. B* **112 (19)**, 6057 (2008) : cited on p. 4

[52] D. De Sancho and R. B. Best. What is the time scale for alpha-helix nucleation? *J. Am. Chem. Soc.* **133 (17)**, 6809 (2011) : cited on p. 4

[53] J. Stigler, F. Ziegler, A. Gieseke, J. C. M. Gebhardt, and M. Rief. The complex folding network of single calmodulin molecules. *Science* **334 (6055)**, 512 (2011) : cited on pp. 4, 5, and 65

[54] F. Noé, S. Doose, I. Daidone, M. Lollmann, M. Sauer, J. D. Chodera, and J. C. Smith. Dynamical fingerprints for probing individual relaxation processes in biomolecular dynamics with simulations and kinetic experiments. *Proc. Natl. Acad. Sci. U.S.A.* **108 (12)**, 4822 (2011) : cited on p. 4

[55] F. Noé, C. Schütte, E. Vanden-Eijnden, L. Reich, and T. R. Weikl. Constructing the equilibrium ensemble of folding pathways from short off-equilibrium simulations. *Proc. Natl. Acad. Sci. U.S.A.* **106 (45)**, 19011 (2009) : cited on pp. 4 and 27

[56] M. Hinczewski, X. Schlagberger, M. Rubinstein, O. Krichevsky, and R. R. Netz. End-monomer dynamics in semiflexible polymers. *Macromolecules* **42 (3)**, 860 (2009) : cited on pp. 4, 117, 118, 124, 126, 128, and 131

[57] M. Hinczewski and R. R. Netz. Global cross-over dynamics of semiflexible polymers. *Europhys. Lett.* **88 (1)**, 18001 (2009) : cited on pp. 4, 117, 124, 128, 131, and 135

[58] R. D. Astumian. Design principles for Brownian molecular machines: How to swim in molasses and walk in a hurricane. *Phys. Chem. Chem. Phys.* **9 (37)**, 5067 (2007) : cited on p. 4

[59] R. Metzler and J. Klafter. The random walk's guide to anomalous diffusion: A fractional dynamics approach. *Phys. Rep.* **339 (1)**, 1 (2000) : cited on p. 4

[60] I. M. Sokolov, J. Klafter, and A. Blumen. Fractional kinetics. *Phys. Today* **55 (11)**, 48 (2002) : cited on p. 4

[61] J. Klafter and I. M. Sokolov. Anomalous diffusion spreads its wings. *Phys. World* **18 (8)**, 29 (2005) : cited on p. 4

[62] I. M. Sokolov and J. Klafter. From diffusion to anomalous diffusion: A century after Einstein's Brownian motion. *Chaos* **15 (2)**, 026103 (2005) : cited on p. 4

[63] M. Kærn, T. C. Elston, W. J. Blake, and J. J. Collins. Stochasticity in gene expression: From theories to phenotypes. *Nat. Rev. Genet.* **6 (6)**, 451 (2005) : cited on p. 4

[64] B. Drossel. Biological evolution and statistical physics. *Adv. Phys.* **50 (2)**, 209 (2001) : cited on p. 4

[65] M. Vergassola, E. Villermaux, and B. I. Shraiman. 'Infotaxis' as a strategy for searching without gradients. *Nature* **445 (7126)**, 406 (2007) : cited on p. 4

[66] Boris S. Kerner. *The Physics of Traffic – Empirical Freeway Pattern Features, Engineering Applications, and Theory*. Springer Series Understanding Complex Systems. Springer, Berlin (2004) : cited on p. 4

[67] J. C. F. Schulz, L. Schmidt, R. B. Best, J. Dzubiella, and R. R. Netz. Peptide chain dynamics in light and heavy water: Zooming in on internal friction. *J. Am. Chem. Soc.* **134 (14)**, 6273 (2012) : cited on pp. 4 and 143

[68] Felix Franks. *Water – A Matrix of Life*. Royal Society of Chemistry, Cambridge, UK, 2nd edition (2000) : cited on p. 5

[69] P. Ball. Water – An enduring mystery. *Nature* **452 (7185)**, 291 (2008) : cited on pp. 5 and 7

[70] J. D. Bryngelson and P. G. Wolynes. Intermediates and barrier crossing in a random energy-model (with applications to protein folding). *J. Phys. Chem.* **93 (19)**, 6902 (1989) : cited on pp. 5 and 47

[71] C. J. Camacho and D. Thirumalai. Kinetics and thermodynamics of folding in model proteins. *Proc. Natl. Acad. Sci. U.S.A.* **90 (13)**, 6369 (1993) : cited on pp. 5 and 47

[72] N. D. Socci, J. N. Onuchic, and P. G. Wolynes. Diffusive dynamics of the reaction coordinate for protein folding funnels. *J. Chem. Phys.* **104 (15)**, 5860 (1996) : cited on pp. 5 and 47

[73] K. A. Dill and H. S. Chan. From Levinthal to pathways to funnels. *Nat. Struct. Biol.* **4 (1)**, 10 (1997) : cited on pp. 5 and 47

[74] G. Hummer, A. E. Garcia, and S. Garde. Conformational diffusion and helix formation kinetics. *Phys. Rev. Lett.* **85 (12)**, 2637 (2000) : cited on pp. 5 and 47

[75] R. B. Best and G. Hummer. Diffusive model of protein folding dynamics with Kramers turnover in rate. *Phys. Rev. Lett.* **96 (22)**, 228104 (2006) : cited on pp. 5 and 47

[76] M. T. Woodside, P. C. Anthony, W. M. Behnke-Parks, K. Larizadeh, D. Herschlag, and S. M. Block. Direct measurement of the full, sequence-dependent folding landscape of a nucleic acid. *Science* **314 (5801)**, 1001 (2006) : cited on pp. 5 and 65

[77] J. C. M. Gebhardt, T. Bornschlögl, and M. Rief. Full distance-resolved folding energy landscape of one single protein molecule. *Proc. Natl. Acad. Sci. U.S.A.* **107 (5)**, 2013 (2010) : cited on pp. 5 and 65

[78] M. Hinczewski, J. C. M. Gebhardt, M. Rief, and D. Thirumalai. From mechanical folding trajectories to intrinsic energy landscapes of biopolymers. *Proc. Natl. Acad. Sci. U.S.A.* **110 (12)**, 4500 (2013) : cited on pp. 5 and 116

[79] L. Le Goff, O. Hallatschek, E. Frey, and F. Amblard. Tracer studies on f-actin fluctuations. *Phys. Rev. Lett.* **89 (25)**, 258101 (2002) : cited on pp. 6, 117, 118, 132, 133, 137, 138, 140, 173, and 174

[80] A. R. Bausch and K. Kroy. A bottom-up approach to cell mechanics. *Nat. Phys.* **2 (4)**, 231 (2006) : cited on pp. 6, 139, 158, and 161

[81] O. Lieleg, M. M. A. E. Claessens, and A. R. Bausch. Structure and dynamics of cross-linked actin networks. *Soft Matter* **6 (2)**, 218 (2010) : cited on pp. 6, 158, and 174

[82] F. H. Stillinger. Water revisited. *Science* **209 (4455)**, 451 (1980) : cited on p. 7

[83] F. S. Csajka and D. Chandler. Transition pathways in a many-body system: Application to hydrogen-bond breaking in water. *J. Chem. Phys.* **109 (3)**, 1125 (1998) : cited on pp. 7 and 24

[84] D. Laage and J. T. Hynes. On the molecular mechanism of water reorientation. *J. Phys. Chem. B* **112 (45)**, 14230 (2008) : cited on pp. 7, 25, and 174

[85] I. M. Svishchev and P. G. Kusalik. Roto-translational motion in liquid water and its structural implication. *Chem. Phys. Lett.* **215 (6)**, 596 (1993) : cited on pp. 7 and 25

[86] A. Luzar and D. Chandler. Hydrogen-bond kinetics in liquid water. *Nature* **379 (6560)**, 55 (1996) : cited on p. 7

[87] A. Luzar and D. Chandler. Effect of environment on hydrogen bond dynamics in liquid water. *Phys. Rev. Lett.* **76 (6)**, 928 (1996) : cited on pp. 7 and 22

[88] Y. M. Rhee, E. J. Sorin, G. Jayachandran, E. Lindahl, and V. S. Pande. Simulations of the role of water in the protein-folding mechanism. *Proc. Natl. Acad. Sci. U.S.A.* **101 (17)**, 6456 (2004) : cited on p. 7

[89] P. L. Geissler, C. Dellago, and D. Chandler. Kinetic pathways of ion pair dissociation in water. *J. Phys. Chem. B* **103 (18)**, 3706 (1999) : cited on pp. 7, 24, and 27

[90] H. J. C. Berendsen, J. R. Grigera, and T. P. Straatsma. The missing term in effective pair potentials. *J. Phys. Chem.* **91 (24)**, 6269 (1987) : cited on pp. 8 and 176

[91] B. Hess, C. Kutzner, D. van der Spoel, and E. Lindahl. Gromacs 4: Algorithms for highly efficient, load-balanced, and scalable molecular simulation. *J. Chem. Theory Comput.* **4 (3)**, 435 (2008) : cited on pp. 8, 30, and 50

[92] D. van der Spoel, E. Lindahl, B. Hess, G. Groenhof, A. E. Mark, and H. J. C. Berendsen. Gromacs: Fast, flexible, and free. *J. Comput. Chem.* **26 (16)**, 1701 (2005) : cited on pp. 8 and 50

[93] H. J. C. Berendsen, J. P. M. Postma, W. F. Vangunsteren, A. Dinola, and J. R. Haak. Molecular-dynamics with coupling to an external bath. *J. Chem. Phys.* **81 (8)**, 3684 (1984) : cited on p. 8

[94] T. Darden, D. York, and L. Pedersen. Particle mesh Ewald: An N.log(N) method for Ewald sums in large systems. *J. Chem. Phys.* **98 (12)**, 10089 (1993) : cited on pp. 8 and 30

[95] U. Essmann, L. Perera, M. L. Berkowitz, T. Darden, H. Lee, and L. G. Pedersen. A smooth particle mesh ewald method. *J. Chem. Phys.* **103 (19)**, 8577 (1995) : cited on pp. 8 and 30

[96] R. Mills. Self-diffusion in normal and heavy-water in the range 1-45 degrees. *J. Phys. Chem.* **77 (5)**, 685 (1973) : cited on p. 10

[97] W. S. Price, H. Ide, and Y. Arata. Self-diffusion of supercooled water to 238 K using PGSE NMR diffusion measurements. *J. Phys. Chem. A* **103 (4)**, 448 (1999) : cited on pp. 9 and 10

[98] P. Mark and L. Nilsson. Structure and dynamics of the TIP3P, SPC, and SPC/E water models at 298 K. *J. Phys. Chem. A* **105 (43)**, 9954 (2001) : cited on p. 10

[99] C. Sendner, D. Horinek, L. Bocquet, and R. R. Netz. Interfacial water at hydrophobic and hydrophilic surfaces: Slip, viscosity, and diffusion. *Langmuir* **25 (18)**, 10768 (2009) : cited on pp. 10, 40, and 41

[100] David Eisenberg and Walter Kauzmann. *The Structure and Properties of Water*. Clarendon Press (1969) : cited on p. 10

[101] P. G. Wolynes. Dynamics of electrolyte-solutions. *Annu. Rev. Phys. Chem.* **31**, 345 (1980) : cited on p. 9

[102] Sangtae Kim and Seppo J. Karrila. *Microhydrodynamics - Principles and Selected Applications*. Dover Publications, Mineola (1991) : cited on pp. 11, 12, 16, 75, 86, and 177

[103] John Happel and Howard Brenner. *Low Reynolds Number Hydrodynamics*. Noordhoff, Leyden (1973) : cited on pp. 11, 12, 16, 119, 177, and 188

[104] M. G. Mazza, N. Giovambattista, F. W. Starr, and H. E. Stanley. Relation between rotational and translational dynamic heterogeneities in water. *Phys. Rev. Lett.* **96 (5)**, 057803 (2006) : cited on pp. 12 and 13

[105] R. Du, V. S. Pande, A. Y. Grosberg, T. Tanaka, and E. S. Shakhnovich. On the transition coordinate for protein folding. *J. Chem. Phys.* **108 (1)**, 334 (1998) : cited on p. 16

[106] Y. M. Rhee and V. S. Pande. One-dimensional reaction coordinate and the corresponding potential of mean force from commitment probability distribution. *J. Phys. Chem. B* **109 (14)**, 6780 (2005) : cited on p. 16

[107] W. N. E and E. Vanden-Eijnden. Transition-path theory and path-finding algorithms for the study of rare events. *Annu. Rev. Phys. Chem.* **61**, 391 (2010) : cited on pp. 16, 24, 27, and 174

[108] P. G. Bolhuis, D. Chandler, C. Dellago, and P. L. Geissler. Transition path sampling: Throwing ropes over rough mountain passes, in the dark. *Annu. Rev. Phys. Chem.* **53**, 291 (2002) : cited on pp. 16, 24, and 174

[109] R. B. Best and G. Hummer. Reaction coordinates and rates from transition paths. *Proc. Natl. Acad. Sci. U.S.A.* **102 (19)**, 6732 (2005) : cited on pp. 16 and 24

[110] W. Humphrey, A. Dalke, and K. Schulten. VMD: Visual molecular dynamics. *J. Mol. Graphics* **14 (1)**, 33 (1996) : cited on pp. 17, 55, and 176

[111] Movies visualizing the motion of water molecules in bulk and at interfaces are included as supplementary material, see MD_h2o_*.mpg (2011-2013) : cited on pp. 17, 31, and 40

[112] N. Agmon. Unified approach to spherically symmetrical diffusion. *Phys. Rev. Lett.* **67 (10)**, 1366 (1991) : cited on p. 18

[113] T. V. Pogorelov and Z. Luthey-Schulten. Variations in the fast folding rates of the λ-repressor: A hybrid molecular dynamics study. *Biophys. J.* **87 (1)**, 207 (2004) : cited on p. 18

[114] S. C. Yang, J. N. Onuchic, A. E. García, and H. Levine. Folding time predictions from all-atom replica exchange simulations. *J. Mol. Biol.* **372 (3)**, 756 (2007) : cited on p. 18

[115] R. B. Best and G. Hummer. Coordinate-dependent diffusion in protein folding. *Proc. Natl. Acad. Sci. U.S.A.* **107 (3)**, 1088 (2010) : cited on pp. 18 and 47

[116] P. Liu, E. Harder, and B. J. Berne. On the calculation of diffusion coefficients in confined fluids and interfaces with an application to the liquid-vapor interface of water. *J. Phys. Chem. B* **108 (21)**, 6595 (2004) : cited on pp. 18, 34, and 37

[117] M. Sega, R. Vallauri, and S. Melchionna. Diffusion of water in confined geometry: The case of a multilamellar bilayer. *Phys. Rev. E* **72 (4)**, 041201 (2005) : cited on p. 18

[118] C. D. Wick and L. X. Dang. Diffusion at the liquid-vapor interface of an aqueous ionic solution utilizing a dual simulation technique. *J. Phys. Chem. B* **109 (32)**, 15574 (2005) : cited on p. 18

[119] J. Mittal, T. M. Truskett, J. R. Errington, and G. Hummer. Layering and position-dependent diffusive dynamics of confined fluids. *Phys. Rev. Lett.* **100 (14)**, 145901 (2008) : cited on pp. 18 and 37

[120] George H. Weiss. First passage time problems in chemical physics. *Adv. Chem. Phys.* **13**, 1 (1966) : cited on pp. 18 and 24

[121] C. A. Emeis and P. L. Fehder. The microscopic mechanism for diffusion and the rates of diffusion-controlled reaction in simple liquid solvents. *J. Am. Chem. Soc.* **92 (8)**, 2246 (1970) : cited on p. 21

[122] P. L. Fehder, C. A. Emeis, and R. P. Futrelle. Microscopic mechanism for self-diffusion and relative diffusion in simple liquids. *J. Chem. Phys.* **54 (11)**, 4921 (1971) : cited on p. 21

[123] G. Hummer. From transition paths to transition states and rate coefficients. *J. Chem. Phys.* **120 (2)**, 516 (2004) : cited on p. 24

[124] B. Peters. p(TP | q) peak maximization: Necessary but not sufficient for reaction coordinate accuracy. *Chem. Phys. Lett.* **494 (1-3)**, 100 (2010) : cited on p. 24

[125] A. Berezhkovskii and A. Szabo. Time scale separation leads to position-dependent diffusion along a slow coordinate. *J. Chem. Phys.* **135 (7)**, 074108 (2011) : cited on p. 27

[126] J. H. Prinz, H. Wu, M. Sarich, B. Keller, M. Senne, M. Held, J. D. Chodera, C. Schütte, and F. Noé. Markov models of molecular kinetics: Generation and validation. *J. Chem. Phys.* **134 (17)**, 174105 (2011) : cited on pp. 27 and 174

[127] Gregor Cevc and Derek Marsh. *Phospholipid Bilayers – Physical Principles and Models*. John Wiley and Sons (1987) : cited on p. 29

[128] Ole G. Mouritsen. *Life – As a Matter of Fat*. Springer (2005) : cited on p. 29

[129] S. K. Pal and A. H. Zewail. Dynamics of water in biological recognition. *Chem. Rev.* **104 (4)**, 2099 (2004) : cited on p. 29

[130] J. L. Rigaud, C. M. Garybobo, and Y. Lange. Diffusion processes in lipid-water lamellar phases. *Biochim. Biophys. Acta.* **266 (1)**, 72 (1972) : cited on p. 29

[131] S. König, E. Sackmann, D. Richter, R. Zorn, C. Carlile, and T. M. Bayerl. Molecular-dynamics of water in oriented DPPC multilayers studied by quasi-elastic neutron-scattering and deuterium-nuclear magnetic-resonance relaxation. *J. Chem. Phys.* **100 (4)**, 3307 (1994) : cited on p. 29

[132] J. Swenson, F. Kargl, P. Berntsen, and C. Svanberg. Solvent and lipid dynamics of hydrated lipid bilayers by incoherent quasielastic neutron scattering. *J. Chem. Phys.* **129 (4)**, 045101 (2008) : cited on p. 29

[133] S. K. Pal, D. Sukul, D. Mandal, and K. Bhattacharyya. Solvation dynamics of DCM in lipid. *J. Phys. Chem. B* **104 (18)**, 4529 (2000) : cited on p. 29

[134] W. Zhao, D. E. Moilanen, E. E. Fenn, and M. D. Fayer. Water at the surfaces of aligned phospholipid multibilayer model membranes probed with ultrafast vibrational spectroscopy. *J. Am. Chem. Soc.* **130 (42)**, 13927 (2008) : cited on p. 29

[135] M. Hishida and K. Tanaka. Long-range hydration effect of lipid membrane studied by terahertz time-domain spectroscopy. *Phys. Rev. Lett.* **106 (15)**, 158102 (2011) : cited on p. 29

[136] J. Szymanski and M. Weiss. Elucidating the origin of anomalous diffusion in crowded fluids. *Phys. Rev. Lett.* **103 (3)**, 038102 (2009) : cited on pp. 29, 30, and 43

[137] N. Malchus and M. Weiss. Anomalous diffusion reports on the interaction of misfolded proteins with the quality control machinery in the endoplasmic reticulum. *Biophys. J.* **99 (4)**, 1321 (2010) : cited on pp. 29 and 43

[138] Jae-Hyung Jeon, Hector Martinez-Seara Monne, Matti Javanainen, and Ralf Metzler. Anomalous diffusion of phospholipids and cholesterols in a lipid bilayer and its origins. *Phys. Rev. Lett.* **109**, 188103 (2012) : cited on pp. 29 and 36

[139] E. Falck, T. Róg, M. Karttunen, and I. Vattulainen. Lateral diffusion in lipid membranes through collective flows. *J. Am. Chem. Soc.* **130 (1)**, 44 (2008) : cited on p. 29

[140] E. Flenner, J. Das, M. C. Rheinstädter, and I. Kosztin. Subdiffusion and lateral diffusion coefficient of lipid atoms and molecules in phospholipid bilayers. *Phys. Rev. E* **79 (1)**, 011907 (2009) : cited on pp. 29 and 36

[141] M. Javanainen, H. Hammaren, L. Monticelli, J. H. Jeon, M. S. Miettinen, H. Martinez-Seara, R. Metzler, and I. Vattulainen. Anomalous and normal diffusion of proteins and lipids in crowded lipid membranes. *Faraday Discuss.* **161**, 397 (2013) : cited on p. 29

[142] S. J. Marrink and H. J. C. Berendsen. Simulation of water transport through a lipid-membrane. *J. Phys. Chem.* **98 (15)**, 4155 (1994) : cited on pp. 29 and 37

[143] S. J. Marrink and H. J. C. Berendsen. Permeation process of small molecules across lipid membranes studied by molecular dynamics simulations. *J. Phys. Chem.* **100 (41)**, 16729 (1996) : cited on p. 29

[144] K. Åman, E. Lindahl, O. Edholm, P. Håkansson, and P. O. Westlund. Structure and dynamics of interfacial water in an L-alpha phase lipid bilayer from molecular dynamics simulations. *Biophys. J.* **84 (1)**, 102 (2003) : cited on p. 29

[145] F. Y. Hansen, G. H. Peters, H. Taub, and A. Miskowiec. Diffusion of water and selected atoms in DMPC lipid bilayer membranes. *J. Chem. Phys.* **137 (20)**, 204910 (2012) : cited on pp. 29 and 33

[146] H. A. Stern and S. E. Feller. Calculation of the dielectric permittivity profile for a nonuniform system: Application to a lipid bilayer simulation. *J. Chem. Phys.* **118 (7)**, 3401 (2003) : cited on p. 30

[147] C. F. Lopez, S. O. Nielsen, M. L. Klein, and P. B. Moore. Hydrogen bonding structure and dynamics of water at the dimyristoylphosphatidylcholine lipid bilayer surface from a molecular dynamics simulation. *J. Phys. Chem. B* **108 (21)**, 6603 (2004) : cited on p. 30

[148] E. Schneck, F. Sedlmeier, and R. R. Netz. Hydration repulsion between biomembranes results from an interplay of dehydration and depolarization. *Proc. Natl. Acad. Sci. U.S.A.* **109 (36)**, 14405 (2012) : cited on p. 30

[149] O. Berger, O. Edholm, and F. Jähnig. Molecular dynamics simulations of a fluid bilayer of dipalmitoylphosphatidylcholine at full hydration, constant pressure, and constant temperature. *Biophys. J.* **72 (5)**, 2002 (1997) : cited on p. 30

[150] B. Hess. P-LINCS: A parallel linear constraint solver for molecular simulation. *J. Chem. Theory Comput.* **4 (1)**, 116 (2008) : cited on p. 30

[151] S. Miyamoto and P. A. Kollman. SETTLE: An analytical version of the shake and rattle algorithm for rigid water models. *J. Comput. Chem.* **13 (8)**, 952 (1992) : cited on p. 30

[152] A. H. de Vries, I. Chandrasekhar, W. F. van Gunsteren, and P. H. Hünenberger. Molecular dynamics simulations of phospholipid bilayers: Influence of artificial periodicity, system size, and simulation time. *J. Phys. Chem. B* **109 (23)**, 11643 (2005) : cited on p. 30

[153] F. Castro-Román, R. W. Benz, S. H. White, and D. J. Tobias. Investigation of finite system size effects in molecular dynamics simulations of lipid bilayers. *J. Phys. Chem. B* **110 (47)**, 24157 (2006) : cited on p. 30

[154] J. B. Klauda, B. R. Brooks, and R. W. Pastor. Dynamical motions of lipids and a finite size effect in simulations of bilayers. *J. Chem. Phys.* **125 (14)**, 144710 (2006) : cited on p. 30

[155] E. Lindahl and O. Edholm. Molecular dynamics simulation of NMR relaxation rates and slow dynamics in lipid bilayers. *J. Chem. Phys.* **115 (10)**, 4938 (2001) : cited on p. 33

[156] J. P. M. Jämbeck and A. P. Lyubartsev. Derivation and systematic validation of a refined all-atom force field for phosphatidylcholine lipids. *J. Phys. Chem. B* **116 (10)**, 3164 (2012) : cited on p. 33

[157] E. Lauga and T. M. Squires. Brownian motion near a partial-slip boundary: A local probe of the no-slip condition. *Phys. Fluids* **17 (10)**, 103102 (2005) : cited on pp. 40, 187, and 188

[158] M. A. Lomholt, I. M. Zaid, and R. Metzler. Subdiffusion and weak ergodicity breaking in the presence of a reactive boundary. *Phys. Rev. Lett.* **98 (20)**, 200603 (2007) : cited on p. 46

[159] S. A. Pabit, H. Roder, and S. J. Hagen. Internal friction controls the speed of protein folding from a compact configuration. *Biochemistry* **43 (39)**, 12532 (2004) : cited on p. 47

[160] T. Cellmer, E. R. Henry, J. Hofrichter, and W. A. Eaton. Measuring internal friction of an ultrafast-folding protein. *Proc. Natl. Acad. Sci. U.S.A.* **105 (47)**, 18320 (2008) : cited on p. 47

[161] M. Buscaglia, L. J. Lapidus, W. A. Eaton, and J. Hofrichter. Effects of denaturants on the dynamics of loop formation in polypeptides. *Biophys. J.* **91 (1)**, 276 (2006) : cited on pp. 47 and 63

[162] A. Möglich, K. Joder, and T. Kiefhaber. End-to-end distance distributions and intrachain diffusion constants in unfolded polypeptide chains indicate intramolecular hydrogen bond formation. *Proc. Natl. Acad. Sci. U.S.A.* **103 (33)**, 12394 (2006) : cited on pp. 47 and 63

[163] R. L. Baldwin. How Hofmeister ion interactions affect protein stability. *Biophys. J.* **71 (4)**, 2056 (1996) : cited on pp. 47 and 48

[164] N. Schwierz, D. Horinek, and R. R. Netz. Reversed anionic Hofmeister series: The interplay of surface charge and surface polarity. *Langmuir* **26 (10)**, 7370 (2010) : cited on p. 47

[165] N. Schwierz, D. Horinek, and R. R. Netz. Anionic and cationic Hofmeister effects on hydrophobic and hydrophilic surfaces. *Langmuir* **29 (8)**, 2602 (2013) : cited on p. 47

[166] L. Vrbka, J. Vondrášek, B. Jagoda-Cwiklik, R. Vácha, and P. Jungwirth. Quantification and rationalization of the higher affinity of sodium over potassium to protein surfaces. *Proc. Natl. Acad. Sci. U.S.A.* **103 (42)**, 15440 (2006) : cited on pp. 47 and 54

[167] J. S. Uejio, C. P. Schwartz, A. M. Duffin, W. S. Drisdell, R. C. Cohen, and R. J. Saykally. Characterization of selective binding of alkali cations with carboxylate by x-ray absorption spectroscopy of liquid microjets. *Proc. Natl. Acad. Sci. U.S.A.* **105 (19)**, 6809 (2008) : cited on pp. 47 and 54

[168] E. F. Aziz, N. Ottosson, S. Eisebitt, W. Eberhardt, B. Jagoda-Cwiklik, R. Vácha, P. Jungwirth, and B. Winter. Cation-specific interactions with carboxylate in amino acid and acetate aqueous solutions: X-ray absorption and ab initio calculations. *J. Phys. Chem. B* **112 (40)**, 12567 (2008) : cited on pp. 47 and 54

[169] M. V. Fedorov, J. M. Goodman, and S. Schumm. To switch or not to switch: The effects of potassium and sodium ions on alpha-poly-L-glutamate conformations in aqueous solutions. *J. Am. Chem. Soc.* **131 (31)**, 10854 (2009) : cited on p. 47

[170] M. Colaco, J. Park, and H. Blanch. The kinetics of aggregation of poly-glutamic acid based polypeptides. *Biophys. Chem.* **136 (2-3)**, 74 (2008) : cited on pp. 47 and 63

[171] D. Madern, C. Ebel, and G. Zaccai. Halophilic adaptation of enzymes. *Extremophiles* **4 (2)**, 91 (2000) : cited on pp. 47 and 63

[172] A. K. Bandyopadhyay, G. Krishnamoorthy, L. C. Padhy, and H. M. Sonawat. Kinetics of salt-dependent unfolding of [2Fe-2S] ferredoxin of Halobacterium salinarum. *Extremophiles* **11 (4)**, 615 (2007) : cited on pp. 47 and 63

[173] R. D. Gray and J. B. Chaires. Kinetics and mechanism of K^+- and Na^+-induced folding of models of human telomeric DNA into G-quadruplex structures. *Nucleic Acids Res.* **36 (12)**, 4191 (2008) : cited on pp. 47 and 63

[174] A. C. Dumetz, A. M. Snellinger-O'Brien, E. W. Kaler, and A. M. Lenhoff. Patterns of protein-protein interactions in salt solutions and implications for protein crystallization. *Protein Sci.* **16 (9)**, 1867 (2007) : cited on p. 48

[175] W. J. Dyer. Protein denaturation in frozen and stored fish. *Food Res.* **16 (6)**, 522 (1951) : cited on p. 48

[176] J. K. Lanyi. Salt-dependent properties of proteins from extremely halophilic bacteria. *Bacteriol. Rev.* **38 (3)**, 272 (1974) : cited on p. 48

[177] M. Karplus and J. A. McCammon. Molecular dynamics simulations of biomolecules. *Nat. Struct. Biol.* **9 (9)**, 646 (2002) : cited on p. 48

[178] S. Marqusee and R. L. Baldwin. Helix stabilization by Glu- ... Lys+ salt bridges in short peptides of de novo design. *Proc. Natl. Acad. Sci. U.S.A.* **84 (24)**, 8898 (1987) : cited on p. 48

[179] S. Marqusee, V. H. Robbins, and R. L. Baldwin. Unusually stable helix formation in short alanine-based peptides. *Proc. Natl. Acad. Sci. U.S.A.* **86 (14)**, 5286 (1989) : cited on p. 48

[180] E. J. Spek, C. A. Olson, Z. S. Shi, and N. R. Kallenbach. Alanine is an intrinsic alpha-helix stabilizing amino acid. *J. Am. Chem. Soc.* **121 (23)**, 5571 (1999) : cited on p. 48

[181] A. Chakrabartty, T. Kortemme, and R. L. Baldwin. Helix propensities of the amino-acids measured in alanine-based peptides without helix-stabilizing side-chain interactions. *Protein Sci.* **3 (5)**, 843 (1994) : cited on p. 48

[182] J. M. Scholtz, E. J. York, J. M. Stewart, and R. L. Baldwin. A neutral, water-soluble, alpha-helical peptide: The effect of ionic-strength on the helix coil equilibrium. *J. Am. Chem. Soc.* **113 (13)**, 5102 (1991) : cited on p. 48

[183] J. Dzubiella. Salt-specific stability and denaturation of a short salt-bridge-forming alpha-helix. *J. Am. Chem. Soc.* **130 (42)**, 14000 (2008) : cited on pp. 48, 49, and 54

[184] D. A. Case. AMBER9.0, University of California, San Francisco (2006) : cited on p. 49

[185] L. X. Dang. Mechanism and thermodynamics of ion selectivity in aqueous-solutions of 18-crown-6 ether: A molecular-dynamics study. *J. Am. Chem. Soc.* **117 (26)**, 6954 (1995) : cited on p. 49

[186] I. S. Joung and T. E. Cheatham. Determination of alkali and halide monovalent ion parameters for use in explicitly solvated biomolecular simulations. *J. Phys. Chem. B* **112 (30)**, 9020 (2008) : cited on p. 49

[187] I. Kalcher and J. Dzubiella. Structure-thermodynamics relation of electrolyte solutions. *J. Chem. Phys.* **130 (13)**, 134507 (2009) : cited on p. 49

[188] J. Dzubiella. Molecular insights into the ion-specific kinetics of anionic peptides. *J. Phys. Chem. B* **114 (20)**, 7098 (2010) : cited on pp. 49 and 63

[189] W. Kabsch and C. Sander. Dictionary of protein secondary structure: Pattern-recognition of hydrogen-bonded and geometrical features. *Biopolymers* **22 (12)**, 2577 (1983) : cited on p. 49

[190] B. Hess. Determining the shear viscosity of model liquids from molecular dynamics simulations. *J. Chem. Phys.* **116 (1)**, 209 (2002) : cited on p. 51

[191] R. Zwanzig. Time-correlation functions and transport coefficients in statistical mechanics. *Annu. Rev. Phys. Chem.* **16**, 67 (1965) : cited on p. 51

[192] T. Chen, B. Smit, and A. T. Bell. Are pressure fluctuation-based equilibrium methods really worse than nonequilibrium methods for calculating viscosities? *J. Chem. Phys.* **131 (24)**, 246101 (2009) : cited on p. 51

[193] M. A. Gonzalez and J. L. F. Abascal. The shear viscosity of rigid water models. *J. Chem. Phys.* **132 (9)**, 096101 (2010) : cited on p. 51

[194] Robert A. Robinson and Robert H. Stokes. *Electrolyte Solutions*. Dover Publications Inc., 2nd edition (2002) : cited on p. 51

[195] K. R. Harris and L. A. Woolf. Temperature and volume dependence of the viscosity of water and heavy water at low temperatures. *J. Chem. Eng. Data* **49 (4)**, 1064 (2004) : cited on p. 51

[196] P. Hänggi, P. Talkner, and M. Borkovec. Reaction-rate theory: 50 years after Kramers. *Rev. Mod. Phys.* **62 (2)**, 251 (1990) : cited on p. 52

[197] R. Metzler and J. Klafter. Kramers' escape problem with anomalous kinetics: Non-exponential decay of the survival probability. *Chem. Phys. Lett.* **321 (3-4)**, 238 (2000) : cited on p. 57

[198] Jean-Louis Barrat and Jean-Pierre Hansen. *Basic Concepts for Simple and Complex Fluids*. Cambridge University Press (2003) : cited on p. 57

[199] S. C. Kou and X. S. Xie. Generalized Langevin equation with fractional Gaussian noise: Subdiffusion within a single protein molecule. *Phys. Rev. Lett.* **93 (18)**, 180603 (2004) : cited on p. 57

[200] T. Neusius, I. Daidone, I. M. Sokolov, and J. C. Smith. Subdiffusion in peptides originates from the fractal-like structure of configuration space. *Phys. Rev. Lett.* **100 (18)**, 188103 (2008) : cited on p. 57

[201] A. K. Sangha and T. Keyes. Proteins fold by subdiffusion of the order parameter. *J. Phys. Chem. B* **113 (48)**, 15886 (2009) : cited on p. 57

[202] V. A. Parsegian, R. P. Rand, and D. C. Rau. Osmotic stress, crowding, preferential hydration, and binding: A comparison of perspectives. *Proc. Natl. Acad. Sci. U.S.A.* **97 (8)**, 3987 (2000) : cited on p. 63

[203] B. Mos, P. Verkerk, S. Pouget, A. van Zon, G. J. Bel, S. W. de Leeuw, and C. D. Eisenbach. The dynamics in polyethyleneoxide-alkali iodide complexes investigated by neutron spin-echo spectroscopy and molecular dynamics simulations. *J. Chem. Phys.* **113 (1)**, 4 (2000) : cited on p. 63

[204] V. P. Denisov, J. Peters, H. D. Hörlein, and B. Halle. Using buried water molecules to explore the energy landscape of proteins. *Nat. Struct. Biol.* **3 (6)**, 505 (1996) : cited on p. 63

[205] J. R. Moffitt, Y. R. Chemla, S. B. Smith, and C. Bustamante. Recent advances in optical tweezers. *Annu. Rev. Biochem.* **77**, 205 (2008) : cited on p. 65

[206] H. Dietz, F. Berkemeier, M. Bertz, and M. Rief. Anisotropic deformation response of single protein molecules. *Proc. Natl. Acad. Sci. U.S.A.* **103 (34)**, 12724 (2006) : cited on pp. 65 and 91

[207] T. Franosch, M. Grimm, M. Belushkin, F. M. Mor, G. Foffi, L. Forró, and S. Jeney. Resonances arising from hydrodynamic memory in Brownian motion. *Nature* **478 (7367)**, 85 (2011) : cited on pp. 65 and 71

[208] A. Jannasch, M. Mahamdeh, and E. Schäffer. Inertial effects of a small Brownian particle cause a colored power spectral density of thermal noise. *Phys. Rev. Lett.* **107 (22)**, 228301 (2011) : cited on pp. 65 and 71

[209] F. Gittes, B. Schnurr, P. D. Olmsted, F. C. MacKintosh, and C. F. Schmidt. Microscopic viscoelasticity: Shear moduli of soft materials determined from thermal fluctuations. *Phys. Rev. Lett.* **79 (17)**, 3286 (1997) : cited on p. 65

[210] J. C. Crocker, M. T. Valentine, E. R. Weeks, T. Gisler, P. D. Kaplan, A. G. Yodh, and D. A. Weitz. Two-point microrheology of inhomogeneous soft materials. *Phys. Rev. Lett.* **85 (4)**, 888 (2000) : cited on pp. 65 and 161

[211] L. Starrs and P. Bartlett. Colloidal dynamics in polymer solutions: Optical two-point microrheology measurements. *Faraday Discuss.* **123**, 323 (2003) : cited on p. 65

[212] J. R. Moffitt, Y. R. Chemla, D. Izhaky, and C. Bustamante. Differential detection of dual traps improves the spatial resolution of optical tweezers. *Proc. Natl. Acad. Sci. U.S.A.* **103 (24)**, 9006 (2006) : cited on pp. 65, 66, and 70

[213] Peter Bloomfield. *Fourier Analysis of Time Series: An Introduction*. John Wiley and Sons (1976) : cited on pp. 66, 78, 80, and 205

[214] K. Berg-Sørensen and H. Flyvbjerg. Power spectrum analysis for optical tweezers. *Rev. Sci. Instrum.* **75 (3)**, 594 (2004) : cited on pp. 66, 67, 69, 75, 78, 79, 81, 82, 86, 116, 195, and 200

[215] I. M. Tolić-Nørrelykke, K. Berg-Sørensen, and H. Flyvbjerg. MatLab program for precision calibration of optical tweezers. *Comput. Phys. Commun.* **159 (3)**, 225 (2004) : cited on p. 66

[216] K. Berg-Sørensen, E. J. G. Peterman, T. Weber, C. F. Schmidt, and H. Flyvbjerg. Power spectrum analysis for optical tweezers. II: Laser wavelength dependence of parasitic filtering, and how to achieve high bandwidth. *Rev. Sci. Instrum.* **77 (6)**, 063106 (2006) : cited on pp. 66, 76, 89, and 191

[217] S. F. Tolić-Nørrelykke, E. Schäffer, J. Howard, F. S. Pavone, F. Jülicher, and H. Flyvbjerg. Calibration of optical tweezers with positional detection in the back focal plane. *Rev. Sci. Instrum.* **77 (10)**, 103101 (2006) : cited on pp. 66 and 85

[218] S. F. Nørrelykke and H. Flyvbjerg. Power spectrum analysis with least-squares fitting: Amplitude bias and its elimination, with application to optical tweezers and atomic force microscope cantilevers. *Rev. Sci. Instrum.* **81 (7)**, 075103 (2010) : cited on p. 66

[219] M. Atakhorrami, G. H. Koenderink, C. F. Schmidt, and F. C. MacKintosh. Short-time inertial response of viscoelastic fluids: Observation of vortex propagation. *Phys. Rev. Lett.* **95 (20)**, 208302 (2005) : cited on pp. 66 and 75

[220] T. B. Liverpool and F. C. MacKintosh. Inertial effects in the response of viscous and viscoelastic fluids. *Phys. Rev. Lett.* **95 (20)**, 208303 (2005) : cited on pp. 66 and 75

[221] M. Atakhorrami, D. Mizuno, G. H. Koenderink, T. B. Liverpool, F. C. MacKintosh, and C. F. Schmidt. Short-time inertial response of viscoelastic fluids measured with Brownian motion and with active probes. *Phys. Rev. E* **77 (6)**, 061508 (2008) : cited on pp. 66 and 75

[222] E. Fällman and O. Axner. Design for fully steerable dual-trap optical tweezers. *Appl. Optics* **36 (10)**, 2107 (1997) : cited on p. 66

[223] Carlos Bustamante, Yann R. Chemla, and Jeffrey R. Moffit. High-resolution dual-trap optical tweezers with differential detection. In Paul R. Selvin and Taekjip Ha, editors, *Single-Molecule Techniques: A Laboratory Manual*, chapter 14. Cold Spring Harbor Laboratory Press, New York, USA (2008) : cited on pp. 66 and 70

[224] P. Mangeol and U. Bockelmann. Interference and crosstalk in double optical tweezers using a single laser source. *Rev. Sci. Instrum.* **79 (8)**, 083103 (2008) : cited on p. 67

[225] M. Atakhorrami, K. M. Addas, and C. F. Schmidt. Twin optical traps for two-particle cross-correlation measurements: Eliminating cross-talk. *Rev. Sci. Instrum.* **79 (4)**, 043103 (2008) : cited on

pp. 67, 75, and 76

[226] X. Perpina, X. Jorda, M. Vellvehi, J. Millan, and N. Mestres. Development of an analog processing circuit for IR-radiation power and noncontact position measurements. *Rev. Sci. Instrum.* **76 (2)**, 025106 (2005) : cited on p. 67

[227] Lev D. Landau and Evgeny M. Lifshitz. *Statistical Physics, Part 1*. Course of Theoretical Physics, Vol. 5. Butterworth-Heinemann, Oxford, UK, 3rd edition (1980) : cited on pp. 68 and 69

[228] J. C. Meiners and S. R. Quake. Direct measurement of hydrodynamic cross correlations between two particles in an external potential. *Phys. Rev. Lett.* **82 (10)**, 2211 (1999) : cited on pp. 68 and 75

[229] P. Bartlett, S. I. Henderson, and S. J. Mitchell. Measurement of the hydrodynamic forces between two polymer-coated spheres. *Philos. Trans. R. Soc. Lond. Ser. A-Math. Phys. Eng. Sci.* **359 (1782)**, 883 (2001) : cited on pp. 68 and 75

[230] S. Henderson, S. Mitchell, and P. Bartlett. Direct measurements of colloidal friction coefficients. *Phys. Rev. E* **64 (6)**, 061403 (2001) : cited on pp. 68 and 75

[231] J. C. Meiners and S. R. Quake. Femtonewton force spectroscopy of single extended DNA molecules. *Phys. Rev. Lett.* **84 (21)**, 5014 (2000) : cited on p. 68

[232] K. C. Neuman and S. M. Block. Optical trapping. *Rev. Sci. Instrum.* **75 (9)**, 2787 (2004) : cited on p. 70

[233] D. A. Weitz, D. J. Pine, P. N. Pusey, and R. J. A. Tough. Nondiffusive Brownian-motion studied by diffusing-wave spectroscopy. *Phys. Rev. Lett.* **63 (16)**, 1747 (1989) : cited on p. 71

[234] H. J. H. Clercx and P. P. J. M. Schram. Brownian particles in shear-flow and harmonic potentials: A study of long-time tails. *Phys. Rev. A* **46 (4)**, 1942 (1992) : cited on p. 71

[235] A. Erbas, R. Podgornik, and R. R. Netz. Viscous compressible hydrodynamics at planes, spheres and cylinders with finite surface slip. *Eur. Phys. J. E* **32 (2)**, 147 (2010) : cited on p. 71

[236] A series of flow field animations is included as supplementary material, see flow_field_*.swf (2012) : cited on pp. 71 and 72

[237] W. van Saarloos and P. Mazur. Many-sphere hydrodynamic interactions. II. Mobilities at finite frequencies. *Physica A* **120 (1-2)**, 77 (1983) : cited on pp. 72, 75, and 85

[238] J. Rotne and S. Prager. Variational treatment of hydrodynamic interaction in polymers. *J. Chem. Phys.* **50 (11)**, 4831 (1969) : cited on pp. 73, 119, 121, 124, and 189

[239] D. L. Ermak and J. A. McCammon. Brownian dynamics with hydrodynamic interactions. *J. Chem. Phys.* **69 (4)**, 1352 (1978) : cited on pp. 73 and 123

[240] Carl W. Oseen. *Neuere Methoden und Ergebnisse in der Hydrodynamik*. Akademische Verlagsgesellschaft (1927) : cited on p. 75

[241] B. H. Zimm. Dynamics of polymer molecules in dilute solution: Viscoelasticity, flow birefringence and dielectric loss. *J. Chem. Phys.* **24 (2)**, 269 (1956) : cited on pp. 75, 125, and 126

[242] M. Reichert and H. Stark. Hydrodynamic coupling of two rotating spheres trapped in harmonic potentials. *Phys. Rev. E* **69 (3)**, 031407 (2004) : cited on p. 75

[243] S. Martin, M. Reichert, H. Stark, and T. Gisler. Direct observation of hydrodynamic rotation-translation coupling between two colloidal spheres. *Phys. Rev. Lett.* **97 (24)**, 248301 (2006) : cited on p. 75

[244] E. J. G. Peterman, M. A. van Dijk, L. C. Kapitein, and C. F. Schmidt. Extending the bandwidth of optical-tweezers interferometry. *Rev. Sci. Instrum.* **74 (7)**, 3246 (2003) : cited on pp. 75, 76, 89,

and 191

[245] J. D. Scargle. Studies in astronomical time-series analysis. II. Statistical aspects of spectral-analysis of unevenly spaced data. *Astrophysical J.* **263 (2)**, 835 (1982) : cited on p. 78

[246] J. H. Horne and S. L. Baliunas. A prescription for period analysis of unevenly sampled time-series. *Astrophysical J.* **302 (2)**, 757 (1986) : cited on p. 78

[247] M. I. A. Lourakis. levmar: Levenberg-Marquardt nonlinear least squares algorithms in C/C++. `http://www.ics.forth.gr/~lourakis/levmar/` (2004) : cited on p. 81

[248] K. Berg-Sørensen, L. Oddershede, E. L. Florin, and H. Flyvbjerg. Unintended filtering in a typical photodiode detection system for optical tweezers. *J. Appl. Phys.* **93 (6)**, 3167 (2003) : cited on pp. 89 and 191

[249] A. R. Bulsara, K. Lindenberg, and K. E. Shuler. Spectral-analysis of a non-linear oscillator driven by random and periodic forces. I. Linearized theory. *J. Stat. Phys.* **27 (4)**, 787 (1982) : cited on p. 91

[250] K. J. Tielrooij, N. Garcia-Araez, M. Bonn, and H. J. Bakker. Cooperativity in ion hydration. *Science* **328 (5981)**, 1006 (2010) : cited on pp. 91 and 171

[251] T. K. Caughey and J. K. Dienes. Analysis of a nonlinear first-order system with a white noise input. *J. Appl. Phys.* **32 (11)**, 2476 (1961) : cited on pp. 91, 98, 104, and 107

[252] N. V. Agudov and A. V. Krichigin. Investigation of stochastic resonance in monostable systems. *Int. J. Bifurcation Chaos* **18 (9)**, 2833 (2008) : cited on pp. 91 and 98

[253] P. Hänggi and H. Thomas. Stochastic-processes: Time evolution, symmetries and linear response. *Phys. Rep.* **88 (4)**, 207 (1982) : cited on pp. 91, 96, and 104

[254] L. Gammaitoni, P. Hänggi, P. Jung, and F. Marchesoni. Stochastic resonance. *Rev. Mod. Phys.* **70 (1)**, 223 (1998) : cited on pp. 91 and 104

[255] J. Casado-Pascual, J. Gómez-Ordóñez, M. Morillo, and P. Hänggi. Rocking bistable systems: Use and abuse of linear response theory. *Europhys. Lett.* **58 (3)**, 342 (2002) : cited on p. 91

[256] R. Zwanzig. Nonlinear generalized Langevin equations. *J. Stat. Phys.* **9 (3)**, 215 (1973) : cited on p. 94

[257] L. Schmidt and R. R. Netz. Criteria for the breakdown of linear response in bistable systems. *Europhys. Lett.* **98 (1)**, 10014 (2012) : cited on pp. 97 and 111

[258] K. S. Nordholm and R. Zwanzig. Strategies for fluctuation renormalization in nonlinear transport-theory. *J. Stat. Phys.* **11 (2)**, 143 (1974) : cited on p. 98

[259] R. F. Rodriguez and N. G. van Kampen. Systematic treatment of fluctuations in a nonlinear oscillator. *Physica A* **85 (2)**, 347 (1976) : cited on p. 98

[260] J. J. Brey, J. M. Casado, and M. Morillo. Spectral density for a nonlinear Fokker-Planck model: Monte-Carlo and analytical studies. *Phys. Rev. A* **32 (5)**, 2893 (1985) : cited on p. 98

[261] John W. Negele and Henri Orland. *Quantum Many-Particle Systems*. Addison-Wesley (1988) : cited on p. 100

[262] V. A. Shneidman, P. Jung, and P. Hänggi. Power spectrum of a driven bistable system. *Europhys. Lett.* **26 (8)**, 571 (1994) : cited on p. 104

[263] V. A. Shneidman, P. Jung, and P. Hänggi. Weak-noise limit of stochastic resonance. *Phys. Rev. Lett.* **72 (17)**, 2682 (1994) : cited on p. 104

[264] B. S. Khatri, M. Kawakami, K. Byrne, D. A. Smith, and T. C. B. McLeish. Entropy and barrier-controlled fluctuations determine conformational viscoelasticity of single biomolecules. *Biophys. J.*

92 (6), 1825 (2007) : cited on p. 113

[265] L. Schmidt. *Stochastic Effects in Coupled Systems*. Diploma thesis, Technical University of Munich, Germany (2011) : cited on p. 114

[266] J. L. Hutter and J. Bechhoefer. Calibration of atomic-force microscope tips. *Rev. Sci. Instrum.* **64 (7)**, 1868 (1993) : cited on p. 116

[267] O. B. Usta, J. E. Butler, and A. J. C. Ladd. Transverse migration of a confined polymer driven by an external force. *Phys. Rev. Lett.* **98 (9)**, 098301 (2007) : cited on p. 117

[268] L. Cannavacciuolo, R. G. Winkler, and G. Gompper. Mesoscale simulations of polymer dynamics in microchannel flows. *Europhys. Lett.* **83 (3)**, 34007 (2008) : cited on p. 117

[269] N. Hoda and S. Kumar. Parameters influencing diffusion dynamics of an adsorbed polymer chain. *Phys. Rev. E* **79 (2)**, 020801(R) (2009) : cited on p. 117

[270] M. Hinczewski and R. R. Netz. Dynamics of DNA: Experimental controversies and theoretical insights. *Physica A* **389 (15)**, 2993 (2010) : cited on pp. 117, 128, and 131

[271] R. Chelakkot, R. G. Winkler, and G. Gompper. Migration of semiflexible polymers in microcapillary flow. *Europhys. Lett.* **91 (1)**, 14001 (2010) : cited on p. 117

[272] D. J. Bonthuis, C. Meyer, D. Stein, and C. Dekker. Conformation and dynamics of DNA confined in slitlike nanofluidic channels. *Phys. Rev. Lett.* **101 (10)**, 108303 (2008) : cited on p. 117

[273] J. Tang, S. L. Levy, D. W. Trahan, J. J. Jones, H. G. Craighead, and P. S. Doyle. Revisiting the conformation and dynamics of DNA in slitlike confinement. *Macromolecules* **43 (17)**, 7368 (2010) : cited on p. 117

[274] R. Shusterman, S. Alon, T. Gavrinyov, and O. Krichevsky. Monomer dynamics in double- and single-stranded DNA polymers. *Phys. Rev. Lett.* **92 (4)**, 048303 (2004) : cited on p. 117

[275] E. P. Petrov, T. Ohrt, R. G. Winkler, and P. Schwille. Diffusion and segmental dynamics of double-stranded DNA. *Phys. Rev. Lett.* **97 (25)**, 258101 (2006) : cited on p. 117

[276] R. Granek. From semi-flexible polymers to membranes: Anomalous diffusion and reptation. *J. de Physique II* **7 (12)**, 1761 (1997) : cited on p. 117

[277] C. Sendner and R. R. Netz. Hydrodynamic lift of a moving nano-rod at a wall. *Europhys. Lett.* **79 (5)**, 58004 (2007) : cited on p. 117

[278] C. Sendner and R. R. Netz. Shear-induced repulsion of a semiflexible polymer from a wall. *Europhys. Lett.* **81 (5)**, 54006 (2008) : cited on p. 117

[279] T. Ando and J. Skolnick. Crowding and hydrodynamic interactions likely dominate in vivo macromolecular motion. *Proc. Natl. Acad. Sci. U.S.A.* **107 (43)**, 18457 (2010) : cited on p. 118

[280] Masao Doi and Samuel F. Edwards. *The Theory of Polymer Dynamics*. Oxford University Press (1988) : cited on pp. 118 and 123

[281] J. R. Blake. Image system for a stokeslet in a no-slip boundary. *Proc. Camb. Phil. Soc.* **70 (2)**, 303 (1971) : cited on p. 118

[282] Y. W. Kim and R. R. Netz. Electro-osmosis at inhomogeneous charged surfaces: Hydrodynamic versus electric friction. *J. Chem. Phys.* **124 (11)**, 114709 (2006) : cited on pp. 119 and 190

[283] N. Hoda and S. Kumar. Brownian dynamics simulations of polyelectrolyte adsorption in shear flow with hydrodynamic interaction. *J. Chem. Phys.* **127 (23)**, 234902 (2007) : cited on pp. 119 and 190

[284] Mauricio D. Carbajal-Tinoco, Ricardo Lopez-Fernandez, and Jose Luis Arauz-Lara. Asymmetry in colloidal diffusion near a rigid wall. *Phys. Rev. Lett.* **99 (13)**, 138303 (2007) : cited on p. 119

[285] G. S. Perkins and R. B. Jones. Hydrodynamic interaction of a spherical-particle with a planar boundary. II. Hard-wall. *Physica A* **189 (3-4)**, 447 (1992) : cited on pp. 119 and 188

[286] M. Stimson and G. B. Jeffery. The motion of two spheres in a viscous fluid. *Proc. Royal Soc. A* **111 (757)**, 110 (1926) : cited on pp. 119 and 188

[287] M. Hinczewski and R. R. Netz. Anisotropic hydrodynamic mean-field theory for semiflexible polymers under tension. *Macromolecules* **44 (17)**, 6972 (2011) : cited on pp. 124, 140, and 174

[288] O. Kratky and G. Porod. Röntgenuntersuchung gelöster Fadenmoleküle. *Recl. Trav. Chim. Pay.-B.* **68 (12)**, 1106 (1949) : cited on p. 124

[289] R. G. Winkler, P. Reineker, and L. Harnau. Models and equilibrium properties of stiff molecular chains. *J. Chem. Phys.* **101 (9)**, 8119 (1994) : cited on p. 125

[290] B. Y. Ha and D. Thirumalai. A mean-field model for semiflexible chains. *J. Chem. Phys.* **103 (21)**, 9408 (1995) : cited on p. 125

[291] R. G. Winkler. Diffusion and segmental dynamics of rodlike molecules by fluorescence correlation spectroscopy. *J. Chem. Phys.* **127 (5)**, 054904 (2007) : cited on pp. 125 and 128

[292] L. Harnau, R. G. Winkler, and P. Reineker. Dynamic structure factor of semiflexible macromolecules in dilute solution. *J. Chem. Phys.* **104 (16)**, 6355 (1996) : cited on pp. 125 and 131

[293] Eugene H. Stanley. *Introduction to Phase Transitions and Critical Phenomena*. Oxford University Press (1987) : cited on p. 131

[294] P. E. Rouse. A theory of the linear viscoelastic properties of dilute solutions of coiling polymers. *J. Chem. Phys.* **21 (7)**, 1272 (1953) : cited on p. 135

[295] M. Manghi, X. Schlagberger, Y. W. Kim, and R. R. Netz. Hydrodynamic effects in driven soft matter. *Soft Matter* **2 (8)**, 653 (2006) : cited on p. 135

[296] A. Srivastava, R. Ben Halevi, A. Veksler, and R. Granek. Tensorial elastic network model for protein dynamics: Integration of the anisotropic network model with bond-bending and twist elasticities. *Proteins* **80 (12)**, 2692 (2012) : cited on p. 139

[297] L. H. Deng, X. Trepat, J. P. Butler, E. Millet, K. G. Morgan, D. A. Weitz, and J. J. Fredberg. Fast and slow dynamics of the cytoskeleton. *Nat. Mater.* **5 (8)**, 636 (2006) : cited on p. 139

[298] H. J. Gao. Application of fracture mechanics concepts to hierarchical biomechanics of bone and bone-like materials. *Int. J. Fracture* **138 (1-4)**, 101 (2006) : cited on p. 139

[299] D. T. N. Chen, Q. Wen, P. A. Janmey, J. C. Crocker, and A. G. Yodh. Rheology of soft materials. *Annu. Rev. Condens. Matter Phys.* **1**, 301 (2010) : cited on p. 139

[300] I. Reviakine, D. Johannsmann, and R. P. Richter. Hearing what you cannot see and visualizing what you hear: Interpreting quartz crystal microbalance data from solvated interfaces. *Anal. Chem.* **83 (23)**, 8838 (2011) : cited on p. 139

[301] A. Basu, Q. Wen, X. M. Mao, T. C. Lubensky, P. A. Janmey, and A. G. Yodh. Nonaffine displacements in flexible polymer networks. *Macromolecules* **44 (6)**, 1671 (2011) : cited on p. 139

[302] M. L. Gardel, M. T. Valentine, J. C. Crocker, A. R. Bausch, and D. A. Weitz. Microrheology of entangled F-actin solutions. *Phys. Rev. Lett.* **91 (15)**, 158302 (2003) : cited on p. 139

[303] J. H. Shin, M. L. Gardel, L. Mahadevan, P. Matsudaira, and D. A. Weitz. Relating microstructure to rheology of a bundled and cross-linked F-actin network in vitro. *Proc. Natl. Acad. Sci. U.S.A.*

101 (26), 9636 (2004) : cited on p. 139

[304] F. Gittes and F. C. MacKintosh. Dynamic shear modulus of a semiflexible polymer network. *Phys. Rev. E* **58 (2)**, R1241 (1998) : cited on p. 139

[305] D. C. Morse. Tube diameter in tightly entangled solutions of semiflexible polymers. *Phys. Rev. E* **63 (3)**, 031502 (2001) : cited on p. 139

[306] D. A. Head, A. J. Levine, and F. C. MacKintosh. Deformation of cross-linked semiflexible polymer networks. *Phys. Rev. Lett.* **91 (10)**, 108102 (2003) : cited on p. 139

[307] J. Wilhelm and E. Frey. Elasticity of stiff polymer networks. *Phys. Rev. Lett.* **91 (10)**, 108103 (2003) : cited on p. 139

[308] M. Das, F. C. MacKintosh, and A. J. Levine. Effective medium theory of semiflexible filamentous networks. *Phys. Rev. Lett.* **99 (3)**, 038101 (2007) : cited on p. 139

[309] C. P. Broedersz, X. M. Mao, T. C. Lubensky, and F. C. MacKintosh. Criticality and isostaticity in fibre networks. *Nat. Phys.* **7 (12)**, 983 (2011) : cited on pp. 139 and 150

[310] N. A. Kurniawan, S. Enemark, and R. Rajagopalan. The role of structure in the nonlinear mechanics of cross-linked semiflexible polymer networks. *J. Chem. Phys.* **136 (6)**, 065101 (2012) : cited on p. 139

[311] M. Das, D. A. Quint, and J. M. Schwarz. Redundancy and cooperativity in the mechanics of compositely crosslinked filamentous networks. *PLoS One* **7 (5)**, e35939 (2012) : cited on pp. 139 and 140

[312] X. M. Mao, O. Stenull, and T. C. Lubensky. Effective-medium theory of a filamentous triangular lattice. *Phys. Rev. E* **87 (4)**, 042601 (2013) : cited on p. 139

[313] X. M. Mao, N. Xu, and T. C. Lubensky. Soft modes and elasticity of nearly isostatic lattices: Randomness and dissipation. *Phys. Rev. Lett.* **104 (8)**, 085504 (2010) : cited on p. 139

[314] K. Sun, A. Souslov, X. M. Mao, and T. C. Lubensky. Surface phonons, elastic response, and conformal invariance in twisted kagome lattices. *Proc. Natl. Acad. Sci. U.S.A.* **109 (31)**, 12369 (2012) : cited on p. 139

[315] E. van der Giessen. Materials Physics: Bending Maxwell's rule. *Nat. Phys.* **7 (12)**, 923 (2011) : cited on p. 140

[316] B. S. Khatri and T. C. B. McLeish. Rouse model with internal friction: A coarse grained framework for single biopolymer dynamics. *Macromolecules* **40 (18)**, 6770 (2007) : cited on p. 144

[317] S. Rode. *Mechanical and Driven Networks in Biological Systems*. Diploma thesis, Technical University of Munich, Germany (2012) : cited on p. 154

[318] A simulation movie of a short semiflexible polymer including the six fluctuating end-point coordinates is included as supplementary material, see BD_semiflexible_polymer.mp4 (2013) : cited on pp. 154 and 155

[319] R. D. Mullins, J. A. Heuser, and T. D. Pollard. The interaction of Arp2/3 complex with actin: Nucleation, high affinity pointed end capping, and formation of branching networks of filaments. *Proc. Natl. Acad. Sci. U.S.A.* **95 (11)**, 6181 (1998) : cited on p. 158

[320] L. Blanchoin, K. J. Amann, H. N. Higgs, J. B. Marchand, D. A. Kaiser, and T. D. Pollard. Direct observation of dendritic actin filament networks nucleated by Arp2/3 complex and WASP/Scar proteins. *Nature* **404 (6781)**, 1007 (2000) : cited on p. 158

[321] K. J. Tielrooij, J. Hunger, R. Buchner, M. Bonn, and H. J. Bakker. Influence of concentration and temperature on the dynamics of water in the hydrophobic hydration shell of tetramethylurea. *J.*

Am. Chem. Soc. **132 (44)**, 15671 (2010) : cited on p. 171

[322] D. Laage and J. T. Hynes. A molecular jump mechanism of water reorientation. *Science* **311 (5762)**, 832 (2006) : cited on p. 174

[323] C. Dellago, P. G. Bolhuis, and P. L. Geissler. Transition path sampling. *Adv. Chem. Phys.* **123**, 1 (2002) : cited on p. 174

[324] P. Faccioli, M. Sega, F. Pederiva, and H. Orland. Dominant pathways in protein folding. *Phys. Rev. Lett.* **97 (10)**, 108101 (2006) : cited on p. 174

[325] M. Sega, P. Faccioli, F. Pederiva, G. Garberoglio, and H. Orland. Quantitative protein dynamics from dominant folding pathways. *Phys. Rev. Lett.* **99 (11)**, 118102 (2007) : cited on p. 174

[326] K. E. Kasza, A. C. Rowat, J. Y. Liu, T. E. Angelini, C. P. Brangwynne, G. H. Koenderink, and D. A. Weitz. The cell as a material. *Curr. Opin. Cell Biol.* **19 (1)**, 101 (2007) : cited on p. 174

[327] D. J. Bicout and A. Szabo. Electron transfer reaction dynamics in non-Debye solvents. *J. Chem. Phys.* **109 (6)**, 2325 (1998) : cited on p. 184

[328] E. M. Gauger, M. T. Downton, and H. Stark. Fluid transport at low Reynolds number with magnetically actuated artificial cilia. *Eur. Phys. J. E* **28 (2)**, 231 (2009) : cited on p. 189

[329] L. P. Ghislain, N. A. Switz, and W. W. Webb. Measurement of small forces using an optical trap. *Rev. Sci. Instrum.* **65 (9)**, 2762 (1994) : cited on p. 195

[330] H. Joseph Weaver. *Theory of Discrete and Continuous Fourier Analysis*. John Wiley and Sons (1989) : cited on p. 199

[331] William Press, Saul Teukolsky, William Vetterling, and Brian Flannery. *Numerical Recipes in C*. Cambridge University Press, 2nd edition (1992) : cited on pp. 199, 204, and 205

[332] V. Vrabie, P. Granjon, and C. Serviere. Spectral kurtosis: From definition to application. In *6th IEEE International Workshop on Nonlinear Signal and Image Processing, Grado-Trieste, Italy* (2003) : cited on p. 205

[333] H. A. Kramers. Brownian motion in a field of force and the diffusion model of chemical reactions. *Physica* **7**, 284 (1940) : cited on p. 206

[334] Lev D. Landau and Evgeny M. Lifshitz. *Theory of Elasticity*. Course of Theoretical Physics, Vol. 7. Butterworth-Heinemann, Oxford, UK, 3rd edition (1986) : cited on p. 207

ABSTRACT

Stochastic concepts are indispensable to understand the fluctuating dynamics of biological systems on the microscopic scale. Devising methods to reliably and efficiently extract the physically relevant information contained in stochastic signals therefore constitutes a major challenge in current biophysical research. In this work, the fluctuating dynamics of various systems are investigated theoretically.

First, the diffusional motion of water molecules and the conformational dynamics of a short peptide are studied based on the trajectories from atomistic simulations. We find a pronounced diffusion anisotropy of water molecules in bulk as well as a remarkably structured diffusivity profile for the relative motion of pairs of water molecules. Near lipid bilayers, water diffusion is suppressed and, due to a coupling of lipids and water molecules, markedly different from the diffusivity at solid surfaces. For the short alpha-helical peptide studied, both the free energy and the diffusivity associated with the conformational dynamics are found to critically depend on the type of co-solutes due to specific ion-peptide interactions.

Second, we establish refined methods to quantitatively analyze and predict the fluctuating signals in biophysical experiments and simulations. We model the signal processing in optical tweezer experiments and develop a Bayesian inference method for the auto- and cross-spectral analysis of the recorded time series, thereby establishing a new framework for the quantitative spectral analysis of single-molecule experiments. From a more fundamental perspective, we investigate the influence of nonlinearities in the equations of motion on the resulting fluctuations by expanding typical dynamic observables in powers of the thermal noise strength. The single-trajectory approach taken also enables us to derive a first-order correction to a recently introduced dynamic convolution theory.

Third, Brownian dynamics simulations and mean-field dynamic theory are used to study the viscoelastic properties of single semiflexible filaments and of crosslinked meshworks. Depending on the dynamic observable, we find a pronounced influence either of hydrodynamic interactions or of filament mechanical properties on the equilibrium fluctuations of single polymers. Based on the anisotropic force response of individual filaments, we finally resolve the rheological properties of extended, crosslinked semiflexible polymer networks using a generalized, two-dimensional dynamic convolution theory.

KURZFASSUNG

Stochastische Konzepte sind unentbehrlich zum Verständnis der fluktuierenden Dynamik von biologischen Systemen auf der Mikroskala. Die Entwicklung von Methoden, welche es erlauben, die physikalisch relevanten Informationen zuverlässig und effizient aus stochastischen Signalen zu extrahieren, stellt daher eine große Herausforderung in der aktuellen biophysikalischen Forschung dar. Gegenstand der vorliegenden Arbeit ist die theoretische Untersuchung der fluktuierenden Dynamik in verschiedenen Systemen.

Erstens werden die Diffusionsbewegung von Wassermolekülen und die Konformationsdynamik eines kurzen Peptids, basierend auf den Trajektorien atomistischer Simulationen, untersucht. Wir entdecken eine ausgeprägte Diffusionsanisotropie der Wassermoleküle im Bulk und ein bemerkenswert strukturiertes Diffusivitätsprofil für die Relativbewegung von Paaren von Wassermolekülen. In der Nähe von Lipidmembranen ist die Wasserdiffusion unterdrückt und unterscheidet sich aufgrund der Kopplung von Lipid- und Wassermolekülen deutlich von der Diffusivität an festen Oberflächen. Für das untersuchte alpha-helikale Peptid hängen aufgrund spezifischer Wechselwirkungen zwischen Ionen und Peptid sowohl die freie Energielandschaft als auch das zur Konformationsdynamik zugehörige Diffusivitätsprofil maßgeblich von der Art der Ionen ab.

Zweitens werden verbesserte Methoden zur quantitativen Analyse und Vorhersage der fluktuierenden Signale in biophysikalischen Experimenten und Simulationen entwickelt. Wir modellieren die Signalverarbeitung in Experimenten mit optischen Pinzetten und entwickeln ein Bayessches Inferenzverfahren für die Analyse von Selbst- und Kreuzspektren der aufgezeichneten Zeitreihen, was eine quantitative spektrale Auswertung von Einzelmolekülexperimenten ermöglicht. Der grundsätzliche Einfluss von Nichtlinearitäten in den Bewegungsgleichungen auf die resultierenden Fluktuationen wird untersucht, indem typische dynamische Observablen in Potenzen der thermischen Rauschintensität entwickelt werden. Die gewählte Einzeltrajektorienperspektive erlaubt zudem, eine Korrektur erster Ordnung für eine kürzlich eingeführte dynamische Konvolutionstheorie herzuleiten.

Drittens dienen Brownsche-Dynamik-Simulationen und eine dynamische Molekularfeldtheorie zur Untersuchung der viskoelastischen Eigenschaften einzelner sowie vernetzter semiflexibler Filamente. Wir stellen abhängig von der dynamischen Observablen einen ausgeprägten Einfluss hydrodynamischer Wechselwirkungen oder der mechanischen Eigenschaften der Filamente auf die Gleichgewichtsfluktuationen einzelner Polymere fest. Schließlich werden, basierend auf den anisotropen Antwortfunktionen einzelner Polymere, die rheologischen Eigenschaften von ausgedehnten Netzwerken semiflexibler Polymere unter Verwendung einer auf zwei Dimensionen verallgemeinerten dynamischen Konvolutionstheorie untersucht.

ERKLÄRUNG

Hiermit erkläre ich, dass ich die vorliegende Dissertationsschrift mit dem Titel

Stochastic Dynamics in Biomolecular Systems

selbständig angefertigt und hierfür keine anderen als die angegebenen Hilfsmittel verwendet habe. Die Arbeit ist weder in einem früheren Promotionsverfahren angenommen noch als ungenügend beurteilt worden.

Berlin, den 14. August 2013

Curriculum Vitae

For data protection reasons the curriculum is not included
in the online version of the thesis.

Aus Datenschutzgründen ist der Lebenslauf
in der Online-Version nicht enthalten.

DANKSAGUNG

Die vorliegende Arbeit ist in den Jahren 2009 bis 2013 am Physik-Department der Technischen Universität München und am Fachbereich Physik der Freien Universität Berlin entstanden. Ich möchte mich an dieser Stelle bei all denjenigen bedanken, die mich bei der Entstehung dieser Arbeit unterstützt und in diesem Lebensabschnitt begleitet haben.

Insbesondere meinem Betreuer Herrn Prof. Roland Netz möchte ich herzlich danken für das Anvertrauen interessanter Forschungsthemen, umfassende Freiheit in der Bearbeitung der Fragestellungen und die fortwährende freundliche Unterstützung. Eine stete Quelle der Inspiration und Motivation stellten die zahlreichen Diskussionen sowie die mir ermöglichten Konferenzbesuche und Forschungsaufenthalte im In- und Ausland dar: In besonderer Erinnerung werden dabei sicherlich die Reisen nach Venedig, Istanbul und Kalifornien bleiben. Nicht zuletzt sorgten die vielen gemeinsamen Lehrstuhlaktivitäten wie Winterschulen, Wandertage, Oktoberfestbesuche, Weihnachtsfeiern und Sommerfeste für eine durchweg angenehme Gruppenatmosphäre – vielen Dank dafür!

Herrn Prof. Sokolov möchte ich dafür danken, die Rolle als Zweitgutachter dieser Dissertation übernommen zu haben.

Für die teils langjährige Zusammenarbeit und die vielen aufschlussreiche Diskussionen möchte ich mich bedanken bei Joachim Dzubiella, Stephan Gekle, Michael Hinczewski, Immanuel Kalcher, Felix Sedlmeier und Sebastian Rode. Besonderer Dank gilt auch unseren experimentellen Kollegen, Herrn Prof. Matthias Rief sowie Alexander Mehlich und Benjamin Pelz.

Nicht unerwähnt bleiben dürfen auch die anderen Kollegen in München und Berlin, denen ich zahlreiche (nicht-)wissenschaftliche Diskussionen verdanke, allen voran Thomas Einert, Aykut Erbas, Emanuel Schneck, Dominik Horinek, Julian Kappler, Won Kyu Kim, Markus Miettinen, Matej Kanduč und Jan Daldrop. Ein besonderes Dankeschön gebührt auch unseren Sekretärinnen Sonja Ortner und Annette Schumann-Welde, welche bei der Bewältigung der Formalitäten stets eine große Hilfe waren. Beim Elitenetzwerk Bayern und Herrn Prof. Andreas Bausch bedanke ich mich für die großzügige Förderung im Rahmen des Graduiertenkollegs *Materials Science of Complex Interfaces*, bei der DFG für finanzielle Unterstützung im Rahmen des SFB 863 und beim Leibniz-Rechenzentrum für Rechenzeit auf dem HLRB II und dem Linux-Cluster.

Meinen Eltern, meiner Schwester Nadège und meiner Freundin Kathrin möchte ich für ihre stete Unterstützung in allen Belangen und für ihren Rückhalt während der gesamten Studien- und Promotionszeit danken.